

# THE QCD, EW, AND HIGGS WORKING GROUP: Summary Report

*Convenors:* C. Buttar<sup>1</sup>, S. Dittmaier<sup>2</sup>, V. Drollinger<sup>3</sup>, S. Frixione<sup>4</sup>, A. Nikitenko<sup>5</sup>, S. Willenbrock<sup>6</sup>  
*Contributing authors:* S. Abdullin<sup>7</sup>, E. Accomando<sup>8,9</sup>, D. Acosta<sup>10</sup>, A. Arbuzov<sup>70</sup>, R.D. Ball<sup>11</sup>,  
 A. Ballestrero<sup>8,9</sup>, P. Bartalini<sup>10</sup>, U. Baur<sup>66</sup>, A. Belhouari<sup>8,9</sup>, S. Belov<sup>12</sup>, A. Belyaev<sup>13</sup>, D. Benedetti<sup>50,54</sup>,  
 T. Binoth<sup>11,64</sup>, S. Bolognesi<sup>8,14</sup>, S. Bondarenko<sup>67</sup>, E.E. Boos<sup>15</sup>, F. Boudjema<sup>58</sup>, A. Bredenstein<sup>2</sup>,  
 V.E. Bunichev<sup>15</sup>, C. Buttar<sup>1</sup>, J.M. Campbell<sup>16</sup>, C. Carloni Calame<sup>44,45</sup>, S. Catani<sup>17,18</sup>, R. Cavanaugh<sup>10</sup>,  
 M. Ciccolini<sup>23</sup>, J. Collins<sup>19</sup>, A.M. Cooper-Sarkar<sup>20</sup>, G. Corcella<sup>21</sup>, S. Cucciarelli<sup>16</sup>, G. Davatz<sup>22</sup>,  
 V. Del Duca<sup>8</sup>, A. Denner<sup>23</sup>, J. D'Hondt<sup>56</sup>, S. Dittmaier<sup>2</sup>, V. Drollinger<sup>3</sup>, A. Drozdetskiy<sup>10</sup>, L.V. Dudko<sup>15</sup>,  
 M. Dührssen<sup>68</sup>, R. Frazier<sup>24</sup>, S. Frixione<sup>4</sup>, J. Fujimoto<sup>59</sup>, S. Gascon-Shotkin<sup>25</sup>, T. Gehrmann<sup>26</sup>,  
 A. Gehrmann-De Ridder<sup>26</sup>, A. Giammanco<sup>62,63</sup>, A.-S. Giolo-Nicollerat<sup>16</sup>, E.W.N. Glover<sup>65</sup>,  
 R.M. Godbole<sup>27</sup>, A. Grau<sup>28</sup>, M. Grazzini<sup>17,18</sup>, J.-Ph. Guillet<sup>58</sup>, A. Gusev<sup>29</sup>, R. Harlander<sup>30</sup>, R. Hegde<sup>27</sup>,  
 G. Heinrich<sup>26</sup>, J. Heyninck<sup>56</sup>, J. Huston<sup>13</sup>, T. Ishikawa<sup>59</sup>, A. Kalinowski<sup>31</sup>, T. Kaneko<sup>59</sup>, K. Kato<sup>60</sup>,  
 N. Kauer<sup>64</sup>, W. Kilgore<sup>32</sup>, M. Kirsanov<sup>69</sup>, A. Korytov<sup>10</sup>, M. Krämer<sup>33</sup>, A. Kulesza<sup>30</sup>, Y. Kurihara<sup>59</sup>,  
 S. Lehti<sup>34</sup>, L. Magnea<sup>8,9</sup>, F. Mahmoudi<sup>35</sup>, E. Maina<sup>8,9</sup>, F. Maltoni<sup>36</sup>, C. Mariotti<sup>8</sup>, B. Mellado<sup>37</sup>,  
 D. Mercier<sup>25</sup>, G. Mitselmakher<sup>10</sup>, G. Montagna<sup>44,45</sup>, A. Moraes<sup>1</sup>, M. Moretti<sup>38,53</sup>, S. Moretti<sup>39</sup>,  
 I. Nakano<sup>40</sup>, P. Nason<sup>41</sup>, O. Nicrosini<sup>44,45</sup>, A. Nikitenko<sup>5</sup>, M.R. Nolten<sup>39</sup>, F. Olness<sup>42</sup>, Yu. Pakhotin<sup>10</sup>,  
 G. Pancheri<sup>43</sup>, F. Piccinini<sup>44,45</sup>, E. Pilon<sup>58</sup>, R. Pittau<sup>8,9</sup>, S. Pozzorini<sup>2</sup>, J. Pumplin<sup>13</sup>, W. Quayle<sup>37</sup>,  
 D.A. Ross<sup>39</sup>, R. Sadykov<sup>71</sup>, M. Sandhoff<sup>46</sup>, V.I. Savrin<sup>15</sup>, A. Schmidt<sup>57</sup>, M. Schulze<sup>30</sup>, S. Schumann<sup>47</sup>,  
 B. Scurlock<sup>10</sup>, A. Sherstnev<sup>15</sup>, P. Skands<sup>7</sup>, G. Somogyi<sup>48,55</sup>, J. Smith<sup>49</sup>, M. Spira<sup>23</sup>, Y. Srivastava<sup>50,54</sup>,  
 H. Stenzel<sup>51</sup>, Y. Sumino<sup>52</sup>, R. Tanaka<sup>40</sup>, Z. Trócsányi<sup>48,55</sup>, S. Tsuno<sup>40</sup>, A. Vicini<sup>41,72</sup>, D. Wackerath<sup>66</sup>,  
 M.M. Weber<sup>46</sup>, C. Weiser<sup>57,61</sup>, S. Willenbrock<sup>6</sup>, S.L. Wu<sup>37</sup>, M. Zanetti<sup>3</sup>

<sup>1</sup> Department of Physics and Astronomy University of Glasgow, G12 8QQ, Glasgow, UK

<sup>2</sup> Max-Planck-Institut für Physik (Werner-Heisenberg-Institut), D-80805 München, Germany

<sup>3</sup> Dipartimento di Fisica "Galileo Galilei", Università di Padova, Padova, Italy

<sup>4</sup> INFN, Sezione di Genova, Genoa, Italy

<sup>5</sup> Imperial College, London, UK

<sup>6</sup> Department of Physics, University of Illinois at Urbana-Champaign, IL, USA

<sup>7</sup> Fermi National Accelerator Laboratory, Batavia, IL-60510, USA

<sup>8</sup> INFN, Sezione di Torino, Turin, Italy

<sup>9</sup> Dipartimento di Fisica Teorica, Università di Torino, Turin, Italy

<sup>10</sup> University of Florida, Gainesville, FL, USA

<sup>11</sup> School of Physics, University of Edinburgh, Edinburgh EH9 3JZ, Scotland, UK

<sup>12</sup> Joint Institute for Nuclear Research, Joliot-Curie 6 Dubna, Moscow region, Russia, 141980

<sup>13</sup> Michigan State University, East Lansing, MI, USA

<sup>14</sup> Dipartimento di Fisica Sperimentale, Università di Torino, Turin, Italy

<sup>15</sup> Scobeltsyn Institute of Nuclear Physics of Lomonosov Moscow State University, Moscow, Russia, 119992

<sup>16</sup> CERN, Geneva, Switzerland

<sup>17</sup> INFN, Sezione di Firenze, Florence, Italy

<sup>18</sup> Dipartimento di Fisica, Università di Firenze, Sesto Fiorentino, Florence, Italy

<sup>19</sup> Penn State University, University Park, PA, USA

<sup>20</sup> Particle Physics, Oxford University, Oxford, OX1 3RH, UK

<sup>21</sup> Dipartimento di Fisica, Università degli Studi di Roma 'La Sapienza', Rome, Italy

<sup>22</sup> Institute for Particle Physics, ETH Zürich, Switzerland

<sup>23</sup> Paul Scherrer Institut, CH-5232 Villigen PSI, Switzerland

<sup>24</sup> H. H. Wills Physics Laboratory, University of Bristol, United Kingdom

<sup>25</sup> Institut de Physique Nucléaire de Lyon/Université Claude Bernard Lyon I, Villeurbanne, France

<sup>26</sup> Institut für Theoretische Physik, Universität Zürich, CH-8057 Zürich, Switzerland

<sup>27</sup> Centre for High Energy Physics, Indian Institute of Science, Bangalore, 560012, India

<sup>28</sup> Departamento de Física Teórica y del Cosmos, Universidad de Granada, Spain

<sup>29</sup> Institute For High Energy Physics, Protvino, Russia

- <sup>30</sup> Institut für Theoretische Teilchenphysik, Universität Karlsruhe, D-76128 Karlsruhe, Germany
- <sup>31</sup> Institute of Experimental Physics, Warsaw University, Poland
- <sup>32</sup> Brookhaven National Laboratory, Upton, NY, USA
- <sup>33</sup> Institut für Theoretische Physik E, EWTW Aachen, Germany
- <sup>34</sup> Helsinki Institute of Physics, 00014 University of Helsinki, Finland
- <sup>35</sup> Physics Department, Mount Allison University, Sackville NB, E4L 1E6 Canada
- <sup>36</sup> Institut de Physique Théorique, Université Catholique de Louvain, Belgium
- <sup>37</sup> University of Wisconsin - Madison, Department of Physics, Madison, WI, USA
- <sup>38</sup> Department of Physics, Ferrara University, Ferrara, Italy
- <sup>39</sup> School of Physics and Astronomy, University of Southampton, Highfield, Southampton SO17 1BJ, UK
- <sup>40</sup> Department of Physics, Okayama University, Okayama, 700-8530, Japan
- <sup>41</sup> INFN, Sezione di Milano, Milan, Italy
- <sup>42</sup> Southern Methodist University, Dallas, TX, USA
- <sup>43</sup> INFN, Laboratori Nazionali di Frascati, Frascati, Italy
- <sup>44</sup> INFN, Sezione di Pavia, Pavia, Italy
- <sup>45</sup> Dipartimento di Fisica Nucleare e Teorica, Università di Pavia, Pavia, Italy
- <sup>46</sup> Bergische Universität Wuppertal, Fachgruppe Physik, 42097 Wuppertal, Germany
- <sup>47</sup> Institute for Theoretical Physics, University of Dresden, Germany
- <sup>48</sup> Institute of Nuclear Research of the Hungarian Academy of Sciences, H-4001 Debrecen, Hungary
- <sup>49</sup> C. N. Yang Institute for Theoretical Physics, SUNY Stony Brook, USA
- <sup>50</sup> Physics Department, University of Perugia, Perugia, Italy
- <sup>51</sup> Justus-Liebig Universität, Giessen, Germany
- <sup>52</sup> Department of Physics, Tohoku University, Sendai, 980-8578, Japan
- <sup>53</sup> INFN, Sezione di Ferrara, Ferrara, Italy
- <sup>54</sup> INFN, Sezione di Perugia, Perugia, Italy
- <sup>55</sup> University of Debrecen, H-4001 Debrecen, Hungary
- <sup>56</sup> Inter-University Institute for High Energies (IIHE), Brussels, Belgium
- <sup>57</sup> Institut für Experimentelle Kernphysik, Universität Karlsruhe, D-76128 Karlsruhe, Germany
- <sup>58</sup> LAPTH CNRS, B.P.110, Annecy-le-Vieux F-74941, France
- <sup>59</sup> KEK, Oho 1-1, Tsukuba, Ibaraki 305-0801, Japan
- <sup>60</sup> Kogakuin University, Nishi-Shinjuku 1-24, Shinjuku, Tokyo 163-8677, Japan
- <sup>61</sup> Physikalisches Institut, Universität Freiburg, D-79104 Freiburg, Germany
- <sup>62</sup> INFN, Sezione di Pisa, Pisa, Italy
- <sup>63</sup> Université Catholique de Louvain, Belgium
- <sup>64</sup> Institut für Theoretische Physik und Astrophysik, Universität Würzburg, D-97074 Würzburg, Germany
- <sup>65</sup> Department of Physics, University of Durham, Durham DH1 3LE, UK
- <sup>66</sup> Dept. of Physics, State University of New York, Buffalo, NY 14260, USA
- <sup>67</sup> II Institute for Theoretical Physics, University of Hamburg, Germany
- <sup>68</sup> Institut für Physik, Albert-Ludwigs Universität Freiburg, Hermann-Herder-Str. 3, 79104, Freiburg, Germany
- <sup>69</sup> INR, Moscow 117312, Russia
- <sup>70</sup> Bogoliubov Laboratory of Theoretical Physics, JINR, Dubna, 141980 Russia
- <sup>71</sup> Dzhelapov Laboratory of Nuclear Physics, JINR, Dubna, 141980 Russia
- <sup>72</sup> Dipartimento di Fisica, Università degli Studi di Milano, Italy

*Report of the Working Group on Quantum Chromodynamics, Electroweak, and Higgs Physics for the Workshop "Physics at TeV Colliders", Les Houches, France, 2–20 May, 2005.*

## Contents

<b>1. Foreword</b>	<b>4</b>
<b>I STANDARD MODEL BENCHMARKS AND BACKGROUNDS</b>	<b>5</b>
2. Model predictions for $\sigma^{\text{tot}}$ at the LHC	5
3. Tuning models for minimum bias and the underlying event	11
4. Small $x$	17
5. Parton-parton luminosity functions for the LHC	34
6. A simple model for large- $x$ resummed parton distributions	40
7. Bottom-quark fragmentation: from $e^+e^-$ data to top and Higgs decays	43
8. Study of jet clustering algorithms at the LHC	48
9. Colour annealing — a toy model of colour reconnections	55
10. Tuned comparison of electroweak corrections to Drell–Yan-like $W^-$ and $Z$ -boson production – a status report	61
11. Electroweak corrections to large transverse momentum production of $Z$ bosons and photons at the LHC	67
12. Impact of weak corrections on LHC jet cross sections	72
13. Search for anomalous couplings in top decay at hadron colliders	74
14. Effective NLO approach in the model of single top quark production	82
15. Progress in $W^+W^-$ production at the LHC	85
16. Top background generation for the $H \rightarrow WW$ channel	101
17. Estimation of $t\bar{t}$ background for $H \rightarrow WW$ channel	106
18. Single resonant top production as background to the $H \rightarrow WW$ search	110
19. Study of PDF and QCD scale uncertainties in $pp \rightarrow ZZ \rightarrow 4\mu$ events at the LHC	113
20. Relative contributions of $t$ - and $s$ -channels to the $ZZ \rightarrow 4\mu$ process	117
21. Sensitivity of the muon isolation cut efficiency to the underlying event uncertainties	121
<b>II HIGGS PHYSICS</b>	<b>126</b>

<b>22. <math>gg \rightarrow H</math> at the LHC: uncertainty due to a jet veto</b>	<b>127</b>
<b>23. Comparison between MCFM and PYTHIA for the <math>gb \rightarrow bh</math> and <math>gg \rightarrow bbh</math> processes at the LHC</b>	<b>132</b>
<b>24. Higgs production in association with bottom quarks</b>	<b>137</b>
<b>25. Associated <math>t\bar{t}H</math> production with <math>H \rightarrow \gamma\gamma</math> at the LHC</b>	<b>144</b>
<b>26. Study of <math>bbZ</math> as a benchmark for MSSM <math>bbH</math></b>	<b>151</b>
<b>27. Data-driven background determination in the channel <math>H \rightarrow WW \rightarrow l\nu l\nu</math> with no hard jets</b>	<b>156</b>
<b>28. Electroweak corrections to the Higgs decays <math>H \rightarrow ZZ/WW \rightarrow 4</math> leptons</b>	<b>160</b>
<b>29. Boson boson scattering at the LHC with PHASE</b>	<b>165</b>
<b>III NLO AND NNLO QCD COMPUTATIONS</b>	<b>169</b>
<b>30. NLO predictions for many-particle production</b>	<b>169</b>
<b>31. One loop gluon initiated corrections in DIPHOX</b>	<b>178</b>
<b>32. The architecture of NNLO cross sections</b>	<b>184</b>
<b>IV MONTE CARLO ISSUES</b>	<b>196</b>
<b>33. On reweighting techniques</b>	<b>196</b>
<b>34. LCG MCDB — database of Monte-Carlo simulated events</b>	<b>200</b>
<b>35. Supporting Monte Carlo generators at the LHC</b>	<b>204</b>

## 1. FOREWORD

The primary goal of the LHC will be that of finding evidence or hints of physics whose signals have not been detected yet by collider experiments. This includes any physics beyond that so successfully described by the Standard Model, but also that relevant to the only sector of the Standard Model which has not been probed directly so far, namely the Higgs sector. The signatures of new physics are vastly diverse, but in the majority of the cases they imply chain decays of massive particles, which in turn will appear in detectors as many-jet events. Although a good understanding of the continuum many-jet QCD production will be needed in order to disentangle such signals from the background, we may consider this situation as a favourable one, since the discovery of new physics will be relatively quick and independent of theoretical assumptions (a much more difficult problem will then be that of understanding which kind of underlying theory is responsible for the signals detected). An even easier case will be that of a very heavy neutral vector boson, whose dilepton decay should be basically background-free. On the other hand, the detection of a Standard Model Higgs will be a pretty complicated affair, since the signal is overwhelmed by huge QCD backgrounds, whose good control is therefore mandatory in order to claim a discovery.

In all cases, the reliability of the outcomes of LHC experiments will depend on their capability of reproducing, and improving, what we know about the Standard Model and QCD, through the studies of a few benchmark processes, the “standard candles”, such as  $W$ ,  $Z$ , and  $t\bar{t}$  production.

The aim of the SM and Higgs Working Group in Les Houches has therefore been twofold. On one hand, we performed a variety of experimental and theoretical studies on standard candles, treating them either as proper signals of known physics, or as backgrounds to unknown physics; we also addressed issues relevant to those non-perturbative or semi-perturbative ingredients, such as Parton Density Functions and Underlying Events, whose understanding will be crucial for a proper simulation of the actual events taking place in the detectors. On the other hand, several channels for the production of the Higgs, or involving the Higgs, have been considered in some details.

This report is organized into four main parts. The first one deals with Standard Model physics, except the Higgs. A variety of arguments are treated here, from full simulation of processes constituting a background to Higgs production, to studies of uncertainties due to PDFs and to extrapolations of models for underlying events, from small- $x$  issues to electroweak corrections which may play a role in vector boson physics. The second part of the report treats Higgs physics from the point of view of the signal. In the third part, reviews are presented on the current status of multi-leg, next-to-leading order and of next-to-next-to-leading order QCD computations. Finally, the fourth part deals with the use of Monte Carlo for simulation of LHC physics.

## Part I

# STANDARD MODEL BENCHMARKS AND BACKGROUNDS

## 2. MODEL PREDICTIONS FOR $\sigma^{\text{tot}}$ AT THE LHC <sup>1</sup>

### 2.1 Introduction

Energy dependence of total hadronic cross-sections has been the focus of intense theoretical interest as a sensitive probe of strong interactions long before the establishment of QCD as “the” theory of hadrons. Even now, notwithstanding creditable successes of perturbative and lattice QCD, alas a first principle description of total/elastic and inelastic hadronic cross-section is unavailable. More pragmatically, for a correct projection of the expected underlying activity at LHC, a reliable prediction of total non-diffractive cross-section is essential to ensure the extraction of new physics from the LHC data. Surely we will have to depend -at the initial stages of LHC- upon predictions based on our current understanding of these matters. Only much later it may become feasible to use the LHC data itself towards this goal. Hence, a critical evaluation of the range of theoretical predictions is absolutely essential.

The hadronic cross-section data exhibit, and require explanation of, three basic features:

- (i) the normalization of the cross section,
- (ii) an initial decrease and
- (iii) a subsequent rise with energy

Various theoretical models exist which are motivated by our theoretical understanding of the strong interactions. The parameters in these models, in most cases, are fitted to explain the observed low-energy data and the model predictions are then extrapolated to give the  $\sigma_{\text{tot}}^{\text{pp}}$  at the LHC energies. There are different classes of models. The highly successful Donnachie-Landschoff parameterisation [1] of the form

$$\sigma_{\text{tot}}(s) = X s^\epsilon + Y s^{-\eta}, \tag{1}$$

---

<sup>1</sup>Contributed by: R.M. Godbole, A. Grau, R. Hegde, G. Pancheri, Y. Srivastava

has been used for a very long time. Here the two terms are understood as arising from the Regge and the Pomeron trajectories, the  $\epsilon$  being approximately close to zero and  $\eta$  being close to 0.5. These values seem to be consistent with a large, but not all, body of the hadronic cross-sections. In this note we will first present phenomenological arguments for the approximate values of these parameters which seem to be required to describe the data satisfactorily. As a matter of fact, there also exist in the literature discussions of the ‘hard’ pomeron [2] motivated by the discrepancies in the rate of energy rise observed by E710 [3], E811 [4] and the CDF [5]. In addition, a variety of models exist wherein the observed energy dependence of the cross-section, along with few very general requirements of factorisation, unitarity and/or ideas of Finite Energy Sum Rules (FESR), is used to determine the values of model parameters [6–11]. The so-obtained parameterisations are then extended to make predictions at the LHC energies. There also exist QCD-motivated models based on the mini-jet formalism [12–14], wherein the energy rise of the total cross-sections is driven by the increasing number of the low- $x$  gluon-gluon collisions. These models need to be embedded in an eikonal formalism [15] to soften the violent energy rise of the mini-jet cross-sections. Even after eikonalisation the predicted energy rise is harder than the gentle one observed experimentally [14, 16]. A QCD-based model where the rise is further tamed by the phenomenon of increasing emission of soft gluons by the valence quarks in the colliding hadrons, with increasing energy [17, 18], offers a consistent description of  $\sigma_{\text{tot}}^{\text{PP}}$ . Thus we have a variety of model predictions for  $\sigma_{\text{tot}}^{\text{PP}}$  at the LHC. In this note we compare these predictions with each other in order to obtain an estimate of the “theoretical” uncertainty on them.

## 2.2 Phenomenological models

The two terms of eq. (1) [1] reflect the well known duality between resonance and Regge pole exchange on the one hand and background and Pomeron exchange on the other, established in the late 60’s through FESR [19]. This correspondence meant that, while at low energy the cross-section could be written as due to a background term and a sum of resonances, at higher energy it could be written as a sum of Regge trajectory exchanges and a Pomeron exchange.

Our present knowledge of QCD and its employment for a description of hadronic phenomena can be used to provide some insight into the “two component” structure of the eq. (1). This begins with considerations about the bound state nature of hadrons which necessarily transcends perturbative QCD. For hadrons made of light quarks ( $q$ ) and gluons ( $g$ ), the two terms arise from  $q\bar{q}$  and  $gg$  excitations. For these, the energy is given by a sum of three terms: (i) the rotational energy, (ii) the Coulomb energy and (iii) the “confining” energy. If we accept the Wilson area conjecture in QCD, (iii) reduces to the linear potential [20, 21]. Then the hadronic rest mass for a state of angular momentum  $J$  can be obtained by minimising the expression for the energy of two massless particles ( $q\bar{q}$  or  $gg$ ) separated by a distance  $r$ . This can then be used to obtain the two sets of linear Regge trajectories  $\alpha_i(s)$

$$\alpha_i(s) = \frac{C_i \bar{\alpha}}{2} + \left(\frac{1}{8C_i \tau}\right)s = \alpha_i(0) + \alpha'_i s. \quad (2)$$

where  $i = 1$  refers to  $q\bar{q}$ ,  $i = 2$  refers to  $gg$ ,  $\tau$  is the “string tension” and the Casimir’s are  $C_1 = C_F = 4/3$ ,  $C_2 = C_G = 3$ .  $\bar{\alpha}$  is the QCD coupling constant evaluated at some average value of  $r$ . Note that  $\alpha_i$  are *not* the coupling constants. Employing our present understanding that resonances are  $q\bar{q}$  bound states while the background, dual to the Pomeron, is provided by gluon-gluon exchanges [21], the above equation can be rewritten as

$$\frac{\alpha_P(0)}{\alpha_R(0)} = C_G/C_F = \frac{9}{4}. \quad (3)$$

If we restrict our attention to the leading Regge trajectory, namely the degenerate  $\rho - \omega - \phi$  trajectory, then  $\alpha_R(0) = \eta \approx 0.48 - 0.5$ , and we obtain for  $\epsilon \approx 0.08 - 0.12$ , a rather satisfactory value. The



same argument for the slopes gives

$$\frac{\alpha'_{gg}}{\alpha'_{q\bar{q}}} = C_F/C_G = \frac{4}{9}. \quad (4)$$

so that if we take for the Regge slope  $\alpha'_R \approx 0.88 - 0.90$ , we get for  $\alpha'_P \approx 0.39 - 0.40$ , in fair agreement with lattice estimates [22].

We now have good reasons for a break up of the amplitude into two components. To proceed further, it is necessary to realize that precisely because massless hadrons do not exist, eq. (1) violates the Froissart bound and thus must be unitarized. To begin this task, let us first rewrite eq. (1) by putting in the ‘‘correct’’ dimensions

$$\bar{\sigma}_{tot}(s) = \sigma_1(s/\bar{s})^\epsilon + \sigma_2(\bar{s}/s)^{1/2}, \quad (5)$$

where we have imposed the nominal value  $\eta = 1/2$ . It is possible further, to obtain [18] rough estimates for the size of the parameters in eq. (5). A minimum occurs in  $\bar{\sigma}_{tot}(s)$  at  $s = \bar{s}$ , for  $\sigma_2 = 2\epsilon\sigma_1$ . If we make this choice, then eq. (5) becomes

$$\bar{\sigma}_{tot}(s) = \sigma_1[1 + 2\epsilon(\bar{s}/s)^{1/2}] + \sigma_1[(s/\bar{s})^\epsilon - 1]. \quad (6)$$

eq. (6) separates cleanly the cross-section into two parts: the first part is a ‘‘soft’’ piece which shows a saturation to a constant value (but which contains no rise) and the second a ‘‘hard’’ piece which has all the rise. In the eikonalised mini-jet model used by us [18] the rising part of the cross-section  $\sigma_{hard}$  is provided by jets which are calculable in perturbative QCD, obviating (at least in principle) the need of an arbitrary parameter  $\epsilon$ . An estimate of  $\sigma_1$  can also be obtained [18] and is  $\sim 40$  mb.

As said earlier, the DL parameterisation [1] is a fit to the existing data of the form given by eq. (1), with  $\epsilon = 0.0808$ ,  $\eta = 0.4525$ . This fit has been extended to include a ‘hard’ pomeron [2] due to the discrepancy between different data sets. The BH model [6] gives a fit to the data using duality constraints. The BH fit for  $\sigma^\pm = \sigma^{\bar{p}p}/\sigma^{pp}$  as a function of beam energy  $\nu$ , is given as,

$$\sigma^\pm = c_0 + c_1 \ln(\nu/m) + c_2 \ln^2(\nu/m) + \beta_{P'}(\nu/m)^{\mu-1} \pm \delta(\nu/m)^{\alpha-1},$$

where  $\mu = 0.5$ ,  $\alpha = 0.415$  and all the other parameters in mb are  $c_0 = 37.32$ ,  $c_1 = -1.440 \pm 0.07$ ,  $c_2 = 0.2817 \pm 0.0064$ ,  $\beta_{P'} = 37.10$ ,  $\delta = -28.56$ . The fit obtained by Igi et al [8] using the finite energy sum rules (FESR) gives LHC predictions very similar to those given by the BH fit. Avila et al. give a fit [9] using analyticity arguments whereas Cudell et al [10] give predictions at the LHC energies by extrapolating fits obtained to the current data using again constraints from unitarity, analyticity of the S-matrix, factorisation, coupled with a requirement that the cross-section asymptotically goes to a constant plus a  $\ln s$  or  $\ln^2 s$  term, in the framework of the COMPETE program.

In the mini-jet models the energy rise of  $\sigma_{tot}^{pp}$  is driven by the increase with energy of the  $\sigma_{jet}^{ab}$  given by

$$\sigma_{jet}^{ab}(s) = \int_{p_{tmin}}^{\sqrt{s}/2} dp_t \int_{4p_t^2/s}^1 dx_1 \int_{4p_t^2/(x_1s)}^1 dx_2 \sum_{i,j,k,l} f_{i|a}(x_1) f_{j|b}(x_2) \frac{d\hat{\sigma}_{ij \rightarrow kl}(\hat{s})}{dp_t}, \quad (7)$$

where subscripts  $a$  and  $b$  denote particles ( $\gamma, p, \dots$ ),  $i, j, k, l$  are partons and  $x_1, x_2$  the fractions of the parent particle momentum carried by the parton.  $\hat{s} = x_1 x_2 s$  and  $\hat{\sigma}$  are hard partonic scattering cross-sections. As said before, the rise with energy of this cross-section is too steep, and hence it has to be imbedded in an eikonal formulation given by,

$$\sigma_{tot}^{ab} = 2 \int d^2\vec{b} [1 - e^{-2\Im\chi(b,s)}] \quad (8)$$

where  $2\Im\chi(b,s) = n(b,s)$  is the average number of multiple collisions which are Poisson distributed. As outlined in eq. (6) this quantity too has contributions coming from soft and hard physics and can be written as

$$n(b,s) = n_{soft} + n_{hard} \simeq A_{soft}(b)\sigma_{soft}(s) + A_{jet}(b)\sigma_{jet}(s). \quad (9)$$

In the second step the number  $n(b, s)$  has been assumed to be factorizable into an overlap function  $A(b)$  and the cross-section  $\sigma$ . The assumption of factorisation as well as the split up between the two contributions, hard and soft, are only approximate. The extent to which this softens the energy rise, depends on the  $b$  dependence of  $n(b, s)$ , i.e., that of  $A(b)$  in the factorised case. The normal assumption of using the same form of  $A(b)$  for both the hard and the soft part, given by the Fourier transform of the electromagnetic Form Factor (FF), still gives too steep a rise even in this Eikonalised Mini-jet Model (EMM) [15]. In our model this rise is tamed by including the effect on the transverse momentum distribution of the partons in the proton, of the soft gluon emission from the valence quarks in the proton [17]; the effect increases with increasing energy. The non-perturbative soft part of the eikonal includes only limited low-energy gluon emission and leads to the initial decrease in the proton-proton cross-section. On the other hand, the rapid rise in the hard, perturbative jet part of the eikonal is tamed into the experimentally observed mild increase by soft gluon radiation whose maximum energy ( $q_{max}$ ) rises slowly with energy. Thus the overlap functions  $A(b)$  are no longer a function of  $b$  alone. We denote the corresponding overlap function by  $A_{BN}(b, q_{max})$  [17] determined by  $q_{max}$ , which depends on the energy and the kinematics of the subprocess. What we use is an average value over all the momentum fractions of the parent partons. We need to further make a model for the 'soft' part which is determined by the nonperturbative dynamics. It is this part of the eikonal that contributes to the  $\sigma_{tot}^{pp}$  at high energies, the turn around from the decreasing Regge behaviour to the softly rising behaviour around  $\sqrt{s} \simeq 15$  GeV, where the hard part contribution is miniscule. We have further postulated that the  $q_{max}$  is the same for the hard and soft processes at low energy, parting company around 10 GeV where the hard processes start becoming important. A good fit to the data requires that  $q_{max}$  at low energies to be a very slowly increasing function of energy, with a value around 0.20 MeV at  $\sqrt{s} = 5$  GeV rising to about 0.24 MeV,  $\sqrt{s} \geq 10$  GeV, the upper value of this soft scale being completely consistent with our picture of the proton. Further, we need to fix one more parameter for nonperturbative region, the  $\sigma_{soft}$ . For the  $pp$  case it is a constant  $\sigma_0$  which will fix the normalization of  $\sigma_{tot}^{pp}$ , whereas for the  $p\bar{p}$  case the duality arguments suggest that there be an additional  $\sqrt{s}$ -dependent piece  $\simeq 1/\sqrt{s}$ . Thus neglecting the real part of the eikonal,  $n(b, s)$  in our model is given by

$$n(b, s) = A_{BN}(b, q_{max}^{soft})\sigma_{soft}^{pp,\bar{p}} + A_{BN}(b, q_{max}^{jet})\sigma_{jet}(s; p_{tmin}), \quad (10)$$

where

$$\sigma_{soft}^{pp} = \sigma_0, \quad \sigma_{soft}^{p\bar{p}} = \sigma_0\left(1 + \frac{2}{\sqrt{s}}\right) \quad (11)$$

Thus the parameters of the model are  $p_{tmin}$  and  $\sigma_0$ . In addition, the evaluation of  $A_{BN}$  involves the  $\alpha_s$  in the infrared region, for which we use a phenomenological form inspired by the Richardson Potential [17]. This involves a parameter  $p$  which for the Richardson Potential takes value 1. Values of  $p_{tmin}$ ,  $\sigma_0$  and  $p$  which give a good fit to the data with the GRV parameterisation of the proton densities [23] are 1.15 GeV, 48 mb and 3/4 respectively, as presented in Ref. [18]. These values are consistent with the expectations of the general argument [18]. We expect these best fit values to change somewhat with the choice of parton density functions (PDF). Since we are ultimately interested in the predictions of the model at TeV energies, we need PDF parameterisations which cover a  $Q^2$  range between 2 and  $10^4$  GeV<sup>2</sup>, as well as are valid up to rather small values of  $x$  ( $\sim 10^{-5}$ ). Further, since our calculation here is only LO, for consistency we have to use LO densities. We have repeated the exercise then for a range of PDF's [24–26] meeting these requirements. We find that it is possible to get a satisfactory description of all the current data, for all the choices of PDF's considered. The corresponding range of values of  $p_{tmin}$ ,  $\sigma_0$  and  $p$  are given in Table 1. The predictions of this modified EMM model span a range which are presented and discussed in the next section.

### 2.3 Model predictions for $\sigma_{tot}^{pp}$ at the LHC

Figure 1 summarises the predictions of the different models described in the previous section. The shaded area gives the range of predictions in the Eikonalised mini-jet model with soft gluon resummation [18]



Table 1: Values of  $p_{tmin}$  and  $\sigma_0$  corresponding to the different parton densities in the proton, for which the EMM (as described in Ref. [18]) gives a satisfactory description of  $\sigma_{tot}^{pp}$ .

PDF	$p_{tmin}$ (GeV)	$\sigma_0$ (mb)	p
GRV [23]	1.15	48	0.75
GRV94lo [24]	1.10	46	0.72
	1.10	51	0.78
GRV98lo [25]	1.10	45	0.70
	1.10	50	0.77
MRST [26]	1.25	47.5	0.74
	1.25	44	0.66

Table 2: Values of  $a_0, a_1, a_2, a_3$  and  $b$  parton densities in the proton, for which the EMM (as described in Ref. [18]) gives a satisfactory description of  $\sigma_{tot}^{pp}$ .

	$a_0$ (mb)	$a_1$ (mb)	b	$a_2$ (mb)	$a_3$ (mb)
Top edge	23.61	54.62	-0.52	1.15	.17
Center	-139.80	193.89	-0.11	13.98	-.14
Lower edge	-68.73	125.80	-0.16	11.05	-.16

(the G.G.P.S. model), the different PDF's used giving the range as described in the earlier section. The solid line gives prediction obtained using the GRV parton densities [23] in the model. The long-dashed dotted curve ( $d$ ), indicates the predictions of the DL fit [1]. The dotted (BH) curve ( $c$ ) and the uppermost dashed curve ( $a$ ), are the results of two analytical models incorporating constraints from unitarity and analyticity, from [6] and [9], respectively. The prediction obtained by Igi et al using FESR follows very closely that given by the BH curve. Furthermore, the short-dash dotted curve ( $b$ ) is the result of a fit by the COMPETE collaboration [10]. The parameterisation for the DL curve and BH curve is already given in the last section. It is gratifying to see that the range of results of our QCD motivated minijet models for the LHC span the other predictions based on models using unitarity, factorisation, analyticity fitting the current data. Thus the predictions seem consistent with each other.

In case of the EMM model results we have parameterised them with a  $\ln^2 s$  fit. We found that in most cases this gave a better representation of our results than a fit of the Regge-Pomeron type of the form of eq. (1). The top edge of the EMM model prediction is obtained for the MRST parameterisation whereas the lower edge for the GRV98lo. We give fits to our results for  $\sigma^{pp}$  of the form,

$$\sigma_{tot}^{pp} = a_0 + a_1 s^b + a_2 \ln(s) + a_3 \ln^2(s). \quad (12)$$

## 2.4 Conclusions

We thus see that the range of the results for the  $\sigma_{tot}^{pp}$  from our QCD motivated EMM model [18] spans the range of predictions made using the current data and general arguments of unitarity and/or factorization. Furthermore, we give  $\ln^2(s)$  parameterisation of the model results for  $\sigma_{tot}^{pp}$  which may be used in evaluating the range of the predictions for the underlying event at the LHC.

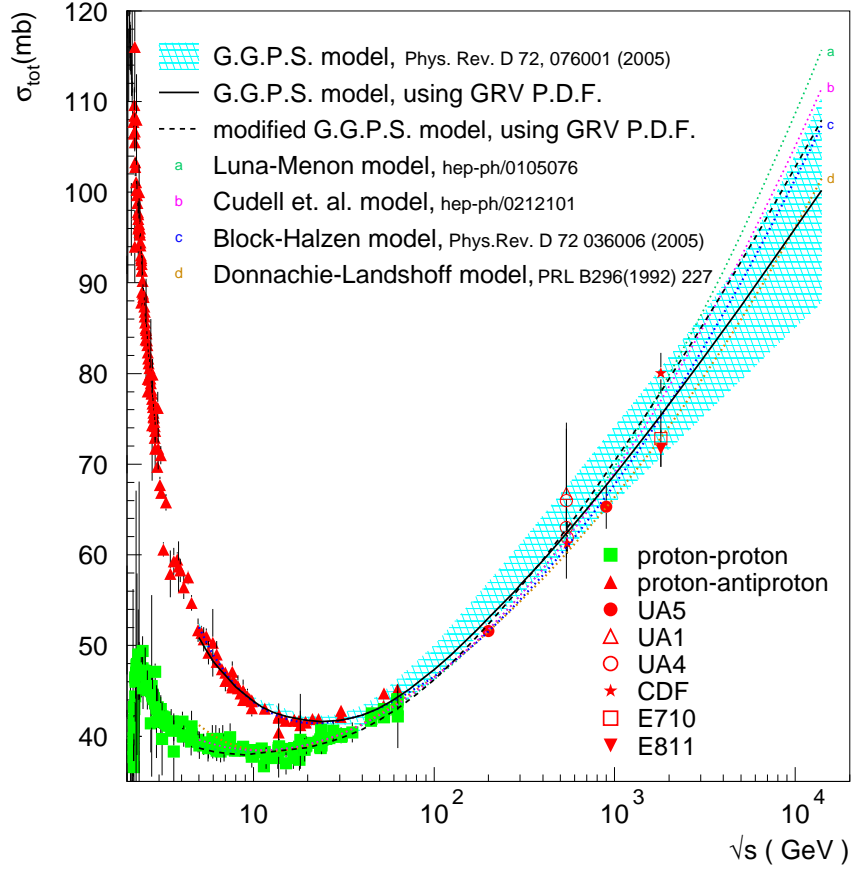


Fig. 1: Predictions for  $\sigma_{\text{tot}}^{\text{pp}}$  in various models. The shaded area gives the range of results in the Eikonalised mini-jet model with soft gluon resummation [18] (the G.G.P.S. model) the solid line giving the prediction obtained using the GRV parton densities [23] in the model. The long-dashed dotted curve (*d*), indicates the predictions for the DL fit [1]. The dotted (BH) curve (*c*) and the uppermost dashed curve (*a*), are the results of two analytical models incorporating constraints from unitarity and analyticity, from [6] and [9], respectively. The prediction obtained by Igi et al, using FESR follows very closely that given by the BH curve. The short dash dotted curve (*b*), is the result of a fit by the COMPETE collaboration [10].

### 3. TUNING MODELS FOR MINIMUM BIAS AND THE UNDERLYING EVENT <sup>2</sup>

#### 3.1 Introduction

PYTHIA version 6.3 introduces major changes related to the description of minimum bias interactions and the underlying event (UE) [27, 28]. There is a new, more sophisticated scenario for multiple interactions, new  $p_T$ -ordered initial- and final-state showers (ISR and FSR), and a new treatment of beam remnants [27, 28].

PYTHIA6.2 has been shown to describe both, minimum bias and underlying event data reasonably well when appropriately tuned [29–31]. A tuning for PYTHIA6.3 as successful as the ATLAS [30] and CDF [31] tunings for 6.2, has yet to be proposed. However, sets of tuned parameters for PYTHIA6.3 which generate minimum bias and underlying event distributions with reasonably good agreement with the data are presented in this report.

JIMMY [32] is a library of routines which should be linked to the HERWIG Monte Carlo (MC) event generator [33] and is designed to generate multiple parton scattering events in hadron-hadron events. JIMMY implements ideas of the eikonal model which are discussed in more detail in Ref. [34]. The multiparton interaction is calculated using the cross-section for the hard subprocess, the conventional parton densities and the area overlap function,  $A(b)$  [32]. JIMMY, however, is limited to the description of the underlying event and should not be used to predict minimum bias events [32].

In this report, in addition to the tunings for PYTHIA6.323 to both, minimum bias [35–39] and the underlying event [40, 41], we also propose a tuning for JIMMY4.1 to the underlying event.

#### 3.2 Minimum bias events

Table 3 displays the relevant PYTHIA6.3 parameters tuned to the minimum bias data [35–39]. It shows the ATLAS tuning [30] used in PYTHIA6.2 in recent ATLAS data challenges [42, 43], and the new proposed PYTHIA6.3 tuning which is labelled as *Min-bias*. The PYTHIA6.323 tuning for the underlying event is also shown in Table 3. The parameters in *Min-bias* were specifically obtained for PYTHIA6.323 with CTEQ6L as the selected PDF set. For the purpose of comparison, the corresponding default values in PYTHIA6.323 [28] are also shown in the table.

##### 3.2.1 Predictions vs. minimum bias data

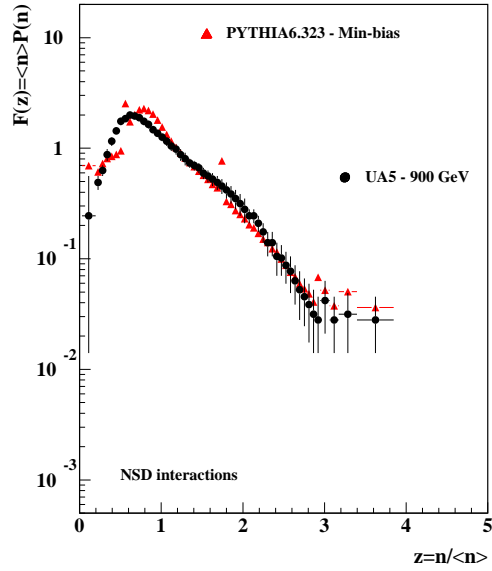
Throughout this report, minimum bias events will be defined as non-single diffractive inelastic (NSD) interactions, following the experimental definition used in [35–39]. In the PYTHIA language, this means that subprocesses 94 and 95 are switched on (MSUB(94)=1 and MSUB(95)=1). The MC distributions have also been adapted to reproduce the particle selection requirements applied to the data by setting  $\pi^0$ ,  $K_s$  and  $\Lambda^0$  as stable particles.

Figure 2 shows distributions generated by PYTHIA6.323 - Min-bias compared to minimum bias data. In Fig. 2(a) the generated charged particle multiplicity distribution (KNO variables) is compared to data measured at  $\sqrt{s} = 900$  GeV. Figure 2(b) compares the Min-bias tuning prediction to the charged particle density distribution,  $dN_{ch}/d\eta$ , at  $\sqrt{s} = 1.8$  TeV. In Fig. 2(c)  $dN_{ch}/d\eta$  at  $\eta = 0$  for a wide range of  $\sqrt{s}$  is shown for PYTHIA6.214 - ATLAS and PYTHIA6.323 - Min-bias. There is a reasonably good agreement between distributions generated with the PYTHIA6.323 - Min-bias tuning and the data.

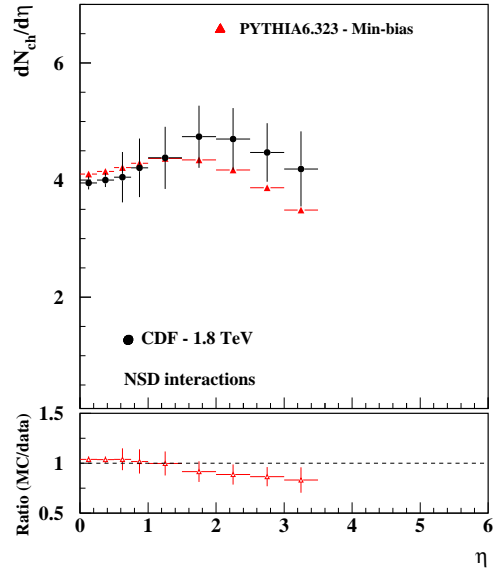
At the qualitative level, the agreement between data and the PYTHIA6.323 - Min-bias tuning is very similar to the agreement seen between the previous ATLAS tuning (PYTHIA6.2 - ATLAS) and the minimum bias data (see Ref. [30]).

---

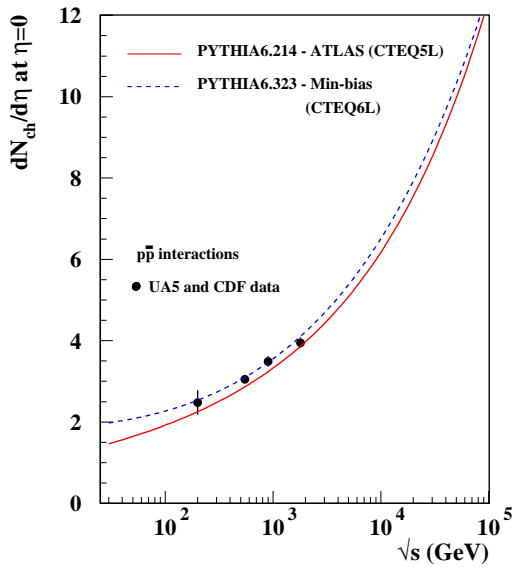
<sup>2</sup>Contributed by: A. Moraes, C. Buttar



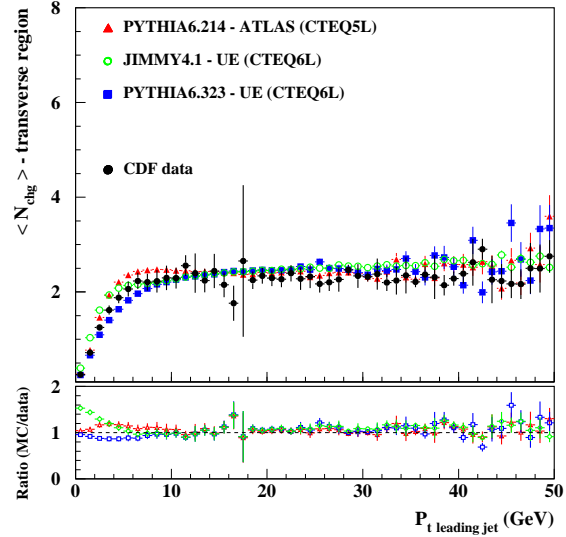
(a)



(b)



(c)



(d)

Fig. 2: (a) Charged multiplicity distributions for NSD  $p\bar{p}$  collisions at  $\sqrt{s} = 900$  GeV; (b)  $dN_{ch}/d\eta$  for NSD  $p\bar{p}$  collisions at 1.8 TeV; (c)  $dN_{ch}/d\eta$  at  $\eta = 0$  for a wide range of  $\sqrt{s}$  shown for PYTHIA6.214 - Rome and PYTHIA6.323 - Min-bias and (d) average charged particles multiplicity in the UE compared to CDF data.

Table 3: PYTHIA6.323 default, Min-bias, UE and PYTHIA6.2 - ATLAS parameters.

Default (PYTHIA6.323) [28]	ATLAS (PYTHIA6.214) [30]	Min-bias (PYTHIA6.323)	UE (PYTHIA6.323)	Comments
MSTP(51)=7 CTEQ5L	MSTP(51)=7 CTEQ5L	MSTP(51)=10042 MSTP(52)=2 CTEQ6L (from LHAPDF)	MSTP(51)=10042 MSTP(52)=2 CTEQ6L (from LHAPDF)	PDF set
MSTP(68)=3	MSTP(68)=1	MSTP(68)=1	MSTP(68)=1	max. virtuality scale and ME matching for ISR
MSTP(70)=1	-	MSTP(70)=2	MSTP(70)=2	regul. scheme for ISR
MSTP(82)=3	MSTP(82)=4	MSTP(82)=4	MSTP(82)=4	complex scenario + double Gaussian matter distribution
-	PARP(67)=1	-	-	parameter regulating ISR
PARP(82)=2.0	PARP(82)=1.8	PARP(82)=2.3	PARP(82)=2.6	$p_{t_{\min}}$ parameter
PARP(84)=0.4	PARP(84)=0.5	PARP(84)=0.5	PARP(84)=0.3	hadronic core radius (only for MSTP(82)=4)
PARP(89)=1.8	PARP(89)=1.0	PARP(89)=1.8	PARP(89)=1.8	energy scale (TeV) used to calculate $p_{t_{\min}}$
PARP(90)=0.25	PARP(90)=0.16	PARP(90)=0.20	PARP(90)=0.24	power of the $p_{t_{\min}}$ energy dependence

### 3.22 LHC predictions for minimum bias events

Figure 3(a) shows charged particle density distributions in pseudorapidity for minimum bias pp collisions at  $\sqrt{s} = 14$  TeV generated by PYTHIA6.214 - ATLAS and PYTHIA6.323 - Min-bias. The charged particle density generated by PYTHIA6.214 - ATLAS and PYTHIA6.323 - Min-bias at  $\eta = 0$  is 6.8 and 7.1, respectively. Note that the  $dN_{ch}/d\eta$  shape is slightly different in the two predictions, especially in the range  $2.5 < \eta < 6.5$ .

Compared to the charged particle density  $dN_{ch}/d\eta$  measured by CDF at 1.8 TeV (Fig. 2(b)), both models indicate a plateau rise of  $\sim 70\%$  at the LHC in the central region.

The average charged particle multiplicity in LHC minimum bias collisions,  $\langle n_{ch} \rangle$ , is 91.04 and 88.72 charged particles as predicted by PYTHIA6.214 - ATLAS and PYTHIA6.323 - Min-bias, respectively. Even though PYTHIA6.323 - Min-bias predicts a higher central plateau, the integrated multiplicity is smaller than that predicted by PYTHIA6.214 - ATLAS because the former also generates a slightly narrower  $dN_{ch}/d\eta$  spectrum compared to the latter.

The  $p_t$  spectrum of charged particles produced in LHC minimum bias events is displayed in Fig. 3(b). Once again, PYTHIA6.323 - Min-bias is compared to PYTHIA6.214 - ATLAS. The “soft” part of the spectrum ( $p_t < 5$  GeV) is very similar as predicted by the two models, however PYTHIA6.323 - Min-bias generates a harder high- $p_t$  tail than PYTHIA6.214 - ATLAS.

### 3.3 Underlying event

The PYTHIA6.323 tuning for the underlying event, labelled *UE*, is also shown in Table 3. As for the *Min-bias* tuning, the parameters in PYTHIA6.323 - UE were specifically obtained for CTEQ6L as the selected PDF set. Note that there are differences between the UE and Min-bias tunings. These can be seen in the  $p_{t_{\min}}$  parameter PARP(82) and in the choice for the hadronic core radius (PARP(84)).

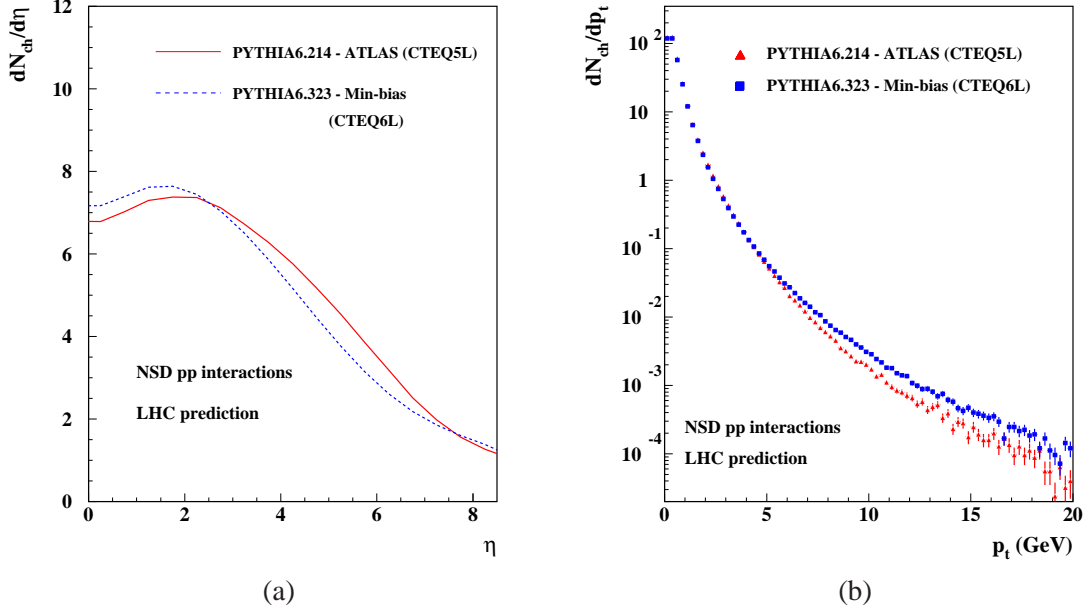


Fig. 3: (a) Charged particle density distributions,  $dN_{ch}/d\eta$ , for NSD pp collisions at  $\sqrt{s} = 14$  TeV. Predictions generated by PYTHIA6.214 - ATLAS and PYTHIA6.323 - Min-bias. (b) Charged particle  $p_t$  spectrum for NSD pp collisions at  $\sqrt{s} = 14$  TeV.

### 3.31 JIMMY4.1 tuning

JIMMY4.1 linked to HERWIG6.507 has been tuned to describe the UE as measured by CDF [40, 41] and the resulting set of parameters, labelled UE, is shown in Table 4. As for PYTHIA6.323, the tuned settings were obtained for CTEQ6L. The default parameters are also included in Table 4 for comparison. JMRAD(91) should also be changed to the same value used for JMRAD(73) when antiprotons are used

Table 4: JIMMY4.1 default and UE parameters for the underlying event.

Default	UE	Comments
JMUEO=1	JMUEO=1	multiparton interaction model
PTMIN=10.0	PTMIN=10.0	minimum $p_T$ in hadronic jet production
PTJIM=3.0	$PTJIM=2.8 \times \left(\frac{\sqrt{s}}{1.8 \text{ TeV}}\right)^{0.274}$	minimum $p_T$ of secondary scatters when JMUEO=1 or 2
JMRAD(73)=0.71	JMRAD(73)=1.8	inverse proton radius squared
PRSOFF=1.0	PRSOFF=0.0	probability of a soft underlying event

in the simulation (e.g. Tevatron events).

Notice that an energy dependent term has been introduced in PTJIM for the UE tuning. This leads to a value of PTJIM=2.1 for  $p\bar{p}$  collisions at  $\sqrt{s} = 630$  GeV and PTJIM=4.9 for the LHC centre-of-mass energy in pp collisions.



### 3.32 Predictions vs. UE data

Based on CDF measurements [40], the UE is defined as the angular region in  $\phi$  which is transverse to the leading charged particle jet.

Figure 2(d) shows PYTHIA6.323 - UE (Table 3) and JIMMY4.1 - UE (Table 4) predictions for the UE compared to CDF data [40] for the average charged particle ( $p_t > 0.5$  GeV and  $|\eta| < 1$ ) multiplicity in the underlying event. A distribution, generated with the ATLAS tuning for PYTHIA6.2 and used in recent ATLAS data challenges is also included in the plot for comparison. There is a reasonably good agreement between the proposed tunings and the data. The distribution shapes are slightly different in the region of  $P_{t_{\text{jet}}} \lesssim 15$  GeV. PYTHIA6.323 - UE underestimates the data while JIMMY4.1 - UE overestimates it at low  $P_{t_{\text{jet}}}$ .

Another measurement of the UE event is made by defining two cones in  $\eta - \phi$  space, at the same pseudorapidity  $\eta$  as the leading  $E_T$  jet (calorimeter jet) and  $\pm 90^\circ$  in the azimuthal direction,  $\phi$  [41]. The total charged track momentum inside each of the two cones is then measured and the higher of the two values used to define the “MAX” cone, with the remaining cone being labelled “MIN” cone. Figure 4 shows PYTHIA6.323 - UE predictions for the UE compared to CDF data [41] for the  $\langle p_t \rangle$  of charged particles in the MAX and MIN cones for  $p\bar{p}$  collisions at (a)  $\sqrt{s} = 630$  GeV and (b) 1.8 TeV. JIMMY4.1 - UE predictions are compared to the data in Fig. 5. Both tunings describe the data with good agreement, however, this only has become possible by tuning the energy dependence terms which regulate the minimum  $p_t$  cut-off parameters in both generators (PARP(82), (89) and (90) for PYTHIA6.3 and PTJIM for JIMMY4.1).

### 3.33 LHC predictions for the UE

Figure 6 shows PYTHIA6.323 - UE (Table 3), JIMMY4.1 - UE (Table 4) and PYTHIA6.2 - ATLAS predictions for the average multiplicity in the UE for LHC pp collisions. The CDF data ( $p\bar{p}$  collisions at  $\sqrt{s} = 1.8$  TeV) for the average multiplicity in the UE is also included in Fig. 6.

A close inspection of predictions for the UE given in Fig. 6, shows that the average charged particle multiplicity in the UE for leading jets with  $P_{t_{\text{jet}}} > 20$  GeV reaches a plateau at  $\sim 6$  charged particles according to JIMMY4.1 - UE,  $\sim 6.5$  for PYTHIA6.214 - ATLAS and  $\sim 7.5$  according to PYTHIA6.323 - UE. Expressed as particle densities per unit  $\eta - \phi$ , where the UE phase-space is given by  $\Delta\eta\Delta\phi = 4\pi/3$  [31, 40], these multiplicities correspond to 1.43, 1.56 and 1.79 charged particles per unit  $\eta - \phi$  ( $p_t > 0.5$  GeV), as predicted by JIMMY4.1 - UE, PYTHIA6.214 - ATLAS and PYTHIA6.323 - UE, respectively.

The distribution shapes also show significant differences between the model predictions. The shape of the multiplicity distribution, generated by PYTHIA6.323 - UE, is considerably different from the other two models in the region of  $P_{t_{\text{jet}}} \lesssim 25$  GeV.

## 3.4 Conclusions

In this report we have proposed minimum bias and underlying event tunings for PYTHIA6.323 and JIMMY4.1 (see Tables 3 and 4).

The minimum bias tuning for PYTHIA6.323 (*Min-bias* - Table 3) has been shown to describe the minimum bias data at different colliding energies (figs. 2(a) - (c)).

LHC predictions from PYTHIA6.323 - Min-bias and PYTHIA6.214 - ATLAS do not show any severe differences. There are some noticeable differences though. The shape of  $dN_{ch}/d\eta$  is narrower in the distribution generated by PYTHIA6.323 - Min-bias compared to that from PYTHIA6.214 - ATLAS. Another difference is seen for  $dN_{ch}/dp_t$ . PYTHIA6.323 - Min-bias generates a  $p_t$  spectrum with a harder tail compared to the prediction from PYTHIA6.214 - ATLAS.

As for the minimum bias tuning for PYTHIA6.323, the underlying event tunings for

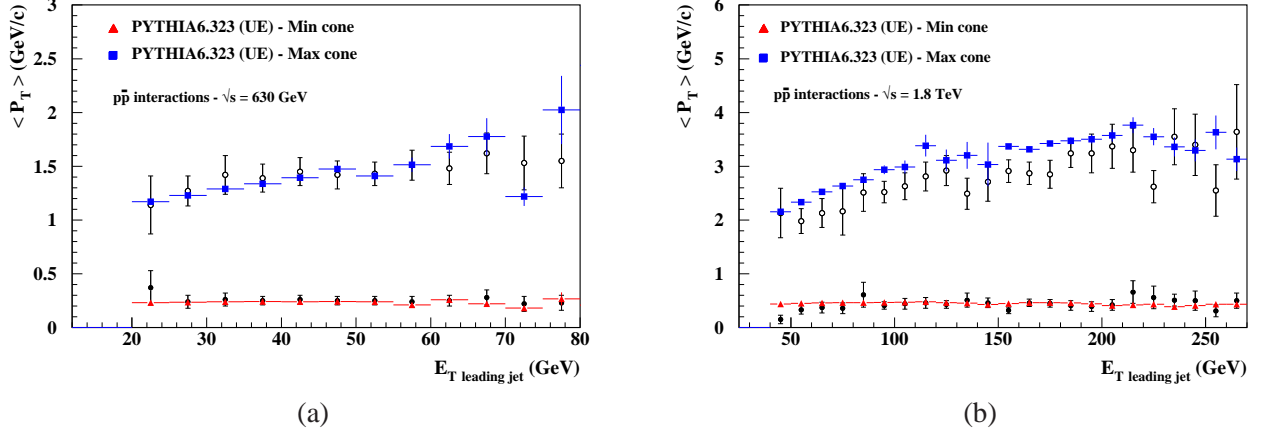


Fig. 4: PYTHIA6.323 - UE predictions for the UE compared to the  $\langle p_t \rangle$  in MAX and MIN cones for (a)  $p\bar{p}$  collisions at  $\sqrt{s} = 630$  GeV and (b) 1.8 TeV.

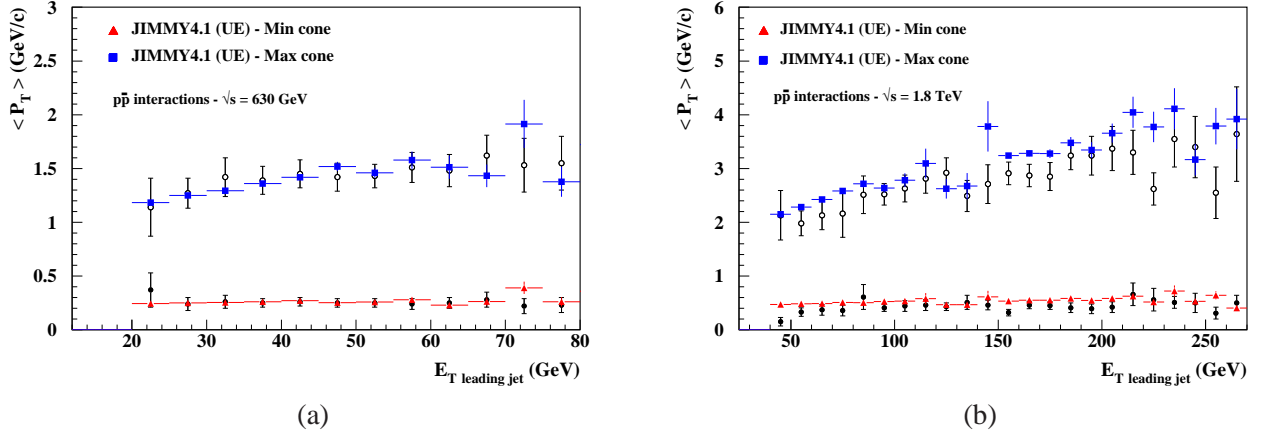


Fig. 5: JIMMY4.1 - UE predictions for the UE compared to the  $\langle p_t \rangle$  in MAX and MIN cones for (a)  $p\bar{p}$  collisions at  $\sqrt{s} = 630$  GeV and (b) 1.8 TeV.

PYTHIA6.323 and JIMMY4.1 (Table 3) have also been shown to describe most of the UE data made available by the CDF Collaboration [40, 41]. However, comparisons to data also indicate that these models need improvements, especially regarding their capability to correctly describe the ratio  $\langle p_t \rangle / \langle N_{chg} \rangle$  in the UE.

Comparing PYTHIA6.323 - UE, JIMMY4.1 - UE and PYTHIA6.214 - ATLAS at the LHC, one can clearly notice differences in the shapes of the distributions predicted by PYTHIA6.323 - UE and the other two models, as shown in Fig. 6.

Tuning the JIMMY parameter PTJIM to include an energy dependent factor made it possible to describe the MAX-MIN  $\langle p_t \rangle$  distributions at different energies.

As a final point, we would like to mention that this is an “ongoing” study. At the moment these are the best parameters we have found to describe the data, but as the models are better understood, the tunings could be improved in the near future.

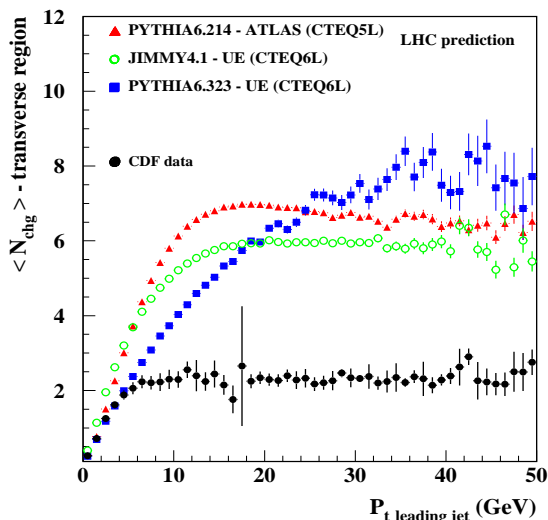


Fig. 6: PYTHIA6.323 - UE, JIMMY4.1 - UE and PYTHIA6.214 - ATLAS predictions for the average multiplicity in the UE for LHC pp collisions.

#### 4. SMALL $x$ <sup>3</sup>

Almost every event recorded at the LHC will involve collisions of partons, mostly gluons, carrying a relatively small proportion of the longitudinal momenta of the colliding beams. Even benchmark cross sections such as  $W$  and  $Z$  production are largely made up of contributions from partons carrying rather small values of  $x$ . However, parton distribution functions and parton evolution are relatively poorly understood when  $x$  is small, due to the small  $x$  logarithms which render the usual (fixed order) perturbation expansion unreliable. This is a serious problem since to make a theoretical prediction for an LHC process we must first obtain reliable parton distribution functions (typically by analysis of data from HERA), and then evolve these partons to scales appropriate for the LHC.

Here we will consider three separate aspects of this problem. Firstly, we consider the sensitivity of the  $W$  and  $Z$  cross sections, and in particular their rapidity distributions, to small  $x$  parton distributions. We also consider how from an experimental perspective these cross sections may eventually be used to improve our knowledge of parton distribution functions. Secondly, we will consider the current theoretical status of small  $x$  resummation, using collinear resummation of the BFKL kernel at LO and NLO, and the prospects for accurate calculations by the time we have LHC data. Finally, we consider how we might search for footprints of BFKL dynamics in LHC data at large rapidities.

#### 4.1 Low- $x$ physics and $W$ and $Z$ production at the LHC<sup>4</sup>

##### 4.11 Introduction

The kinematic plane for the LHC is shown in Fig. 7, which translates the kinematics for producing a state of mass  $M$  and rapidity  $y$  into the deep inelastic scattering variables,  $Q^2$ , the scale of the hard sub-process, and the Bjorken  $x$  values of the participating partons. The scale of the process is given by  $Q^2 = M^2$  and the Bjorken  $x$  values by,  $x_1 = (M/\sqrt{s})\exp(y)$ , and,  $x_2 = (M/\sqrt{s})\exp(-y)$ , where  $y$  is the parton rapidity,  $y = \frac{1}{2} \ln \frac{(E+pl)}{(E-pl)}$ . Thus, at central rapidity, these  $x$  values are equal, but as one moves away from central rapidity, one parton moves to higher  $x$  and one to lower  $x$ , as illustrated by the

<sup>3</sup>Contributed by: R.D. Ball, M. Cooper-Sarkar, V. Del Duca

<sup>4</sup>Author: A.M. Cooper-Sarkar

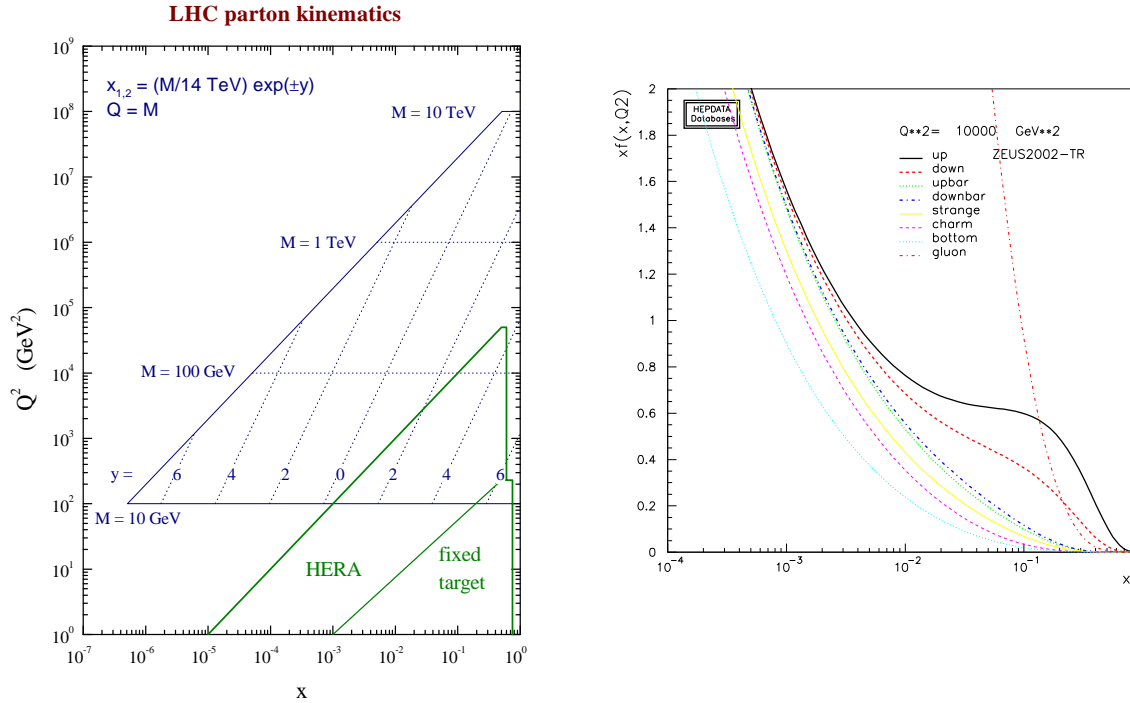


Fig. 7: Left plot: The LHC kinematic plane (thanks to James Stirling). Right plot: PDF distributions at  $Q^2 = 10,000 \text{ GeV}^2$ .

lines of constant  $y$  on the plot. The first physics to be studied at the LHC will be at relatively low scales, where the large cross sections ensure that even low luminosity running will yield copious numbers of events. Thus the LHC will begin by studying standard model (SM) physics, calibrating our knowledge of the detectors on these well known processes. Study of Fig. 7 makes it clear that the cross sections for these processes are only well known if the parton distribution functions (PDFs) of the proton are well known at small- $x$ . This assumes that the theoretical formalism of NLO QCD, as embodied in the DGLAP equations, is valid at small- $x$ , since this is the formalism used for determining PDFs. In the present contribution we address the question of how PDF uncertainties at low  $x$  affect the SM processes of  $W$  and  $Z$  production at the LHC.

The major source of information on low- $x$  physics in the last decade has been the HERA data. One of the most striking results of HERA was observation of an unexpected rise of the  $F_2$  structure function at low- $x$ . The interpretation of the rise in  $F_2$ , in the DGLAP formalism, attributes it to a strong rise in the gluon distribution function at low- $x$ , since the gluon drives the sea distributions by  $g \rightarrow q\bar{q}$  splitting. In fact, the DGLAP equations predict that, at high  $Q^2$  ( $\gtrsim 100 \text{ GeV}^2$ ), a steep rise of the gluon and the sea at low- $x$  will evolve from flat input shapes at a low  $Q^2$  ( $\sim 4 \text{ GeV}^2$ ). Nevertheless, the rise was unexpected, firstly, because most theoreticians expected any such tendency to be tamed either by screening effects, or by gluon recombination at high gluon density. Secondly, because the rise was already present for low  $Q^2$  ( $\sim 1 - 2 \text{ GeV}^2$ ) - even lower than the conventional starting scale for QCD evolution. Hence the observation of the rise led to excitement in a somewhat orthogonal section of the theoretical community, where a steep rise at low  $Q^2$  had been predicted in the BFKL formalism, which resums diagrams involving  $\ln(1/x)$ . Such resummations are not part of the conventional DGLAP  $\ln(Q^2)$  summations.

However, even though the observation of a rise of  $F_2$  at low  $x$  and low  $Q^2$  defied conventional prejudice, it can be accommodated within the conventional DGLAP formalism provided sufficiently flexible input shapes are used at a low enough input scale (now taken to be  $Q^2 \sim 1 \text{ GeV}^2$ ). In fact it turns out that whereas the input sea distribution is still rising at low- $x$ , the input gluon distribution has

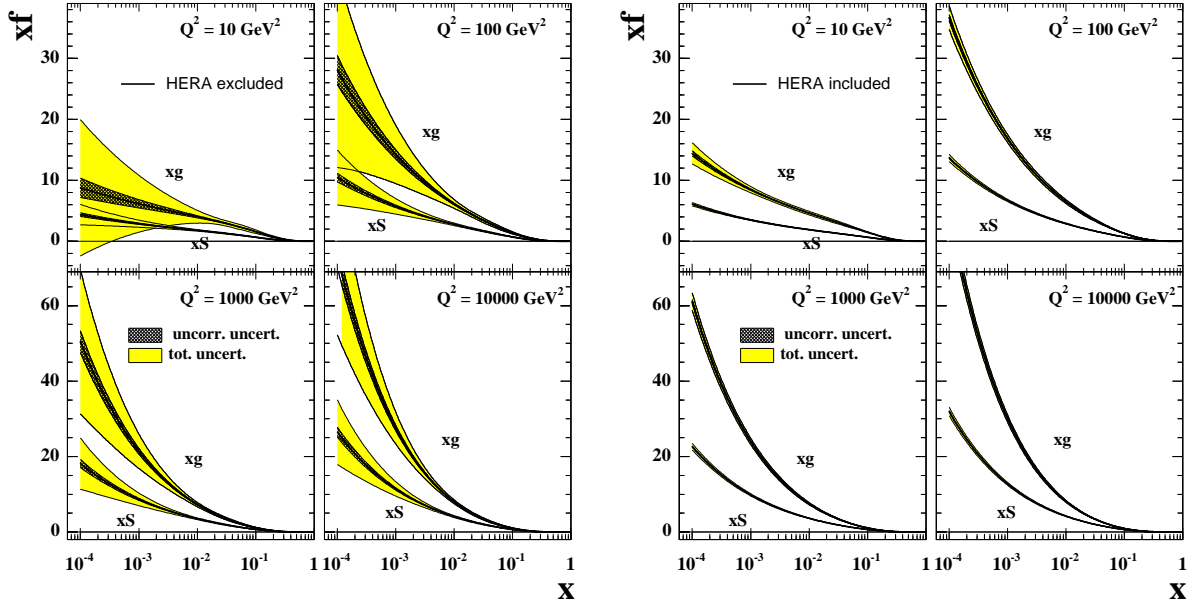


Fig. 8: Sea ( $xS$ ) and gluon ( $xg$ ) PDFs, as a function of  $x$ , for various  $Q^2$  values; left plot: from the ZEUS-S global PDF analysis not including HERA data; right plot: from the ZEUS-S global PDF analysis including HERA data.

turned over to become valence-like, and is even allowed to become negative in some parameterizations. This counter intuitive behaviour has led many QCD theorists to believe that the conventional formalism is in need of extension [44]. In Sec. 4.2 we describe recent work in this area. The present section is concerned with how well the PDFs are known at low- $x$ , within the conventional framework, and how this affects the predictions for  $W$  and  $Z$  production at the LHC. These processes have been suggested as ‘standard-candles’ for the measurement of luminosity because their cross sections are ‘well known’. In the present contribution we investigate to what extent this is really true - and what might be done about it.

#### 4.12 $W$ and $Z$ Production at the LHC

At leading order (LO),  $W$  and  $Z$  production occur by the process,  $q\bar{q} \rightarrow W/Z$ . Consulting Fig. 7, we see that at central rapidity, the participating partons have small momentum fractions,  $x \sim 0.005$ , and over the measurable rapidity range,  $|y| < 2.4$ ,  $x$  values remain in the range,  $5 \cdot 10^{-4} < x < 0.05$ . Thus, in contrast to the situation at the TeVatron, the scattering is happening dominantly between sea quarks and anti-quarks. Furthermore, the high scale of the process  $Q^2 = M^2 \sim 10,000 \text{ GeV}^2$  ensures that the gluon is the dominant parton as also illustrated in Fig. 7, where the PDFs for all parton flavours are shown for  $Q^2 \sim 10,000 \text{ GeV}^2$ . Hence the sea quarks have mostly been generated by the flavour blind  $g \rightarrow q\bar{q}$  splitting process. Thus the precision of our knowledge of  $W$  and  $Z$  cross sections at the LHC is crucially dependent on the uncertainty on the momentum distribution of the gluon at low- $x$ . This is where the HERA data come in.

Figure 8 shows the sea and gluon PDFs (and their uncertainties) extracted from an NLO QCD PDF fit analysis to world data on deep inelastic scattering, before and after HERA data are included. The latter fit is the ZEUS-S global fit [45], whereas the former is a fit using the same fitting analysis but leaving out the ZEUS data. The full PDF uncertainties for both fits are calculated from the eigenvector PDF sets of the ZEUS-S analysis using LHAPDF [46]. The improvement in the level of uncertainty is striking.

Figure 9 illustrates how this improved knowledge of the gluon and sea distributions has improved our knowledge of  $W$  and  $Z$  cross sections. It shows  $W$  and  $Z$  rapidity spectra predicted using the PDFs extracted from the global PDF fit which does not include the HERA data, compared to those extracted

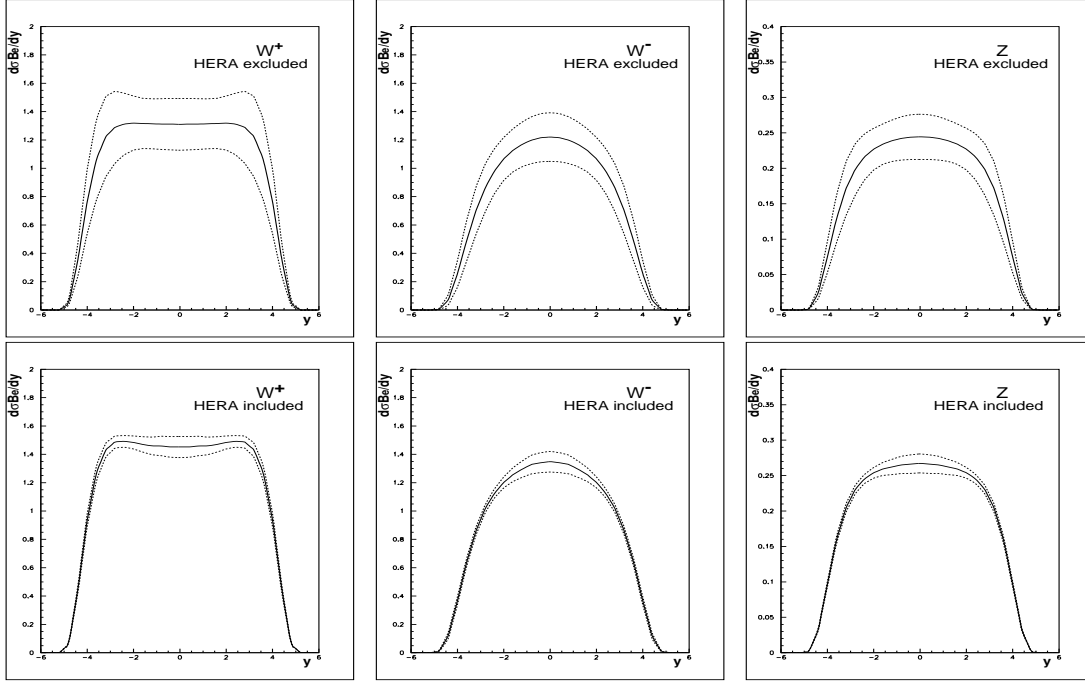


Fig. 9: LHC  $W^+$ ,  $W^-$ ,  $Z$  rapidity distributions and their PDF uncertainties: top row: from the ZEUS-S global PDF analysis not including HERA data; left plot  $W^+$ ; middle plot  $W^-$ ; right plot  $Z$ ; bottom row: from the ZEUS-S global PDF analysis including HERA data; left plot:  $W^+$ ; middle plot:  $W^-$ ; right plot:  $Z$ .

Table 5: LHC  $W$  and  $Z$  cross sections for decay via the lepton mode, for various PDFs

PDF Set	$\sigma(W^+).B(W^+ \rightarrow l^+\nu_l)$	$\sigma(W^-).B(W^- \rightarrow l^-\bar{\nu}_l)$	$\sigma(Z).B(Z \rightarrow l^+l^-)$
ZEUS-S no HERA	$10.63 \pm 1.73$ nb	$7.80 \pm 1.18$ nb	$1.69 \pm 0.23$ nb
ZEUS-S	$12.07 \pm 0.41$ nb	$8.76 \pm 0.30$ nb	$1.89 \pm 0.06$ nb
CTEQ6.1	$11.66 \pm 0.56$ nb	$8.58 \pm 0.43$ nb	$1.92 \pm 0.08$ nb
MRST01	$11.72 \pm 0.23$ nb	$8.72 \pm 0.16$ nb	$1.96 \pm 0.03$ nb

from the similar global PDF fit which does include HERA data. The corresponding predictions for the  $W$  and  $Z$  cross sections, decaying to the lepton decay mode, are summarized in Table 5. The uncertainties in the predictions for these cross sections have decreased from  $\sim 16\%$  pre-HERA to  $\sim 3.5\%$  post-HERA. There could clearly have been no talk of using these processes as standard candle processes, without the HERA data.

The post-HERA level of precision, illustrated in Fig. 9, is taken for granted in modern analyses. However, when considering the PDF uncertainties on the Standard Model (SM) predictions it is necessary not only to consider the uncertainties of one particular PDF analysis, but also to compare PDF analyses. Figure 10 compares the predictions for  $W^+$  production for the ZEUS-S PDFs with those of the CTEQ6.1 [47] PDFs and the MRST01 [48] PDFs<sup>5</sup>. The corresponding  $W^+$  cross sections for decay to the leptonic mode are given in Table 5. Comparing the uncertainty at central rapidity, rather than the total cross section, we see that the uncertainty estimates are somewhat larger:  $\sim 6\%$  for ZEUS-S;  $\sim 8\%$  for CTEQ6.1M and  $\sim 3\%$  for MRST01. The difference in the central value between ZEUS-S and CTEQ6.1 is  $\sim 4\%$ . Thus the spread in the predictions of the different PDF sets is comparable to the uncertainty estimated by the individual analyses. Since the measurable rapidity range is restricted to central rapidity, it is more prudent to use these uncertainty estimates when considering if  $W$ ,  $Z$  cross sections can be used as luminosity monitors. Comparing the results from the three PDF extractions it seems reasonable to use the generous estimate of the CTEQ6.1 analysis,  $8\%$ , as an estimate of how well the luminosity could

<sup>5</sup>MRST01 PDFs are used because the full error analysis is available for this PDF set.



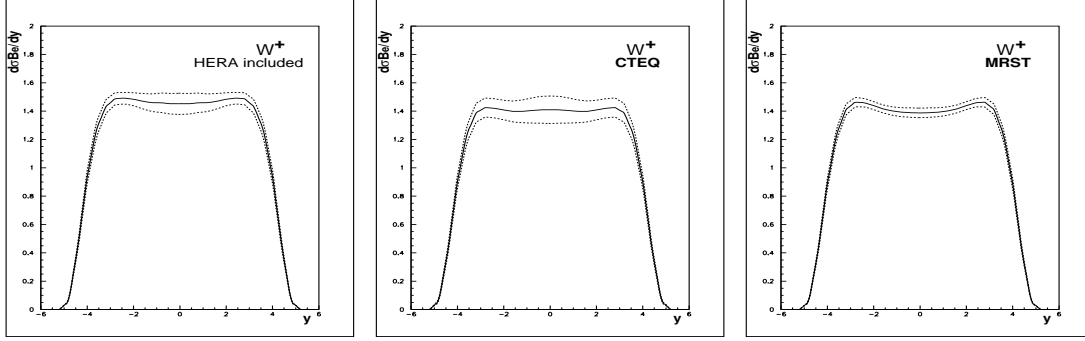


Fig. 10: LHC  $W^+$  rapidity distributions and their PDF uncertainties; left plot: ZEUS-S PDFs; middle plot: CTEQ6.1 PDFs; right plot: MRST01 PDFs.

be measured, at the present level of uncertainty. We subject this estimate to some further reality checks below and in Sec. 4.13 and we discuss the possibility of improving this estimate with early LHC data in Sec. 4.14

Since the PDF uncertainty feeding into the  $W^+$ ,  $W^-$  and  $Z$  production is mostly coming from the gluon PDF for all three processes, there is a correlation in their uncertainties, which can be removed by taking ratios. The upper half of Fig. 11 shows the  $W$  asymmetry

$$A_W = (W^+ - W^-)/(W^+ + W^-).$$

for CTEQ6.1 PDFs. The PDF uncertainties on the asymmetry at central rapidity are about 5%, smaller than those on the  $W$  spectra themselves, and a PDF eigenvector decomposition indicates that sensitivity to  $u$  and  $d$  quark flavour distributions is now evident. Even this residual flavour sensitivity can be removed by taking the ratio

$$A_{ZW} = Z/(W^+ + W^-)$$

as also shown in Fig. 11. This quantity is almost independent of PDF uncertainties, which are now as small as 0.5%, within the CTEQ6.1 PDF analysis.

However, as before, it is necessary to compare these quantities between different PDF analyses. The variation in the predictions for the ratio  $A_{ZW}$  between PDF analyses (MRST01, ZEUS-S and Alekhin02 PDFs have been compared to CTEQ6.1) is outside the PDF uncertainty estimates of the different analyses, but it is still only  $\sim 5\%$ . Hence this ratio could be used as an SM benchmark measurement. The ratio  $A_W$  shows a much more striking difference between MRST01 PDFs and the others. This is illustrated in the lower half of Fig. 11 for the ZEUS-S, CTEQ6.1 and MRST01 PDFs, in the measurable rapidity range. There is a difference of  $\sim 25\%$  in the predictions. The origin of this difference between MRST and other PDFs is in the valence spectra. At leading order, the dominant contribution to  $A_W$  is

$$A_W = \frac{u\bar{d} - d\bar{u}}{u\bar{d} + d\bar{u}}. \quad (13)$$

At central rapidity,  $x \sim 0.005$ , for both partons and consequently  $\bar{u} \approx \bar{d}$ <sup>6</sup>. Thus

$$A_W = \frac{u - d}{u + d} = \frac{u_v - d_v}{u_v + d_v + 2\bar{q}} \quad (14)$$

and  $A_W$  depends on the difference of the valence quarks. The quantity  $u_v - d_v$ , is different for MRST and CTEQ, and this difference is outside the PDF uncertainty estimates of either analysis. However,

<sup>6</sup>Even if some fairly wild assumptions as to the shape of  $\bar{d} - \bar{u}$  are made for low  $Q^2$ , the absolute size of  $\bar{q}$  evolves with  $Q^2$  to become very large at  $Q^2 = M_W^2$ , whereas the difference does not evolve, and becomes relatively small.

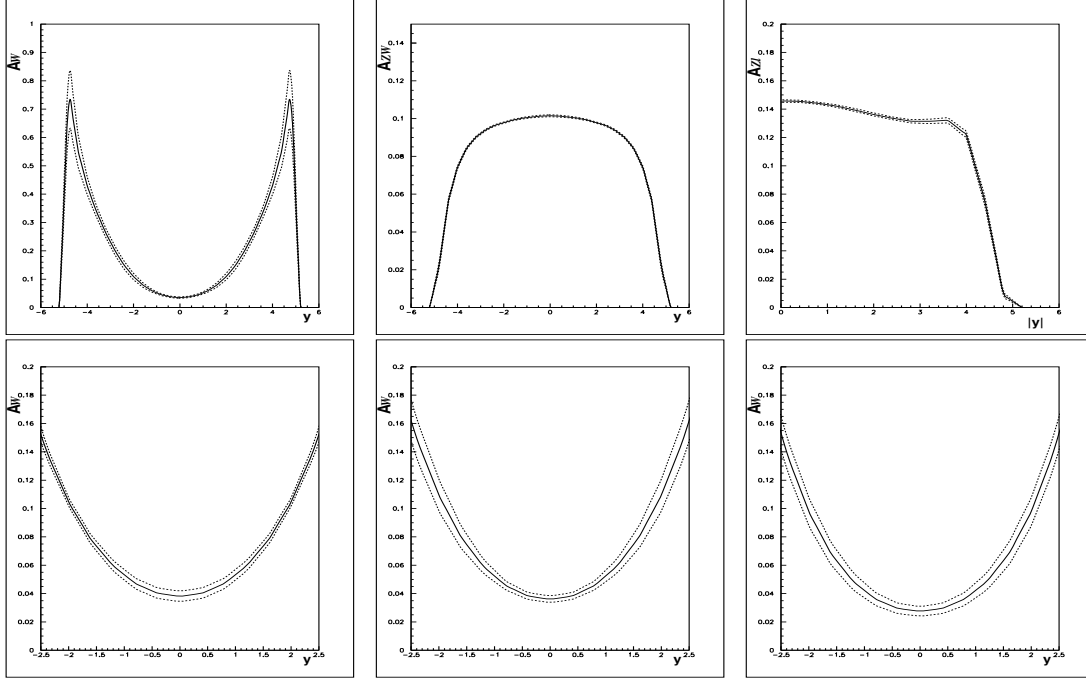


Fig. 11: Top row: predictions from the CTEQ6.1 PDFs: left plot: the  $W$  asymmetry  $A_W$ ; middle plot: the ratio  $A_{ZW}$ ; right plot: the ratio  $A_{Zl}$ . Bottom row: the  $W$  asymmetry  $A_W$  within the measurable rapidity range, as predicted using different PDF analyses: left plot: ZEUS-S; middle plot: CTEQ6.1; right plot: MRST01.

these uncertainty estimates are themselves unreliable for valence spectra at  $x \sim 0.005$ , since there is no data on valence quantities at such small  $x$ . The LHC can provide the first such measurement.

In order to assess, if LHC measurements will actually be discriminating, we must first account for the fact that  $W$  bosons decay and are most easily detected from their leptonic final states. Thus we actually measure the decay lepton rapidity spectra rather than the  $W$  rapidity spectra. The upper half of Fig. 12 shows these rapidity spectra for positive and negative leptons from  $W^+$  and  $W^-$  decay together with the lepton asymmetry,

$$A_l = (l^+ - l^-)/(l^+ + l^-)$$

for the CTEQ6.1 PDFs. A cut of,  $p_t > 25$  GeV, has been applied on the decay lepton, since it will not be possible to identify leptons with small  $p_t$ . A particular lepton rapidity can be fed from a range of  $W$  rapidities so that the contributions of partons at different  $x$  values are smeared out in the lepton spectra. Nevertheless, the broad features of the  $W$  spectra and the sensitivity to the gluon parameters are reflected in the lepton spectra, resulting in a similar estimate ( $\sim 8\%$ ) of PDF uncertainty at central rapidity for the CTEQ6.1 PDFs. The lepton asymmetry shows the change of sign at large  $y$  which is characteristic of the  $V - A$  structure of the lepton decay. The cancellation of the uncertainties due to the gluon PDF is not so perfect in the lepton asymmetry as in the  $W$  asymmetry. Even so, in the measurable rapidity range, the PDF uncertainty in the asymmetry is smaller than in the lepton spectra, being  $\sim 5\%$ , for the CTEQ6.1 PDFs. The  $Z$  to  $W$  ratio  $A_{ZW}$  has also been recalculated as a  $Z$  to leptons ratio,

$$A_{Zl} = Z/(l^+ + l^-)$$

illustrated in Fig. 11. Just as for  $A_{ZW}$ , the overall uncertainty in  $A_{Zl}$  is very small ( $\sim 0.5\%$ ) for CTEQ6.1 PDFs.

It is again necessary to consider the difference between different PDF analyses for the predictions of the lepton spectra,  $A_{Zl}$  and  $A_l$ . For the lepton spectra, the spread in the predictions of the different PDF analyses of MRST01, CTEQ6.1 and ZEUS-S is comparable to the uncertainty estimated by the

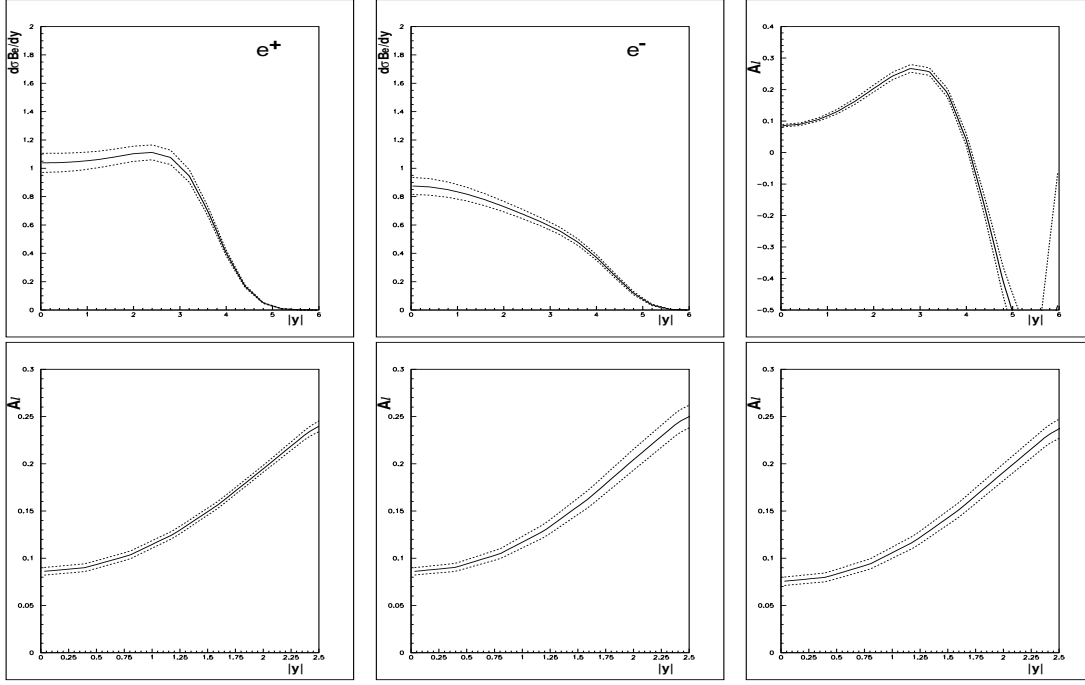


Fig. 12: Top row: lepton spectra from the CTEQ6.1 PDFs; left plot: decay  $e^+$  rapidity spectrum; middle plot: decay  $e^-$  rapidity spectrum; right plot: lepton asymmetry  $A_l$ . Bottom row: the lepton asymmetry  $A_l$  from different PDF analyses: left plot: ZEUS-S; middle plot: CTEQ6.1; right plot: MRST01.

individual analyses, just as for the  $W$  spectra, and this is shown later in Fig. 13. Just as for  $A_{ZW}$ , there are greater differences in the predictions for  $A_{Zl}$  between PDF analyses than within any PDF analysis, but these differences remain within  $\sim 5\%$  preserving this quantity as an SM benchmark measurement. Thus our previous estimate of the usefulness of these processes as luminosity monitors and SM benchmarks survives the reality check of the fact that we will measure the leptons, not the  $W$  bosons.

The significant differences which we noticed between the predictions of the different PDF analyses for  $A_W$ , remain in the predictions for  $A_l$ . The lower half of Fig. 12 compares these predictions for the ZEUS-S PDFs with those of the CTEQ6.1 PDFs and the MRST01 PDFs, in the measurable rapidity range. The discrepancy of  $\sim 25\%$  which was found in  $A_W$  has been somewhat diluted to  $\sim 15\%$  in  $A_l$ , but this should still be large enough for LHC measurements to discriminate, and hence to give information on the low- $x$  valence distributions.

#### 4.13 How well can we actually measure $W$ spectra at the LHC?

The remainder of this contribution will be concerned with the question: how accurately can we measure the lepton rapidity spectra and can we use the early LHC data to improve on the current level of uncertainty?

We have simulated one million signal,  $W \rightarrow e\nu_e$ , events for each of the PDF sets CTEQ6.1, MRST2001 and ZEUS-S using HERWIG (6.505). For each of these PDF sets the eigenvector error PDF sets have been simulated by PDF re-weighting and k-factors have been applied to approximate an NLO generation. A study has been made of the validity of both PDF re-weighting and k-factor re-weighting and this is reported in ref. [49]. The conclusion is that PDF re-weighting is valid for re-weighting the rapidity spectra when the PDF sets are broadly similar, as they are within any one PDF analysis. The k-factor re-weighting to simulate NLO is also valid for the rapidity spectra for which it was designed.

The top part of Fig. 13, shows the  $e^\pm$  and  $A_l$  spectra at the generator level, for all of the PDF sets superimposed. As mentioned before, it is clear that the lepton spectra as predicted by the different PDF analyses are compatible, within the PDF uncertainties of the analyses. The events are then passed through ATLFAST, the fast simulation of the ATLAS detector. This applies loose kinematic cuts:

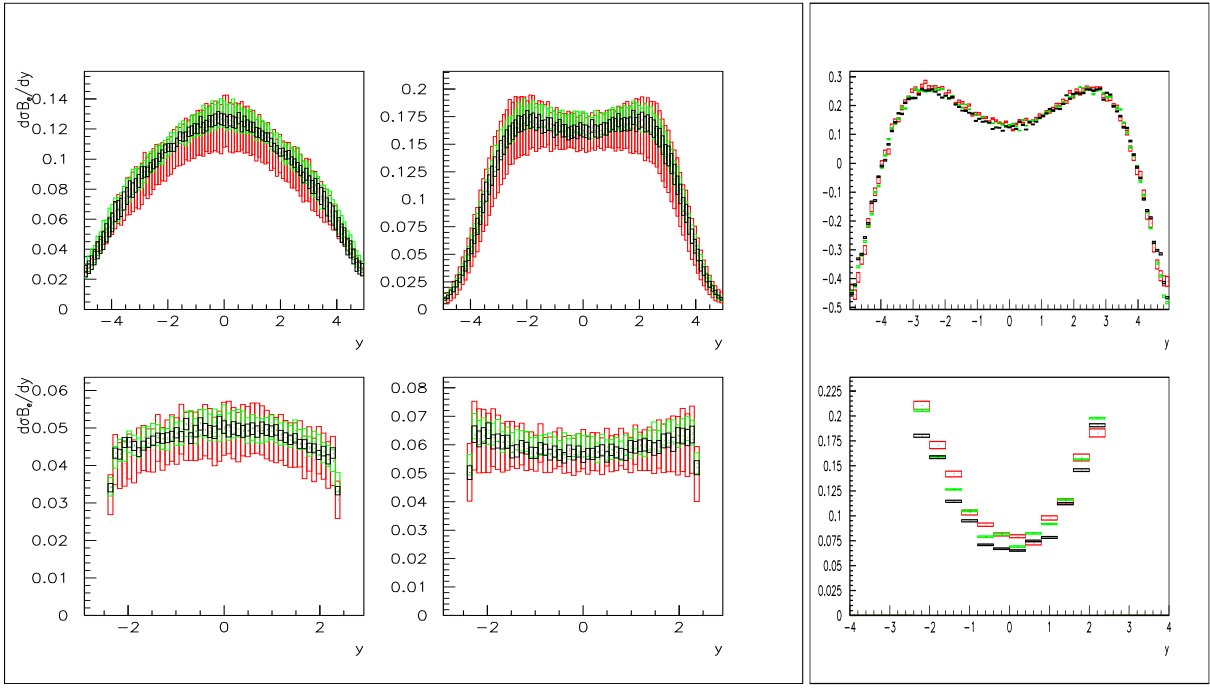


Fig. 13: Top row:  $e^-$ ,  $e^+$  and  $A_e$  rapidity spectra for the lepton from the  $W$  decay, generated using HERWIG + k factors and CTE6.1 (red), ZEUS-S (green) and MRST2001 (black) PDF sets with full uncertainties. Bottom row: the same spectra after passing through the ATLFast detector simulation and selection cuts.

$|\eta| < 2.5$ ,  $p_{te} > 5 \text{ GeV}$ , and electron isolation criteria. It also smears the 4-momenta of the leptons to mimic momentum dependent detector resolution. We then apply further cuts, designed to eliminate the background preferentially. These criteria are:

- pseudorapidity,  $|\eta| < 2.4$ , to avoid bias at the edge of the measurable rapidity range
- $p_{te} > 25 \text{ GeV}$ , high  $p_t$  is necessary for efficient electron identification
- missing  $E_t > 25 \text{ GeV}$ , the  $\nu_e$  in a signal event will have a correspondingly large missing  $E_t$
- no reconstructed jets in the event with  $p_t > 30 \text{ GeV}$ , to discriminate against QCD background
- recoil of the  $W$  boson in the transverse plane  $p_t^{\text{recoil}} < 20 \text{ GeV}$ , to discriminate against QCD background

These cuts ensure that background from the processes:  $W \rightarrow \tau\nu_\tau$ ;  $Z \rightarrow \tau^+\tau^-$ ; and  $Z \rightarrow e^+e^-$ , is negligible ( $\lesssim 1\%$ ) [49]. Furthermore, a study of charge misidentification has established that the lepton asymmetry will need only very small corrections ( $\lesssim 0.5\%$ ), within the measurable rapidity range [49].

The lower half of Fig. 13, shows the  $e^\pm$  and  $A_l$  spectra at the detector level after application of these cuts for all of the PDF sets superimposed. The level of precision of each PDF set, seen in the analytic calculations of Fig. 10, appears somewhat degraded at detector level, so that a net level of PDF uncertainty in the lepton spectra of  $\sim 10\%$  is expected at central rapidity. Thus the usefulness of these processes as a luminosity monitor is somewhat compromised if a measurement to better than 10% is required.

The anticipated cancellation of PDF uncertainties in the asymmetry spectrum is observed, within each PDF set, such that the uncertainties predicted by each PDF set are  $\sim 5\%$ , but the spread between the MRST and CTEQ/ZEUS-S PDF sets is as large as  $\sim 15\%$ . Thus measurements, which are accurate to about  $\sim 5\%$ , could provide useful information on the valence distributions at low  $x$ .

#### 4.14 Using LHC data to improve precision of PDFs

We now consider the possibility of improving on the current level of PDF uncertainty by using LHC data itself. The high cross sections for  $W$  production at the LHC ensure that it will be the experimental

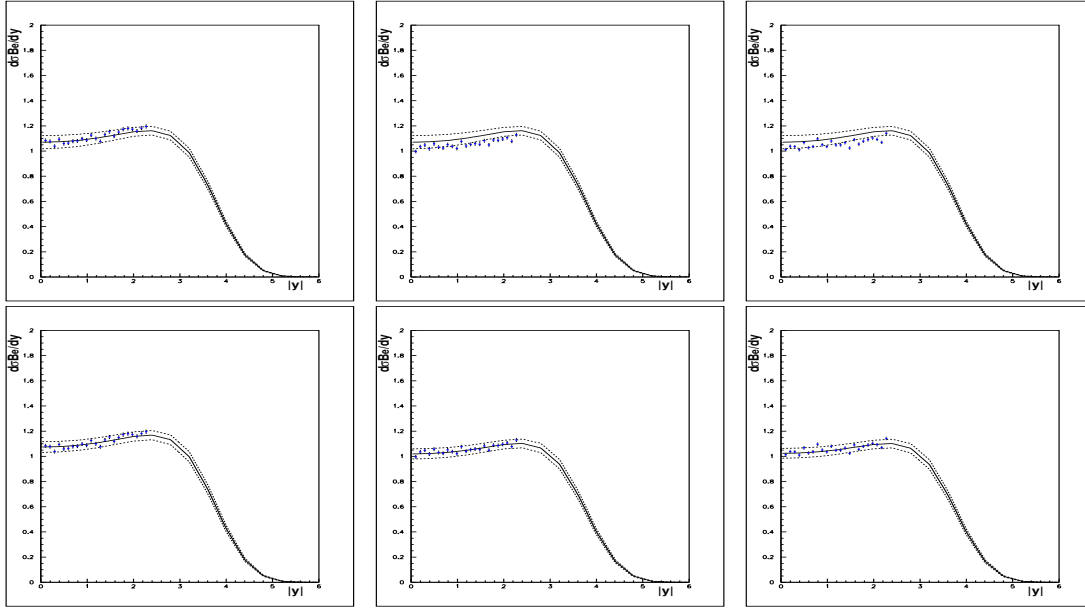


Fig. 14: Top row:  $e^+$  rapidity spectra generated from: left plot: ZEUS-S PDFs; middle plot: CTEQ6.1 PDFs; right plot: CTEQ6.1 PDFs which have been passed through the ATLFast detector simulation and corrected back to generator level using ZEUS-S PDFs; compared to the analytic prediction using ZEUS-S PDFs. Bottom row: the same lepton rapidity spectra as above compared to the analytic prediction *after* including these lepton pseudo-data in the ZEUS-S PDF fit.

systematic errors, rather than the statistical errors, which are determining. Our experience with the detector simulation leads us to believe that a systematic precision of  $\sim 5\%$  could be achievable. We have optimistically imposed a random 4% scatter on our samples of one million  $W$  events, generated using different PDFs, in order to investigate if measurements at this level of precision will improve PDF uncertainties at central rapidity significantly, if they are input to a global PDF fit.

The upper left hand plot of Fig. 14 shows the  $e^+$  rapidity spectrum for events generated from the ZEUS-S PDFs compared to the analytic predictions for the same ZEUS-S PDFs. The lower left hand plot illustrates the result if these events are then included in the ZEUS-S PDF fit (together with the  $e^-$  spectra which are not illustrated). The size of the PDF uncertainties, at  $y = 0$ , decreases from 6% to 4.5%. The largest improvement is in the PDF parameter  $\lambda_g$ , controlling the low- $x$  gluon at the input scale,  $Q_0^2$ :  $xg(x) \sim x^{\lambda_g}$  at low- $x$ ,  $\lambda_g = -0.199 \pm 0.046$ , before the input of the LHC pseudo-data, compared to,  $\lambda_g = -0.196 \pm 0.029$ , after input. Note that whereas the relative normalizations of the  $e^+$  and  $e^-$  spectra are set by the PDFs, the absolute normalization of the data is free in the fit, so that no assumptions are made on our ability to measure luminosity. Secondly, we repeat this procedure for events generated using the CTEQ6.1 PDFs. This is illustrated in the middle section of Fig. 14. Before they are input to the fit, the cross section for these events is on the lower edge of the uncertainty band of the ZEUS-S predictions (upper middle plot). If these events are then input to the fit the central value shifts and the uncertainty decreases (lower middle plot). The value of the parameter  $\lambda_g$  becomes,  $\lambda_g = -0.189 \pm 0.029$ , after input of these pseudo-data. Finally, to simulate the situation which really faces experimentalists, we generate events with CTEQ6.1, and pass them through the ATLFast detector simulation and cuts. We then correct back from detector level to generator level using a different PDF set - in this cases the ZEUS-S PDFs - since in practice we will not know the true PDFs. The upper right hand plot of Fig. 14 shows that the resulting corrected data look pleasingly like CTEQ6.1, but they are more smeared. When these data are input to the PDF fit the central values shift and errors decrease (lower right plot) just as for the perfect CTEQ6.1 pseudo data. The value of  $\lambda_g$  becomes,  $\lambda = -0.181 \pm 0.030$ , after input of these pseudo data. Thus we see that the bias introduced by the correction procedure from detector to generator level is small compared to the PDF uncertainty, and that measurements at the  $\sim 4\%$  level should be able to improve the level of uncertainty of the PDF predictions.

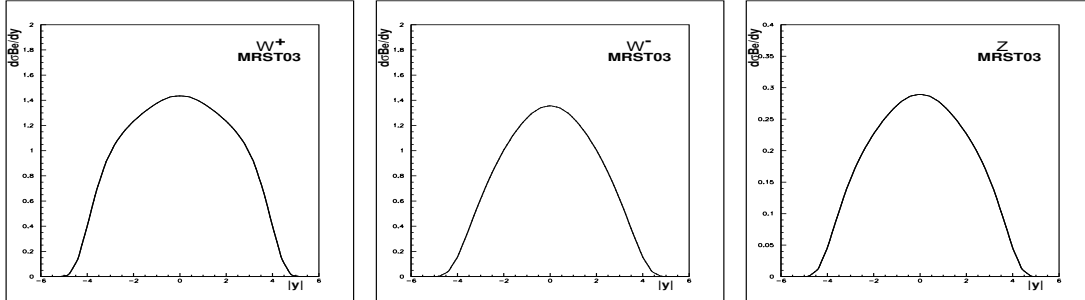


Fig. 15:  $W^+$ ,  $W^-$  and  $Z$  rapidity distributions for the MRST03 PDFs at the LHC: left plot:  $W^+$ ; middle plot:  $W^-$ ; right plot:  $Z$ .

#### 4.15 Conclusions

We have investigated the PDF uncertainty on the predictions for  $W$  and  $Z$  production at the LHC, using the electron decay channel for the  $W$  bosons and taking into account realistic expectations for the measurement accuracy and the cuts on data which will be needed to identify signal events from background processes. We conclude that, at the present level of PDF uncertainty, the decay lepton spectra can be used as a luminosity monitor but it is only good to  $\sim 10\%$ . However, we have also investigated the measurement accuracy necessary for early measurements of these decay lepton spectra to be useful in further constraining the PDFs. A systematic measurement error of  $\sim 4\%$  could provide useful extra constraints.

The ratio of  $Z$  to  $W^+ + W^-$  production (measured via the lepton spectra) can provide an SM measurement which is relatively insensitive to PDF uncertainties. By contrast, a measurement of the lepton asymmetry can provide the first measurements of the valence difference  $u_v - d_v$  at small  $x$ .

We now return to the caveat made in the introduction: the current study has been performed using standard PDF sets which are extracted using NLO QCD in the DGLAP formalism. The extension to NNLO is straightforward, giving small corrections  $\sim 1\%$ . PDF analyses at NNLO including full accounting of the PDF uncertainties are not extensively available yet, so this small correction has not been pursued here. However, there may be much larger uncertainties in the theoretical calculations because the kinematic region involves low- $x$ . The MRST group recently produced a PDF set, MRST03, which does not include any data for  $x < 5 \times 10^{-3}$ , in order to avoid the inappropriate use of the DGLAP formalism at small- $x$ . Thus the MRST03 PDF set should only be used for  $x > 5 \times 10^{-3}$ . What is needed is an alternative theoretical formalism for smaller  $x$ , as explained in Sec. 4.2. It is clear that the use of this formalism would bring greater changes than the small corrections involved in going to NNLO. There may even be a need for more radical extensions of the theory at low- $x$  due to high density effects.

The MRST03 PDF set may be used as a toy PDF set, to illustrate the effect of using very different PDF sets on our predictions. A comparison of Fig. 15 with Fig. 9 or Fig. 10 shows how different the analytic predictions are from the conventional ones, and thus illustrates where we might expect to see differences due to the need for an alternative formalism at small- $x$ . Whereas these results may seem far fetched, we should remind ourselves that moving into a different kinematic regime can provide surprises - as it did with the HERA data itself!

## 4.2 Resummed Perturbative Evolution at High Energy <sup>7</sup>

### 4.21 Introduction

Logarithmic enhancement of higher order perturbative result may take place when more than one large scale ratio is present. In DIS and DY this happens in the two opposite limits when the centre-of-mass energy of the partonic collision is close to the threshold for the production of the final state, or much

<sup>7</sup>Author: R.D. Ball



higher than the characteristic scale of the process. These correspond respectively to the small- $x$  and large- $x$  kinematical regions, where  $0 \leq x \leq 1$  is defined in terms of the invariant mass of the non-leptonic final state  $\frac{(1-x)Q^2}{x}$ . The corresponding perturbative contributions are respectively enhanced by powers of  $\ln \frac{1}{x}$  and  $\ln(1-x)$ , or, equivalently, in the space of Mellin moments, by powers of  $\frac{1}{N}$  and  $\ln N$ , where  $N \rightarrow 0$  moments dominate as  $x \rightarrow 0$  while  $N \rightarrow \infty$  moments dominate as  $x \rightarrow 1$ . Here we will be concerned only with the small- $x$  (and thus small  $N$ ) region.

In the DGLAP evolution equation one resums collinear logarithms first, resulting at LO and NLO in a good description of many data sets, and in particular the HERA  $F_2$  data at perturbative  $Q^2$  and values of  $x$  as low as  $10^{-4}$  [50–52]. However in the singlet (gluonic) channel the fixed order splitting functions contain small- $x$  logarithms also, which at NNLO [53] begin to destabilise the perturbative expansion, so that a further resummation is needed if the evolution is to be reliable at small  $x$ . Small- $x$  logarithms may be resummed by using the BFKL equation [54–56]. However the fixed order kernels of this equation, currently known to NLO [57] are perturbatively unstable for all realistic values of  $\alpha_s$ , and are thus by themselves useless for reliable calculations [58–60]. This is because they contain collinear logarithms, which must be resummed even at LO if reliable predictions are to be obtained [61]. This collinear resummation of the BFKL kernel restores longitudinal momentum conservation [62], and leads ultimately to a stable expansion.

Two approaches to the simultaneous resummation of these two classes of logs have recently reached the stage where their phenomenological application can be envisaged. In the duality (ABF) approach [62–68] one concentrates on the problem of obtaining an improved anomalous dimension (splitting function) for DIS which reduces to the ordinary perturbative result at large  $N$  (large  $x$ ), while including resummed BFKL corrections at small  $N$  (small  $x$ ), determined through the BFKL kernel. The CCSS approach [69–72] is built up within the BFKL framework, by improving the whole hierarchy of subleading kernels in the collinear region consistently with the renormalization group. The BFKL equation is then solved and a perturbative splitting function extracted numerically.

Here we will briefly review the theoretical underpinnings of the duality approach, and then compare phenomenological results obtained in both approaches.

#### 4.22 High Energy Duality

In the ABF approach one constructs an improved anomalous dimension (splitting function) for DIS which reduces to the ordinary perturbative result at large  $N$  (large  $x$ ) given by:

$$\gamma(N, \alpha_s) = \alpha_s \gamma_0(N) + \alpha_s^2 \gamma_1(N) + \alpha_s^3 \gamma_2(N) \dots \quad (15)$$

while including resummed BFKL corrections at small  $N$  (small  $x$ ) which are determined by the aforementioned BFKL kernel  $\chi(M, \alpha_s)$ :

$$\chi(M, \alpha_s) = \alpha_s \chi_0(M) + \alpha_s^2 \chi_1(M) + \dots, \quad (16)$$

which is the Mellin transform of the angular-averaged kernel  $K$  with respect to  $t = \ln \frac{k^2}{k_0^2}$ . The main theoretical tool which enables this construction is the duality relation between the kernels  $\chi$  and  $\gamma$

$$\chi(\gamma(N, \alpha_s), \alpha_s) = N, \quad (17)$$

which is a consequence of the fact that the solutions of the BFKL and DGLAP equations coincide at leading twist [60, 62, 73]. Further improvements are obtained exploiting the symmetry under gluon interchange of the BFKL gluon-gluon kernel and through the inclusion of running coupling effects.

By using duality, one can construct a more balanced expansion for both  $\gamma$  and  $\chi$ , the "double leading" (DL) expansion, where the information from  $\chi$  is used to include in  $\gamma$  all powers of  $\alpha_s/N$  and, conversely,  $\gamma$  is used to improve  $\chi$  by all powers of  $\alpha_s/M$ . A great advantage of the DL expansion is

that it resums the collinear poles of  $\chi$  at  $M = 0$ , enabling the imposition of the physical requirement of momentum conservation  $\gamma(1, \alpha_s) = 0$ , whence, by duality:

$$\chi(0, \alpha_s) = 1. \quad (18)$$

This procedure eliminates in a model-independent way the alternating sign poles  $+1/M, -1/M^2, \dots$  that appear in  $\chi_0, \chi_1, \dots$ . These poles make the perturbative expansion of  $\chi$  unreliable even in the central region of  $M$ : e.g.,  $\alpha_s \chi_0$  has a minimum at  $M = 1/2$ , while, at realistic values of  $\alpha_s$ ,  $\alpha_s \chi_0 + \alpha_s^2 \chi_1$  has a maximum.

At this stage, while the poles at  $M = 0$  are eliminated, those at  $M = 1$  remain, so that the DL expansion is still not finite near  $M = 1$ . The resummation of the  $M = 1$  poles can be accomplished by exploiting the collinear-anticollinear symmetry, as in the CCSS approach [69–71]. In Mellin space, this symmetry implies that at the fixed-coupling level the kernel  $\chi$  for evolution in  $\ln \frac{s}{kk_0}$  must satisfy  $\chi(M) = \chi(1 - M)$  order by order in perturbation theory. This symmetry is however broken by the DIS choice of variables  $\ln \frac{1}{x} = \ln \frac{s}{Q^2}$  and by the running of the coupling. In the fixed-coupling limit the kernel  $\chi_{\text{DIS}}$ , dual to the DIS anomalous dimension, is related to the symmetric one  $\chi_\sigma$  through the implicit equation [57]

$$\chi_{\text{DIS}} \left( M + \frac{1}{2} \chi_\sigma(M) \right) = \chi_\sigma(M). \quad (19)$$

Hence, the  $M = 1$  poles can be resummed by performing the double-leading resummation of  $M = 0$  poles of  $\chi_{\text{DIS}}$ , determining the associated  $\chi_\sigma$  through eq. (19), then symmetrizing it, and finally going back to DIS variables by using eq. (19) again in reverse. Using the momentum conservation eq. (18) and eq. (19), it is easy to show that  $\chi_\sigma(M)$  is an entire function of  $M$ , with  $\chi_\sigma(-1/2) = \chi_\sigma(3/2) = 1$ , and thus necessarily has a minimum at  $M = 1/2$ . Through this procedure one obtains order by order from the DL expansion a symmetrized DL kernel  $\chi_{\text{DIS}}$ , and its corresponding dual anomalous dimension  $\gamma$ . The kernel  $\chi_{\text{DIS}}$  has to all orders a minimum and satisfies a momentum conservation constraint  $\chi_{\text{DIS}}(0) = \chi_{\text{DIS}}(2) = 1$ .

The final ingredient of the ABF approach is a treatment of the running coupling corrections to the resummed terms. Indeed, their inclusion in the resummed anomalous dimension greatly softens the asymptotic behavior near  $x = 0$ . Hence, the dramatic rise of structure functions at small  $x$ , which characterized resummations based on leading-order BFKL evolution, and is ruled out phenomenologically, is replaced by a much milder rise. This requires a running coupling generalization of the duality equation (17), which is possible noting that in  $M$  space the running coupling  $\alpha_s(t)$  becomes a differential operator, since  $t \rightarrow d/dM$ . Hence, the BFKL evolution equation for double moments  $G(N, M)$ , which is an algebraic equation at fixed coupling, becomes a differential equation in  $M$  for running coupling. In the ABF approach, one solves this differential equation analytically when the kernel is replaced by its quadratic approximation near the minimum. The solution is expressed in terms of an Airy function if the kernel is linear in  $\alpha_s$  [64], for example in the case of  $\alpha_s \chi_0$ , or of a Bateman function in the more general case of a non linear dependence on  $\alpha_s$  [68] as is the case for the DL kernels. The final result for the improved anomalous dimension is given in terms of the DL expansion plus the ‘‘Airy’’ or ‘‘Bateman’’ anomalous dimension, with the terms already included in the DL expansion subtracted away.

For example, at leading DL order, i.e. only using  $\gamma_0(N)$  and  $\chi_0(M)$ , the improved anomalous dimension is

$$\begin{aligned} \gamma_I^{NL}(\alpha_s, N) &= [\alpha_s \gamma_0(N) + \alpha_s^2 \gamma_1(N) + \gamma_s \left( \frac{\alpha_s}{N} \right) - \frac{n_c \alpha_s}{\pi N}] \\ &\quad + \gamma_A(c_0, \alpha_s, N) - \frac{1}{2} + \sqrt{\frac{2}{\kappa_0 \alpha_s} [N - \alpha_s c_0]}. \end{aligned} \quad (20)$$

The terms within square brackets give the LO DL approximation, i.e. they contain the fixed-coupling information from  $\gamma_0$  and (through  $\gamma_s$ ) from  $\chi_0$ . The ‘‘Airy’’ anomalous dimension  $\gamma_A(c_0, \alpha_s, N)$  contains

the running coupling resummation, i.e. it is the exact solution of the running coupling BFKL equation which corresponds to a quadratic approximation to  $\chi_0$  near  $M = 1/2$ . The last two terms subtract the contributions to  $\gamma_A(c_0, \alpha_s, N)$  which are already included in  $\gamma_s$  and  $\gamma_0$ . In the limit  $\alpha_s \rightarrow 0$  with  $N$  fixed,  $\gamma_I(\alpha_s, N)$  reduces to  $\alpha_s \gamma_0(N) + O(\alpha_s^2)$ . For  $\alpha_s \rightarrow 0$  with  $\alpha_s/N$  fixed,  $\gamma_I(\alpha_s, N)$  reduces to  $\gamma_s(\frac{\alpha_s}{N}) + O(\alpha_s^2/N)$ , i.e. the leading term of the small- $x$  expansion. Thus the Airy term is subleading in both limits. However, if  $N \rightarrow 0$  at fixed  $\alpha_s$ , the Airy term replaces the leading singularity of the DL anomalous dimension, which is a square root branch cut, with a simple pole, located on the real axis at rather smaller  $N$ , thereby softening the small- $x$  behaviour. The quadratic approximation is sufficient to give the correct asymptotic behaviour up to terms which are of subleading order in comparison to those included in the DL expression in eq. (20).

The running coupling resummation procedure can be applied to a symmetrized kernel, which possesses a minimum to all orders, and then extended to next-to-leading order [67, 68]. This entails various technical complications, specifically related to the nonlinear dependence of the symmetrized kernel on  $\alpha_s$ , to the need to include interference between running coupling effects and the small  $x$  resummation, and to the consistent treatment of next-to-leading  $\log Q^2$  terms, in particular those related to the running of the coupling.

### 4.23 Results

Even though the basic underlying physical principles of the ABF and CCSS approaches are close, there are technical differences in the construction of the symmetrized DL kernel, in the derivation from it of an anomalous dimension and associated splitting function, and in the inclusion of running coupling effects. Therefore, we will compare results for the resummed fixed-coupling  $\chi$  kernel (BFKL characteristic function), then the corresponding fixed-coupling splitting functions, and finally the running coupling splitting functions which provide the final result in both approaches. In order to assess the phenomenological impact on parton evolution we will finally compare the convolution of the splitting function with a “typical” gluon distribution.

In fig. 16 we show the solution  $\chi_{\text{DIS}}$  of eq. (19) for the symmetrized NLO DL kernel. The pure  $Lx$  and  $NLx$  (BFKL) and next-to-leading  $\ln Q^2$  (DGLAP) are also shown. All curves are determined with frozen coupling ( $\beta_0 = 0$ ), and with  $n_f = 0$ , in order to avoid complications related to the diagonalization of the DGLAP anomalous dimension matrix and to the choice of scheme for the quark parton distribution. Also shown is the corresponding resummed kernel in the RGI CCSS approach. The resummed ABF and CCSS results are very close, the main difference being due to the fact that at small  $M$  the ABF result coincides by construction with NLO DGLAP, whereas for very small  $M$  (i.e. large  $x$ ) the CCSS result reduces to LO DGLAP. Because of the underlying symmetry this small difference is also seen in the anticollinear region  $M \sim 1$ , though the two curves coincide by construction at the momentum conservation points  $M = 0$  and  $M = 2$ . In comparison to DGLAP, the resummed kernels have a minimum, related to the fact that both collinear and anticollinear logs are resummed. In comparison to BFKL, which has a minimum at LO but not NLO, the resummed kernels always have a perturbatively stable minimum, characterized by a lower intercept than leading-order BFKL: specifically, when  $\alpha_s = 0.2$ ,  $\lambda \sim 0.25$  instead of  $\lambda \sim 0.5$ . This corresponds to a softer small- $x$  rise of the associated splitting function.

The fixed-coupling resummed splitting functions up to NLO are shown in figure 17, along with the unresummed DGLAP splitting functions up to NNLO. For  $n_f = 0$  the NLO DGLAP splitting function has the property that it vanishes at small  $x$  — this makes it relatively straightforward to combine not just LO DGLAP but also NLO DGLAP with the NLL $x$  resummation. In the ABF approach the splitting function is the inverse Mellin transform of the anomalous dimension obtained using duality eq. (17) from the symmetrized DL  $\chi$  kernel. Hence, the LO and NLO resummed result respectively reproduce all information contained in the LO and NLO  $\chi$  and  $\gamma$  kernel with the additional constraint of collinear-anticollinear symmetry. Both the ABF LO and NLO results are shown in figure 17. The CCSS  $NLx+LO$

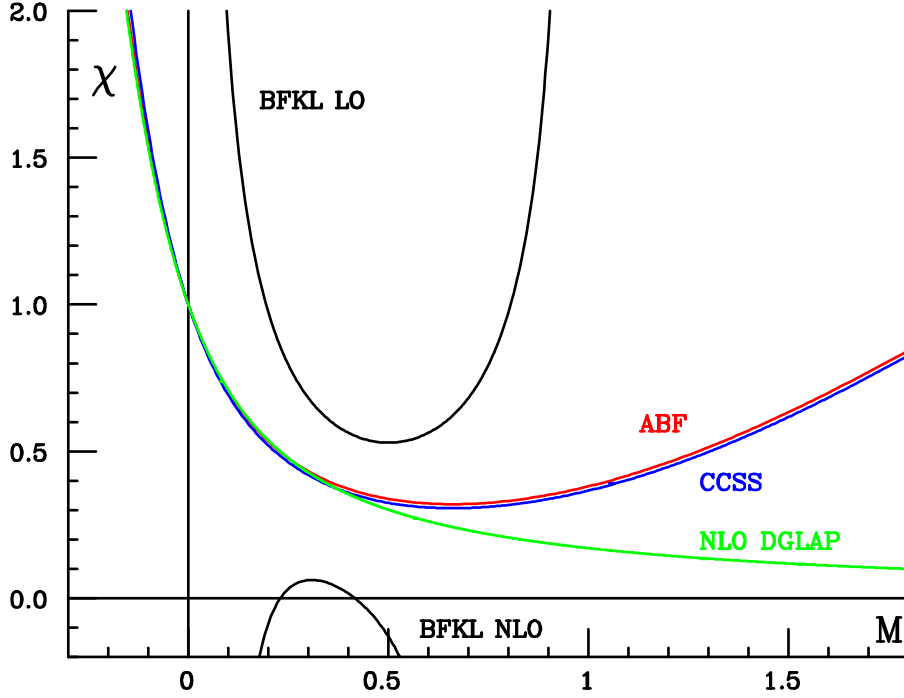


Fig. 16: The kernel  $\chi$  (BFKL characteristic function) for fixed coupling ( $\beta_0 = 0$ )  $\alpha_s = 0.2$  and  $n_f = 0$ . The BFKL curves are the LO and NLO truncations of eq. (16), the DGLAP curve is the dual eq. (17) of the NLO anomalous dimension eq. (15), while the ABF and CCSS curves are respectively the solution  $\chi_{\text{DIS}}$  of eq. (19) and the solution for  $\omega$  of a similar eqn. in the CCSS approach.

and  $NLx+NLO$  curves are also shown for comparison.

In comparison to unresummed results, the resummed splitting functions display the characteristic rise at small  $x$  of fixed-coupling leading-order BFKL resummation, though the small- $x$  rise is rather milder ( $\sim x^{-0.25}$  instead of  $\sim x^{-0.5}$  for  $\alpha_s = 0.2$ ). At large  $x$  there is good agreement between the resummed results and the corresponding LO (dashed) or NLO (solid) DGLAP curves. At small  $x$  the difference between the ABF LO and CCSS  $NLx+LO$  (dashed) curves is mostly due to the different way the symmetrization is implemented, as both approaches contain the same dominant small- $x$  terms. This difference is reduced when one compares the CCSS  $NLx+nLO$  with ABF NLO, and it might be taken as an estimate of the intrinsic ambiguity of the fixed-coupling resummation procedure. At intermediate  $x$  the NLO resummed splitting functions is of a similar order of magnitude as the NLO DGLAP result even down to quite small  $x$ , but with a rather different shape, characterized by a dip at  $x \sim 10^{-3}$ . The unstable small- $x$  drop of the NNLO DGLAP result is consequence of the unresummed  $\frac{\alpha_s^3}{N^2}$  double pole in the NNLO anomalous dimension.

The running-coupling resummed splitting functions are displayed in figure 18. Note that the unresummed curves are the same as in the fixed coupling case since their dependence on  $\alpha_s$  is just through a prefactor of  $\alpha_s^k$ , whereas in the resummed case there is an interplay between the running of the coupling and the structure of the small- $x$  logs. All the resummed curves display a considerable softening of the small- $x$  behaviour in comparison to their fixed-coupling counterparts, due to the softening of the leading small- $x$  singularity in the running-coupling case [64, 69]. As a consequence, the various resummed results are closer to each other than in the fixed-coupling case, and also closer to the unresummed LO and NLO DGLAP results. The resummed perturbative expansion appears to be stable, subject to moderate theoretical ambiguity, and qualitatively close to NLO DGLAP.

Finally, to appreciate the impact of resummation it is useful to investigate not only the properties of the splitting function, but also its convolution with a physically reasonable gluon distribution. We take

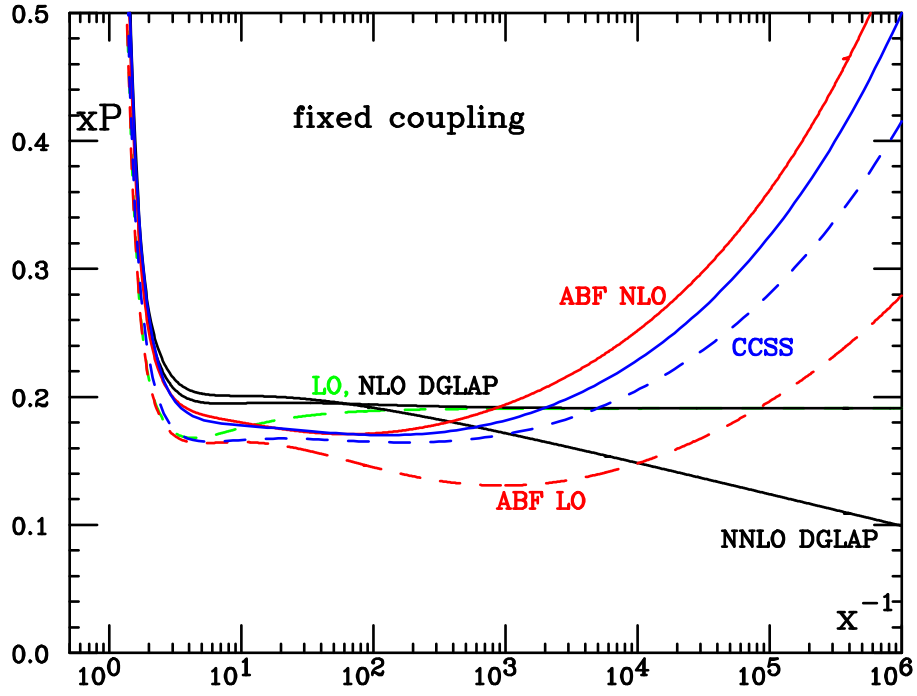


Fig. 17: The fixed coupling ( $\beta_0 = 0$ )  $xP_{gg}(x)$  splitting function, evaluated with  $\alpha_s = 0.2$  and  $n_f = 0$ . The dashed curves are LO for DGAP, symmetrized LO DL for ABF, and  $NLx+LO$  for CCSS, while the solid curves are NLO and NNLO for DGLAP, symmetrized NLO DL for ABF and  $NLx+NLO$  for CCSS.

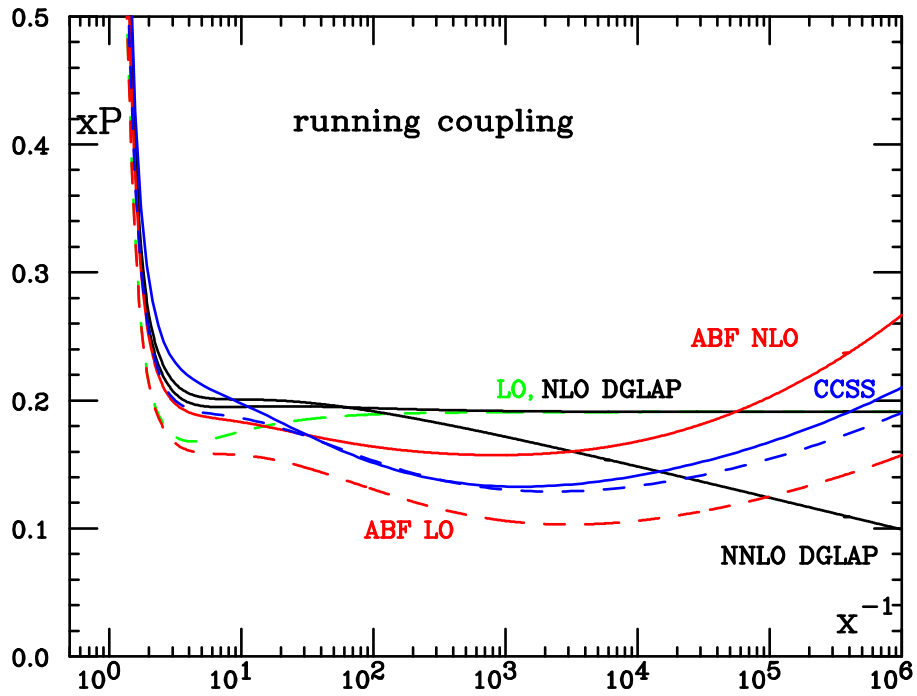


Fig. 18: The running coupling  $xP_{gg}(x)$  splitting function, evaluated with  $\alpha_s = 0.2$  and  $n_f = 0$ . The various curves correspond to the same cases as in figure 17.

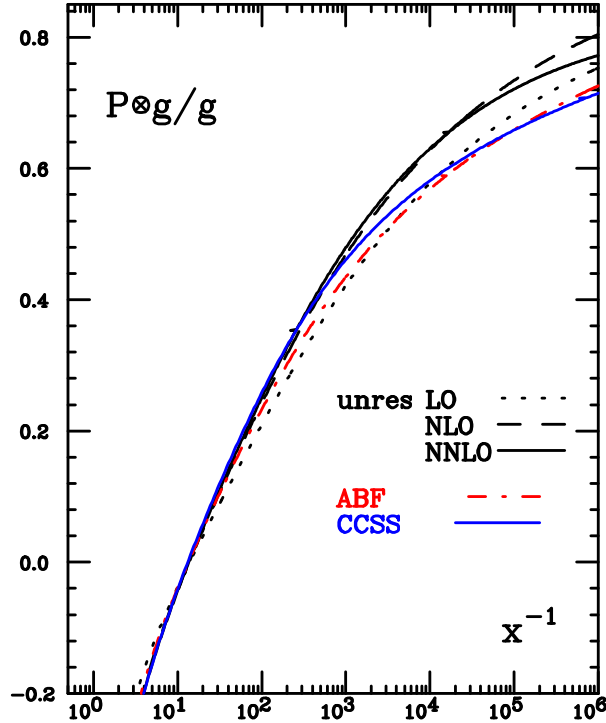


Fig. 19: Convolution of resummed and fixed-order  $P_{gg}$  splitting functions with a toy gluon distribution, eq. (21), normalised to the gluon distribution itself, with  $\alpha_s = 0.2$  and  $n_f = 0$ . The resummed ABF and CCSS curves are obtained using respectively the ABF NLO and CCSS  $NLx+NLO$  splitting function shown in fig. 18.

the following toy gluon

$$xg(x) = x^{-0.18}(1-x)^5, \quad (21)$$

and show in fig. 19 the result of its convolution with various splitting functions of fig. 18. The differences between resummed and unresummed results, and between the ABF and CCSS resummations are as expected partly washed out by the convolution, even though the difference between the unresummed LO and NLO DGLAP results is clearly visible. In particular, differences between the fixed-order and resummed convolution start to become significant only for  $x$  below  $10^{-2} - 10^{-3}$ , even though resummation effects started to be visible in the splitting functions at somewhat larger  $x$ . However it should be clear from this figure why the structure function data from HERA were so well described by LO and NLO GLAP evolution [50–52]: significant deviations from GLAP will only be seen for smaller  $x$  and larger  $Q^2$  than is accessible at HERA, but may well be important for many important processes at the LHC.

### 4.3 Hunting BFKL at Hadron Colliders <sup>8</sup>

#### 4.3.1 Introduction

With its unprecedented kinematic range, the LHC offers an unique opportunity to explore strong-interaction processes characterised by two large and disparate scales. In inclusive di-jet production, for instance, jets of transverse energy  $E_T = 50$  GeV may span a rapidity interval of up to about 10 units of rapidity. Processes with two large and disparate scales may contain large logarithms of the ratio of those scales. The interest in such processes arises from the Balitsky-Fadin-Kuraev-Lipatov (BFKL) equation [54–56], which performs an all-order resummation in  $\alpha_S$  of the leading logarithms (LL) of  $\ln(\hat{s}/|\hat{t}|)$ , with  $\hat{s}$  the squared parton centre-of-mass energy,  $\hat{t}$  a typical momentum transfer, and  $\hat{s} \gg |\hat{t}|$ .

<sup>8</sup>Author: V. Del Duca



The generality of the resummation is based on the fact that gluon exchange in the  $t$  channel dominates in any scattering process with  $\hat{s} \gg |\hat{t}|$ . The BFKL formalism then re-sums the multiple gluon radiation out of the gluon exchanged in the  $t$  channel. The LL terms are obtained in the approximation of a strong rapidity ordering of the emitted gluons. The resummation yields an integral equation which describes the evolution of the gluon propagator in the  $t$  channel, and whose kernel is formed by the emission of a gluon along the ladder and by the LL contribution to a gluon-loop exchange in the ladder. By putting together the emission of two close-in-rapidity gluons [74, 75] and a  $q\bar{q}$  pair [76–80] along the ladder, the one-loop corrections [81–84] to the emission of a gluon along the ladder, and the next-to-leading-logarithmic (NLL) [85–89] contribution to a gluon two-loop exchange in the ladder, also the NLL corrections [57, 90, 91] to the BFKL equation have been computed.

#### 4.32 Jets at large rapidity intervals

During the last two decades, a large body of work has been dedicated to predict and detect footprints of emission of BFKL gluon radiation in strong-interaction processes, like di-jet production at large rapidity intervals [92–97],  $W$ -boson production in association with jets [98], heavy-quark production at hadron colliders [79, 80, 99, 100]; forward-jet production [101–111], forward-pion production [103, 112, 113] and transverse-energy flow [101, 113, 114] in DIS;  $\gamma^*\gamma^*$  collisions in double-tag events,  $e^+e^- \rightarrow e^+e^- +$  hadrons [115–123]. All that the processes above have in common is a large logarithm: in di-jet production at large rapidity intervals, for instance, the large logarithm is the rapidity interval between the jets,  $\Delta y \simeq \ln(\hat{s}/E_{T1}E_{T2})$ , with  $E_{T1}$  and  $E_{T2}$  the transverse energies of the two tagged jets; in forward-jet production in DIS the large logarithm is  $\ln(x/x_{bj})$ , where  $x_{bj}$  is the Bjorken scaling variable and  $x$  the momentum fraction of the parton entering the hard scattering; in  $\gamma^*\gamma^*$  collisions in  $e^+e^- \rightarrow e^+e^- +$  hadrons, the large logarithm is  $Y = \ln(y_1y_2S/\sqrt{Q_1^2Q_2^2})$ , with  $S$  the  $e^+e^-$  centre-of-mass energy, and  $y_i$  and  $Q_i^2$  the light-cone momentum fraction and the virtuality of the virtual photon  $i$ , with  $i = 1, 2$ .

From a theoretical point of view, di-jet production at large rapidity intervals is the simplest process to which to apply the BFKL resummation, because at leading order in  $\alpha_S$  it is just parton-parton scattering, which at large rapidity intervals is dominated by gluon exchange in the  $t$  channel. In fact, the  $t$ -channel gluon dominance is also used as a diagnostic tool for discriminating between different dynamical models for parton scattering. In the measurement of di-jet angular distributions, models which feature gluon exchange in the  $t$  channel, like QCD, predict the characteristic  $\sin^{-4}(\theta^*/2)$  di-jet angular distribution [124, 125], while models featuring contact-term interactions, which do not have gluon exchange in the  $t$  channel, predict a flattening of the di-jet angular distribution at large  $\hat{s}/|\hat{t}|$  [126, 127]. The phenomenological analysis of di-jet production at large rapidity intervals, though, is not so simple as its theoretical construct: since  $\hat{s} = x_a x_b S$ , with  $S$  the hadron centre-of-mass energy and  $x_a, x_b$  the momentum fractions of the partons entering the hard scattering, once the jet transverse energies are fixed, there are two ways of increasing  $\Delta y \simeq \ln(x_a x_b s/E_{T1}E_{T2})$ : by increasing the  $x$ 's in a fixed-energy collider; or viceversa, by fixing the  $x$ 's and letting  $S$  grow, in a ramping-run collider experiment. The former set-up, the only feasible at a collider run at fixed energy, like the Tevatron or the LHC, has been proven to be unpractical, since in the di-jet production rate  $d\sigma/d\Delta y$  as a function of  $\Delta y$  it is difficult to disentangle the BFKL-driven rise of the parton cross section from the steep fall-off of the parton densities [95]. The latter set-up, even though the first to be proposed [94], has been analysed only in the late 90's [93], because it required a collider running at different centre-of-mass energies, and it has become feasible only when the Tevatron has undertaken for a few days a run at  $\sqrt{S} = 630$  GeV, in addition to the usual  $\sqrt{S} = 1800$  GeV of Run I. However, a careful analysis at fixed  $x$ 's [97] has shown that in the kinematic reach of Tevatron di-jet production at large rapidity intervals is far from the BFKL asymptotic regime. Other processes of BFKL interest at hadron colliders are  $W$ -boson production in association with jets and heavy-quark production. The former is simpler to analyse experimentally than di-jet production, which is hindered by the complexity of triggering on jets in the forward calorimetry. In fact, if the  $W$  boson decays leptonically, it is more advantageous to trigger on the  $W$  decay products [98].

Heavy-quark production, although potentially interesting, is hampered by the fact that gluon exchange in the  $t$  channel is a higher-order effect: it occurs only at two orders of  $\alpha_S$  higher than the leading order, and the logarithms  $\ln(\hat{s}/|\hat{t}|)$  are not large enough, within the kinematic reach of Tevatron and LHC, to offset that initial handicap [100].

Forward-jet production in DIS consists of tagging a jet far in rapidity from the current-fragmentation region. In such a way, it is guaranteed that the momentum fraction  $x$  of the parton entering the hard scattering is much larger than the Bjorken-scaling variable  $x_{bj}$ , and a large logarithm  $\ln(x/x_{bj})$  arises. In such a case, gluon exchange in the  $t$  channel occurs at NLO (the leading order is the creation of a quark pair or of a quark and a gluon, because the parton-model process of a virtual photon knocking a quark off is constrained by  $x = x_{bj}$ , and thus it is forbidden by the forward-jet requirement). Although the NLO analysis falls short of describing the data [101–103], the LL BFKL prediction overshoots the data, calling for a NLL BFKL analysis which so far has not yet been performed. Recently, the improved statistics have allowed for an analysis of three-jet production in DIS, with one forward jet out of the three jets [104]. This process offers the advantage of having gluon exchange in the  $t$  channel already at leading order, thus the NLO analysis guarantees a better control over the theoretical uncertainties. In this case, the data are in good agreement with the NLO prediction for three-jet production [128].

$\gamma^*\gamma^*$  collisions in double-tag events,  $e^+e^- \rightarrow e^+e^- + \text{hadrons}$  have been analysed by the LEP collaborations [115–118]. There is good agreement with the NLO analysis [122], except for the higher values of  $Y$ . This is understandable, because gluon exchange in the  $t$  channel occurs only at NNLO. However, although a complete NNLO calculation is beyond the reach of the present technology, the contributions which feature gluon exchange in the  $t$  channel can be included exactly in the theoretical prediction. Doing so [123] improves the agreement between the data and the theory at the higher values of  $Y$ .

In conclusion, it is difficult to find strong, compelling evidence of the BFKL resummation in the comparison between the data and the theoretical analysis. That may be in part due to the fact that within the kinematic reach of the present colliders, the asymptotic region where the BFKL resummation is supposed to be applicable does not seem to have been reached yet. But also to the fact that the LL BFKL predictions are plagued by large theoretical uncertainties, while the NLL resummation, for which the analytic solution [57] and numerical Monte Carlo studies [129–133] exist, is not in a form yet that can be readily applied to the phenomenological analyses outlined above.

## 5. PARTON-PARTON LUMINOSITY FUNCTIONS FOR THE LHC <sup>9</sup>

### 5.1 Introduction

The number of events anticipated at the LHC for a process with a cross section  $\sigma$  can be calculated by multiplying the cross section times the beam-beam luminosity. There are a number of programs available to calculate cross sections for processes of interest at leading-order, next-to-leading order and next-to-next-to-leading order, and in some cases with parton showering and hadronization effects included [134]. But it is sometimes also useful to be able to make quick order-of-magnitude estimates for the sizes of cross sections. For hard interactions, the collision is not between the protons per se but between the partons in the two protons, carrying fractions  $x_1$  and  $x_2$  of their parent proton's momentum. A plot showing the parton kinematics at the LHC is shown in Fig. 20, indicating the relationship between the two parton  $x$  values and the mass  $M = \sqrt{\hat{s}}$  and rapidity  $y = \frac{1}{2} \ln(x_1/x_2)$  of the produced system. Thus, for example, a final state with a mass  $M = 100 \text{ GeV}$  and a rapidity  $y = 4$  is produced by two partons with  $x$  values of approximately 0.00015 and 0.35.

Because the interacting partons carry only a fraction of the parent proton's momentum, it is useful

---

<sup>9</sup>Contributed by: A. Belyaev, J. Huston, J. Pumplin

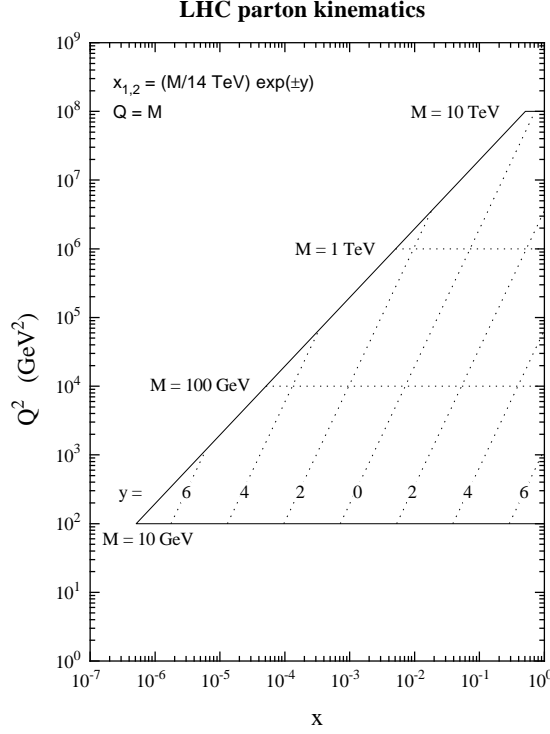


Fig. 20: Parton kinematics for the LHC.

to define the differential parton-parton luminosity  $dL_{ij}/d\hat{s} dy$  and its integral  $dL_{ij}/d\hat{s}$ :

$$\frac{dL_{ij}}{d\hat{s} dy} = \frac{1}{s} \frac{1}{1 + \delta_{ij}} [f_i(x_1, \mu) f_j(x_2, \mu) + (1 \leftrightarrow 2)] . \quad (22)$$

The prefactor with the Kronecker delta avoids double-counting in case the partons are identical. The generic parton-model formula

$$\sigma = \sum_{i,j} \int_0^1 dx_1 dx_2 f_i(x_1, \mu) f_j(x_2, \mu) \hat{\sigma}_{ij} \quad (23)$$

can then be written as

$$\sigma = \sum_{i,j} \int \left( \frac{d\hat{s}}{\hat{s}} dy \right) \left( \frac{dL_{ij}}{d\hat{s} dy} \right) (\hat{s} \hat{\sigma}_{ij}) . \quad (24)$$

(This result is easily derived by defining  $\tau = x_1 x_2 = \hat{s}/s$  and observing that the Jacobian  $\frac{\partial(\tau, y)}{\partial(x_1, x_2)} = 1$ .)

Equation 24 can be used to estimate the production rate for a hard scattering process at the LHC as follows. Figure 21(left) shows a plot of the luminosity function integrated over rapidity,  $dL_{ij}/d\hat{s} = \int (dL_{ij}/d\hat{s} dy) dy$ , at the LHC value  $\sqrt{s} = 14$  TeV for various parton flavor combinations, calculated using the CTEQ6.1 parton distribution functions [135]. The widths of the curves indicate an estimate for the PDF uncertainties. We assume  $\mu = \sqrt{\hat{s}}$  for the scale. (Similar plots made with earlier PDFs are shown in Ellis, Stirling, Webber [136].) On the other hand, Fig. 21(right) presents the second product,  $[\hat{s} \hat{\sigma}_{ij}]$ , for various  $2 \rightarrow 2$  partonic processes. The parton level cross sections are given for a parton  $p_T > 0.1 \times \sqrt{\hat{s}}$  cut and for fixed  $\alpha_s = 0.118$ . We have used the CalcHEP package [137] to estimate these cross sections. As expected, the  $gg$  luminosity is large at low  $\sqrt{\hat{s}}$  but falls rapidly with respect to

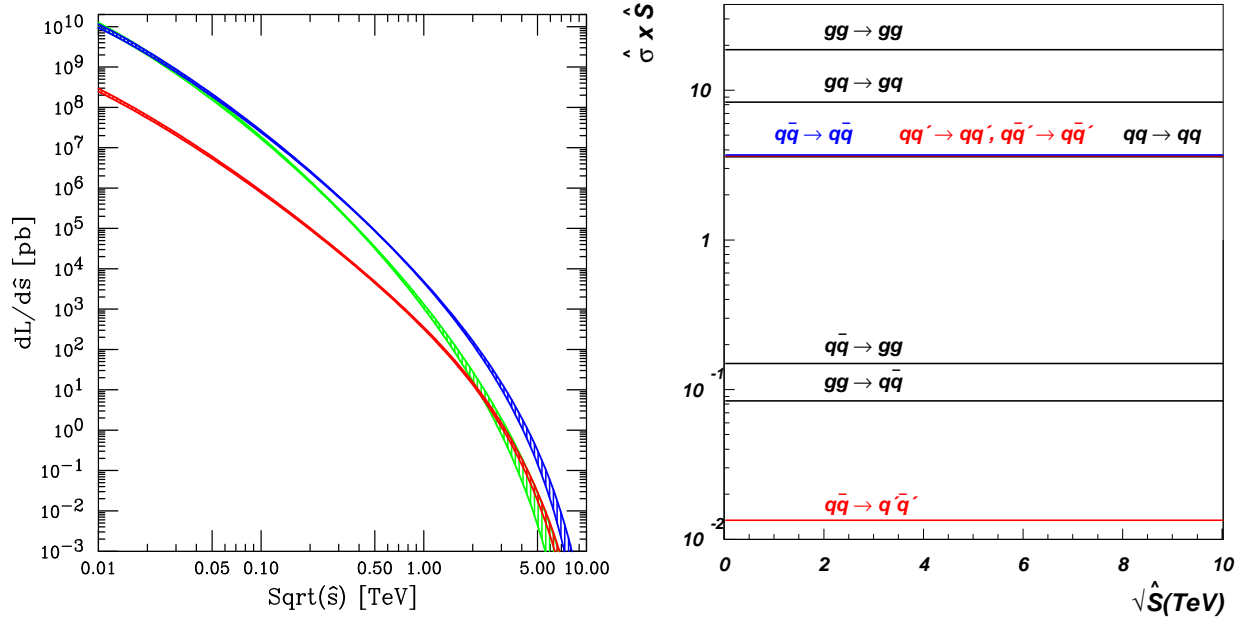


Fig. 21: Left: luminosity  $\left[\frac{1}{\hat{s}} \frac{dL_{ij}}{d\tau}\right]$  in pb integrated over  $y$ . Green= $gg$ , Blue= $g(d+u+s+c+b) + g(\bar{d}+\bar{u}+\bar{s}+\bar{c}+\bar{b}) + (d+u+s+c+b)g + (\bar{d}+\bar{u}+\bar{s}+\bar{c}+\bar{b})g$ , Red= $d\bar{d} + u\bar{u} + s\bar{s} + c\bar{c} + b\bar{b} + \bar{d}d + \bar{u}u + \bar{s}s + \bar{c}c + \bar{b}b$ . Right: parton level cross sections  $[\hat{s}\hat{\sigma}_{ij}]$  for various processes

the other parton luminosities. The  $gq$  luminosity is large over the entire kinematic region plotted.

One can use Equation 24 in the form

$$\sigma = \frac{\Delta\hat{s}}{\hat{s}} \left( \frac{dL_{ij}}{d\hat{s}} \right) (\hat{s}\hat{\sigma}_{ij}). \quad (25)$$

and Fig. 21 to estimate the production cross sections for QCD jets for a given  $\Delta\hat{s}$  interval. For example, for the gluon pair production rate for  $\hat{s}=1$  TeV and  $\Delta\hat{s} = 0.01\hat{s}$ , we have  $\frac{dL_{gg}}{d\hat{s}} \simeq 10^3$  pb and  $\hat{s}\hat{\sigma}_{gg} \simeq 20$  leading to  $\sigma \simeq 200$  pb (for the  $p_T^g > 0.1 \times \sqrt{\hat{s}}$  cut we have assumed above). Note that for a given small  $\Delta\hat{s}/\hat{s}$  interval, the corresponding invariant mass  $\Delta\sqrt{\hat{s}}/\sqrt{\hat{s}}$  interval, is  $\Delta\sqrt{\hat{s}}/\sqrt{\hat{s}} \simeq \frac{1}{2}\Delta\hat{s}/\hat{s}$ . One should also mention that all hard cross sections presented in Fig.21 are proportional to  $\alpha_s^2$  and have been calculated for  $\alpha_s = 0.118$ , so production rates can be easily rescaled for a certain  $\alpha_s$  at a given scale.

One can further specify the parton-parton luminosity for a specific rapidity  $y$  and  $\hat{s}$ ,  $dL_{ij}/d\hat{s} dy$ . If one is interested in a specific partonic initial state, then the resulting differential luminosity can be displayed in families of curves as shown in Fig. 22, where the differential parton-parton luminosity at the LHC is shown as a function of the subprocess center-of-mass energy  $\sqrt{\hat{s}}$  at various values of rapidity for the produced system for several different combinations of initial state partons. One can read from the curves the parton-parton luminosity for a specific value of mass fraction and rapidity. (It is also easy to use the Durham PDF plotter to generate the pdf curve for any desired flavor and kinematic configuration [138].)

It is also of great interest to understand the uncertainty for the parton-parton luminosity for specific kinematic configurations. Some representative parton-parton luminosity uncertainties are shown in Figs. 23-26. The PDF uncertainties were generated from the CTEQ6.1 Hessian error analysis using the standard  $\Delta\chi^2$  100 criterion. Except for kinematic regions where one or both partons is a gluon at high  $x$ , the pdf uncertainties are of the order of 5-10%. Even tighter constraints will be possible once the LHC Standard Model data is included in the global pdf fits. Again, the uncertainties for individual PDF's can also be calculated online using the Durham pdf plotter.

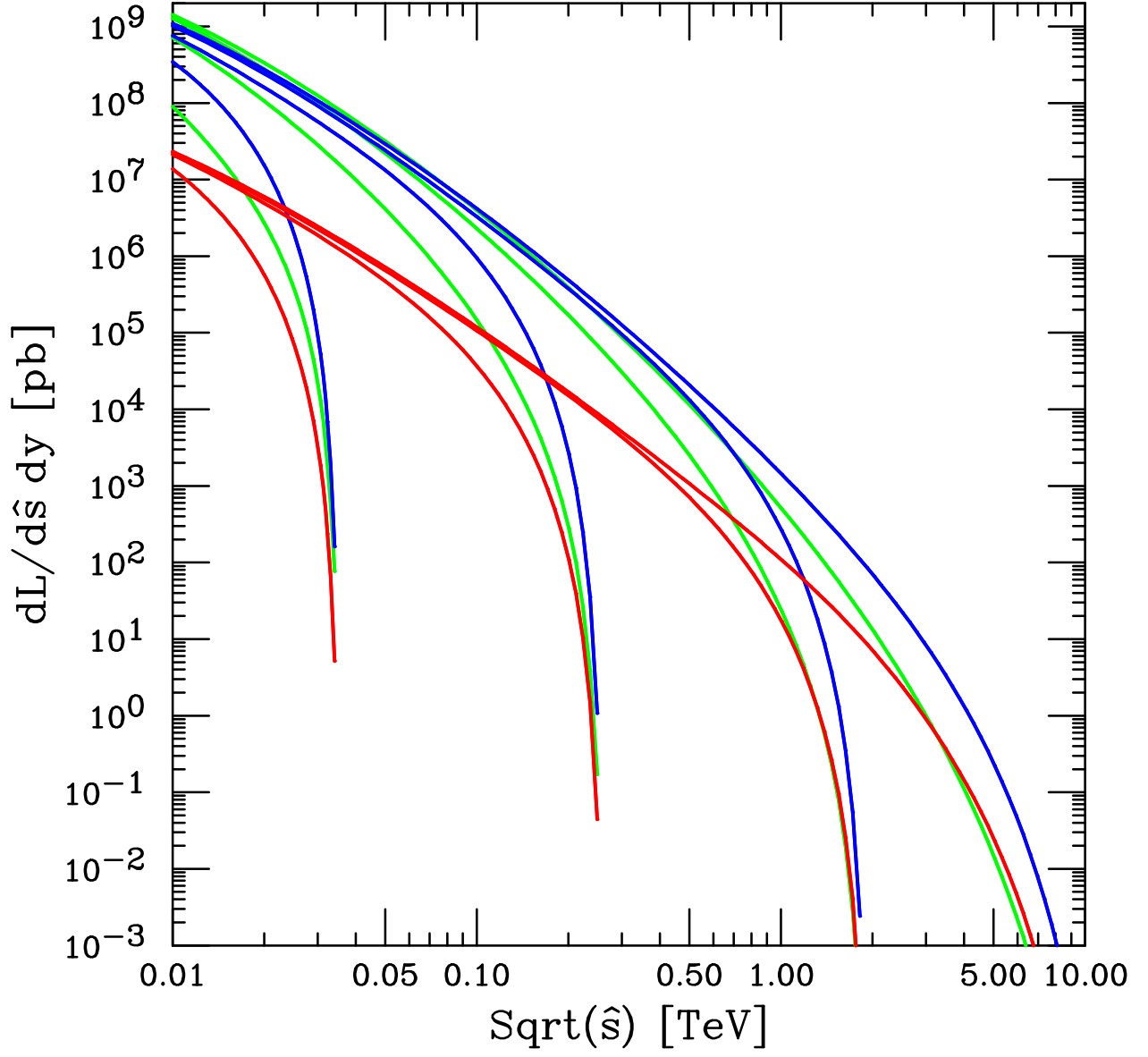


Fig. 22: dLuminosity/dy at  $y = 0, 2, 4, 6$ . Green= $gg$ , Blue= $g(d + u + s + c + b) + g(\bar{d} + \bar{u} + \bar{s} + \bar{c} + \bar{b}) + (d + u + s + c + b)g + (\bar{d} + \bar{u} + \bar{s} + \bar{c} + \bar{b})g$ , Red= $d\bar{d} + u\bar{u} + s\bar{s} + c\bar{c} + b\bar{b} + \bar{d}d + \bar{u}u + \bar{s}s + \bar{c}c + \bar{b}b$ .

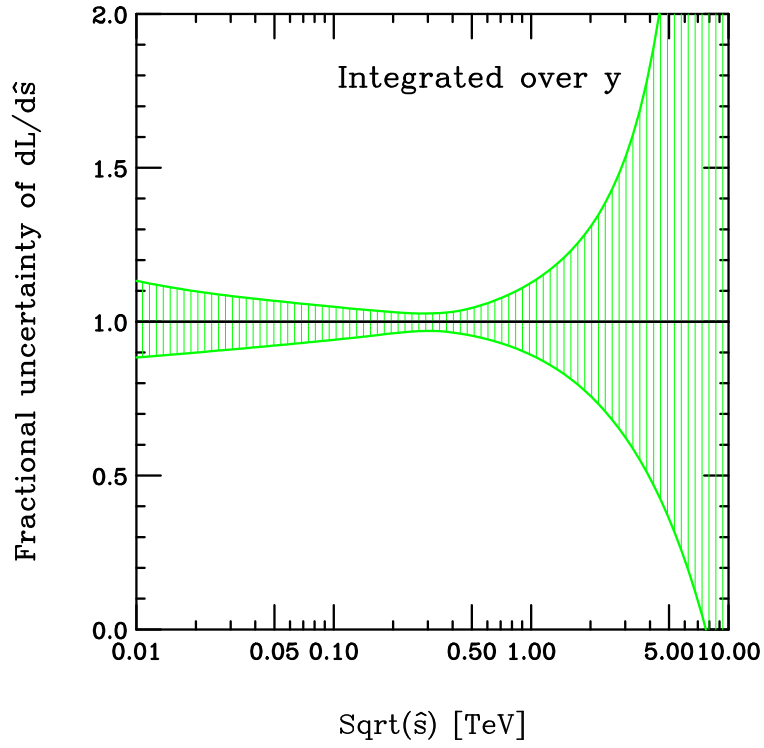


Fig. 23: Fractional uncertainty of  $gg$  luminosity integrated over  $y$ .

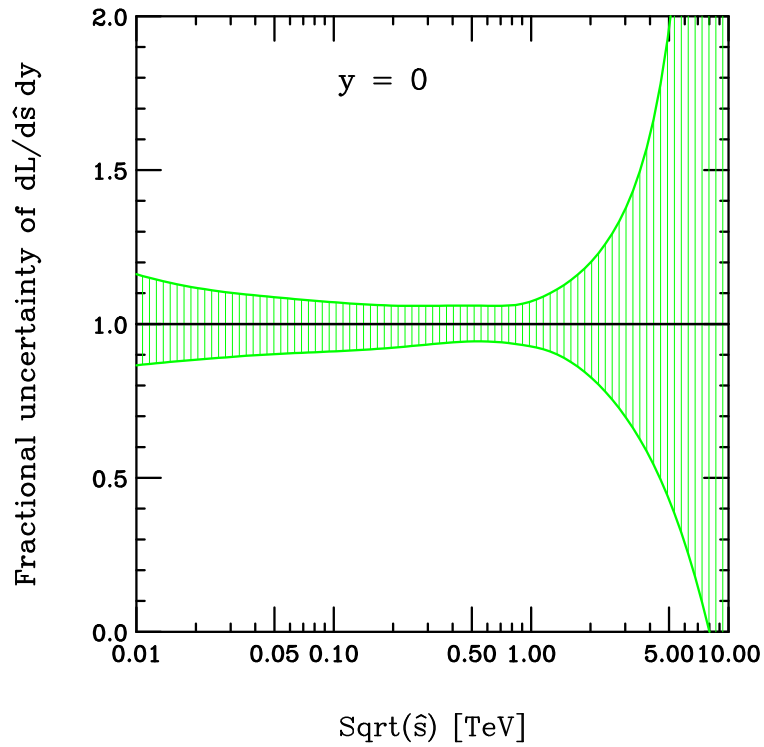


Fig. 24: Fractional uncertainty of  $gg$  luminosity at  $y = 0$ .

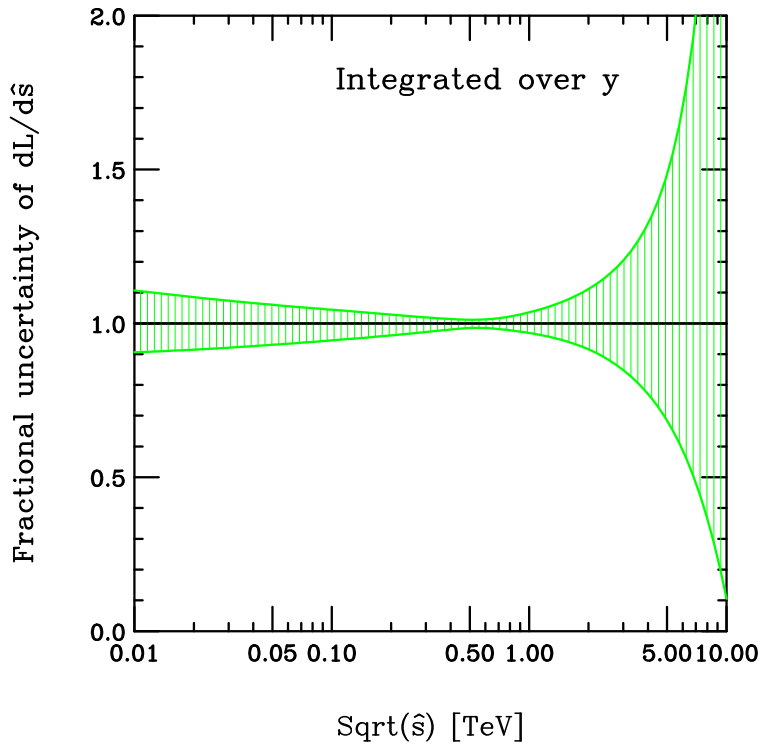


Fig. 25: Fractional uncertainty for Luminosity integrated over  $y$  for  $g(d + u + s + c + b) + g(\bar{d} + \bar{u} + \bar{s} + \bar{c} + \bar{b}) + (d + u + s + c + b)g + (\bar{d} + \bar{u} + \bar{s} + \bar{c} + \bar{b})g$ ,

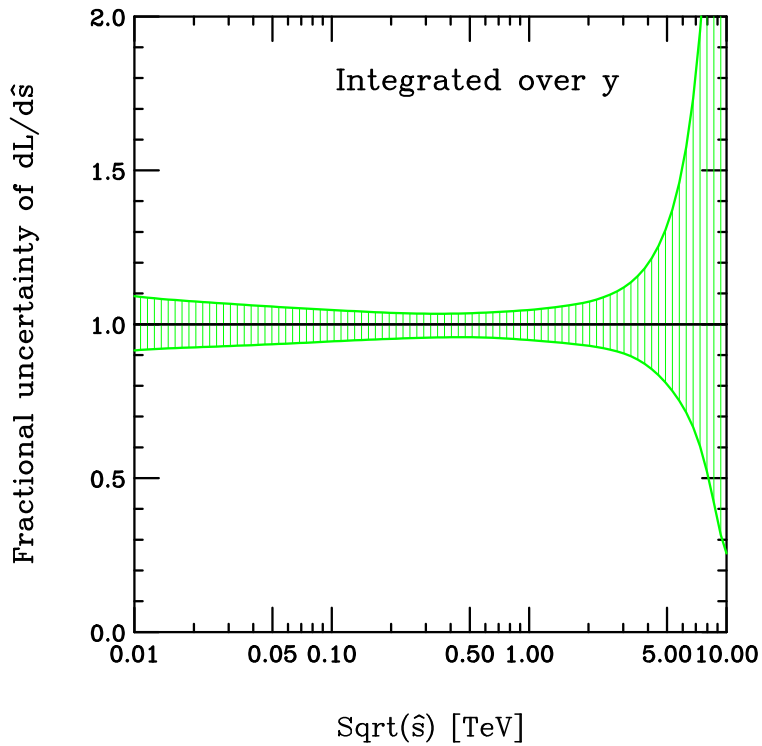


Fig. 26: Fractional uncertainty for Luminosity integrated over  $y$  for  $d\bar{d} + u\bar{u} + s\bar{s} + c\bar{c} + b\bar{b} + \bar{d}d + \bar{u}u + \bar{s}s + \bar{c}c + \bar{b}b$ .



## 5.2 Conclusions

Some representative parton-parton luminosity and luminosity uncertainty plots have been presented. A more complete set will be maintained at the Standard Model benchmark website started at Les Houches 2005: [www.pa.msu.edu/~huston/Les\\_Houches\\_2005/Les\\_Houches\\_SM.html](http://www.pa.msu.edu/~huston/Les_Houches_2005/Les_Houches_SM.html) and will also be included in a review article to be published in the near future.

## Acknowledgements

We would like to thank J. Campbell, W.J. Stirling and W.K. Tung for useful discussions and comments.

## 6. A SIMPLE MODEL FOR LARGE- $x$ RESUMMED PARTON DISTRIBUTIONS <sup>10</sup>

The achievement of precision goals of the LHC and other high-energy colliders crucially depends on the knowledge of parton distribution functions (PDF's). One of the phase space regions in which parton densities are less constrained is the large- $x$  region, where limited data exist and NLO fits do not work well due to the presence of large higher-order and power corrections. The range of applicability of perturbative methods can be extended in this region by applying soft-gluon resummation techniques, which are available for many hard processes. Here we will be concerned with estimating the effects of resummation on PDF's. To this end, we will present a simple analysis of Deep Inelastic Scattering (DIS) structure function data, which will allow us to extract next-to-leading order (NLO) and resummed parton distribution functions at large  $x$ .

DIS structure functions  $F_i(x, Q^2)$  are given by the convolution of coefficient functions and PDF's. NLO coefficient functions are known to contain terms that become large and dominant at large  $x$ , originating from soft and collinear gluon emission. These contributions need to be resummed to all orders to improve the validity of the perturbative prediction. Large- $x$  resummation for the DIS coefficient function was performed in [139, 140] in the massless approximation, and in [141, 142] with the inclusion of quark-mass effects, which are relevant when the focus is on heavy quark production.

Soft resummation is naturally performed in Mellin moment space, where large- $x$  terms correspond, at  $\mathcal{O}(\alpha_s)$ , to single ( $\alpha_s \ln N$ ) and double ( $\alpha_s \ln^2 N$ ) logarithms of the variable  $N$ . Such logarithms exponentiate in a Sudakov form factor: in the next-to-leading logarithmic (NLL) approximation, terms  $\mathcal{O}(\alpha_s^n \ln^{n+1} N)$  (LL) and  $\mathcal{O}(\alpha_s^n \ln^n N)$  (NLL) are resummed in the Sudakov exponent. Using large- $x$  resummed coefficient functions, we can extract resummed PDF's from DIS structure function data, and compare them with a NLO fit. We shall consider recent charged-current (CC) data from neutrino-iron scattering, collected by the NuTeV collaboration [143], and neutral-current (NC) data from the NMC [144] and BCDMS [145, 146] collaborations.

We have used NuTeV data on  $F_2(x)$  and  $xF_3(x)$  at the test values of  $Q^2 = 31.62 \text{ GeV}^2$  and  $12.59 \text{ GeV}^2$ . The structure function  $F_2$  contains a gluon-initiated contribution  $F_2^g$ , which is not soft-enhanced and is very small at large  $x$ : we extracted  $F_2^g$  from a global fit, e.g. CTEQ6M [47], and limited our fit to the quark-initiated term  $F_2^q$ . We chose a parametrization of the form  $F_2^q(x) = F_2(x) - F_2^g(x) = Ax^{-\alpha}(1-x)^\beta(1+bx)$ ;  $xF_3(x) = Cx^{-\rho}(1-x)^\sigma(1+kx)$ . The best-fit parameters and the  $\chi^2$  per degree of freedom from the fit are quoted in [147]. In Figs. 27 and 28, we present the NuTeV data on  $F_2(x)$  and  $xF_3(x)$  at  $Q^2 = 12.59 \text{ GeV}^2$ , along with the best-fit curves. In order to extract individual quark distributions, we need to consider also NC data. We use NMC and BCDMS results, and employ the parametrization of the nonsinglet structure function  $F_2^{\text{ns}} = F_2^p - F_2^D$  provided by the NNPDF collaboration [148, 149]. The parametrization [148, 149] is based on neural networks trained on Monte-Carlo copies of the data set, which include all information on errors and correlations: this gives an unbiased representation of the probability distribution in the space of structure functions. Fig. 29 shows  $F_2^{\text{ns}}(x, Q^2)$ , computed with the neural parametrization at our chosen values of  $Q^2$ , for

<sup>10</sup>Contributed by: G. Corcella, L. Magnea

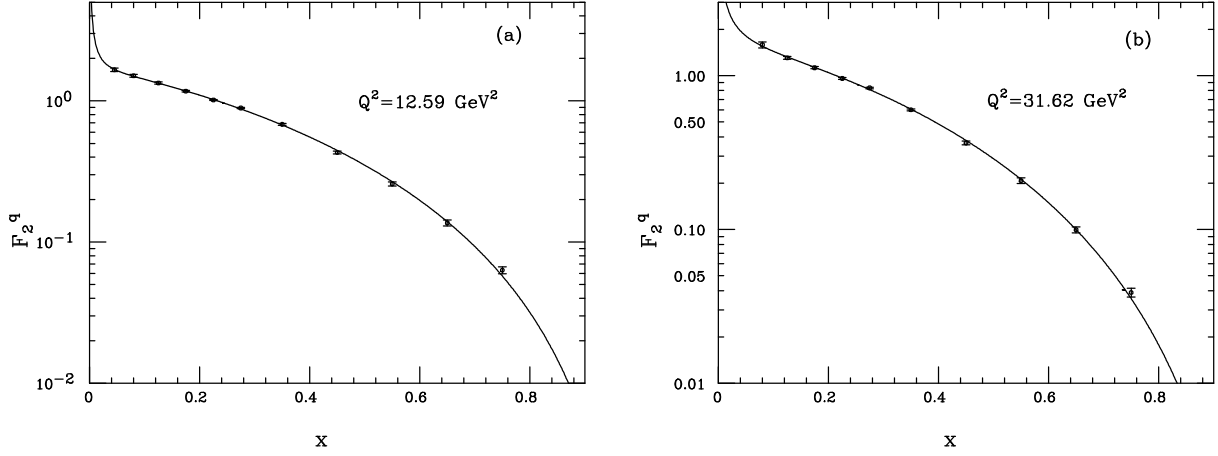


Fig. 27: NuTeV data and best-fit curves for the structure function  $F_2^q$  at  $Q^2 = 12.59 \text{ GeV}^2$  (a) and  $31.62 \text{ GeV}^2$  (b).

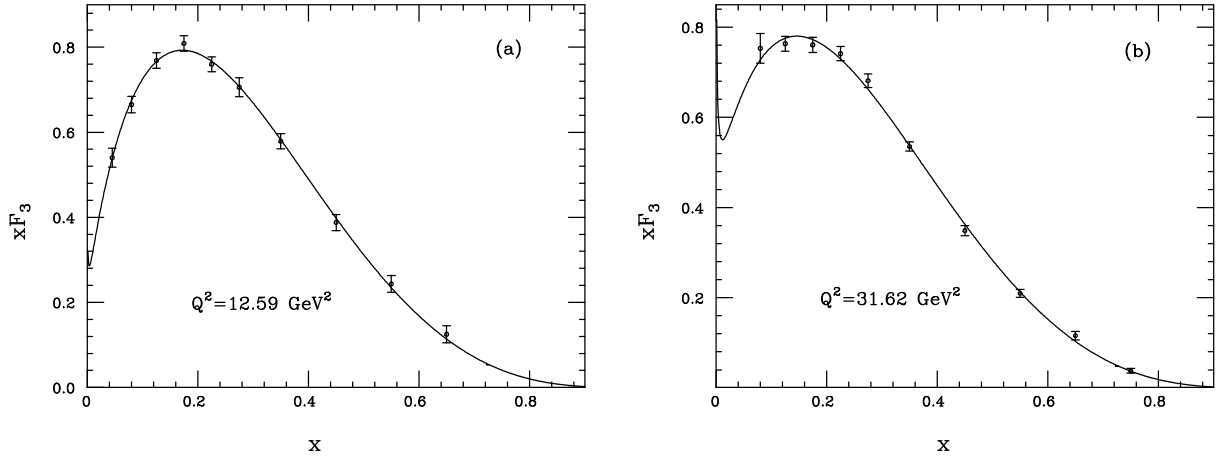


Fig. 28: As in Fig. 27, but for the structure function  $F_3$ .

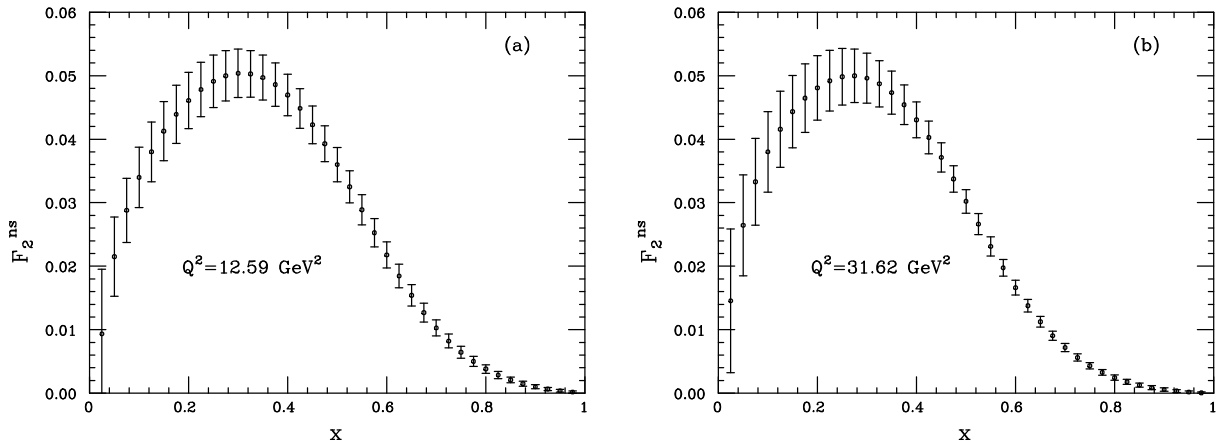


Fig. 29: A sampling of the neural parametrization of NMC and BCDMS data for  $F_2^{ns}(x, Q^2)$  at  $Q^2 = 12.59 \text{ GeV}^2$  (a) and at  $Q^2 = 31.62 \text{ GeV}^2$  (b), from the NNPDF Collaboration [148].

$x = n/40$ ,  $n = 1, \dots, 39$ . The central values are given by the averages of the results obtained with the one thousand neural networks of the NNPDF collaboration, and the error bars are the corresponding standard deviations. The errors are quite large, because  $F_2^{ns}(x, Q^2)$  is the difference between proton and

deuteron structure functions, which implies a loss of precision.

Writing  $F_2$ ,  $xF_3$  and  $F_2^{\text{ns}}$  in terms of their parton content, we can extract NLO and NLL-resummed quark distributions, according to whether we use NLO or NLL coefficient functions. In order to solve for individual quark distributions, we assume isospin symmetry of the sea, i.e.  $s = \bar{s}$  and  $\bar{u} = \bar{d}$ , we neglect the charm density, and impose a relation of the form  $\bar{s} = \kappa \bar{u}$ . We obtain a system of three equations, explicitly presented and solved in [147] in terms of  $u$ ,  $d$  and  $s$ . We begin by working in  $N$ -space, where the resummation has a simpler form and quark distributions are just the ratio of the appropriate structure function and coefficient function. We will then invert the results to  $x$ -space using a simple parametrization,  $q(x) = Dx^{-\gamma}(1-x)^\delta$ .

Figs. 30–31 show the effect of the resummation on the up-quark distribution at  $Q^2 = 12.59$  and  $31.62 \text{ GeV}^2$ , in  $N$ - and  $x$ -space, for  $\kappa = 1/2$ . As for the result in  $x$ -space, the best-fit values of  $D$ ,  $\gamma$  and  $\delta$ , along with the  $\chi^2/\text{dof}$ , are quoted in Table 6.

The impact of the resummation is noticeable at large  $N$  and  $x$ : the coefficient function and its moments in that region are enhanced by the resummation, and therefore quark densities are suppressed when extracted from a given set of structure function data. The effect is larger at  $Q^2 = 12.59 \text{ GeV}^2$ , as expected from the running of the strong coupling. In Fig. 31 we also present the up-quark density according to the MRST2001 set [26], in the NLO approximation. Given the various approximations which we made in our analysis, the limited data set and the emphasis on large- $x$  data, we do not expect that our results should agree with the MRST2001 global fit. We note however that at low  $x$  the MRST2001 up-quark distribution is within the error range of the densities extracted from our fit. At large  $x$  it looks closer to our NLL-resummed PDF rather than to the NLO one. In fact, as observed in [150], the MRST2001 set was fitted to CCFR structure function data [151], which are lower than NuTeV at large  $x$ . It is therefore reasonable that the NLO MRST2001 PDF's be lower than the NLO ones which we extracted from a fit to NuTeV, and therefore closer to our resummed PDF's. The discrepancy between NuTeV and CCFR at large  $x$  is now described as understood [143]. In principle, also  $d$  and  $s$  densities are affected by the resummation; we found, however, that the errors on these PDF's within our fit are too large to display sensitivity to soft resummation.

Table 6: Best-fit values and errors for the up-quark  $x$ -space parametrization, at the chosen values of  $Q^2$ .

$Q^2$	PDF	$D$	$\gamma$	$\delta$
12.59	NLO	$3.025 \pm 0.534$	$0.418 \pm 0.101$	$3.162 \pm 0.116$
	RES	$4.647 \pm 0.881$	$0.247 \pm 0.109$	$3.614 \pm 0.128$
31.62	NLO	$2.865 \pm 0.420$	$0.463 \pm 0.086$	$3.301 \pm 0.098$
	RES	$3.794 \pm 0.583$	$0.351 \pm 0.090$	$3.598 \pm 0.104$

Fig. 32 shows the impact of the resummation on the ratio  $\Delta u(x) = (u_{\text{NLO}}(x) - u_{\text{res}}(x)) / u_{\text{NLO}}(x)$ , at both values of  $Q^2$ , for the central values of the best-fit parameters, as quoted in Table 6. We observe that the suppression of the resummed up quark distribution with respect to the NLO one is about 5% at  $x \simeq 0.58$ , 10% at  $x \simeq 0.65$  and 20% at  $x \simeq 0.75$  for  $Q^2 = 12.59 \text{ GeV}^2$ , while for  $Q^2 = 31.62 \text{ GeV}^2$  the same suppression factors are reached at  $x \simeq 0.61$ ,  $x \simeq 0.69$  and  $x \simeq 0.8$ , respectively.

We note that our results on fixed-order and resummed quark distributions at the two values of  $Q^2$  are consistent with NLO perturbative evolution. This is shown in Fig. 33: NLO and NLL-resummed moments obtained from a fit of the data at  $12.59 \text{ GeV}^2$  are consistent with the ones obtained via NLO evolution from the values fitted at  $31.62 \text{ GeV}^2$ , just within one standard deviation. It should be observed, however, that the evolution of resummed moments is less consistent than the NLO one, which might be due to effects of power corrections, which are entangled to the resummation and have not been accounted for in our work.

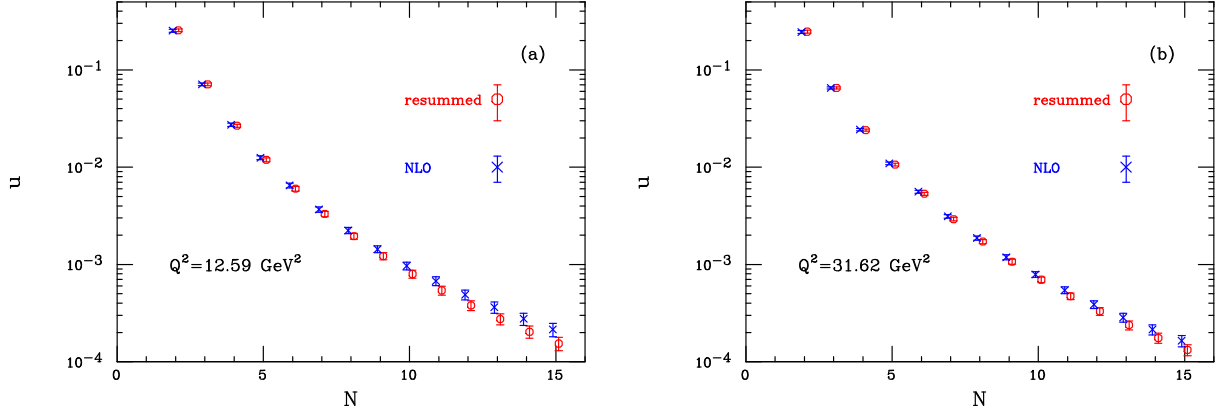


Fig. 30: NLO and resummed moments of the up quark distribution at  $Q^2 = 12.59 \text{ GeV}^2$  (a) and  $31.62 \text{ GeV}^2$  (b).

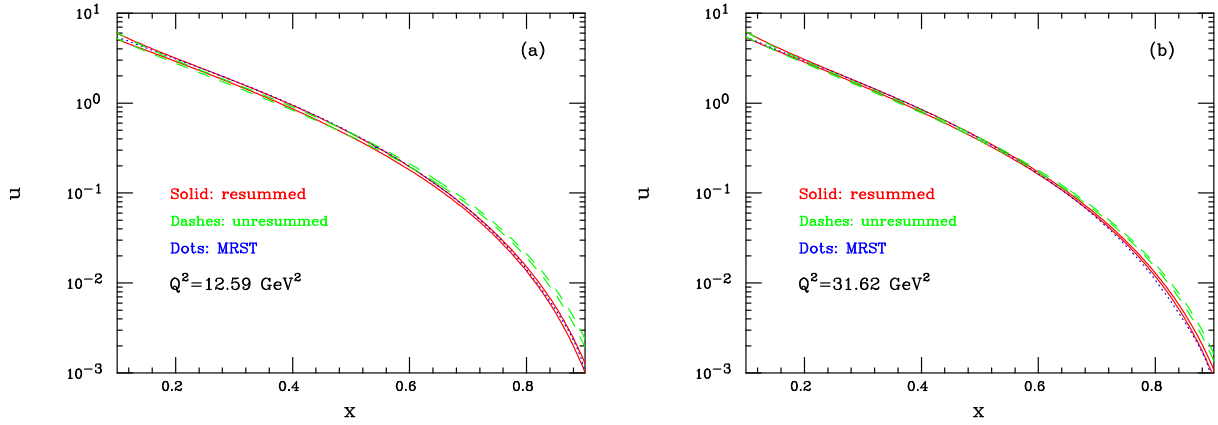


Fig. 31: NLO and NLL up-quark density in  $x$ -space at  $Q^2 = 12.59 \text{ GeV}^2$  (a) and  $31.62 \text{ GeV}^2$  (b). Plotted are the edges of statistical bands at one-standard-deviation confidence level. For the sake of comparison, the MRST2001 result is also shown.

In conclusion, we have fitted fixed-target large- $x$  DIS structure function data, and extracted NLO and NLL-resummed parton densities. We found an impact of the resummation on valence quark densities, which are suppressed by about 10 – 20% at  $x > 0.5$  and moderate  $Q^2$ . Our results show that higher-order perturbative effects should not be neglected in parton fits at large  $x$ . A NNLO analysis [26] is bound to include some of the effects discussed here and is a step in right direction. Whenever resummed hard partonic cross sections are employed, however, it would be desirable to have at hand resummed PDF's as well: our results in fact show that in some cases the Sudakov enhancement of the partonic cross section which is typical of soft resummation could be partly compensated by a suppression of large- $x$  partons when the same physical effects are consistently included in their determination.

## 7. BOTTOM-QUARK FRAGMENTATION: FROM $e^+e^-$ DATA TO TOP AND HIGGS DECAYS<sup>11</sup>

### 7.1 Introduction

We investigate  $B$ -hadron production in  $e^+e^-$  annihilation ( $e^+e^- \rightarrow b\bar{b}$ ), top decay ( $t \rightarrow bW$ ) and the Standard-Model-Higgs decay  $H \rightarrow b\bar{b}$ , which is relevant at the LHC for  $m_H < 135 \text{ GeV}$ , and to Higgs production in association with vector bosons [152] or  $t\bar{t}$  pairs [153, 154].

We describe  $b$ -quark production using resummed calculations, based on the formalism of pertur-

<sup>11</sup>Contributed by: G. Corcella, V. Drollinger

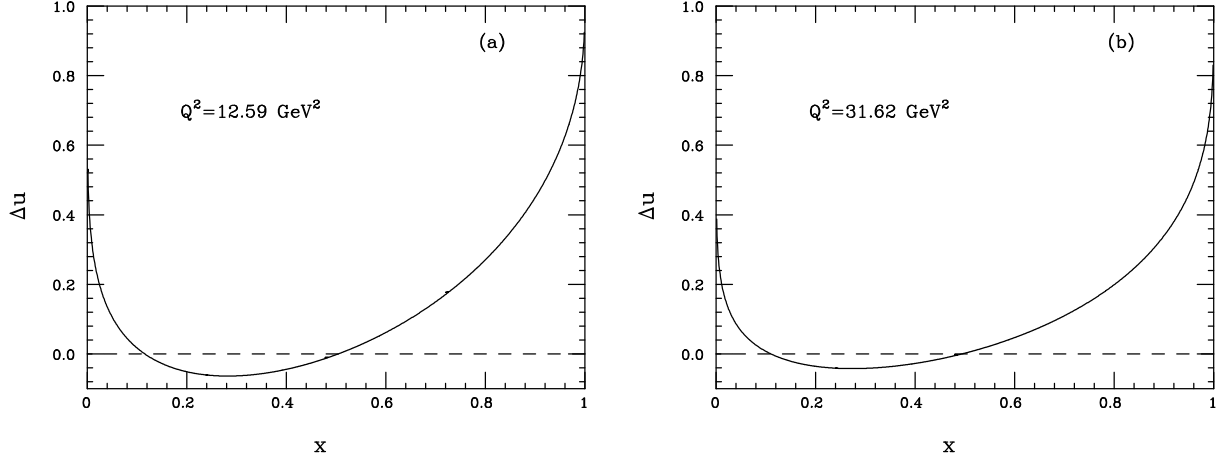


Fig. 32: Relative effect of large- $x$  resummation on the up-quark density at  $Q^2 = 12.59 \text{ GeV}^2$  (a) and  $31.62 \text{ GeV}^2$ .

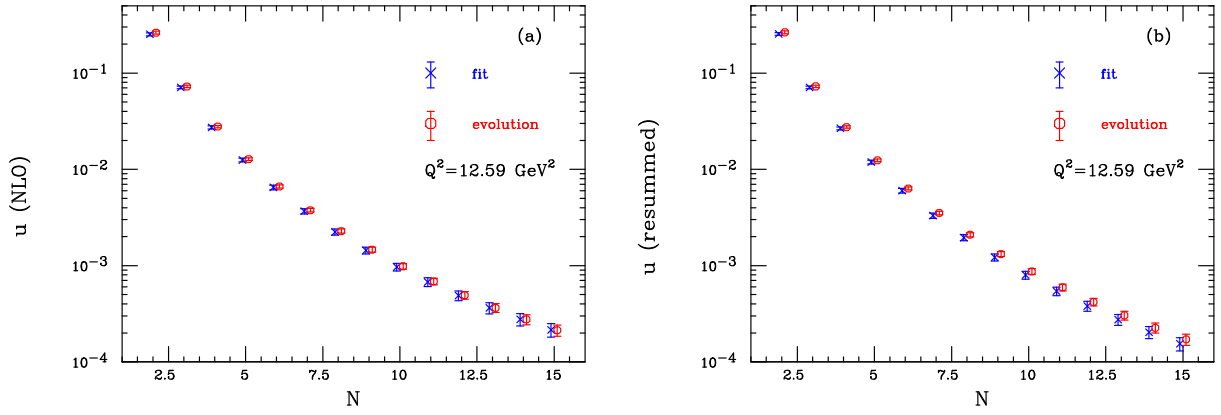


Fig. 33: Comparison of fitted moments of the up-quark distributions at  $Q^2 = 12.59 \text{ GeV}^2$ , with moments obtained via NLO evolution from  $Q^2 = 31.62 \text{ GeV}^2$ .

bative fragmentation functions [155], and the HERWIG [33] and PYTHIA [27, 156] Monte Carlo event generators. We use  $e^+e^-$  data on the  $B$ -hadron spectrum collected by the SLD [157], ALEPH [158] and OPAL [159] experiments to fit the cluster and string hadronization models, implemented by HERWIG and PYTHIA, and the Kartvelishvili non-perturbative fragmentation function [160], used in the framework of the resummed calculation. We shall employ the fitted models to predict the  $B$ -energy distribution in top and Higgs decays. Furthermore, we shall use data from DELPHI [161] in Mellin moment space to extract the moments of the non-perturbative fragmentation function and predict the  $N$ -space  $B$ -spectrum in  $t \rightarrow bW$  and  $H \rightarrow b\bar{b}$ .

## 7.2 Bottom-quark production and multi-parton radiation

We shall first consider  $b$ -quark production at the next-to-leading order (NLO) in  $Z$ ,  $H$  and top decays:

$$P(Q) \rightarrow b(p_b)\bar{b}(p_{\bar{b}})(g(p_g)), \quad (26)$$

with  $P = Z$  or  $H$ , and

$$t(Q) \rightarrow b(p_b)W(p_W)(g(p_g)). \quad (27)$$

We shall neglect powers of  $(m_b^2/Q^2)^p$  and consider the  $b$ -quark energy fraction

$$x_b = \frac{1}{1-w} \frac{2p_b \cdot Q}{Q^2}, \quad (28)$$

with  $w = 0$  in Higgs and  $Z$  decays and  $w = m_W^2/m_t^2$  in  $t \rightarrow bW$ . The approach of perturbative fragmentation functions [155] expresses the  $x_b$  distribution as the convolution of a massless coefficient function and a perturbative fragmentation function  $D(m_b, \mu_F)$ , associated with the transition of a light parton into a heavy quark:

$$\frac{1}{\Gamma_0} \frac{d\Gamma_b}{dx_b}(x_b, Q, m_b) = \int_{x_b}^1 \frac{dz}{z} \left[ \frac{1}{\Gamma_0} \frac{d\hat{\Gamma}_b}{dz}(z, Q, \mu, \mu_F) \right]^{\overline{\text{MS}}} D_b^{\overline{\text{MS}}}\left(\frac{x_b}{z}, \mu_F, m_b\right). \quad (29)$$

In Eq. (29),  $d\hat{\Gamma}_b/dz$  is the differential width for the production of a massless  $b$ , after subtraction of the collinear singularity in the  $\overline{\text{MS}}$  factorization scheme ( $\overline{\text{MS}}$  coefficient function),  $\mu$  and  $\mu_F$  are the renormalization and factorization scales. The NLO coefficient functions have been computed in [155, 162, 163] for  $e^+e^-$  collisions, top and Higgs decays, respectively.

The perturbative fragmentation function follows the Dokshitzer–Gribov–Lipatov–Altarelli–Parisi (DGLAP) evolution equations and its initial condition at a scale  $\mu_{0F}$  is process-independent [155, 164]. Solving the DGLAP equations for an evolution from  $\mu_{0F}$  to  $\mu_F$ , with an NLO kernel, allows one to resum leading (LL)  $\alpha_S^n \ln^n(\mu_F^2/\mu_{0F}^2)$  and next-to-leading (NLL)  $\alpha_S^n \ln^{n-1}(\mu_F^2/\mu_{0F}^2)$  logarithms (collinear resummation). Setting  $\mu_{0F} \simeq m_b$  and  $\mu_F \simeq Q$ , one resums the large mass logarithm  $\ln(Q^2/m_b^2)$ , which appears in the massive spectrum [155].

Moreover, the coefficient functions and the initial condition of the perturbative fragmentation present terms which become large for  $x_b \rightarrow 1$ , which corresponds to soft-gluon radiation. NLL soft resummation in the initial condition of the perturbative fragmentation function is process-independent and has been carried out in [164]. In [163–165], NLL soft terms in the coefficient functions of  $Z \rightarrow b\bar{b}$ ,  $t \rightarrow bW$  and  $H \rightarrow b\bar{b}$  processes have been resummed. In terms of the Mellin variable  $N$ , such calculations resum LLs ( $\alpha_S^n \ln^{n+1} N$ ) and NLLs ( $\alpha_S^n \ln^n N$ ) in the Sudakov exponent.

As far as Monte Carlo event generators are concerned, HERWIG and PYTHIA implement LO processes, such as  $Z(H) \rightarrow b\bar{b}$  and  $t \rightarrow bW$ , and the subsequent parton radiation is treated in the collinear approximation. As discussed, e.g., in [166], this is equivalent to a LL resummation, with the inclusion of some NLL terms as well.

In order to allow hard and large-angle radiation, parton showers are provided with matrix-element corrections. PYTHIA uses the collinear approximation to populate the full phase space and the tree-level exact matrix element corrects the first emission [167, 168]. PYTHIA 6.220, which we shall use hereafter, contains matrix-element corrections to all the considered processes. Unlike PYTHIA, the standard HERWIG algorithm completely suppresses the radiation in the so-called ‘dead zone’, corresponding to hard and/or large-angle radiation. The exact matrix element populates the dead zone (hard correction) and corrects the shower every time an emission is the ‘hardest so far’ (soft correction) [169]. HERWIG 6.506, our default version, includes the corrections to  $e^+e^-$  annihilation [170] and top decay [171]. More recently, the corrections to  $H \rightarrow b\bar{b}$  processes have been implemented [172], and we shall account for them in the following.

### 7.3 $B$ -hadron spectrum in $x_B$ -space

In order to describe hadron production, both resummed calculations and Monte Carlo parton showers need to be supplemented by hadronization models, which contain parameters which need to be tuned to experimental data. In particular, PYTHIA and HERWIG implement the string and the cluster model, respectively. As far as the resummed computation is concerned, we shall convolute the  $b$  spectrum with the Kartvelishvili non-perturbative fragmentation function:

$$D^{\text{np}}(x; \gamma) = (1 + \gamma)(2 + \gamma)(1 - x)x^\gamma, \quad (30)$$

and fit the parameter  $\gamma$  to data.



Table 7: Parameters of HERWIG and PYTHIA hadronization models tuned to  $e^+e^-$  data, along with the  $\chi^2/\text{dof}$ .

HERWIG	PYTHIA
CLSMR(1) = 0.4	
CLSMR(2) = 0.3	PARJ(41) = 0.85
DECWT = 0.7	PARJ(42) = 1.03
CLPOW = 2.1	PARJ(46) = 0.85
PSPLT(2) = 0.33	
$\chi^2/\text{dof} = 222.4/61$	$\chi^2/\text{dof} = 45.7/61$

We shall consider data from SLD, ALEPH and OPAL on the  $B$ -hadron energy fraction  $x_B$ , which is the hadron-level counterpart of Eq. (28). As in [172], when using the resummation, we consider the data in the range  $0.18 \leq x_B \leq 0.94$ , to avoid the regions  $x_B \rightarrow 0$  and  $x_B \rightarrow 1$ , where the calculation is unreliable. In fact, the predicted parton- and hadron-level spectra become negative at very small and very large  $x$ , owing to the presence of unresummed terms and to non-perturbative corrections, relevant especially at large  $x$ . In the considered range, we obtain:  $\gamma = 17.178 \pm 0.303$ , with  $\chi^2/\text{dof} = 46.2/53$ .

As for HERWIG and PYTHIA, the default parametrization of the hadronization models would not be able to fit such data, as one would get  $\chi^2/\text{dof} = 739.4/61$  for HERWIG and  $\chi^2/\text{dof} = 467.9/61$  for PYTHIA. In [172], the cluster and string models were tuned to the data and the results are reported in Table 7. The new  $\chi^2$  are  $\chi^2/\text{dof} = 45.7/61$  for PYTHIA and  $\chi^2/\text{dof} = 222.4/61$  for HERWIG: although HERWIG is still not able to fit well the data, the comparison is greatly improved after the tuning. Major improvements in the description of  $b$ -fragmentation are nonetheless present in the C++ version HERWIG++ (whose use is beyond the goals of our analysis), which is able to describe well the data, after fitting only the shower cutoff [173]. More details about the fits are discussed in [172], where it is also pointed out that our tuning works well also for the new model implemented in PYTHIA 6.3 [27]. Using options and parameters as they are defined in the new scenario (model 1), we get  $\chi^2/\text{dof} = 45.7/61$ . In Fig. 34 we present the  $x_B$  data, and the spectra given by the resummed calculation, convoluted with the Kartvelishvili model, by HERWIG and by PYTHIA. Default HERWIG and PYTHIA are quite far from the data; after the tuning, PYTHIA reproduces the data quite well, while HERWIG yields a broader distribution.

Using the fitted parameters, we can predict the  $B$  spectrum in top and Higgs decays: this is shown in Fig. 35, for  $m_t = 175$  GeV and  $m_H = 120$  GeV. In top decay, PYTHIA reproduces the peak of the resummed calculation rather well, while it is below the NLL prediction at  $x_B < 0.7$  and above at  $x_B > 0.9$ . HERWIG is below the resummed spectrum in most the  $x_B$  range, and above only at large  $x_B$ . As for  $H \rightarrow b\bar{b}$  processes, PYTHIA fares rather well with respect to the NLL calculation and, although small discrepancies are visible, the overall agreement looks acceptable. HERWIG yields instead a broader spectrum, which is higher than the NLO+NLL one at intermediate and large  $x_B$ , and lower around the peak.

## 7.4 Results in moment space

We now turn to the results on  $B$ -hadron production in Mellin moment space, where the moments  $\Gamma_N$  of the differential width read:

$$\Gamma_N = \int_0^1 dz z^{N-1} \frac{1}{\Gamma} \frac{d\Gamma}{dz}(z). \quad (31)$$

In Ref. [161], the DELPHI collaboration presented the moments for  $B$  production in  $e^+e^-$  annihilation. From the point of view of resummed calculations, working in moment space is better since, in  $N$ -space, convolutions become ordinary products, and the thus relation between parton- and hadron-level cross sections becomes  $\sigma_N^B = \sigma_N^b D_N^{\text{np}}$ , where  $D_N^{\text{np}}$  the  $N$ -space counterpart of the non-perturbative fragmen-

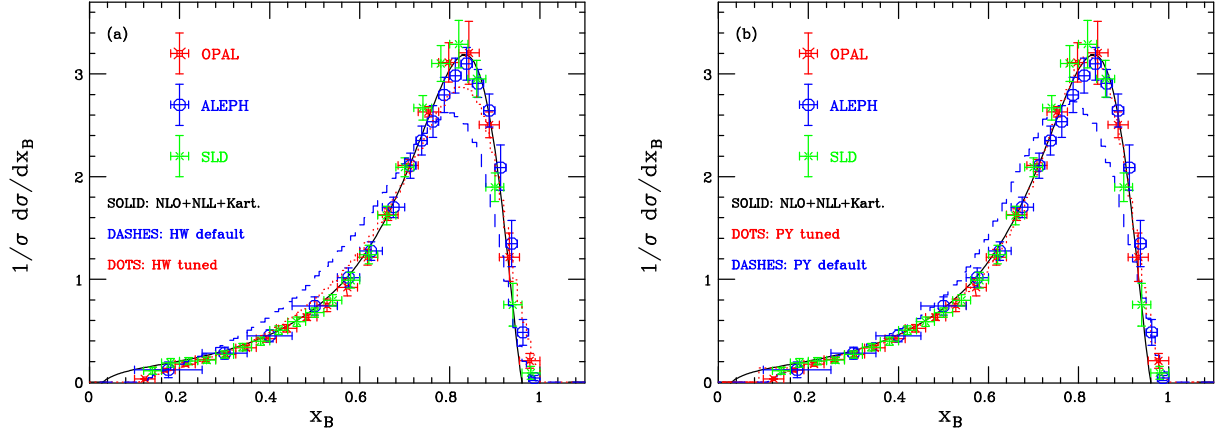


Fig. 34: Comparison of OPAL, ALEPH and SLD data with HERWIG (a), PYTHIA (b) and the NLO+NLL calculation.

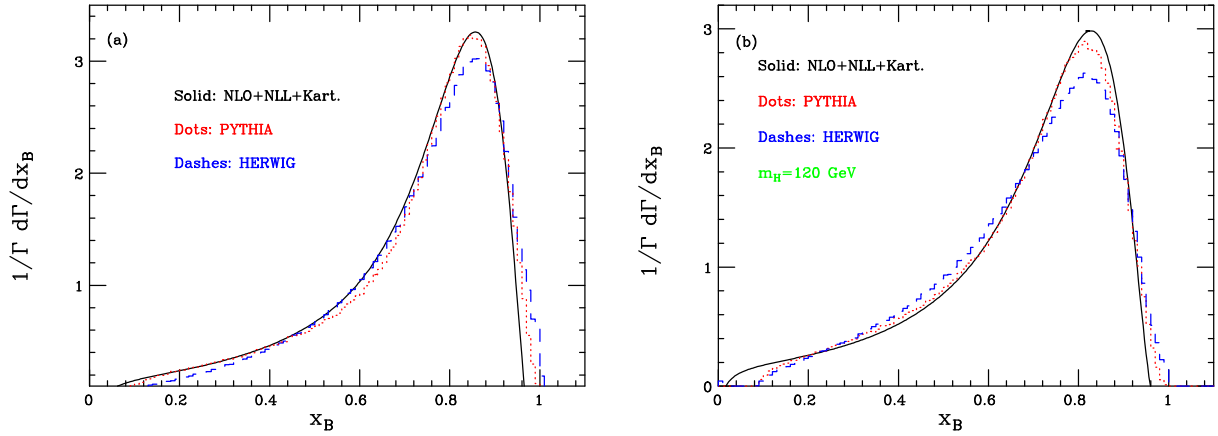


Fig. 35:  $B$  spectrum in top (a) and Higgs (b) decays, using HERWIG, PYTHIA and NLO+NLL calculations.

tation function. Therefore, there is no need to assume any functional form for the non-perturbative fragmentation function in  $x$ -space. Moreover, resummed calculations are well defined in  $N$ -space, and do not exhibit the problems of the  $x_B$  spectra, which become negative at small or large  $x_B$ .

In Table 8 we quote the data from DELPHI, the moments yielded by HERWIG, PYTHIA and the NLO+NLL calculation in  $Z$ ,  $t$  and  $H$  decays. The moments given by HERWIG and PYTHIA in  $e^+e^-$  annihilation are consistent, within the error ranges, with the ones measured by DELPHI. Although problems are present when fitting the  $x_B$  data from LEP and SLD, it is remarkable that HERWIG is compatible with the DELPHI moments within one standard deviation.

The results for top and Higgs decays exhibit similar features to the  $x_B$  spectra. In top decay, PYTHIA is very close to the NLL calculation which uses  $D_N^{\text{np}}$  extracted from the DELPHI data, while HERWIG, whose predictions are shifted toward larger  $x_B$ , yields larger moments. For  $H \rightarrow b\bar{b}$ , PYTHIA and HERWIG give moments which are compatible within 1%.

## 7.5 Conclusions

In summary, we have investigated  $b$ -quark fragmentation in  $e^+e^-$  annihilation, top and Higgs  $H \rightarrow b\bar{b}$  decays. We have described  $b$  production using resummed calculations, based on the perturbative fragmentation approach, HERWIG and PYTHIA. We have fitted a few hadronization models to LEP and SLD data on  $B$ -hadron production and performed predictions on the  $B$  spectrum in top and Higgs decays. Tuning the HERWIG and PYTHIA hadronization models played a crucial role, as the default

Table 8: Moments  $\sigma_N^B$  from DELPHI [161], and moments in  $e^+e^-$  annihilation, Higgs ( $H$ ) and top ( $t$ ) decay, using NLL resummed calculations, HERWIG (HW) and PYTHIA (PY).

	$\langle x \rangle$	$\langle x^2 \rangle$	$\langle x^3 \rangle$	$\langle x^4 \rangle$
$e^+e^-$ data $\sigma_N^B$	$0.7153 \pm 0.0052$	$0.5401 \pm 0.0064$	$0.4236 \pm 0.0065$	$0.3406 \pm 0.0064$
$e^+e^-$ NLL $\sigma_N^b$	0.7801	0.6436	0.5479	0.4755
$D_N^{\text{np}}$	0.9169	0.8392	0.7731	0.7163
$e^+e^-$ HW $\sigma_N^B$	0.7113	0.5354	0.4181	0.3353
$e^+e^-$ PY $\sigma_N^B$	0.7162	0.5412	0.4237	0.3400
$H$ -dec. NLL $\Gamma_N^b$	0.7580	0.6166	0.5197	0.4477
$H$ -dec $\Gamma_N^B$	0.6950	0.5175	0.4018	0.3207
$H$ -dec. HW $\Gamma_N^B$	0.6842	0.5036	0.3877	0.3076
$H$ -dec. PY $\Gamma_N^B$	0.6876	0.5080	0.3913	0.3099
$t$ -dec. NLL $\Gamma_N^b$	0.7883	0.6615	0.5735	0.5071
$t$ -dec. NLL $\Gamma_N^B$	0.7228	0.5551	0.4434	0.3632
$t$ -dec. HW $\Gamma_N^B$	0.7325	0.5703	0.4606	0.3814
$t$ -dec. PY $\Gamma_N^B$	0.7225	0.5588	0.4486	0.3688

parametrizations would not be able to reproduce the  $e^+e^-$  data. Moreover, we have analysed data from the DELPHI Collaboration in moment space, extracted the non-perturbative fragmentation function in  $N$ -space, and compared the moments given by resummed calculations, HERWIG and PYTHIA.

## 8. STUDY OF JET CLUSTERING ALGORITHMS AT THE LHC <sup>12</sup>

### 8.1 Introduction

A wide spectrum of new physics topologies, as well as known processes like top quark production, will have quarks in the final state of proton-proton collisions at the LHC. When reconstructing the quark's kinematics, jet reconstruction is of major importance, which is a complex task and not necessarily robust. Ambiguities in the jet definition not only arise from the theoretical point of view if higher order corrections are taken into account, but also experimentally, due to the magnetic field, the calorimeter response and the different configuration possibilities of jet clustering algorithms.

This study concentrates on the algorithmic task of clustering the input objects (e.g simulated particles or calorimeter cells) into jets. This is performed from an analysis perspective, which means that the jet clustering is considered to be optimal if the reconstruction efficiency of the complete kinematics of the primary quark event topology is maximized. This reconstruction efficiency will be defined in terms of quality criteria or quality markers, relative to the performance of a typical analysis like the reconstruction of the mass of a resonance decaying into quarks. The distance between the generated primary partons  $i$  and the reconstructed jets  $j$ , and therefore the error of the jets, should be minimized in both energy and momentum (angular) space, for example  $\epsilon_\theta = \theta_j^{\text{jet}} - \theta_i^{\text{quark}}$ .

Physics effects like pile-up, underlying event and radiation enlarge this mean error. The scope of this study is to find the most efficient configuration for jet finding algorithms in the presence of these effects, in order to maximize the fraction of events for which all quarks have smaller errors than some predefined criteria. Hence, events suffering from a large amount of hard gluon radiation will be rejected.

The resulting efficiency does not only depend on the configuration of the jet finding but also on the event topology. This will be investigated for processes with two, four, six and eight primary quarks in the final state, covering a significant spectrum of physics processes at the LHC.

<sup>12</sup>Contributed by: D. Benedetti, S. Cucciarelli, J. D'Hondt, A. Giammanco, J. Heyninck, A. Schmidt, C. Weiser

To disentangle detector effects from pure algorithmic and physics effects, the study is performed with simulated particle information as input to the jet finding algorithms. The comparison with a realistic detector is beyond the general scope of this contribution. It will be described in dedicated papers for the specific experiments.

## 8.2 Jet Clustering Algorithms

The following jet reconstruction algorithms are considered in this study: the *Iterative Cone* algorithm (IC), the inclusive  $k_T$  algorithm ( $k_T$ ) and the *MidPoint Cone* algorithm (MC). A description of these algorithms and the definition of their parameters can be found in Ref. [174]. For all algorithms the energy recombination scheme and the  $\eta, \phi$ -metric is used. The main parameters that are varied for the different algorithms are: the cone radius for the *Iterative Cone* algorithm; the R-parameter that reflects a radius-like role for the  $k_T$  algorithm; the cone radius and the shared energy fraction threshold for merging for the *MidPoint Cone* algorithm.

For all algorithms generated and stable final state particles are used as input. Muons and neutrinos are excluded, and the effects of the magnetic field are not taken into account. All particles are assumed to emerge from the primary vertex, where the clustering is performed.

## 8.3 Event Generation

Proton collisions at 14 TeV have been generated at a luminosity of  $2 \times 10^{33} \text{ cm}^{-2}\text{s}^{-1}$ . Final states like fully leptonic and semileptonic  $t\bar{t}$ , and semileptonic and hadronic  $t\bar{t}H \rightarrow t\bar{t}b\bar{b}$  events, have been selected to represent topologies with two, four, six and eight primary quarks. The  $t\bar{t}$  events were generated using PYTHIA version 6.2 and the  $t\bar{t}H$  events were generated with compHEP version 41.10, interfaced to PYTHIA version 6.215. For the leptonic decay of the W boson, only electrons and muons are considered.

## 8.4 Event Selection

A realistic event selection is applied. The reconstructed jets are required to have a transverse energy larger than 20 GeV, and to be within the tracker acceptance for a proper  $b$ -tagging performance ( $|\eta| < 2.4$  for the CMS experiment). Isolated signal leptons from the W-decay are removed from the jet finding input. Only if the number of jets passing these criteria is larger than or equal to the number of primary partons the event is considered for the analysis.

An iterative procedure is used to match the reconstructed jets to the generated primary partons based on the  $\Delta R$  distance in the  $(\eta, \phi)$  plane. For each possible jet-quark couple the  $\Delta R$ -value is calculated, and the smallest value is considered as a correct jet-quark matching and is removed from the list for the next iteration. When more jets have a minimal  $\Delta R$ -value with the same quark, the couple with the lowest  $\Delta R$ -value is taken. This procedure is iterated until all jets have their respective quark match.

## 8.5 Description of the Quality Markers

In order to obtain an efficient reconstruction of the kinematics of the primary partons, the selected jets should match both in energy and direction the primary partons. Variables called quality markers are defined to quantify the goodness of the event reconstruction from that perspective. Although physics effects of pile-up, gluon radiation and underlying event will degrade the overall event reconstruction efficiency, their magnitude is equal for all considered jet definitions. Hence, the relative comparison between jet definitions is meaningful.

### 8.5.1 Event Selection Efficiency “ $\epsilon_s$ ”:

This efficiency is defined as the fraction of events that pass the event selection. When the selection is applied on quark level, the efficiency is equal to 80% for the two quarks final state, 62% for the four

quarks final state, 61% for the six quarks final state and 52% for the eight quarks final state.

### 8.52 Angular Distance between Jet and Parton “Frac $\alpha_{jp}^{max}$ ”:

A jet is considered to be well reconstructed, if the  $\Delta R$  distance between its direction and its best matched quark direction,  $\alpha_{jp}$ , is sufficiently small. For each event, this results in a list of increasing  $\alpha_{jp}^i$ -values,  $\{\alpha_{jp}^1, \dots, \alpha_{jp}^n = \alpha_{jp}^{max}\}$ , where  $n$  is the amount of primary quarks in the considered event topology. Hence,  $\alpha_{jp}^{max}$  is defined as the maximum  $\alpha_{jp}^i$ -value of all  $i$  jet-quark pairs in the event. The  $\alpha_{jp}^i$  distributions for a four quarks final state are shown in Fig.36. The last one of these plots represents the  $\alpha_{jp}^{max}$

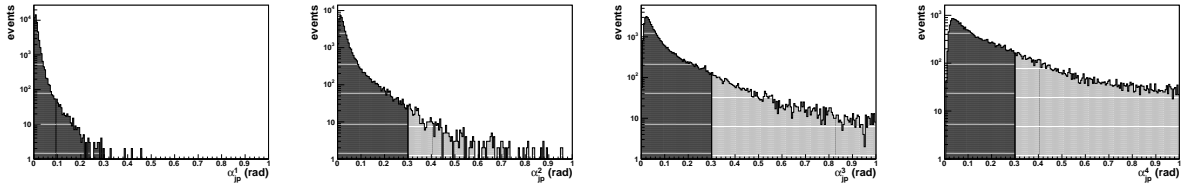


Fig. 36: Distributions of  $\alpha_{jp}^i$  in increasing order for the IC algorithm with a cone radius of 0.4 in the case of a final state with four quarks. The 0.3 rad criteria as discussed in the text is indicated.

variable. To quantify the angular reconstruction performance of a particular jet definition, a quality marker is defined as the fraction of events with a  $\alpha_{jp}^{max}$  value lower than 0.3 and denoted as “Frac  $\alpha_{jp}^{max}$ ”. The choice of the worst jet is motivated by the reasoning that the directions of all primary quarks in the event are required to be well determined.

### 8.53 Energy Difference “Frac $\beta_{jp}^{max}$ ”:

The reconstructed energy of the primary quarks is usually biased and has a broad resolution. Figure 37 shows the average fraction of the quark energy that is reconstructed for a specific algorithm configuration as a function of the reconstructed transverse jet energy. Such a calibration curve can be interpreted as an estimator for the expected reconstructed energy. For this plot only well matched ( $\alpha_{jp} < 0.3$ ), non-overlapping jets were taken into account. For the iterative cone algorithm, a jet is considered to be non-overlapping, if its  $\Delta R$  distance to any other jet is larger than twice the value of the cone radius parameter of the algorithm. It is the aim of jet calibration studies to determine these average corrections to be applied on the reconstructed jet energies. Therefore the remaining component is the energy resolution.

The  $\beta_{jp}^i$  values are defined for each primary quark  $i$  as the distance from the expected energy fraction (deduced from the fitted function in Fig. 37) in units of standard deviations. For each selected event, the primary quark with the highest  $\beta_{jp}^i$  value, called  $\beta_{jp}^{max}$  is considered to be the one with the worst reconstruction performance from the energy point of view. An example for the  $\beta_{jp}^{max}$  distribution is shown in Fig. 38. An energy related quality marker is defined as the fraction of events with a  $\beta_{jp}^{max}$  lower than 2 standard deviations, and denoted as “Frac  $\beta_{jp}^{max}$ ”.

### 8.54 Combined Variable “Frac( $\alpha_{jp}^{max} + \beta_{jp}^{max}$ )”:

The combined variable is defined as the fraction of events in which both the direction and the energy of the  $n$  primary quarks are well reconstructed using the definitions in Section 8.52 and 8.53. The correlation between  $\alpha_{jp}^{max}$  and  $\beta_{jp}^{max}$  is shown in Fig. 39, where applying both quality criteria defines a rectangular area in which the kinematics of the primary quarks are well reconstructed. As an illustration of the power of this combined variable in identifying well reconstructed events, the reconstructed spectrum of the hadronic top quark mass in the semileptonic  $t\bar{t}$  final state is shown in Fig. 40. The light grey histogram shows the spectrum from events where the kinematics of the primary quarks have been badly reconstructed according to the combined variable.

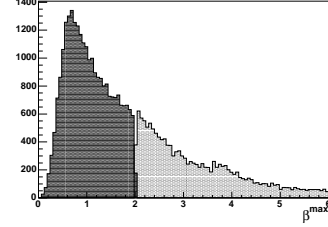
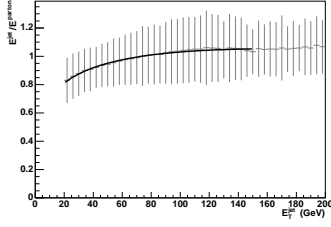


Fig. 37: Example of a  $\frac{E_T^{jet}}{E_{parton}^{jet}}$  vs.  $E_T^{parton}$  curve for the IC algo- Fig. 38: Distribution of  $\beta_{jp}^{max}$  for the IC algorithm with a cone rithm with a cone radius of 0.4, applied on a final state with four primary quarks. The vertical bars illustrate the resolution.

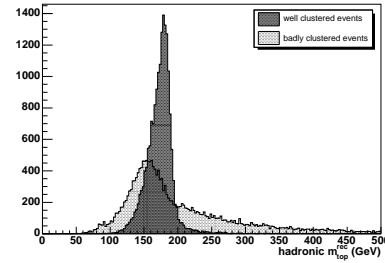
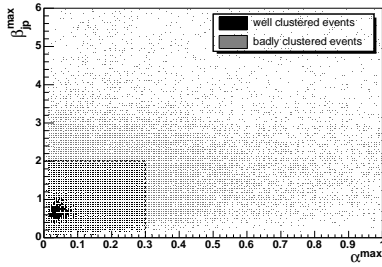


Fig. 39: Box plot of  $\beta_{jp}^{max}$  vs.  $\alpha_{jp}^{max}$  for the IC algorithm with Fig. 40: Distribution of the hadronic top quark mass, using jets a cone radius of 0.4, applied on a final state with four primary clustered with the IC algorithm with a cone radius of 0.4, ap- quarks. quarks.

### 8.55 Overall Quality Marker "FracGood"

The fraction of selected and well reconstructed events, i.e. the selection efficiency  $\epsilon_s$ , multiplied by the combined variable  $\text{Frac}(\alpha_{jp}^{max} + \beta_{jp}^{max})$  is defined as "FracGood".

This last quality marker is interpreted as an estimate for the reconstruction efficiency of the kinematics of the primary quarks of the complete event, and therefore used to compare different algorithms and their corresponding configurations. Although this variable gives a powerful overall indication of a reasonable jet definition, it is sometimes useful to consider the partial information of the individual quality markers. Depending on the priorities of a specific physics analysis, one would be interested in the average number of reconstructed jets, or the energy resolution for non-overlapping jets, or the efficiency of the angular matching between primary quark and jet. The average number of jets gives an idea of the sensitivity to pile-up, underlying event, and the rate of fake jets, while the energy resolution can be linked to the issue of jet calibration.

## 8.6 Results

In this section the most important observations for each jet clustering algorithm considered are summarized.

### 8.61 Iterative Cone Algorithm

Fig. 42 shows the "FracGood" variable as a function of the cone radius. The maximum fraction of well reconstructed events is obtained for a cone radius varying from 0.3 to 0.5, depending on the event topology. The dependence of the fraction of well reconstructed events on the minimal transverse energy of the jet seed is found to be negligible. A stronger dependence as well as a larger optimal cone radius is however expected when the jet input is changed from simulated to reconstructed particles. due to a



magnet field, will result in a stronger dependence of the number of reconstructed jets with respect to a minimal seed  $E_T$ -value.

Another important observation is the decrease of the optimal cone radius for increasing jet multiplicity. This behaviour can be explained by the higher probability of overlapping jets for higher jet multiplicities. The generally lower selection efficiency (Fig.41) for high multiplicities is interpreted as due to higher probability for overlapping jets, the different  $p_t$  spectrum of the jets, and moreover to the fact that an increase of the average center of mass energy for  $t\bar{t}H$ -production compared to  $t\bar{t}$ -production will result in extra hard gluon jets.

Furthermore, a lower selection efficiency  $\epsilon_s$  is observed for very low jet radii. This can be explained by the transverse energy cut of 20 GeV which is more severe for small opening angles.

Both effects will result in a more difficult jet clustering task for high jet multiplicities. Compared to 55% of well clustered events in the two quark final state, only 6% of the events in an eight quark topology pass all the criteria using the optimum cone radius in each case.



Fig. 41: Fraction of selected events versus the cone radius (IC Fig. 42: Fraction of well clustered and selected events versus the cone radius (IC algorithm)).

The angular and energy resolutions for different cone radii are shown in Fig. 45. The points closest to the origin can be considered to give the best resolutions and they are in good agreement with the clustering parameters obtained for the optimal reconstruction efficiency.

### 8.62 Inclusive $k_T$ Algorithm

Fig. 44 shows the result for the scan of the R-parameter of the inclusive  $k_T$  algorithm. Again, a strong dependence on the jet multiplicity is observed. For the two quark topology, R=0.6 gives the best performance, while this value is reduced to 0.3 for the 8 quark topology. This behaviour is expected keeping in mind that the R-parameter plays a comparable role for the inclusive  $k_T$  algorithm as the jet radius does for the *Iterative Cone* algorithm. Compared to the optimal configuration of the *Iterative Cone* algorithm, this algorithm performs almost identical for the two quark case, but is able to get higher reconstruction efficiencies for larger jet multiplicities.



Fig. 43: Fraction of selected events versus the R-parameter ( $k_T$  Fig. 44: Fraction of well clustered and selected events versus the R-parameter ( $k_T$  algorithm)).

The resolution plot in Fig. 45 shows a similar behaviour as for the *Iterative Cone* algorithm. The resolution seems to be optimal for a R-parameter value for which also the fraction of selected and well clustered events is maximized.



Fig. 45: Relative energy resolution versus angular resolution ( $\Delta R$  distance between jet and quark) for the IC algorithm (left) and  $k_T$  algorithm (right). The markers of the same type represent the seven different IC cone radii (0.2-0.8) or the ten R-parameter values (0.1-1). The values on the top left are the ones with the smallest cone radii or R-parameter values, respectively. The energy resolution is defined as the RMS divided by the mean value of the  $E^{jet}/E^{quark}$  distribution, and the angular resolution is defined by the width of a gaussian fit to the symmetrized  $\Delta R$  distribution. For this plot, the two quark-jet pairs with the worst matching (only the worst one in the case of two jets) have been removed to reduce the effect of radiation.

### 8.63 Midpoint Cone algorithm

The scan of the cone radius is shown in Fig. 46 and the dependence on the shared energy fraction threshold for merging is shown in Fig. 47. For high jet multiplicities, the *MidPoint Cone* algorithm is able to



Fig. 46: Fraction of well clustered and selected events versus Fig. 47: Fraction of well clustered and selected events versus the cone radius for a merging threshold of 0.5 and a cone area the threshold for merging for a cone radius of 0.3 and an area fraction of 0.25 (MC algorithm).

reach slightly higher efficiencies than the *Iterative Cone* algorithm. Surprisingly, almost no dependence on the shared energy fraction threshold for merging has been found. This behaviour might be related to the fact that simulated particles have been used as input.

### 8.64 Summary of the Main Observations

Table 9 summarizes the optimal parameter values for the three jet clustering algorithms, and for each of the considered event topologies. For each optimal jet configuration, the respective estimate of the fraction of well reconstructed events is given.

### 8.65 Correlation Between Optimized Configurations

The correlation between the optimized *Iterative Cone* algorithm and the inclusive  $k_T$  algorithm for the final state with four primary quarks is shown in Fig. 48 and 49, for the  $\alpha_{jp}^{max}$  and  $\beta_{jp}^{max}$  variables.

Table 9: Overview of the optimal parameter values with their respective estimate of the fraction of well reconstructed events.

	IC		$k_T$		MC		MC	
	jet radius		R-parameter		jet radius		Overlap Threshold	
	<i>Value</i>	<i>FracGood</i>	<i>Value</i>	<i>FracGood</i>	<i>Value</i>	<i>FracGood</i>	<i>Value</i>	<i>FracGood</i>
2 quarks	0.5	53.9	0.6	54.9	0.5	42.4	0.40	40.3
4 quarks	0.5	22.3	0.5	23.8	0.3	22.8	0.40-0.50	22.9
6 quarks	0.3	11.2	0.4	12.9	0.2	12.1	0.50-0.60	11.8
8 quarks	0.3	4.85	0.3	5.93	0.2	5.72	0.60	5.0

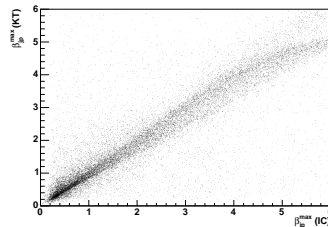
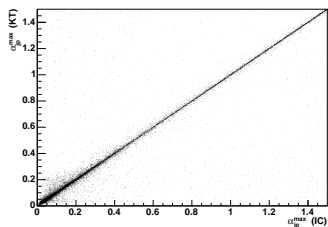


Fig. 48: Correlation between the IC and  $k_T$  algorithms for the  $\alpha_{jp}^{max}$  variable in the case of the final state with four primary quarks. Fig. 49: Correlation between the IC and  $k_T$  algorithms for the  $\beta_{jp}^{max}$  variable in the case of the final state with four primary quarks.

### 8.66 Robustness Of The Method Against Hard Radiation

The sensitivity of the overall observations to the radiation of gluons with a large transverse momentum relative to their mother quark, or from the initial state proton system, is investigated in the following. The distributions of the  $\alpha_{jp}^i$ -values ordered by their magnitude within an event are shown in Fig. 50 for a sample without initial and final state radiation<sup>13</sup>. This has to be compared directly to Fig. 36 which

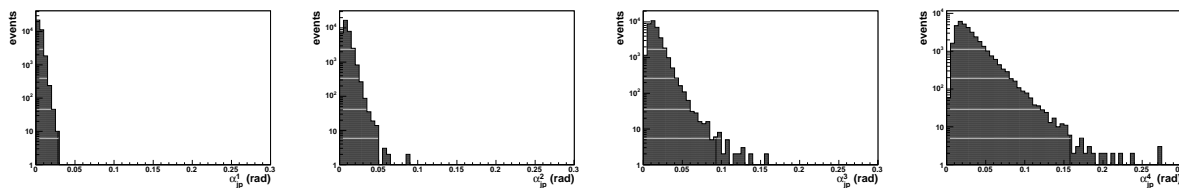


Fig. 50: Distributions of  $\alpha_{jp}^i$  in increasing order of magnitude for the IC algorithm in the case of a final state with four primary quarks which do not radiate hard gluons.

shows the same plots including final state radiation. Obviously, the long tails are not present in the case without radiation which indicates that the  $\Delta R$  cut of 0.3 for the worst jet is not expected to have an effect in this case. The observation is indeed, that the  $\text{Frac}(\alpha_{jp}^{max} + \beta_{jp}^{max})$  quality marker has a flat distribution, but not the selection efficiency and therefore the “FracGood” quality marker.

Fig. 51 shows the fraction of selected, well clustered semileptonic  $t\bar{t}$  events with and without initial and final state radiation for the *Iterative Cone* algorithm. The addition of radiation results in an overall lower efficiency, but the optimal cone radius and the shape of the curve are robust. A similar observation was obtained for the inclusive  $k_T$  algorithm in Fig. 52.

In order to quantify the effect of radiation on the resolutions, Fig. 53 shows the two cases for the *Iterative Cone* and the inclusive  $k_T$  algorithm. As expected, the overall resolutions are better in the case without radiation, but the shape of the curves remains invariant.

<sup>13</sup>PYTHIA parameters *MSTP* 61 and 71 were switched off.

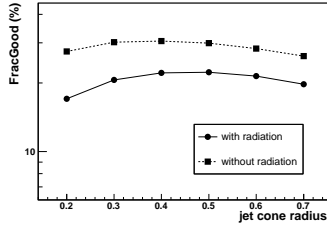


Fig. 51: Influence of hard gluon radiation on the fraction of selected, well clustered events, as a function of the IC cone radius selected, in the case with four primary quarks in the final state.

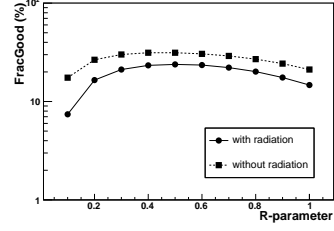


Fig. 52: Influence of hard gluon radiation on the fraction of selected, well clustered events, as a function of the  $k_T$  R-parameter in the case with four primary quarks in the final state.

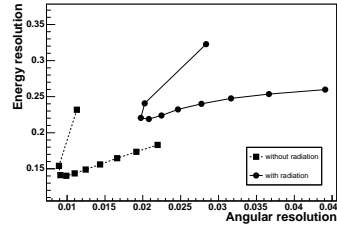
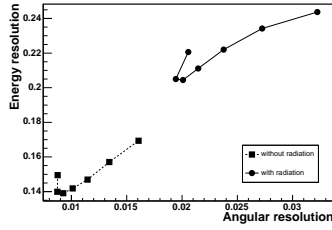


Fig. 53: Energy resolution versus angular resolution ( $\Delta R$  distance between jet and quark) for the IC algorithm (left) and  $k_T$  algorithm (right) in the case of four jets in the final state. The definitions are identical to them in Fig. 45.

## 8.7 Conclusions

In this paper three jet clustering algorithms (the *Iterative Cone* algorithm, the inclusive  $k_T$  algorithm and the *MidPoint Cone* algorithm) are compared according to some pre-defined performance criteria based on reconstruction efficiencies of the kinematics of the primary quarks. A scan of the most important algorithm parameters is performed in order to determine the optimal jet clustering from an analysis point of view, i.e. to maximize the reconstruction efficiency.

As a proof of concept for the quality definition of the jet clustering, the top quark mass was determined from reconstructed jets. The quality markers were able to isolate the narrow, gaussian top quark mass peak in a broad distribution.

The study was performed on different event samples with topologies ranging from two primary quarks (fully leptonic and semileptonic top quark pairs) up to eight ( $t\bar{t}H \rightarrow bq\bar{q}b\bar{q}q\bar{b}\bar{b}$ ). As expected, it was found that smaller opening angles are better suited for higher jet multiplicities.

The presented results have been obtained using simulated particle information at the vertex, and without a magnetic field, but similar results have already been extracted for a full detector simulation. These results will be published in dedicated papers for the specific experiments.

## 9. COLOUR ANNEALING — A TOY MODEL OF COLOUR RECONNECTIONS <sup>14</sup>

### 9.1 Introduction

Among the central objectives of collider physics is the precise measurement of the elementary particle masses and couplings. Striking recent examples are the measurements both at LEP and at the Tevatron of the mass of the W boson to a precision better than one per mille [175, 176] — a precision giving truly valuable insight into the mechanism of electroweak symmetry breaking as well as in probing for the quantum effects of New Physics.

At present, with the top quark in focus at the Tevatron and the physics programme of the LHC

<sup>14</sup>Contributed by: M. Sandhoff, P. Skands

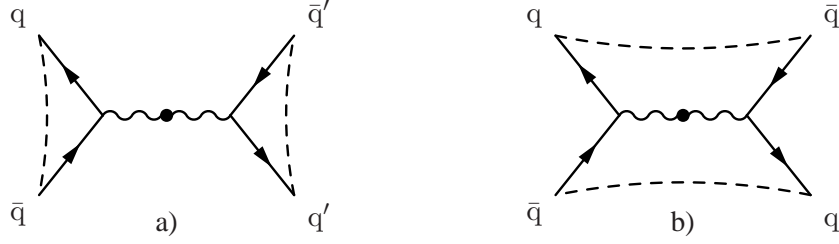


Fig. 54: a) the original colour topology in hadronic  $e^+e^- \rightarrow WW$  events, and b) a reconnected version. Note that these are not Feynman diagrams but rather spatial diagrams depicting the situation after the annihilation, with the production point at the origin. Arrows pointing against the direction of motion signify antifermions.

only a few years distant, the solid understanding of QCD phenomena beyond leading-order perturbation theory is becoming increasingly more important, with a large range of both experimental and theoretical methods and tools being developed. The aim, to achieve theoretical and systematic uncertainties capable of matching the expected statistical precision of the large data samples becoming available.

Apart from developments in flavour physics and lattice QCD, essentially all of these approaches focus on the perturbative domain of QCD — in brief: including more legs/loops/logarithms in the calculations. The point we wish to stress here is that, even assuming these approaches to one day deliver predictions with negligible uncertainties associated with uncalculated perturbative orders, there still remains the non-perturbative aspects, for which current understanding cannot be called primitive, but certainly not crystal clear either.

Recently, the structure and physics of the underlying event has received some attention [177–180], but again the main theoretical thrust, with few exceptions [181, 182], has taken place in the perturbative modeling, in the form of more sophisticated models for multiple perturbative interactions [29, 34, 183]. While non-perturbative aspects certainly play a significant role, and enter into the descriptions in the form of various phenomenological parameters, they generally suffer from being hard to quantify, hard to calculate, and hard to test. In this study, we shall focus on precisely such a source of potential uncertainty: colour reconnection effects in the final state, in particular in the context of measurements made at hadron colliders.

In Section 9.2 we briefly discuss some previous celebrations on colour reconnections, and in Section 9.3 present our own toy model, for use in the present study. In Section 9.4 we give a few explicit examples and show some results for  $t\bar{t}$  events at the Tevatron. Section 9.5 contains a summary and outlook.

## 9.2 Colour Reconnections

The subject of colour rearrangements was first studied by Gustafson, Pettersson, and Zerwas (GPZ) [184], there in a mainly qualitative way, and in the context of rearrangements taking place already at the perturbative level. They observed that, e.g. in hadronic  $WW \rightarrow (q_1\bar{q}_2)(q_3\bar{q}_4)$  events at LEP, illustrated in Fig. 54a with colour connections traced by dashed lines, interference effects and gluon exchanges between the decay products could lead to a reconfiguration of the colour topology into the one depicted in Fig. 54b. In the reconnected topology, both the perturbative QCD cascade and the subsequent hadronisation phase would be substantially different, leading to very large effects.

Sjöstrand and Khoze (SK) [185, 186] subsequently argued that such large effects were most likely unrealistic. A reconnection already at the perturbative level requires at least two perturbative gluon vertices, leading to an  $\alpha_s^2$  suppression. Moreover, the relevant reconnection diagram is colour suppressed by  $1/N_c^2$  with respect to the leading (non-reconnected)  $\mathcal{O}(\alpha_s^2)$  diagrams. Finally, for the decay products of the two W bosons to radiate coherently, they must, in the language of wave mechanics, be in phase, which only occurs for radiation at energies smaller than the W width. In other words, gluons with

wavelengths smaller than the typical separation of the two  $W$  decay vertices will be radiated (almost) incoherently. For these reasons, SK considered a scenario where reconnections occur as part of the non-perturbative hadronisation phase.

The SK model is based on the standard Lund string fragmentation model [187], in which the chromo-electric flux lines formed between colour charges separated at distances larger than  $\sim 1\text{fm}$  are represented by simple massless strings. SK argued that, if two such strings overlap in space and time, there should be a finite possibility for them to ‘cut each other up’ and rearrange themselves, much as has been recently discussed for the case of cosmic and mesonic superstrings [188, 189]. However, since we do not yet know whether QCD strings behave more like flux tubes in a Type II or a Type I superconductor (roughly speaking whether the topological information is stored in a small core region or not), SK presented two distinct models, commonly referred to as SK-II and SK-I, respectively. As would be expected, both models resulted in effects much smaller than in the GPZ model, leading to a predicted total uncertainty on the  $W$  mass from this source of  $\sigma_{M_W} < 40\text{ MeV}$ . SK also performed a study of QCD interconnection effects in  $t\bar{t}$  production [190], but only in the context of  $e^+e^-$  collisions.

Subsequently, a number of alternative models have also been proposed, most notably the ones proposed by the Lund group, based on QCD dipoles [191–193], and one based on clusters by Webber [194]. Apart from  $WW$  physics, colour reconnections have also been proposed to model rapidity gaps [195–197] and quarkonium production [198].

Returning to  $e^+e^-$ , experimental investigations at LEP II have not found conclusive evidence of the effect [199, 200], but were limited to excluding only the more dramatic scenarios, such as GPZ and versions of SK-I with the recoupling strength parameter close to unity. Hence, while colour reconnection effects cannot be arbitrarily large, there is room for further speculation. In addition, as we shall argue below, it may be possible that the effect is enhanced in hadron collisions over  $e^+e^-$  — with the added complication that the environment at hadron colliders is necessarily much less benign to this sort of measurement than was the case at LEP.

### 9.3 Our Toy Model — Colour Annealing

In electron–positron annihilation, the two incoming states carry electromagnetic charge — giving rise to a dilute cloud of virtual photons surrounding them — but no strong charge. From the QCD point of view, the vacuum state is thus undisturbed in the initial state, at least up to effects of order  $\alpha^2$ , i.e.  $e \rightarrow e'\gamma^* \rightarrow e'q\bar{q}$ . After the production of, say, a  $WW$  pair, e.g. with both  $W$  bosons decaying hadronically,  $e^+e^- \rightarrow W^+W^- \rightarrow (q_1\bar{q}_2)(q_3\bar{q}_4)$ , further QCD radiation and hadronisation then develops, in the background of this essentially pure vacuum state. As discussed above, the final state colour topology during the perturbative part of the QCD cascade, at least down to energies of order the  $W$  width, in all likelihood is the one depicted in Fig. 54a. For gluon energies smaller than the  $W$  width, however, the question is still relatively open.

Going to (inelastic, non-diffractive) hadron-hadron collisions, the initial state already contains strong charges. Using a simple bag model for illustration, the vacuum at the collision point and in the space-time area immediately surrounding it would not be the undisturbed one above, but would rather correspond to the vacuum *inside* the hadronic bag. Though detailed modeling is beyond the scope of the present discussion, we note that soft colour fields living inside this bag, with wavelengths of order the hadron size  $\sim$  hadronisation length, could impact in a non-trivial way the formation of colour strings at the time of hadronisation [195, 196], effects that would not have been present in  $e^+e^-$  collisions.

We are not aware of any detailed studies, neither experimental nor theoretical at this time. Several of the models mentioned above would still be more or less directly applicable, but the noisier environment of hadron colliders makes it daunting to attempt to look for any effect. In this paper, we propose a simple toy model, to give a first indication of the possible size of the effect, in particular for  $t\bar{t}$  production at the Tevatron.



Since we do not expect the difference in background vacuum to affect the short-distance physics, we take the arguments of SK concerning the absence of colour reconnections at the perturbative level to still be valid. Though one could still imagine reconnections below the relevant resonance widths, we shall not consider this. That is, we let the entire perturbative evolution remain unchanged, and implement our model at the hadronisation level only. Having no explicit model for how the presence of soft background fields would affect the collapse of the colour wave functions at hadronisation time, we consider an extreme case, where the quarks and gluons completely forget their colour ‘history’. Instead, what determines between which partons hadronising strings form is a minimization of the total potential energy stored in strings. Specifically, we propose that the partons, regardless of their formation history, will tend to be colour connected to the partons closest to them in momentum space, hence minimizing the string length and thereby the average particle multiplicity produced by the configuration, as measured by the so-called ‘Lambda measure’ [181,201], here given for massless partons for simplicity:

$$\Lambda = \prod_{i=1}^N \frac{m_i^2}{M_0^2} \quad , \quad (32)$$

where  $i$  runs over the number of colour-anticolour pairs (dipoles) in the event,  $N$ ,  $m_i$  is the invariant mass of the  $i$ ’th dipole, and  $M_0$  is a constant normalisation factor of order the hadronisation scale. The average multiplicity produced by string fragmentation is proportional to the logarithm of  $\Lambda$ . Technically, the model implementation starts by erasing the colour connections of all final state coloured partons, including ones from  $W$  decays etc. It then begins an iterative procedure (which unfortunately can be quite time-consuming):

1. Loop over all final state coloured partons.
2. For each such parton with a still unconnected colour or anticolour charge,
  - (a) Compute the  $\Lambda$  measure for each possible string connection from that parton to other final state partons which have a compatible free colour charge.
  - (b) Store the connection with the smallest  $\Lambda$  measure for later comparison.
3. Compare all the possible ‘minimal string pieces’ found, one for each parton. Select the largest of these to be carried out physically. That parton is in some sense the one that is currently furthest away from all other partons.
4. If any ‘dangling colour charges’ are left, repeat from 1.
5. At the end of the iteration, if the last parton is a gluon, and if all other partons already form a complete colour singlet system, the remaining gluon is simply attached between the two partons where its presence will increase the total  $\Lambda$  measure the least.

This procedure will find a local minimum of the  $\Lambda$  measure. More aggressive models could still be constructed, most noticeably by refining the algorithm to avoid being trapped in shallow local minima. As a side remark, we note that the above procedure, which we shall refer to as Type II below, as it stands would tend to result in a number of small closed gluon loops. Hence, we also consider a variant (Type I) where closed gluon loops are suppressed, if other possibilities exist, see illustration in Fig. 55. Both variants of the annealing algorithm are implemented in PYTHIA 6.326, and are carried over to PYTHIA 6.4, where they can be accessed using the `MSTP(95)` switch, see also the update notes [202] and the PYTHIA 6.4 manual [203].

## 9.4 Results

As a first application of the new models, we consider their effects on semileptonic  $t\bar{t}$  events at the Tevatron. Specifically, whether an effect could be observable in the light-quark jet system from the hadronic  $W$  decay. This is closely related to the work presented in [204].

For any fragmentation model, the first step is to make a (re)tune of the minimum-bias and underlying-event (UE) parameters. Ideally, the whole range of model parameters should come under

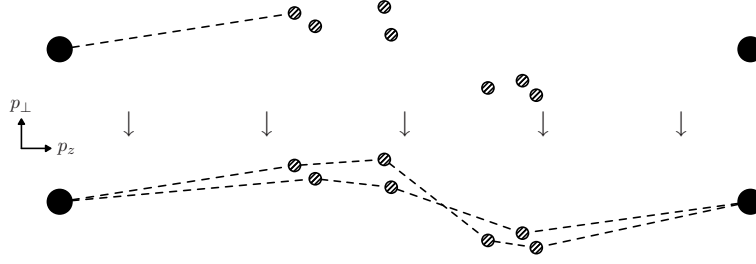


Fig. 55: Type I colour annealing in a schematic  $gg \rightarrow gg$  scattering. Black dots: beam remnants. Smaller dots: gluons emitted in the perturbative cascade. All objects here are colour octets, hence each dot must be connected to two string pieces. Upper: the first connection made. Lower: the final string topology.

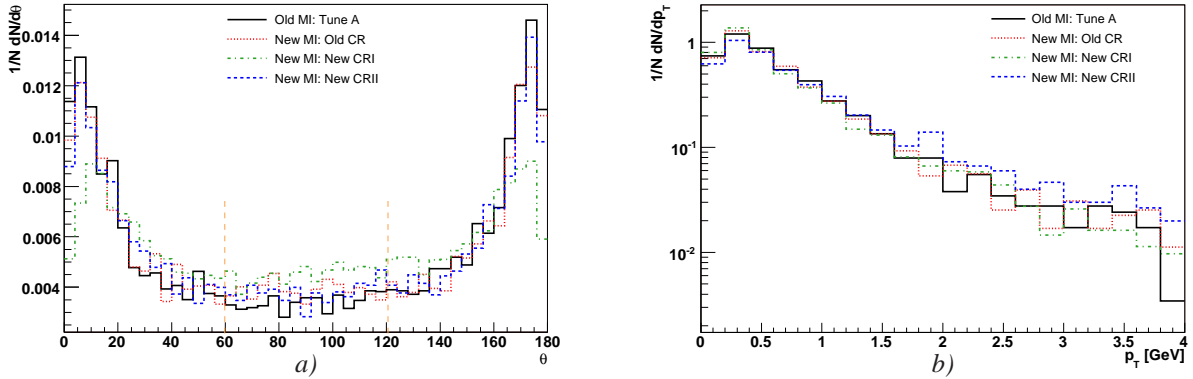


Fig. 56: Semi-leptonic top events at the Tevatron (see text). *a*) Charged particle density between the  $W$  jets (note the zero suppression) and *b*)  $p_{\perp}$  spectra for charged particles in the region  $60^{\circ} < \theta < 120^{\circ}$ .

scrutiny, however for the present study we limit ourselves to a one-parameter retuning of the multiple interactions colour-screening cutoff in PYTHIA ( $\text{PARP}(82)$ ), requiring the retuned models to agree with the average charged particle multiplicity of Tune A [177]. Below, we compare Tune A to a preliminary tune of the new UE framework (Old CR) adapted from the Low FSR tune in [183], and to the same model with Type I and Type II colour reconnections applied. For the 4 models,  $\text{PARP}(82) = 2.0, 2.1, 2.2, 1.55$ , respectively.

Next, for each of the tuned models, 50000  $t\bar{t}$  events were generated at  $E_{CM} = 1960$  GeV, corresponding to approximately  $8\text{fb}^{-1}$  of integrated luminosity. Out of the semi-leptonic fraction of this sample, events with exactly four charged particle jets were selected (clustered with an exclusive kT jet algorithm [205] with  $d_{\text{cut}} = 150 \text{ GeV}^2$ ). Finally, the jets have to be uniquely identified to the correct parton. This was done requiring that the (and only the) dedicated jet has a minimal  $\Delta R$  between its axis and the initial parton.

In the undisturbed colour topology, three string pieces are relevant; one spanned between the  $W$  jets, one between the  $b$  quark and the  $p$  beam remnant, and one between the  $\bar{b}$  and the  $\bar{p}$  remnant. To maximise the overlap of these strings, and hence create a bias towards situations where colour reconnections should be enhanced, we reject events that do not fulfill either condition A)  $\eta_q > \eta_{\bar{q}} > \eta_b$  or B)  $\eta_{\bar{b}} > \eta_q > \eta_{\bar{q}}$ .

For each accepted event, we perform a boost to the rest frame of the hadronic  $W$ , then a polar rotation to line up the decay jets along the  $z$  axis (for condition A (B), the quark is rotated to  $0^{\circ}$  ( $180^{\circ}$ )), and finally an azimuthal rotation to bring the  $b$  jet from the associated top decay into the  $(x, z)$  plane, in the positive- $x$  hemisphere. We then reject events where the other  $b$  jet is not also in the positive- $x$  hemisphere, so that the negative- $x$  hemisphere between the  $W$  jets should, at least to some extent, be free from extraneous hadronic activity.

We consider two observables, in both cases only including particles in the negative- $x$  hemisphere. First, in Fig. 56a, the charged particle multiplicity between the jets,  $1/N_{\text{ch}}dN_{\text{ch}}/d\theta$ , and second, in Fig. 56b, the transverse momentum distribution  $1/N_{\text{ch}}dN_{\text{ch}}/dp_{\perp}$  for particles in the inter-jet region,  $60^{\circ} < \theta < 120^{\circ}$ , indicated in Fig. 56a by dashed vertical markers.

In Fig. 56a, the asymmetry between the left and right peak sizes is due to the rapidity constraints and to the way we performed the rotations; conditions A and B then both force the associated  $b$  quark to be closer to the right-hand jet. Given the subtle nature of the effect, and the noisy hadronic environment, the variations in Fig. 56 are quite large (the distortion of the peak shape at small angles for Type I is, however, probably too large to be realistic). However, notice that the reconnected scenarios do *not* lead to a significant reduced charged particle density in the inter-jet region, which would have been the effect we should naively have been looking for, by comparison to the  $e^{+}e^{-}$  studies. We note, however, that the most aggressive of the new models, Type II (blue dashed curve), does produce fewer particles in the fragmentation region than its sister Type I (green dot-dashed), and also (as shown in figure 56b) that the charged particles produced in Type II have a higher average  $p_{\perp}$ .

What is going on is that, as for so many aspects of hadron-hadron physics, the end result is not controlled by one effect alone, but by a combination of factors. Multiplicity will be increased by allowing more underlying-event activity and will be decreased by allowing more colour reconnections. Hence the same multiplicity can be arrived at through different mixes of these. By first tuning to the min-bias data we are to some extent cancelling these effects against each other. This illustrates an essential point: in a hadron-hadron environment, the multiplicity alone may not be a discriminating variable. However, the mixes are not completely equivalent. While they may lead to the same result in one distribution, they will differ for another. Specifically, by combining the particle flow with the energy flow, some discriminating power can be gained. One way of realising this is to consider that the underlying activity is pumping energy into the event. To maintain the same multiplicity distribution, the particle hardness must then be a function of the underlying activity, as is illustrated by Fig. 56. While we shall terminate our discussion here, the subject of disentangling these effects certainly merits further consideration.

## 9.5 Conclusions

We have presented a few simple toy models of colour reconnections, based on an annealing-like algorithm. These models are quite general and are directly applicable to any process, unlike many previous models for which only implementations specific to WW events exist.

As a first application, we have studied the effects on two simple observables in semileptonic  $t\bar{t}$  events at the Tevatron. We find that, while we cannot discern the presence or absence of a classical string effect in the multiplicity distributions alone, it may still be possible to distinguish between different models by including energy-flow information. The natural next step would be to consider the extent to which measurements of the top mass at the Tevatron and LHC are influenced by these effects. For instance, an attractive possibility is to use the hadronically reconstructed  $W$  mass in these events to set the jet energy scale, hence the degree to which the hadronic  $W$  mass reconstruction is affected by the effects discussed here would be interesting to examine.

We intend this study mostly for illustration and for communicating a few essential remarks. As such, we have freely (ab)used Monte Carlo truth information and have skipped lightly over a number of aspects, which would have to be more carefully addressed in a real analysis. We hope that this work may nevertheless serve to stimulate further efforts in this exciting and presently little understood field.

## Acknowledgements

We are grateful to the organisers of Les Houches 2005, “Physics at TeV Colliders” for a wonderful workshop, and to T. Sjöstrand for enlightening discussions and comments on the manuscript. Furthermore we would like to thank P. Mättig and T. Harenberg for their support. This work was supported by Uni-

versities Research Association Inc. under Contract No. DE-AC02-76CH03000 with the United States Department of Energy.

## 10. TUNED COMPARISON OF ELECTROWEAK CORRECTIONS TO DRELL–YAN-LIKE $W$ - AND $Z$ -BOSON PRODUCTION – A STATUS REPORT <sup>15</sup>

### 10.1 Introduction

The basic parton processes for single vector-boson production are  $qq' \rightarrow W \rightarrow l\nu_l$  and  $q\bar{q} \rightarrow \gamma/Z \rightarrow l^+l^-$ , with charged leptons  $l$  in the final state. Experimental measurements in the vicinity of the  $W$  and  $Z$  resonances allow for a precise determination of the  $W$ -boson mass and, from the forward-backward asymmetry, of the effective weak mixing angle. Above resonance, the off-shell tails of appropriate distributions are sensitive to the gauge-boson decay widths. At high invariant masses, for example, of the  $l^+l^-$  pair, deviations from the standard cross section and  $A_{\text{FB}}$  could indicate new physics, such as an extra heavy  $Z'$  or extra dimensions. Finally, the Drell–Yan-like  $W$  and  $Z$  production processes may be used as a luminosity monitor or to further constrain PDFs at the LHC.

Predictions for Drell–Yan processes do not only receive sizeable QCD corrections, which are known up to NNLO [206, 207], but also important corrections of electroweak origin. Unfortunately, existing Monte Carlo generators, such as HORACE [208, 209], RESBOS [210, 211], WINHAC [212] and WGRAD [213] / ZGRAD [214], do not yet combine the complete knowledge on strong *and* electroweak higher-order effects. A first step towards this goal has been taken in Ref. [215] where the combined effect of soft-gluon summation and final-state photon radiation has been studied for  $W$ -boson production. For more details on predictions for Drell–Yan processes we refer to the literature [216–219].

In this article we focus on electroweak corrections, which are completely known in  $\mathcal{O}(\alpha)$ . Historically, a first step to include electroweak corrections was already made in Ref. [220], where effects of final-state radiation in the gauge-boson decay stage were taken into account. For  $W$  production the approximation of Ref. [220] has been improved later in Ref. [213] by the inclusion of  $\mathcal{O}(\alpha)$  corrections to resonant  $W$  bosons and in Refs. [221, 222] by the full corrections of  $\mathcal{O}(\alpha)$ . For  $Z$  production the  $\mathcal{O}(\alpha)$  QED corrections have been presented in Ref. [223] and completed by the corresponding weak contributions in Ref. [214]. The particular importance of final-state photon radiation demands a treatment that goes beyond  $\mathcal{O}(\alpha)$ . Such multi-photon effects have been studied both for  $W$ - and  $Z$ -boson production in Refs. [208, 212] and Ref. [209], respectively. A comparison of these two calculations can be found in Ref. [224].

In the following we focus on precision calculations of electroweak corrections as performed by various groups in recent years and present a status report of a comparison for a common set of input parameters and a uniformly tuned setup (input-parameter scheme, PDFs etc.). In particular, the recently released  $\mathcal{O}(\alpha)$ -improved PDFs “MRST2004QED” [225] are employed. This set of PDFs includes a photon distribution function resulting from the  $\mathcal{O}(\alpha)$ -driven evolution of the PDFs, i.e. the Drell–Yan cross section receives a new type of real correction from photon-induced processes.

The different approaches that are compared are briefly summarized in the next section, the precise setup is described in Section 10.3, and Section 10.4 contains the numerical results.

### 10.2 Different approaches and codes

The following collaborations have contributed to the tuned comparison of results on electroweak corrections to Drell–Yan processes:

- DK: Ref. [221] contains a detailed description of the calculation of the  $\mathcal{O}(\alpha)$  corrections to  $W$  production at hadron colliders and a discussion of results for the Tevatron and the LHC. In particular,

---

<sup>15</sup>Contributed by: A. Arbuzov, U. Baur, S. Bondarenko, C. Carloni Calame, S. Dittmaier, M. Krämer, G. Montagna, O. Nicrosini, R. Sadykov, A. Vicini, D. Wackerroth

the full  $\mathcal{O}(\alpha)$  calculation is compared with a pole approximation for the W resonance. The case of Z-boson production is not considered. For the present analysis, the calculation of Ref. [221] has been extended (i) to include final-state radiation beyond  $\mathcal{O}(\alpha)$  via structure functions and (ii) by implementing the  $\mathcal{O}(\alpha)$ -corrected PDF set MRST2004QED. The photon-induced processes  $\gamma q \rightarrow q' l \nu_l$  and  $\gamma \bar{q}' \rightarrow \bar{q} l \nu_l$  have been calculated as described in Ref. [226]. The evaluation of the  $q\bar{q}'$  channel has been technically improved by employing a generalization of the dipole subtraction approach [227] to non-collinear-safe observables, as partially described in Ref. [228].

- HORACE [208, 209] is a Monte Carlo generator for single W/Z boson production at hadron colliders. In its published version [208, 209] it simulates final-state-like multiple photon emission corrections via the QED parton-shower algorithm developed in Refs. [229, 230]. For the present study, HORACE has been extended (i) by including the exact  $\mathcal{O}(\alpha)$  electroweak corrections to W production and (ii) by implementing the MRST2004QED set of PDFs. Photon-induced processes, as well as the exact  $\mathcal{O}(\alpha)$  corrections to Z production, are not taken into account in the present version. A version of the generator, where the exact  $\mathcal{O}(\alpha)$  corrections and the parton-shower are matched, is in preparation. The theoretical and computational details of the calculation of the exact  $\mathcal{O}(\alpha)$  corrections to W production and its matching with QED radiation beyond  $\mathcal{O}(\alpha)$  will be presented elsewhere [231].
- SANC [232] (see <http://sanc.jinr.ru> and <http://pcphysanc.cern.ch>) is an automated system which provides complete parton level results for the electroweak one-loop corrections to both neutral- and charged-current Drell-Yan processes. SANC is based on the construction of helicity amplitudes and electroweak form factors. It automatically generates results in FORTRAN format which can be implemented in Monte Carlo event generators. The integration over the phase space for hard photon emission can be performed either (semi-)analytically or by means of a Monte Carlo integrator. Although the semi-analytical treatment of the hard photon contribution does not allow to impose all required cuts (i.e. the cut on the missing transverse momentum), it provides an important check of the Monte Carlo calculation. A detailed description of the SANC calculation of the charged-current Drell-Yan process can be found in Ref. [233].
- WGRAD [213,222] and ZGRAD2 [214] (see <http://ubpheno.physics.buffalo.edu/~dow/>) are two Monte Carlo programs that include the complete  $\mathcal{O}(\alpha)$  electroweak radiative corrections to  $p\bar{p} \rightarrow W^\pm \rightarrow \ell^\pm \nu$  (WGRAD) and  $p\bar{p} \rightarrow \gamma, Z \rightarrow l^+ l^- X$  ( $l = e, \mu$ ) (ZGRAD2). Both Monte Carlo programs use the phase space slicing method described in Refs. [234–236]. Charged lepton mass effects  $\propto \ln(\hat{s}/m_l^2)$  associated with collinear final-state photon radiation are included in the calculation while very small terms of  $\mathcal{O}(m_l^2/\hat{s})$  have been neglected. For this comparison the MRST2004QED structure functions have been implemented, and the lepton selection cuts and photon-lepton recombination procedure have been modified according to the specifications given in this report. Radiative corrections beyond  $\mathcal{O}(\alpha)$  that are partially implemented in WGRAD and ZGRAD2 have been switched off.



### 10.3 Common setup for the calculations

#### 10.3.1 Input parameters and scheme definitions

The relevant input parameters are

$$\begin{aligned}
G_\mu &= 1.16637 \times 10^{-5} \text{ GeV}^{-2}, & \alpha(0) &= 1/137.03599911, & \alpha_s &= 0.1187, \\
M_W &= 80.425 \text{ GeV}, & \Gamma_W &= 2.124 \text{ GeV}, & & \\
M_Z &= 91.1876 \text{ GeV}, & \Gamma_Z &= 2.4952 \text{ GeV}, & M_H &= 115 \text{ GeV}, \\
m_e &= 0.51099892 \text{ MeV}, & m_\mu &= 105.658369 \text{ MeV}, & m_\tau &= 1.77699 \text{ GeV}, \\
m_u &= 66 \text{ MeV}, & m_c &= 1.2 \text{ GeV}, & m_t &= 178 \text{ GeV}, \\
m_d &= 66 \text{ MeV}, & m_s &= 150 \text{ MeV}, & m_b &= 4.3 \text{ GeV}, \\
|V_{ud}| &= 0.975, & |V_{us}| &= 0.222, & & \\
|V_{cd}| &= 0.222, & |V_{cs}| &= 0.975, & & 
\end{aligned} \tag{33}$$

which essentially follow Ref. [237]. For the top-quark mass  $m_t$  the value of Ref. [238] is taken. The masses of the light quarks are adjusted to reproduce the hadronic contribution to the photonic vacuum polarization of Ref. [239]. The CKM matrix is included via global factors to the partonic cross sections.

The lowest-order cross section is parametrized in the “ $G_\mu$  scheme” as defined in Ref. [221], i.e. the electromagnetic coupling  $\alpha$  is derived according to  $\alpha_{G_\mu} = \sqrt{2}G_\mu M_W^2(1 - M_W^2/M_Z^2)/\pi$ , so that the results are practically independent of the masses of the light quarks. Moreover, this procedure absorbs the corrections proportional to  $m_t^2/M_W^2$  in the fermion–W-boson couplings and the running of  $\alpha(Q^2)$  from  $Q^2 = 0$  to the electroweak scale. In the relative radiative corrections, however,  $\alpha(0)$  is used as coupling parameter, which is the correct effective coupling for real photon emission. Note that the  $\mathcal{O}(\alpha)$  corrections in the  $G_\mu$  scheme receive a constant contribution from the quantity  $\Delta r$ , as described in Ref. [221]. The W- and Z-boson resonances are treated with fixed widths without any running effects.

The  $\mathcal{O}(\alpha)$ -improved set of PDFs “MRST2004QED” [225] is used throughout. The factorization of the photonic initial-state quark-mass singularities is done in the DIS-like factorization scheme, i.e. *not* in the  $\overline{\text{MS}}$  scheme as frequently done in the past, because photon radiation off incoming quarks was ignored in the  $F_2$  fit to HERA data [240] (see also Ref. [226]). The factorization scale is set to the weak boson mass, i.e. to  $M_W$  and  $M_Z$  for W- and Z-boson production, respectively.

#### 10.3.2 Phase-space cuts and event selection

In the following the same set of phase-space and event selection cuts are used as described in Ref. [221] for W production at the LHC ( $\sqrt{s} = 14 \text{ TeV}$ ). In detail, for the experimental identification of the process  $pp \rightarrow W^+ \rightarrow \nu_l l^+ (+\gamma)$  the set of phase-space cuts

$$p_{T,l} > 25 \text{ GeV}, \quad p_{T,\text{missing}} > 25 \text{ GeV}, \quad |\eta_l| < 1.2, \tag{34}$$

is adopted, where  $p_{T,l}$  and  $\eta_l$  are the transverse momentum and the rapidity of the charged lepton  $l^+$ , respectively, and  $p_{T,\text{missing}} = p_{T,\nu_l}$  is the missing transverse momentum carried away by the neutrino. Note that these cuts are not “collinear safe” with respect to the lepton momentum, so that observables in general receive corrections that involve large lepton-mass logarithms of the form  $\alpha \ln(m_l/M_W)$ . This is due to the fact that photons within a small collinear cone around the charged lepton momentum are not treated inclusively, i.e. the cuts assume a perfect isolation of photons from the charged lepton. While this is (more or less) achievable for muon final states, it is not realistic for electrons. In order to be closer to the experimental situation for electrons, the following photon recombination procedure is considered:

1. Photons with a rapidity  $|\eta_\gamma| > 2.5$ , which are close to the beams, are treated as invisible, i.e. they are considered as part of the proton remnant.
2. If the photon survived the first step, and if the resolution  $R_{l\gamma} = \sqrt{(\eta_l - \eta_\gamma)^2 + \phi_{l\gamma}^2}$  is smaller than 0.1 (with  $\phi_{l\gamma}$  denoting the angle between lepton and photon in the transverse plane), then the

photon is recombined with the charged lepton, i.e. the momenta of the photon and of the lepton  $l$  are added and associated with the momentum of  $l$ , and the photon is discarded.

3. Finally, all events are discarded in which the resulting momentum of the charged lepton does not pass the cuts given in (34).

While the electroweak corrections differ for final-state electrons and muons without photon recombination, the corrections become universal in the presence of photon recombination, since the lepton-mass logarithms cancel in this case, in accordance with the KLN theorem.

## 10.4 Numerical results

### 10.4.1 $W$ -boson production

Table 10 compares results on integrated cross sections as given in Table 2 of Ref. [221], i.e. for  $pp \rightarrow W^+ \rightarrow \nu_l l^+ (+\gamma)$  with the different lower cuts on  $p_{T,l}$ . The quantities  $\delta_{e^+\nu_e}$  and  $\delta_{\mu^+\nu_\mu}$  correspond to the corrections relative to the lowest-order prediction  $\sigma_0$  for the case that no photon recombination is applied. The corrections for the  $e^+\nu_e$  final state are larger in size compared to the  $\mu^+\nu_\mu$  because of the existence

Table 10: Integrated lowest-order cross sections  $\sigma_0$  for  $W$  production at the LHC for different ranges in  $p_{T,l}$  and corresponding relative corrections  $\delta$ , as obtained from the various calculations.

pp $\rightarrow \nu_l l^+ (+\gamma)$ at $\sqrt{s} = 14$ TeV						
$p_{T,l}/\text{GeV}$	25– $\infty$	50– $\infty$	100– $\infty$	200– $\infty$	500– $\infty$	1000– $\infty$
$\sigma_0/\text{pb}$						
DK	2112.2(1)	13.152(2)	0.9452(1)	0.11511(2)	0.0054816(3)	0.00026212(1)
HORACE	2112.21(4)	13.151(6)	0.9451(1)	0.11511(1)	0.0054812(4)	0.00026211(2)
SANC	2112.22(2)	13.1507(2)	0.94506(1)	0.115106(1)	0.00548132(6)	0.000262108(3)
WGRAD	2112.3(1)	13.149(1)	0.94510(5)	0.115097(5)	0.0054818(2)	0.00026209(2)
$\delta_{e^+\nu_e}/\%$						
DK	-5.19(1)	-8.92(3)	-11.47(2)	-16.01(2)	-26.35(1)	-37.92(1)
HORACE	-5.23(1)	-8.98(1)	-11.49(1)	-16.03(1)	-26.36(1)	-37.92(2)
WGRAD	-5.10(1)	-8.55(5)	-11.32(1)	-15.91(2)	-26.1(1)	-38.2(2)
$\delta_{\mu^+\nu_\mu}/\%$						
DK	-2.75(1)	-4.78(3)	-8.19(2)	-12.71(2)	-22.64(1)	-33.54(2)
HORACE	-2.79(1)	-4.84(1)	-8.21(1)	-12.73(1)	-22.65(1)	-33.57(1)
SANC	-2.80(1)	-4.82(2)	-8.17(2)	-12.67(2)	-22.63(2)	-33.50(2)
WGRAD	-2.69(1)	-4.53(1)	-8.12(1)	-12.68(1)	-22.62(2)	-33.6(2)
$\delta_{\text{recomb}}/\%$						
DK	-1.73(1)	-2.45(3)	-5.91(2)	-9.99(2)	-18.95(1)	-28.60(1)
HORACE	-1.77(1)	-2.51(1)	-5.94(1)	-10.02(1)	-18.96(1)	-28.65(1)
SANC	-1.89(1)	-2.56(1)	-5.97(1)	-10.02(1)	-18.96(1)	-28.61(1)
WGRAD	-1.71(1)	-2.32(1)	-5.94(1)	-10.11(2)	-19.08(3)	-28.73(6)
$\delta_{\gamma q}/\%$						
DK	+0.071(1)	+5.24(1)	+13.10(1)	+16.44(2)	+14.30(1)	+11.89(1)

of fermion-mass logarithms originating from collinear final-state radiation. As explained above, these mass-singular corrections cancel if the photon is recombined, rendering the corresponding correction  $\delta_{\text{recomb}}$  smaller. At large  $p_{T,l}$  the electroweak corrections are dominated by Sudakov logarithms of



Table 11: Integrated lowest-order cross sections  $\sigma_0$  for W production at the LHC for different ranges in  $M_{T,\nu_l l}$  and corresponding relative corrections  $\delta$ . The transverse mass is defined by  $M_{T,\nu_l l} = \sqrt{2p_{T,l}p_{T,\nu_l}(1 - \cos \phi_{\nu_l l})}$ , where  $\phi_{\nu_l l}$  is the angle between the lepton and the missing momentum in the transverse plane.

pp $\rightarrow \nu_l l^+ (+\gamma)$ at $\sqrt{s} = 14$ TeV						
$M_{T,\nu_l l}/\text{GeV}$	50– $\infty$	100– $\infty$	200– $\infty$	500– $\infty$	1000– $\infty$	2000– $\infty$
$\sigma_0/\text{pb}$						
DK	2112.2(1)	13.152(2)	0.9452(1)	0.057730(5)	0.0054816(3)	0.00026212(1)
HORACE	2112.21(4)	13.151(6)	0.9451(1)	0.057730(2)	0.0054812(4)	0.00026211(2)
WGRAD	2112.2(1)	13.150(1)	0.9450(4)	0.057728(2)	0.0054811(2)	0.00026210(1)
$\delta_{e^+\nu_e}/\%$						
DK	-5.20(1)	-7.95(2)	-10.19(2)	-16.69(2)	-24.52(1)	-35.24(1)
HORACE	-5.21(1)	-8.00(1)	-10.20(1)	-16.70(1)	-24.53(1)	-35.25(1)
WGRAD	-5.09(1)	-7.73(2)	-10.12(2)	-16.69(3)	-24.50(4)	-35.3(3)
$\delta_{\mu^+\nu_\mu}/\%$						
DK	-2.75(1)	-5.03(2)	-7.98(1)	-14.43(1)	-21.99(1)	-32.15(1)
HORACE	-2.77(1)	-5.08(1)	-8.01(1)	-14.44(1)	-21.99(1)	-32.16(1)
SANC	-2.76(2)	-5.06(2)	-7.96(2)	-14.41(2)	-21.94(2)	-32.12(2)
WGRAD	-2.69(1)	-4.84(1)	-7.96(1)	-14.48(1)	-22.03(1)	-32.3(1)
$\delta_{\text{recomb}}/\%$						
DK	-1.73(1)	-3.43(2)	-6.52(2)	-12.55(1)	-19.51(1)	-28.75(1)
HORACE	-1.75(1)	-3.48(1)	-6.54(1)	-12.57(1)	-19.54(1)	-28.77(1)
WGRAD	-1.66(1)	-3.27(1)	-6.52(1)	-12.62(2)	-19.60(2)	-29.0(1)
$\delta_{\gamma q}/\%$						
DK	+0.0567(3)	+0.1347(1)	+0.2546(1)	+0.3333(1)	+0.3267(1)	+0.3126(1)

the form  $-\alpha/\pi \log^2(\hat{s}/M_W^2)$  which are independent of the lepton species. Comparing the results in Table 10 we find that the various calculations are, in general, consistent with each other. More detailed comparisons are in progress to further improve the agreement.

The corrections originating from the photon-induced processes are not included in  $\delta_{e^+\nu_e}$ ,  $\delta_{\mu^+\nu_\mu}$ , and  $\delta_{\text{recomb}}$ , but are shown separately as  $\delta_{\gamma q}$  in Table 10. They are enhanced at large  $p_{T,l}$  because of a new type of contribution where a W boson is exchanged in the  $t$ -channel. The photon-induced processes could in principle be used to extract information on the photon content of the proton. However, they are overwhelmed by QCD corrections and QCD uncertainties which strongly affect the  $p_{T,l}$  spectrum, see e.g. Ref [215]. If, on the other hand, one considers the distribution in the transverse mass  $M_{T,\nu_l l}$ , which is much less sensitive to QCD uncertainties, the impact of  $\delta_{\gamma q}$  is below the per-cent level. This is demonstrated in Table 11 where the  $\mathcal{O}(\alpha)$  cross section predictions with cuts on  $M_{T,\nu_l l}$  are shown.

Figure 57 shows the relative electroweak correction  $\delta$  as a function of the lepton transverse momentum  $p_{T,l}$ , and the transverse mass  $M_{T,\nu_l l}$  in pp  $\rightarrow W^+ \rightarrow \nu_l l^+ (+\gamma)$  for the LHC. The results from the DK, HORACE and SANC collaborations are in good agreement. Near  $p_{T,l} \approx M_W/2$  and  $M_{T,\nu_l l} \approx M_W$  the correction  $\delta$  reaches the order of 10% for bare muons. Since these enhanced corrections originate from collinear final-state radiation, they are negative for higher  $p_{T,l}$  and redistribute events to lower transverse momenta. The correction  $\delta$  is reduced to a few per cent after photon recombination, which eliminates the artificial lepton-mass logarithms.

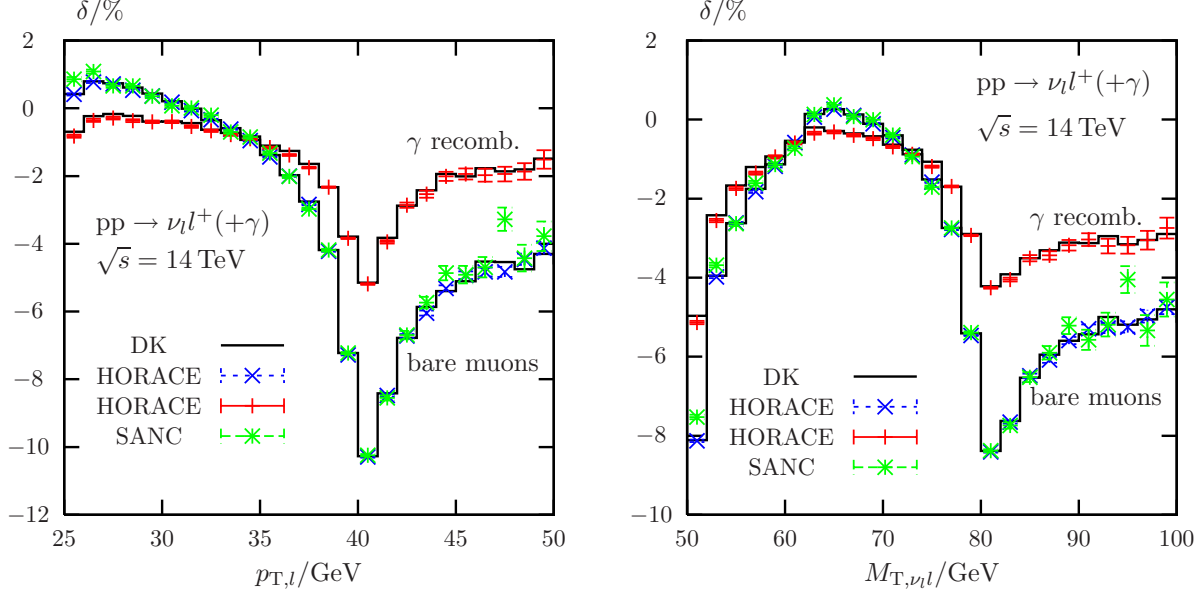


Fig. 57: Relative corrections  $\delta$  as a function of the transverse-momentum  $p_{T,l}$  and the transverse mass  $M_{T,\nu_l l}$ , as obtained from the DK, HORACE and SANC calculations. The contributions from the photon-induced processes have not been included in this comparison.

Table 12: Integrated lowest-order cross sections  $\sigma_0$  for Z production at the LHC for different ranges in  $M_{l+l-}$  and corresponding relative corrections  $\delta$ , as obtained from the HORACE and SANC calculations. The experimental lepton identification cuts  $p_{T,l} > 25$  GeV and  $|\eta_l| < 1.2$  have been applied.

pp $\rightarrow l^+l^- (+\gamma)$ at $\sqrt{s} = 14$ TeV						
$M_{l+l-}/\text{GeV}$	50– $\infty$	100– $\infty$	200– $\infty$	500– $\infty$	1000– $\infty$	2000– $\infty$
$\sigma_0/\text{pb}$						
HORACE	254.64(1)	10.571(1)	0.45303(3)	0.026996(2)	0.0027130(2)	0.00015525(1)
SANC	254.65(2)	10.572(7)	0.45308(3)	0.026996(2)	0.0027131(2)	0.000155246(6)
$\delta_{\mu^+\mu^-}/\%$						
SANC	-3.18(2)	-8.63(2)	-2.62(3)	-5.51(3)	-9.74(3)	-15.26(4)

#### 10.42 Z-boson production

Table 12 shows results on integrated cross sections for  $pp \rightarrow Z/\gamma \rightarrow l^+l^- (+\gamma)$  with the different lower cuts on  $M_{l+l-} = \sqrt{(p_{l^+} + p_{l^-})^2}$ , as obtained by the HORACE and SANC collaborations. Note that the experimental lepton identification cuts  $p_{T,l} > 25$  GeV and  $|\eta_l| < 1.2$  (cf. Eq. (34)) have been applied. The corrections do not contain contributions from the photon-induced processes.

### 10.5 Conclusions

We have presented precision calculations for electroweak corrections to the Drell–Yan-like production of W and Z bosons at the LHC from various theoretical collaborations. The calculations have been based on a common theoretical setup and choice of the input parameters, and are using the  $\mathcal{O}(\alpha)$ -improved MRST2004QED set of parton distribution functions. We have compared cross section predictions and differential distributions in the lepton transverse-momentum  $p_{T,l}$  and in the transverse mass  $M_{T,\nu_l l}$ , and find, in general, good agreement between the various calculations. We have also presented first results for the photon-induced processes which turn out to be large for large  $p_{T,l}$  but do not contribute significantly to the  $M_{T,\nu_l l}$  distribution. Work is in progress to further extend and improve the comparison of the

various calculations.

## Acknowledgements

The HORACE authors are grateful to Fulvio Piccinini for stimulating discussions. Three of us (A.A., S.B., R.S.) are grateful to Dmitri Bardin, Pena Christova, Lidia Kalinovskaya, and all the SANC collaboration members for help and their contributions to the SANC system, which were relevant for this study.

## 11. ELECTROWEAK CORRECTIONS TO LARGE TRANSVERSE MOMENTUM PRODUCTION OF $Z$ BOSONS AND PHOTONS AT THE LHC <sup>16</sup>

### 11.1 Introduction

The Large Hadron Collider (LHC) with its high center-of-mass energy and design luminosity will offer a unique possibility to explore production of gauge bosons with very large transverse momentum ( $p_T$ ). Being embedded in the environment of hadronic collisions, the reaction necessarily involves hadronic physics, like parton distributions, and depends on the strong coupling constant. In turn, the cross section for the  $Z$ -boson or direct photon production at large  $p_T$  is an important means to constrain information on the parton distribution functions (PDFs). For this class of production processes at the LHC, electroweak (EW) corrections from virtual boson exchange become important. This is due to the presence of the logarithmic terms of the form  $\alpha^k \log^{2k-i}(\hat{s}/M_W^2)$  (with  $i = 0$  for the leading logarithmic (LL) terms,  $i = 1$  for the next-to-leading logarithmic (NLL) terms, etc.) at the  $k$ -loop level. These corrections, also known as electroweak Sudakov logarithms, may well amount to several tens of per cent. A recent survey of the literature on logarithmic EW corrections can be found in Ref. [241]. Specifically, full one-loop weak corrections to the hadronic  $Z$ -boson and prompt photon production at large  $p_T$  have been studied in Refs. [242, 243]. Numerical results for the one-loop corrections to these two processes can be also found in Ref. [244]. In the following we briefly discuss the calculation of Refs. [242, 243] and present compact analytic expressions for the  $Z$ -boson and direct photon production in the high energy approximation, derived from the exact one-loop results in Refs. [242, 243]. Moreover, we also present the NLL contributions to the two-loop EW corrections, calculated in Refs. [243, 245]. Corresponding numerical results are discussed.

Of course, to achieve reliable predictions at high  $p_T$ , the QCD corrections in next-to-leading order (NLO) need to be taken into account as they can amount to several tens of per cent correction for both processes. However, in the following we are interested only in the EW corrections to the leading order (LO) in the strong coupling constant  $\alpha_S$  cross section for the process  $pp \rightarrow Vj$  ( $V = \gamma, Z$ ;  $j = \text{jet}$ ).

### 11.2 Calculation

In the calculation of the one-loop corrections to the hadronic production of  $Z$  bosons [242] and the hadronic production of photons [243] at large  $p_T$  we consider only weak contributions, i.e. we do not include photonic corrections. The quarks are assumed massless and diagrams involving couplings of quarks to Higgs bosons or would-be-Goldstone bosons are neglected. Moreover, we omit quark-mixing effects in the calculations. The calculation for the  $\bar{q}q \rightarrow Vg$  ( $V = \gamma, Z$ ) subprocess is performed at the level of matrix elements and allows for full control over polarization effects. Results for the other contributing subprocesses,  $q\bar{q} \rightarrow Vg$ ,  $gq \rightarrow Vq$ ,  $qg \rightarrow Vq$ ,  $\bar{q}q \rightarrow V\bar{q}$  and  $g\bar{q} \rightarrow V\bar{q}$  are easily obtained from CP symmetry and crossing transformations. The one-loop amplitude is split into two parts: Abelian and non-Abelian, as the structure of the gauge group generators in front of each term contributing to the amplitude can be classified as either Abelian (characteristic for Abelian theories) or non-Abelian (originating from non-commutativity of weak interactions). Tensor loop integrals, appearing in the expressions for one-loop corrections are reduced to scalar integrals by means of Passarino-Veltman technique. For

<sup>16</sup>Contributed by: A. Kulesza, S. Pozzorini, M. Schulze

the  $Z$ -boson and photon production the electroweak coupling constants are renormalized in the  $\overline{\text{MS}}$  and on-shell (OS) scheme, respectively. The wave functions of all external particles are always renormalized according to the on-shell prescription. The weak-boson masses need not to be renormalized since they do not enter the tree-level amplitudes. Further details of the calculation can be found in Refs. [242, 243].

### 11.21 Analytical results

The  $p_{\text{T}}$  distribution for the partonic reaction  $\bar{q}q \rightarrow Vg$  ( $V = \gamma, Z$ ) reads

$$\frac{d\hat{\sigma}^{\bar{q}q \rightarrow Vg}}{dp_{\text{T}}} = \frac{p_{\text{T}}}{8\pi N_c^2 \hat{s} |\hat{t} - \hat{u}|} \left[ \overline{\sum} |\mathcal{M}^{\bar{q}q \rightarrow Vg}|^2 + (\hat{t} \leftrightarrow \hat{u}) \right], \quad (35)$$

where  $N_c = 3$ ,  $\overline{\sum} = \frac{1}{4} \sum_{\text{pol}} \sum_{\text{col}}$ ,  $\hat{s} = (p_{\bar{q}} + p_q)^2$ ,  $\hat{t} = (p_{\bar{q}} - p_V)^2$ ,  $\hat{u} = (p_q - p_V)^2$  and  $p_V^2 = M_V^2$ . To  $\mathcal{O}(\alpha^2 \alpha_S)$  for the unpolarized squared matrix element we have

$$\begin{aligned} \overline{\sum} |\mathcal{M}_1^{\bar{q}q \rightarrow Vg}|^2 &= 8\pi^2 \alpha \alpha_S (N_c^2 - 1) \sum_{\lambda=R,L} \left\{ (I_{q_\lambda}^V)^2 \left[ H_0^V (1 + 2\delta C_{q_\lambda}^{V,A}) \right. \right. \\ &\quad \left. \left. + \frac{\alpha}{2\pi} \sum_{V'=Z,W^\pm} \left( I^{V'} I^{\bar{V}'} \right)_{q_\lambda} H_1^{V,A}(M_{V'}^2) \right] + \frac{U_{VW^3}}{s_W} T_{q_\lambda}^3 I_{q_\lambda}^V \left[ 2H_0^V \delta C_{q_\lambda}^{V,N} + \frac{\alpha}{2\pi} \frac{1}{s_W^2} H_1^{V,N}(M_W^2) \right] \right\}, \end{aligned} \quad (36)$$

where  $I_{q_\lambda}^V$  represents the coupling of an electroweak gauge boson  $V$  to right-handed ( $\lambda = R$ ) or left-handed ( $\lambda = L$ ) quarks. In terms of the electric charge  $Q_q$ , the weak isospin  $T_{q_\lambda}^3$  and the weak hypercharge  $Y_{q_\lambda}$  we have  $I_{q_\lambda}^\gamma = -Q_q$ ,  $I_{q_\lambda}^Z = c_W/s_W T_{q_\lambda}^3 - s_W Y_{q_\lambda}/(2c_W)$ , with the shorthands  $c_W = \cos \theta_w$  and  $s_W = \sin \theta_w$  for the weak mixing angle  $\theta_w$ . Moreover the relevant elements of the Weinberg rotation matrix  $U$  are given by  $U_{\gamma W^3} = -s_W$  and  $U_{Z W^3} = c_W$ . The term  $H_0^V = (\hat{t}^2 + \hat{u}^2 + 2\hat{s}M_V^2)/(\hat{t}\hat{u})$  in Eq. (36) represents the Born contribution.  $\delta C_{q_\lambda}^{V,A/N}$  summarize the counterterms associated with the renormalization of the couplings and the gauge-boson wave function. The contributions resulting from the bare loop diagrams and the fermionic wave-function renormalization correspond to the functions  $H_1^{V,A/N}$ . The complete analytic expressions for these functions and for the counterterms, as well as details concerning the choice of the renormalization scheme, can be found in Ref. [242] for the  $Z$ -boson production and in Ref. [243] for photon production. In the following we concentrate on the high-energy asymptotic behaviour of the corrections, more precisely the next-to-next-to-leading logarithmic (NNLL) approximation of the full result. Formally we consider the limit where  $M_W^2/\hat{s} \rightarrow 0$  and  $\hat{t}/\hat{s}$ ,  $\hat{u}/\hat{s}$  are constant. In this limit the one-loop weak corrections are strongly enhanced by logarithms of the form  $\log(\hat{s}/M_W^2)$ . The functions  $H_1^{V,A/N}$  assume the general form

$$H_1^{V,A/N}(M_{V'}^2) \stackrel{\text{NNLL}}{=} \text{Re} \left[ g_0^{V,A/N}(M_{V'}^2) \frac{\hat{t}^2 + \hat{u}^2}{\hat{t}\hat{u}} + g_1^{V,A/N}(M_{V'}^2) \frac{\hat{t}^2 - \hat{u}^2}{\hat{t}\hat{u}} + g_2^{V,A/N}(M_{V'}^2) \right]. \quad (37)$$

We find  $g_i^{\gamma,A} = g_i^{Z,A}$  for  $i = 0, 1, 2$  and  $g_j^{\gamma,N} = g_j^{Z,N}$  for  $j = 1, 2$ . For  $V = \gamma, Z$  one has:

$$\begin{aligned} g_0^{V,A}(M_{V'}^2) &= -\log^2 \left( \frac{-\hat{s}}{M_{V'}^2} \right) + 3 \log \left( \frac{-\hat{s}}{M_{V'}^2} \right) + \frac{3}{2} \left[ \log^2 \left( \frac{\hat{t}}{\hat{s}} \right) + \log^2 \left( \frac{\hat{u}}{\hat{s}} \right) \right. \\ &\quad \left. + \log \left( \frac{\hat{t}}{\hat{s}} \right) + \log \left( \frac{\hat{u}}{\hat{s}} \right) \right] + \frac{7\pi^2}{3} - \frac{5}{2}, \end{aligned} \quad (38)$$

$$g_1^{V,N}(M_{V'}^2) = -g_1^{V,A}(M_{V'}^2) + \frac{3}{2} \left[ \log \left( \frac{\hat{u}}{\hat{s}} \right) - \log \left( \frac{\hat{t}}{\hat{s}} \right) \right] = \frac{1}{2} \left[ \log^2 \left( \frac{\hat{u}}{\hat{s}} \right) - \log^2 \left( \frac{\hat{t}}{\hat{s}} \right) \right],$$

$$g_2^{V,N}(M_{V'}^2) = -g_2^{V,A}(M_{V'}^2) = -2 \left[ \log^2 \left( \frac{\hat{t}}{\hat{s}} \right) + \log^2 \left( \frac{\hat{u}}{\hat{s}} \right) + \log \left( \frac{\hat{t}}{\hat{s}} \right) + \log \left( \frac{\hat{u}}{\hat{s}} \right) \right] - 4\pi^2.$$

The non-Abelian function  $g_0^{V,N}$  is given by ( $\delta_{VV'} = 1$  for  $V = V'$ , otherwise  $\delta_{VV'} = 0$ ):

$$g_0^{V,N}(M_W^2) = 2 \left[ \bar{\Delta}_{UV} - \delta_{V\gamma} \log \left( \frac{M_W^2}{M_Z^2} \right) \right] + \log^2 \left( \frac{-\hat{s}}{M_W^2} \right) - \log^2 \left( \frac{-\hat{t}}{M_W^2} \right) - \log^2 \left( \frac{-\hat{u}}{M_W^2} \right) \\ + \log^2 \left( \frac{\hat{t}}{\hat{u}} \right) - \frac{3}{2} \left[ \log^2 \left( \frac{\hat{t}}{\hat{s}} \right) + \log^2 \left( \frac{\hat{u}}{\hat{s}} \right) \right] - 2\pi^2 + 2\delta_{VZ} \left( -\frac{\pi^2}{9} - \frac{\pi}{\sqrt{3}} + 2 \right). \quad (39)$$

The ultraviolet singularity,  $\bar{\Delta}_{UV} = 2/(4-D) - \gamma_E + \log(4\pi\mu^2/M_Z^2)$  is cancelled by the counterterms [242, 243].

The size of the logarithmically enhanced contributions grows with energy and for transverse momenta of hundreds of GeV also the two-loop logarithms become important. At the NLL accuracy, our results for the two-loop corrections include contributions with terms of the form  $\alpha^2 L_{\hat{s}}^4$  and  $\alpha^2 L_{\hat{s}}^3$  where  $L_{\hat{r}}^k = \log^k(|\hat{r}|/M_W^2)$ . The expressions presented here have been obtained using results of Refs. [246–248]. Since at two-loop level the purely weak corrections cannot be isolated from the complete electroweak corrections in a gauge-invariant way, we have to consider the combination of weak and electromagnetic virtual corrections. The latter are regularized by means of a fictitious photon mass<sup>17</sup>  $\lambda = M_W$ . For the unpolarized squared matrix element we have  $\overline{\sum} |\mathcal{M}_2^{\bar{q}q \rightarrow Vg}|^2 - \overline{\sum} |\mathcal{M}_1^{\bar{q}q \rightarrow Vg}|^2 \stackrel{\text{NLL}}{=} 2\alpha^3 \alpha_S (N_c^2 - 1) H_0^V A^{V,(2)}$  where

$$A^{V,(2)} = \sum_{\lambda=L,R} \left\{ \frac{1}{2} (I_{q\lambda}^V C_{q\lambda}^{\text{ew}} + S_{q\lambda}^V) \left[ I_{q\lambda}^V C_{q\lambda}^{\text{ew}} (L_{\hat{s}}^4 - 6L_{\hat{s}}^3) \right. \right. \\ \left. \left. + S_{q\lambda}^V (L_{\hat{t}}^4 + L_{\hat{u}}^4 - L_{\hat{s}}^4) \right] - (\delta_{VZ} - \delta_{V\gamma}) \frac{T_{q\lambda}^3 Y_{q\lambda}}{8s_W^4} (L_{\hat{t}}^4 + L_{\hat{u}}^4 - L_{\hat{s}}^4) \right. \\ \left. + \frac{1}{6} I_{q\lambda}^V \left[ I_{q\lambda}^V \left( \frac{b_1}{c_W^2} \left( \frac{Y_{q\lambda}}{2} \right)^2 + \frac{b_2}{s_W^2} C_{q\lambda} \right) + S_{q\lambda}^V b_2 \right] L_{\hat{s}}^3 \right\}. \quad (40)$$

Here  $C_{q\lambda}^{\text{ew}} = Y_{q\lambda}^2/(4c_W^2) + C_{q\lambda}/s_W^2$  is the electroweak Casimir operator for quarks, with  $C_{q_L} = 3/4$  and  $C_{q_R} = 0$ .  $S_{q\lambda}^V$  is defined as  $S_{q\lambda}^V = C_{VV'}^{\text{ew}} I_{q\lambda}^{V'}/2$  where  $C_{VV'}^{\text{ew}}$  is the electroweak Casimir operator in the adjoint representation [246, 249] and  $S_{q\lambda}^\gamma = -T_{q\lambda}^3/s_W^2$ ,  $S_{q\lambda}^Z = c_W T_{q\lambda}^3/s_W^3$ . The one-loop  $\beta$ -function coefficients read  $b_1 = -41/(6c_W^2)$  and  $b_2 = 19/(6s_W^2)$ . We stress that although the above one- and two-loop results for the photon and  $Z$ -boson production can be put in the same form, their derivation requires separate calculation for each of the processes.

## 11.22 Numerical results

The hadronic cross sections are obtained using LO MRST2001 PDFs [26]. We choose  $p_T^2$  as the factorization scale and, similarly as the scale at which the running strong coupling constant is evaluated. We also adopt the value  $\alpha_S(M_Z^2) = 0.13$  and use the one-loop running expression for  $\alpha_S(\mu^2)$ , in accordance with the LO PDF extraction method of the MRST collaboration. We use the following values of parameters [237]:  $M_Z = 91.19$  GeV,  $M_W = 80.39$  GeV and  $\alpha = 1/137.0$ ,  $s_W^2 = 1 - c_W^2 = 1 - M_W^2/M_Z^2$  for the  $\gamma$  production (OS scheme with  $\alpha$  in the Thompson limit) or  $\alpha = 1/128.1$ ,  $s_W^2 = 0.2314$  for the  $Z$ -boson production ( $\overline{\text{MS}}$  scheme, as discussed above, with  $M_Z^2$  as the renormalization scale).

First, we study the behaviour of the one-loop EW corrections to the transverse momentum distributions of photons and  $Z$  bosons produced at the LHC, see Fig. 58. The contribution provided by

<sup>17</sup>This approach permits to separate the finite and infrared-divergent parts of the photonic corrections in a gauge-invariant way (for a detailed discussion see Sect. 2 of [245]). In our results we include only the finite part, defined through  $\lambda = M_W$ . The remaining part, which contains infrared-divergent logarithms of  $\lambda/M_W$ , is gauge-invariant and can thus be treated separately and combined with real photon radiation.

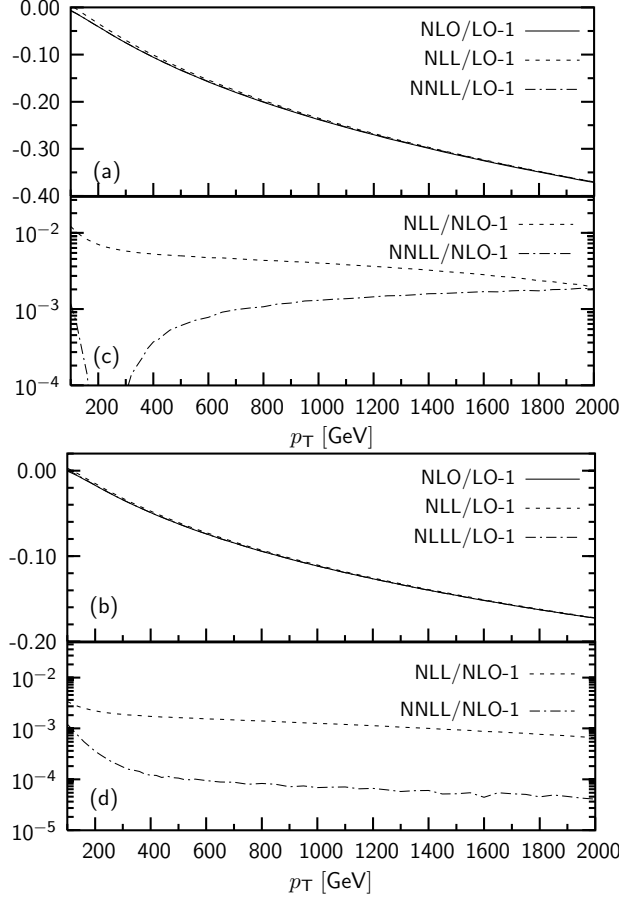


Fig. 58: Upper plots: relative NLO (solid), NNL (dotted) and NNLL (dot-dashed) weak corrections wrt. the LO  $p_T$  distribution for the process (a)  $pp \rightarrow Zj$  and (b)  $pp \rightarrow \gamma j$  at  $\sqrt{s} = 14$  TeV. Lower plots: NLL (dotted) and NNLL (dot-dashed) approximation compared to the full NLO result for (c)  $pp \rightarrow Zj$  and (d)  $pp \rightarrow \gamma j$  at  $\sqrt{s} = 14$  TeV.

the NLO correction is negative and increases in size with  $p_T$ , reaching -37% (-17%) for the  $Z$ -boson (photon) production at  $p_T = 2$  TeV. We also conclude that the NLL approximation works good, at a per cent (or better) level of accuracy both for the photon and  $Z$ -boson production. In comparison, the quality of the NNLL approximation is excellent, at the level of accuracy of  $10^{-3}$  or better in the entire  $p_T$  range for both processes.

To demonstrate the relevance of the EW effects for the transverse momentum distributions of the gauge bosons produced at the LHC, in Fig. 59 we present the relative NLO and next-to-next-to-leading order (NNLO)<sup>18</sup> corrections for the cross section, integrated over  $p_T$  starting from  $p_T = p_T^{\text{cut}}$ , as a function of  $p_T^{\text{cut}}$ . This is compared with the statistical error, defined as  $\Delta\sigma_{\text{stat}}/\sigma = 1/\sqrt{N}$  with  $N = \mathcal{L} \times \sigma_{\text{LO}}$ . We assume a total integrated luminosity  $\mathcal{L} = 300 \text{ fb}^{-1}$  for the LHC. It is clear from Fig. 59, that the size of the one-loop (two-loop logarithmic) corrections is much bigger than (comparable to) the statistical error for both the  $Z$ -boson and the  $\gamma$  production.

In Fig. 60, we plot the ratio of the  $p_T$  distribution for the  $\gamma$  production to the  $p_T$  distribution for the  $Z$ -boson production. Such ratio is expected to be less sensitive to theoretical errors than the distributions themselves, since many uncertainties such as the scale at which  $\alpha_S$  is calculated or the choice of PDFs cancel to a large extent in the ratio. Moreover, due to a similar cancellation mechanism, the ratio should

<sup>18</sup>Our NNLO predictions include the exact NLO contributions combined with the leading and next-to-leading logarithmic two-loop terms (40).

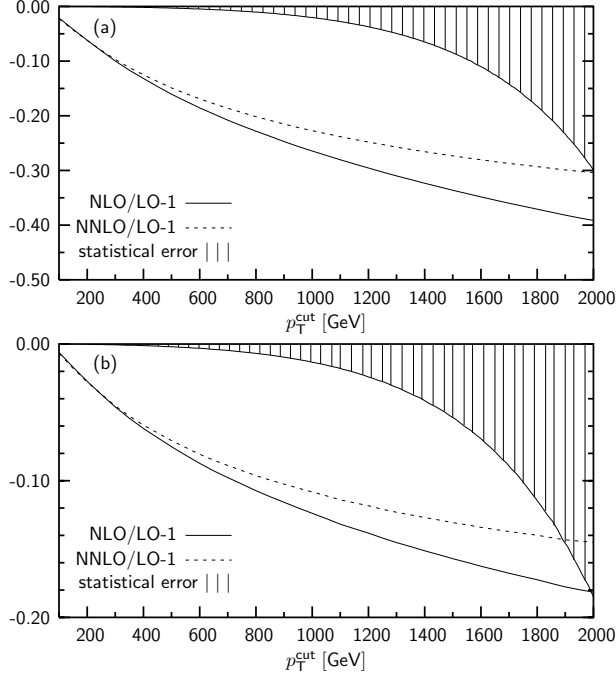


Fig. 59: Relative NLO (solid) and NNLO (dotted) corrections wrt. the LO prediction and estimated statistical error (shaded area) for the unpolarized integrated cross section for (a)  $pp \rightarrow Zj$  and (b)  $pp \rightarrow \gamma j$  at  $\sqrt{s} = 14$  TeV as a function of  $p_T^{\text{cut}}$ .

remain stable against QCD corrections. From Fig. 60 we observe that the EW corrections modify the production ratio considerably. The effect is the strongest at high  $p_T$ . In this region, the LO photon cross section is smaller than the cross section for  $Z$ -boson production by about 25%. The relatively large NLO corrections for  $Z$ -boson production, as compared to  $\gamma$  production, cause the full NLO production rates to become equal at the highest  $p_T$  considered here, i.e.  $p_T \sim 2$  TeV. The two-loop corrections modify the ratio and lead to a few per cent decrease at high  $p_T$ .

### 11.3 Conclusions

At the LHC, the transverse momentum of  $Z$  bosons or photons produced in the process  $pp \rightarrow Vj$  ( $V = \gamma, Z$ ) will reach the TeV scale. In this  $p_T$  regime one-loop weak corrections are negative and large, of the order of tens of per cent. In the high-energy limit these corrections are approximated with

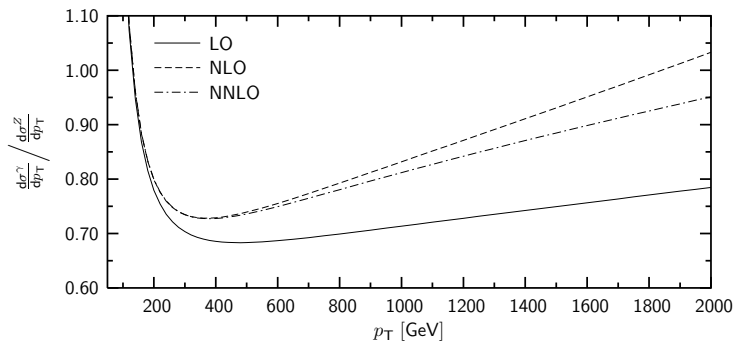


Fig. 60: Ratio of the transverse momentum distributions for the processes  $pp \rightarrow \gamma j$  and  $pp \rightarrow Zj$  at  $\sqrt{s} = 14$  TeV for the LO (solid), NLO (dashed) and NNLO (dotted) predictions.



an excellent accuracy by the compact analytical expressions presented here. We also present expressions for the dominant logarithmic part of the two-loop EW corrections and point out that these corrections are important for the correct interpretation of the measurements. Moreover, we find that the EW corrections modify significantly the ratio of the  $Z$ -boson and  $\gamma$  transverse momentum distributions at high  $p_T$ .

## 11.4 Acknowledgments

We are grateful to J. H. Kühn for the collaboration on the project. This work was supported in part by BMBF Grant No. 05HT4VKA/3 and by the Deutsche Forschungsgemeinschaft (SFB/TR-9 “Computational Particle Physics”). M. S. acknowledges financial support from the Graduiertenkolleg “Hochenergiephysik und Teilchenastrophysik”. A.K. would like to thank the organizers for the kind hospitality and stimulating atmosphere during the workshop.

## 12. IMPACT OF WEAK CORRECTIONS ON LHC JET CROSS SECTIONS <sup>19</sup>

### 12.1 Weak corrections at TeV scales

The purely weak (W) component of next-to-leading order (NLO) Electro-Weak (EW) effects produce leading corrections of the type  $\alpha_W \log^2(E_T^2/M_W^2)$ , where  $\alpha_W \equiv \alpha_{EM}/\sin^2\theta_W$ , with  $\alpha_{EM}$  the Electro-Magnetic coupling constant and  $\theta_W$  the Weinberg angle. In fact, for large enough  $E_T$  values, the jet transverse energy, such EW effects may be competitive not only with next-to-NLO (NNLO) (as  $\alpha_W \approx \alpha_S^2$ ) but also with NLO QCD corrections (e.g., for  $E_T = 0.5$  TeV,  $\log^2(E_T^2/M_W^2) \approx 10$ ).

These ‘double logs’ are due to a lack of cancellation between virtual and real  $W$ -emission in higher order contributions. This is in turn a consequence of the violation of the Bloch-Nordsieck theorem in non-Abelian theories [250]. The problem is in principle present also in QCD. In practice, however, it has no observable consequences, because of the final averaging of the colour degrees of freedom of partons, forced by their confinement into colourless hadrons. This does not occur in the EW case, where the initial state has a non-Abelian charge, as in proton-(anti)proton scattering. Besides, these logarithmic corrections are finite (unlike in QCD), since  $M_W$  provides a physical cut-off for  $W$ -emission. Hence, for typical experimental resolutions, softly and collinearly emitted weak bosons need not be included in the production cross section and one can restrict oneself to the calculation of weak effects originating from virtual corrections only. By doing so, similar logarithmic effects,  $\sim \alpha_W \log^2(E_T^2/M_W^2)$ , are generated also by  $Z$ -boson corrections. Finally, at least in some cases (like the present one), all these purely weak contributions can be isolated in a gauge-invariant manner from EM effects which therefore may not be included in the calculation.

In view of all this, it becomes of crucial importance to assess the quantitative relevance of such weak corrections affecting, in particular, key QCD processes at present and future hadron colliders, such as jet and heavy quark pair production. Published analyses for  $b$ -jet production at the Tevatron and Large Hadron Collider (LHC) already exist [251] – see also the previous Les Houches proceedings [252] and Refs. [241, 253] – and those for  $t\bar{t}$  production are in progress [254–260]. (For Standard Model (SM) corrections to heavy quark pairs based on Sudakov leading logarithms only, see [261, 262].) We show here results for the case of jet production at the LHC, a preliminary account of which was given in [263]. (For the case of Tevatron, see Ref. [264].)

### 12.2 Corrections to jet production

It is the aim of this note to report on the computation of the full one-loop weak effects<sup>20</sup> entering all possible ‘2 parton  $\rightarrow$  2 parton’ scatterings, through the perturbative order  $\alpha_S^2\alpha_W$ . (See Ref. [265] for tree-level  $\alpha_S\alpha_{EW}$  interference effects – hereafter,  $\alpha_{EW}$  exemplifies the fact that both weak and EM

<sup>19</sup>Contributed by: S. Moretti, M.R. Nolten, D.A. Ross

<sup>20</sup>We neglect here purely EM effects (as well as interferences between these and the weak ones) through  $\mathcal{O}(\alpha_S^2\alpha_{EM})$ , as they are not associated with logarithmic enhancements either.

effects are included at the given order). We will instead ignore altogether the contributions of tree-level  $\alpha_S^2\alpha_W$  terms involving the radiation of real  $W$  and  $Z$  bosons. Therefore, apart from  $gg \rightarrow gg$  (which is not subject to order  $\alpha_S^2\alpha_W$  corrections), there are in total fifteen subprocesses to consider,

$$gg \rightarrow q\bar{q} \quad (41)$$

$$q\bar{q} \rightarrow gg \quad (42)$$

$$qg \rightarrow qg \quad (43)$$

$$\bar{q}g \rightarrow \bar{q}g \quad (44)$$

$$qq \rightarrow qq \quad (45)$$

$$\bar{q}\bar{q} \rightarrow \bar{q}\bar{q} \quad (46)$$

$$qQ \rightarrow qQ \text{ (same generation)} \quad (47)$$

$$\bar{q}\bar{Q} \rightarrow \bar{q}\bar{Q} \text{ (same generation)} \quad (48)$$

$$qQ \rightarrow qQ \text{ (different generation)} \quad (49)$$

$$\bar{q}\bar{Q} \rightarrow \bar{q}\bar{Q} \text{ (different generation)} \quad (50)$$

$$q\bar{q} \rightarrow q\bar{q} \quad (51)$$

$$q\bar{q} \rightarrow Q\bar{Q} \text{ (same generation)} \quad (52)$$

$$q\bar{q} \rightarrow Q\bar{Q} \text{ (different generation)} \quad (53)$$

$$q\bar{Q} \rightarrow q\bar{Q} \text{ (same generation)} \quad (54)$$

$$q\bar{Q} \rightarrow q\bar{Q} \text{ (different generation)}, \quad (55)$$

with  $q$  and  $Q$  referring to quarks of different flavours and where the latter are limited to  $u$ -,  $d$ -,  $s$ -,  $c$ - and  $b$ -type (all taken as massless). While the first four processes (with external gluons) were already computed in Ref. [266], the eleven four-quark processes are new to this study. Besides, unlike the former, the latter can be (soft and collinear) divergent, so that gluon bremsstrahlung effects ought to be evaluated to obtain a finite cross section at the considered order. In addition, for completeness, we have also included the non-divergent ‘2 parton  $\rightarrow$  3 parton’ subprocesses

$$qg \rightarrow qq\bar{q} \quad (56)$$

$$\bar{q}g \rightarrow \bar{q}q\bar{q} \quad (57)$$

$$qg \rightarrow qQ\bar{Q} \text{ (same generation)} \quad (58)$$

$$\bar{q}g \rightarrow \bar{q}\bar{Q}Q \text{ (same generation)}. \quad (59)$$

Notice that in our treatment we identify the jets with the partons from which they originate and we adopt the cut  $|\eta| < 2.5$  in pseudorapidity to mimic the LHC detector coverage and the standard jet cone requirement  $\Delta R > 0.7$  to emulate their jet data selection (although we eventually sum the two- and three-jet contributions). Furthermore, as factorisation and renormalisation scale we use  $\mu = \mu_F \equiv \mu_R = E_T/2$  while we adopt CTEQ6L1 [47] as Parton Distribution Functions.

Fig. 12.2 exemplifies the relevance that  $\alpha_S^2\alpha_W$  effects can have at the LHC. The  $\alpha_S^2\alpha_W$  corrections are rather large and grow steadily with the jet transverse energy, as the total (i.e., via all partonic channels) results through  $\mathcal{O}(\alpha_S^2 + \alpha_S^2\alpha_W)$  [labelled NLO weak] differ with respect to the prediction of total LO QCD through  $\mathcal{O}(\alpha_S^2)$  [LO QCD] by up to an astounding  $-40\%$ , in the vicinity of 4 TeV, the highest  $E_T$  point that may be reached at the LHC after full luminosity. In fact, already at  $E_T = 1$  TeV, the effects amount to  $-10\%$ . In the case of subprocesses initiated by (anti)quarks only, one also has LO EW effects through  $\mathcal{O}(\alpha_S\alpha_{EW})$ , which can only reach a 3(16)% effect at  $E_T = 1(4)$  TeV, as shown in the same plot. (Here LO SM identifies the sum of terms of  $\mathcal{O}(\alpha_S^2)$ ,  $\mathcal{O}(\alpha_S\alpha_{EW})$  and  $\mathcal{O}(\alpha_{EW}^2)$ ). Between the two kind of corrections then, are the one-loop ones that dominates over those at tree-level. Finally, the plot also presents the contributions of only those subprocesses that are not initiated by gluons: it is clear that at large  $E_T$  are these channels that dominates.

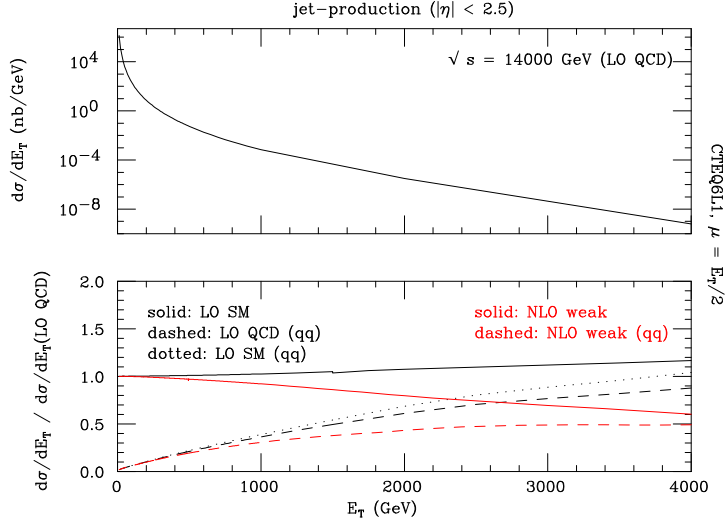


Fig. 61: Top: The total single jet inclusive distribution in transverse energy through  $\mathcal{O}(\alpha_S^2)$  at the LHC, via all partonic subprocesses. Bottom: The effects of the one-loop  $\mathcal{O}(\alpha_S^2\alpha_W)$  and tree-level  $\mathcal{O}(\alpha_S\alpha_{EW})$  corrections relative to the spectrum above. The label (qq) refers to the case of subprocesses with no gluons in the initial state.

### 12.3 Conclusions

In summary, at the LHC,  $\mathcal{O}(\alpha_S^2\alpha_W)$  terms are important contributions to the inclusive jet cross section at large transverse energy. For the expected highest reach of the machine,  $E_T \approx 4$  TeV, they can be as large as  $-40\%$ . Therefore, they ought to be included while comparing experiment *versus* theory. However, particular care should be devoted to the treatment of real  $W$  and  $Z$  production and decay in the definition of the inclusive jet data sample, as this will determine whether (positive) tree-level  $W$  and  $Z$  bremsstrahlung effects have to be included in the theoretical predictions through  $\mathcal{O}(\alpha_S^2\alpha_W)$ , which would tend to counterbalance the negative effects due to the one-loop  $W$  and  $Z$  exchange estimated here. As these were not included in our calculation, the matter is currently under study.

## 13. SEARCH FOR ANOMALOUS COUPLINGS IN TOP DECAY AT HADRON COLLIDERS <sup>21</sup>

### 13.1 Introduction

Since the top quark was discovered at the Tevatron [267, 268] the number of the observed top quark events in the Tevatron Run II experiment is increasing with the integrated luminosity, and now reaching of the order of a few hundred. At LHC, of the order of  $\sim 10^7$  top quarks will be produced in the first year of operation. The study of top quark properties is expected to reveal the fundamental structure of top quark interactions currently at the Tevatron, and in the future at the LHC and the ILC.

Among various interactions of the top quark, the study of the top quark decay properties is particularly interesting. In the Standard Model, the top quark decays via electroweak interaction before hadronization, so that the top quark's spin information is transferred directly to its decay products, and their properties can be predicted reliably using perturbative calculations. Thus, the top quark spin can be used as a powerful analyzer to study top quark decays.

The anomalous couplings of top decays can be derived indirectly from a constraint to the  $W$  polarization state from the top quark by using the lepton helicity angle [269, 270]. The sensitivity of the anomalous couplings has also been studied using single top events by looking at the differential

<sup>21</sup>Contributed by: S. Tsuno, I. Nakano, Y. Sumino, R. Tanaka

distributions for signal and background events [271]. However, single top events have not yet been observed at the Tevatron [272, 273]. Due to the low number of signal events and due to the difficult separation of the signal from the backgrounds, the experimental results are still poor.

In this article, we propose a new method for reconstructing an effective spin direction of the top quark using the  $t\bar{t}$  production process [274, 275]. In particular, the new feature of this technique is that we do not need to reconstruct the spin of the anti-top side in a  $t\bar{t}$  event, i.e. we do not make use of the correlation between the top and anti-top spins. We rather make use of the correlation between the top spin and the directions of its decay products. So that, even in the *lepton + jets* channel, the spin direction of the top quark can be easily reproduced using the information of one only top quark, and a high event statistics is obtained with good signal and background separation. Our method is expected to improve the sensitivity to anomalous couplings considerably compared to other measurements.

### 13.2 Anomalous couplings in top decay vertices

The interaction with an anomalous coupling in the top decay vertex can be expressed as

$$\Gamma_{Wtb}^\mu = -\frac{g}{\sqrt{2}}V_{tb}\bar{u}(p_b)\left[\gamma^\mu f_1 P_L - \frac{i\sigma^{\mu\nu}k_\nu}{M_W}f_2 P_R\right]u(p_t) \quad , \quad (60)$$

where  $V_{tb}$  is the CKM (Cabibbo-Kobayashi-Maskawa) matrix element,  $P_{L,R} = (1 \mp \gamma_5)/2$  is the left-handed/right-handed projection operator, and  $k$  is the momentum of the  $W$ . We take the convention in which the energy scale is represented by  $M_W$  (on-shell). For simplicity of the analysis, we assume that the interactions preserve the  $CP$  symmetry and also neglect the couplings of the right-handed bottom quark. Two form factors  $f_1$  and  $f_2$  are thus treated as real, and then their values are  $f_1 = 1$  and  $f_2 = 0$  at tree-level in the SM.

From Eq. 60, we may separate the dependence of the decay distribution on  $f_1$  and on  $f_2/f_1$ . A variation of  $f_1$  changes only the normalization of the (partial) decay width of the top quark, while a variation of  $f_2/f_1$  changes both, the normalization and the differential decay distributions. Since it is difficult to measure the absolute value of the decay width accurately in the near future, our primary goal will be to constrain the value of  $f_2/f_1$  from the measurement of the differential decay distribution. Since the transverse  $W$  boson ( $W_T$ ) is more sensitive to  $f_2$  than the longitudinal  $W$  boson ( $W_L$ ), we can enhance the contribution of  $W_T$  using the decay distribution. It is well known that the contribution of  $W_T$  is dominant when the  $W$  is emitted opposite to the top spin direction in the decay  $t \rightarrow bW$  and also when the lepton ( $l$ ) is emitted in the opposite direction to the  $W$  in the decay  $W \rightarrow l\nu$ . Hence, we can select this kinematic region in order to enhance the sensitivity to  $f_2/f_1$ .

The differential decay distribution of the  $W$  and the  $l$  in the semi-leptonic decay from a top quark with definite spin orientation,  $N^{-1}d\Gamma(t \rightarrow bl\nu)/d\cos\theta_W d\cos\theta_l$ , is shown in Fig. 62 for (a)  $(f_1, f_2) = (1, 0)$  (tree-level SM) and (b)  $(f_1, f_2) = (1, 0.3)$ , respectively.  $\theta_W$  is defined as the angle between the top spin direction and the direction of the  $W$  in the top quark rest frame.  $\theta_l$  is defined as the lepton helicity angle, which is the angle of the charged lepton in the rest frame of the  $W$  with respect to the original direction of flight of the  $W$ . Comparing the two figures, the effects of varying  $f_2$  are indeed enhanced in the regions  $\cos\theta_W \simeq -1$  and  $\cos\theta_l \simeq -1$ , in accord with the enhancement of the  $W_T$  contributions in these regions. Thus, it is crucial to reconstruct the top quark's spin orientation in this method. At hadron collider experiments, it is much less trivial to reconstruct the top quark spin direction, as compared to  $e^+e^-$  collider experiments. We discuss how to reconstruct the top spin direction in the next section.

### 13.3 Effective spin reconstruction

At hadron colliders, top quarks are produced predominantly through  $t\bar{t}$  production processes. At the Tevatron, 85% of the produced  $t\bar{t}$  pairs come from  $q\bar{q}$  initial states, while 15% come from  $gg$  initial states. On the other hand, at the LHC, the corresponding fractions are 10% ( $q\bar{q}$ ) and 90% ( $gg$ ), respectively. At

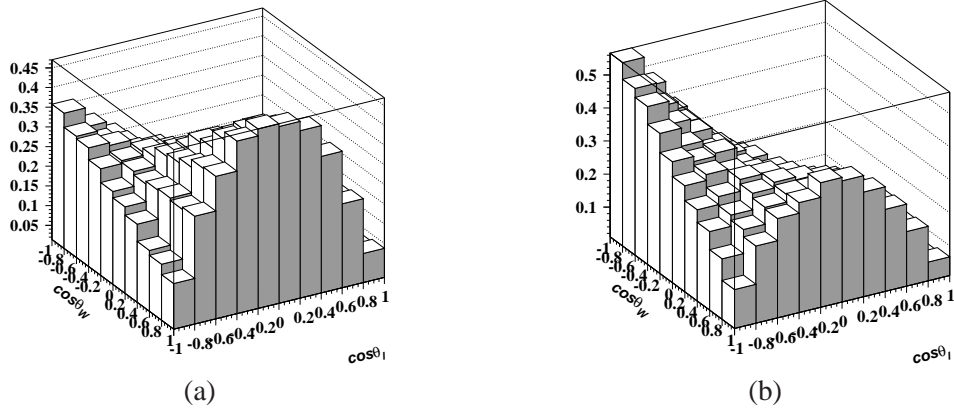


Fig. 62: Normalized differential decay distributions (a) for  $(f_1, f_2) = (1, 0)$ , and (b) for  $(f_1, f_2) = (1, 0.3)$ . They are normalized to unity upon integration.

these colliders, the polarization of the produced top quarks is rather small: at tree level, top quarks are produced unpolarized; at NLO, the polarization of top quarks is reported to be very small [276, 277].

In our analysis of the anomalous couplings, we want to utilize correlations between the top quark spin direction and the distribution of its decay products. In conventional approaches to reconstruct the top quark spin, the top anti-top spin correlation in  $t\bar{t}$  events has been used [278–280]. A serious deficit of such methods is that they are quite complicated. For instance, the direction of the down-type quark in the hadronic decay of anti-top quark is maximally correlated with the  $\bar{t}$  spin. Hence, in order to reconstruct the spin of the anti-top quark, we should distinguish the charges of the quarks from the  $W$  decay. This is a highly non-trivial task and we anticipate that rather large systematic errors will be involved before eventually reconstructing the top quark spin. On the other hand, if we want to use leptonic decays both, of the top and of the anti-top quarks, we suffer from the lack of statistics as well as from non-trivial event kinematics due to the two missing momenta of the neutrinos.

Here we take another route for reconstructing (effectively) the top quark spin. We use the correlation between the top spin and the direction of the charged lepton in the top decay for reconstructing the parent top quark’s spin. Then we use this information to analyze the anomalous couplings in the decay of the same top quark. Since we reconstruct the spin and analyze the spin-dependent decay distribution using the *same top decay process*, we should make sure that we use independent correlations in the former and latter procedures to avoid obtaining a meaningless outcome. For this purpose, we take advantage of the following facts: (1) Within the SM, the charged lepton is known to be the best analyzer of the parent top quark’s spin and is produced preferentially in the direction of the top spin [281]. (2) The angular distribution of the charged lepton with respect to the top spin direction (after all other kinematic variables are integrated out) is hardly affected by the anomalous couplings of top quark, if the anomalous couplings are small [282].<sup>22</sup> Therefore, we may project the direction of the charged lepton onto an appropriate spin basis; then the reconstructed top quark spin is scarcely affected by the existence of the anomalous couplings  $f_1$  and  $f_2$ , when they are small. We define an effective spin direction by the projection of the lepton direction onto the helicity basis:

$$\vec{S}_{\text{SH}} = \text{sign}(\cos \Theta) \times \frac{\vec{p}_t}{|\vec{p}_t|} , \quad (61)$$

where  $\Theta$  is the angle between the charged lepton and the original direction of top quark (opposite of the anti-top direction) in the top rest frame;  $\vec{p}_t$  is the top quark momentum in the  $t\bar{t}$  c.m. frame. We refer to the effective spin direction above as *signed-helicity* (SH) direction.

<sup>22</sup>More precisely, the angular distributions of the  $\ell^\pm$  are independent of the anomalous couplings up to (and including) linear terms in these couplings.



In order to verify how well this effective spin direction reproduces the true top spin direction, we demonstrate in Fig. 63 the angular correlations between the directions of the decay products of the top quark and the signed-helicity direction (61). (Obviously, it is tautological to use the signed-helicity direction for the analysis of the charged lepton angular distribution, so we do not show the lepton angular distribution.) In the same figure, the angular correlations using the true top spin direction for 100% polarized top quarks are shown. It is customary to parametrize an angular correlation with the linear relation  $\frac{1}{2}(1 + \alpha \cos \theta)$ , where  $\alpha$  is a correlation coefficient [278]. The correlation coefficients  $\alpha$  of the  $b$  and the  $W$  for the signed-helicity direction are about twice as large as those for the true top spin direction. This comes from a purely kinematic origin, as can be understood as follows: consider a hypothetical case, in which no correlation between the true spin direction and direction of the  $W$  exists (the decay is isotropic). Even in this case, there is a positive correlation between the signed-helicity direction and the  $W$  in the top rest frame, since the charged lepton is emitted more in the direction of the  $W$  due to the boost of the  $W$ . The angular correlation of the neutrino with the signed-helicity direction does not obey a linear relation.<sup>23</sup> In this case, the correlation is somewhat stronger than that with the true spin direction, too. Thus, the signed-helicity direction reproduces qualitatively correct the angular correlations with the decay products, although the angular correlations are biased to be somewhat larger than those of the true spin direction. In addition, it is important that the dependence of the distributions on the anomalous couplings is approximately reproduced in this spin reconstruction method.

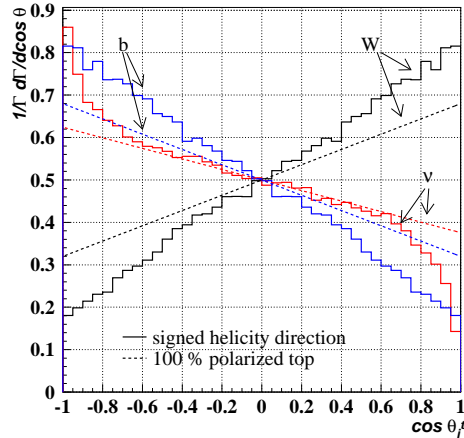


Fig. 63: Angular correlations between the directions of top decay products and the top spin direction in the top rest frame, when using the signed-helicity direction (solid lines) and when using the ideal off-diagonal basis (dashed lines) for the spin directions, respectively. We use the parton information at the generator level, with the initial state as produced at the Tevatron with  $\sqrt{s} = 1.96$  TeV.

### 13.4 Simulation

In order to estimate the sensitivity to anomalous couplings in the top decay, we perform a Monte Carlo (MC) event generation and a detector simulation. The events are produced with both, Tevatron Run II ( $p\bar{p}$  collisions with  $\sqrt{s} = 1.96$  TeV) and LHC ( $pp$  collisions with  $\sqrt{s} = 14$  TeV) conditions.

The event generation for the  $t\bar{t}$  signal samples is performed by the GR@PPA event generator [283] which is interfaced to PYTHIA v6.226, a showering MC [284]. GR@PPA produces the hard process based on a  $t\bar{t}$  matrix element calculation at tree level. The whole decay chain of the top quark is included in the diagram calculation, so that the spin correlations in top decays are fully reproduced. The anomalous couplings in the top decay are also included. PYTHIA performs fragmentation, parton

<sup>23</sup>This dependence is a result of the 100% anticorrelation of the lepton and the  $\nu$  directions (back-to-back) in the  $l\nu$  c.m. frame plus the effect of the boost of the  $W$ .

showering, hadronization, and so on and so forth. On the other hand, underlying events are produced by PYTHIA alone, using the parameters tuned to reproduce the real data from the Tevatron.

The detector simulation is performed by smearing energies for the stable particles deposited into a proper segmentation of the calorimeter geometry similar to the CDF and ATLAS detectors. Jets are clustered by the cone clustering algorithm in PARTHIA (PYCELL) with cone size 0.4. We do not simulate  $b$  tagging. Instead, a  $b$ -jet is identified as the nearest jet with the minimum separation  $\Delta R$  between a jet and a  $b$ -quark at the generator level. The separation ( $\Delta R$ ) is defined as

$$\Delta R = \sqrt{\Delta\phi^2 + \Delta\eta^2} \quad , \quad (62)$$

where  $\Delta\phi$  and  $\Delta\eta$  are the separation in the azimuthal angle and the pseudorapidity for every pair of a jet and a  $b$ -quark at generator level, respectively. As for leptons, we use the generator level information.

We select the  $lepton + jets$  channel in the  $t\bar{t}$  production process by requiring to pass the cuts

	Tevatron	LHC
lepton	$p_T \geq 20$ GeV, $ \eta  \leq 1.0$	$p_T \geq 20$ GeV, $ \eta  \leq 2.5$
$b$ -jet	$E_T \geq 15$ GeV, $ \eta  \leq 1.0$	$E_T \geq 30$ GeV, $ \eta  \leq 2.5$
other jet	$E_T \geq 15$ GeV, $ \eta  \leq 2.0$	$E_T \geq 30$ GeV, $ \eta  \leq 2.5$
	$\cancel{E}_T \geq 20$ GeV	$\cancel{E}_T \geq 20$ GeV

where  $\cancel{E}_T$  is the missing transverse energy calculated by the vectorial sum of the selected lepton and the four jets. We require two  $b$ -jets out of least 4 jets in each event.

Although our MC simulation is not fully realistic, we consider it to be useful for giving a rough estimate of the sensitivity to anomalous couplings before performing a full simulation. In particular, as for the Tevatron experiments, our MC simulation would give quite reasonable results. On the other hand, for LHC studies, there are some other important ingredients that should be taken into account before giving more realistic estimates of the sensitivity. Among them, the most important effect would be the presence of events with extra jets, i.e.  $t\bar{t} + n$ -jets events, which are not included in our event generation. (This effect is expected to be small at the Tevatron.)

The full kinematic event reconstruction for the  $lepton + 4jets$  channel is performed by a likelihood fitting reconstruction method [285] with constrained top and  $W$  masses on event-by-event basis.<sup>24</sup> This technique has the advantage to choose the correct jet-parton assignment by maximizing the likelihood function for each  $t\bar{t}$  candidate event, as well as a better kinematic reconstruction than the naive reconstruction without this likelihood fitting technique.

### 13.5 Sensitivity study

As already explained, we measure the double angular distribution of the  $W$  and the charged lepton using the effective spin reconstruction method. The top quark helicity axis is defined in the top quark rest frame as (the opposite of) the direction of the momentum of the hadronically decaying anti-top quark, which sequentially decays into three jets. The sign of the top spin is defined by the direction of the charged lepton in the top rest frame. The reconstructed top quark momentum is also used to measure the helicity angle of the charged lepton, since the original direction of the  $W$  in the  $W$  rest frame is equivalent to the opposite of the leptonically decaying top quark direction in the  $W$  rest frame

We show in Fig. 64 the double angular distributions  $d\Gamma/d\cos\theta_W \cos\theta_l$  using MC events, after event selection and event reconstruction by the kinematic likelihood fitting. Comparing with the corresponding parton distributions at generator level in Fig. 62, one can see that, even after cuts, the dependence on the anomalous couplings remains in the  $W_T$  region ( $\cos\theta_W \sim -1$ ,  $\cos\theta_l \sim -1$ ). The

<sup>24</sup>Ref. [285] is a dedicated study for top quark reconstruction at future  $e^+e^-$  linear colliders. In order to apply it to hadron collider experiments, some modifications are implemented.



difference is maximized in the  $W_T$  region ( $\cos \theta_W \sim -1, \cos \theta_l \sim -1$ ) and minimized in its diagonal opposite region ( $\cos \theta_W \sim 1, \cos \theta_l \sim 1$ ). The other two (diagonal) regions depend weaker on anomalous couplings.

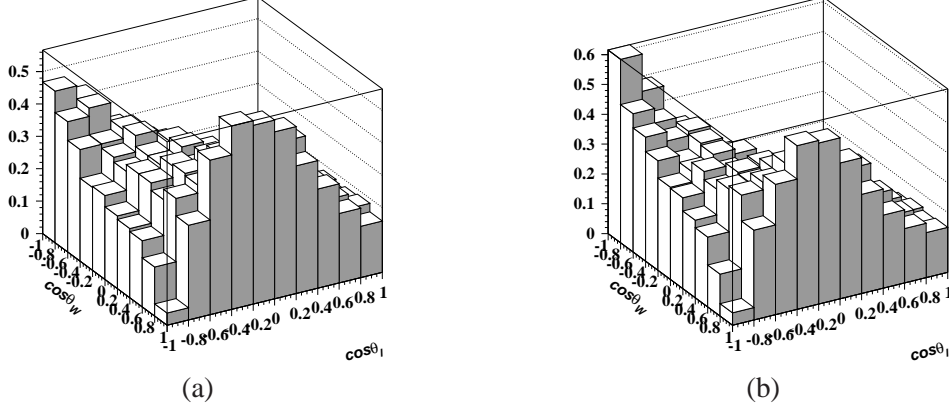


Fig. 64: Normalized differential decay distributions using the signed-helicity direction *after event reconstruction and kinematic cuts* (a) for  $(f_1, f_2) = (1, 0)$ , and (b) for  $(f_1, f_2) = (1, 0.3)$ .

When the signal statistics is small or the background contribution is not well-understood, a simple but not elaborate method to determine the anomalous couplings would be practical for a first analysis. Hence, we divide the kinematic region into 4 regions and simply count the number of events in each region. The regions are defined as follows:

$$\begin{aligned}
 \text{Region A :} & \quad -1 \leq \cos \theta_W \leq 0 \quad \text{and} \quad -1 \leq \cos \theta_l \leq 0 \\
 \text{Region B :} & \quad -1 \leq \cos \theta_W \leq 0 \quad \text{and} \quad 0 \leq \cos \theta_l \leq 1 \\
 \text{Region C :} & \quad 0 \leq \cos \theta_W \leq 1 \quad \text{and} \quad -1 \leq \cos \theta_l \leq 0 \\
 \text{Region D :} & \quad 0 \leq \cos \theta_W \leq 1 \quad \text{and} \quad 0 \leq \cos \theta_l \leq 1 \quad ,
 \end{aligned} \tag{63}$$

where  $\cos \theta_l$  is the lepton helicity angle and  $\cos \theta_W$  is the angle between the  $W$  and the signed-helicity direction in the top rest frame.

The dependences of the event fractions in these regions on the anomalous couplings are shown in Fig. 65. The regions A and D are the regions which are most sensitive to anomalous couplings, while the regions B and C are less sensitive. We can see that the event fraction in region A increases with  $f_2/f_1$  when  $f_2/f_1 > 0$ , and takes a minimum value around  $f_2/f_1 \approx -0.45$ , and then increases again if we decrease  $f_2/f_1$  below  $-0.45$ . The event fraction in region D has an opposite behavior to that of region A. All the event fractions take maximum or minimum values around  $f_2/f_1 = -M_W/M_t \approx -0.45$ , where the transverse component of the  $W$  is canceled. Note that since  $f_1$  only contributes to the normalization of the differential angular distribution, which does not affect the shape of the distribution, the event fractions depend only on  $x = f_2/f_1$  regardless of the various choices of  $f_1$  and  $f_2$ .

We fit the MC data as a function of  $f_2/f_1$ , shown by discrete points in Fig. 65, with analytic functions estimated by the integration over each of the regions A–D, where the sum of the event fractions in four regions is normalized to one. The fitting results of the event fractions in each region are also shown as functions of  $f_2/f_1$  in Fig. 65. The minimum  $\chi^2$  per degree of freedom takes a reasonable value  $\approx 1.20$ . The functions, determined by the fit, are used to estimate the sensitivity to the anomalous couplings.

In Table 13, the expected bounds on the coupling ratio at 95% C.L. are shown, which are corresponding to 100 and 1000 selected events (after cuts) for the Tevatron experiment and 100k selected events (after cuts) for the LHC experiment, respectively.<sup>25</sup> The input parameters of the MC simulations

<sup>25</sup>Using the detection efficiencies, 100 and 1000 double  $b$ -tagged events at Tevatron are translated roughly to 1 and 10  $\text{fb}^{-1}$  integrated luminosities, respectively, and 100k events to 10  $\text{fb}^{-1}$  at LHC.

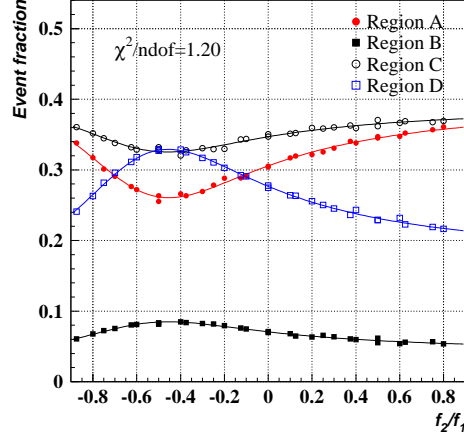


Fig. 65: MC data and fit results of the event fractions in each region as a functions of  $f_2/f_1$ . All regions are defined in Eq. (63).

Table 13: Expected bounds at 95% C.L. corresponding to 100 and 1000 events (after cuts) for Tevatron and 100k events (after cuts) for LHC. Input parameters of the MC simulations are taken as  $(f_1, f_2) = (1, 0)$ . Only statistical errors are taken into account. For comparison, the bounds using an ideal off-diagonal direction, and those using only the events with correct assignment of the two  $b$ -jets in the signed helicity method are presented.

Number of events	Tevatron (1.96 TeV)		LHC (14 TeV)
	100	1000	100k
Signed-helicity direction	$-0.93 < \frac{f_2}{f_1} < 0.57$	$-0.12 < \frac{f_2}{f_1} < 0.14,$ $-0.81 < \frac{f_2}{f_1} < -0.70$	$-0.01 < \frac{f_2}{f_1} < 0.01,$ $-0.74 < \frac{f_2}{f_1} < -0.72$
Ideal off-diagonal direction	$-0.84 < \frac{f_2}{f_1} < 0.50$	$-0.11 < \frac{f_2}{f_1} < 0.12,$ $-0.73 < \frac{f_2}{f_1} < -0.61$	Not applicable
Signed-helicity direction with correct $b$ assignment	$-0.29 < \frac{f_2}{f_1} < 0.39,$ $-0.89 < \frac{f_2}{f_1} < -0.59$	$-0.09 < \frac{f_2}{f_1} < 0.10,$ $-0.80 < \frac{f_2}{f_1} < -0.71$	$-0.01 < \frac{f_2}{f_1} < 0.01,$ $-0.75 < \frac{f_2}{f_1} < -0.74$

are taken as  $(f_1, f_2) = (1, 0)$  (tree-level SM values). Only statistical errors are taken into account to obtain the allowed regions. For comparison, we present the allowed regions using an ideal off-diagonal direction (for the Tevatron), in which the spin direction is reconstructed using the off-diagonal basis with the sign ambiguity resolved by looking into the information at the generator level; we may consider that this ideal off-diagonal direction approximates the true spin direction well, so that the corresponding results can be used as references (although these include effects of kinematic cuts as well as contamination from fake events). We also present the allowed regions using only events with a correct assignment of two  $b$ -jets using the signed helicity direction.

In Table 13, the bounds using the signed helicity direction are not very different from those using the ideal off-diagonal spin direction at the Tevatron. Since the latter results can be regarded as references for optimal reconstruction of the top spin, it is seen that the signed helicity direction is quite efficient for this analysis. In addition, the sensitivities can be improved if we can remove the misassignment of the  $b$ -jets.

Finally, we show the expected excluded regions in the  $(f_2, f_1)$ -plane at 95% C.L. for the Tevatron case in Fig. 66. We thus anticipate that our method allows us to cover a wide region in the parameter space even in this simplified counting experiment.

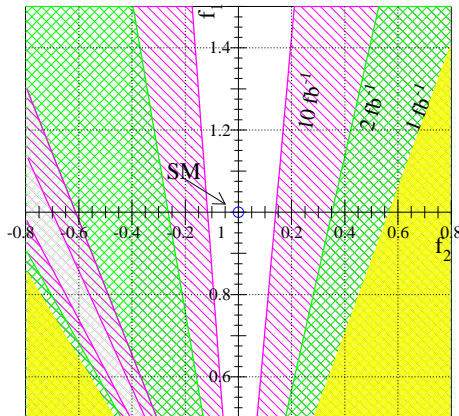


Fig. 66: Expected excluded regions at 95% C.L. in the  $(f_2, f_1)$ -plane at Tevatron. The shaded regions correspond to  $1 \text{ fb}^{-1}$ ,  $2 \text{ fb}^{-1}$ , and  $10 \text{ fb}^{-1}$  integrated luminosities, respectively. The input SM point is located at  $(f_2, f_1) = (0, 1)$ .

### 13.6 Conclusions

We have studied the sensitivities to anomalous couplings  $f_1$  and  $f_2$  in top quark decays at hadron colliders, taking into account realistic experimental conditions expected at the Tevatron and the LHC.

We have analyzed a double angular distribution  $d\Gamma(t \rightarrow b\nu)/d\cos\theta_W d\cos\theta_l$  by using a new method to reconstruct the top quark spin direction effectively (referred to as *signed-helicity direction*). This method does not require the reconstruction of the spin of the top quark on the other side, hence it helps to elude possibly large systematic uncertainties. These techniques, when used in combination, turned out to be quite powerful for the sensitivity study. The  $W_T$  region  $\cos\theta_W \sim -1$ ,  $\cos\theta_l \sim -1$  of the distribution is sensitive to the ratio of the anomalous couplings  $f_2/f_1$ . We confirmed that this feature is preserved even after kinematic cuts.

In order to give reliable estimates, we have developed an event generator incorporating in the matrix element proper spin correlations of the partons as well as the anomalous couplings in the top decay vertices. We also simulate the detector effects by assuming a simple geometry and energy resolutions based on the CDF and ATLAS detectors for the Tevatron and the LHC colliders, respectively. After the event selection, the event kinematics is reconstructed by the kinematic likelihood fitting on an event by event basis. It not only improves the jet energy scale from the measured jet energy to the corresponding parton energy but also helps to select the correct configuration of the jets in the top event topology.

As a first analysis, we have simply counted the event fractions of the double angular distribution divided into 4 regions. Then we have performed  $\chi^2$ -fits to these event fractions in order to find the sensitivities to  $f_2/f_1$ . The results can be summarized as follows. The bounds obtained at 95% C.L. read

$$\begin{aligned}
 & -0.93 < \frac{f_2}{f_1} < 0.57 && \text{for 100 reconstructed events at Tevatron,} \\
 & -0.81 < \frac{f_2}{f_1} < -0.70, \quad -0.12 < \frac{f_2}{f_1} < 0.14 && \text{for 1000 reconstructed events at Tevatron,} \\
 & -0.74 < \frac{f_2}{f_1} < -0.72, \quad -0.01 < \frac{f_2}{f_1} < 0.01 && \text{for 100k reconstructed events at LHC.}
 \end{aligned} \tag{64}$$

We have taken into account only the statistical errors. Due to characteristic dependences of the event fractions on  $f_2/f_1$ , the bound on  $f_2/f_1$  shrinks quickly as the number of top quark events increases up to a few hundred. For more events, the bound scales with  $1/\sqrt{N}$ , and there remains a twofold ambiguity for the allowed ranges of  $f_2/f_1$ .

Although some simplifications have been made, we consider that our MC study for the Tevatron experiment reflects realistic experimental conditions closely enough to give reasonable estimates for the sensitivities to anomalous couplings. On the other hand, as for the LHC case, some important ingredients

are still missing in the MC simulation (the most important one would be  $t\bar{t} + n$ -jets events), so our results should be taken as first rough estimates.

Since our methods for event reconstruction and effective top spin reconstruction are fairly simple, we would expect that they can be applied to other analyses, such as precise determination of the  $W$  polarization states in top decays.

## Acknowledgments

S.T. is grateful to the organizers of the Physics at TeV Colliders workshop (Les Houches 2005) to give an opportunity for fruitful discussions.

## 14. EFFECTIVE NLO APPROACH IN THE MODEL OF SINGLE TOP QUARK PRODUCTION<sup>26</sup>

### 14.1 Introduction

The dedicated event generator SingleTop for the simulation of the electroweak production of a single top and its subsequent decays at the Tevatron and LHC has been achieved with the help of the CompHEP package [286]. Single top is expected to be discovered at the Tevatron Run II and will be a very interesting subject of detailed studies at the LHC (see the review [287]).

There are three main processes for single top production at hadron colliders which could be distinguished by the virtuality  $Q_W^2$  of the  $W$ -boson involved in the process:  $t$ -channel,  $s$ -channel and associated  $tW$  mechanisms.

The generator SingleTop includes all the three processes and provides Monte-Carlo unweighted events at the NLO QCD level. In [288] it was shown that the NLO distributions for the  $s$ -channel process are the same as the LO once rescaled by a known  $K$ -factor. We discuss shortly here only the main process with the largest rate, the  $t$ -channel production. The representative LO and NLO diagrams are shown in Fig.67. The top decay is not shown, however it is included with all the spin correlations.

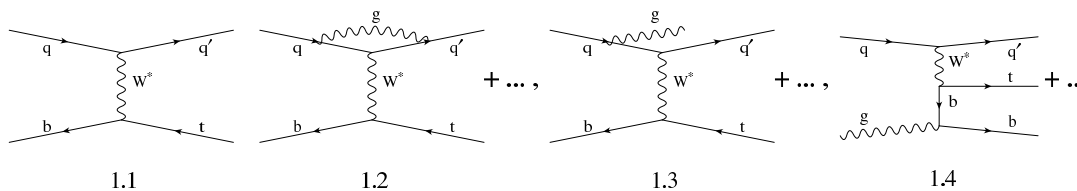


Fig. 67: LO and representative loop and tree NLO diagrams of the  $t$ -channel single top production

### 14.2 Overview of the effective NLO approach

We compute by means of CompHEP the LO process  $2 \rightarrow 2$  with the  $b$ -quark in the initial state including the three-body decay of the top taking into account spin correlation. This is fed into PYTHIA [27]. We also switch on ISR and FSR. Then with CompHEP we compute the NLO tree level corrections -  $2 \rightarrow 3$  processes with additional  $b$ - and light quarks or gluons in the final state including also the top decay with spin correlations. We split the phase space region in "soft" and "hard" parts according to the  $p_T$  of those additional  $b$  and light jets. The "soft" radiation is taken from PYTHIA radiation while the "hard" region is a matrix element calculation through CompHEP. The soft part is normalised in such a way that the value of the total cross section at NLO, known from [289, 290] ( $\sigma_{NLO}^{t\text{-channel}} = 242.6(1.9)$  pb for the LHC (Tevatron)), is correctly reproduced. The splitting parameters are tuned based on the

<sup>26</sup>Contributed by: E.E. Boos, V.E. Bunichev, L.V. Dudko, V.I. Savrin, A.V. Sherstnev

requirements that all the distributions become smooth after normalization. The performed cross checks show an agreement with exact NLO calculations where the computed NLO distributions are correctly reproduced by our method. Therefore, the generator “SingleTop” designed this way does not have a double counting problem, gives the NLO rate and distributions and includes all the spin correlations.

The first release of the generator [291] did not include the hard radiation of the light jets, while the latest version [292] currently used in the analysis by the Fermilab DO and the LHC CMS collaborations includes all the mentioned properties.

### 14.3 Practical implementation of the method in generator SingleTop

The generator “SingleTop” realizes the effective NLO approach of event generation by taking into account the main NLO corrections. It is based on the phase space slicing method.

The cross sections for the  $t$ -channel process in the Born approximation include the full set of Feynman diagrams where the top-quark appears with additional  $b$  and light quarks in the final state ( $2 \rightarrow 3$ ). However, the calculation of the process  $2 \rightarrow 3$  at tree level does not include the large logarithmic QCD corrections (related to the splitting  $g \rightarrow b\bar{b}$ ) that appears in the “soft” phase space region where the  $b$  quark has a small  $P_T$ . It is possible to calculate this effect via the standard renormalization procedure and include it into the partonic distributions of the  $b$ -quarks in the proton. In this case the reaction  $2 \rightarrow 2$  (with  $b$ -quark in the initial state) would be the LO approach of the  $t$ -channel process. In the same way another  $b$ -quark should appear also in the final state. It follows from the fact that  $b$ -quark can be produced in the proton only through  $b\bar{b}$  pairs from the virtual gluon. One can simulate the final  $b$ -quark in the process  $2 \rightarrow 2$  via ISR. In this case the  $b$ -quark could be produced by initial state radiation and will appear in the final state within a branch of parton shower, from the splitting function  $g \rightarrow b\bar{b}$ . One of this  $b$ -quarks (from gluon splitting) is the initial hard parton and the second one goes to the final state.

Calculations of the process  $2 \rightarrow 3$  at the tree level approach does not include large logarithmic corrections (related to the process  $g \rightarrow b\bar{b}$ ) but the exact tree level calculations correctly simulate the behavior of the  $b$ -quark in the “hard” phase space region that corresponds to large  $P_T$ . We will demonstrate that the combination of the processes  $2 \rightarrow 2$  and  $2 \rightarrow 3$  allows us to construct MC samples at “effective” NLO level approach. We can prepare correct events with “soft”  $b$ -quark via ISR simulation. But in this case we lose the significant contribution of the “hard”  $b$ -quark. We can probably get the appropriate result if we use different strategies of simulation in the different kinematic regions of phase space. Unfortunately, we can not naively combine the samples with  $2 \rightarrow 2$  and  $2 \rightarrow 3$  processes because in this case we get double counting of some phase space regions. To avoid the problem of double counting we propose to use different methods of MC simulation in the different phase space regions and combine them based on some kinematic parameters.

Figures 68, 69 show the normalized distributions at Tevatron energies (the distributions at the LHC energies have almost the same dependencies). On these plots we can see the distributions for  $P_T$  and pseudorapidity of the top and light quarks looks similar, but the distributions of additional  $b$ -quark (that comes not from  $t$ -quark decay) differ significantly. The distribution in pseudorapidity of additional ISR  $b$ -quarks, have pikes at the larger values than the distributions for processes  $2 \rightarrow 3$  at tree level. Moreover the  $P_T$  spectra for the events derived from PYTHIA with the ISR simulation are “softer” than in the tree level calculation. The main contribution from the large logarithmic appears in the “soft” region of  $P_T(b)$ . Therefore, it is reasonable to use the transverse momentum of the additional  $b$ -quark as a kinematical parameter for slicing the phase space between the hard and soft regions. To prepare events at NLO effective approach we apply the following procedure: first, we prepare the CompHEP events  $2 \rightarrow 3$  (at tree level) with  $P_T(b)$  larger than some critical value  $P_T^0$ . Then we prepare events  $2 \rightarrow 2$  in the “soft” region of the phase space with  $P_T(b) < P_T^0$ . The cross section of  $2 \rightarrow 2$  events in the “soft” region is multiplied by the  $K$ -factor. This takes into account loop corrections which do not change significantly the distributions. The value for the  $K$ -factor is derived by normalising the NLO

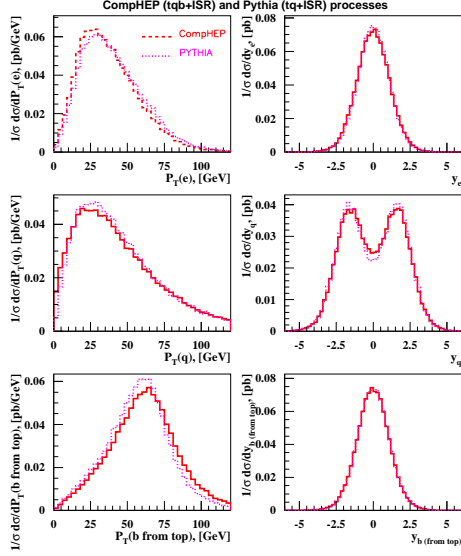


Fig. 68: The comparison of  $P_T$  and  $\eta$  distributions for the  $pp \rightarrow tq + b_{ISR}$  (PYTHIA) and  $pp \rightarrow tq + b_{LO}$  (CompHEP) simulations for the Tevatron. The distributions are normalized to unity and no cuts applied.

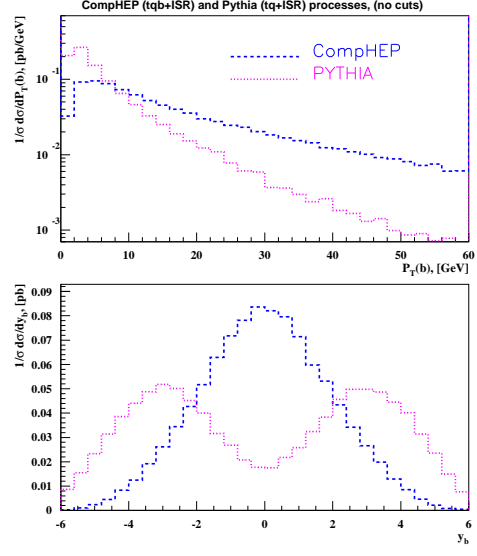


Fig. 69: The comparison of  $P_T$  and  $\eta$  distributions for the  $b_{ISR}$  and  $b_{LO}$  in the  $pp \rightarrow tq + b_{ISR}$  (PYTHIA) and  $pp \rightarrow tq + b_{LO}$  (CompHEP) simulations for the Tevatron. The distributions are normalized to unity and no cuts applied.

cross section to a normalised  $2 \rightarrow 2$  from Pythia and  $2 \rightarrow 3$  from CompHEP through

$$\sigma_{NLO} = K \cdot \sigma_{PYTHIA}(2 \rightarrow 2)|_{P_T(b) < P_T^0} + \sigma_{CompHEP}(2 \rightarrow 3)|_{P_T(b) > P_T^0}.$$

The  $K$ -factor here is a function of the slicing parameter  $P_T^0$ . The total NLO cross section we know from exact NLO calculations [289, 290].

In case of LHC collider we have:

$$\sigma_{CompHEP}(2 \rightarrow 3)|_{P_T^b > 20\text{GeV}} \approx 108.7 \text{ pb},$$

$$\sigma_{CompHEP}(2 \rightarrow 3)|_{P_T^b > 10\text{GeV}} \approx 125.7 \text{ pb}$$

and  $K=0.89$  for  $P_T^0 = 20 \text{ GeV}$ , and  $k=0.77$  for  $P_T^0 = 10 \text{ GeV}$ .

In case of the TEVATRON we have:

$$\sigma_{CompHEP}(2 \rightarrow 3)|_{P_T^b > 20\text{GeV}} \approx 0.46 \text{ pb}$$

$$\sigma_{CompHEP}(2 \rightarrow 3)|_{P_T^b > 10\text{GeV}} \approx 0.72 \text{ pb}.$$

and  $k=1.32$  for  $P_T^0 = 20 \text{ GeV}$ , and  $k=1.21$  for  $P_T^0 = 10 \text{ GeV}$ .

The natural requirement for the correct slicing parameter  $P_T^0$  is a smoothness of the final  $P_T$  distribution in the whole kinematic region for the additional  $b$ -quark. After a series of iterations we have found that the  $P_T$  distribution becomes smooth enough with  $P_T^0 = 10 \text{ GeV}$ . The result is shown in Figure 70. The distributions for the LHC collider are shown in the figure 71 for the same value of  $P_T^0 = 10 \text{ GeV}$ . The algorithm described above we have named the "effective NLO approach".



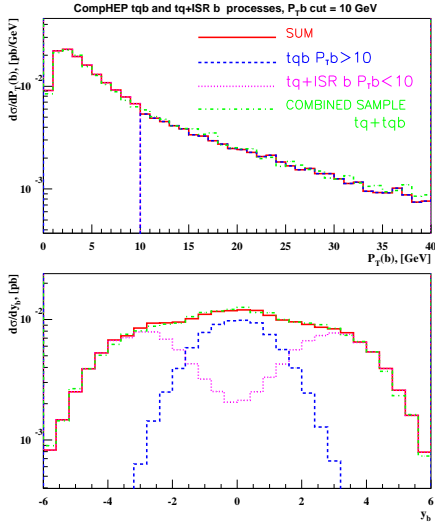


Fig. 70: The combined distributions for the "soft"  $pp \rightarrow tq + b_{ISR}$  (PYTHIA) and "hard"  $pp \rightarrow tq + b_{LO}$  (CompHEP) regions for the Tevatron collider with  $P_T^0(b) = 10$  GeV.

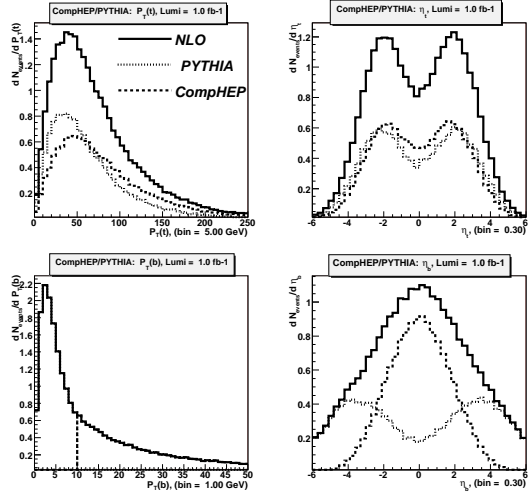


Fig. 71: The combined distributions for the "soft"  $pp \rightarrow tq + b_{ISR}$  (PYTHIA) and "hard"  $pp \rightarrow tq + b_{LO}$  (CompHEP) regions for the LHC collider with  $P_T^0(b) = 10$  GeV.

#### 14.4 Comparison of the results

To check the correctness of our approach we compare our results with two independent NLO calculations. The programs ZTOP [288] and MCFM [293] provides the kinematic distributions at NLO level. The MCFM takes into account the NLO corrections in the decay of  $t$ -quark as well as in the production. The ZTOP includes NLO corrections only in the production of top quark. The ZTOP and MCFM programs provide the possibility to calculate NLO distributions, but do not simulate events which are important in the real analysis. We should note, that due to the model of showering for the final partons, the generator "SingleTop" takes into account most of the part of the NLO corrections in the decay of the  $t$ -quark as well as in the production. We compare the representative distributions from our effective NLO approach with exact NLO calculations. The results are shown in Figures 72, 73. We can see how the events simulated in the effective NLO approach correctly reproduces the exact NLO distributions which are plotted with the ZTOP and MCFM programs. The good agreement in the distributions demonstrates the correctness of the simple approach to model the most important part of the NLO QCD corrections on the level of event simulations.

#### Acknowledgements

The work is partly supported by RFBR 04-02-16476, RFBR 04-02-17448, Universities of Russia UR.02.02.503, and Russian Ministry of Education and Science NS.1685.2003.2 grants.

### 15. PROGRESS IN $W^+W^-$ PRODUCTION AT THE LHC <sup>27</sup>

The production of vector boson pairs in hadron collisions is an important process within and beyond the Standard Model (SM). Vector boson pairs directly probe the gauge structure of the  $SU(2) \otimes U(1)$  electroweak theory. Experimentally, various interesting measurements are possible at hadron colliders.

<sup>27</sup>Contributed by: T. Binoth, M. Ciccolini, G. Davatz, V. Drollinger, M. Dürrssen, A.-S. Giolo-Nicollerat, M. Grazzini, N. Kauer, M. Krämer, M. Zanetti



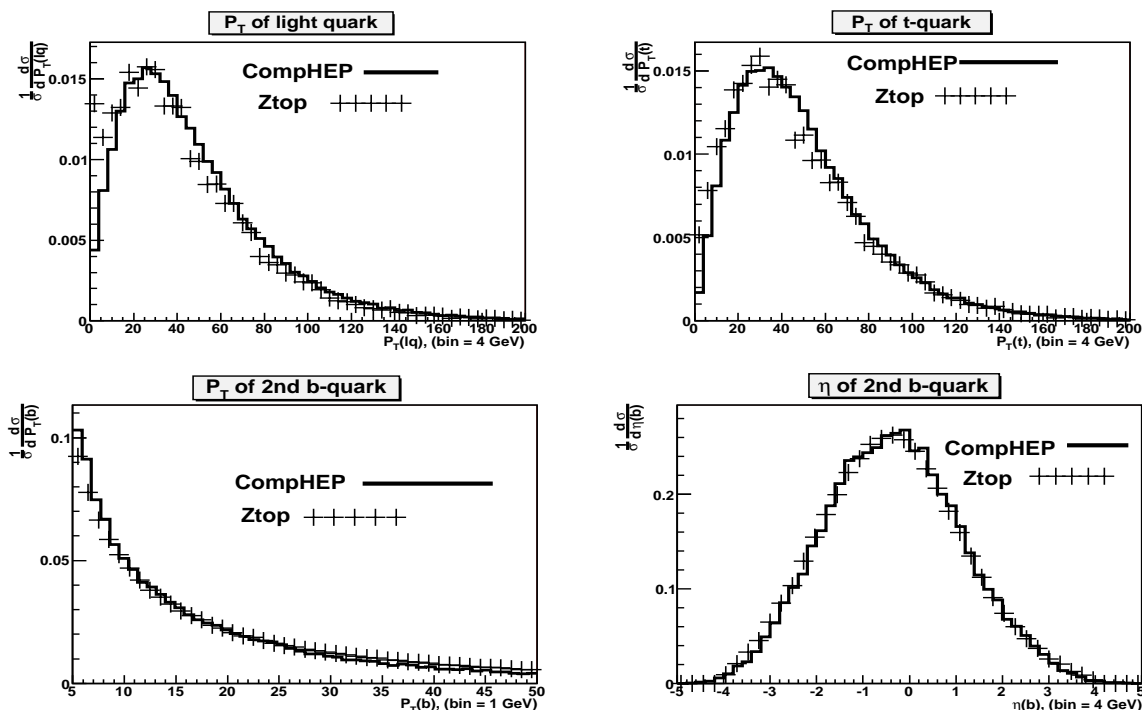


Fig. 72: The  $P_T$  and pseudorapidity distributions of final quarks in effective NLO approach (“SingleTop”) and exact NLO calculations (ZTOP) for the Tevatron collider.

This has been demonstrated at the Tevatron already, for instance by measuring the  $W^+W^-$  cross section or the trilinear vector boson couplings [294, 295].

On the other hand,  $pp \rightarrow W^+W^-$  has to be considered as a background process in many analyses. One of the most prominent examples is the search for  $h \rightarrow W^+W^- \rightarrow \ell^+\nu\ell^-\bar{\nu}$ , which is the most important SM Higgs search channel in the mass range between 155 GeV and 170 GeV at the LHC [296, 297]. Here,  $W$  pairs are the irreducible background to the resonant production of  $W$  pairs coming from the Higgs decay. An accurate theoretical prediction for the  $W^+W^-$  background process is crucial to fully exploit the  $h \rightarrow W^+W^-$  discovery channel, in particular as no Higgs mass peak can be reconstructed from leptonic  $W$  decays with two neutrinos in the final state.

In the following, recent progress in the understanding of  $W$  pairs is presented. The  $W^+W^-$  cross section is presently known at NLO, and the contribution from the one-loop  $gg \rightarrow W^+W^- \rightarrow \ell^+\nu\ell^-\bar{\nu}$  diagrams has been evaluated recently. Although this is only a part of the (presently unknown) full NNLO contribution, this calculation is now available also as event generator. Analyses of this process show that the event properties differ substantially from the LO and NLO quark-scattering contributions to the  $pp \rightarrow W^+W^-$  process. In addition, the event generator for  $gg \rightarrow W^+W^-$  has been interfaced to a parton shower program.

For the general case of  $W$  pair production soft gluon effects are studied in a resummed higher order calculation. A solid understanding of soft gluon effects is important for kinematic properties of  $W^+W^-$  events, such as the transverse momentum of the  $W$  pair. Furthermore the results of this calculation are compared with MC@NLO, in which the spin correlations have been included quite recently.

After some more comparisons and cross checks, two  $W^+W^-$  background normalization strategies are presented for the Higgs search in the  $h \rightarrow W^+W^- \rightarrow \ell^+\nu\ell^-\bar{\nu}$  channel, and the corresponding theoretical uncertainties are evaluated. The uncertainties turn out to be reduced significantly, when the new achievements are taken into account.

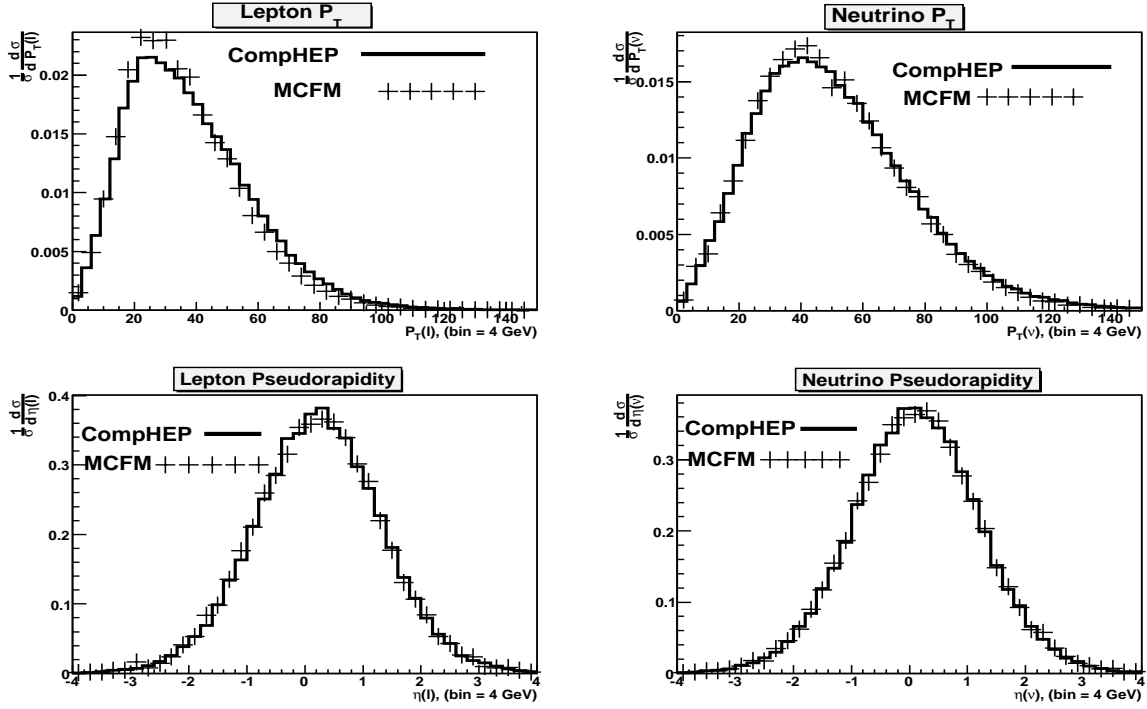


Fig. 73: The  $P_T$  and pseudorapidity distributions of final leptons from top-quark decay in effective NLO approach (“Single-Top”) and exact NLO calculations (MCFM) for the Tevatron collider.

### 15.1 Soft-gluon effects in $W^+W^-$ production<sup>28</sup>

At present, the  $WW$  production cross section is known at NLO accuracy. The NLO corrections were first obtained with the traditional method by summing over the  $W$ ’s polarizations [298, 299]. Later the calculation has been extended to fully include spin correlations in the  $W$ ’s decay [300, 301]. The NLO effect increases the cross section by about 40% at LHC energies.

The fixed-order NLO calculations provide a reliable estimate of  $W^+W^-$  cross sections and distributions as long as the scales involved in the process are all of the same order. When the transverse momentum of the  $W^+W^-$  pair  $p_T^{WW}$  is much smaller than its invariant mass  $M_{WW}$  the validity of the fixed-order expansion may be spoiled since the coefficients of the perturbative expansion can be enhanced by powers of the large logarithmic terms,  $\ln^n M_{WW}/p_T^{WW}$ . This is certainly the case for the  $p_T^{WW}$  spectrum, which, when evaluated at fixed order, is even divergent as  $p_T^{WW} \rightarrow 0$ , and thus requires an all-order resummation of the logarithmically enhanced terms. Resummation effects, however, can be visible also in other observables, making it important to study them in detail.

In the following we report on a study of soft-gluon effects in  $W^+W^-$  production at hadron colliders [302]. We use the helicity amplitudes of Ref. [303] and work in the narrow width approximation (i.e. we only consider double-resonant contributions), but fully include the decays of the  $W$  bosons, keeping track of their polarization in the leptonic decay. In the large  $p_T^{WW}$  region we use LO perturbation theory ( $W^+W^-+1$  parton); in the region  $p_T^{WW} \ll M_{WW}$  the large logarithmic contributions are resummed to NLL and (almost) NNLL [304, 305] accuracy<sup>29</sup>.

To perform the resummation we use the formalism of Refs. [306, 307]. In this approach, the resummation is achieved at the level of the partonic cross section and the large logarithmic contributions are exponentiated in a process-independent manner, being constrained to give vanishing contribution to

<sup>28</sup>Author: M. Grazzini

<sup>29</sup>The inclusion of NNLL terms cannot be complete [302], since two-loop corrections to  $W^+W^-$  production are not yet known.

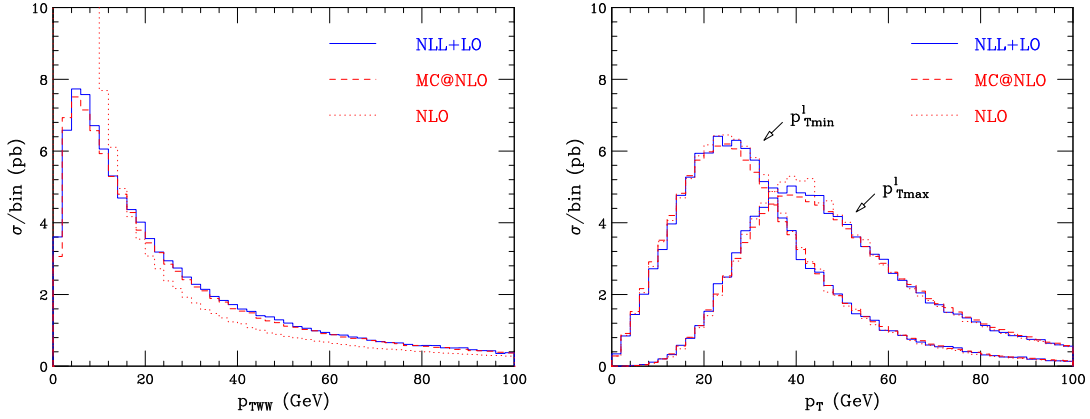


Fig. 74: Left: Comparison of the transverse momentum spectra of the  $W^+W^-$  pair obtained at NLL+LO, NLO and with MC@NLO. No cuts are applied. Right: corresponding predictions for the transverse momentum spectra of the lepton with minimum and maximum  $p_T^l$ .

the total cross section. Our results have thus uniform NLO accuracy over the entire range of transverse momenta but consistently include the all-order resummation of logarithmically enhanced terms in the region  $p_T^{WW} \ll M_{WW}$ .

We present predictions for the transverse momentum spectrum of the  $W^+W^-$  pair, but also for a few leptonic distributions, comparing our results with those obtained at NLO with the program MCFM [301], and with the ones from the general purpose event generator MC@NLO [308, 309] which, in its latest release [310], partially includes the effect of spin correlations in the  $W$ 's decay. More details can be found in Ref. [302].

To compute the  $W^+W^-$  cross section we use MRST2002 NLO densities [311] and  $\alpha_S$  evaluated at two-loop order. Our resummed predictions depend on renormalization, factorization and resummation scales. Unless stated otherwise, the resummation scale is set equal to the invariant mass  $M_{WW}$  of the  $W^+W^-$  pair, whereas renormalization and factorization scales are set to  $2M_W$ . The latter choice allows us to exploit our unitarity constraint and to exactly recover the total NLO cross section when no cuts are applied. At NLO we consistently use  $\mu_F = \mu_R = 2M_W$  as default choice, whereas in MC@NLO  $\mu_F$  and  $\mu_R$  are set to the default choice, the average transverse mass of the  $W$  bosons.

We start by considering the inclusive cross sections. Our NLL+LO result is 115.6 pb, and agrees with the NLO one (116.0 pb) to better than 1%. The cross section from MC@NLO is instead lower, about 114.7 pb. The above difference is due to the different choice of the scales, and to the different convention in the choice of the electroweak couplings adopted in MC@NLO.

In Fig. 74 (left) we show the  $p_T^{WW}$  distribution, computed at NLO (dotted), NLL+LO (solid) and with MC@NLO (dashed). We see that the NLO result diverges to  $+\infty$  as  $p_T^{WW} \rightarrow 0$ . The NLL+LO and MC@NLO results are instead finite as  $p_T^{WW} \rightarrow 0$  and are in good agreement, showing a kinematical peak around  $p_T^{WW} \sim 5$  GeV.

We now consider the  $p_T$  spectra of the leptons. For each event, we classify the transverse momenta of the two charged leptons into their minimum and maximum values,  $p_{T_{\min}}^l$  and  $p_{T_{\max}}^l$ . In Fig. 74 (right) we plot the corresponding  $p_T$  spectra, computed at NLL+LO (solid), NLO (dotted) and with MC@NLO (dashes). All the three predictions are clearly in good agreement: the effect of resummation, which is essential in the  $p_T^{WW}$  spectrum, is hardly visible in the leptonic spectra.

To further assess the effect of resummation in the leptonic observables, we consider the application of the following cuts, suggested by the study of Ref. [312]:

- For each event,  $p_{T_{\min}}^l$  should be larger than 25 GeV and  $p_{T_{\max}}^l$  should be between 35 and 50 GeV.

- The invariant mass  $m_{ll}$  of the charged leptons should be smaller than 35 GeV.
- The missing  $p_T$  of the event should be larger than 20 GeV.
- The azimuthal charged lepton separation in the transverse plane  $\Delta\phi$  should be smaller than  $45^\circ$ .
- A jet veto is mimicked by imposing that the transverse momentum of the  $W^+W^-$  pair should be smaller than 30 GeV. This cut is perfectly legitimate in our resummed calculation and is exactly equivalent to a jet veto at NLO.

These cuts, designed for the search of a Higgs boson with  $M_h = 165$  GeV, strongly select the small  $\Delta\phi$  region. The jet veto is usually applied in order to reduce the  $t\bar{t}$  contribution, which is expected to produce large- $p_T$   $b$ -jets from the decay of the top quark.

The NLL+LO (MC@NLO) accepted cross section is 0.599 pb (0.570 pb) which should be contrasted with the NLO result, which is 0.691 pb, about 20% higher. This relative large difference is due to the fact that these cuts enhance the relevance of the small- $p_T^{WW}$  region, where the NLO calculation is not reliable.

In Fig. 75 the  $p_{T\min}^l$  and  $p_{T\max}^l$  distributions are presented. We see that although the three predictions are in reasonable agreement in shape, differences are now evident. In particular, the  $p_{T\min}^l$  distribution at NLO is steeper than the other two. Comparing NLL+LO and MC@NLO spectra, we see that the former are steeper than the latter: with the application of strong cuts the differences between NLL+LO and MC@NLO predictions are enhanced.

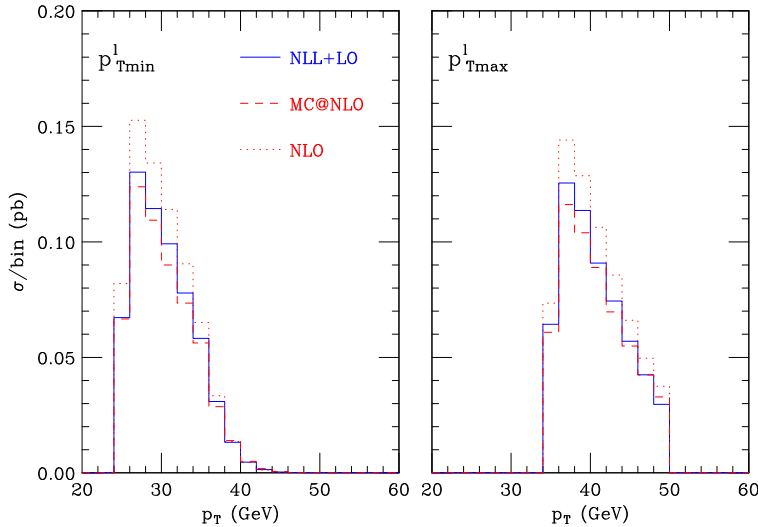


Fig. 75: Distributions of  $p_{T\min}^l$  and  $p_{T\max}^l$  when cuts are applied.

In the search for the Higgs boson in the  $h \rightarrow W^+W^- \rightarrow \ell^+\nu\ell^-\bar{\nu}$  channel an important difference between the signal and the background is found in the  $\Delta\phi$  distribution. Since the Higgs is a scalar, the charged leptons tend to be produced quite close in angle. As a consequence, the signal is expected to be peaked at small values of  $\Delta\phi$ , whereas the  $\Delta\phi$  distribution for the background is expected to be reasonably flat. It is thus important to study the effect of resummation on this distribution, which is also known to be particularly sensitive to spin correlations. In Fig. 76 (left) the  $\Delta\phi$  distribution is displayed. We see that the shapes of the three results are in good agreement with each other, although a slightly different slope of the NLL+LO result with respect to MC@NLO and NLO appears. We remind the reader that the NLO and NLL+LO calculations exactly include spin correlations, whereas MC@NLO neglects spin correlations in the finite (non-factorized) part of the one-loop contribution.

In Fig. 76 (right) we finally consider the transverse-mass distribution of the  $W^+W^-$  system, defined as in Ref. [313]. The NLO result (dotted) is compared to the NLL+LO one (solid) and to MC@NLO

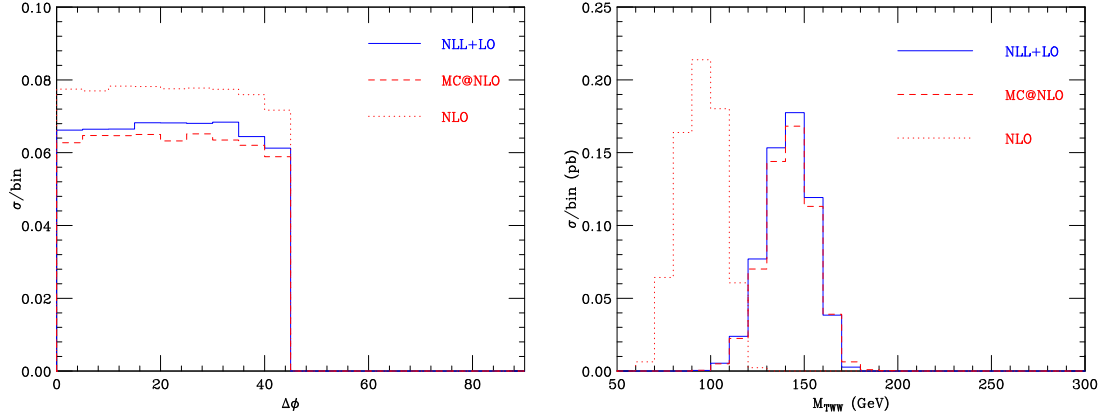


Fig. 76: Left:  $\Delta\phi$  distribution when cuts are applied. Right: Transverse-mass distribution.

(dashes). We see that the effects of soft-gluon resummation are dramatic for this distribution: the NLL+LO result is shifted towards larger values of  $M_{TWW}$  by about 50 GeV, which is mainly due to the divergence of the NLO curve, shown in Fig. 74. We find that this big difference is mainly due to the leptonic cuts: removing the jet veto the shift in the transverse-mass distribution is basically unchanged. Comparing the shapes of the histograms we see that at NLO the shape is fairly different with respect to NLL+LO and MC@NLO. Also the NLL+LO and MC@NLO distributions now show clear differences: the position of the peak is the same, but the NLL+LO result is steeper and softer than the MC@NLO one.

In this contribution we have examined soft-gluon effects in  $W^+W^-$  production at the LHC. We find that resummation has a mild impact on inclusive leptonic distributions. On the other hand, when stringent cuts are applied, the effects of resummation are strongly enhanced. The most significant effect is seen in the transverse mass distribution, for which the NLO calculation is clearly not reliable. Our resummed predictions are generally in good agreement with those of the MC@NLO event generator.

## 15.2 Gluon-induced $W^+W^-$ background to Higgs boson searches<sup>30</sup>

### 15.2.1 Introduction

The hadronic production of  $W$  pairs has been studied extensively in the literature (see e.g. Ref. [216]). In this short note we focus on the gluon-induced loop process  $gg \rightarrow W^*W^* \rightarrow \ell\bar{\nu}\ell'\nu'$ . Although suppressed by two powers of  $\alpha_s$  relative to quark-antiquark annihilation, the importance of the gluon-gluon induced background process is enhanced by the experimental Higgs search cuts which exploit the longitudinal boost and the spin correlations of the  $W^+W^-$  system to suppress  $W$  pair continuum production through quark-antiquark annihilation. We present the first complete calculation of the gluon-fusion process  $gg \rightarrow W^*W^* \rightarrow \ell\bar{\nu}\ell'\nu'$ , including spin and decay angle correlations and allowing for arbitrary invariant masses of the  $W$  bosons. This work extends our previous calculation [314], which did not include the contribution from the intermediate top-bottom massive quark loop.

Our calculation demonstrates that the gluon-fusion contribution to on-shell  $W$  pair production only provides a 5% correction to the inclusive  $W$  pair production cross section at the LHC. However, after taking into account realistic experimental cuts, the process  $gg \rightarrow W^*W^* \rightarrow \ell\bar{\nu}\ell'\nu'$  becomes sizeable and enhances the theoretical  $W^+W^-$  background estimate for Higgs searches by about 30%. In the following we will present a brief discussion of the numerical results. Details of the calculation can be found in Ref. [314] and in a forthcoming article. We note that an independent calculation of the  $gg \rightarrow W^+W^-$  background has been performed in Ref. [315]. A comparison of the two calculations

<sup>30</sup>Authors: T. Binoth, M. Ciccolini, N. Kauer, M. Krämer

Refs. [314] and [315] is in progress.

## 15.22 Results

In this section we present numerical results for the process  $pp \rightarrow W^*W^* \rightarrow \ell\bar{\nu}\ell'\nu'$  at the LHC, where  $\ell = e$  or  $\mu$ . We tabulate the total cross section and the cross section for two sets of experimental cuts. In addition, we show various differential distributions. The experimental cuts include a set of ‘‘standard cuts’’ [216], motivated by the finite acceptance and resolution of the detectors, where we require all charged leptons to be produced at  $p_{T,\ell} > 20$  GeV and  $|\eta_\ell| < 2.5$ , and a missing transverse momentum  $\cancel{p}_T > 25$  GeV. Cross sections calculated with this set of cuts will be labeled  $\sigma_{\text{std}}$ . We also present results after imposing Higgs search cuts following a recent experimental study [312]. In addition to the ‘‘standard cuts’’ defined above, we require that the opening angle between the two charged leptons in the plane transverse to the beam direction must satisfy  $\Delta\phi_{T,\ell\ell} < 45^\circ$  and that the dilepton invariant mass  $M_{\ell\ell}$  be less than 35 GeV. Furthermore, the larger and smaller of the lepton transverse momenta are restricted as follows:  $25 \text{ GeV} < p_{T,\text{min}}$  and  $35 \text{ GeV} < p_{T,\text{max}} < 50 \text{ GeV}$ . Finally, a jet-veto is imposed that removes events with jets where  $p_{T,\text{jet}} > 20$  GeV and  $|\eta_{\text{jet}}| < 3$ . Cross sections evaluated with the Higgs selection cuts will be labeled  $\sigma_{\text{bkg}}$ .

To obtain numerical results we use the following set of input parameters:  $M_W = 80.419$  GeV,  $M_Z = 91.188$  GeV,  $G_\mu = 1.16639 \times 10^{-5}$  GeV $^{-2}$ ,  $\Gamma_W = 2.06$  GeV,  $\Gamma_Z = 2.49$  GeV, and  $V_{\text{CKM}} = 1$ . The weak mixing angle is given by  $c_w = M_W/M_Z$ ,  $s_w^2 = 1 - c_w^2$ . The electromagnetic coupling is defined in the  $G_\mu$  scheme as  $\alpha_{G_\mu} = \sqrt{2}G_\mu M_W^2 s_w^2/\pi$ . The masses of external fermions are neglected. The values of the heavy quark masses in the intermediate loop are set to  $m_{\text{top}} = 178$  GeV and  $m_b = 4.4$  GeV. The  $pp$  cross sections are calculated at  $\sqrt{s} = 14$  TeV employing the CTEQ6L1 and CTEQ6M [47] parton distribution functions at tree- and loop-level, corresponding to  $\Lambda_5^{\text{LO}} = 165$  MeV and  $\Lambda_5^{\overline{\text{MS}}} = 226$  MeV with one- and two-loop running for  $\alpha_s(\mu)$ , respectively. The renormalization and factorization scales are set to  $M_W$ . Fixed-width Breit-Wigner propagators are used for unstable gauge bosons.

We compare results for  $W^+W^-$  production in gluon scattering with LO and NLO results for the quark scattering processes. Since we are interested in  $W^+W^-$  production as a background, the  $gg \rightarrow h \rightarrow W^+W^-$  signal amplitude is not included. The LO and NLO quark scattering processes are computed with MCFM [301], which implements helicity amplitudes with full spin correlations [303] and includes finite-width effects and single-resonant corrections. Table 14 shows gluon and quark scattering cross sections for the LHC. Total cross sections ( $\sigma_{\text{tot}}$ ) are compared with cross sections when standard

Table 14: Cross sections for the gluon and quark scattering contributions to  $pp \rightarrow W^*W^* \rightarrow \ell\bar{\nu}\ell'\nu'$  at the LHC ( $\sqrt{s} = 14$  TeV) without selection cuts (tot), with standard LHC cuts (std:  $p_{T,\ell} > 20$  GeV,  $|\eta_\ell| < 2.5$ ,  $\cancel{p}_T > 25$  GeV) and Higgs search selection cuts (bkg, see main text) applied. The integration error is given in brackets. We also show the ratio of the NLO to LO cross sections and the ratio of the combined NLO+ $gg$  contribution to the NLO cross section.

	$\sigma(pp \rightarrow W^*W^* \rightarrow \ell\bar{\nu}\ell'\nu') [\text{fb}]$				
	$gg$	$q\bar{q}$		$\frac{\sigma_{\text{NLO}}}{\sigma_{\text{LO}}}$	$\frac{\sigma_{\text{NLO}+gg}}{\sigma_{\text{NLO}}}$
		LO	NLO		
$\sigma_{\text{tot}}$	60(1)	875.8(1)	1373(1)	1.57	1.04
$\sigma_{\text{std}}$	29.8(6)	270.5(1)	491.8(1)	1.82	1.06
$\sigma_{\text{bkg}}$	1.41(3)	4.583(2)	4.79(3)	1.05	1.29

LHC cuts ( $\sigma_{\text{std}}$ ) and selection cuts optimized for Higgs boson searches ( $\sigma_{\text{bkg}}$ ) are applied (see above for the definition of the cuts). The  $gg$  process only yields a 5% correction to the total  $W^+W^-$  cross section calculated from quark scattering at NLO QCD. When realistic Higgs search selection cuts are applied the correction increases to 30%. Note that the experimental Higgs search cuts include a jet



veto which suppresses large contributions from gluon-quark scattering at NLO and thereby reduces the K-factor for  $q\bar{q} \rightarrow W^+W^-$  from 1.6 to 1.1. For the  $gg \rightarrow W^+W^-$  process we find a renormalization and factorization scale uncertainty of approximately 25%. The scale uncertainty of the  $q\bar{q} \rightarrow W^+W^-$  process is approximately 5% [314].

The massive top-bottom loop increases the result based on intermediate light quarks [314] by 12% and 15% for the inclusive cross section,  $\sigma_{\text{tot}}$ , and the cross section with standard cuts,  $\sigma_{\text{std}}$ , respectively. After imposing Higgs search cuts, however, the contribution of the massive quark loop is reduced to 2% only. This reduction can largely be attributed to the cut on  $\Delta\phi_{T,\ell\ell}$  as can be seen in Fig. 78 (right) below. We note that the impact of the massive quark loop contribution is mainly due to the interference with the massless loops.

Selected differential distributions for  $pp \rightarrow W^*W^* \rightarrow \ell\bar{\nu}\bar{\ell}'\nu'$  at the LHC are shown in Figs. 77 and 78. The standard set of cuts defined above has been applied throughout. Figure 77 shows the distribution in the invariant mass of the pair of charged leptons. We compare the gluon-gluon induced contribution with the quark scattering process in LO and NLO. In order to facilitate the comparison with Ref. [314], the gluon-fusion cross section is shown with and without the top-bottom intermediate loop. We observe that the invariant mass distribution of the gluon-gluon induced process is similar in shape to the quark scattering contributions and suppressed by more than one order of magnitude in normalization.

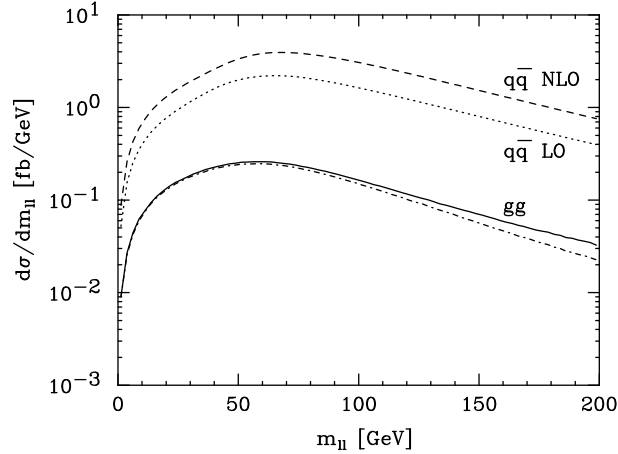


Fig. 77: Distributions in the charged lepton-pair invariant mass  $m_{\ell\ell}$  for the gluon scattering process (solid) and the quark scattering process in LO (dotted) and NLO QCD (dashed) of  $pp \rightarrow W^*W^* \rightarrow \ell\bar{\nu}\bar{\ell}'\nu'$  at the LHC. The dashed-dotted line shows the gluon scattering process without the intermediate top-bottom loop [314]. The input parameters are defined as in the main text. Standard LHC cuts have been applied (see main text and Table 14).

W-boson pairs produced in quark-antiquark scattering at the LHC are in general strongly boosted along the beam axis. Gluon induced processes on the other hand result in  $W^+W^-$  events at more central rapidities. This feature is born out by the distribution in the pseudorapidity of the negatively charged lepton shown in Fig. 78 (left). In order to distinguish the shapes of the various contributions we have chosen a linear vertical scale and plot the gluon-gluon contribution multiplied by a factor 10. Compared to LO quark-antiquark scattering, the lepton distribution of the gluon-gluon process shows a more pronounced peak at central rapidities. We also observe an enhancement of the NLO corrections at central rapidities which is due to the substantial contribution of gluon-quark processes at NLO.

Figure 78 (right) finally shows the distribution in the transverse-plane opening angle of the charged leptons. This observable reflects the spin correlations between the  $W^+W^-$  pair and allows one to discriminate W bosons originating from scalar Higgs decays and  $W^+W^-$  continuum production. Note that the importance of the gluon-gluon process is enhanced by the Higgs search selection cuts which require

a small opening angle  $\Delta\phi_{T,\ell\ell} < 45^\circ$ . This selection cut, on the other hand, reduces the contribution of the intermediate top-bottom loop to the gluon-fusion cross section.

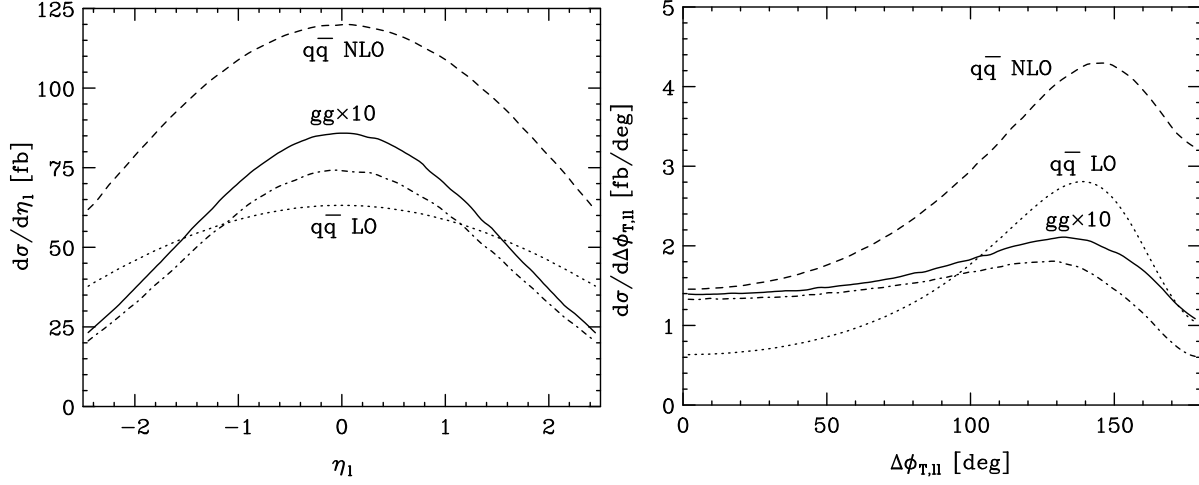


Fig. 78: Left: distributions in the pseudorapidity  $\eta_{\ell^-}$  of the negatively charged lepton. Right: distributions in the transverse-plane opening angle of the charged leptons  $\Delta\phi_{T,\ell\ell}$ . Details as in Fig. 77. The  $gg$  distribution is displayed after multiplication with a factor 10. The dashed-dotted line shows the gluon scattering process without the intermediate top-bottom loop [314].

### 15.23 Conclusions

We have calculated the loop-induced gluon-fusion process  $gg \rightarrow W^*W^* \rightarrow \ell\bar{\nu}\ell'\nu'$  which provides an important background for Higgs boson searches in the  $h \rightarrow W^+W^-$  channel at the LHC. We have presented numerical results for the total cross section, the cross section with two sets of experimental cuts and various differential distributions. The results extend our previous calculation [314] by including the intermediate top-bottom loop. Our calculation demonstrates that the gluon-fusion contribution to on-shell W pair production only yields a 5% correction to the inclusive W pair production cross section at the LHC. However, after imposing realistic Higgs search selection cuts, the process  $gg \rightarrow W^*W^* \rightarrow \ell\bar{\nu}\ell'\nu'$  becomes the dominant higher-order correction to the  $W^+W^-$  background estimate and enhances the theoretical prediction from quark-antiquark scattering at NLO by approximately 30%. We conclude that gluon-gluon induced W pair production is essential for a reliable description of the background and has to be taken into account to exploit the discovery potential of Higgs boson searches in the  $pp \rightarrow h \rightarrow W^+W^- \rightarrow \text{leptons}$  channel at the LHC.

### 15.3 Effect of parton showering on gluon-induced $W^+W^-$ production <sup>31</sup>

The main background for the Higgs search decaying in  $W^+W^- \rightarrow \ell^+\nu\ell^-\bar{\nu}$  is the continuum  $W^+W^-$  production,  $q\bar{q} \rightarrow W^+W^-$ . Recently a NNLO correction to this process was calculated, the gluon-induced  $W^+W^-$  production,  $gg \rightarrow W^+W^-$  [314, 315]. This process represents only a 4% correction to the inclusive  $W^+W^-$  production cross section at NLO. However, when the selection cuts specific to Higgs search in the  $W^+W^-$  channel are applied, this fraction increases to 30%. This is due to the fact that  $gg \rightarrow W^+W^-$  tends to have leptons emitted more centrally than continuum  $W^+W^-$  production, rendering the Higgs selection cuts less efficient against this background.

So far  $gg \rightarrow W^+W^-$  was only studied using a parton-level generator. In the following the effects of adding a parton shower to this process will be investigated. The  $gg \rightarrow W^+W^-$  parton-level program provided by N. Kauer was linked to PYTHIA for the showering step. The W bosons were then forced to

<sup>31</sup>Authors: G. Davatz, A.-S. Giolo-Nicollerat, M. Zanetti

decay into leptons. The addition of a parton shower is expected to have mainly an effect on the lepton isolation requirement and on the jet veto efficiency. In order to study this effect, the initial state radiation was switched on and off, and the distributions of characteristic variables were compared after specific cuts have been applied. The same selection and reconstruction as in the “Top background generation in the  $h \rightarrow W^+W^-$  channel” chapter of these proceedings was used.

The addition of the parton shower reduces the efficiency of finding two isolated leptons in the final state by 20%. Adding a jet veto after all other selection cuts are applied reduces the total efficiency by 10%. The changes to the jet veto efficiency due to the addition of parton shower is thus smaller than its effect on the lepton isolation. The shapes of the other cut variables remain similar with or without initial state radiation. Figure 79 shows a comparison of the  $p_t$  spectrum of the lepton with the highest  $p_t$  and the angle between the leptons in the transverse plane for a  $gg \rightarrow W^+W^-$  sample produced without (black solid line) and with (red dashed line) initial state radiation.

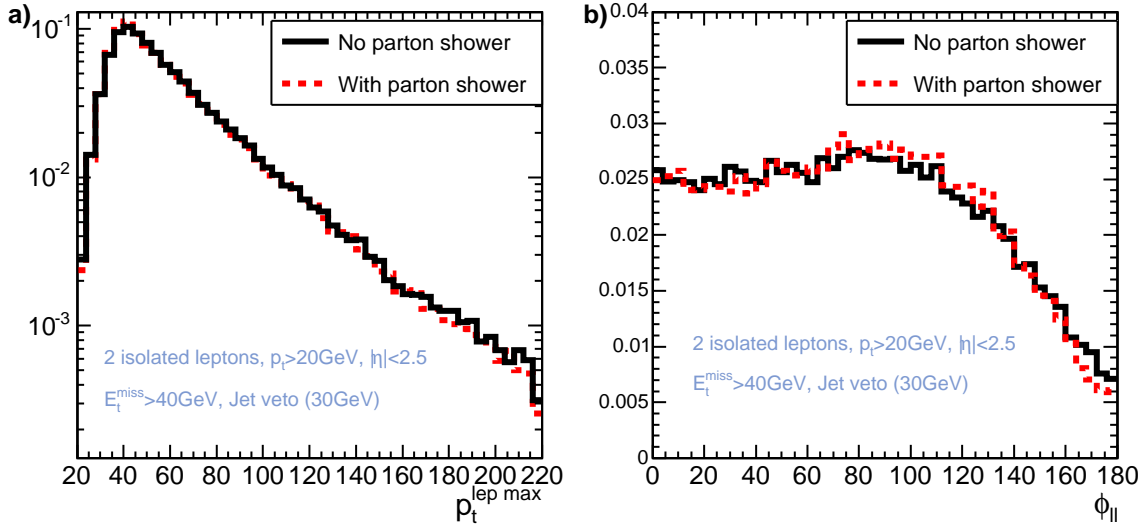


Fig. 79: The  $p_t$  spectrum of the lepton with the highest  $p_t$  (a) and the opening angle between the leptons in the transverse plane (b) for a sample simulated without initial state radiation (black solid line) and with initial state radiation (red dotted line) for events with two isolated leptons, a missing energy higher than 40 GeV and no jets with  $E_T > 30$  GeV.

Since the gluon-induced  $W^+W^-$  production is known at LO only, it is not possible to know if the parton shower will describe accurately the inclusion of higher order QCD corrections. Moreover when applying a jet veto, essentially only the leading order part of this process remains. For further simulation of this process with parton showering we recommend to apply a jet veto in order to be in the correct kinematic region but to set its efficiency to one to take into account the fact that the contribution from  $gg \rightarrow W^+W^-$  is only known at LO, where no additional jets are expected.

An analysis with detailed CMS detector simulation of this process has been performed. After all selection cuts for the  $h \rightarrow W^+W^-$  analysis [316],  $gg \rightarrow W^+W^-$  still represents a contribution of about 30% to the continuum  $W$  pair production cross section at NLO.

## 15.4 Modeling the production of $W$ pairs<sup>32</sup>

### 15.41 Introduction

In order to measure the contribution from the  $W^+W^-$  background in the Higgs signal region it is necessary to extrapolate the number of  $W^+W^-$  events from an almost pure background region to the signal

<sup>32</sup>Authors: V. Drollinger, M. Dührssen

region. In general, it is favorable to study the behavior of such an extrapolation from a clean subsample of the corresponding background events. In this particular case, no method is known how to isolate  $W^+W^-$  background events in a clean way. The only option left, is to rely on theoretical predictions.

The scope of this work is to study effects which could lead to systematic uncertainties in the measurement of  $W^+W^-$  events. After the events are generated with various programs, a basic selection of the events is applied which follows the selection proposed for the  $h \rightarrow W^+W^- \rightarrow \ell^+\nu\ell^-\bar{\nu}$  [296] analysis. For the selected events a set of kinematic distributions is compared. In particular, the main attention is drawn to the  $\Delta\phi(\ell^+, \ell^-)$  distribution which is characteristic for both, signal and background, and therefore is a good candidate for the normalization of the  $W^+W^-$  background.

**Event Generators** There are many programs available to generate  $W^+W^-$  events. For simplicity, only the final state with two muons and two neutrinos is generated. Different event generators have been employed in order to compare the kinematic distributions: PYTHIA, CompHEP, MC@NLO, and GG2WW. All generators can be run with different parameters and options and have different strengths and weaknesses.

PYTHIA [284] is a well known program which generates everything starting from the hard interaction at LO until the complete final state, including showers and the underlying event, in a self consistent way. PYTHIA is used to study the effect of spin correlations and scale dependence.

CompHEP [286] is an event generator which allows to generate the hard processes of almost any tree digram. Among the programs considered, it is the only one which calculates the full  $2 \rightarrow 4$  (two particles in the initial state and four particles in the final state) matrix elements. The showering is done in a separate step with PYTHIA.

MC@NLO [308, 309] is used to evaluate the effect of higher order corrections to  $W^+W^-$  production as well as the effect of spin correlations which have been included recently and are available in version 3.10 [310]. The events are weighted with constant weights which differ only in the sign. The showering is performed with HERWIG [33].

GG2WW [317] is an event generator that generates the hard process of  $gg \rightarrow W^+W^-$  at LO and decays the W bosons. It has all important features: all six quarks (top and bottom quarks massive), W bosons are allowed to be off shell, and all spin correlations are taken into account. Higher order corrections, which are expected to be similar to other gluon induced processes at the LHC, are unknown at present. On the other hand,  $gg \rightarrow W^+W^-$  can be considered as a higher order partonic sub-process to  $pp \rightarrow W^+W^-$  production in general, where the sub-process  $q\bar{q} \rightarrow W^+W^-$  represents the lowest order.

**Event Selection** In order to be able to compare events in a phase space region that is typical for an analysis, the pre-selection cuts of the  $h \rightarrow W^+W^- \rightarrow \ell^+\nu\ell^-\bar{\nu}$  analysis, as suggested in Ref. [296] (cuts 1 to 6), are applied. The lepton isolation (cut 3) is omitted because the leptons from W decays are typically isolated anyway. The cuts, which will be applied in all cases, are  $p_T(\mu_1^\pm) > 20 \text{ GeV}/c$  and  $p_T(\mu_2^\pm) > 10 \text{ GeV}/c$ ,  $|\eta(\mu^\pm)| < 2$  for both muons,  $m(\mu^+, \mu^-) < 80 \text{ GeV}/c^2$ ,  $p_T(\mu^+ + \mu^-) > 20 \text{ GeV}/c$ , and  $\Delta\phi(\mu^+, \mu^-) < 2.4 \text{ rad}$ .

The following naming conventions are used:  $\mu_1$  is the muon with the highest  $p_T$  in the event,  $\mu_2$  is the muon with the second highest  $p_T$ ,  $W_1$  is the W boson that decays to  $\mu_1$ , and  $W_2$  is the W boson that decays to  $\mu_2$ . Kinematic distributions for W boson pairs and muon pairs are compared in the following in case the events have passed the selection described above. The distributions of W pairs are not accessible experimentally, but important to understand some event properties. All distributions are normalized to unit area in order to be able to compare the shapes of the distributions more easily.

### 15.42 Results and discussion

In the following, various kinematic properties of W pair events are compared for the different event generators in the first part. The  $\Delta\phi(\mu^+, \mu^-)$  distribution, which turns out to be the most sensitive observable, is discussed in more detail in the second and the third part.

**Comparison of Generators** In order to get an idea about the importance of HO corrections and spin correlations, six typical distributions of W pair production are compared in Fig. 80. Both effects are clearly visible, when MC@NLO and PYTHIA are compared with spin correlations switched “on” and “off” in both cases. There is also difference possible due to the different underlying events of MC@NLO (HERWIG) and PYTHIA. This difference is expected to disappear, after both event generators have been tuned consistently to LHC data. Recently, the soft gluons have been resummed up to NNLL for W pair production at NLO in Ref. [302], summarized in section 15.1. The result is in good agreement with the prediction of MC@NLO. The approximation of generating W pairs in a  $2 \rightarrow 2$  process and then

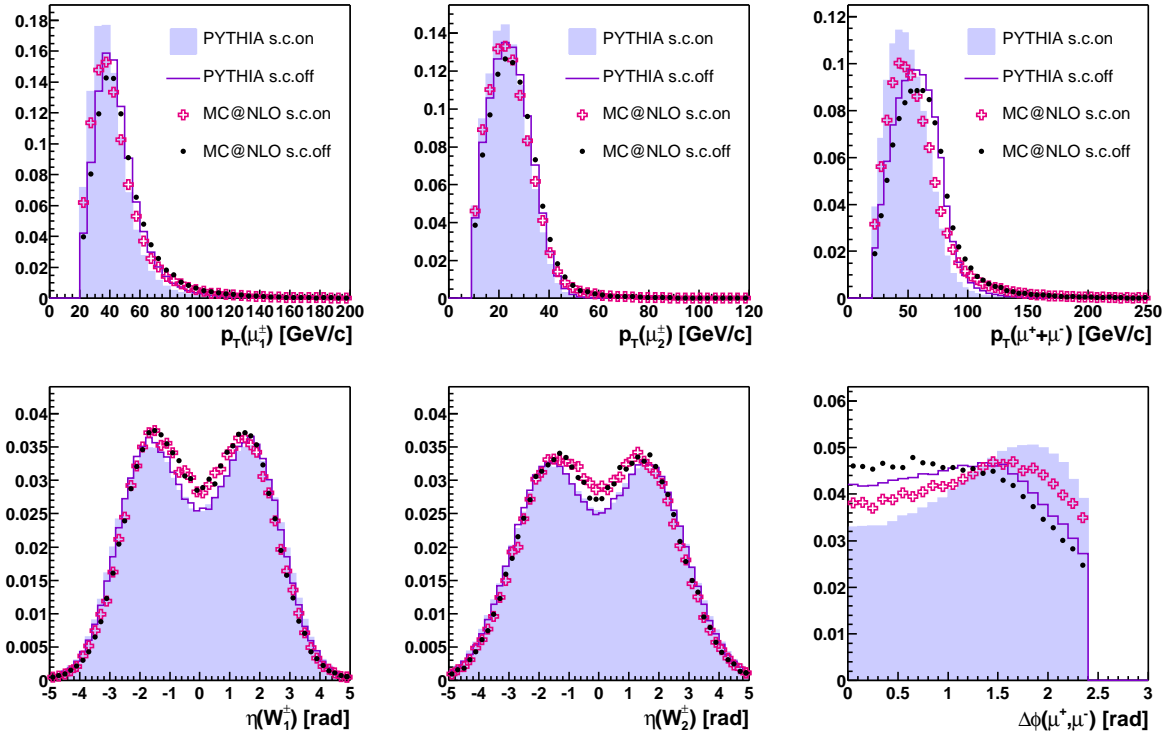


Fig. 80: Comparison of W boson and muon distributions: there is a clear difference visible between the simulation of the hard process at LO and NLO. The effect of spin correlations (labelled “s.c.”) plays an important role, too, at LO and at NLO.

performing the W decays in an separate step has no visible effect on the kinematic distributions, when PYTHIA is compared with CompHEP which computes the full  $2 \rightarrow 4$  matrix element. Even the fact that contributions from Feynman diagrams with only one W boson are not present in case of PYTHIA does not lead to recognizable differences, because the contribution from processes with only one W boson is strongly suppressed.

In this study, no emphasis is placed on the comparison of the cross sections which are summarized in Table 15 before and after the event selection. The selection efficiencies give an idea about the quantitative differences of the various simulations. These differences should not be understood as the uncertainty of the W pair production process, because it becomes clear that a proper choice of the event generator, in this case MC@NLO (with spin correlations), can describe all important features with a better accuracy than the differences between the scenarios investigated.

Table 15: Cross sections and selection efficiencies for the scenarios considered.

program and setup	total $\sigma \times \text{BR}$	$\sigma \times \text{BR}$ after selection	selection efficiency
PYTHIA: spin correlations “on”	828 fb	122 fb	14.7%
PYTHIA: spin correlations “off”	828 fb	137 fb	16.5%
CompHEP: $q\bar{q} \rightarrow WW \rightarrow 2\mu 2\nu$	900 fb	127 fb	14.1%
CompHEP: $q\bar{q} \rightarrow W_{\mu\nu} \rightarrow 2\mu 2\nu$	900 fb	127 fb	14.1%
MC@NLO: spin correlations “on”	1287 fb	206 fb	16.0%
MC@NLO: spin correlations “off”	1287 fb	212 fb	16.5%
GG2WW: six quarks, Ws off shell	60 fb	19 fb	31.4%

**Theoretical Uncertainties at NLO** Once all features are included in an event generator - in this case MC@NLO - the shape of  $\Delta\phi(\mu^+, \mu^-)$  is still not perfectly known. There are two theoretical uncertainties than can be potentially large in this particular example. In order to study the PDF uncertainty, each PDF parameter is varied independently by one standard deviation. In case of the structure function MRS, this leads to thirty error PDFs. The  $\Delta\phi(\mu^+, \mu^-)$  shape variation, shown in Fig. 81 (left), turns out to be small.

In order to study the uncertainties due to higher order corrections, often the scale dependence of the renormalization scale  $\mu_r$  and factorization scale  $\mu_f$  are varied independently by a factor of two in both directions, which results in nine different scales including the nominal scale. The shape of the  $\Delta\phi(\mu^+, \mu^-)$  distribution of MC@NLO is stable against the variation of the scales as shown in Fig. 81 (right). But this is not only the case at NLO. The shape variation is similar at LO, even though both shapes are different. What is the reason for this discrepancy? Whereas initial states at LO is always  $q\bar{q}$ , the possible initial states at NLO are  $q\bar{q}$ ,  $qg$  and  $g\bar{q}$ . The events with gluons in the initial state have different spin properties which are visible in the  $\Delta\phi(\mu^+, \mu^-)$  distribution. A cross check for this hypothesis is also shown in Fig. 81 (right), where the NLO events with  $q\bar{q}$  initial state are shown separately. This shape is remarkably close<sup>33</sup> to the shape at LO. In conclusion, the new partonic process coming in at NLO is not reflected by the scale variations, which means that the method of changing the scales does not work in this particular case. In order to study the scale uncertainties in a reliable way, all partonic sub-processes have to be taken into account, which means that in case of W pair production the contribution from the  $gg$  initial state has to be added.

**Contribution from  $gg \rightarrow W^+W^-$**  Compared to the process  $q\bar{q} \rightarrow W^+W^-$  the cross section for  $gg \rightarrow W^+W^-$  is more than an order of magnitude smaller. On the other hand, the latter process has a higher selection efficiency, as shown in Table 15, and becomes more important after cuts relative to  $q\bar{q} \rightarrow W^+W^-$ . In Fig. 82 (left) the shape of  $gg \rightarrow W^+W^- \rightarrow \mu^+\nu\mu^-\bar{\nu}$  events is compared with the corresponding distribution from MC@NLO. There is a clear difference visible, which means that the addition of the  $gg \rightarrow W^+W^-$  contribution changes the shape of the sum of all partonic sub-processes.

In order to get the whole picture the  $gg \rightarrow W^+W^-$  events are added to the events, generated with MC@NLO, taking into account the different cross sections after cuts. Three scaling factors for  $gg \rightarrow W^+W^-$  are shown in Fig. 82 (right), namely  $k_{gg \rightarrow W^+W^-} = 0, 1, 2$ . The largest deviation from the nominal ( $k_{gg \rightarrow W^+W^-} = 1$ ) shape is the shape without contribution from  $gg \rightarrow W^+W^-$ . In order to get a feeling for the uncertainty due to the missing NLO corrections for  $gg \rightarrow W^+W^-$ , this sub-process is multiplied with a factor of two, which is roughly the k-factor of  $gg \rightarrow h$ , another process with two gluons in the initial state. In a comparable case,  $gg \rightarrow \gamma\gamma$  at NLO [318], the k-factor turns out to be even lower than two. The change of the shape of the  $\Delta\phi(\mu^+, \mu^-)$  distribution due to the  $gg \rightarrow W^+W^-$

<sup>33</sup>There is a difference visible which is due to the different underlying events, and the somewhat different  $p_T$  spectra of the  $W^+W^-$  system, respectively.



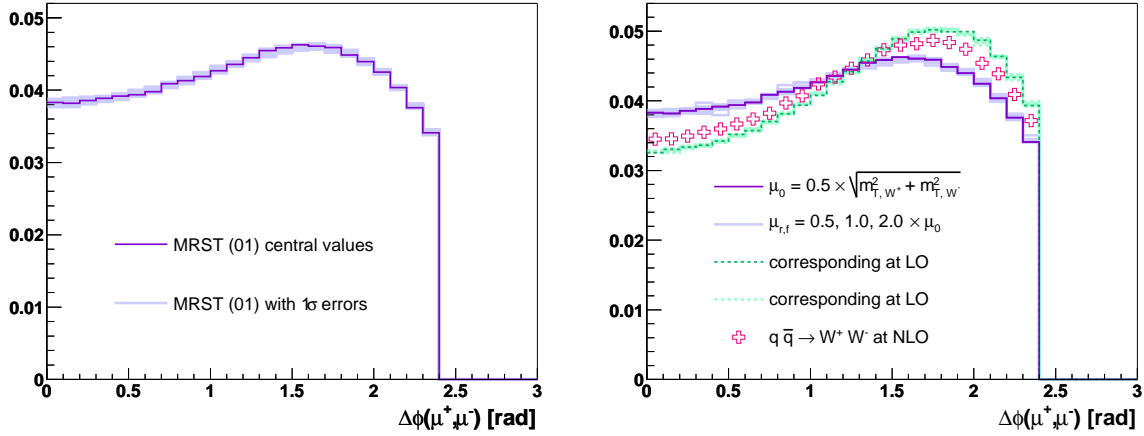


Fig. 81: Left: PDF uncertainties with MC@NLO: shown are the nominal MRST structure functions with one set of nominal parameters and with 30 sets of parameters where one parameter is varied by one standard deviation at a time. Right: Scale uncertainties with MC@NLO: the scales  $\mu_r$  and  $\mu_f$  are varied independently by factors of two with respect to the nominal scale  $\mu_0$ . The scale dependence at LO is studied correspondingly with PYTHIA, which yields shapes close to  $q\bar{q} \rightarrow W^+W^-$  at NLO. Note that there are small statistical fluctuations which contribute to the width of the error bands, too.

contribution is small for this particular selection, but it has to be kept in mind that the fraction of this sub-process can be enhanced further with additional cuts.

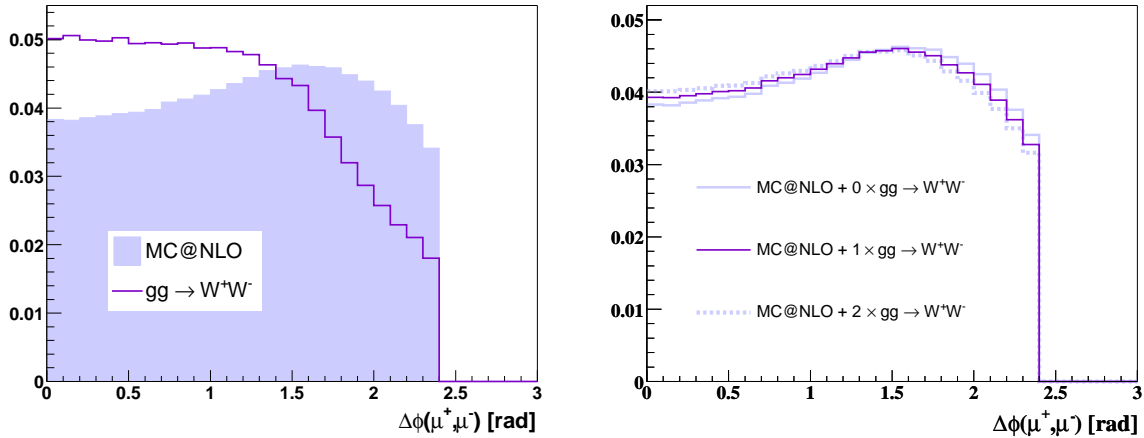


Fig. 82: Left: Shape comparison of  $gg \rightarrow W^+W^-$  (GG2WW) events with MC@NLO, which includes the partonic sub-processes  $q\bar{q} \rightarrow W^+W^-$ ,  $qg \rightarrow W^+W^-$  and  $\bar{q}g \rightarrow W^+W^-$ . Right:  $pp \rightarrow W^+W^-$  with all partonic sub-processes. Three scenarios for the partonic sub-process  $gg \rightarrow W^+W^-$  are assumed: zero times the nominal LO cross section, one times the nominal LO cross section, and two times the nominal LO cross section.

#### 15.43 Analyzing the transverse Mass Distribution of W Pairs

Besides the transverse opening angle  $\Delta\phi(\ell^+, \ell^-)$  also the distribution of the pseudorapidity of the sum of the two leptons  $\eta(\ell^+ + \ell^-)$  and the transverse mass  $M_T$  promise some discrimination power between a Higgs boson signal and the  $W^+W^-$  background (The invariant mass  $m(\ell^+ + \ell^-)$  of the two leptons is strongly correlated to  $\Delta\phi(\ell^+, \ell^-)$  and not used here). For simplicity only relaxed pre-selection cuts are applied: two leptons ( $e^\pm$  or  $\mu^\pm$ ) with

- $p_T(\ell_1^\pm) > 20 \text{ GeV}/c$  and  $p_T(\ell_2^\pm) > 10 \text{ GeV}/c$

- $|\eta(\ell^\pm)| < 2.5$
- $p_T^{\text{miss}} = p_T(\nu_1 + \nu_2) > 20 \text{ GeV}/c$ .

The usual definition of the transverse mass is  $M_T = \sqrt{2 \cdot p_T(\ell^+ + \ell^-) \cdot p_T^{\text{miss}} \cdot (1 - \cos \phi_T)}$  for the  $h \rightarrow W^+W^-$  analysis, where  $\phi_T$  is the transverse opening angle between the vector sum of the two leptons and  $p_T^{\text{miss}}$ . This definition works best if the two leptons are almost collinear. For increasing opening angle between the leptons,  $M_T$  decreases since both  $p_T(\ell^+ + \ell^-)$  and  $p_T^{\text{miss}}$  get smaller. To compensate for this the definition  $M'_T = \sqrt{M_T^2 + m^2(\ell^+ + \ell^-)}$  is used rather than  $M_T$ .

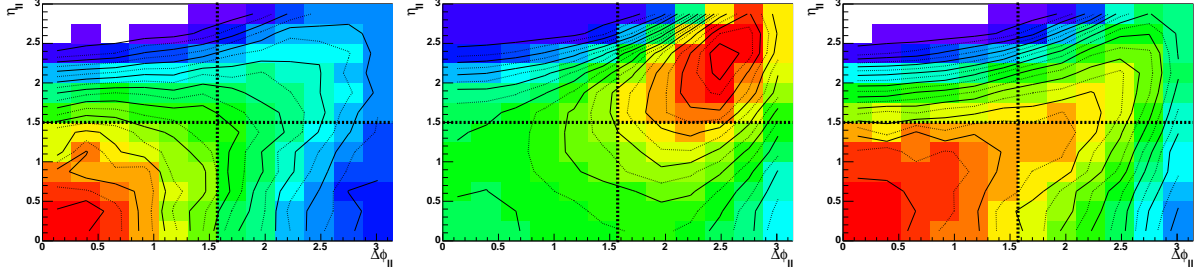


Fig. 83: Event distribution for  $W^+W^- \rightarrow \ell^+\nu\ell^-\bar{\nu}$  in the plane of  $\eta_u = \eta(\ell^+ + \ell^-)$  and  $\Delta\phi_u = \Delta\phi(\ell^+, \ell^-)$ . For the normalization of the  $M'_T$  shape the plane is split into four regions at  $\eta(\ell^+ + \ell^-) = 1.5$  and  $\Delta\phi(\ell^+, \ell^-) = \frac{\pi}{2}$ .

Left:  $gg \rightarrow h \rightarrow W^+W^-$  (MC@NLO). Center:  $q\bar{q} \rightarrow W^+W^-$  (MC@NLO). Right:  $gg \rightarrow W^+W^-$  (GG2WW).

**Defining signal and normalization regions** In Fig. 83 the distribution of events in the plane of  $\eta(\ell^+ + \ell^-)$  vs.  $\Delta\phi(\ell^+, \ell^-)$  is shown for a Higgs boson of 170 GeV (left),  $q\bar{q} \rightarrow W^+W^-$  (center) and  $gg \rightarrow W^+W^-$  (right). A potential Higgs boson signal would appear dominantly in the signal region  $\eta(\ell^+ + \ell^-) < 1.5$  and  $\Delta\phi(\ell^+, \ell^-) < \frac{\pi}{2}$  (very similar to  $gg \rightarrow W^+W^-$ ). On the other hand the dominant  $q\bar{q} \rightarrow W^+W^-$  background is found in the normalization regions  $\eta(\ell^+ + \ell^-) > 1.5$  or  $\Delta\phi(\ell^+, \ell^-) > \frac{\pi}{2}$ .

The aim is to normalize the shape of  $M'_T$  for  $q\bar{q} \rightarrow W^+W^-$  in the signal region using the shape of  $M'_T$  in the normalization region. Such a shape normalization to data has the advantage that experimental uncertainties that enter  $M_T$  due to the missing transverse momentum can be reduced in the ratio.

For a systematic comparison of the  $M'_T$  shapes the  $\eta(\ell^+ + \ell^-)$  vs.  $\Delta\phi(\ell^+, \ell^-)$  plane is split into four regions at  $\eta(\ell^+ + \ell^-) = 1.5$  and  $\Delta\phi(\ell^+, \ell^-) = \pi/2$ .

**Normalizing the  $M'_T$  shape for  $q\bar{q} \rightarrow W^+W^-$**  The shape of  $M'_T$  for  $q\bar{q} \rightarrow W^+W^-$  and  $gg \rightarrow W^+W^-$  is shown in Fig. 84 for each region of Fig. 83 (histograms normalized to unity). For additional comparison the shape of  $M'_T$  in the signal region is shown for Higgs boson events. Also in this shape  $gg \rightarrow W^+W^-$  is very similar to a Higgs boson with a mass close to 170 GeV.

In Fig. 85 the ratio of the  $M'_T$  shape in the signal region and the  $M'_T$  shape in the normalization regions is shown for MC@NLO. The colored error band gives the systematic uncertainty on the shape of MC@NLO from scale and PDF variations. The QCD factorization and renormalization scale inside MC@NLO is varied independently within factors of 2. PDF uncertainties are evaluated by scanning through the CTEQ6 [47] error PDFs. The width of the error band is actually consistent with the statistical fluctuations expected from the independent Monte Carlo samples and therefore gives an upper limit on the systematic uncertainty on the ratio. The ratio given by PYTHIA [27] and HERWIG [319] shows a slight shift to smaller values of  $M'_T$  (the main reason is the missing  $gq$  and  $qg$  initial state as shown in section 15.42). In the relevant mass range of  $100 \text{ GeV} < M'_T < 200 \text{ GeV}$  a systematic uncertainty of less than 10% on these ratios can be expected (not including experimental uncertainties from  $p_T^{\text{miss}}$ ).

The most promising way of normalizing the  $M'_T$  shape in the signal region is from the normalization region  $\eta(\ell^+ + \ell^-) > 1.5$  and  $\Delta\phi(\ell^+, \ell^-) < 1.5$  (Fig. 85 left), which has the same  $\Delta\phi(\ell^+, \ell^-)$

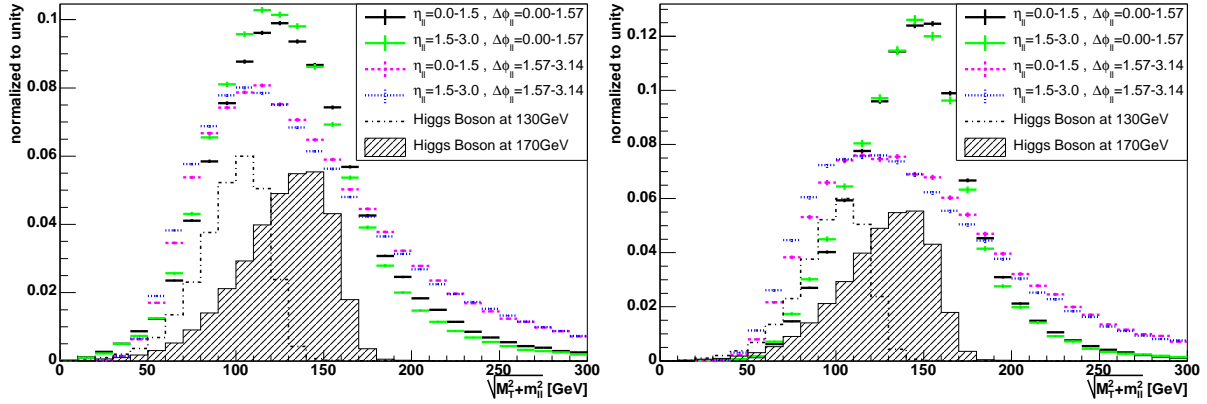


Fig. 84: Distribution of  $M'_T$  for  $q\bar{q} \rightarrow W^+W^-$  (left) and  $g\bar{g} \rightarrow W^+W^-$  (right) in four different regions of the  $\eta(\ell^+ + \ell^-)$  vs.  $\Delta\phi(\ell^+, \ell^-)$  plane of Fig. 83 (normalized to unity). The error bars give the Monte Carlo statistical error on the points. For comparison the dashed-dotted and the hashed histogram give the shape of  $h \rightarrow W^+W^-$  events in the signal region ( $\eta(\ell^+ + \ell^-) < 1.5$ ,  $\Delta\phi(\ell^+, \ell^-) < \frac{\pi}{2}$ ), arbitrary normalization).

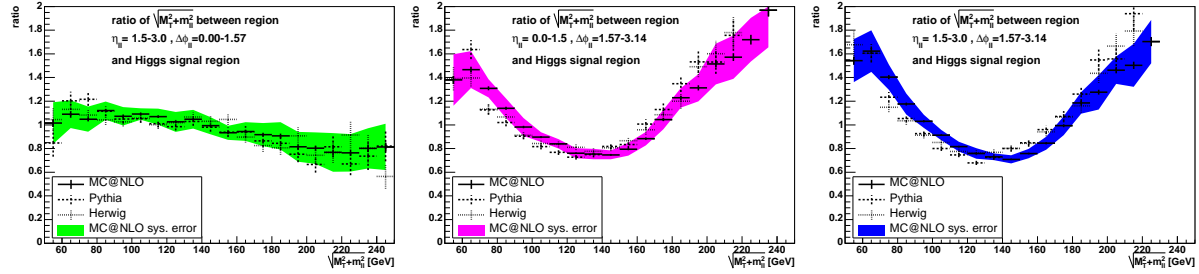


Fig. 85: Ratio between the  $M'_T$  distribution in the three normalization regions and the signal region for MC@NLO. The error bars give the Monte Carlo statistical error on the shape. The colored error band gives an upper limit on the systematic uncertainty on this shape from QCD factorization and renormalization scale variation (each within a factor 2) and one sigma error PDF variation. The width of this error band is dominated by statistical fluctuations, the true uncertainty should be much smaller. For comparison also the leading order shape from PYTHIA and HERWIG is shown.

distribution as the signal region. Since the ratio is relatively flat, systematic shifts in  $M'_T$  are uncritical. However, this region suffers from low experimental event statistics and has already some Higgs boson signal contribution as can be seen in Fig. 83.

The normalization regions with  $\Delta\phi(\ell^+, \ell^-) > \frac{\pi}{2}$  should be cleanly measurable, but the ratio to the signal region is not flat and systematic uncertainties on  $p_T^{\text{miss}}$  might affect the ratio (this needs further experimental studies).

Once the  $M'_T$  shape of the background is measured, one could go beyond number counting in the signal region and use the information contained in the  $M'_T$  distribution. One could follow two approaches: By using  $\Delta\phi(\ell^+, \ell^-)$  to normalize the  $W^+W^-$  background one could subtract the extrapolated  $M'_T$  shape in the signal region and look for the Jacobian Higgs peak. Alternatively one could use the extrapolated  $M'_T$  shape to normalize the  $W^+W^-$  background directly by using the sideband  $M'_T > 200$  GeV. This would be an independent method of normalizing the background directly in the Higgs boson signal region.

Using both methods it should also be possible to measure the Higgs boson mass from the position of the Jacobian peak. Without any background determination from data, this might prove difficult, since the peak of the background and the peak of the signal are very close together.

The shape of the ratios in Fig. 85 is very similar for  $g\bar{g} \rightarrow W^+W^-$  and also for  $t\bar{t}$ , which contributes as additional background to  $h \rightarrow W^+W^-$  searches. This reduces the dependency of the

extrapolation on the relative normalization of the various backgrounds.

#### 15.44 Conclusions

The modeling of  $W$  pair production at the LHC has been investigated by comparing several event generators with different features. MC@NLO turns out to be the most reliable program available. The prediction of  $pp \rightarrow W^+W^-$  is improved further by combining  $gg \rightarrow W^+W^-$  events with the events from MC@NLO. More results and details can be found in Ref. [320].

After the event selection, which is borrowed from the  $h \rightarrow W^+W^-$  analysis, the shape of the  $\Delta\phi$  distribution can be used to extrapolate the number of  $W$  pair events from the background control region ( $1.4 \text{ rad} < \Delta\phi < 2.4 \text{ rad}$ ) into the Higgs signal region ( $\Delta\phi < 0.8 \text{ rad}$ ). For this particular example the theoretical uncertainties of the  $\Delta\phi$  shape are  $\delta_{\text{PDF}} < 0.7\%$  for the PDF uncertainty of MC@NLO,  $\delta_{\text{scale}} < 2.0\%$  for the scale uncertainty of MC@NLO, and  $\delta_{gg \rightarrow W^+W^-} \approx 3.8\%$  for the uncertainty of the  $gg \rightarrow W^+W^-$  contribution. For comparison, ignoring either the spin correlations or the higher order corrections would lead to uncertainties of the order of 30%.

By measuring the distribution of the transverse mass  $M'_T$  at large  $\Delta\phi(\ell^+, \ell^-)$  or  $\eta(\ell^+ + \ell^-)$  an extrapolation to the transverse mass distribution into the Higgs boson signal region seems feasible. The theoretical uncertainty on this extrapolation estimated from PDF and scale uncertainties of MC@NLO is less than 10%. Using this extrapolation an independent normalisation of  $W^+W^-$  and an observation of the Jacobian Higgs boson peak should be possible.

#### Acknowledgements

Special thanks to Stefano Frixione for including the important spin correlations in MC@NLO, and many thanks to Alexandre Sherstnev for the nice introduction to the use of CompHEP and to Edward Boos for giving further details. Many thanks to Massimiliano Grazzini for his very useful comments about higher order uncertainties. Work supported in part by the European Community's Human Potential Programme under contract HPRN-CT-2002-00326, [V.D.].

## 16. TOP BACKGROUND GENERATION FOR THE $H \rightarrow WW$ CHANNEL <sup>34</sup>

### 16.1 Introduction

The  $t\bar{t}$  production is known as an important background for many processes at the LHC. Large uncertainties can be expected from the different Monte Carlo simulations. We will study the  $t\bar{t}$  background in the phase space specific for the SM Higgs channel  $H \rightarrow WW \rightarrow \ell\nu\ell\nu$  by comparing four different Monte Carlo event generators: HERWIG [319], MC@NLO [308, 309], PYTHIA [27] and TopReX [321].

The Higgs decay into two  $W$  bosons and subsequently into two charged leptons is expected to be the main discovery channel for intermediate Higgs mass, between  $2m_W$  and  $2m_Z$  [296]. The signature of this decay is characterized by two leptons and high missing transverse energy. However, since no narrow mass peak can be reconstructed, a good control of the background, together with a high signal to background ratio, is needed. The most important backgrounds, which give similar signature as the signal (i.e. two leptons and missing energy), are the continuum  $WW$  production and the  $t\bar{t}$  production. In order to separate the signal from the backgrounds, one has to require a small opening angle between the leptons in the plane transverse to the beam against the continuum  $WW$  production and apply a jet veto against  $t\bar{t}$  production. This implies a restriction to a very specific region of the phase space.

First, we estimate how well Leading Order (LO) Monte Carlos generate top production in the phase space relevant for Higgs search with respect to NLO Monte Carlos by comparing MC@NLO with HERWIG. Then by comparing PYTHIA and HERWIG we determine the effect of using different parton shower

<sup>34</sup>Contributed by: G. Davatz, A.-S. Giolo-Nicollerat, M. Zanetti

models. Finally, we estimate the effect of spin correlations between the  $t$  and the  $\bar{t}$ . More details about this study can be found in Ref. [322].

## 16.2 Generating top background

For each Monte Carlo program, one million  $pp \rightarrow t\bar{t} \rightarrow WbWb \rightarrow \ell\nu\ell\nu b\bar{b}$  events are generated ( $\ell = e, \mu$  and  $\tau$ ). The PDF chosen for HERWIG, PYTHIA and TopReX is CTEQ5L and for MC@NLO CTEQ5M1. No underlying event is generated. The top mass is set to 175 GeV. The events are reconstructed using stable detectable particles. First, a pre-selection requires two isolated opposite charged leptons with  $p_t > 20$  GeV and  $|\eta| < 2$ , cuts which can easily be satisfied by CMS and ATLAS. This pre-selection is always applied in the following. The final selection requires:

- rejecting all events including a jet<sup>35</sup> with  $p_t$  higher than 30 GeV and  $|\eta| < 2.5$  (jet veto)
- $E_t^{\text{miss}} > 40$  GeV ( $E_t^{\text{miss}}$  is formed with the sum of isolated leptons and jets transverse momenta)
- $\phi_{\ell\ell} < 45^\circ$  (angle between the leptons in the transverse plane)
- $5 \text{ GeV} < m_{\ell\ell} < 40$  GeV (the invariant mass of the two leptons)
- $30 \text{ GeV} < p_{t \text{ lep max}} < 55$  GeV (lepton with the maximal  $p_t$ )
- $p_{t \text{ lep min}} > 25$  GeV (lepton with the minimal  $p_t$ )

## 16.3 Comparison between HERWIG and MC@NLO

To estimate the effect of an accurate inclusion of NLO matrix elements, HERWIG 6.508 and MC@NLO 2.31 were compared<sup>36</sup>. The spin correlations between  $t$  and  $\bar{t}$  are not included in MC@NLO. HERWIG events were therefore also simulated without these spin correlations. As the same showering model is used, the difference between the two simulations should be mostly due to the additional NLO matrix elements in MC@NLO.

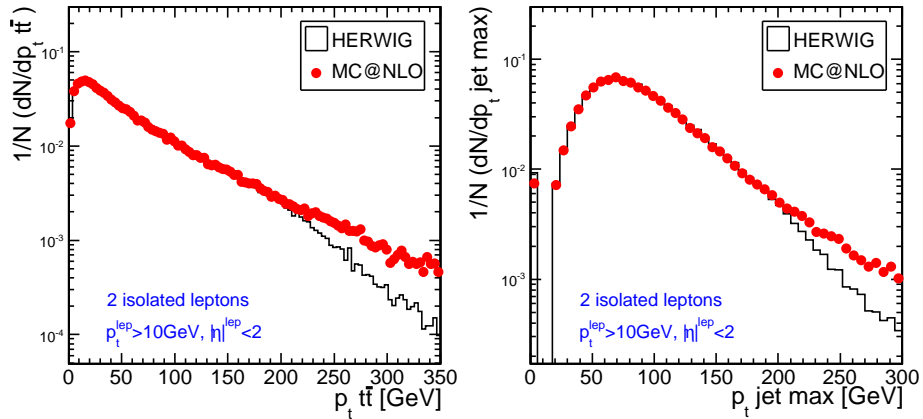


Fig. 86: The  $p_t$  distribution of the  $t\bar{t}$  system (left) and the leading jet (right) in HERWIG and MC@NLO.

Figure 86 (left) shows the transverse momentum of the  $t\bar{t}$  system for HERWIG and MC@NLO. At low  $p_t$ , the two Monte Carlos are very similar, as the soft and collinear emissions are generated by HERWIG in both simulations. The  $t\bar{t}$  system is balanced by gluon emissions from the initial state radiation. MC@NLO produces in addition to the hard process up to one hard jet accurate to NLO. Therefore,

<sup>35</sup>The jets are reconstructed using an iterative cone algorithm with a cone size,  $\Delta R$ , of 0.5. A jet is kept if its  $p_t$  is higher than 20 GeV and  $|\eta| < 4.5$ .

<sup>36</sup>HERWIG 6.508 was also used for the showering step in MC@NLO. HERWIG 6.508 is an update of the HERWIG 6.507 version with a bug fixed concerning the top decay.

the high  $p_t$  region of the  $t\bar{t}$  system is harder in MC@NLO.

In Fig. 86 (right), the  $p_t$  of the hardest jet is shown, taking into account all jets in the final state (from the hard process and from the gluon emission).  $p_{t \text{ jet max}}$  equal to zero means that there is no reconstructed jet with  $p_t$  higher than 20 GeV and  $|\eta| < 4.5$  in the event. In the high  $p_t$  region the leading jet is harder in MC@NLO, but again at low  $p_t$ , the two simulations are very similar. The region relevant for the  $H \rightarrow WW \rightarrow \ell\nu\ell\nu$  signal selection is the very low  $p_t$  region, where HERWIG and MC@NLO agree very well. In addition, the shapes of all the other cut variables are very similar in MC@NLO and HERWIG without spin correlations. After comparing the relative efficiencies of the different cuts, the differences between the two Monte Carlos are essentially due to the jet veto cut and smaller than 10%. Since there are already two b-jets in the  $t\bar{t}$  final state, the jet veto tends to be less sensitive to additional jet activity. From this comparison one can conclude that implementing accurately the NLO contribution in the simulation has a small effect on the shapes of the variables considered and the selection efficiencies for the phase space relevant for the  $H \rightarrow WW$  search. The region where NLO makes a difference is at very high  $p_t$ , whereas the bulk of the selected events is in the low  $p_t$  region.

#### 16.4 Effect of showering models, differences between HERWIG and PYTHIA

In the following, we study how different showering models influence the variable shapes and selection efficiencies. For this, PYTHIA 6.325, based on the Lund hadronization model, was compared with HERWIG without spin correlations, based on the cluster model for hadronization. Furthermore, we simulate two PYTHIA samples, one with the default  $Q^2$ -ordered parton shower model (so-called 'old showering') and one with the  $p_t$ -ordered parton showering model (so-called 'new showering'). For all three simulations, default scales are chosen.

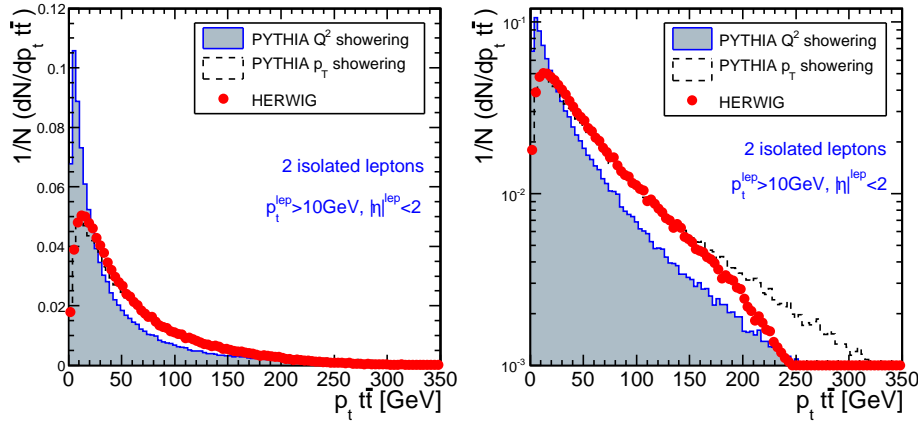


Fig. 87: The  $p_t$  spectrum of the  $t\bar{t}$  system in HERWIG, PYTHIA new ( $p_t$ -ordered) and old ( $Q^2$ -ordered) showering.

In Fig. 87, the  $p_t$  spectrum of the  $t\bar{t}$  system is shown. The PYTHIA old showering tends to produce a much softer spectrum than HERWIG and the PYTHIA new showering model. The  $p_t$  spectrum of the  $t\bar{t}$  system in HERWIG and the new showering model in PYTHIA agree very well, except in the high  $p_t$  region, which is due to the fact that HERWIG applies no matrix element corrections at all.

Figure 88 shows the  $p_t$  spectrum of the hardest jet for PYTHIA and HERWIG. The leading jets in the new showering program are harder than in the old one. As the jets are harder, the number of jets increase with respect to the old showering model, as can be seen in Fig. 89. If one compares the other cut variables, the old showering model in PYTHIA and HERWIG agree well, whereas the new showering model in PYTHIA produces softer leptons, as shown in Fig. 89. Comparing the relative efficiencies after the selection cuts were applied, the biggest differences come from the jet veto and the lepton isolation cut



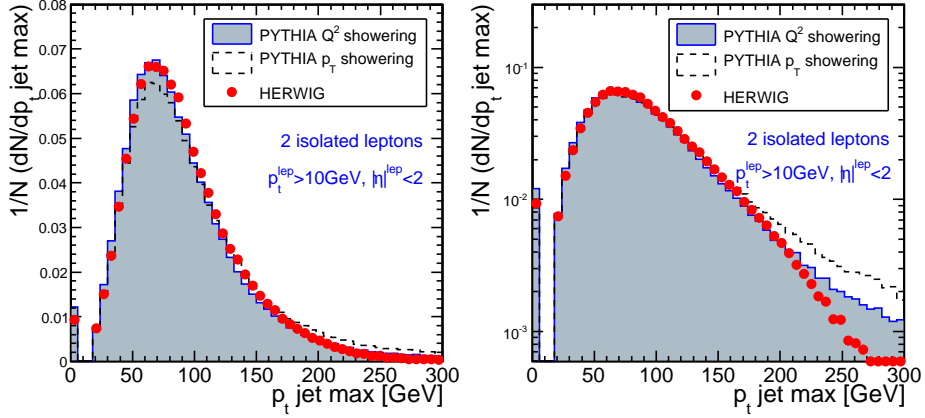


Fig. 88: The  $p_t$  spectrum of the leading jet in HERWIG, PYTHIA new ( $p_t$ -ordered) and old ( $Q^2$ -ordered) showering.

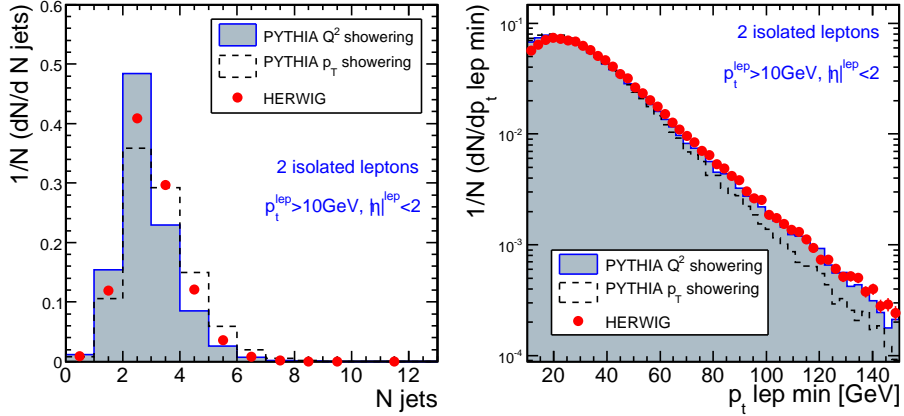


Fig. 89: The number of jets (left) and the  $p_t$  distribution of the softest lepton (right) in HERWIG, PYTHIA new ( $p_t$ -ordered) and old ( $Q^2$ -ordered) showering.

efficiencies. While PYTHIA with the old showering model and HERWIG have about the same isolation efficiency, PYTHIA with the new showering model has a 20% lower efficiency for the isolation of the leptons. This is due to the fact that particles from the new shower have on average higher  $p_t$  than the ones from the old shower, making the leptons less isolated.

The jet veto efficiencies from HERWIG and the new showering model in PYTHIA are very similar, whereas the veto is less effective in the old showering model due to the fact that the jets are softer and therefore more events pass the jet veto. This leads to a difference in the jet veto efficiency of about 20%. In order to get lower uncertainties from the use of different Monte Carlos, it will be very important to tune the Monte Carlos with data.

### 16.5 Effect of the spin correlations

In the  $H \rightarrow WW$  Higgs search, a cut has to be applied on the opening angle between the leptons in the transverse plane ( $\phi_{\ell\ell}$ ) in order to differentiate the signal from continuum  $WW$  background. The variable  $\phi_{\ell\ell}$ , as much as the mass of the di-lepton system  $m_{\ell\ell}$ , are sensitive to spin correlations. In the following, the influence of the inclusion of spin correlations in the  $t\bar{t}$  process is studied. PYTHIA does not include the spin correlation between  $t$  and  $\bar{t}$ . Thus we use TopReX with and without spin correlations,

interfaced to PYTHIA for the showering step<sup>37</sup>. Figure 90 shows the angle  $\phi_{\ell\ell}$  between the leptons for the simulations with and without spin correlations. On the left, the only requirements are two isolated leptons with  $p_t > 10$  GeV and  $|\eta| < 2$ . On the right, a jet veto is applied in addition. As  $\phi_{\ell\ell}$  and  $m_{\ell\ell}$  are correlated, we only show the  $\phi_{\ell\ell}$  distribution. PYTHIA and TopReX without spin correlations show the same  $\phi_{\ell\ell}$  distribution. Including spin correlations leads to a flatter  $\phi_{\ell\ell}$  distribution. The same is studied with HERWIG with spin correlations, compared to HERWIG and MC@NLO without spin correlations. The difference due to the inclusion of spin correlations is slightly bigger in the comparison of TopReX and PYTHIA. Again, HERWIG without spin correlations has the same  $\phi_{\ell\ell}$  distribution as MC@NLO. After a jet veto is applied, the distributions with and without spin correlations look more similar in both cases.

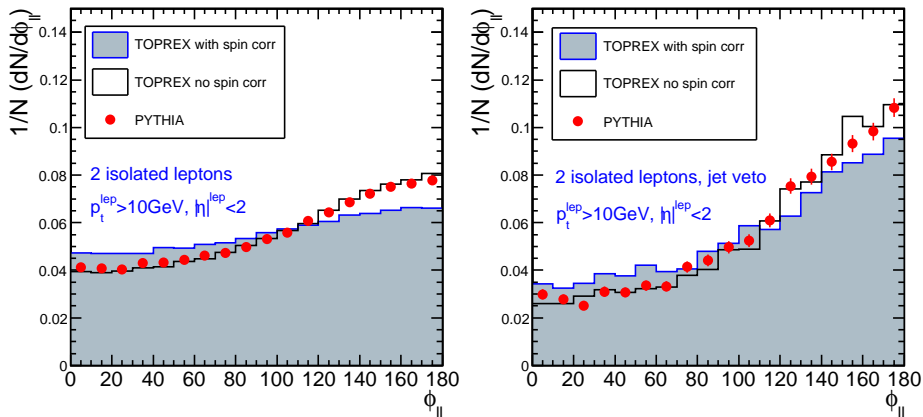


Fig. 90:  $\phi_{\ell\ell}$  is the angle between the leptons in the plane transverse to the beam. TopReX with and without spin correlations is shown, as well as PYTHIA. On the left, only very basic cuts are applied, whereas on the right a jet veto is applied in addition. The region important for the Higgs signal search is the low  $\phi_{\ell\ell}$  region.

The difference of the relative efficiencies with and without spin correlations in HERWIG is about 10% and the same difference can be observed in TopReX. However, the relative efficiency for the  $\phi_{\ell\ell}$  cut in TopReX is slightly higher than in HERWIG.

In conclusion, the following approach could be used to generate the  $t\bar{t}$  background: since the difference between MC@NLO and HERWIG without spin correlations is rather small in our region of interest, HERWIG with spin correlations could be used, re-weighted to the NLO cross section with an inclusive K-factor.

The new showering model of PYTHIA predicts similar shapes for the jets and the  $t\bar{t}$  system as HERWIG, but the isolation of the leptons leads to a difference of about 20% and the other lepton variables are softer. On the other hand, the old showering model of PYTHIA is more similar to HERWIG in the lepton isolation and the lepton variable shapes, but has much softer jets. This needs to be studied further.

When data is available, these uncertainties can be reduced by tuning the different Monte Carlos to data. In any case, it will be important to estimate the  $t\bar{t}$  background contribution for the Higgs search using data by defining normalization regions.

## Acknowledgements

We would like to thank Gennaro Corcella, Torbjörn Sjöstrand, Peter Richardson and Stefano Frixione for the useful discussions and help on the topic.

<sup>37</sup>The difference between PYTHIA and TopReX without spin correlation is mostly due to the fact that the top quarks are not allowed to radiate gluons in TopReX, and the different treatment of  $m_{top}$ . For this comparison, the old showering model is chosen in PYTHIA.

## 17. ESTIMATION OF $t\bar{t}$ BACKGROUND FOR $H \rightarrow WW$ CHANNEL <sup>38</sup>

### 17.1 $t\bar{t}$ normalization from data

The presence of two neutrinos in the final state of the  $H \rightarrow W^+W^- \rightarrow \ell^+\nu\ell^-\bar{\nu}$  decay chain does not allow the reconstruction of a narrow invariant mass peak. Moreover, the rejection needed to reduce the different background processes is very high, in the specific case of  $t\bar{t}$  being  $\mathcal{O}(10^{-5})$ . The precise understanding of the backgrounds is the most critical issue concerning this Higgs discovery channel. The most reliable approach to address this problem is to measure the different sources of background directly from the data. The commonly used method consists on selecting a signal-free phase space region (control region), where a given background process is enhanced. The contribution of that background in the signal region is then extrapolated from the control region taking into account the observed amount of events. This procedure relies on the relation:

$$N_{signal\_reg} = \frac{N_{signal\_reg}^{MonteCarlo}}{N_{control\_reg}^{MonteCarlo}} N_{control\_reg} = \frac{\sigma_{signal\_reg} \cdot \epsilon_{signal\_reg}}{\sigma_{control\_reg} \cdot \epsilon_{control\_reg}} N_{control\_reg} \quad (65)$$

where  $N_{signal\_reg}^{MonteCarlo}$  and  $N_{control\_reg}^{MonteCarlo}$  are the numbers of events predicted by the Monte Carlo simulation in the signal and control region. Each of this two numbers can be expressed as a product of the theoretical cross section in that phase space area,  $\sigma_{signal\_reg, control\_reg}$ , and the experimental efficiency of reconstructing events in the same region,  $\epsilon_{signal\_reg, control\_reg}$ <sup>39</sup>. This will allow to better point out the different sources of systematic uncertainties. In particular the theoretical predictions enter the procedure only via the ratio  $\sigma_{signal\_reg}/\sigma_{control\_reg}$ , leading to a much smaller scale dependency and thus to smaller theoretical uncertainties.

The theoretical issues concerning the  $t\bar{t}$  normalization have been deeply studied in [323], following the work done in the Les Houches Workshop in the year 2003. The primary goal of this note is to provide a reliable description of the experimental aspects, specifically the ones related to the CMS detector. For this study a full detector simulation has then been exploited.

The main requirement from the experimental side on the choice of the control region is to limit as much as possible the error due to the “ $\epsilon$ ” terms in relation (65). This implies to use similar selections as for the signal region. Moreover the contamination from other physical and instrumental backgrounds should be negligible.

In order to estimate the  $t\bar{t}$  contribution in the signal region, we exploit the presence of two additional high  $E_t$  jets coming from the top quark decay. Two procedures are proposed: the first based on the tagging of the two jets as originating from  $b$  quarks, and the other is requiring simply the  $E_t$  of the jets to be above a certain threshold. Both control regions will be defined by the same selections on the leptons as for the signal region.

The cuts used to define the signal region together with the corresponding number of events expected for  $1 \text{ fb}^{-1}$  for the fully simulated signal (for a Higgs mass of 165 GeV),  $t\bar{t}$  and  $Wt$  are summarized in Table 16.

The main cut to reject the  $t\bar{t}$  is the jet veto. An event is rejected, if there is at least one reconstructed jet with  $E_t > 15 \text{ GeV}$  within  $|\eta| = 2.5$ . In order to reduce the fake jets, when the measured jet  $E_t$  is between 15 and 20 GeV, the ratio of the sum of the  $p_t$  of all tracks inside the jet over the transverse jet energy deposited in the calorimeter, referred to as “ $\alpha$ ”, is required to be greater than 0.2.

#### 17.11 $b$ -tagging jets based $t\bar{t}$ normalization

The presence of two  $b$ -tagged jets together with two isolated leptons is a striking evidence for  $t\bar{t}$  events. In addition to the requirement of two  $b$ -jets, the control region for  $t\bar{t}$  extrapolation is defined by all the

<sup>38</sup>Contributed by: G. Davatz, A.-S. Giolo-Nicollerat, M. Zanetti

<sup>39</sup>The experimental uncertainties could modify the boundaries defining the phase space where the cross section is calculated theoretically. This is the case in particular when the selections involve jets. The “ $\epsilon$ ” terms in relation (65) are assumed to account also for this effect.

Table 16: The expected number of events for a luminosity of  $1 \text{ fb}^{-1}$  for the signal with a Higgs mass of 165 GeV and the  $t\bar{t}$  and  $t\text{W}b$  background. The relative efficiency with respect to the previous cut is given inside the brackets.

		$H \rightarrow WW$ ( $m_H = 165 \text{ GeV}$ )	$t\bar{t}$	$t\text{W}b$
	$\sigma \times \text{BR}(e, \mu, \tau)$ [fb]	2360	86200	3400
1)	Trigger	1390 (59%)	57380 (67%)	2320 (68%)
2)	lepton ID	393 (28%)	15700 (27%)	676 (29%)
3)	$E_t^{\text{miss}} > 50 \text{ GeV}$	274 (70%)	9332 (59%)	391 (58%)
4)	$\phi_{\ell\ell} < 45$	158 (58%)	1649 (18%)	65 (17%)
5)	$12 \text{ GeV} < m_{\ell\ell} < 40 \text{ GeV}$	119 (75%)	661 (40%)	28 (43%)
6)	$30 \text{ GeV} < p_t^{\ell \text{max}} < 55 \text{ GeV}$	88 (74%)	304 (46%)	13 (46%)
7)	$p_t^{\ell \text{min}} > 25 \text{ GeV}$	75 (85%)	220 (73%)	9.2 (71%)
8)	Jet veto	46 (61%)	9.8 (4.5%)	1.4 (15%)

cuts in Table 16 but the jet veto.

The algorithm, used to discriminate whether a jet is originated from a  $b$  quark, is based on the impact parameters of charged particle tracks associated to the jet [324]. The parameter, in the following called “discriminator”, that characterizes the efficiency and the mistagging rate of the algorithm, is the impact parameter significance  $\sigma_{IP}$  of a minimum number of tracks associated to the jet. In this study, a jet is tagged as a  $b$ -jet if its measured  $E_t$  is greater than  $20 \text{ GeV}$  and if there are at least 2 tracks with  $\sigma_{IP}$  above a given threshold. The dependence of the efficiency of selecting  $t\bar{t}$  and the purity of the events selected on the discriminator value is shown in the plots of Fig. 91.

A discriminator value of 2 for jet  $b$ -tagging is used in this analysis. In this case the double  $b$ -tagging efficiency is  $\mathcal{O}(30\%)$  while the mistagging rate is  $\mathcal{O}(3\%)$ . Table 17 summarizes the number of events expected for  $10 \text{ fb}^{-1}$  in the control region for  $t\bar{t}$ ,  $Wt$  and the signal in the case of  $2\mu$ ,  $2e$  and  $e\mu$  final states.

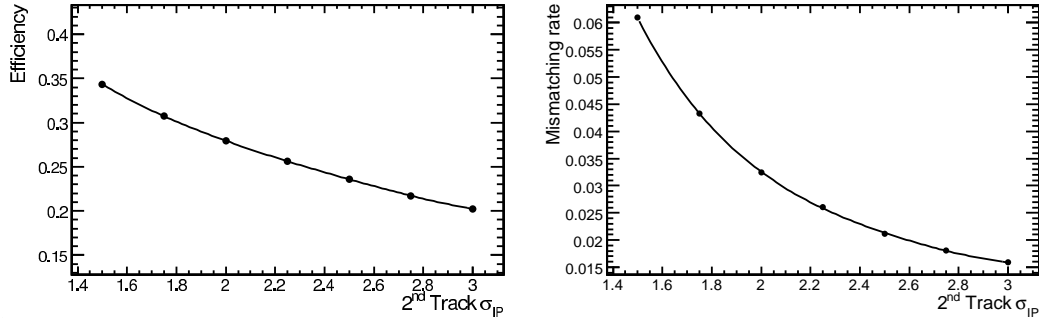


Fig. 91: Tagging efficiency and mistagging rate as a function of the discriminator. Left plot shows the efficiency of  $b$ -tagging both the jets originated from  $b$  quarks in  $t\bar{t}$  events, whereas right plot shows the percentage of mistagged jets.

Not all the processes with  $2\ell + 2b + E_t^{\text{miss}}$  as final state have been fully simulated for this analysis. Nevertheless, general considerations and fast Monte Carlo level checks can lead to exclude other relevant sources of backgrounds.

The more natural concurrent process is  $W^+W^-b\bar{b} \rightarrow 2\ell 2\nu b\bar{b}$  which is anyway  $\alpha_{\text{weak}}^2$  suppressed with respect to  $t\bar{t}$ . Its cross section is indeed expected to be smaller than  $1 \text{ pb}$ . Assuming the same efficiency for the kinematic selections as for the  $W^+W^- \rightarrow 2\ell$ , i.e.  $\mathcal{O}(10^{-3})$ , less than 10 events are expected for  $10 \text{ fb}^{-1}$  in the control region even without taking into account the double- $b$  tagging efficiency. In the case of same flavor leptons in the final state,  $\gamma^*/Z^* \rightarrow 2\ell + b\bar{b}$  (the vector boson mass being away

Table 17: Number of events of  $t\bar{t}$ , signal and  $Wt$  expected for  $10 \text{ fb}^{-1}$  in the two control regions, described in the text, and in the signal region. The results are shown for  $2\mu$ ,  $2e$ ,  $e\mu$  final states.

	“b-tagging” control region			“hard jets” control region			signal region		
	$2\mu$	$2e$	$e\mu$	$2\mu$	$2e$	$e\mu$	$2\mu$	$2e$	$e\mu$
$t\bar{t}$	194	107	245	-	-	411	33	22	44
$Wt$	1	< 1	2	-	-	6	5	3	6
<i>Signal</i> ( $m_H = 165$ )	< 1	< 1	1	-	-	11	156	89	214

from the  $Z$  peek, i.e.  $m_{\ell\ell} < 40 \text{ GeV}$ ) could also contribute as an instrumental background, when an high value of  $E_t^{miss}$  is yielded by the imperfect hermeticity of the detector and due the finite resolution of the calorimeters, respectively. Anyway for a fully simulated sample of  $\gamma^*/Z^* \rightarrow 2\ell + 2jets$  with jets’  $E_t$  grater than 20 GeV, the fraction of events with  $E_t^{miss} > 50 \text{ GeV}$  (the actual cut applied for the signal selection) is smaller than 1%. Applying the same kinematic selection, but the  $E_t^{miss}$  cut on a  $pp \rightarrow \gamma^*/Z^* \rightarrow 2\ell + b\bar{b}$  sample generated with MadGraph [325], 200 events are expected for  $10 \text{ fb}^{-1}$  which vanish if the rejection due to a realistic  $E_t^{miss}$  selection is included.

### 17.12 Two high $E_t$ jets based $t\bar{t}$ normalization

Although very powerful, the method proposed above for the estimation of the  $t\bar{t}$  background from data relies entirely on jet b-tagging which is known to be a sophisticated procedure from the hardware as well as from the algorithmic point of view. In order to avoid the systematics due to this method, it is then worth to have alternative methods to estimate the  $t\bar{t}$  background from data.

Each of the two  $b$  quarks in the  $t\bar{t}$  final state come from a  $175 \text{ GeV}$  central object; their  $E_t$  spectra are then rather hard. An alternative method to define a  $t\bar{t}$  control region is thus to require simply two hard jets in the detector in addition to the signal cuts listed in Table 16.

In analogously to the normalization, based on b-tagging, Drell Yan can be a dangerous background. In this case, the general  $2\ell + 2j$  final state has a much higher cross section with respect to the  $2\ell + 2b$  one. As a fully simulated sample based on matrix element calculations was not available, a Monte Carlo level analysis has been performed, leading to the result that, after applying the  $\mathcal{O}(10^{-2})$  reduction due to the  $E_t^{miss}$  cut, the contribution of this process in the control region can not be neglected. In order to get rid of this additional background, only the  $e\mu$  final state has been considered.

The thresholds on the jet transverse energy that maximize the signal ( $t\bar{t}$ ) over the background ( $Wt$ +signal) ratio and minimize the statistical error have been found to be 50 and 30 GeV. The number of events expected events for  $10 \text{ fb}^{-1}$  for  $t\bar{t}$ ,  $Wt$  and the signal are summarized in Table 17.

A background process, not considered in the full simulation analysis, is  $W^+W^- \rightarrow \mu\nu_\mu + e\nu_e + 2j$ . The cross section, after geometrical acceptance cuts, is  $0.4 \text{ pb}$ , whereas the signal selection cut efficiency is smaller than  $5 \cdot 10^{-4}$  (with an uncertainty of  $\sim 8\%$  from the limited Monte Carlo statistics). The contribution of this background can then be assumed to be at maximum of the order as the signal.

In case one jet is misidentified as an electron,  $W^\pm \rightarrow \mu\nu_\mu + 3j$  could be a source of background, too. For the CMS detector, the probability of electron misidentification is estimated to be  $\mathcal{O}(10^{-4})$ <sup>40</sup>. Given its cross section, calculated to be  $\sim 200 \text{ pb}$  after the geometrical acceptance cuts, the latter rejection factor together with the kinematic selection efficiency, estimated again from a generator level study is  $\mathcal{O}(10^{-4})$ , lead to neglect this process as a source of contamination of the  $t\bar{t}$  control region.

<sup>40</sup>The muon misidentification rate is at least one order of magnitude smaller

## 17.2 $t\bar{t}$ normalization procedure uncertainties

### 17.21 Systematics uncertainties

Our proposed procedure to estimate the number of  $t\bar{t}$  events in the signal phase space region exploits relation (65). In order to compute the systematic uncertainties on the final result we consider separately those related to each term present in the formula.

- **Theoretical uncertainty**

Taking the ratio of the  $t\bar{t}$  cross sections in the signal and control region avoids much of the theoretical systematic uncertainties. This is in fact the main justification of rel. (65), first proposed in Ref. [323]. In that paper the theoretical uncertainty on the ratio  $\sigma_{signal\_reg}/\sigma_{control\_reg}$  has been studied at parton level with LO precision by varying the renormalization and factorization scales. The error has been estimated to range between 3% to 10%, mostly due to the choice of the PDF. In Ref. [326], the NLO effects on  $t\bar{t}$  simulation have been studied, with the result that the shapes of the distributions involved in the normalization procedure, i.e. the  $E_t$  spectra of the jets and the jet multiplicity are not affected by higher orders contributions. However, the comparison of different showering models shows some discrepancies either in the jet multiplicity or the jets  $E_t$  spectra, introducing a further uncertainty with respect to the one due to the PDF set.

For what concerns the proposed normalization procedure, the dependence on the showering model has been studied in this analysis. Nevertheless, the Monte Carlo predictions concerning  $t\bar{t}$  will be intensively compared and tuned directly with the data, also considering the very high  $t\bar{t}$  rate at the LHC. A 10% systematical error due to theoretical uncertainty will be assumed as reported in Ref. [323], although baring in mind that this could be an optimistic estimate.

- **Jet energy scale uncertainty**

In the background normalization procedures, we propose, the jet energy scale (JES) uncertainty is particularly important since it affects in opposite manners the signal region, defined by vetoing the jets, and the control region where the presence of two jets is required. To take into account this sort of anti-correlation of  $\epsilon_{signal\_reg}$  and  $\epsilon_{control\_reg}$ , we estimate the effect of the JES uncertainty directly on their ratio by rescaling the measured jet four momentum by an amount corresponding to the fractional uncertainty (i.e.  $P_{jet}^\mu = (1 + \lambda)P_{jet}^\mu$ ).

In the plot of Fig. 92 the relative variation of  $\frac{\epsilon_{signal\_reg}}{\epsilon_{control\_reg}}$  for various values of  $\lambda$  is shown. In the plot the triangles represent the control region, defined by requiring two jets with  $E_t$  greater than 50 and 35 GeV, whereas the squares stand for the control region defined by requiring two b-tagged jets<sup>41</sup>

A realistic estimation of the JES uncertainty of CMS after integrating  $10 fb^{-1}$  of LHC is  $\mathcal{O}(5\%)$ . The corresponding relative variation of  $\epsilon_{signal\_reg}/\epsilon_{control\_reg}$  is  $\sim 8\%$  for the double b-tagging defined control region and  $\sim 10\%$  for the two high  $E_t$  jets control region.

- **$\alpha$  criterion uncertainty**

In order to prevent the contamination from fakes when vetoing jets down to a raw transverse energy of 15 GeV, it is useful to cut on the track content of the jets. For jets with  $E_t$  between 15 and 20 GeV the  $\alpha$  criterion is then exploited, as explained before. In order to estimate the systematic uncertainty due to this criterion, the cut on  $\alpha$  has been varied from 0.15 to 0.25. Moreover, different values of the minimum  $p_t$  for a track, to be included in the sum, have been tried from 2 to 3 GeV. The consequent variation of the jet veto efficiency ( $\epsilon_{signal\_reg}$ ) is relatively small, i.e. of the order of 4%.

- **b-tagging uncertainty**

In Ref. [327] the precision, with which the b-tagging efficiency of CMS will be known at CMS, is expected to be 11% for  $1 fb^{-1}$  integrated luminosity and it is foreseen to improve till 7% with

---

<sup>41</sup>The reason, why the ratio  $\epsilon_{signal\_reg}/\epsilon_{control\_reg}$  in the latter case is less sensitive to the JES uncertainty is that the  $E_t$  threshold for the b-jets candidates is 20 GeV and the fraction of  $t\bar{t}$  events with b-tagged jets with  $E_t$  close to that threshold is very small.



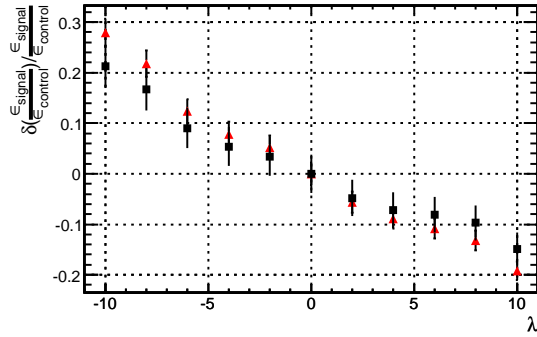


Fig. 92: Relative variation of  $\frac{\epsilon_{signal-reg}}{\epsilon_{control-reg}}$  as a function the jet momentum rescaling factor  $\lambda$ . The red triangles represent the control region defined by two hard jets whereas the black squares correspond to the two b-tagged jets phase space area.

10  $fb^{-1}$ . These values represent directly the uncertainty on  $\epsilon_{control-reg}$  in the case of the control region defined by requiring two b-tagged jets.

- **Uncertainties on  $N_{control-reg}$**

It has been shown in the previous section that  $t\bar{t}$  is plainly the dominant process in both control regions. With the cuts used for selecting these control regions, i.e. the signal kinematic cuts plus two b-tagged jets or two high  $E_t$  jets, we expect to identify almost purely  $t\bar{t}$  events. In the worst case, i.e. when the control region is defined by two high  $E_t$  jets, the fraction of events coming from other processes is smaller than 4%. Provided that this fraction is small, it is safe to simply neglect this source of systematic uncertainty.

For 10  $fb^{-1}$ , the experimental uncertainties listed above account for a systematic error of  $\sim 11\%$  for both  $t\bar{t}$  control regions. Including the theoretical uncertainty this error does not exceed 16%.

### 17.22 Statistical uncertainties

The statistical precision with which the number of  $t\bar{t}$  events in the signal region can be known depends on the expected number of  $t\bar{t}$  events in the control region. From the numbers quoted in Table 17 and assuming a Poissonian behavior it is clear that the error due to systematic uncertainties is predominant with respect to the statistical ones for both of the proposed normalization procedures.

## 18. SINGLE RESONANT TOP PRODUCTION AS BACKGROUND TO THE $H \rightarrow WW$ SEARCH<sup>42</sup>

At leading order, the inclusive double resonant top production process,  $pp \rightarrow t\bar{t} \rightarrow WbWb \rightarrow \ell\nu\ell\nu b\bar{b}$ , where  $\ell = e, \mu, \tau$ , has a cross section times branching ratio of about 52 pb. Single resonant top production  $pp \rightarrow Wtb$  represents a contribution about ten times smaller. After applying a jet veto, the singly resonant top contribution is increased with respect to the doubly resonant one, since the b-jet is typically produced at much lower transverse momentum. It is this contribution which we will study in detail here.

In order to resum large logarithms of the form  $\log[(m_t + m_W)/m_b]$ , it is preferable to view the singly resonant process as one in which a b quark is probed directly inside the proton. In this case, the single resonant leading order process is  $gb \rightarrow Wt$ , as depicted in Fig. 93. Starting from this process one can calculate NLO corrections, which naively include the doubly resonant diagrams in the real radiation contribution. Previous attempts to remove these contributions have either relied on subtracting the doubly resonant cross section [328] or on applying a mass window cut [329], both of which suffer from ambiguities related to the interference between the singly and doubly resonant graphs. However,

<sup>42</sup>Contributed by: J. Campbell, G. Davatz, A.-S. Giolo-Nicollerat, F. Maltoni, S. Willenbrock, M. Zanetti

by applying a veto on the presence of an extra b quark, the interference effect is greatly suppressed and the contribution from the doubly resonant diagrams can be unambiguously removed [330].

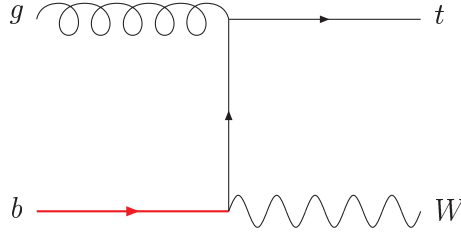


Fig. 93: A lowest order diagram for the singly resonant top production process. A b quark is produced inside the proton via gluon splitting and the resulting anti-b is unobserved.

Therefore we can estimate the singly resonant top production rate at NLO in a region where a jet veto is applied, which in the case of the Higgs search corresponds to the signal region. Clearly, the NLO prediction for the rate depends on the region of phase space which is probed, in particular on the definition of the jet veto. In the following, we will study the sensitivity to NLO corrections of the different kinematic variables used for  $H \rightarrow WW \rightarrow \ell\nu\ell\nu$ .

The NLO corrections to  $Wt$  production, implemented using a veto on an extra b quark, are calculated using the Monte Carlo program MCFM [330, 331]. The factorization and renormalization scales chosen to be equal to the jet veto value used, i.e. 40 GeV. We have calculated the efficiencies obtained for the Higgs selection cuts, which are defined in the chapter, ‘Top background generation in the  $H \rightarrow WW$  channel’ of these proceedings. A comparison between the LO and NLO results is shown in Table 18. We note that, since MCFM is a parton level generator, the jet veto actually corresponds to a veto directly on the partons, requiring no parton with  $p_t > 40$  GeV. Moreover, no requirement on the lepton isolation is added. Without selection cuts, the effect of the NLO corrections is to increase the LO cross section by a factor of about 1.4. After all selection cuts, this factor drops to approximately 0.7 almost entirely due to the effect of the jet veto. This is expected since the presence of an extra parton in the NLO calculation means that a jet is vetoed more frequently. The efficiency for the other selection cuts are very similar at LO and NLO. In order to account for the difference in the jet veto efficiency between NLO and LO, the K-factor that will be used to approximate the NLO cross section is determined in the signal region by the ratio of the NLO to LO cross sections of MCFM.

The cut selection efficiency obtained with MCFM is then compared to a simulation performed using TopReX [321], in which the effects of a parton shower are included. The cut efficiencies obtained using this approach are shown in the third column of Table 18. TopReX and MCFM lead to very similar results, with the exception of the jet veto.

The difference between the efficiencies of the jet veto is a direct consequence of the limitations of the parton level generator, MCFM. Whereas MCFM includes no showering and thus applies the jet veto directly at the parton level, the events produced by TopReX can be vetoed according to jets produced by the shower<sup>43</sup>. It is clear that the transverse momentum of the jet produced by the shower is not the same as the  $p_t$  of the parton that is produced in the hard interaction. We find that, at leading order, requiring no parton with  $p_t > 40$  GeV has a similar efficiency as requiring no jets with  $p_t > 30$  GeV. Thus a parton cut at 40 GeV will correspond to a jet cut at 30 GeV. Fig. 94 shows the selection efficiency as a function of the  $p_t$  of the b for finding two leptons with  $p_t > 20$  GeV and vetoing all clustered jets with  $p_t > 30$  GeV, for the TopReX sample. In this case, 85% of the events have  $p_t(b) < 40$  GeV and 94% have  $p_t(b) < 60$  GeV.

<sup>43</sup>For this study, as before, the jets are reconstructed using a cone algorithm on the stable particles from the MC tree.

Table 18: Higgs selection cut efficiencies for the singly resonant Wt process at LO and NLO, simulated with MCFM (parton level) [331] and TopReX (LO and parton shower). Here a veto is applied on the  $p_t$  of the generated b and is set to 40 GeV. The cross section is given after the following branching ratio has been included,  $[W^+ \rightarrow e^- \nu][t \rightarrow e^- \nu \bar{b}]$ .

	MCFM				TopReX
	LO		NLO		LO
Selection cuts	$\sigma \times \text{BR}$ (fb)	rel. eff	$\sigma \times \text{BR}$ (fb)	rel. eff	rel. eff
No cuts	271		377		
2 lep, $ \eta  < 2$ , $p_t > 20$ GeV	204	0.75	277	0.73	
$E_t^{\text{miss}} > 40$	148	0.73	209	0.75	0.75
$\phi_{\ell\ell} < 45$	20.8	0.14	34.4	0.16	0.17
$5 \text{ GeV} < m_{\ell\ell} < 40 \text{ GeV}$	10.6	0.51	15.6	0.45	0.50
Partonic jet veto, 40 GeV	1.55	0.15	1.12	0.07	0.16
$30 \text{ GeV} < p_t^{\ell \text{max}} < 55 \text{ GeV}$	1.08	0.70	0.73	0.65	0.63
$p_t^{\ell \text{min}} > 25 \text{ GeV}$	0.73	0.68	0.49	0.67	0.67

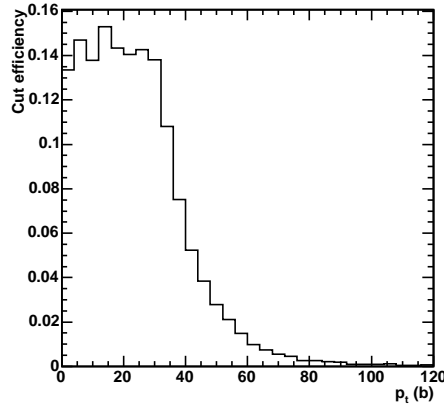


Fig. 94: Cut efficiency as a function of the transverse momentum of the b quark, after requiring two isolated leptons with  $p_t > 20$  GeV,  $|\eta| < 2$  and no reconstructed clustered jet with  $p_t > 30$  GeV for a simulation with TopReX.

A leading order parton shower Monte Carlo should thus already provide a good approximation of this process. A NLO K-factor of 0.7 has been determined in the signal region for the Higgs search in the WW channel. In particular, the veto on additional jet activity occurs at a transverse momentum of 30 GeV, corresponding to a parton-level veto of 40 GeV. The theoretical error on the Wt cross section is estimated to be of the order of 10-20%, including PDF and scale variation [330]. Therefore a conservative estimate of the Wt background in this region could be obtained by simply using the LO cross section without any additional K-factor, since it is predicted to be slightly less than unity at most.

## 19. STUDY OF PDF AND QCD SCALE UNCERTAINTIES IN $pp \rightarrow ZZ \rightarrow 4\mu$ EVENTS AT THE LHC <sup>44</sup>

### 19.1 Introduction

The  $q\bar{q} \rightarrow ZZ \rightarrow 4\mu$  process is the main irreducible background in searches for the Higgs boson via its  $H \rightarrow ZZ \rightarrow 4\mu$  decay mode. Theoretical uncertainties affect the current estimation of the physics reach for the search analysis and may turn into contributions to the total systematic errors on significance estimators, as background evaluation on a specific 4-muon mass range often relies on extrapolations from regions with larger background statistics, which are based on Monte Carlo Models. Normalization to higher rate processes like single  $Z$  production may help to reduce these uncertainties. This work concentrates on the estimation of current errors in the calculations for total and differential cross sections for the process  $q\bar{q} \rightarrow ZZ \rightarrow 4\mu$  arising from PDF and perturbative uncertainties, following the guidelines described in [332] for the evaluation of theoretical uncertainties in LHC analyses.

### 19.2 Event Generation

All results are obtained at NLO with MCFM [331] version 4.0 interfaced to the standard Les Houches accord PDF package LHAPDF [333]. The cross sections are evaluated within a typical experimental acceptance and for momentum cuts summarised in Section 19.3 The calculations with MCFM are carried out for a given fixed set of electroweak input parameters using the effective field theory approach. The PDF family CTEQ61 provided by the CTEQ collaboration [135] is taken as nominal PDF input. Quantitative error analysis is performed following the prescription of reference [334] using the 40 sets of CTEQ61. Errors are propagated via re-weighting to the final observables. MRST2001E given by the MRST group [311] is considered as an additional cross check. The value of the strong coupling  $\alpha_s$  is not a free input parameter for the cross section calculation but taken from the corresponding value in the PDF.

The dependence of the observables on the choice for renormalization and factorization scales is unphysical and should be regarded as one important contribution to the total uncertainty in the theoretical predictions accounting for missing higher orders in QCD calculations. The reference cross sections and distributions are obtained with  $\mu_R = \mu_F = 2M_Z$ . Missing higher orders are estimated by independent variations of the two scales in the range  $M_Z < \mu < 4M_Z$ , following prescriptions applied to other processes [335].

### 19.3 Definition of observables and event selection

In order to perform a generator-level study with MCFM, we select events fulfilling acceptance and momentum cuts very much along the lines of the ones optimized for full simulation-level analysis (in progress). General pre-selection cuts and three different sets of selection cuts are defined, the latter being driven by the Higgs search in four muon final states at low, average and high Higgs masses ( $M_H = 150, 250, \text{ and } 500 \text{ GeV}$  respectively).

The pre-selection cuts are:

- There should be at least four such muons (2 opposite sign muon pairs) for an event to be considered.
- $PT > 7 \text{ GeV}$  for all the four muons.
- Selected opposite sign muon pairs arising from  $Z/\gamma$  decays should have invariant mass  $M_{\mu^+\mu^-} > 12 \text{ GeV}$ . This cut on  $M_{\mu^+\mu^-}$  removes low-mass resonances.

The selection cuts are obtained from the pre-selection cuts, increasing the lower PT threshold on the four muons to 10, 16 and 25 GeV for  $m_H = 150, 250, \text{ and } 500 \text{ GeV}$  respectively.

~~The notations we use in this work include:~~

<sup>44</sup>Contributed by: S. Abdullin, D. Acosta, P. Bartalini, R. Cavanaugh, A. Drozdetskiy, A. Korytov, G. Mitselmakher, Yu. Pakhotin, B. Scurlock, A. Sherstnev, H. Stenzel

Table 19: Relative uncertainty on total cross section  $\sigma(q\bar{q} \rightarrow ZZ \rightarrow 4\mu)$  with pre-selection cuts and on  $d\sigma/dM_{4\mu}$  evaluated for three values of  $M_{4\mu}$  with selection cuts. Reference figures correspond to CTEQ61 PDF set and  $\mu_F = \mu_R = 2 * M_Z$ . Asymmetric errors arising from the choice of the QCD scales are obtained adopting independent variations of  $\mu_F$  and  $\mu_R$  in the range  $M_Z < \mu < 4M_Z$ . Symmetric errors from PDF parameterization are obtained using the CTEQ61 error sets. Comparison with reference MRST2001E predictions is also reported.

	$\Delta(\sigma)$	$\Delta(d\sigma/dM_{4\mu})$	$\Delta(d\sigma/dM_{4\mu})$	$\Delta(d\sigma/dM_{4\mu})$
	(pre-selection cuts)	( $M_H=150$ GeV)	( $M_H=250$ GeV)	( $M_H=500$ GeV)
$\mu_F$ and $\mu_R$	+3.2%	+2.3%	+3.4%	+3.8%
scales	-4.0%	-4.4%	-4.3%	-2.5%
PDF (CTEQ61)	$\pm 4.8\%$	$\pm 5.1\%$	$\pm 4.7\%$	$\pm 4.4\%$
$\Delta$ (MRST2001E)	+4.6%	+0.4%	+4.8%	+6.6%

- $M_{4\mu}$  is the invariant mass of the four selected muons.
- $PT_{4\mu}$  is the transverse momentum of the four muons system.
- Z1 ( $M_{\mu^+\mu^-}$ ) refers to the muon pair with invariant mass closest to the  $Z^0$  mass and Z2 refers to the second muon pair selected from the rest of the muons with the highest PT.

#### 19.4 Study of uncertainties from PDF and QCD scales

The total effective cross section  $\sigma(q\bar{q} \rightarrow ZZ \rightarrow 4\mu)$  with pre-selection cuts for CTEQ61 PDF set and  $\mu_F = \mu_R = 2 * M_Z$  turns out to be 18.6 fb. The  $M_{4\mu}$  distribution is given in Fig. 95, along with uncertainties from CTEQ61 error analysis; the corresponding relative uncertainties are also reported in Fig. 96, which indicates a flat behaviour for  $M_{4\mu} > 150$  GeV. An additional cross check is made in Fig. 97, which reports the comparison between the predictions of CTEQ61 and MRST2001E PDFs.

The effect of  $\mu_F$  and  $\mu_R$  variations on  $M_{4\mu}$  is shown in Fig. 98; one may notice that each of the four different combinations turns out to be dominant as lower (or upper) error boundary in a given  $M_{4\mu}$  region, with an overall effect which results in flat boundaries. Adopting just  $\mu_F - \mu_R$  correlated variations would underestimate the contribution of QCD scales to the total theoretical uncertainty.

All these results are summarized in Table 19. We quote 3-4% effects arising from the variation of the QCD scales and 4-5% effects from CTEQ61 error analysis, while MRST2001 predictions turn out to be consistent with CTEQ61 error boundaries. No sensitive dependency of the error boundaries with  $M_{4\mu}$  is observed.

In general, CTEQ61 error analysis achieves similar results for all the single muon, di-muons and four-muons kinematic distributions in  $q\bar{q} \rightarrow ZZ \rightarrow 4\mu$  events. QCD scale variations also achieve similar results for single muon distributions. However, more sensitive relative uncertainties of around 10-15% are observed on four-muons and di-muons PT and pseudorapidity distributions in  $q\bar{q} \rightarrow ZZ \rightarrow 4\mu$  events. See for example Fig. 99, which reports the  $PT_{4\mu}$  distribution and Fig. 100, which shows the effect of  $\mu_F$  and  $\mu_R$  variations on  $PT_{4\mu}$ .

Fig. 101 reports the invariant mass distribution of the Z2 along with uncertainties from CTEQ61 error analysis (corresponding to a relative error of around 4% on the overall Z2 mass spectrum), while Fig. 102 shows the effect of  $\mu_F$  and  $\mu_R$  variations on the same distribution, which turns out to be slightly more pronounced on the nominal mass of the  $Z$  resonance.

The effects of the complete logarithmic electroweak  $O(\alpha)$  corrections on the production of vector-boson pairs at the LHC have been studied in [336]. These corrections, that we don't take into account, turn out to be relevant for  $M_{4\mu}$  of the order of several 100GeV lowering the Born level predictions by more than 10% for  $M_{4\mu} > 500$ GeV.

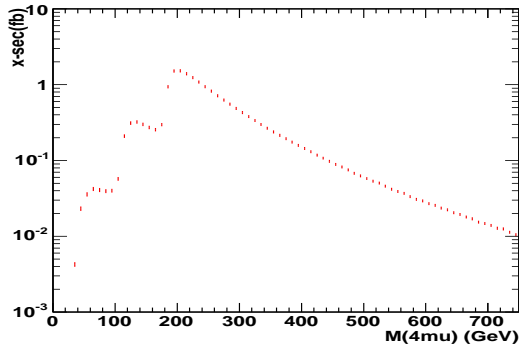


Fig. 95:  $M_{4\mu}$  = four muon invariant mass distribution, normalized to femtobarns per 10 GeV bins. PDF = CTEQ61;  $\mu_F = \mu_R = 2 * M_Z$ . Symmetric error bars result from full error analysis with the CTEQ61 error sets: they are reported as relative uncertainties in Fig. 96.

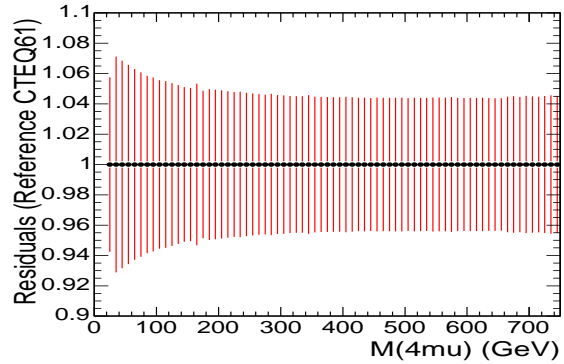


Fig. 96:  $M_{4\mu}$  distribution: symmetric relative uncertainties from full error analysis with the CTEQ61 error sets.

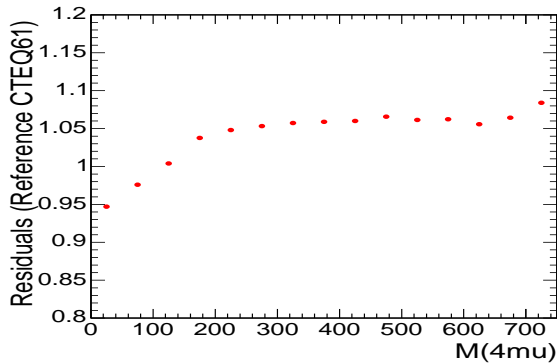


Fig. 97: Ratio between  $M_{4\mu}$  distributions obtained with PDF = MRST2001 and PDF = CTEQ61 respectively.

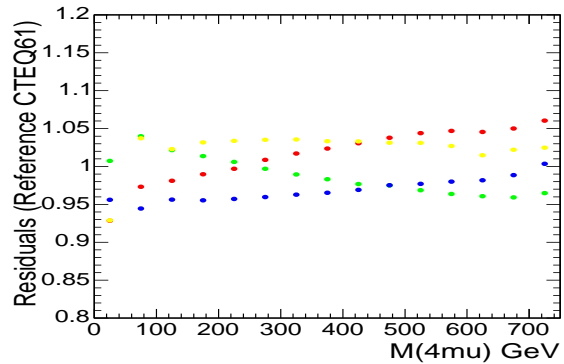


Fig. 98:  $M_{4\mu}$  distribution according to four different renormalization and factorization scale settings with respect to the reference one ( $\mu_F = \mu_R = 2M_Z$ ):  $\mu_F = M_Z, \mu_R = M_Z$  (red);  $\mu_F = 4M_Z, \mu_R = M_Z$  (yellow);  $\mu_F = M_Z, \mu_R = 4M_Z$  (green);  $\mu_F = 4M_Z, \mu_R = 4M_Z$  (blue).



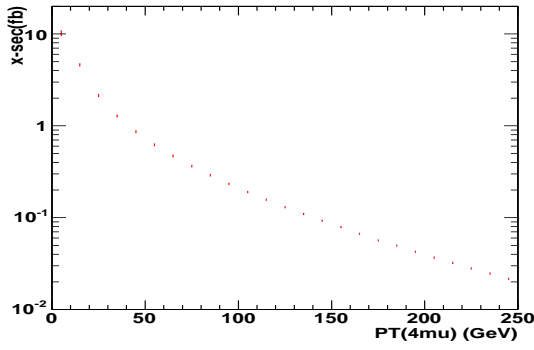


Fig. 99:  $PT(4\mu)$  = transverse momentum of the  $4\mu$  system. PDF = CTEQ61;  $\mu_F = \mu_R = 2 * M_Z$ . Symmetric error bars result from full error analysis with the CTEQ61 error sets.

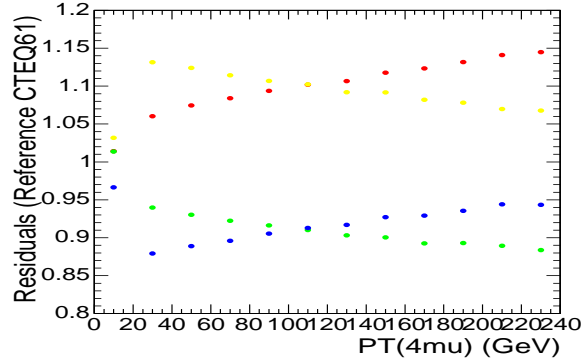


Fig. 100:  $PT(4\mu)$  distribution according to four different renormalization and factorization scale settings with respect to the reference one ( $\mu_F = \mu_R = 2M_Z$ ):  $\mu_F = M_Z, \mu_R = M_Z$  (red);  $\mu_F = 4M_Z, \mu_R = M_Z$  (yellow);  $\mu_F = M_Z, \mu_R = 4M_Z$  (green);  $\mu_F = 4M_Z, \mu_R = 4M_Z$  (blue).

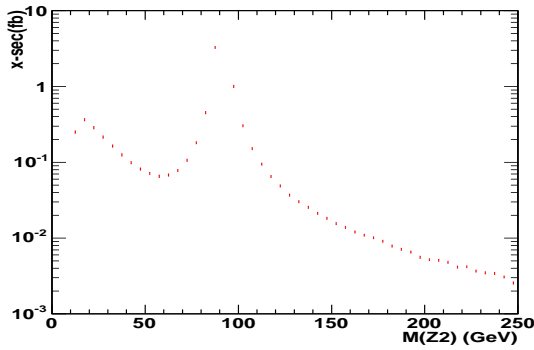


Fig. 101: Invariant mass of the  $Z2$  candidate. PDF = CTEQ61;  $\mu_F = \mu_R = 2 * M_Z$ . Symmetric error bars result from full error analysis with the CTEQ61 error sets.

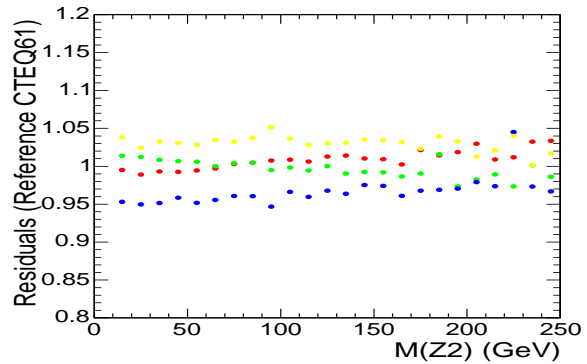


Fig. 102: Invariant mass of the  $Z2$  candidate according to four different renormalization and factorization scale settings with respect to the reference one ( $\mu_F = \mu_R = 2M_Z$ ):  $\mu_F = M_Z, \mu_R = M_Z$  (red);  $\mu_F = 4M_Z, \mu_R = M_Z$  (yellow);  $\mu_F = M_Z, \mu_R = 4M_Z$  (green);  $\mu_F = 4M_Z, \mu_R = 4M_Z$  (blue).

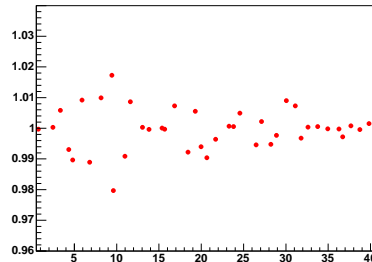


Fig. 103: Normalized ratio between  $ZZ \rightarrow 4\mu$  and  $Z \rightarrow 2\mu$  cross sections according to the 40 members of the CTEQ61 sets.

## 19.5 Normalization to Drell-Yan

Normalization to higher rate processes involving  $q\bar{q}$  initial state may provide us with an experimental methodology to absorb part of the theoretical uncertainties arising from PDF and QCD scales. Single  $Z$  boson events decaying to  $\mu^+\mu^-$  events are generated with MCFM with pre-selection cuts (applied to di-muons final states) described in section 19.3. The total effective cross section  $\sigma(q\bar{q} \rightarrow Z \rightarrow \mu^+\mu^-)$  turns out to be 924 pb. Fig. 103 shows the prediction for the normalized ratio  $\sigma(q\bar{q} \rightarrow ZZ \rightarrow 4\mu)/\sigma(q\bar{q} \rightarrow Z \rightarrow 2\mu)$  with pre-selection cuts according to the 40 members of CTEQ61. PDF uncertainty on the ratio reduces to  $\pm 3.2\%$ , against  $\pm 4.8\%$  which is the value quoted for  $\sigma(q\bar{q} \rightarrow ZZ \rightarrow 4\mu)$  (Table 19). A similar approach is followed for the uncertainty on the ratio arising from QCD scale variations, which gives an asymmetric error of +3.5 % and -2.8%.

As mentioned in the previous section, this study doesn't take into account electroweak corrections. Although the size of these corrections turns out to be similar [337] between for single and double boson production, corrections to the ratio might be sensitive in the high  $M_{4\mu}$  region.

## 19.6 Acknowledgments

We would like to thank M. Aldaya, P. Arce, D. Bourilkov, J. Caballero, J. Campbell, B. Cruz, S. Ferrag, U. Gasparini, P. Garcia, J. Hernandez, I. Josa, E.R. Morales, N. Neumeister, A. Nikitenko, T. Sjostrand for their active participation in the analysis discussions and comments on this letter.

## 20. RELATIVE CONTRIBUTIONS OF $t$ - and $s$ -CHANNELS TO THE $ZZ \rightarrow 4\mu$ PROCESS <sup>45</sup>

### 20.1 Introduction

The  $q\bar{q} \rightarrow ZZ \rightarrow 4\mu$  process is the main irreducible background in searches for the Higgs boson via its  $H \rightarrow ZZ \rightarrow 4\mu$  decay mode. Figures 104 and 105 show the  $t$ - and  $s$ -channel contribution diagrams. PYTHIA [284], an event generator commonly used for simulation of this process at the LHC is unfortunately missing the  $s$ -channel contribution. In this note, we show that the  $s$ -channel sub-process and its interference with the  $t$ -channel cannot be neglected if one aims to simulate the  $ZZ$ -background with a precision of 10% or better.

One may notice that very different kinematics are expected for the  $s$ - and  $t$ -channel events. For example, the invariant mass of the four muons for the  $s$ -channel contribution will tend to have a peak around the  $Z^0$  mass with a tail to high invariant masses, because a  $Z$  is radiated from one of the muon legs in the decay of the first  $Z$ , whereas the  $t$ -channel has a more complicated structure with at least two distinct peaks around the  $Z^0$  mass and twice the  $Z^0$  mass, with a tail to even higher values.

### 20.2 Event Generation

For this study we used event samples of  $ZZ$  (by  $Z$  in the  $ZZ$  process here and below we mean  $Z/Z^*/\gamma^*$ ) background produced with PYTHIA only (PYTHIA parameters: MSEL = 0, MSUB 22 = 1) and with CompHEP-PYTHIA. The latter uses the CompHEP [286] matrix element (ME) generator interfaced to PYTHIA, which is used for showering and hadronization in the same way and with the same parameters as for the pure-PYTHIA sample. Below, we refer to CompHEP-PYTHIA samples simply as CompHEP samples. The main subprocesses resulting in a  $4\mu$  final state are:

$$ZZ \rightarrow 4\mu$$

$$ZZ \rightarrow 2\tau 2\mu \rightarrow 4\mu \text{ (not used in this analysis)}$$

$$ZZ \rightarrow 2b 2\mu \rightarrow 4\mu \text{ (not used in this analysis)}$$

---

<sup>45</sup>Contributed by: S. Abdullin, D. Acosta, P. Bartalini, R. Cavanaugh, A. Drozdetskiy, A. Korytov, G. Mitselmakher, Yu. Pakhotin, B. Scurlock, A. Sherstnev

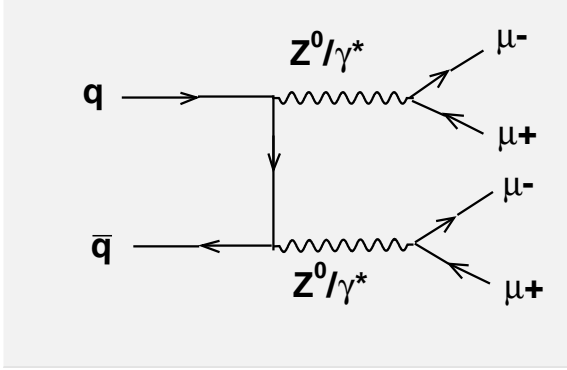


Fig. 104: ZZ background: t-channel diagram.

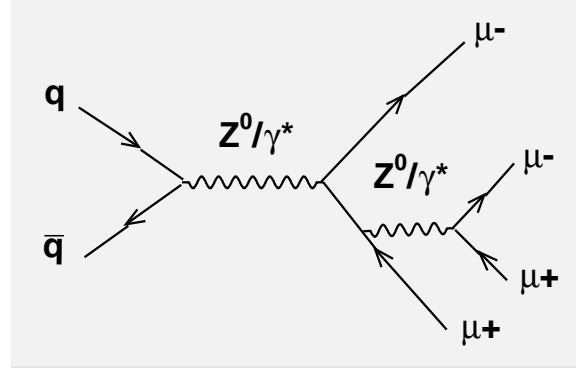


Fig. 105: ZZ background: s-channel diagram.

For normal analysis cuts, which select a region of  $4\mu$  invariant masses between about 110 and 170 GeV, we expect about 33 events from the first process, about 4 events for the second and about 3 events for the third. The latter one will become negligible after isolation cuts. All event numbers in this note are normalized to  $30\text{fb}^{-1}$  of integrated luminosity.

We used the CTEQ5L PDF [338] and the  $\hat{s} Q^2$  scale parameter [284] in both CompHEP and PYTHIA (the  $\hat{s} Q^2$  scale is not a default in PYTHIA 6.223). Generator-level “pre-selection” cuts are:  $PT > 3$  GeV,  $|\eta| < 2.5$  for all four muons. The PYTHIA sample’s generation-level “pre-selection” cuts:  $PT > 3$  GeV,  $|\eta| < 2.5$  for the four selected muons. Additional cuts on the invariant masses of any two pairs of selected opposite sign muons are:  $5 < M_{\mu^+\mu^-} < 150$  GeV (the cross sections, especially for the s-channel, are sensitive to the lower limit; the upper limit, once it is sufficiently higher than  $m_{Z^0}$ , is not important).

### 20.3 Event selection and analysis cuts

To perform a generator-level study, we select events as for the full simulation-level analysis in progress (selection cuts).

The selection cuts are:

- $PT > 7$  GeV (for the barrel,  $|\eta| < 1.1$ ) or  $P > 9$  GeV (for the endcaps,  $|\eta| > 1.1$ ) for all considered muons. These cuts correspond to a muon reconstruction efficiency of 80-90%.
- There should be at least four such muons (2 opposite sign muon pairs) for an event to be considered.
- All four permutations of opposite sign muon pairs should have invariant mass  $M_{\mu^+\mu^-} > 12$  GeV (for the four muons selected). This cut on  $M_{\mu^+\mu^-}$  removes low-mass resonances.

We also use in this study an example of analysis cuts optimized for small Higgs boson masses ( $m_H < 160$  GeV for the full simulation-level analysis in progress), as listed in Table 20.

The notations we use for the analysis-level cuts include:

- Z1 ( $M_{\mu^+\mu^-}$ ) refers to the muon pair with invariant mass closest to the  $Z^0$  mass and Z2 refers to the second muon pair selected from the rest of the muons with the highest PT.
- $\mu_1, \dots, \mu_4$  are the four selected muons when they are sorted by PT, largest to smallest.
- $M_{4\mu}$  is the invariant mass of the four selected muons.

### 20.4 CompHEP vs. PYTHIA: comparison of t-channel only samples

Before making a comparison of events for which the s- and t-channel diagrams are included (CompHEP) with t-channel diagram events only (pure-PYTHIA), we compare t-channel CompHEP and t-channel

Table 20: Analysis-level cuts (example of cuts optimized for the small Higgs boson mass region,  $M_{4\mu} < 160$  GeV).

parameter	cut, GeV
PT $\mu_1$	14
PT $\mu_2$	10
PT $\mu_3$	10
PT $\mu_4$	7
Z1 ( $M_{\mu+\mu-}$ )	> 60
Z1 ( $M_{\mu+\mu-}$ )	< 110
Z2 ( $M_{\mu+\mu-}$ )	> 12
Z2 ( $M_{\mu+\mu-}$ )	< 60
$M_{4\mu}$	> 110

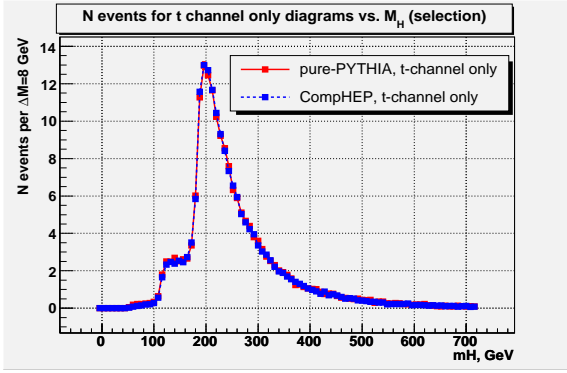


Fig. 106:  $4\mu$  invariant mass distribution after selection cuts,  $L = 30 \text{ fb}^{-1}$ . Comparison of t-channel CompHEP generated events and t-channel PYTHIA ones. Error bars include the MC statistical contribution only.

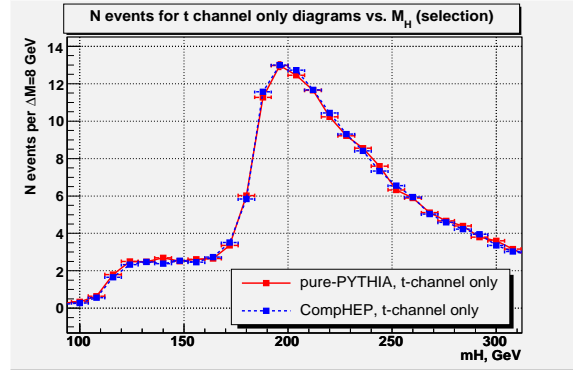


Fig. 107: Enlarged part of Fig. 106,  $100 < M_{4\mu} < 300$  GeV.

pure-PYTHIA events. This cross check is necessary to be sure that the effect, if it exists, is not due to a difference in internal cuts, model parameters or something similar, but indeed is a consequence of taking the  $s$ -channel into account, as well as interference between the  $s$ - and  $t$ -channels.

Figures 106, 107, 108 and 109 show the results of the  $t$ -channel only comparison. Figure 106 shows the entire  $M_{4\mu}$  interval of interest, and Figs. 107, 108 and 109 show different sub-intervals for better comparison. It is clear, that the  $t$ -channel only samples generated with PYTHIA and with CompHEP have almost identical  $M_{4\mu}$  spectra (up to the level of the statistical precision of the results).

## 20.5 Comparison of $t$ - and $s$ -channel sample (CompHEP) vs. $t$ -channel sample only (pure-PYTHIA)

We now compare the  $s$ - and  $t$ -channel CompHEP events to  $t$ -channel only PYTHIA events.

There are three regions of interest in the  $4\mu$  invariant mass ( $M_{4\mu}$ ). The first one is near the  $Z^0$  mass. Because of the  $s$ -channel, in particular, this region has a peak. The peak is clearly seen after both selection and analysis cuts (optimized for small  $m_H$  region), see Figs. 110 and 111.

Another region of interest is the low mass region with  $M_{4\mu} < 160$  GeV. This is where we applied our example set of analysis cuts (optimized for small  $m_H$  region). In this region, due to the  $s$ -channel presence and interference between the  $t$ - and  $s$ -channels, we see an excess of events over the  $t$ -channel-only case at the level of 10-15% (even after the analysis cuts), see Fig. 112.

Even in the third region of interest ( $M_{4\mu} > 160$  GeV), the  $s$ -channel contribution still is not negli-

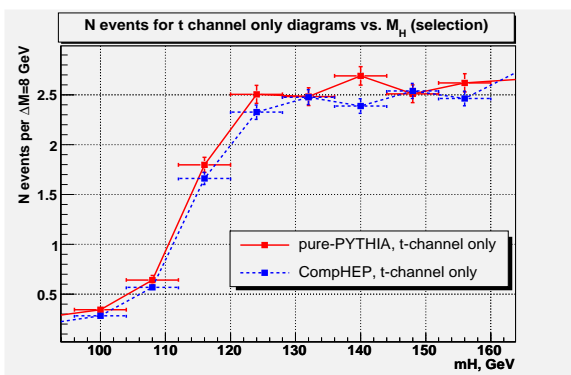


Fig. 108: Enlarged part of Fig. 106,  $100 < M_{4\mu} < 160$  GeV.

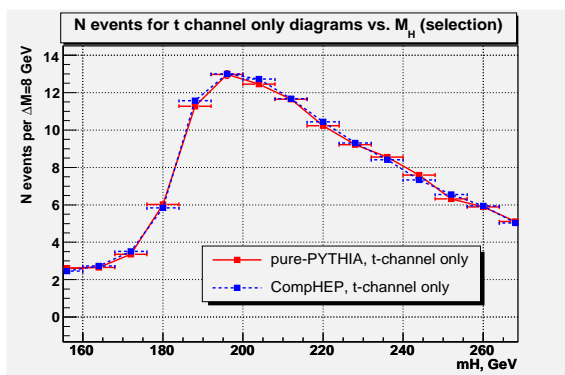


Fig. 109: Enlarged part of Fig. 106,  $160 < M_{4\mu} < 260$  GeV.

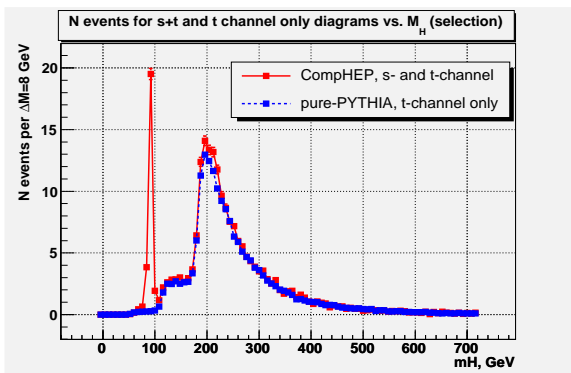


Fig. 110:  $4\mu$  invariant mass distribution after selection cuts,  $L = 30 \text{ fb}^{-1}$ . Comparison of s- plus t-channel CompHEP generated events and t-channel only PYTHIA ones. Error bars include MC statistical contribution only.

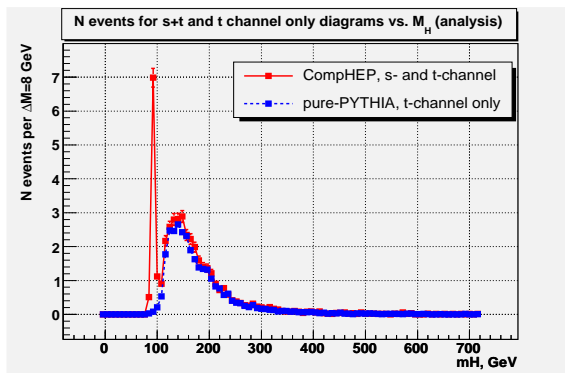


Fig. 111: Same as Fig. 110 but after analysis cuts (see Table 20).

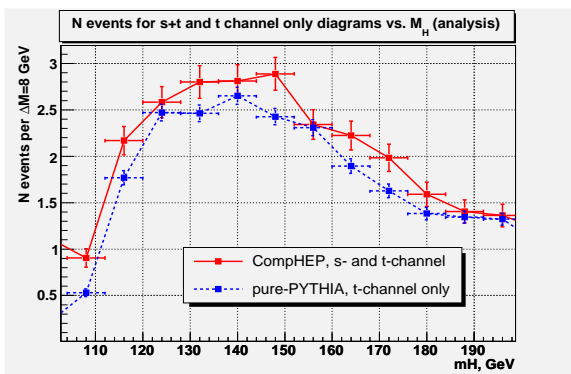


Fig. 112: Enlarged part of Fig. 111.

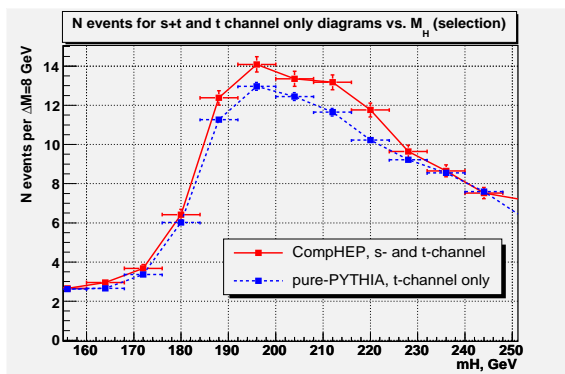


Fig. 113: Enlarged part of Fig. 110 for  $M_{4\mu} > 160$  GeV.

gible,  $\sim 5 - 7\%$  (Fig. 113).

The overall numbers of  $4\mu$  events after different cuts are shown in Table 21. "Pre-selection" cuts are defined in Section 20.2, "selection" and "analysis" cuts are defined in Section 20.3. The numbers for the t-channel contributions for the PYTHIA- and CompHEP-produced samples in the first two columns ( $\sigma$  (pre-selection) in fb and the corresponding N (pre-selection) of expected events) are different because of different pre-selection cuts for these two generators. Once the cut on the invariant mass of all four permutations of  $\mu^+\mu^-$ -pairs is introduced (and other cuts are the same as well), the expected event numbers for the t-channel contribution for the PYTHIA and CompHEP samples are the same up to the level of statistical precision.

Table 21: Cross section values for the t- and s-channel CompHEP sample, the t-channel CompHEP and PYTHIA samples and the corresponding expected numbers of events for  $30 \text{ fb}^{-1}$  integrated luminosity with MC statistical errors (numbers and corresponding statistical errors are scaled according to cross-section and integrated luminosity from a much larger number of MC generated events).

process	$\sigma$ (pre-selection), fb	N (pre-selection)	N (selection)	N (analysis)
CompHEP, s- and t-channel	65.0	$1950 \pm 4.6$	$224 \pm 1.6$	$42.6 \pm 0.68$
CompHEP, t-channel only	18.8	$565 \pm 1.1$	$184 \pm 0.64$	$29.3 \pm 0.25$
pure PYTHIA	9.93	$298 \pm 0.98$	$186 \pm 0.77$	$30.4 \pm 0.31$

## 20.6 Summary

PYTHIA does not include the s-channel (and its interference with the t-channel) in ZZ background generation.

We have shown that the s-channel contribution to the ZZ background in the analysis of  $H \rightarrow 4\mu$  with  $M_{4\mu} > 115 \text{ GeV}$  (area of interest for the Standard Model Higgs boson search at LHC: lower limit is from LEP studies) is non-negligible and remains non-negligible after applying analysis cuts optimised for a low mass Higgs search.

## Acknowledgments

We would like to thank M. Aldaya, P. Arce, J. Caballero, B. Cruz, T. Ferguson, U. Gasparini, P. Garcia, J. Hernandez, I. Josa, P. Moisenz, E.R. Morales, N. Neumeister, A. Nikitenko, F. Palla, T. Sjostrand and I. Vorobiev for their active participation in the analysis discussions and comments on this letter.

## 21. SENSITIVITY OF THE MUON ISOLATION CUT EFFICIENCY TO THE UNDERLYING EVENT UNCERTAINTIES<sup>46</sup>

### 21.1 Introduction

In future searches for the Higgs boson at the LHC via its 4-muon decay channel,  $H \rightarrow ZZ \rightarrow 4\mu$ , the muon isolation cut plays a key role in suppressing many otherwise dominating backgrounds where all or some muons originate from hadronic decays ( $t\bar{t}$  and  $Zb\bar{b}$  are the most important processes in this category). In reducing the  $t\bar{t}$  and  $Zb\bar{b}$  backgrounds to a negligible level, the ZZ background and signal is also suppressed. Therefore, one must worry about the efficiency of the muon isolation cut with respect to the ZZ background and Higgs boson signal and, even more, about the sensitivity of this efficiency to the large theoretical uncertainties associated with a poor understanding of the underlying event (UE) physics. The UE is defined as [339] all the remnant activity from the same proton-proton interaction. The goal of the studies presented in this letter was not to optimize the muon isolation cut in order to

<sup>46</sup>Contributed by: S. Abdullin, D. Acosta, P. Bartalini, R. Cavanaugh, A. Drozdetskiy, A. Korytov, G. Mitselmakher, Yu. Pakhotin, B. Scurlock, A. Sherstnev



maximize the signal-over-background significance, but rather to understand how well can we predict the isolation cut efficiency using the current Monte Carlo generators, and to determine how to measure the isolation cut efficiency using the experimental data themselves.

In these generator-level studies, we looked only at the tracker-based isolation cut.

The analysis presented in this letter is done in accordance with CMS guidelines described in [339] for estimating uncertainties arising due to the UE.

## 21.2 Event generation parameters for PYTHIA

Higgs boson,  $t\bar{t}$  and Z-inclusive data samples were generated with PYTHIA 6.223 [284]. The ZZ data sample was generated at the matrix-element level with CompHEP [286] and, then, PYTHIA was used to complete the event simulation (parton shower development, UE, hadronization, and particle decays). The PYTHIA parameters that drive the UE simulation were consistently chosen to match those selected for the Data Challenge 2005 (DC05) CMS official production (see Table 22). Detailed discussion of the associated phenomenology and the corresponding references can be found elsewhere [339].

Table 22: Parameters in PYTHIA for multi-parton interactions (MI) and UE for CDF, ATLAS and CMS.

parameter	CDF	ATLAS	CMS (DC04)	CMS (DC05)	comment
PARP(82)	2	1.8	1.9	2.9	regularization scale of PT spectrum for MI
PARP(84)	0.4	0.5	0.4	0.4	parameter of matter distribution inside hadrons
PARP(85)	0.9	0.33	0.33	0.33	probability in MI for two gluons with color connections
PARP(86)	0.95	0.66	0.66	0.66	probability in MI for two gluons (as a closed loop)
PARP(89)	1800	1000	1000	14000	reference energy scale
PARP(90)	0.25	0.16	0.16	0.16	power of the energy-rescaling term
$pt_{\text{cut-off}}$	3.34	2.75	2.90	2.90	final $pt_{\text{cut-off}}$

The most critical parameter affecting the UE activity is  $pt_{\text{cut-off}}$ , the lowest PT allowed for multi-parton interactions. The smaller  $pt_{\text{cut-off}}$  is, the larger is the number of tracks associated with the underlying event. The  $pt_{\text{cut-off}}$  value and its evolution with the center of mass energy of proton-proton collisions are defined via the following formula:

$$pt_{\text{cut-off}} = \text{PARP}(82) * (14000/\text{PARP}(89))^{\text{PARP}(90)}$$

The three parameters, PARP(82,89,90), have meaning only in this combination. The parameters PARP(89) and PARP(90) are fixed at 14,000 and 0.16, correspondingly. We decided to vary  $pt_{\text{cut-off}}$  by  $\pm 3\sigma$ , or  $\pm 0.5$  GeV, which seems to be a sensible estimation of theoretical uncertainties arising from UE modeling [340]. Note that  $pt_{\text{cut-off}} = 3.34$  GeV, as extracted from CDF's Tune A of PYTHIA MI parameters, differs from the default values used by ATLAS (2.75 GeV) and CMS (2.9 GeV) by  $\sim 0.5$  GeV because it was done using a different PYTHIA parameter tuning model and is listed for completeness only in Table 22.

## 21.3 Monte Carlo sample production

Processes used in these studies were:  $t\bar{t}$  (PYTHIA parameter MSEL = 6); Higgs boson signal ( $m_H = 150$  GeV, PYTHIA parameters MSEL = 0, MSUB(102,123,124) = 1 with H allowed to decay to  $Z/\gamma^*$  only,  $Z/\gamma^*$  allowed to decay to  $e/\mu/\tau$  pair only and  $\tau$  allowed to decay to  $e/\mu$  only); ZZ (PYTHIA parameters MSEL = 0, MSUB(1) = 22 with  $Z/\gamma^*$  allowed to decay to  $e/\mu/\tau$  pair only and  $\tau$  allowed to decay to  $e/\mu$  only); Z-inclusive (PYTHIA parameters MSEL = 0, MSUB(1) = 1 with Z allowed to decay to muon pair only). For Higgs boson signal, we used PHOTOS as a generator of bremsstrahlung photons.

Generator-level cuts:

- $t\bar{t}$ : at least four muons with  $PT > 7$  GeV and  $|\eta| < 2.4$ ;

- Higgs boson signal: at least four muons with  $PT > 7$  GeV and  $|\eta| < 2.4$ ;  $5 < M_{\text{inv}}(\mu^+\mu^-) < 150$  GeV for 2 intermediate resonances ( $Z/\gamma^*$ );
- ZZ-sample: same as for signal;
- Z-inclusive: no user defined cuts.

## 21.4 Event selection

Event-selection cuts were further imposed on the produced Monte Carlo samples. These cuts were chosen to mimic those optimized for the future data analysis. There are two distinct sets of such cuts.

First, only "good muons" were selected. A muon was considered to be "good" if it had  $PT > 7$  GeV in the barrel region ( $|\eta| < 1.1$ ) or  $P > 9$  GeV in the endcaps ( $1.1 < |\eta| < 2.4$ ). This ensures that the muon reconstruction efficiencies are flat with respect to PT or P, which helps minimize systematic uncertainties on the muon reconstruction efficiency.

Then, event-selection cuts similar to the full analysis cuts were applied. They are:

- At least 2 opposite sign muon pairs with invariant masses for all  $\mu^+\mu^-$  pair permutations being greater than 12 GeV (this cut suppresses heavy-quark resonances).
- PT of all four selected muons must be greater than 10 GeV (signal-over-background optimization).
- invariant mass of the four muons must be greater than 110 GeV and less than 700 GeV (Higgs boson with  $M < 114.4$  GeV is excluded at LEP, Higgs boson with mass over 700 GeV is strongly disfavored by theory and, also, would have too low a production cross section).
- $ISOL = \sum PT_i$  (PT with respect to the beam direction) should be less or equal to 0, 0, 1, 2 GeV for the four muons when the muons are sorted by the ISOL parameter. The sum runs over only charged particle tracks with PT greater then 0.8 GeV and inside a cone of radius  $R = \sqrt{(\Delta\phi)^2 + (\Delta\eta)^2} = 0.3$  in the azimuth-pseudorapidity space. A PT threshold of 0.8 GeV roughly corresponds to the PT for which tracks start looping inside the CMS Tracker. Muon tracks were not included in the calculation of the ISOL parameter.

## 21.5 Tracker-based muon isolation cut efficiency

Figures 114, 115 and 116 show the muon isolation cut efficiency averaged over all "good" muons (see section 21.4) for the  $t\bar{t}$  sample and the Higgs boson. For  $t\bar{t}$  background, we show two plots: one for muons originating from  $W \rightarrow \mu\nu$  and  $W \rightarrow \tau\nu \rightarrow \mu\nu\nu\nu$  decays and the other for muons originating from hadronic decays (typically, the former would tend to be isolated and the latter non-isolated). The average isolation efficiency per "good" muon is calculated as the ratio of the number of "good" muons with the isolation parameter ISOL below a particular threshold to the total number of "good" muons. Figure 117 shows the isolation cut efficiency for the least isolated muon out of four (Higgs boson sample). We use a cut at  $ISOL=2$  GeV for such muons. One can see that this cut alone will have  $\sim 80\%$  efficiency with  $\pm 5\%$  uncertainty due to the UE model.

Figure 118 compares the muon isolation cut efficiency curves for the main irreducible ZZ background and for the Higgs boson events. Clearly, these efficiencies are very similar.

### 21.51 Sensitivity to kinematical cuts

Figure 119 demonstrates another very important feature of the tracker-based muon isolation cut: its efficiency is not very sensitive to the kinematical analysis cuts. The figure has two sets of efficiency curves: one is obtained for "good" muons and another for "good" muons passing further event selection cuts as described in section 21.4. One can hardly see any difference. Therefore, the conclusions of this analysis will not depend on the choice of the final event selection cuts.

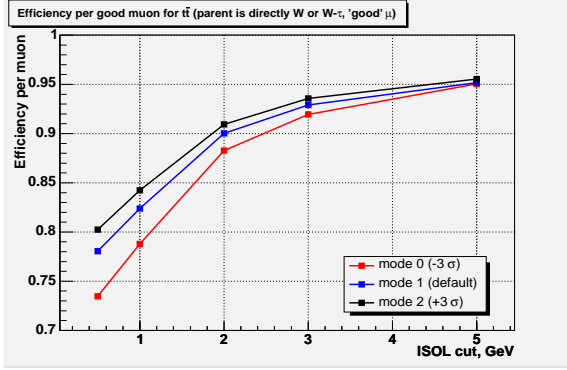


Fig. 114: Muon isolation cut efficiency averaged over selected muons whose parents are W bosons ( $t\bar{t}$  events). The blue middle line is for the default MI  $pt_{\text{cut-off}}$ , the black upper line is for downward  $-3\sigma$  variation of  $pt_{\text{cut-off}}$  value, the red lower line is for upward  $+3\sigma$  variation.

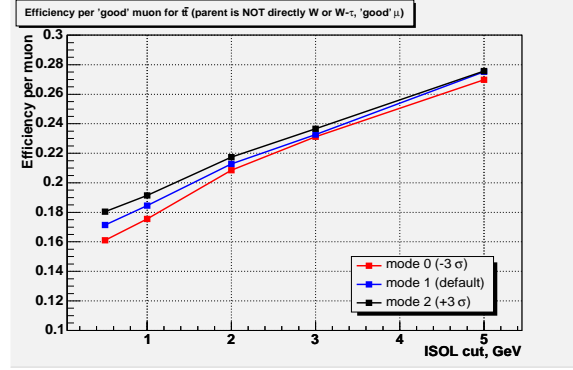


Fig. 115: Similar to Fig. 114 for muons from hadronic decays ( $t\bar{t}$  events).

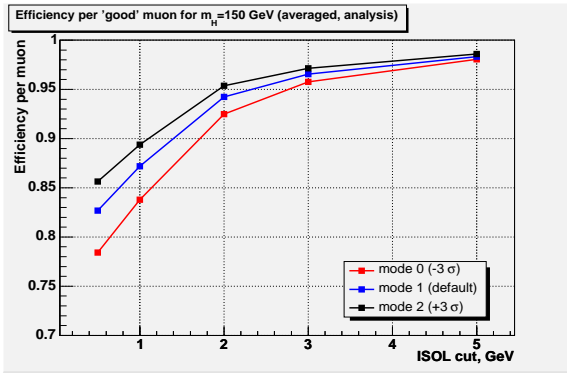


Fig. 116: Similar to Fig. 114 for Higgs boson events.

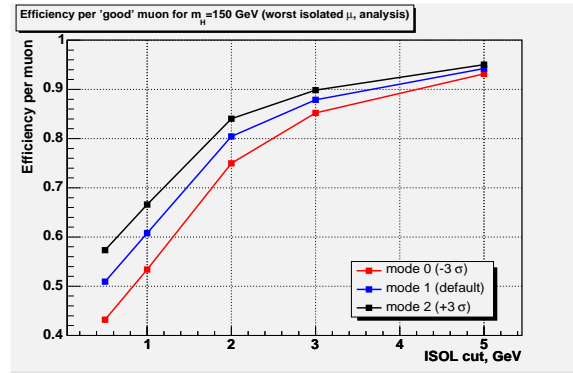


Fig. 117: Muon isolation cut efficiency for the least isolated muon from 4 selected ones in Higgs boson events.

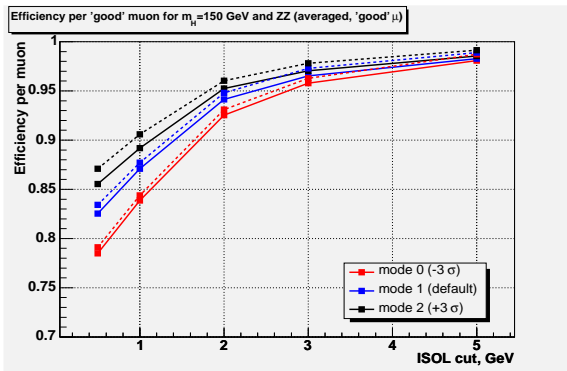


Fig. 118: Muon isolation cut efficiency averaged over 4 selected muons for signal events (solid lines, Fig. 116) and ZZ background (dashed lines). The blue middle line is for the default MI  $pt_{\text{cut-off}}$ , the black upper line is for downward  $-3\sigma$  variation of  $pt_{\text{cut-off}}$  value, the red lower line is for upward  $+3\sigma$  variation.

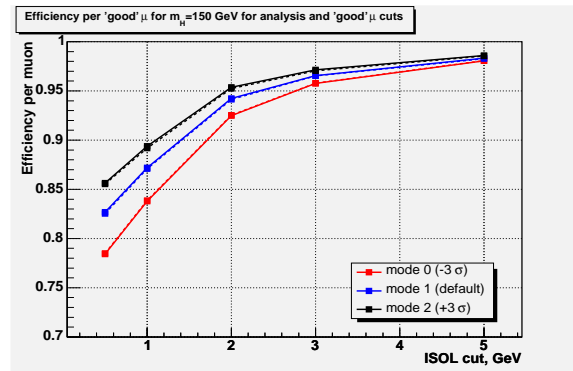


Fig. 119: Muon isolation cut efficiency averaged over 4 selected muons for signal events. Solid lines are for good muons from events after analysis cuts (same as Fig. 116) and dashed lines are for good muons from events before analysis cuts. There is no difference at statistical precision level for two graph sets. Color notations are the same as for Fig. 118.

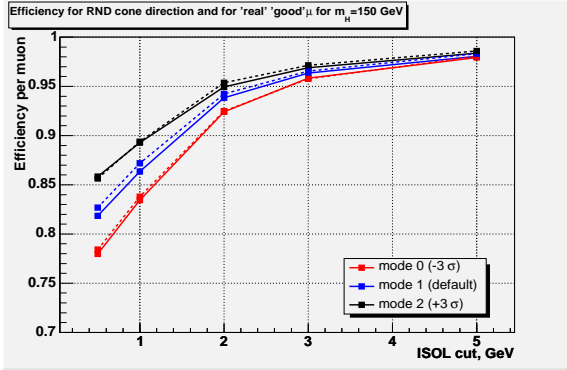


Fig. 120: Muon isolation cut efficiency for random-cone directions (solid lines) and for muons (dashed lines) for signal events. The blue middle lines are for the default MI  $pt_{\text{cut-off}}$ , the black upper lines are for downward  $-3\sigma$  variation of  $pt_{\text{cut-off}}$  value, the red lower lines are for upward  $+3\sigma$  variation.

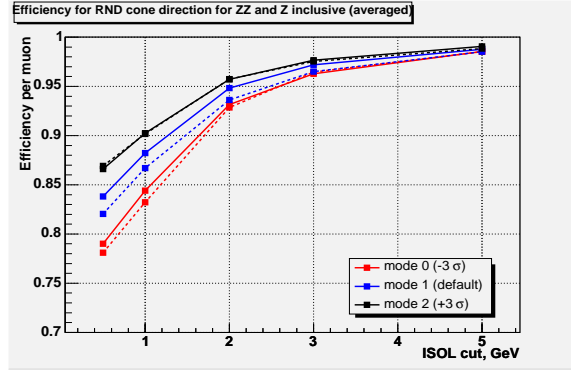


Fig. 121: Muon isolation cut efficiency for random-cone directions for Z-inclusive (dashed lines) and for ZZ (solid lines) events. The blue middle lines are for the default MI  $pt_{\text{cut-off}}$ , the black upper lines are for downward  $-3\sigma$  variation of  $pt_{\text{cut-off}}$  value, the red lower lines are for upward  $+3\sigma$  variation.

### 21.52 Evaluation of the muon isolation cut efficiency from data using random-cone directions

Figure 120 shows the isolation cut efficiency as calculated for random directions uniformly distributed in  $\eta - \phi$  space ( $|\eta| < 2.4$ ). The algorithm of the ISOL parameter calculation is the same as for “real” MC muons, except that now the ISOL parameter is calculated from the sum of PT for tracks around random directions in the acceptance region. The Higgs boson Monte Carlo sample was used to make these plots. We see that the graphs obtained for the random cone (solid lines) and for “real” muons (dashed line; identical to Figures 116 and 119) look very similar. In fact, they agree within statistical uncertainties. This observation motivated us to investigate whether we can measure the isolation cut efficiency by using some distinct reference data sample and applying the random-cone technique. The reference data sample must have a large cross section (to provide good statistics), be relatively clean from backgrounds, and have a similar underlying structure to ZZ events. Inclusive  $Z \rightarrow \mu\mu$  seems to be just what we need. The cross section is  $\sim 1.6$  nb,  $Z \rightarrow \mu\mu$  has a very clean signature.

Figure 121 shows the isolation cut efficiencies computed for random-cone directions in Z-inclusive Monte Carlo sample. One can see that the isolation cut efficiencies for muons in the ZZ sample are very well mimicked by the efficiencies calculated for random cones in the Z-inclusive sample. The variations in the UE  $pt_{\text{cut-off}}$  have nearly identical effects on both data samples.

### 21.53 $4\mu$ Isolation cut efficiency per event

Efficiencies per event are listed in Table 23. We observe that the values for Signal, ZZ-background, and Z-inclusive using random-cone technique samples are in agreement with each other for all three tested UE scenarios. The range of efficiencies for the ZZ-background spans from  $\sim 0.72$  to  $\sim 0.84$ . This range of  $\pm 6\%$  absolute of the central value can be associated with the uncertainties on the 4-muon isolation cut efficiency arising from theoretical uncertainties on considered UE parameters in PYTHIA.

On the other hand, it appears possible to use the Z-inclusive sample to gauge the UE activity and evaluate the 4-muon isolation cut efficiency experimentally. There might be a small systematic shift of the order of  $\sim 2\%$  in efficiencies between the ZZ and Z-inclusive samples, and this is a shift can be evaluated from data, and the result is then to a large degree independent from a particular UE scenario. For the three different UE simulations we used in these studies, we obtain the following offsets:  $0.018 \pm 0.008$ ,  $0.015 \pm 0.009$ ,  $0.017 \pm 0.007$ . Much larger Monte Carlo samples would be needed to pin it down

Table 23: Efficiency per event using different events samples: Higgs boson signal with  $m_H = 150$  GeV, ZZ background, Z-inclusive (4 RND muons),  $t\bar{t}$  background. “4 RND muons” means that for a particular process in each event 4 random cone directions were used to calculate the ISOL parameter and the corresponding values were treated as ones for “real” muons.

process/case	efficiency (default)	efficiency ( $-3\sigma$ )	efficiency ( $+3\sigma$ )
signal, $m_H = 150$ GeV	$0.775 \pm 0.004$	$0.707 \pm 0.005$	$0.812 \pm 0.004$
ZZ background	$0.780 \pm 0.004$	$0.721 \pm 0.005$	$0.838 \pm 0.004$
4 RND muons, Z-inclusive events	$0.762 \pm 0.007$	$0.706 \pm 0.007$	$0.821 \pm 0.006$
$t\bar{t}$ background	$0.016 \pm 0.001$	$0.013 \pm 0.001$	$0.015 \pm 0.001$

more accurately. However, conservatively, one may ignore this correction and assign a 2% systematic uncertainty on the Z-sample-based estimate of the 4-muon isolation cut efficiency for ZZ-background and Higgs boson signal events as it is already much smaller in comparison to the other systematics such as theoretical uncertainties associated with the choice of PDF’s and QCD scale, NLO/NNLO corrections, etc.

The efficiency for accepting  $t\bar{t}$ -events is of the order of  $0.015 \pm 0.001$ . Its sensitivity to the UE could not be studied due to lack of statistics, but it is not expected to be too large as it is dominated by the jet activity. In fact, if the reducible  $t\bar{t}$ - and  $Zb\bar{b}$ -backgrounds could not be suppressed well below the ZZ-background, one would need to study their sensitivity to the UE physics, as well as to the jet fragmentation modeling.

## 21.6 Summary

The isolation cut efficiency per muon due to uncertainties in the UE can vary as much as  $\pm 5\%$  (the efficiency itself and its uncertainty strongly depend on how tight the ISOL cut is). The 4-muon isolation cut efficiency per event for  $ZZ \rightarrow 4\mu$  background is measured to be  $\sim (78 \pm 6)\%$ .

To decrease these large uncertainties to a negligible level with respect to other systematic uncertainties, one can calibrate the isolation cut efficiency from data using Z-inclusive events ( $Z \rightarrow 2\mu$ ) and the random-cone technique. We show that this indeed significantly decreases uncertainties associated with the poor understanding of the UE physics. There might be  $\sim 2\%$  systematic shift in the 4-muon isolation cut efficiencies obtained this way. In principle, one can correct for this shift, but it does not appear to be necessary as this uncertainty is already very small.

The results and described techniques in this letter may be of interest for all analyses relying on lepton isolation cuts.

## 21.7 Acknowledgments

We would like to thank M. Aldaya, P. Arce, J. Caballero, B. Cruz, G. Dissertori, T. Ferguson, U. Gasparini, P. Garcia, J. Hernandez, I. Josa, M. Konecki, P. Moisenz, E.R. Morales, N. Neumeister, A. Nikitenko, F. Palla and I. Vorobiev for their active participation in the analysis discussions and comments on this letter.

## Part II

# HIGGS PHYSICS

### 22. $gg \rightarrow H$ AT THE LHC: UNCERTAINTY DUE TO A JET VETO <sup>47</sup>

#### 22.1 Overview

The experimental cross section  $\sigma_{meas}$  of the Higgs signal and other final states is given by

$$\sigma_{meas} = N_s / (\epsilon_{sel} \times L_{pp}) \quad (66)$$

with  $N_s$  being the number of signal events,  $\epsilon_{sel}$  the efficiency after all signal selection cuts are applied and  $L_{pp}$  the integrated proton-proton luminosity. In order to get an estimation of the cross section uncertainty, the statistical and systematic uncertainties have to be determined. The systematic uncertainties come from the experimental selection, background and luminosity uncertainties.

In the Higgs mass range between 155 and 180 GeV,  $H \rightarrow WW \rightarrow \ell\nu\ell\nu$  is considered to be the main Higgs discovery channel [296, 312]. The signal consists of two isolated leptons with a small opening angle and large missing  $E_T$ . In order to reduce the top background, a jet veto has to be applied. The signal over background ratio is found to be around 2:1 at a Higgs mass of 165 GeV. For lower and higher Higgs masses, this signal over background ratio decreases slightly [312].

As the signal over background ratio is small in this channel, the systematic uncertainties should be known very well. This study concentrates on the uncertainty of the signal efficiency due to the jet veto. The systematics were obtained using different Monte Carlo simulations.

Three different Monte Carlo generators are compared: PYTHIA 6.319, HERWIG 6.507 and MC@NLO 2.31 [33, 183, 308, 309]. All three are so-called parton shower Monte Carlos.

PYTHIA is a general purpose Leading Order (LO) Monte Carlo, based on LO matrix elements and Lund hadronization. HERWIG is also a Leading Order Monte Carlo based on the Cluster model for hadronization. MC@NLO matches Next-to-Leading Order (NLO) calculations to a parton shower Monte Carlo. Its total cross section is calculated with NLO accuracy. In MC@NLO, HERWIG is used for the showering.

The three Monte Carlos treat the high transverse momentum ( $p_T$ ) region in different ways: PYTHIA includes matrix element corrections in the  $m_{top} \rightarrow \infty$  limit, whereas HERWIG has no hard matrix element corrections included in  $gg \rightarrow H$  so far. MC@NLO includes the NLO matrix elements in an exact way.

For PYTHIA, two different samples have been generated for comparison: One with the default  $Q^2$  ordered showering model and one with the new  $p_T$  ordered showering model. In the beginning, we make the comparisons with the default  $Q^2$  ordered showering and then also include the new  $p_T$  ordered showering model.

In the following, the pdf set chosen for HERWIG and PYTHIA is CTEQ5L, while for MC@NLO CTEQ5M is taken. Jets are reconstructed using an iterative cone algorithm with cone size 0.5. The leading particle (seed) of the jet has to have a  $p_T$  higher than 1 GeV. The  $|\eta|$  of the jet should be smaller than 4.5 (here the CMS detector acceptance is chosen [341]). An event is rejected if it contains a jet with a  $p_T$  higher than 30 GeV. The Higgs mass for this study is chosen to be 165 GeV, which is the region where the best signal over background ratio can be found. The top mass is set to 175 GeV. First, all events are studied without considering the underlying event. Finally, PYTHIA is also studied including different underlying event schemes.

A similar study was done in the content of the HERA/LHC workshop, with the CASCADE pro-

---

<sup>47</sup>Contributed by: G. Davatz, A. Nikitenko



gram included in the comparison [342]<sup>48</sup>.

At LO, the  $p_T$  of the Higgs is zero. However, parton shower Monte Carlos emit soft gluons which balance the Higgs boson and introduce a transverse momentum in LO parton shower Monte Carlos. As the Higgs is balanced by jets, the transverse momentum is very sensitive to the jet veto and therefore also the efficiency of a jet veto depends strongly on  $p_T$  Higgs.

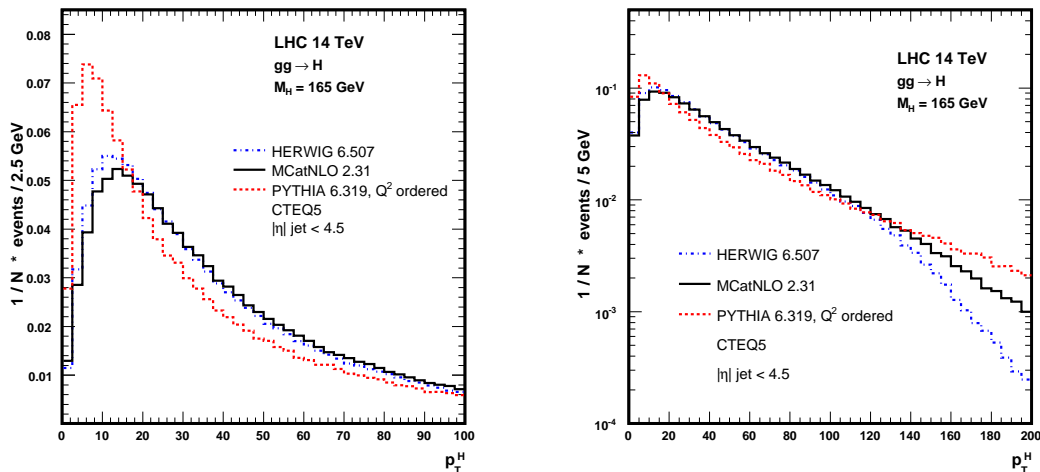


Fig. 122:  $p_T$  Higgs spectra for PYTHIA, HERWIG and MC@NLO in linear and logarithmic scale.

## 22.2 Comparing PYTHIA with $Q^2$ ordered showering, HERWIG and MC@NLO

In this section, PYTHIA with the default  $Q^2$  ordered showering, HERWIG and MC@NLO is compared. In Fig. 122, the normalized  $p_T$  Higgs spectra are shown for the three Monte Carlos. In the linear scale, one can see that at low  $p_T$ , HERWIG and MC@NLO are very similar. This can be expected as the soft and collinear emissions of MC@NLO are treated by HERWIG. In the low  $p_T$  region, PYTHIA predicts a softer leading jet spectrum than HERWIG and therefore also a softer  $p_T$  Higgs spectrum in this region. At high  $p_T$  however, PYTHIA is harder than HERWIG. Figure 123(left) shows the leading jet spectrum in the logarithmic scale. HERWIG implements angular ordering exactly and thus correctly sums the  $LL$  (Leading Log) and part of the  $N^k LL$  (Next-to-Leading Log) contributions. However, the current version of HERWIG, available on the web, does not treat hard radiations in a consistent way. Hence the spectrum drops quickly at high  $p_T$  Higgs (Fig. 122(right)) and high  $p_T$  of the leading jet (Fig. 123(left)). In contrast, PYTHIA does not treat angular ordering in an exact way, but includes hard matrix element corrections. Therefore, PYTHIA looks more similar to MC@NLO at high  $p_T$ . MC@NLO on the other hand correctly treats the hard radiation up to NLO, combining the high  $p_T$  spectrum with the soft radiation of HERWIG.

In Fig. 123(right), the efficiency of the jet veto is shown for the three different Monte Carlos as a function of  $p_T$  Higgs. One observes a strong dependency of the  $p_T$  Higgs on the jet veto. Once a jet veto is defined, the efficiency starts to drop quickly as soon as the  $p_T$  of the Higgs is close to the  $p_T$  used to define a jet veto. However, as the Higgs  $p_T$  can be balanced by more than one jet, the efficiency is not zero above this value.

<sup>48</sup>CASCADE is a full hadron level Monte Carlo generator for ep and pp scattering at small x built according to the CCFM evolution equation [343].

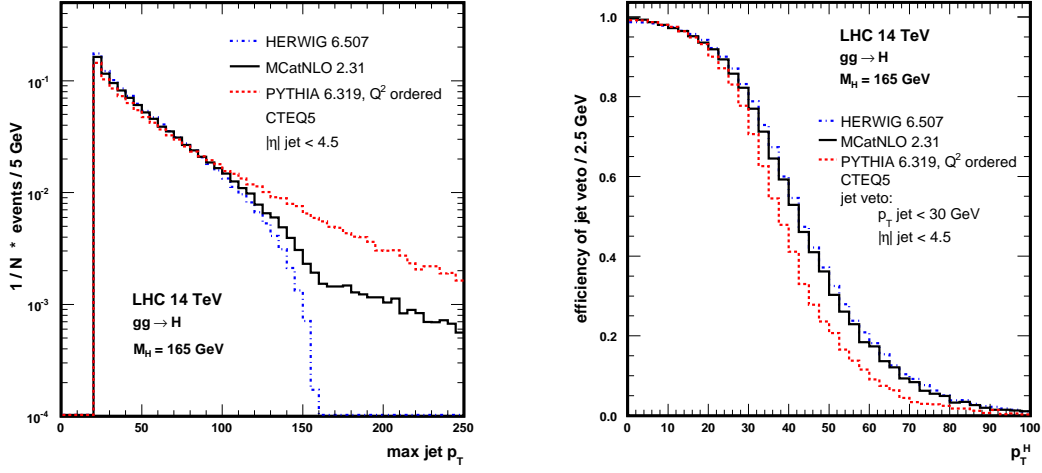


Fig. 123:  $p_T$  of the leading jet for PYTHIA, HERWIG and MC@NLO (left), and efficiency of the jet veto with 30 GeV as a function of  $p_T$  Higgs (right).

### 22.3 HERWIG + matrix element corrections and PYTHIA with new $p_T$ ordered shower model

G. Corcella provided a preliminary version of HERWIG including hard matrix element corrections for  $gg \rightarrow H$  [344]. The hard matrix element corrections lead to harder jets (Fig. 124(left)) and therefore the jet veto is more effective. At high  $p_T$ , PYTHIA and HERWIG become now very similar (Fig. 124(middle)).

Also the new  $p_T$  ordered showering model in PYTHIA is tested. Figure 124(right) shows the  $p_T$  Higgs spectrum for the default  $Q^2$  ordered and the new  $p_T$  ordered showering models. The jets from the new showering model are shifted to higher  $p_T$  in the low  $p_T$  region and therefore also the  $p_T$  of the Higgs boson is more similar to HERWIG and MC@NLO in this region. In Fig. 125, the efficiency after a jet veto is applied (left) and the  $p_T$  Higgs distribution (right) for HERWIG with matrix element corrections, PYTHIA with new  $p_T$  ordered shower model and MC@NLO is shown.

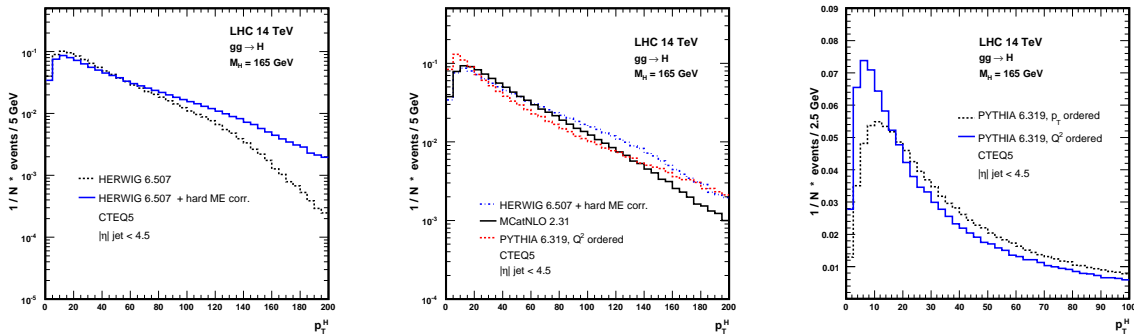


Fig. 124: The  $p_T$  Higgs spectrum for HERWIG with and without hard matrix element corrections (left) and HERWIG with matrix element corrections in comparison with PYTHIA and MC@NLO (middle). On the right, the  $p_T$  Higgs spectrum for the default  $Q^2$  ordered and the new  $p_T$  ordered showering models is shown.

Table 24 shows the number for the efficiency of a jet veto of 30 GeV for MC@NLO, PYTHIA and HERWIG with and without matrix element corrections. In the first row, the number of the efficiency for a

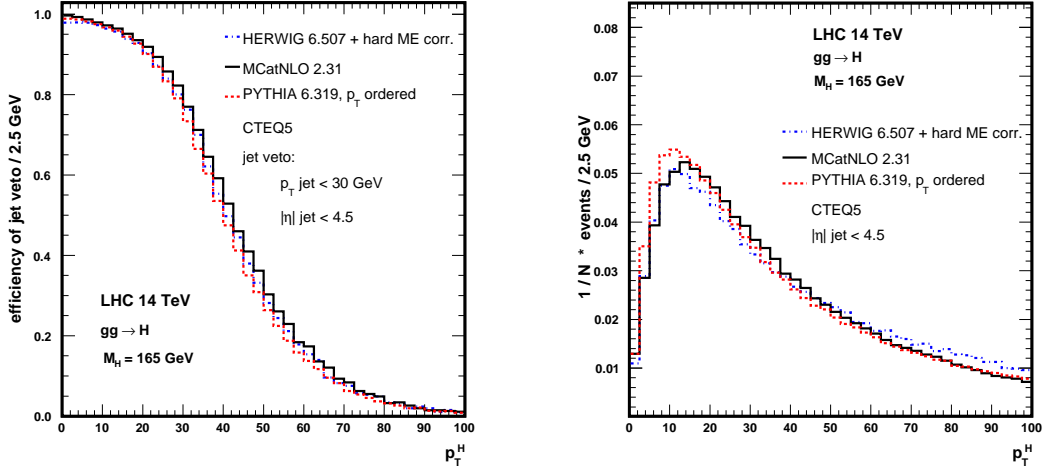


Fig. 125: Efficiency after a jet veto is applied and  $p_T$  Higgs distribution for HERWIG with matrix element corrections, PYTHIA with new  $p_T$  ordered shower model and MC@NLO.

$p_T$  Higgs between 0 and 80 GeV is shown. The second row shows the inclusive efficiency over all events. One has to keep in mind that after all selection cuts are applied, only the low  $p_T$  Higgs region is important [312]. One can see that in the region important for the Higgs search in the WW channel (first row), the difference between the new  $p_T$  ordered PYTHIA version, HERWIG with matrix element corrections and MC@NLO is only around 1%. The overall uncertainty between all these different simulations is around 10%.

Table 24: Efficiency of the jet veto for MC@NLO, PYTHIA with  $Q^2$ - and  $p_T$ - ordered shower models, HERWIG with and without matrix element corrections.

	Efficiency for events with a $p_T$ Higgs between 0 and 80 GeV	Inclusive efficiency (all events)
MC@NLO 2.31	0.69	0.58
PYTHIA 6.319, $Q^2$ ordered	0.73	0.62
PYTHIA 6.319, $p_T$ ordered	0.68	0.53
HERWIG 6.507	0.70	0.63
HERWIG 6.507 + ME Corrections	0.68	0.54

In Ref. [342], the effect of including a realistic detector resolution, NNLO calculations (described in Ref. [312]) and different tunings for the underlying event were studied in addition. As a result, the effect on the jet veto efficiency, when smearing the  $E_T$  of a jet with the jet resolution of e.g. CMS [341], is less than 1%. The uncertainty of the jet veto efficiency does not change significantly including higher order corrections with the re-weighting method described in Ref. [312]. The biggest part of the events is at low  $p_T$ , while the effect of higher order corrections occurs mostly at very high  $p_T$ . PYTHIA with  $Q^2$  showering model was studied with different underlying event tuning schemes, which are the ATLAS Tune [345], CDF Tune A [180] and PYTHIA default (MSTP(81)=1, MSTP(82)=3 [183]). The different tunings lead to about the same efficiency, and also the difference in the efficiency with and without underlying event is less than 1%.

## 22.4 MC@NLO: Effect of varying the factorization and renormalization scale

To get an estimate of the uncertainty due to different factorization and renormalization scales, three MC@NLO samples were produced with scales  $\mu_{\text{fac,rec}}$  between  $M_H/2$  and  $2M_H$ . In Fig. 126(left), the  $p_T$  Higgs spectrum and in Fig. 126(right) the efficiency after a jet veto of 30 GeV is applied are shown for these three samples. The only difference is at very high  $p_t$ , whereas the bulk of the events is at low  $p_T$ . Therefore, as can be seen also in Table 25, the effect of different scales on the jet veto efficiency is negligible.

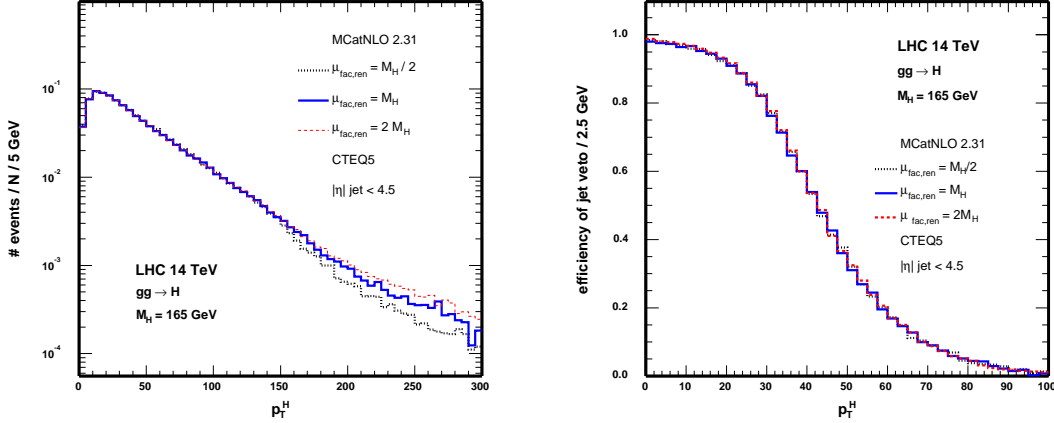


Fig. 126: Number of events and efficiency after a jet veto 30 GeV is applied for MC@NLO with different scale choices.

Table 25: Efficiency of the jet veto for MC@NLO with different scale choices.

	Efficiency for events with a $p_T$ Higgs between 0 and 80 GeV	Inclusive efficiency (all events)
$\mu_{\text{fac,rec}} = M_H/2$	0.685	0.585
$\mu_{\text{fac,rec}} = M_H$	0.692	0.583
$\mu_{\text{fac,rec}} = 2M_H$	0.687	0.582

## 22.5 Conclusions

We have studied the uncertainty of the jet veto efficiency due to the use of different Monte Carlo generators in the  $gg \rightarrow H$  channel. The uncertainty between PYTHIA, HERWIG and MC@NLO without underlying event lies within 10%. Including higher order QCD corrections does not increase this uncertainty significantly. Also the effect of including a realistic jet  $E_T$  resolution (for this study we took the CMS jet  $E_T$  resolution) is very small. We also studied the effect of the underlying event with different tuning models in PYTHIA (PYTHIA default, ATLAS Tune and CDF Tune A). The tuning models considered lead to about the same efficiency and the effect of including underlying events or not is smaller than 1%. Taking into account the new  $p_T$  ordered showering model of PYTHIA and a preliminary version of HERWIG with matrix element corrections reduces the uncertainty in the region which is relevant for the Higgs to WW signal search to 1%.

## Acknowledgements

We would like to thank G. Corcella, M. Dittmar, S. Frixione, M. Seymour and T. Sjostrand for useful discussions and comments.

## 23. COMPARISON BETWEEN MCFM AND PYTHIA FOR THE $gb \rightarrow bh$ and $gg \rightarrow bbh$ PROCESSES AT THE LHC <sup>49</sup>

### 23.1 Introduction

An accurate generation of the  $gb \rightarrow bh$  and  $gg \rightarrow b\bar{b}h$  processes is crucial both for the measurement of the MSSM  $gg \rightarrow b\bar{b}h$ ,  $h \rightarrow 2\tau$  cross section and for constraining  $\tan(\beta)$  from event-counting at the LHC [346]. The production of a MSSM Higgs boson in association with b quarks is the dominant production process at high  $\tan(\beta)$  and for  $M_h > 150\text{-}200 \text{ GeV}/c^2$ . The CMS experimental selections include single b-tagging, a veto on the other jets in the event (excluding  $\tau$  jets), a cut on the angle between the two  $\tau$  leptons in the transverse plane and a cut on the reconstructed mass of the  $\tau$ -lepton pair using the missing transverse energy. Thus, the correct generation of the pseudorapidity and  $p_T$  of the b quarks and the Higgs boson is very important.

In PYTHIA [284], both the  $gb \rightarrow bh$  ( $2 \rightarrow 2$ ) and  $gg \rightarrow b\bar{b}h$  ( $2 \rightarrow 3$ ) processes are available, each of which produces a  $b\bar{b}h$  final state. In the  $gb \rightarrow bh$  process the second b quark ( $\bar{b}$ ) comes from the gluon splitting ( $g \rightarrow b\bar{b}$ ) in the initial state parton shower and is always present in the PYTHIA event.

In this paper we compare the kinematics of the PYTHIA  $2 \rightarrow 2$  and  $2 \rightarrow 3$  processes with the next-to-leading order (NLO) calculations implemented in the MCFM program [347]. The NLO calculations in MCFM start from the leading order (LO)  $gb \rightarrow bh$  process, with the LO  $gg \rightarrow b\bar{b}h$  contribution included as part of the NLO calculation. The LO MCFM calculations were also compared with the PYTHIA  $2 \rightarrow 2$  process when both the initial and final state radiation was switched off.

### 23.2 Simulation setup

The kinematic distributions were compared for two values of the Higgs boson mass,  $m_h=200$  and  $500 \text{ GeV}/c^2$ . PYTHIA 6.227 was used to generate the processes  $gg \rightarrow b\bar{b}h$  (MSUB(121)=1, KFPR(121,2)=5) and  $gb \rightarrow bh$  (MSUB(32)=1 with gluon and b quark as incoming partons). The CTEQ6L1 PDF was used with the renormalization and the factorization scales equal and set to  $\mu_R = \mu_F = (m_h + 2m_b)/4$ . The primordial parton  $k_T$  was switched off in PYTHIA (MSTP(91)=0). To reduce the CPU time, the fragmentation, decays and multiple interactions were switched off in PYTHIA (MSTP(111)=0, MSTP(81)=0). For the  $gb \rightarrow bh$  process, a lower cut of  $20 \text{ GeV}/c$  was set on the  $p_T$  of the outgoing partons in the rest frame of the hard interaction (CKIN(3)=20 in PYTHIA). The jets were reconstructed from the partons using the simple cone algorithm with a cone size of 0.7.

### 23.3 Comparison of PYTHIA and MCFM at leading order

The distributions for the  $gb \rightarrow bh$  process in PYTHIA and LO MCFM were compared. The initial and the final state radiation in PYTHIA was switched off, so that a direct comparison of the LO matrix element implementation in PYTHIA and MCFM could be performed. The distributions of the b quark  $p_T$  and the Higgs boson mass are shown in Figures 127 and 128 respectively, for  $m_h=500 \text{ GeV}/c^2$ . The dashed line shows the PYTHIA distributions, whereas the dotted line shows the MCFM distributions. There is a clear difference between the PYTHIA and MCFM curves. The dominant reason is that, in PYTHIA the matrix elements make use of the kinematic relation  $s + t + u = m_h^2$ . In contrast, MCFM uses  $s + t + u = Q^2$ , where  $Q^2$  is the virtuality of the Higgs boson. This is the appropriate form to use when the Higgs boson is allowed off-shell using the Breit-Wigner approximation; it gives rise to a large discrepancy when the Higgs boson is very far off-shell (for instance,  $Q^2 \gg m_h^2$ ). Corrections to the PYTHIA matrix elements were made by substituting  $Q^2$  for  $m_h^2$  where appropriate<sup>50</sup> and the solid lines in Figures 127 and 128 reflect the PYTHIA results after this change. With the corrected matrix elements the discrepancy between PYTHIA and MCFM is significantly reduced. The remaining difference in the Higgs boson mass distribution is due to the different treatment of the Higgs boson propagator. MCFM

<sup>49</sup>Contributed by: J.M. Campbell, A. Kalinowski, A. Nikitenko

<sup>50</sup>Thanks to T. Sjöstrand for providing the fixed matrix element.

uses the fixed width approach, whereas PYTHIA uses a width which is dependent on  $Q^2$ . In particular, the drop near  $160 \text{ GeV}/c^2$  corresponds to the closure of the WW decay channel for the Higgs boson. This calculation is most useful in the resonance region. Away from the resonance peak, once the decay of the Higgs boson is included contributions from other interfering diagrams (such as ones in which the Higgs is replaced by a Z boson) can change the shape of the prediction.

### 23.4 Comparison of next-to-leading order MCFM and PYTHIA

The comparison between the MCFM NLO predictions and PYTHIA was made when the initial and the final state radiation in PYTHIA was switched on. In all figures shown below the solid line represents the distribution for the PYTHIA  $gb \rightarrow bh$  process generated with the corrected matrix element and  $\hat{p}_T > 20 \text{ GeV}/c$ , the dashed line shows the distribution for the PYTHIA  $gg \rightarrow b\bar{b}h$  process and the dotted line corresponds to the MCFM  $gb \rightarrow bh$  process at NLO.

The  $p_T$  distribution of the highest  $p_T$  b jet with  $|\eta| < 2.4$  is shown in Figure 129 for  $m_h=200 \text{ GeV}/c^2$  and Figure 130 for  $m_h=500 \text{ GeV}/c^2$ . Each of the histograms is normalized to unity in the region  $p_T > 20 \text{ GeV}/c$ . One sees that both PYTHIA processes show good agreement with MCFM.

The efficiency of the central jet veto (after single b tagging) depends, in particular, on the  $p_T$  and  $\eta$  distributions of the second (less energetic) b jet. The  $p_T$  distribution of the second b jet within  $|\eta| < 2.4$  is shown in Figure 131 for  $m_h=200 \text{ GeV}/c^2$  and Figure 132 for  $m_h=500 \text{ GeV}/c^2$ , after requiring that the first (most energetic) b jet be in the tagging range  $p_T^{\text{b jet}} > 20 \text{ GeV}/c$  and  $|\eta^{\text{b jet}}| < 2.4$ . Once again, the histograms are normalized to unity in the region  $p_T > 20 \text{ GeV}/c$ . One can see that the second b jet in the PYTHIA  $gb \rightarrow bh$  process is much softer than in NLO MCFM, while this calculation agrees well with the PYTHIA  $gg \rightarrow b\bar{b}h$  process. This is to be expected since the second b quark ( $\bar{b}$ ) in the  $gb \rightarrow bh$  process is produced by the parton shower in the initial state. At high  $p_T$  one expects the  $2 \rightarrow 3$  process, which is included as a NLO effect in MCFM, to provide a better description and one sees that this is indeed the case.

Figures 133, 134, 135 and 136 show the pseudorapidity distributions for the first and the second b jets for Higgs boson masses of 200 and 500  $\text{GeV}/c^2$ . The content of the histograms is normalized to unity in the  $\eta$  interval between -2 and +2. The PYTHIA distributions for the leading b jet for the Higgs boson mass of 200  $\text{GeV}/c^2$  agree well with the MCFM result (Figure 133), whereas for  $m_h=500 \text{ GeV}/c^2$  the MCFM  $\eta$  distribution is less central than in PYTHIA (Figure 134). The second b jet in the  $gb \rightarrow bh$  process is distributed in the forward/backward direction more in PYTHIA than in MCFM (Figures 135 and 136). This is again due to the aforementioned reason that the second b quark is produced in PYTHIA from the parton shower. The  $\eta$  distribution of the second b jet in the PYTHIA  $gg \rightarrow b\bar{b}h$  process is close to MCFM, but there is still some difference which is more pronounced for  $m_h=200 \text{ GeV}/c^2$  than for  $m_h=500 \text{ GeV}/c^2$ .

The experimental selections include cuts on the visible  $\tau$ -lepton energy, on the angle between the two  $\tau$  leptons in the transverse plane and on the mass reconstructed from the missing transverse energy. Therefore the selection efficiency depends, in particular, on the  $p_T$  spectrum of the Higgs boson. Figures 137 and 138 show the Higgs boson  $p_T$  spectrum after cuts which imitate the experimental selections of single b tagging and a jet veto. These cuts require that:

- the first b jet must lie in the tagging range,  $p_T^{\text{b jet}} > 20 \text{ GeV}/c$  and  $|\eta^{\text{b jet}}| < 2.4$ ;
- no other jets should be observed in the central region,  $p_T^{\text{other jet}} < 20 \text{ GeV}/c$  or  $|\eta^{\text{other jet}}| > 2.4$ .

Since MCFM includes the b quark as a massless particle, predictions are only available when applying a cut on the b quark  $p_T$ . By momentum balance, this means that the Higgs boson transverse momentum is constrained at LO to be greater than the jet cut of  $20 \text{ GeV}/c$ . However, when moving to NLO, the region below this begins to be populated. This feature means that the NLO calculation does not provide reliable predictions in the close vicinity of the jet cut. Therefore we perform the comparison only for  $p_T > 30 \text{ GeV}/c$  and normalize the histograms in Figures 137 and 138 to unity in the  $p_T$  interval between 30 and



200 GeV/c. One can see that the Higgs boson  $p_T$  spectrum calculated to NLO in MCFM is slightly softer than either PYTHIA prediction. The effect on the selection efficiency requires further study but is expected to be small.

### 23.5 Conclusions

A comparison of the shapes of the kinematic distributions of b quarks and the Higgs boson was performed for the PYTHIA  $gb \rightarrow bh$  and  $gg \rightarrow b\bar{b}h$  processes and the  $gb \rightarrow bh$  process implemented at LO and NLO in MCFM. The study was performed for two masses of the Higgs boson, 200 and 500 GeV/c<sup>2</sup>, which lie at either end of the interesting analysis region.

It was observed that the  $p_T$  spectrum of the leading b jet in the PYTHIA  $gg \rightarrow b\bar{b}h$  process is in good agreement with the one obtained from the NLO MCFM  $gb \rightarrow bh$  process. The PYTHIA  $gb \rightarrow bh$  process leads to the second b jet being produced with a softer  $p_T$  spectrum, due to the parton shower. Neither of the two PYTHIA processes agrees exactly with the  $\eta$  spectrum of the b jets in the NLO MCFM  $gb \rightarrow bh$  process, but the PYTHIA  $gg \rightarrow b\bar{b}h$  process shows better agreement. The  $p_T$  spectrum of the Higgs boson in the PYTHIA processes is slightly harder than in NLO MCFM.

The  $p_T$  shapes for the b jet and the Higgs boson were compared for  $p_T^{b \text{ jet}} > 20 \text{ GeV}/c$  and  $p_T^H > 30 \text{ GeV}/c$ . Since the experimental jet energy resolution for 20 GeV jets in CMS is of the order of 40%, it would be very desirable to make a comparison with NLO calculations using a much lower cut-off, for instance  $\simeq 5 \text{ GeV}/c$ . However, such an exercise would require further theoretical input, namely a calculation which extends the MCFM treatment to include effects due to the mass of the final state b quark.

### Acknowledgments

We would like to thank S. Willenbrock, F. Maltoni, M. Spira, M. Krämer and J. Collins for very useful discussions.

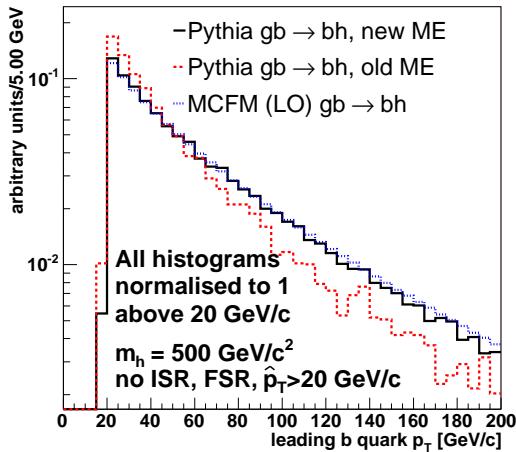


Fig. 127: The  $p_T$  of the b quark in PYTHIA and LO MCFM for  $gb \rightarrow bh$  process,  $m_h=500 \text{ GeV}/c^2$ . See more explanations in the text.

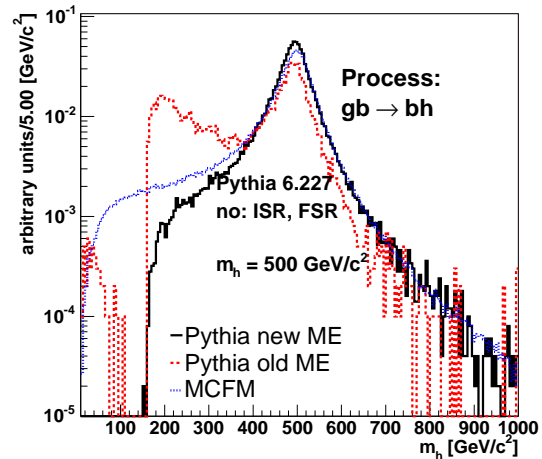


Fig. 128: The Higgs boson mass distribution in PYTHIA and MCFM for  $m_h=500 \text{ GeV}/c^2$ .

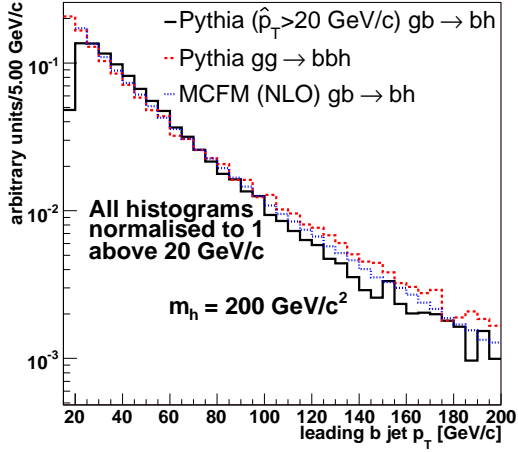


Fig. 129: The  $p_T$  of the leading b jet in PYTHIA and in MCFM for  $m_h=200 \text{ GeV}/c^2$ .

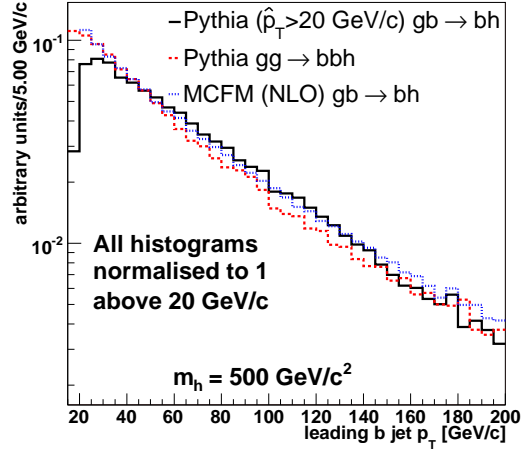


Fig. 130: The  $p_T$  of the leading b jet in PYTHIA and in MCFM for  $m_h=500 \text{ GeV}/c^2$ .

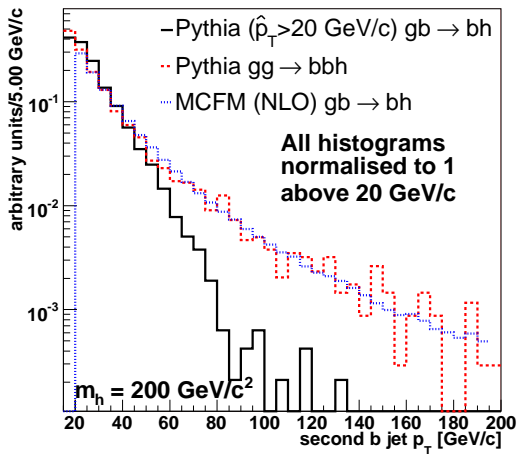


Fig. 131: The  $p_T$  of the second b jet in PYTHIA and in MCFM for  $m_h=200 \text{ GeV}/c^2$ .

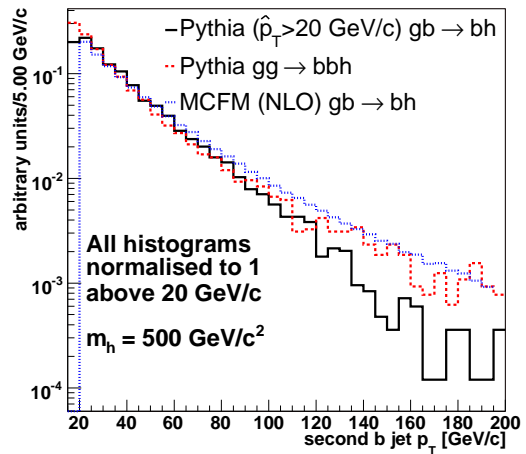


Fig. 132: The  $p_T$  of the second b jet in PYTHIA and in MCFM for  $m_h=500 \text{ GeV}/c^2$ .

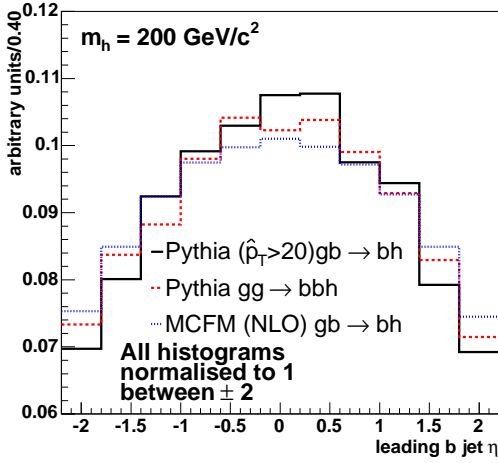


Fig. 133: The  $\eta$  of the leading b jet in PYTHIA and in MCFM for  $m_h=200 \text{ GeV}/c^2$ .

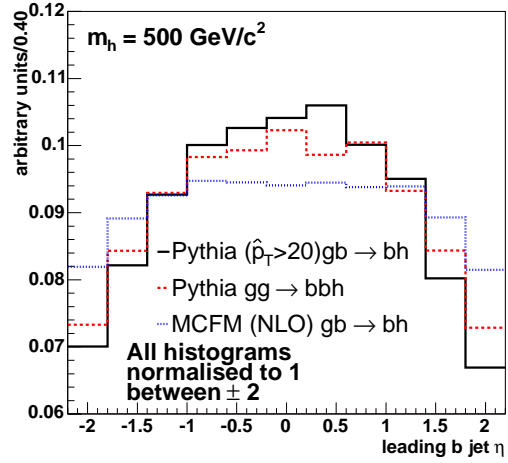


Fig. 134: The  $\eta$  of the leading b jet in PYTHIA and in MCFM for  $m_h=500 \text{ GeV}/c^2$ .

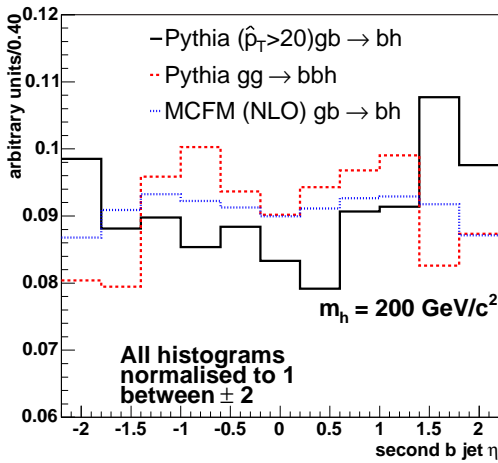


Fig. 135: The  $\eta$  of the second b jet in PYTHIA and in MCFM for  $m_h=200 \text{ GeV}/c^2$ .

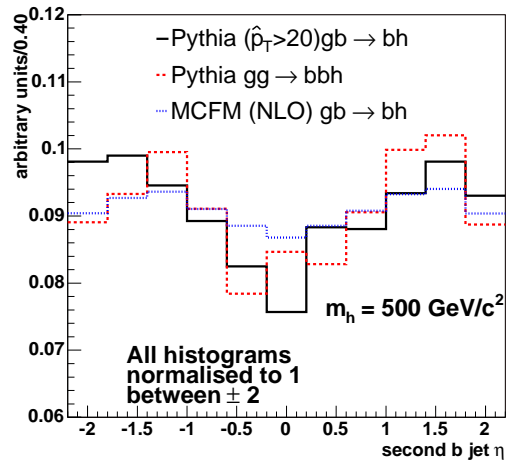


Fig. 136: The  $\eta$  of the second b jet in PYTHIA and in MCFM for  $m_h=500 \text{ GeV}/c^2$ .

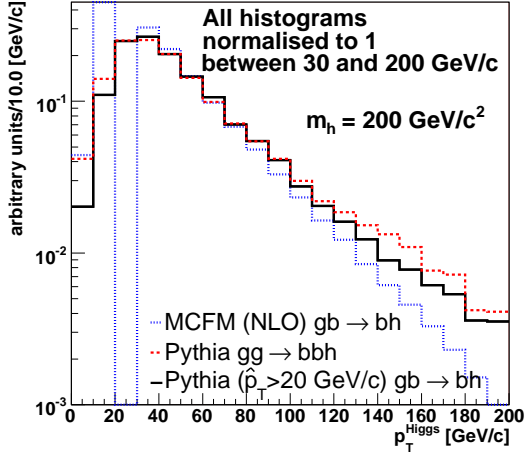


Fig. 137: The  $p_T$  of the Higgs boson for the leading  $b$  jet in the tagging range and no other jets in the central region,  $m_h=200$   $\text{GeV}/c^2$ .

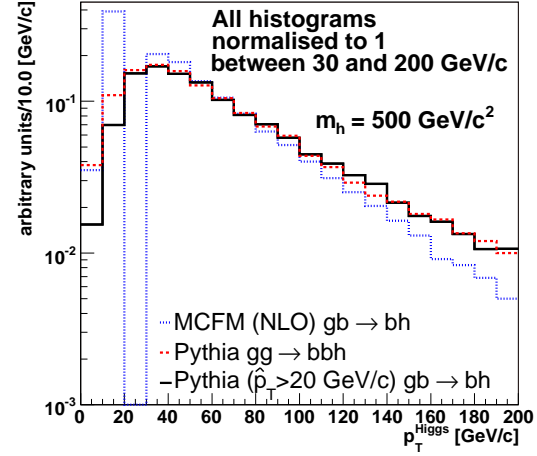


Fig. 138: The  $p_T$  of the Higgs boson for the leading  $b$  jet in the tagging range and no other jets in the central region,  $m_h=500$   $\text{GeV}/c^2$ .

## 24. HIGGS PRODUCTION IN ASSOCIATION WITH BOTTOM QUARKS <sup>51</sup>

### 24.1 Introduction

At large values of  $\tan\beta$ , some or all of the MSSM Higgs bosons have enhanced couplings to bottom quarks. The neutral MSSM Higgs bosons may therefore be copiously produced in association with bottom quarks. There are two different formalisms that have been employed to calculate the cross sections for such processes. The four-flavor scheme begins with  $gg \rightarrow b\bar{b}h$  as the leading-order (LO) process. The cross sections with zero, one, or two high- $p_T$   $b$  jets are known at next-to-leading order (NLO) in QCD [348–351]. In contrast, the five-flavor scheme uses a bottom-quark distribution function in the initial state. The inclusive cross section begins with  $b\bar{b} \rightarrow h$  at LO, and has been calculated at NLO [352–354] and NNLO [355]. The cross section with one high- $p_T$   $b$  jet begins with  $gb \rightarrow hb$  at LO and is known at NLO [347]. The cross section with two high- $p_T$   $b$  jets can only be calculated in the four-flavor scheme.

The five-flavor scheme has two advantages with respect to the four-flavor scheme. Collinear logarithms, proportional to powers of  $\alpha_s \ln(\mu_F/m_b)$  ( $\mu_F$  is the factorization scale), that appear in the four-flavor scheme are resummed to all orders in the five-flavor scheme. Thus one expects a more convergent perturbation series in the five-flavor scheme. The second advantage is that the LO process in the five-flavor scheme is simpler, and makes higher-order corrections tractable. For example, the inclusive cross section for Higgs production in association with  $b$  quarks is known at NNLO in the five-flavor scheme [355], but only at NLO in the four-flavor scheme [348, 351].

Comparisons between calculations of Higgs production in the two schemes have been carried out in Refs. [350, 351, 356]. Generally speaking, the two calculations agree within their respective uncertainties. However, there are various ways in which the comparisons can and should be improved.

Let us focus on the inclusive cross section for Higgs production in association with bottom quarks. A comparison of the four- and five-flavor calculations, taken from the 2003 Les Houches proceedings [356], is shown in Fig. 139. The five-flavor calculation has a smaller uncertainty since it is NNLO, while

<sup>51</sup>Contributed by: J. Campbell, S. Catani, J. Collins, S. Dittmaier, S. Frixione, R. Harlander, W. Kilgore, M. Krämer, L. Magnea, F. Maltoni, S. Moretti, P. Nason, F. Olness, S. Schumann, J. Smith, M. Spira, S. Willenbrock

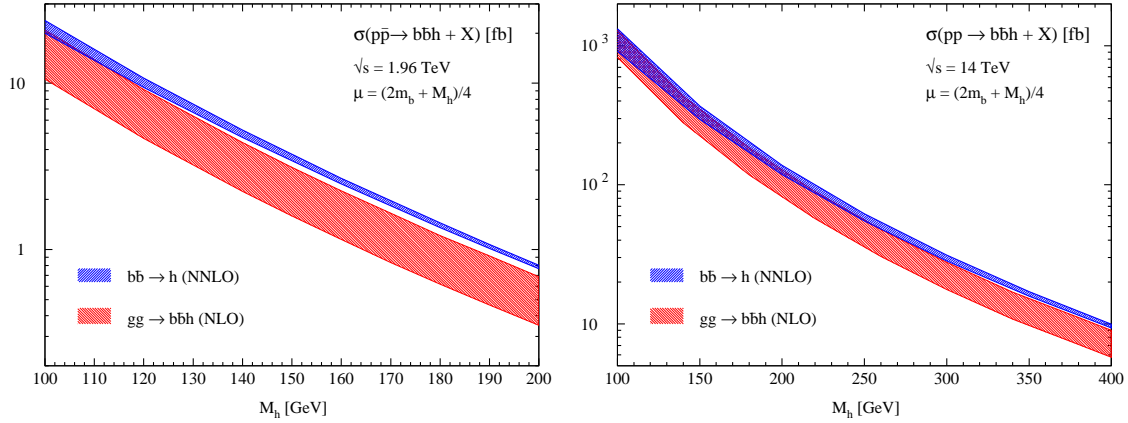


Fig. 139: Inclusive cross sections for  $p\bar{p}(pp) \rightarrow b\bar{b}h + X$  at the Tevatron and the LHC as a function of the Higgs mass  $M_h$ . The error bands correspond to varying the scale from  $\mu_R = \mu_F = (2m_b + M_h)/8$  to  $\mu_R = \mu_F = (2m_b + M_h)/2$ . The NNLO curves are from Ref. [355].

the four-flavor calculation is NLO. Although they are consistent with each other, the five-flavor cross section lies near the top of the uncertainty band of the four-flavor cross section. This may be due in part to the fact that the five-flavor calculation is one order higher, and that it also resums collinear logarithms. However, there are also ways in which the comparison could be made more fairly.

In this review, we discuss some of the ways that the comparison between the four- and five-flavor scheme calculations could be improved. After a review of the formalism, we discuss the effect of a finite  $b$  mass; top-loop diagrams; four- and five-flavor parton distribution functions; and NNLO parton distribution functions. We also estimate the effect of the resummation of collinear logarithms. We conclude with a summary of our results.

## 24.2 Formalism

If the characteristic energy scale  $\mu$  is small compared to the  $b$ -quark mass,  $m_b$ , then the  $b$  quark decouples from the dynamics and *does not* appear as a partonic constituent of the hadron; that is,  $b(x, \mu < m_b) = 0$  and we are working in a four-flavor scheme. In such a scheme, the Higgs is produced in the  $\mathcal{O}(\alpha_s^2)$  process  $gg \rightarrow b\bar{b}h$ . Calculations in the four-flavor scheme have the advantage that they do not need to introduce the  $b$  distribution function.

If instead we consider energy scales much larger than the  $b$ -quark mass ( $\mu \gg m_b$ ), then we work in a five-flavor scheme where the  $b$  quark *does* appear as a partonic constituent of the hadron,  $b(x, \mu > m_b) > 0$ . In this regime, the  $b$ -quark mass enters as powers of  $\alpha_s \ln(\mu^2/m_b^2)$  which are resummed via the DGLAP equations. This scheme has the advantage that it involves lower-order Feynman graphs, and the  $\alpha_s \ln(\mu^2/m_b^2)$  terms are resummed.

Ideally, there is an intermediate region where the 4-flavor and 5-flavor schemes are both a good representation of the physics; in this region we can make a transition from the low-energy 4-flavor scheme to the high-energy 5-flavor scheme thereby obtaining a description of the physics that is valid throughout the entire energy range from low to high scales.<sup>52</sup>

When we evolve the  $b$  distribution function in the context of the DGLAP evolution equation  $db \sim P_{b/i} \otimes f_i$ , we have the option to use splitting kernels which are either mass-dependent [ $P_{b/i}(m_b \neq 0)$ ] or mass-independent [ $P_{b/i}(m_b = 0)$ ]. While one might assume that using  $P_{b/i}(m_b \neq 0)$  yields more

<sup>52</sup>We label the four-flavor and five-flavor schemes as “fixed-flavor-number” (FFN) schemes since the number of partons flavors is fixed. The hybrid scheme which combines these FFS is a “variable-flavor-number” (VFN) scheme since it transitions from a four-flavor scheme at low energy to a five-flavor scheme at high energy [357, 358].

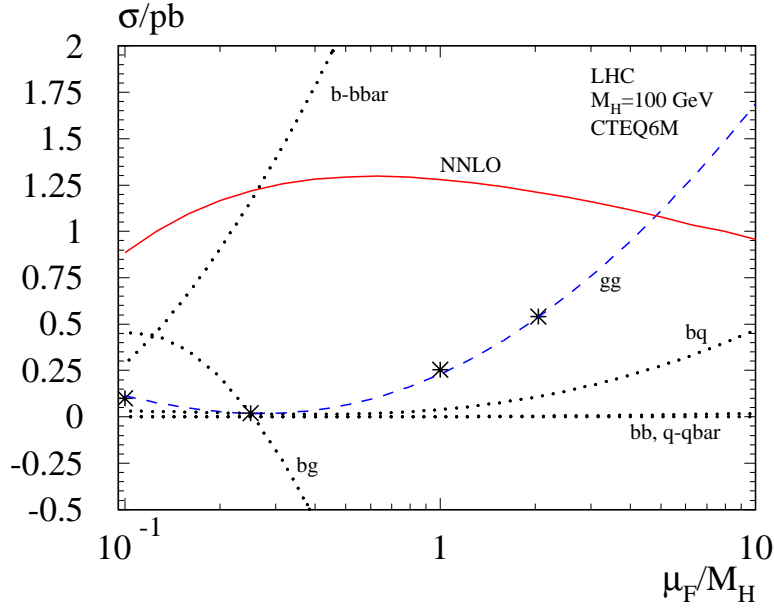


Fig. 140: The cross section for the process  $b\bar{b} \rightarrow h + X$  (LHC,  $m_h = 100$  GeV) at NNLO (solid line), split into the individual sub-processes (dashed and dotted). The markers denote the contribution from the  $gg$  sub-processes, with mass divergences subtracted minimally, and bottom quark mass terms kept in the matrix element calculation.

accurate results, this is not the case. The choice of  $P_{b/i}(m_b \neq 0)$  or  $P_{b/i}(m_b = 0)$  is simply a choice of scheme, and both schemes yield identical results up to high-order corrections [359]. For simplicity, it is common to use the mass-independent scheme since the  $P_{b/i}(m_b = 0)$  coincide with the  $\overline{\text{MS}}$  kernels.

When the factorization proof of the ACOT scheme was extended to include massive quarks, it was realized that fermion lines with an initial or internal “cut” could be taken as massless [360]. This simplification, referred to as the simplified-ACOT (S-ACOT) scheme, is *not* an approximation; it is again only a choice of scheme, and both the results of the ACOT and S-ACOT schemes are identical up to high-order corrections [361]. The S-ACOT scheme can lead to significant technical simplifications by allowing us to ignore the heavy quark masses in many of the individual Feynman diagrams. Furthermore, the mass of the heavy quark in the initial state must be set to zero in order to avoid infrared divergences that appear starting at NNLO [362–366].

### 24.3 Finite $b$ mass

The NNLO calculation of  $b\bar{b} \rightarrow h$  was carried out with  $m_b = 0$  throughout [355]. This is not an approximation at LO or NLO, since all diagrams have at least one  $b$  quark in the initial state. However, at NNLO the process  $gg \rightarrow bbh$  arises, and here the bottom-quark mass may be kept finite. The numerical impact of neglecting the  $b$ -quark mass can be determined by extracting this contribution from the fully massless result of Ref. [355] and comparing it to the terms denoted by “LO+1/ $\ln+1/\ln^2$ ” in Ref. [354], where a finite  $b$ -quark mass was used. In both cases, the mass divergences are subtracted in the  $\overline{\text{MS}}$  scheme, and the difference between them is expected to be of order  $(m_b/m_h)^2$ .

The results for the LHC are shown in Fig. 140, where the dashed line denotes the massless result, and the markers represent individual values read off of the relevant curve in Fig. 7 of Ref. [354]. As expected, the markers hardly deviate from the curve, thus showing that the bottom quark mass effects are indeed negligible.

Another observation is that the  $gg$  channel in the  $\overline{\text{MS}}$  scheme almost vanishes at a factorization



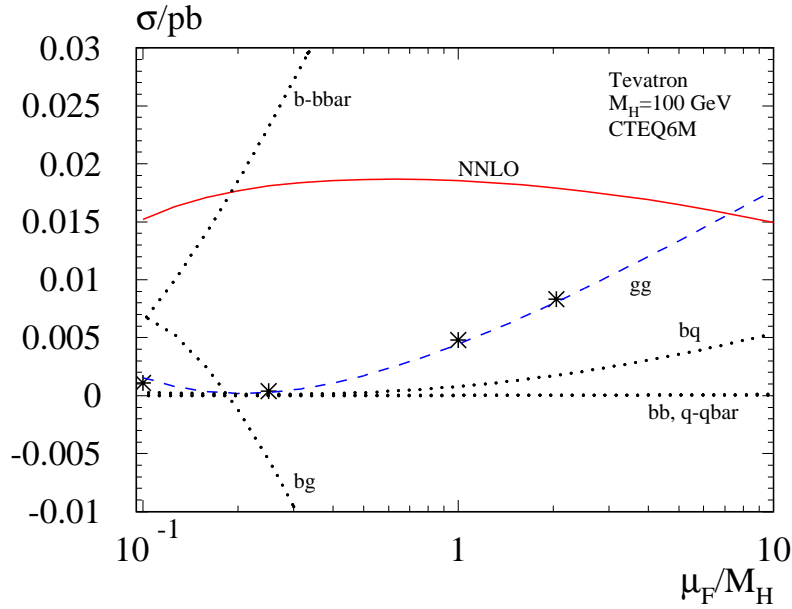


Fig. 141: Same as Fig. 140, but for the Tevatron (1.96 TeV).

scale of  $\mu_F = m_h/4$ ; in fact, this is true for *all* sub-processes (dash-dotted lines), except for the  $b\bar{b}$  channel. This supports  $\mu_F \approx m_h/4$  as the factorization scale for this process, as argued in Ref. [354] based on the collinear behavior of the NLO correction. The solid line is the sum of all sub-processes and thus represents the NNLO result (note, however, that we used a NLO parton density set to make these curves).

The analogous plot for the Tevatron is shown in Fig. 141. Qualitatively, one observes the same behavior as for the LHC, only the factorization scale at which only the  $b\bar{b}$  curve contributes to the rate is a little lower ( $\mu_F \approx m_h/5$ ).

#### 24.4 Top loop

In both the four- and five-flavor schemes, one encounters higher-order diagrams where the Higgs boson couples to a top-quark loop, not to the bottom quark. Such a diagram is shown in Fig. 142. In both schemes it contributes via its interference with the tree diagram  $gg \rightarrow b\bar{b}h$ , which is proportional to  $m_b$  due to the chiral structure of the diagrams. In the comparison of the inclusive cross sections, shown in

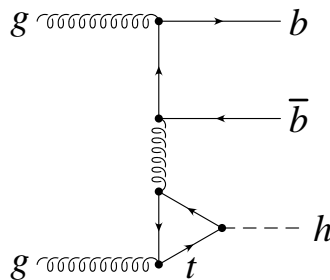


Fig. 142: Higgs production via a top-quark loop. This diagram interferes with the tree diagram for  $gg \rightarrow b\bar{b}h$ .

Fig. 139, this class of diagrams was included in the four-flavor scheme calculation but not in the five-flavor scheme. This contribution is negative, and accounts for about 4% of the difference in the two schemes at the Tevatron, and about 9% at the LHC, for  $m_h = 120$  GeV [356].

Upon further reflection, it seems more appropriate to regard the class of diagrams involving a top loop as being associated with the process  $gg \rightarrow h$ , which also contributes to inclusive Higgs production. The cross sections shown in Fig. 139 do not include this process. From this point of view, the top-loop contribution discussed above is not really a radiative correction to  $gg \rightarrow b\bar{b}h$  (four-flavor scheme) or  $b\bar{b} \rightarrow h$  (five-flavor scheme), but rather an interference between these processes and  $gg \rightarrow h$ . It is common to find that two different LO processes interfere at higher order.

The most systematic way to organize the calculation is in powers of the Yukawa couplings  $y_b$  and  $y_t$ . The inclusive cross section contains terms proportional to  $y_b^2$  and  $y_t^2$ , as well as interference terms proportional to  $m_b y_b y_t$ .

Regardless of one's point of view, a fair comparison of the four- and five-flavor schemes should treat the class of diagrams containing a top-quark loop identically. These diagrams are treated consistently in Refs. [350, 351].

## 24.5 Four- and five-flavor parton distribution functions

A four-flavor calculation should use a four-flavor set of parton distribution functions, that is, one in which there is no  $b$  distribution function. Unfortunately, no such set is available in the standard parton distribution sets. Here we estimate the numerical impact that a four-flavor set would make on the calculation of  $gg \rightarrow b\bar{b}h$ .

To illustrate how the active number of “heavy” flavors affects the “light” partons, in Fig. 143(a) we show the momentum fraction of the gluon vs. the factorization scale  $\mu$ . We have started with a single PDF set at  $\mu = 1.3$  GeV, and evolved from this scale invoking the “heavy” flavor thresholds as appropriate for the specified number of flavors. While all three PDF sets start with the same initial momentum fraction, once we go above the charm threshold ( $m_c = 1.3$  GeV) the  $N_F = \{4, 5\}$  momentum fractions are depleted by the  $g \rightarrow c\bar{c}$  process. In a similar fashion, the momentum fraction for  $N_F = 5$  is depleted compared to  $N_F = 4$  by the  $g \rightarrow b\bar{b}$  channel above the bottom threshold ( $m_b = 5$  GeV).

To gauge the effect of the different number of flavors on the cross section, we compute the gluon-gluon luminosity which is defined as  $d\mathcal{L}_{gg}/d\tau = g \otimes g$ . We choose a scale of  $\mu \approx m_h/4 = 30$  GeV which is characteristic of a Higgs of mass 120 GeV. In terms of the luminosity, the cross section is given as  $d\sigma/d\tau \sim [d\mathcal{L}_{gg}/d\tau] [\hat{\sigma}(\hat{s} = \tau s)]$  with  $\tau = \hat{s}/s = x_1 x_2$ .

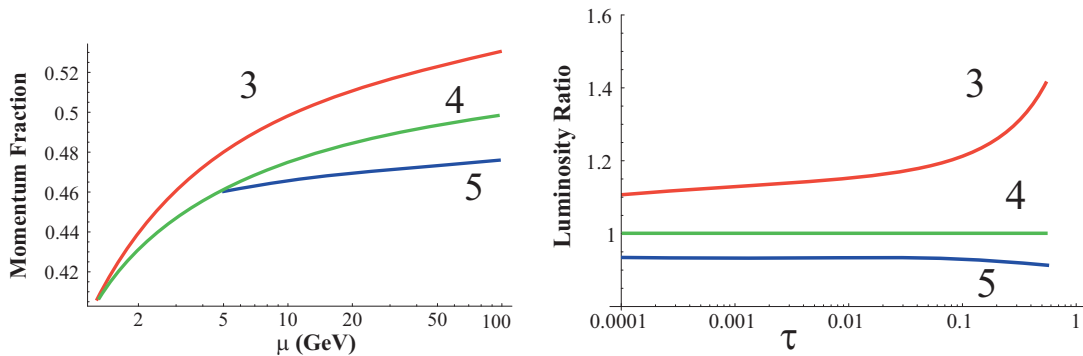


Fig. 143: (a) Integrated momentum fraction,  $\int_0^1 x f_g(x, \mu) dx$  vs.  $\mu$  of the gluon for  $N_F = \{3, 4, 5\} = \{\text{Red, Green, Blue}\}$ . (b) The ratio of the gluon-gluon luminosity ( $d\mathcal{L}_{gg}/d\tau$ ) vs.  $\tau$  for  $N_F = \{3, 4, 5\} = \{\text{Red, Green, Blue}\}$  as compared with  $N_F = 4$  at  $\mu = 30$  GeV.

To highlight the effect of the different  $N_F$  PDF's, we plot the ratio of the luminosity as compared to the  $N_F = 4$  case in Fig. 143(b). We see that the effects of Fig. 143(a) are effectively squared, as expected, when examining the curves of Fig. 143(b).

The blue (bottom-most) curve in Fig. 143(b) shows that by using a five-flavor set in the four-flavor calculation of  $gg \rightarrow b\bar{b}h$ , one is underestimating the cross section by about 7%. While this is not a very large effect, it does go in the correct direction to improve the agreement between the four- and five-flavor calculations of inclusive Higgs production.

## 24.6 NNLO parton distribution functions

The production of heavy quarks in deep-inelastic scattering (DIS) and the incorporation of heavy quarks into parton densities are related and interesting topics. The fixed-flavor NLO QCD corrections to charm quark electro-production were calculated in Ref. [367] in the three-flavor scheme. At high energies, the three-flavor scheme should be replaced by a four-flavor scheme, and eventually a five-flavor scheme. In the intermediate region, a variable flavor number scheme should provide a smooth switch from the three-flavor scheme to the four-flavor scheme. [368]

The treatment of the heavy quark as a parton density requires the identification of the large logarithmic terms  $\log(Q^2/m^2)$ , which was done in Ref. [369] through next-to-next-leading order (NNLO). Then based on a two-loop analysis of the heavy quark structure functions from an operator point of view, it was shown in Refs. [370], [371] and [372] how to incorporate these large logarithms into charm (and bottom) densities. Two different NNLO variable flavor number schemes were defined in Refs. [373] and [374], where it was shown how they could be matched to the three-flavor scheme at small  $Q^2$ , the four-flavor scheme at large  $Q^2$ , and the five-flavor scheme at even larger  $Q^2$ .

This NNLO analysis yielded two important results. One was the complete set of NNLO matching conditions for massless parton evolution between  $N$  and  $N + 1$  flavor schemes. Unlike the NLO case, the NNLO matching conditions are discontinuous at these flavor thresholds. Such matching conditions are necessary for any NNLO calculation at the LHC, and have already been implemented in parton evolution packages by [375], [376] but unfortunately not yet in the programs which make global fits to experimental data. Note that the NNLO matching conditions on the running coupling  $\alpha_s(N_F, Q^2)$  as  $Q^2$  increases across heavy-flavor flavor thresholds have been calculated in [377, 378] and [379, 380]. Furthermore, the NNLO two-loop calculations above explicitly showed that the heavy quark structure functions in variable flavor approaches are not infrared safe. A precise definition of the heavy-flavor content of the deep inelastic structure function requires one to either define a heavy quark-jet structure function, or introduce a fragmentation function to absorb the uncanceled infrared divergence. Similar issues arise for inclusive  $Z$  production in association with heavy quarks [381]. In either case, a set of contributions to the inclusive light parton structure functions must be included at NNLO.

A dedicated analysis [382] for charm electro-production showed that even at relatively large  $Q^2$  one could not distinguish between the fixed order NLO calculation of [367] and the NNLO VFNS calculation of [371], given the large error bars on the experimental data then available in the year 2000. This demonstrates that terms in  $\ln(Q^2/m^2)$  in fixed flavor number schemes are proportional to the convolution of small terms and therefore do not necessarily make a large contribution to the deep-inelastic cross section. To quantify this statement one requires more precise data from the HERA collider on charm and bottom quark electro-production analyzed in both fixed-flavor and variable flavor schemes. Since there is an increasing use of variable flavor schemes with massless charm and bottom parton densities in hadronic collisions it is important to clarify this topic.

## 24.7 Resummation

The fundamental difference between the  $gg \rightarrow b\bar{b}h$  process and the  $b\bar{b} \rightarrow h$  process amounts to whether the radiative splittings (e.g.,  $g \rightarrow b\bar{b}$ ) are computed by the DGLAP equation as a part of the parton evo-

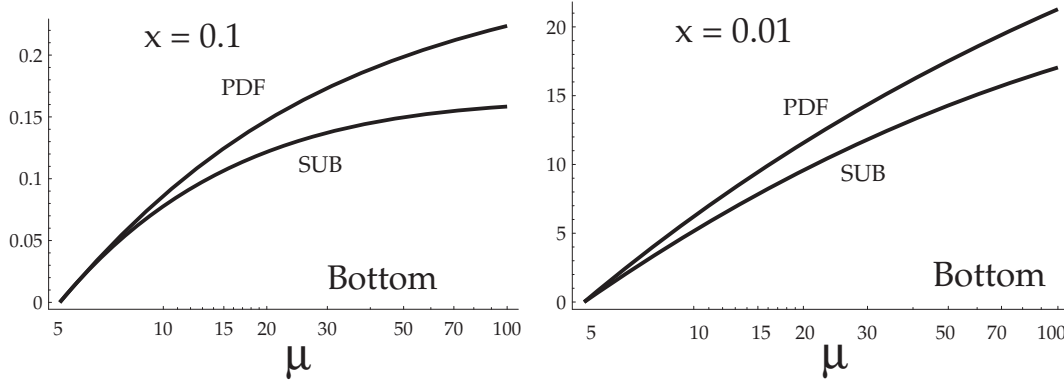


Fig. 144: Comparison of the evolved PDFs,  $b(x, \mu)$  (labeled PDF), and perturbative PDFs,  $\tilde{b}(x, \mu) \sim P_{b/g} \otimes g$  (labeled SUB), as a function of the renormalization scale  $\mu$  for bottom at a)  $x = 0.1$  and b)  $x = 0.01$ .

lution, or whether they are external to the hadron and computed explicitly. In essence, both calculations are represented by the same perturbation theory with two different expansion points; while the full perturbation series will yield identical answers for both expansion points, there will be differences in the truncated series.

To understand the source of this difference, we examine the contributions which are resummed into the  $b$ -quark distribution function by the DGLAP evolution equation,  $df \sim P \otimes f$ . Solving this equation perturbatively in the region of the  $b$ -quark threshold, we obtain  $\tilde{b} \sim P_{b/g} \otimes g$ . This term simply represents the first-order  $g \rightarrow b\bar{b}$  splitting that is fully contained in the  $\mathcal{O}(\alpha_s^2) gg \rightarrow b\bar{b}h$  calculation.

In addition to this initial splitting, the DGLAP equation resums an infinite series of such splittings into the perturbatively-evolved PDF,  $b$ . Both  $b$  and  $\tilde{b}$  are shown in Fig. 144 for two choices of  $x$  [383]. Near threshold, we expect  $b$  to be dominated by the single splitting contribution, and this is verified in the figure. In this region,  $b$  and  $\tilde{b}$  are comparable, and we expect the four-flavor  $gg \rightarrow b\bar{b}h$  calculation should be reliable in this region.

As we move to larger scales, we see  $b$  and  $\tilde{b}$  begin to diverge at a few times  $m_b$  since  $b$  includes higher-order splitting such as  $\{P^2, P^3, P^4, \dots\}$  which are not contained in  $\tilde{b}$ . We expect the five-flavor  $b\bar{b} \rightarrow h$  calculation should be most reliable in this region since it resums the iterative splittings.

Fig. 144 shows that the resummation is a bigger effect at larger values of  $\mu$ , as expected. This may explain why the five-flavor curves in Fig. 139 deviate more from the four-flavor curves at larger values of the Higgs mass. Fig. 144 also shows that the resummation is a bigger effect at larger values of  $x$ , which may explain why the Tevatron curves deviate more from each other than the LHC curves.

This analysis also explains a puzzling difference between the two formalisms. The  $b\bar{b} \rightarrow h$  calculation appears to be affected by Sudakov logarithms due to soft and collinear gluon emission, yielding for example terms of the form  $\alpha_s^2 \log^4 N$  at NNLO, with  $N$  the Mellin variable conjugate to  $m_h^2/\hat{s}$ . The presence of these logarithms would suggest the need to perform a resummation. In the  $gg \rightarrow b\bar{b}h$  calculation, however, Sudakov logarithms are subleading because each final-state quark provides a suppression factor, roughly  $1 - m_h^2/\hat{s}$  as  $\hat{s} \rightarrow m_h^2$ , corresponding to a  $1/N$  suppression of the Mellin transform. However, this is not a real difference, just a rearrangement the perturbative series: in the  $b\bar{b} \rightarrow h$  calculation, the  $1/N$  suppression factors are provided by the  $b$ -quark distribution, which is evaluated perturbatively, and acquires a  $1/N$  factor through the Mellin transform of the splitting kernel  $P_{b/g}$ .

## 24.8 Conclusions

In this review we have discussed a few improvements that could be made in the calculation of Higgs production in association with bottom quarks in the four- and five-flavor schemes. A consistent treatment of top-quark loop diagrams would improve the agreement between the inclusive cross sections, shown in Fig. 139, by 4% at the Tevatron and 9% at the LHC for  $m_h = 120$  GeV. We estimate that using a four-flavor set of parton distribution functions in the four-flavor calculation would improve the agreement by about another 7%. We showed that using a finite  $b$  mass in the NNLO five-flavor calculation has no numerical impact. The NNLO parton distributions used in that calculation could be improved by implementing a proper matching at heavy-flavor thresholds, but we cannot estimate what the numerical impact will be. Finally, we discussed how resummation could explain some of the features of the comparison between the four- and five-flavor calculations.

## 25. ASSOCIATED $t\bar{t}H$ PRODUCTION WITH $H \rightarrow \gamma\gamma$ AT THE LHC <sup>53</sup>

### 25.1 Introduction

A Standard Model or two-doublet neutral Higgs boson produced in association with a  $t\bar{t}$  pair, with  $H(h^0) \rightarrow \gamma\gamma$  would share a fully reconstructible mass peak with the inclusive  $H(h^0) \rightarrow \gamma\gamma$  signature. But like the other associated-production channels  $WH$  and  $ZH$  [384], the signature could contain an isolated high-transverse-momentum charged lepton which can be used both to discriminate against QCD background and reconstruct the primary vertex; the associated production channels could hence be less dependent on photon energy resolution. In particular, the presence of two top quarks would tend to produce high-multiplicity events, which could offer additional discriminating power against light jet QCD background. And in the case of the two-doublet MSSM the gluon fusion Higgs production channel could in fact be subject to suppression with respect to the associated production channels in the case of top-stop degeneracy ("maximal mixing") [385]. Prior generator-level studies for the detection of the SM ([386]) and MSSM [387] Higgs bosons in CMS [388] via this channel have indicated a signal-to-background ratio of approximately 1. A full simulation study in the ATLAS Physics Technical Design Report [389] has predicted a signal significance of  $S/\sqrt{B} = 4.3-2.8$  for  $m_H = 100-140$  GeV with a signal efficiency of  $\sim 30\%$ . A more recent, related ATLAS study involving a 2-photon signature accompanied by missing energy [390] has indicated, for  $100 \text{ fb}^{-1}$  a signal-to-background ratio of  $\sim 2$  for  $m_H = 120$  GeV.

### 25.2 Signal production cross-sections and event rates

Production cross-sections for  $t\bar{t}H$  have been calculated at next-to-leading order [391–393]. Taking the branching ratio for  $H \rightarrow \gamma\gamma$  from HDECAY [394] and assuming in addition that the decay of one of the top quarks yields a lepton (electron or muon) from  $W^\pm \rightarrow l + \nu_l$  (including the possibility of tau lepton decays to muons or electrons), we estimate for several Higgs boson masses the number of signal events for 30 and  $100 \text{ fb}^{-1}$  (Table 26):

Table 26: Estimated number of signal events for  $t\bar{t}H, H \rightarrow \gamma\gamma$ , assuming NLO production cross sections [392], Higgs branching ratios to 2 photons [394], and 1 electron or muon from top decay (including from tau lepton decays).

Higgs Mass (GeV)	After $30 \text{ fb}^{-1}$	After $100 \text{ fb}^{-1}$
115	20.75	69.18
120	19.53	65.10
130	15.92	53.05
140	11.18	37.28

Figure 145 shows typical Feynman diagrams of the signal process.

<sup>53</sup>Contributed by: S. Dittmaier, R. Frazier, S. Gascon-Shotkin, M. Krämer, F. Maltoni, D. Mercier, M. Moretti, A. Nikitenko, F. Piccinini, R. Pittau, M. Spira

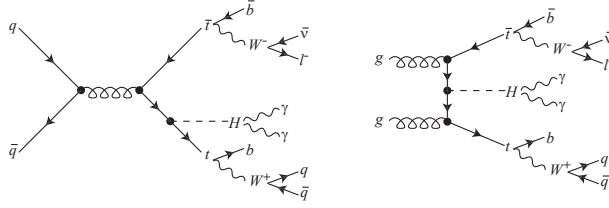


Fig. 145: Typical s- and t-channel diagrams for  $t\bar{t}H$  production with  $H \rightarrow \gamma\gamma$  and at least one charged lepton from the decay of a top or antitop quark.

Signal events were generated with both the MADGRAPH [325,395,396] and ALPGEN [397–399] LO exact matrix element generators, for each of the Higgs masses shown in Table 1 (at least 30000 events per mass value with statistical error below 1%). Events from both generators were found to yield comparable LO cross-section results and kinematical distributions. The LO cross-sections were also found to agree with those from the program HQQ [400] at the percent level.

It should be noted that for the current study all signal events have been generated such that exactly one of the two W bosons from the two top quarks decays leptonically. It can be assumed, however, that the event selection which will be described below will also have some efficiency for events where both W bosons yield leptons, thus potentially increasing the total number of signal events expected to be observed. This will be evaluated in a later study.

### 25.3 Identified background processes and event generation

Standard Model processes resulting in both irreducible and reducible backgrounds have been identified. A background is called irreducible if it is capable of giving rise to the same signature on the particle level as that searched for in a signal event, that is to say, a lepton and two photons ( $l\gamma\gamma$ ). Among the irreducible processes, special care has been taken to properly treat the  $t\bar{t}\gamma\gamma$  background. Feynman diagrams of three possible types of  $t\bar{t}\gamma\gamma$  processes considered are shown in Figure 146. In the first case, called “Type 1”, both photons are radiated from either outgoing top quark or incoming parton lines. In the third case, called “Type 3”, both are radiated from top quark decay products. The second case, “Type 2” combines one photon radiated according to “Type 1” with the second radiated according to “Type 3”. (A fourth process arises from both photons being radiated from different decay products of the *same* top quark; for the relevant event selection (see pertinent section below) with  $m_{\gamma\gamma} > 70$  GeV we have verified that this contribution is completely negligible). Since at the time of undertaking the study no matrix element generator included either the Types 2 or 3 processes, a collaboration was begun with the authors of ALPGEN to add them. Also added to ALPGEN was the process  $W\gamma\gamma + 4$  jets. The performance of this sample versus an inclusive  $W\gamma\gamma$  sample (with all possible extra jets coming from parton showering), also considered, is evaluated in subsequent sections. Where applicable in the ALPGEN samples, top quarks and W bosons are decayed within ALPGEN which assures preservation of spin correlation information which could impact kinematical distributions.

Table 27 lists the considered irreducible background processes, the generators used to either generate or cross-check event samples, the LO cross-section with statistical errors, the number of events expected for 30 (100)  $\text{fb}^{-1}$  of integrated luminosity, the number of events generated and the statistical weight of each generated event for 30 (100)  $\text{fb}^{-1}$  of integrated luminosity. The cross-sections reflect preselection criteria imposed at generator-level which are described in the next section. In the processes involving real top quarks as well as in the  $W\gamma\gamma + 4j$  process, one top quark/the W boson was forced to decay leptonically, and the stated cross-section therefore implicitly includes the relevant branching ratio. It can be seen that the effect of the inclusion of background Types 2 and 3 is to augment the total initial contribution (before selection) from  $t\bar{t}\gamma\gamma$  by approximately one order of magnitude.

A background is called reducible if at least one element of the final-state signature is mistakenly



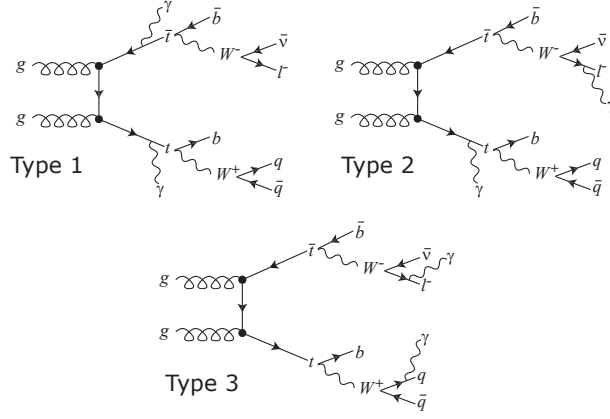


Fig. 146: A subsample of the relative Feynman graphs illustrating the three types of  $t\bar{t}\gamma\gamma$  processes.

Table 27: Cross-sections at leading order (statistical errors in parentheses), number of events generated, numbers of events and statistical weight/generated event for 30 and 100  $\text{fb}^{-1}$  of integrated luminosity for the irreducible backgrounds considered.

Process	$\sigma \times \text{BR}$ (1 $W \rightarrow l\nu$ )	Ngen	N 30 $\text{fb}^{-1}$	Wgt 30 $\text{fb}^{-1}$	N 100 $\text{fb}^{-1}$	Wgt 100 $\text{fb}^{-1}$	Generator
$tt\gamma\gamma$ 1	1.6 fb ( $\leq 1/\text{mil}$ )	9296	48	.0052	160	.0172	AL, MG
$tt\gamma\gamma$ 2	6.1 fb ( $\leq 1\%$ )	2310	183	.0792	610	.2641	AL
$tt\gamma\gamma$ 3	4.9 fb ( $\leq 1\%$ )	914	147	.1608	490	.5361	AL
$bb\gamma\gamma$	318.1 fb	159829	9543	.0597	31810	0.1990	MG
$W\gamma\gamma$ 4j	11.5 fb (1.2%)	4587	345	0.0752	1150	.2507	AL
$Z\gamma\gamma$	29.0 fb	50005	870	0.0174	2900	0.0580	MG
$W\gamma\gamma$	23.6 fb	112000	708	0.0063	2360	0.0211	MG

identified due to incomplete detector coverage or other instrumental effects. This could arise if one or more electrons or jets are misidentified as photons, or a jet as an electron or a muon. Therefore possible background processes can be grouped into the following signature categories:  $ll\gamma$ ,  $llj$ ,  $ljj$ ,  $l\gamma j$ ,  $\gamma\gamma j$ ,  $\gamma jj$ ,  $jjj$ , where  $l$  is a lepton and  $j$  is a jet. Table 28 lists the reducible background processes to be considered for each category. It should be noted that several processes could contribute to more than one signature category.

During the time horizon of the workshop, due to the implementation of the many new generator processes, it has been possible to study only the irreducible backgrounds with acceptable statistics, so only these will be presented in this report. Low-statistics tests on most of the processes in Table 28 have been performed, and as many of these processes as possible will be included with high statistics in a definitive study now in progress with events fully simulated and reconstructed in the CMS detector.

All generated signal and background events were fragmented and hadronized with PYTHIA [27, 284] version 6.227.

## 25.4 Description of preselections

No generator-level preselections were made on signal events. For the irreducible background events, the following preselection was made:

- $m_{\gamma\gamma} \geq 80 \text{ GeV}$  + where applicable:
- $p_{T\gamma} \geq 20 \text{ GeV}$ ,  $|\eta_{\gamma}| \leq 2.5$  or  $p_{T\gamma} \geq 15 \text{ GeV}$ ,  $|\eta_{\gamma}| \leq 2.7$
- $p_{Tj,l,b} \geq 15 \text{ GeV}$ ,  $|\eta_{j,l,b}| \leq 2.7$ ,  $\Delta R(l,j \text{ or } j,j \text{ or } b,b \text{ or } \gamma,j \text{ or } \gamma,\gamma) \geq 0.3$

where  $p_T$  refers to the transverse momentum of the particle,  $\eta$  its rapidity and  $\Delta R = \sqrt{(\Delta\eta^2 + \Delta\phi^2)}$  where  $\phi$  is the azimuthal angle.

Table 28: Identified reducible background processes to be considered for each signature category.

Signature	Process
$\gamma\gamma j$	$m\gamma + \text{njets}$
$l\gamma$	$ll\gamma$
$l\gamma j$	$W(Z)\gamma + \text{njets}$
	$b\bar{b}\gamma + \text{njets}$
	$t\bar{t}\gamma + \text{njets}$
$\gamma jj$	$m\gamma + \text{njets}$
	$b\bar{b}\gamma + \text{njets}$
	$t\bar{t}\gamma + \text{njets}$
	$W(Z)\gamma + \text{njets}$
$ljj, llj$	$W(Z) + t\bar{t} + \text{njets}$
	$W(Z) + b\bar{b} + \text{njets}$
	$kW+mZ+\text{njets}$
	$t\bar{b}(W)+\text{njets}$
	$t + \text{njets}, Wt\bar{b} + \text{njets}$
	$b\bar{b}t\bar{t} + \text{njets}$
	$b\bar{b}b\bar{b} + \text{njets}$
	$t\bar{t}t\bar{t} + \text{njets}$
$jjj$	$W(Z) + t\bar{t} + \text{njets}$
	$W(Z) + b\bar{b} + \text{njets}$
	$kW+mZ+\text{njets}$
	$t\bar{b}(W)+\text{njets}$
	$t + \text{njets}, Wt\bar{b} + \text{njets}$
	$b\bar{b}t\bar{t} + \text{njets}$
	$b\bar{b}b\bar{b} + \text{njets}$
	$t\bar{t}t\bar{t} + \text{njets}$

The logical .OR. of the above generator-level criteria were then imposed on all signal event samples at the particle level as well as the following fiducial acceptances on signal as well as on background events:

- $|\eta_{\gamma,e}| \leq 2.5, |\eta_{\mu}| \leq 2.1,$
- $\Delta R_{\gamma_1, \gamma_2} \geq 0.3$  where  $\gamma_1$  and  $\gamma_2$  are  $p_T$ -ordered

### 25.5 Description of preliminary particle-level selection

After the preselection, the selection imposed on all signal and background events includes the following criteria: first, that the two photons from the Higgs boson decay as well as the lepton coming from one of the top quarks will have significant  $p_T$ :

- $p_{T\gamma_1, \gamma_2, lepton} \geq 50, 25, 20$  GeV
- $p_{T\gamma_1} + p_{T\gamma_2} \geq 120$  GeV

Second, that the two Higgs photons and the lepton from a top quark will be isolated:

- $\Delta R_{\gamma_1, lepton}, \Delta R_{\gamma_2, lepton} \geq 0.4, 0.6$
- The  $\Delta R$  of the closest charged particle with  $p_T > 1$  GeV to  $\gamma_1$  ( $\gamma_2$ ) must be greater than or equal to 0.2 (0.15)
- The  $\Delta R$  of the closest charged particle with  $p_T > 1$  GeV to the lepton must be greater than or equal to 0.15 and less than or equal to 2
- The absolute value of the scalar product of the  $\gamma_1$  and lepton momenta must be greater than or equal to  $300 \text{ GeV}^2$

Third, that the scalar nature of the Higgs boson will assure a flat distribution of the variable  $\cos \theta^*$  for signal events, where  $\tan \theta^* = \frac{|\vec{p}_i| \sin \theta_i}{\gamma(|\vec{p}_i| \cos \theta_i - \beta E_i)}$ , and  $E_i$  and  $\theta_i$  refer respectively to the energy of and the 3-space angle between either of the two Higgs photon directions and the direction of their joint

4-vector, in the laboratory frame. The same distribution should be peaked in the forward and backward directions for background events. The requirement imposed is :  $\cos \theta^* \leq 0.9$ .

Fourth, that the presence of a real  $t\bar{t}$  pair in signal events should result in a multiplicity significantly greater than for background events from processes not containing such a pair. Events must therefore contain at least eight particle-level jets as constructed with the PYCELL algorithm of the PYTHIA package.

Finally, the invariant mass of the two photons selected as coming from a Higgs boson must lie within a 3 GeV-wide window around the putative Higgs boson mass corresponding to the signal event sample considered.

## 25.6 Preliminary particle-level results for the Standard Model Higgs boson

Table 29 shows, for each of the Standard Model Higgs boson masses considered, the signal selection efficiency and the number of signal ( $N_S$ ) and background events expected, from each irreducible background process, for  $30 \text{ fb}^{-1}$  of integrated luminosity (corresponding to approximately the first three years of LHC running at  $10^{33} \text{ cm}^{-2} \text{ s}^{-1}$ ) after application of the selection described in the previous section. It can be seen that the leading-order  $W\gamma\gamma$  sample seems to strongly underestimate the contribution to the total background, as compared to the  $W\gamma\gamma+4$  jet sample. Therefore, for the current study we include the  $W\gamma\gamma+4$  jet contribution instead of the  $W\gamma\gamma$  contribution when calculating the total number of expected background events ( $N_B$ ) and the signal significance as reflected by the quantity  $N_S/\sqrt{N_B}$ , both of which are also shown in Table 29. It should be noted however that, by the same argument, the leading-order  $Z\gamma\gamma$  sample considered probably also represents an underestimated contribution relative to that of a hypothetical  $Z\gamma\gamma+4$  jet sample, not available at the time of the study. This contribution may be of the same order as that from the  $W\gamma\gamma+4$  jet sample, though perhaps slightly reduced in analogy with the relative importances of the leading-order  $W\gamma\gamma$  and  $Z\gamma\gamma$  contributions. This will be evaluated with a soon-to-be-available  $Z\gamma\gamma+4$  jet sample.

Table 29: Estimated number of signal and background events, signal selection efficiency and signal significance for  $t\bar{t}H, H \rightarrow \gamma\gamma$ , after  $30 \text{ fb}^{-1}$  of integrated luminosity.

Higgs Mass (GeV)	115	120	130	140
Signal Selection Efficiency (%)	19.09	20.78	24.65	25.58
Number Signal Evts ( $N_S$ )	3.96	4.06	3.92	2.86
$t\bar{t}\gamma\gamma$ Type 1	0.17	0.11	0.14	0.16
$t\bar{t}\gamma\gamma$ Type 2	0.08	0.16	0.08	0.16
$t\bar{t}\gamma\gamma$ Type 3	<0.2	0.2	<0.2	<0.2
$Z\gamma\gamma$	0.23	0.21	0.24	0.16
$W\gamma\gamma+4j$	0.4	0.9	1.9	1.4
$bb\gamma\gamma$	< 0.06	0.06	0.06	< 0.06
Total Number Background Evts. ( $N_B$ )	0.88	1.63	2.42	1.88
Signal Significance	4.22	3.18	2.52	2.09
$W\gamma\gamma$	0.37	0.42	0.37	0.39

Table 30 shows the same results for  $100 \text{ fb}^{-1}$  of integrated luminosity (corresponding to approximately one year of LHC running at  $10^{34} \text{ cm}^{-2} \text{ s}^{-1}$ ).

For both cases it can be seen that the contributions to the total surviving background from the  $t\bar{t}\gamma\gamma$  Type 2 and, in the limit of generated statistics, Type 3 processes are of the same order of magnitude as the Type 1 process.

The limited-statistics samples of the reducible background processes considered have not resulted in a significant contribution to the number of surviving background events, in the context of this particle-level study.

The above results would indicate a possibility of signal observability in excess of  $3\sigma$  for Higgs bo-

Table 30: Estimated number of signal and background events, signal selection efficiency and signal significance for  $t\bar{t}H, H \rightarrow \gamma\gamma$ , after  $100 \text{ fb}^{-1}$  of integrated luminosity

Higgs Mass (GeV)	115	120	130	140
Signal Selection Efficiency (%)	19.09	20.78	24.65	25.58
Number Signal Evts ( $N_S$ )	13.2	13.5	13.1	9.5
$t\bar{t}\gamma\gamma$ Type 1	0.57	0.38	0.48	0.53
$t\bar{t}\gamma\gamma$ Type 2	0.3	0.5	0.3	0.5
$t\bar{t}\gamma\gamma$ Type 3	<0.5	0.5	<0.5	<0.5
$Z\gamma\gamma$	0.8	0.7	0.8	0.5
$W\gamma\gamma 4j$	1.5	3.0	6.2	4.7
$bb\gamma\gamma$	<0.2	0.2	0.2	<0.2
Total Number Background Evts. ( $N_B$ )	3.17	5.28	7.98	6.23
Signal Significance	7.41	5.88	4.64	3.81
$W\gamma\gamma$	1.25	1.35	1.23	1.27

son masses below 120 GeV after  $30 \text{ fb}^{-1}$ , with approximately four signal events observed corresponding to the signal selection efficiencies of approximately 20%.

For  $100 \text{ fb}^{-1}$ , there would be discovery potential in excess of  $5\sigma$  and ranging as high as over  $7\sigma$  for Higgs boson masses up to 120 GeV. For masses up to 140 GeV there would be a possibility of signal observability in excess of  $3\sigma$ .

## 25.7 Conclusions and future work

The preliminary particle-level selection presented above has not yet been optimized. Furthermore, there is a possibility to enhance its performance via the inclusion of variables involving missing energy and/or momentum, or the identification of b quark jets, which may be effective in vetoing background events not including real top quarks but nonetheless having high jet multiplicity. The present study would indicate that it is this type of process (for example  $W + \gamma\gamma + N$  jets) which will prove to be the most challenging background.

The method used to select the two putative Higgs photons in each event may also have an effect on the selection's performance. In some prior studies of associated Higgs production [384], the two photons with the highest values of  $p_T$  have been assumed to have come from the Higgs boson. However we have observed (see Figure 147) that the use of this criterion results in considerable sidebands in the two-photon invariant mass distribution, at the level of approximately 10% for  $t\bar{t}H$  events with  $H \rightarrow \gamma\gamma$ . Investigation has shown that this faulty combinatorial choice concerns overwhelmingly the photon with the second-highest  $p_T$ , since the photon with the highest  $p_T$  is not a Higgs photon only at the level of approximately 1/mil, as calculated from signal events. The origin of these 'fake' second Higgs photons is approximately 80% from  $\pi^0$ 's, 10% from  $\eta$ 's, a few percent from  $\omega$ 's, and the remainder from other particles. Fully 80% of these fake Higgs photon 'mother' particles appear to come from parton showers whose origin is one of the two final-state top quarks, and as such are peculiar to the  $t\bar{t}H$  process. The other 20% come from showering from the initial-state protons and hence are common to all the associated production channels. In this way we can estimate that the level of the effect on the WH and ZH processes would be approximately 2-3%.

In addition to the pure combinatorial effect discussed above, which in itself would be damaging to signal selection efficiency, the selection of 'fake' Higgs photons could result in biased kinematical distributions used to construct the selection itself, whether this last is composed of the mere sequential imposition of criteria or of a more sophisticated nature such as likelihood or neural network-based selections. An example of this possibility is shown in Fig. 148, where the total distribution of the photon with the second-highest  $p_T$  in each event is plotted, with that for those events in which the second photon is not a Higgs photon superposed on it, on the left-hand side. The plot on the right-hand side shows the

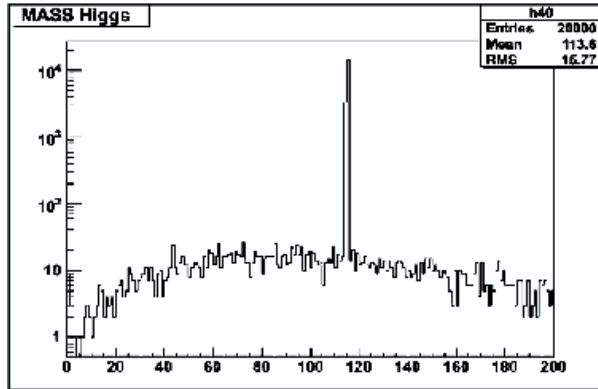


Fig. 147: Invariant  $\gamma\gamma$  mass from events from the signal process  $t\bar{t}H$  production with  $H \rightarrow \gamma\gamma$  and at least one charged lepton from the decay of a top or antitop quark ( $m_H = 115$  GeV), where the two photons with the highest values of  $p_T$  have been identified as the Higgs photons.

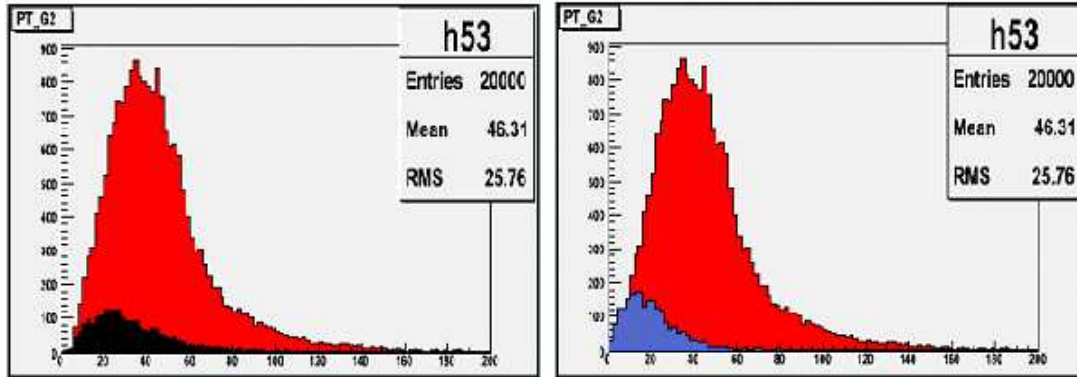


Fig. 148: Distribution of the transverse momentum for the second-highest  $p_T$  photon in each event. (Left) The shaded superimposed distribution corresponds to events where this photon is not from Higgs boson decay. (Right) The shaded superimposed distribution corresponds to the true Higgs photon in the same events.

same total distribution, but the superimposed sub-distribution is that of the true Higgs photons in the same events. Techniques are currently under investigation to try to improve the Higgs photon selection so as to correct this problem, both at the particle level as well as in the context of a detailed CMS simulation and reconstruction study, which is now ongoing. In this detailed simulation and reconstruction study we will study the contributions of the reducible as well as the irreducible backgrounds. We will interpret the results in the context of models with two Higgs doublets as well as attempt to estimate the sensitivity of the  $t\bar{t}H$  process to the CP nature of the Higgs boson, as has been suggested by some authors [401].

### Acknowledgements

The authors would like to thank the organizers and session convenors of the Les Houches Workshop. S. G.-S. is indebted to Peter Skands for his invaluable help on the ALPGEN/PYTHIA interface for the new ALPGEN processes. R.P. acknowledges the financial support of MIUR, under contract n. 2004021808 009.

## 26. STUDY OF $bbZ$ AS A BENCHMARK FOR MSSM $bbH$ <sup>54</sup>

### 26.1 Introduction

The Z boson production process with associated b jets  $gg/q\bar{q} \rightarrow b\bar{b}Z$  is topologically similar to  $gg/q\bar{q} \rightarrow b\bar{b}H$ . In the MSSM the associated Higgs production dominates at large values of  $\tan\beta$ . At large  $\tan\beta$  the most important decay modes for the Higgs boson are  $H \rightarrow b\bar{b}$  and  $H \rightarrow \tau\tau$ . Here we concentrate on Higgs decaying into  $\tau$ 's with  $\tau$  decaying to an electron or muon.

The  $b\bar{b}Z$  production at the LHC can be used as a benchmark for testing the Higgs boson reconstruction methods [381]. The Z mass is known with a good precision, which can be used to verify the mass reconstruction method. It is also possible to measure the  $b\bar{b}Z$  cross section to verify NLO calculations, and b jet and Z transverse momentum spectra to verify the kinematics.

The aim of this study is to show that the Higgs boson mass peak can be reconstructed by reconstructing and understanding the Z mass peak, and to show that it is possible to extract the signal from the background and to measure the cross section. If that can be done, the same method should work similarly for the Higgs boson in  $gg/q\bar{q} \rightarrow b\bar{b}H$ .

### 26.2 Cross sections

The signal consists of  $Z/\gamma^*$  events produced in association with b quarks. The Z boson and  $\gamma^*$  are allowed to decay to electron, muon or tau pairs, tau decaying leptonically. Two possibilities exist, either to select any two lepton final state, or to select  $e+\mu$  final states only. The former has a larger cross section, but the latter has a significantly smaller background [402].

The signal ( $b\bar{b}Z/\gamma^*$ ) is generated, and the signal cross sections calculated with CompHEP [286]. The LO signal cross section for any two-lepton final state is 58 pb. No  $p_T$  and  $\eta$  cuts are applied on massive b quarks in  $b\bar{b}Z/\gamma^*$  process generation. The background comes mainly from two sources,  $Z/\gamma^*$  associated with light quark and gluon jets, generated with PYTHIA [27], and  $t\bar{t}$ ,  $tW$  events, generated with TopReX [321]. An NLO cross section of 1891 pb [403], calculated with MCFM [331], is used for Drell-Yan  $Z/\gamma^* \rightarrow LL$  ( $LL = ee, \mu\mu$  or  $\tau\tau$ ) events with  $m_{LL} > 80 \text{ GeV}/c^2$ . For  $t\bar{t}$  and  $tW$  a cross section of 840 and 60 pb is used, respectively [287]. The  $Z/\gamma^*$  background sample consists also of events with two associated b quarks, but to prevent double counting, those events are removed using the available generation level information of the events.

As shown in Table 31, the cross section for  $gg/q\bar{q} \rightarrow b\bar{b}Z/\gamma^*, Z/\gamma^* \rightarrow \tau\tau \rightarrow \ell\ell + X$  is quite small, in fact of the order of the Higgs boson cross section at  $m_A = 200 \text{ GeV}/c^2$ ,  $\tan\beta \sim 25$ . As the mass of the Z boson is lower than that of the Higgs boson, the leptons and jets have lower  $p_T$ , and the selection efficiency for the associated  $Z/\gamma^* \rightarrow \tau\tau \rightarrow \ell\ell$  events is lower. Therefore, studying  $gg/q\bar{q} \rightarrow b\bar{b}Z/\gamma^*, Z/\gamma^* \rightarrow \tau\tau \rightarrow \ell\ell + X$  as a benchmark for the Higgs boson in  $e+\mu$  final states is not feasible. However, it is possible to study the mass reconstruction using inclusive  $Z/\gamma^* \rightarrow \tau\tau$  events.

Other potential backgrounds are  $b\bar{b}$ , WW, WZ and ZZ events. The contribution from these backgrounds turn out, however, to be negligible after the selection. The cross sections for signal and main background processes are shown in Table 31.

### 26.3 Detector simulation

The detector simulation is done using full GEANT [404] simulation in the ORCA [405] framework. Version ORCA\_8\_7\_4 of CMS OO reconstruction software is used. The CMS detector is simulated with the complete ideal detector, no staging and no misalignment of the detector elements is assumed. The ORCA reconstruction is based on official CMS digitized datasets with pile-up included (3.4 minimum bias events superimposed per event crossing for a luminosity of  $2 \times 10^{33} \text{ cm}^{-2} \text{ s}^{-1}$ ).

<sup>54</sup>Contributed by: S. Lehti



Table 31: Cross sections for signal and background processes.

Signal $b\bar{b}Z/\gamma^*$	pb	Background	pb
$\tau\tau b\bar{b}$ ( $60 < m_{\tau\tau} < 100 \text{ GeV}/c^2$ )	3.29	$Z/\gamma^* \rightarrow \tau\tau \rightarrow \ell\ell$ ( $80 < m_{\tau\tau} < 100 \text{ GeV}/c^2$ )	223.2
$\tau\tau b\bar{b}$ ( $m_{\tau\tau} > 100 \text{ GeV}/c^2$ )	0.132	$Z/\gamma^* \rightarrow \tau\tau \rightarrow \ell\ell$ ( $m_{\tau\tau} > 100 \text{ GeV}/c^2$ )	10.1
$\mu\mu b\bar{b}$ ( $60 < m_{\mu\mu} < 100 \text{ GeV}/c^2$ )	26.2	$Z/\gamma^* \rightarrow \mu\mu$ ( $m_{\mu\mu} > 80 \text{ GeV}/c^2$ )	1891
$\mu\mu b\bar{b}$ ( $m_{\mu\mu} > 100 \text{ GeV}/c^2$ )	1.05	$Z/\gamma^* \rightarrow ee$ ( $m_{ee} > 80 \text{ GeV}/c^2$ )	1891
$ee b\bar{b}$ ( $60 < m_{ee} < 100 \text{ GeV}/c^2$ )	26.3	$t\bar{t} \rightarrow ee/\mu\mu/\tau\tau$	86.2
$ee b\bar{b}$ ( $m_{ee} > 100 \text{ GeV}/c^2$ )	1.05	$tW \rightarrow ee/\mu\mu/\tau\tau$	6.16

## 26.4 Event selection

### 26.4.1 Trigger

The events are triggered with a single and double electron and muon trigger. The  $p_T$  threshold for single muons is 19 GeV/c, for single electrons 29 GeV/c, for double muons 7 GeV/c and for double electrons 17 GeV/c [406]. The Level 1 trigger efficiency for the signal is 0.914. The overall trigger efficiency for signal is found to be 0.826. Stronger trigger thresholds and lower efficiency on single and double electrons suppress the electron final states with respect to the muon final states. An offline cut on lepton  $p_T > 20$  GeV/c balances the different thresholds for events passing the two electron and two muon trigger, but the events triggered with single electron trigger are still suppressed. Therefore, there are more muon events than electron events from the signal and the background passing the trigger.

### 26.4.2 Offline selection

The basic event selection is a requirement of two isolated leptons  $p_T > 20$  GeV/c in the central detector acceptance region  $|\eta| < 2.5$  coming from a reconstructed primary vertex. These cuts reduce efficiently the backgrounds with soft leptons ( $pp \rightarrow b\bar{b}, c\bar{c}, \dots$ ). The leptons are defined isolated when there are no other tracks from the primary vertex with  $p_T > 1$  GeV/c within a cone  $\Delta R = \sqrt{\Delta\varphi^2 + \Delta\eta^2} \leq 0.4$  around the lepton. Other methods, which are used to suppress the backgrounds, are b tagging and central jet veto. The missing transverse energy, reconstructed from high  $p_T$  objects, such as leptons and jets, is used to suppress  $t\bar{t}$  events, and it is also needed in the  $H \rightarrow \tau\tau$  mass reconstruction method due to neutrinos in the final state.

B jets, associated with the Z boson, provide a powerful tool to separate the  $b\bar{b}Z/\gamma^*$  events from the  $Z/\gamma^*$  background. The  $Z/\gamma^*$  events are mostly produced with no significant jet activity, and the associated jets are mostly light quark and gluon jets. Therefore, the  $Z/\gamma^*$  background can be suppressed by requiring reconstructed jets to be present in the event, and even further by requiring that the associated jets are identified as b jets. There are two possibilities available, either to require one b tagged jet per event and veto other jets, or to require two b tagged jets in the event. Here the 2b-tagging option is used in order to have a more pure sample of  $b\bar{b}Z/\gamma^*$  events. A  $E_T$  threshold of 20 GeV is used for both jets.

B jets associated with the Higgs and Z bosons are generally very soft, which makes their tagging a challenging task. In a low  $E_T$  jet, the track multiplicity and momenta tend to be low, and many jets do not have enough significant tracks to be identified as b jets. As a consequence, the b tagging efficiency is not very high. In this study, a b tagging algorithm based on the reconstruction of the secondary decay vertex of the decaying B hadron [407] is chosen. The discriminator of that algorithm is shown in Fig. 149 for b, c and light quark and gluon jets. A cut of discriminator  $> 2$  gives on average 22% b tagging efficiency per jet ( $b\bar{b}Z/\gamma^*$ ) with 0.091% mistagging rate ( $jjZ/\gamma^*$ ). A cut stronger than this suppresses the signal too much with respect to  $t\bar{t}$  events, for which the b jets are more energetic, more central, and therefore easier to reconstruct and to b tag.

The  $t\bar{t}$  events have more jet activity than  $b\bar{b}Z/\gamma^*$ , and a jet veto is used to suppress the  $t\bar{t}$  background. Events with jets  $E_T > 20$  GeV within the tracker acceptance region in addition to the two b jets

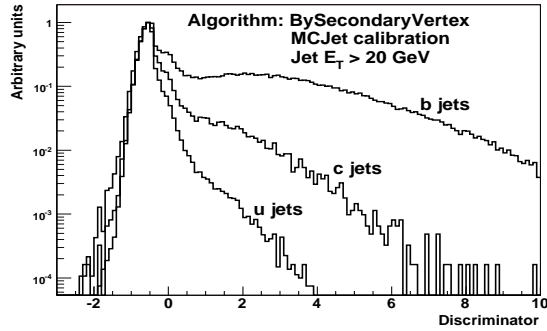


Fig. 149: The output of the b tagging algorithm for b-, c- and light quark and for gluon jets in  $t\bar{t}$  events.

are rejected.

In  $t\bar{t}$  events the leptons come from W decays, so there are always neutrinos in the final state. For the signal there are no neutrinos in the final state ( $b\bar{b}Z/\gamma^* \rightarrow b\bar{b}\tau\tau \rightarrow b\bar{b}\ell\ell + X$  represents only a tiny fraction of the signal events) and missing transverse energy is expected only due to measurement error. The missing  $E_T$  (MET) is reconstructed from the high  $E_T$  objects in the event: the two leptons, and the jets coming from the primary vertex. A jet is defined to be coming from the primary vertex, if at least half of its tracks are coming from the primary vertex. A MC jet correction [407] on jet energy scale is used. A MET cut  $MET < 30$  GeV is applied, which is already close to the detector MET resolution.

A strong method to separate the Z boson events from the  $t\bar{t}$  background is to reconstruct the invariant Z mass. The two leptons are measured with a good accuracy, and the invariant mass distribution in Fig. 150 shows a clear peak at the nominal Z boson mass. Events with invariant a mass of  $85 < m_{\ell\ell} < 95$  GeV/ $c^2$  are chosen for further analysis.

After the selection described above, from the total number of passed events (1065 events for  $30 \text{ fb}^{-1}$ ) the fraction of signal events ( $b\bar{b}Z/\gamma^*$ ) is 70%, the fraction of  $Z/\gamma^*$  with no associated b jets is 11%, and the fraction of  $t\bar{t}$  events is 19%. All other backgrounds are negligible.

## 26.5 Results

### 26.51 Mass reconstruction

In the  $H_{\text{SUSY}} \rightarrow \tau\tau$  analysis the Higgs boson mass is reconstructed using a collinear approximation method. Due to neutrinos in the final state a precise mass reconstruction is impossible. In the collinear approximation the neutrinos are assumed to be emitted along the leptons, which is a valid assumption for the signal events due to large Lorentz boosts of the two  $\tau$ 's. The missing transverse energy is projected along the lepton transverse momentum directions, giving an estimate for the neutrino momentum including the z component of the neutrino momentum. The reconstructed mass is the invariant mass of the summed lepton and neutrino 4-momenta.

Mass reconstruction using the collinear approximation is possible, when the two leptons are not in a back-to-back configuration. Events in back-to-back configuration are removed with a cut  $\Delta\varphi(\ell_1, \ell_2) < 175^\circ$ , where  $\Delta\varphi(\ell_1, \ell_2)$  is the angle between the two leptons in the transverse plane. The mass reconstructed using the collinear approximation is shown in Fig. 151. The  $e+\mu$  final states are chosen to select events with intermediate  $\tau$ 's. In the Higgs boson studies one b jet is required present in the event with a veto on additional jets. Similar events are chosen here, one associated jet is required in the event, but no b tagging is used. Since the leptons are generally well measured, the mass peak position and width are highly dependent on the quality of the missing transverse energy measurement.

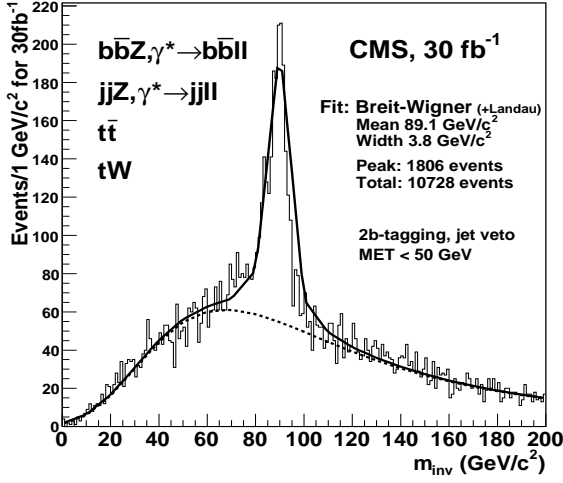


Fig. 150: Invariant mass of the two leptons.

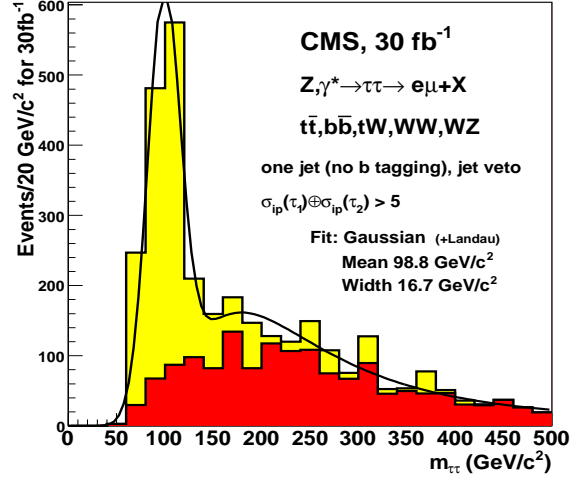


Fig. 151: Mass reconstructed using collinear approximation.

### 26.52 Verification of Monte Carlo

The verification of the Monte Carlo for  $b\bar{b}Z/\gamma^*$  events includes the verification of the cross section, the associated  $b$  jet  $E_T$  and  $\eta$  distributions, and the  $Z$   $p_T$  distribution. These has been studied in Ref. [408]. Each of these distributions consists of both, signal and background events, the measured distribution is a convolution of different signal and background distributions. The shapes of the background distributions can be measured from the data, both  $Z/\gamma^*$  cross section with associated light quark and gluon jets and the  $t\bar{t}$  cross section are large compared to the signal cross section. This information can be used to estimate the shape of the convoluted distributions, which can then be compared with the measured distributions.

Due to a large cross section and a small width, the invariant  $Z$  mass peak can be reconstructed and measured from data with high statistics. Using the signal selection cuts to extract the  $b\bar{b}Z/\gamma^*$  events from the background, the fraction of the  $b\bar{b}Z/\gamma^*$  cross section from the inclusive  $Z/\gamma^*$  cross section can be measured. The number of  $t\bar{t}$  (+ $tW$ ) events can be estimated from the fit shown in Fig. 150. The fraction of  $Z/\gamma^*$  events with associated light quark and gluon jets can be estimated using the known  $b$  tagging efficiency and mis-tagging rate, which can be estimated with good statistics from the measured  $t\bar{t}$  events [407].

The  $b$  tagged jet  $E_T$  and  $\eta$  distributions are shown in Figs. 152 and 153. The measured distributions consist of 70% signal events (dashed histograms). The contribution from  $Z, \gamma^*$  events with soft initial and final state radiation jets, misidentified as  $b$  jets, comes in mostly at low values of jet  $E_T$ . This is shown as a gap between the points and the solid histogram in the figures. Due to the hard  $b$  tagging cut, used the purity of the measured  $b$  jets in  $b\bar{b}Z/\gamma^*$  events is very high, close to one, and dropping to 0.96 at low values of jet  $E_T$ .

The  $Z$  boson  $p_T$  reconstructed from the two leptons is shown in Fig. 154. Again the shapes of the background distributions are needed, and they can be measured from data. The contribution of other backgrounds is taken into account as described above. Since the  $Z$  boson  $p_T$  is reconstructed from the two well measured leptons, the difference between reconstructed and generated  $Z$  boson  $p_T$  is small, about 2.3 %.

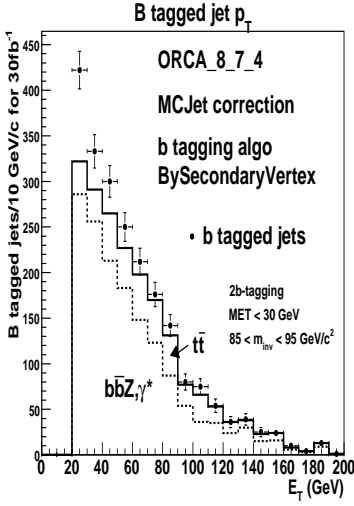


Fig. 152: Reconstructed and b tagged jet  $p_T$  (points) and the fraction of  $b\bar{b}Z/\gamma^*$  (dashed histogram) and  $t\bar{t}$  events (solid histogram).

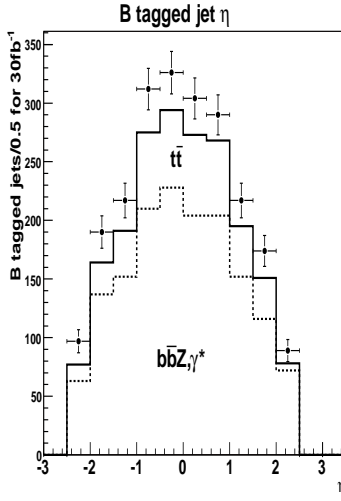


Fig. 153: Reconstructed and b tagged jet  $\eta$  (points) and the fraction of  $b\bar{b}Z/\gamma^*$  (dashed histogram) and  $t\bar{t}$  events (solid histogram).

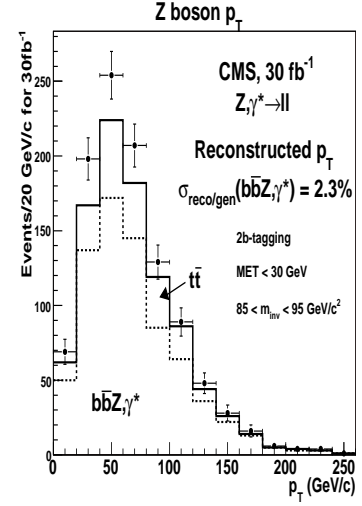


Fig. 154: Z boson  $p_T$  reconstructed from the two leptons (points) and the fraction of  $b\bar{b}Z/\gamma^*$  (dashed histogram) and  $t\bar{t}$  events (solid histogram).

### 26.53 Systematic uncertainties

The uncertainty of the signal selection efficiency is related to the uncertainty of the lepton identification, the absolute calorimeter scale and the b tagging efficiency. An error in the calorimeter scale introduces an error in the jet energy measurement. Here a 1% error on calorimeter scale leads to a 3.4% error on the signal selection efficiency. The uncertainty of the b tagging efficiency can be estimated from  $t\bar{t}$  events as in Ref. [407]. A value of 5% can be used as a conservative estimate. A lepton identification uncertainty of 2% is used for both, electrons and muons.

The uncertainty of the  $t\bar{t}$  background can be evaluated from the signal+background fit shown in Fig. 150. The error of the fit gives the uncertainty. The number of  $t\bar{t}$  events for  $30 \text{ fb}^{-1}$  integrated from the fit is 8922 and the error  $\Delta N_{t\bar{t}} = 147.3$ , which corresponds to a  $t\bar{t}$  background uncertainty  $\Delta N_{t\bar{t}}/N_{t\bar{t}} = 1.7\%$ . The uncertainty of the number of  $jjZ/\gamma^*$  events  $N_{jjZ/\gamma^*} = \epsilon_{\text{mistag}}(\text{jet}_1) \times \epsilon_{\text{mistag}}(\text{jet}_2) \times N_{jjZ/\gamma^*}^{\text{nobtag}}$  is  $\Delta N_{jjZ/\gamma^*}/N_{jjZ/\gamma^*} = \sigma_{\text{fit}} \oplus 2\sigma_{\text{mistag}}$ , where  $\sigma_{\text{fit}}$  is the uncertainty of the Z peak fit when no b tagging is used. Assuming a 5% mistagging uncertainty and a 1.7% error from the Z peak fit without b tagging, the uncertainty of the  $jjZ/\gamma^*$  background is  $\Delta N_{jjZ/\gamma^*}/N_{jjZ/\gamma^*} = 10.1\%$ .

The total systematic uncertainty of the above measurements, including the luminosity uncertainty of 5%, yields a 14.2% uncertainty on the cross section measurement.

## 26.6 Conclusions

It is shown that the  $b\bar{b}Z/\gamma^*$  events can be used as a benchmark for the MSSM Higgs production  $gg/qq \rightarrow b\bar{b}H$ . The  $b\bar{b}Z/\gamma^*$  cross section can be measured and compared with the highest order theoretical calculation available. The associated jet  $E_T$  and  $\eta$  distributions as well as Z  $p_T$  distribution can be measured and compared with the expected theoretical distributions. Understanding the  $b\bar{b}Z/\gamma^*$  events helps us to understand and better trust the theoretical predictions for  $b\bar{b}H$  events, if a heavy neutral MSSM Higgs boson is found in the  $H \rightarrow \tau\tau$  decay channel.

Table 32: Cut flows (in fb) for  $M_H = 160$  GeV in the  $e\mu$  channel.

Cut	$gg \rightarrow H$	VBF	$t\bar{t}$	EW WW	$gg \rightarrow WW$	$qq \rightarrow WW$	$Z/\gamma^*$
Trigger and $Z$ rej.	185	25.1	7586	11.4	48.5	792	151
Hard Jet Veto	90.0	1.48	51.6	0.16	21.2	451	31.4
B Veto	89.6	1.46	37.6	0.16	21.1	449	30.8
$P_T^{Higgs}$	53.2	1.23	33.0	0.09	13.1	177	23.6
$M_{ll}$	42.9	1.10	7.85	0.02	6.31	65.2	22.0
$\Delta\phi_{ll}$	33.1	0.93	5.23	0.02	5.14	42.8	0.07
$M_T$	31.2	0.86	3.64	0.01	3.61	36.8	0.06

## Acknowledgements

The author would like to thank the ARDA/ASAP team for a magnificent grid tool they have created, and A. Nikitenko and R. Kinnunen for reading the manuscript.

## 27. DATA-DRIVEN BACKGROUND DETERMINATION IN THE CHANNEL $H \rightarrow WW \rightarrow l\nu l\nu$ WITH NO HARD JETS<sup>55</sup>

### 27.1 Introduction

The search for the Higgs boson called for by the Standard Model is arguably one of the most important topics in high-energy particle physics today. For a very broad range of masses the dominant decay mode of the Standard Model Higgs boson is the decay  $H \rightarrow WW$  [296]. In this work we study the theoretical uncertainties involved in a data-driven background determination strategy. In Section 27.2, we describe our Monte Carlo samples, event selection, and method for in-situ background determination. We then discuss the most important systematic errors in Sections 27.3 and 27.4

### 27.2 Monte Carlo and Analysis Method

We consider the following signal and background processes:

- Higgs production. We model the gluon-initiated process with the generator provided in MC@NLO and normalize the cross-section for the signal to the values given in [409]. The small contribution from Weak Boson Fusion (VBF) is modelled with Pythia [284, 410].
- QCD  $WW$  production is modelled with the generator provided in MC@NLO version 3.1 [308, 309]. A non-negligible number of  $WW$  events come from  $gg \rightarrow WW$  diagrams that are not included in MC@NLO; we model this contribution using the generator documented in [314].
- $t\bar{t}$  production. The (dominant) doubly-resonant contribution is modelled with MC@NLO. To estimate the impact of the singly-resonant and non-resonant  $WWbb$  contributions to the background, we perform a comparison between leading-order calculations of  $pp \rightarrow WWbb$  and  $pp \rightarrow t\bar{t} \rightarrow WWbb$  using MadEvent [325, 395].
- QCD  $Z/\gamma$  production, with  $Z \rightarrow ee/\mu\mu/\tau\tau$ . We model this background with MC@NLO.

Although we do not expect detector effects to be important in this study, it is convenient to simulate a detector using the last FORTRAN-based release of ATLFAST, and we apply the jet energy corrections in ATLFAST-B [411]<sup>56</sup>. Our event selection consists of the following cuts:

<sup>55</sup>Contributed by: B. Mellado, W. Quayle, S.L. Wu

<sup>56</sup>We also apply a small correction to the energy of jets for which HERWIG was used for the parton showering and hadronization; the correction is given by  $(1 - 5 \times 10^{-5} P_T^{jet} + 0.042)$  where the jet  $P_T$  is measured in GeV.

Table 33: Cross-sections (in fb) in the two control samples discussed in Section 27.2 for  $M_H = 160$  GeV for all lepton flavors.

Sample	$gg \rightarrow H$	VBF	$t\bar{t}$	EW WW	$gg \rightarrow WW$	$qq \rightarrow WW$	$Z/\gamma^*$
Primary	1.86	0.03	33.4	0.08	6.19	121.0	7.96
b-tagged	0.18	0.007	17.02	0.0001	0.08	1.51	1.29

- Trigger and topology cuts. We require that the event has exactly two leptons with transverse momentum greater than 15 GeV in the region with  $|\eta| < 2.5$ , and we apply a lepton identification efficiency of 90% for each lepton. The dilepton invariant mass is required to be less than 300 GeV.
- $Z$  rejection. The event is rejected if the leptons have an invariant mass between 82 and 98 GeV. We require a large missing transverse momentum  $P_T^{miss} > 30$  GeV, which is raised to 40 GeV if the two leptons have the same flavor. (This cut is already included in the first line of the table.) To reduce the nontrivial background from the decay  $Z \rightarrow \tau\tau \rightarrow ll + P_T^{miss}$ , we calculate, using the collinear approximation,  $x_\tau^1$  and  $x_\tau^2$ , the energy fractions carried by the visible decay products of the  $\tau$  leptons, and  $M_{\tau\tau}$ , the invariant mass of the two  $\tau$  leptons. We reject the event if  $x_\tau^1 > 0$ ,  $x_\tau^2 > 0$ , and  $|M_{\tau\tau} - M_Z| < 25$  GeV.
- Jet veto. We reject the event if there are any jets with  $P_T > 30$  GeV anywhere in the detector, or if it contains any b-tagged jets with  $P_T > 20$  GeV and  $|\eta| < 2.5$ . We assume a b-tagging efficiency of 60% with rejections of 10 and 100 against jets from  $c$  quarks and light jets, respectively.
- Transverse momentum of the Higgs candidate, defined as the vector sum of the transverse momenta of the leptons and the missing  $P_T$ . We require that  $P_T^{Higgs} > 11.1$  GeV.

In the signal-like region, we apply three more cuts: we require that the dilepton mass has  $6.3 < M_{ll} < 64.1$  GeV, that the azimuthal opening angle between the leptons satisfies  $\Delta\phi_{ll} < 1.5$  radians, and that the transverse mass obeys  $50 < M_T < M_H + 10$  GeV (where  $M_H$  is the Higgs mass hypothesis). The distribution of the dilepton opening angle in the transverse plane, shown in Fig. 155, owes its discriminating power to the difference in the helicity states of the  $W$  pairs in signal and background. For brevity, we have omitted plots of the other variables. The cross-sections after successive cuts for a representative Higgs mass of 160 GeV in the  $e\mu$  channel are shown in Table 32. We also consider two control samples:

- The primary control sample is defined the same way as the signal-like region, but with different cuts on the dilepton opening angle in the transverse plane and the dilepton invariant mass. We require  $\Delta\phi_{ll} > 1.5$  radians and  $80 < M_{ll} < 300$  GeV; we remove the cut on the transverse mass.
- The b-tagged control sample cuts are the same as in the primary control sample, except that instead of applying a b-jet veto, we require that there is a b-tagged jet with  $P_T$  between 20 GeV and 30 GeV; we also remove the lower bound on the dilepton invariant mass.

Table 33 shows the cross-sections in these two control samples. In order to make meaningful estimates of systematic errors, it is helpful to define the following three quantities:

- $\alpha_{WW}$ : The ratio of the QCD  $WW$  cross-section in the signal-like region over the QCD  $WW$  cross-section in the primary control sample.
- $\alpha_{t\bar{t}}$ : The ratio of the  $t\bar{t}$  cross-section in the signal-like region over the  $t\bar{t}$  cross-section in the b-tagged control sample.
- $\alpha_{t\bar{t}}^{WW}$ : The ratio of the  $t\bar{t}$  cross-section in the primary control sample over the  $t\bar{t}$  cross-section in the b-tagged control sample.

With these ratios taken from Monte Carlo, we estimate the number of  $t\bar{t}$  events in the signal-like region as  $N_{t\bar{t}}^{signal-like} = \alpha_{t\bar{t}} N_{b-tagged}$  and the number of  $WW$  background events in the signal-like region as

$$N_{WW}^{signal-like} = \alpha_{WW} N_{WW}^{primary} = \alpha_{WW} (N_{total}^{primary} - \alpha_{t\bar{t}}^{WW} N_{b-tagged} - \text{small backgrounds})$$



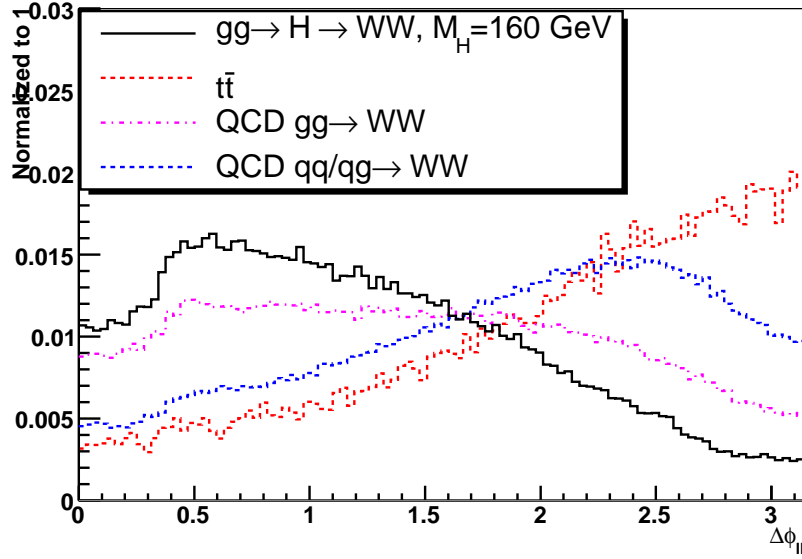


Fig. 155: The distribution of the azimuthal angle (in the transverse plane) between the leptons after cuts.

where  $N_{tt}^{b\text{-tagged}}$  is the number of events in the b-tagged control sample,  $N_{total}^{primary}$  is the total number of events in the primary control sample, and the “small backgrounds” consist mostly of Drell-Yan events. Our task is now to estimate the uncertainty in  $\alpha_{WW}$ ,  $\alpha_{tt}$ , and  $\alpha_{tt}^{WW}$ .

### 27.3 Theoretical Uncertainties in the WW Background

We begin with the theoretical uncertainties in the extrapolation coefficient  $\alpha_{WW}$ . Here, the theoretical error is dominated by the uncertainty in the normalization of the  $gg \rightarrow WW$  contribution; recent studies have shown that this contribution can be in excess of 30% for the cuts used in those studies [314,315].

We compute the the theoretical error as the sum in quadrature of the uncertainty due to the fit error in the parton density function parameterization and the uncertainty due to the choice of  $Q^2$  scale. To estimate the parton density function (PDF) uncertainty, we have used the CTEQ6 PDF set and its error sets; using equation (3) in [47], we find that the uncertainty in  $\alpha_{WW}$  is 2.8%. To assess the uncertainty due to the choice of  $Q^2$  scale, we have varied the renormalization and factorization scales by factors of 8.<sup>57</sup> We examine four choices of scale variations: Scale 1 has  $Q_{ren} \rightarrow 8Q_{ren}$ ,  $Q_{fac} \rightarrow Q_{fac}/8$ ; Scale 2 has  $Q_{ren} \rightarrow Q_{ren}/8$ ,  $Q_{fac} \rightarrow 8Q_{fac}$ ; Scale 3 has  $Q_{ren} \rightarrow 8Q_{ren}$ ,  $Q_{fac} \rightarrow 8Q_{fac}$ ; and Scale 4 has  $Q_{ren} \rightarrow Q_{ren}/8$ ,  $Q_{fac} \rightarrow Q_{fac}/8$ . Table 34 shows the cross-sections before and after cuts in the signal-like region and primary control sample for the  $gg \rightarrow WW$  and  $qq \rightarrow WW$  contributions, with the central-value  $Q^2$  scales and the four modified scale choices. The largest variation in  $\alpha_{WW}$  we observe is 4.1%, and we take this to be the theoretical error due to the choice of  $Q^2$  scale. The total theoretical uncertainty we calculate on the prediction of  $\alpha_{WW}$  is therefore 5%.

### 27.4 Theoretical Uncertainties in the Top Background

We now turn our attention to the uncertainties in  $\alpha_{tt}$  and  $\alpha_{tt}^{WW}$ . Here, the most important question to ask is how to handle single top production. A procedure for generating both  $pp \rightarrow t\bar{t}$  and  $pp \rightarrow Wt$  without

<sup>57</sup>This is an unusually large scale variation to choose; typically, a scale uncertainty will be quoted based on a scale variation of 2 or at most 4. Our motivation for this choice is the fact that we expect the K-factor for  $gg \rightarrow WW$  to be large, since the K-factor for  $gg \rightarrow \gamma\gamma$  has been calculated and it is slightly less than 2 [318].

Table 34: Cross-sections before and after cuts for the signal-like region and the primary control sample, with the corresponding extrapolation coefficients, using the nominal assumptions and the 4 altered scale choices. For historical reasons, the upper bound on the dilepton invariant mass ( $M_{ll} < 300$  GeV) is not applied to the control sample in the values reported in this table.

Scale Choice	No cuts		Sig. Reg.		Cont. Samp.		$\alpha_{WW}$
	$gg \rightarrow WW$	$qq \rightarrow WW$	$gg$	$qq$	$gg$	$qq$	
Central	487.77	11302.44	6.45	63.20	6.38	130.10	0.5103
scale1	239.93	12862.82	2.92	69.25	3.33	143.83	0.4904
scale2	1058.97	9076.86	14.5	49.03	13.46	107.44	0.5255
scale3	278.17	11189.52	3.81	65.02	3.54	131.92	0.5081
scale4	913.38	11702.80	11.1	61.81	12.66	133.51	0.4988

Table 35: Cross-sections (in fb) and extrapolation coefficients for the  $t\bar{t}$  background for various masses, using MadGraph to model the  $WWbb$  background.

Process	Signal-like	Cont. Samp.	b-tagged	$\alpha_{t\bar{t}}$	$\alpha_{t\bar{t}}^{WW}$
$WWbb$	13.34	109.41	47.13	0.2829	2.3211
$t\bar{t} \rightarrow WWbb$	9.80	80.77	37.72	0.2599	2.1413

double-counting at leading order was presented in [329], and a calculation including off-shell effects and spin correlations in the  $WWbb$  system at tree level was presented in [412]. Unfortunately, we know of no event generator available at the time of this writing which also takes into account the one-loop radiative corrections to  $WWbb$  production, so we will perform our uncertainty estimate at tree-level.

In addition to the  $t\bar{t}$  Monte Carlo sample (from MC@NLO) that we have used in the other sections of this note, we have generated two separate  $WWbb$  Monte Carlo samples using MadGraph. One includes only doubly-resonant top quark pair production, and the other includes the full  $WWbb$  final state. For these events, we have allowed the b-quarks to be generated with  $P_T$  as low as 1 GeV, and with pseudorapidity as high as 100. One would expect a disproportionately large contribution from the region where one b-quark is soft or forward, and we therefore feel it is likely that the single-top contribution is overestimated in our non-resonant  $WWbb$  Monte Carlo. This is exactly what we want if we are to prove that our analysis is robust. We have applied the cuts for the signal-like region and both of the control regions to these two Monte Carlo samples to assess the importance of single-top production in this analysis.

Table 35 shows the  $WWbb$  background cross-sections in the signal-like region, the primary control sample, and the b-tagged control sample obtained with the leading-order doubly-resonant  $t\bar{t}$  and inclusive  $WWbb$  samples. We note that although the difference in the absolute cross-section given by the two samples is approximately 30%, the corresponding differences in the predictions of  $\alpha_{t\bar{t}}$  and  $\alpha_{t\bar{t}}^{WW}$  are only about 9%. It is worth noting that this figure is only a general guideline, since the exact values of  $\alpha_{t\bar{t}}$  and  $\alpha_{t\bar{t}}^{WW}$  are strongly dependent on the particulars of the b-tagging algorithm used. Our intent in this section is only to give a rough idea of what the theoretical uncertainty on the extrapolation from a b-tagged sample to a b-vetoed sample should be. In practice, this uncertainty should be addressed in detail using full detector simulation by any experimenter performing a  $H \rightarrow WW$  search like the one outlined here.

## 27.5 Summary

We have proposed a method to estimate the normalization of the dominant backgrounds in the  $H \rightarrow WW \rightarrow l\nu l\nu$  channel using two control samples in the data, one b-tagged, and the other b-vetoed;

in our approach, the systematic errors must be given in terms of the ratios  $\alpha_{WW}$ ,  $\alpha_{tt}$ , and  $\alpha_{tt}^{WW}$ . We have computed the theoretical uncertainty on  $\alpha_{WW}$ ; the result is 5%. We have shown that, for a b-tagging algorithm operating only on jets with  $P_T > 20$  GeV and  $|\eta| < 2.5$ , such that  $\epsilon_b = 60\%$  and the rejections against light quarks and c-quarks are 100 and 10 respectively, the effect of singly-resonant and non-resonant  $WWbb$  diagrams is less than 10% on  $\alpha_{tt}$  and  $\alpha_{tt}^{WW}$ . A study using these uncertainties and this background extraction technique is in progress for the ATLAS experiment; the preliminary result is that a Higgs discovery at  $M_H = 160$  GeV would require less than  $2 \text{ fb}^{-1}$  of integrated luminosity [413]. However, final calculations of the uncertainties on these last two extrapolation coefficients, as well as final results on the overall sensitivity of the search we have presented here, must be computed within the context of the LHC experiments.

## Acknowledgement

The authors are grateful to N. Kauer, and S. Frixione. This work was supported in part by the United States Department of Energy through Grant No. DE-FG0295-ER40896.

## 28. ELECTROWEAK CORRECTIONS TO THE HIGGS DECAYS $H \rightarrow ZZ/WW \rightarrow 4 \text{ LEP-TONS}$ <sup>58</sup>

### 28.1 Introduction

The primary task of the LHC will be the detection and the investigation of the Higgs boson. If it is heavier than 140 GeV, it decays dominantly into gauge-boson pairs, i.e. into 4 fermions. These decays offer the largest discovery potential for a Higgs boson with a mass  $\gtrsim 130$  GeV [414, 415], and the decay  $H \rightarrow ZZ \rightarrow 4\ell$  will allow for the most accurate measurement of the Higgs-boson mass above 130 GeV [416]. At an  $e^+e^-$  linear collider, these decays will enable precision measurements of the corresponding branching ratios and couplings at the per-cent level.

A kinematical reconstruction of the Higgs boson and of the virtual W and Z bosons requires the study of distributions. Thereby, it is important to include radiative corrections, in particular real photon radiation. In addition, the verification of the spin and the CP properties of the Higgs boson relies on the study of angular and invariant-mass distributions [417, 418]. As a consequence a Monte Carlo generator for  $H \rightarrow ZZ/WW \rightarrow 4f$  including electroweak corrections is needed.

In the literature the electroweak  $\mathcal{O}(\alpha)$  corrections are only known for decays into on-shell gauge bosons  $H \rightarrow ZZ/WW$  [419–422]. In this case, also some leading higher-order corrections have been calculated. However, below the gauge-boson-pair thresholds only the leading order is known, and in the threshold region the on-shell approximation becomes unreliable. Only recently electroweak corrections to  $H \rightarrow ZZ/WW \rightarrow 4f$  have been considered. Progress on a calculation of the electromagnetic corrections to  $H \rightarrow ZZ \rightarrow 4f$  has been reported at the RADCOR05 conference by Carloni Calame [423]. At this conference we have also presented first results of our calculation of the complete  $\mathcal{O}(\alpha)$  corrections to the general  $H \rightarrow 4f$  processes [424]. In this note we sketch the calculation and provide some numerical results. More results and details of the calculation can be found in Ref. [425]. The electroweak corrections have been implemented into a Monte Carlo generator called *PROPHECY4f*.

### 28.2 Computational details

We have calculated the complete  $\mathcal{O}(\alpha)$  virtual and real photonic corrections to the processes  $H \rightarrow 4f$ . This includes both the corrections to the decays  $H \rightarrow ZZ \rightarrow 4f$  and  $H \rightarrow WW \rightarrow 4f$  and their interference. The calculation of the one-loop diagrams has been performed in the conventional 't Hooft–Feynman gauge and in the background-field formalism using the conventions of Refs. [426] and [427],

<sup>58</sup>Contributed by: A. Bredenstein, A. Denner, S. Dittmaier, M.M. Weber

respectively. The masses of the external fermions have been neglected whenever possible, i.e. everywhere but in the mass-singular logarithms.

For the implementation of the finite width of the gauge bosons we use the “complex-mass scheme”, which was introduced in Ref. [428] for lowest-order calculations and generalized to the one-loop level in Ref. [429]. In this approach the W- and Z-boson masses are consistently considered as complex quantities, defined as the locations of the propagator poles in the complex plane. To this end, bare real masses are split into complex renormalized masses and complex counterterms. Since the bare Lagrangian is not changed, double counting does not occur. Perturbative calculations can be performed as usual, only parameters and counterterms, in particular the electroweak mixing angle defined from the ratio of the W- and Z-boson masses, become complex. Since we only perform an analytic continuation of the parameters, all relations that follow from gauge invariance, such as Ward identities, remain valid. As a consequence the amplitudes are gauge independent, and unitarity cancellations are respected. Moreover, the on-shell renormalization scheme can straightforwardly be transferred to the complex-mass scheme [429].

The amplitudes have been generated with *FeynArts*, using the two independent versions 1 and 3, as described in Refs. [430] and [431], respectively. The algebraic evaluation has been performed in two completely independent ways. One calculation is based on an in-house program implemented in *Mathematica*, the other has been completed with the help of *FormCalc* [432]. The amplitudes are expressed in terms of standard matrix elements and coefficients of tensor integrals [426]. The reduction to standard matrix elements is performed as described in the appendix of Ref. [433].

The tensor coefficients are evaluated as in the calculation of the corrections to  $e^+e^- \rightarrow 4$  fermions [429]. They are recursively reduced to master integrals at the numerical level. The scalar master integrals are evaluated for complex masses using the methods and results of Refs. [434–436]. UV divergences are regulated dimensionally and IR divergences with an infinitesimal photon mass. Tensor and scalar 5-point functions are directly expressed in terms of 4-point integrals [437]. Tensor 4-point and 3-point integrals are reduced to scalar integrals with the Passarino–Veltman algorithm [438] as long as no small Gram determinant appears in the reduction. If small Gram determinants occur, two alternative schemes are applied [439]. One method makes use of expansions of the tensor coefficients about the limit of vanishing Gram determinants and possibly other kinematical determinants. In this way, again all tensor coefficients can be expressed in terms of the standard scalar functions. In the second, alternative method we evaluate a specific tensor coefficient, the integrand of which is logarithmic in Feynman parametrization, by numerical integration. Then the remaining coefficients as well as the standard scalar integral are algebraically derived from this coefficient. The results of the two different codes, based on the different methods described above are in good numerical agreement.

Since corrections due to the self-interaction of the Higgs boson become important for large Higgs masses, we have included the dominant two-loop corrections to the decay  $H \rightarrow VV$  proportional to  $G_\mu^2 M_H^4$  in the large-Higgs-mass limit which were calculated in Refs. [440, 441].

The matrix elements for the real photonic corrections are evaluated using the Weyl–van der Waerden spinor technique as formulated in Ref. [442] and have been successfully checked against the result obtained with *Madgraph* [395]. The soft and collinear singularities are treated both in the dipole subtraction method following Refs. [227, 443] and in the phase-space slicing method following closely Refs. [213, 444, 445]. For the calculation of non-collinear-safe observables we use the extension of the subtraction method introduced in Ref. [228]. Final-state radiation beyond  $\mathcal{O}(\alpha)$  is included at the leading-logarithmic level using the structure functions given in Ref. [446] (see also references therein).

The phase-space integration is performed with Monte Carlo techniques. One code employs a multi-channel Monte Carlo generator similar to the one implemented in *RacoonWW* [428, 443] and *Lusifer* [447], the second one uses the adaptive multi-dimensional integration program *VEGAS* [448].

### 28.3 Numerical results

We use the  $G_\mu$  scheme, i.e. we define the electromagnetic coupling by  $\alpha_{G_\mu} = \sqrt{2}G_\mu M_W^2 s_w^2 / \pi$ . Our lowest-order results include the  $\mathcal{O}(\alpha)$ -corrected width of the gauge bosons. For the results presented here, we define distributions in the rest frame of the Higgs boson and apply no cuts. We show results without photon recombination and results where the photon has been recombined with the nearest charged fermion if the invariant mass of the photon–fermion pair is below 5 GeV. More details about the setup as well as all input parameters are provided in Ref. [425].

In the two upper plots of Fig. 156 we show the partial decay widths for  $H \rightarrow \nu_e e^+ \mu^- \bar{\nu}_\mu$  and  $H \rightarrow e^- e^+ \mu^- \mu^+$  as a function of the Higgs-boson mass. The lower plots show the corrections relative to the lowest-order results. For  $H \rightarrow \nu_e e^+ \mu^- \bar{\nu}_\mu$ , the corrections are at the level of 2–8% in the considered Higgs-mass region. Around 160 GeV, the corrections are dominated by the Coulomb singularity and at about 180 GeV the ZZ threshold is visible. Note that corrections behave smoothly as a function of the Higgs-boson mass across the thresholds owing to the use of the complex-mass scheme. For the final state  $e^- e^+ \mu^- \mu^+$ , the corrections are between 1% and 5%. The effects of the W-pair and Z-pair thresholds are clearly visible.

The lower plots of Fig. 156 show also a comparison with HDECAY [394]. To this end, we have defined

$$\Gamma^{\text{HDECAY}} = \Gamma_{\text{HVV}}^{\text{HDECAY}} \frac{\Gamma_{Vf_1f_2,0}}{\Gamma_{V,1}} \frac{\Gamma_{Vf_3f_4,0}}{\Gamma_{V,1}} \quad (67)$$

and have divided this by the lowest-order width for  $H \rightarrow f_1 \bar{f}_2 f_3 \bar{f}_4$ . HDECAY agrees well with the lowest-order  $H \rightarrow 4f$  width below threshold, because there  $\Gamma_{\text{HVV}}^{\text{HDECAY}}$  consistently takes into account the off-shell effects of the gauge bosons. Above threshold the gauge bosons are treated as stable, and leading radiative corrections due to the Higgs-boson self-coupling are incorporated. In a small window between the two regions HDECAY interpolates between the two results. The large difference between HDECAY and our lowest-order prediction above threshold is due to the difference of the on-shell and off-shell phase space and has nothing to do with the Coulomb singularity. In particular, for  $H \rightarrow e^- e^+ \mu^- \mu^+$  there is no Coulomb singularity, but the phase-space effect with respect to HDECAY is present, and the corresponding off-shell effects amount to more than 5%.

In Fig. 157 we study the invariant-mass distribution of the two fermions resulting from the decay of the Z bosons in the decay  $H \rightarrow e^- e^+ \mu^- \mu^+$ . The plot on the l.h.s. shows the distribution for  $\mu^- \mu^+$  including  $\mathcal{O}(\alpha)$  corrections. The plot on the r.h.s. compares the relative corrections for  $e^- e^+$  and  $\mu^- \mu^+$ . If we do not recombine photons with collinear fermions, we get very large corrections for invariant masses below the W-boson mass [228, 449]. This is because we define the invariant mass from the fermion pair excluding the photon. The corrections depend logarithmically on the fermion masses and are thus different for electrons and muons. If we recombine the photons with the fermions, the corrections are much smaller and independent on the fermion masses.

The investigation of angular correlations between the fermionic decay products is an essential tool for investigating the spin and parity properties of the Higgs boson. In Ref. [418] it was demonstrated how the parity of the Higgs boson can be determined by looking at the angle between the decay planes of the two Z bosons in the decay  $H \rightarrow ZZ$ . Including the Z-boson decay, this angle can be defined as

$$\begin{aligned} \cos \phi' &= \frac{(\mathbf{k}_+ \times \mathbf{k}_1)(\mathbf{k}_+ \times \mathbf{k}_3)}{|\mathbf{k}_+ \times \mathbf{k}_1| |\mathbf{k}_+ \times \mathbf{k}_3|}, \\ \text{sgn}(\sin \phi') &= \text{sgn}\{\mathbf{k}_+ \cdot [(\mathbf{k}_+ \times \mathbf{k}_1) \times (\mathbf{k}_+ \times \mathbf{k}_3)]\}, \end{aligned} \quad (68)$$

where  $\mathbf{k}_+ = \mathbf{k}_1 + \mathbf{k}_2$ . The l.h.s. of Fig. 158 shows the decay width for  $H \rightarrow e^- e^+ \mu^- \mu^+$  as a function of  $\phi'$  revealing a  $\cos 2\phi'$  term. As was noticed in Ref. [418] this term is characteristic for a scalar. For a pseudo scalar a term proportional to  $(-\cos 2\phi')$  would be present instead. Photon recombination has no significant effect for the distribution in  $\phi'$ , because adding a soft or collinear photon to a fermion momentum does not change its direction significantly.

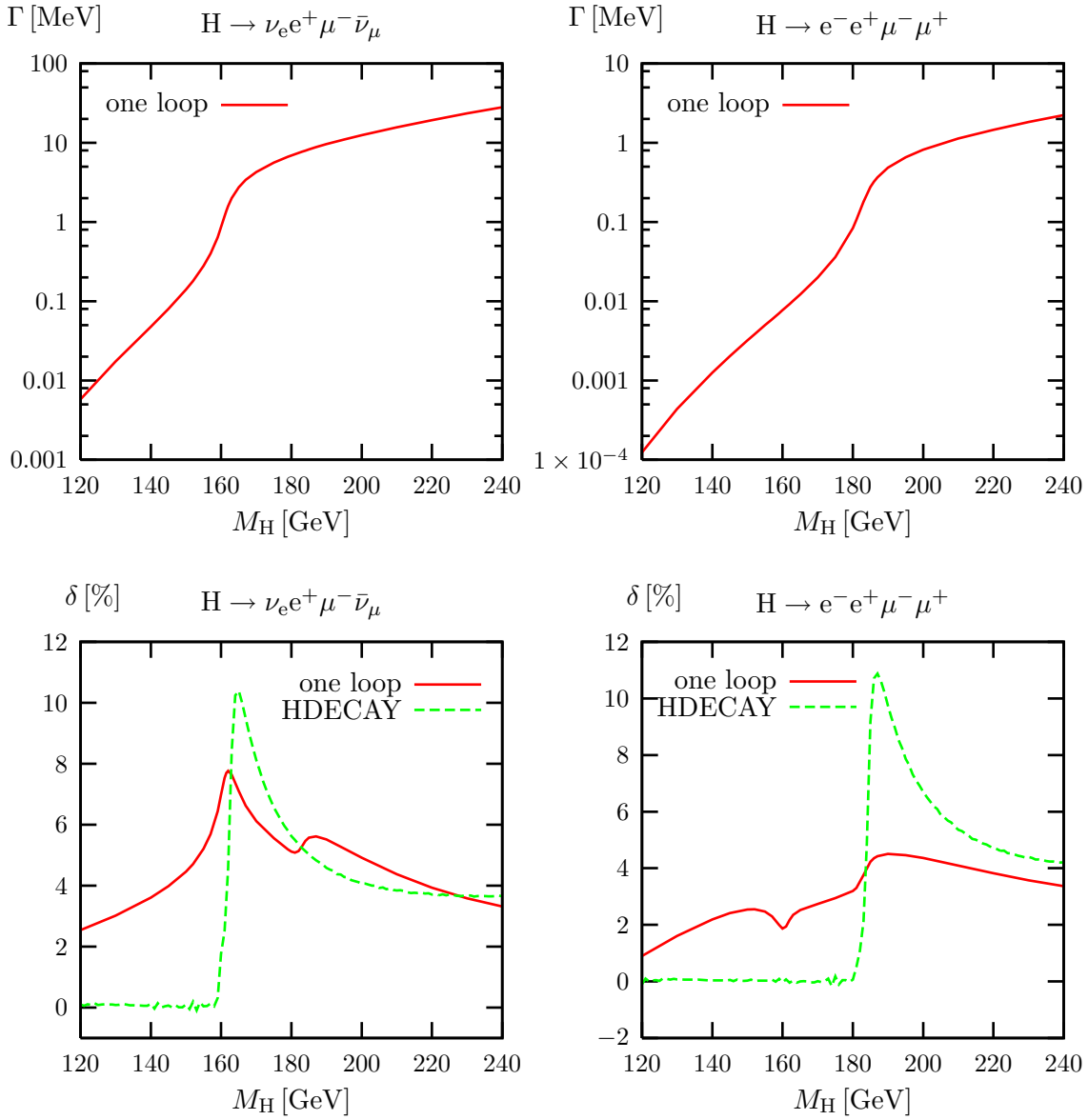


Fig. 156: Partial decay widths for  $H \rightarrow \nu_e e^+ \mu^- \bar{\nu}_\mu$  (l.h.s.) and  $H \rightarrow e^- e^+ \mu^- \mu^+$  (r.h.s.) as a function of the Higgs-boson mass. The upper plots show the absolute predictions including  $\mathcal{O}(\alpha)$  corrections, and the lower plots show the relative  $\mathcal{O}(\alpha)$  corrections and the predictions of the program HDECAY relative to the complete lowest-order prediction.



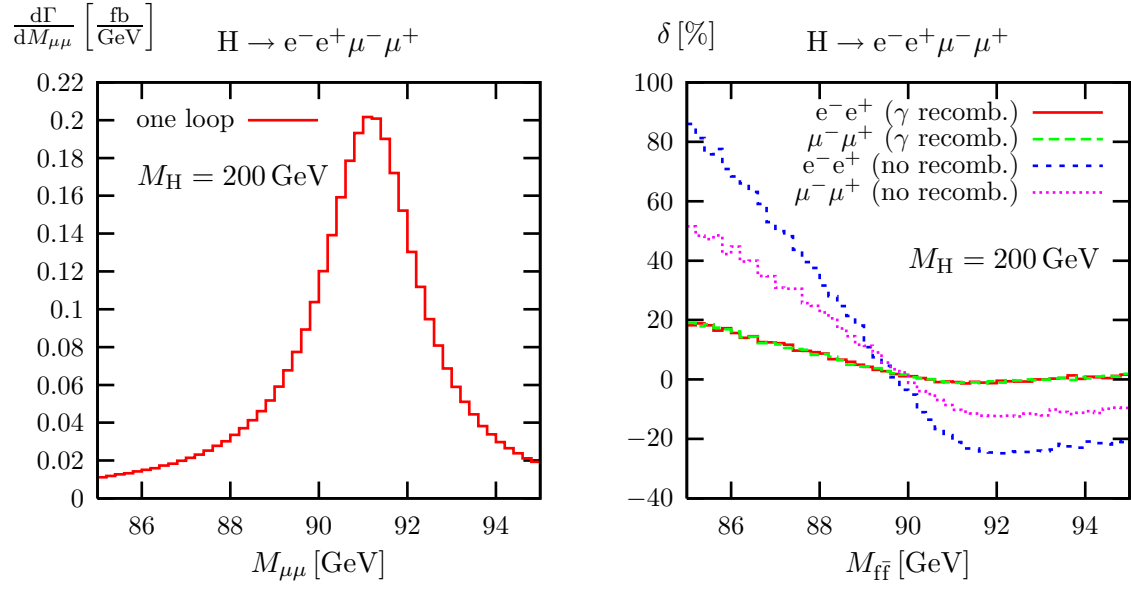


Fig. 157: Invariant-mass distribution of  $\mu^- \mu^+$  (l.h.s.) and relative corrections for the invariant-mass distribution of  $e^- e^+$  and  $\mu^- \mu^+$  (r.h.s.) in the reaction  $H \rightarrow e^- e^+ \mu^- \mu^+$  for  $M_H = 200$  GeV.

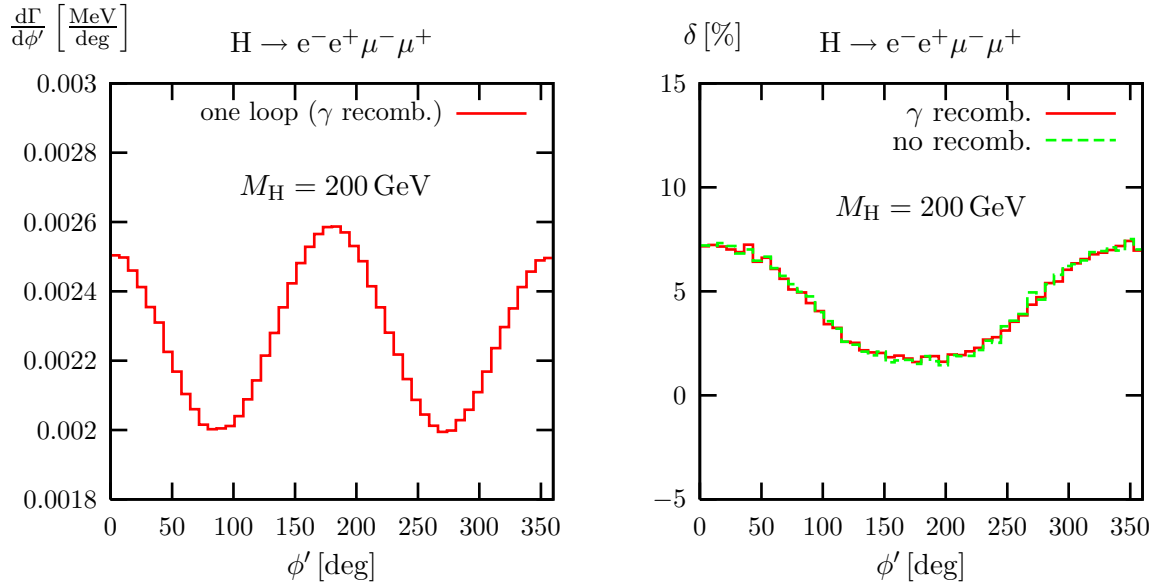


Fig. 158: Distribution in the angle between the decay planes of the two Z bosons in the reaction  $H \rightarrow e^- e^+ \mu^- \mu^+$  and relative corrections with and without applying photon recombination for  $M_H = 200$  GeV.

## 28.4 Conclusions

We have presented results from a calculation of the complete electroweak  $\mathcal{O}(\alpha)$  radiative corrections to the Higgs-boson decays into 4 leptons,  $H \rightarrow 4\ell$ , in the electroweak Standard Model. We find corrections to the partial widths in the range of 1–8%. If predictions with an accuracy of better than 5% are needed, off-shell effects and radiative corrections have to be taken into account.

## 29. BOSON BOSON SCATTERING AT THE LHC WITH PHASE <sup>59</sup>

### 29.1 Introduction

The large energies available at the LHC will make it possible to access many-particle final states with much higher statistics than before. Among these final states, six-fermion signals are of particular interest for Higgs boson discovery and for analyzing vector boson scattering. At the LHC, the SM Higgs production is driven by gluon-gluon fusion. The fusion of W and Z gauge bosons represents the second most important contribution to the Higgs production cross section <sup>60</sup>. The Higgs decay channel into WW, giving rise to two forward-backward jets plus four leptons or two leptons and two jets from the W's, is particularly clean and has been found to be quite promising in the low-intermediate mass range ( $115 < M_H < 200$  GeV). If the Higgs boson is not present, the complementary approach to the question of electroweak symmetry breaking is to study vector boson scattering. In the absence of the Higgs boson, general arguments based on unitarity imply that massive gauge bosons become strongly interacting at the TeV scale. Processes, mediated by massive vector boson scattering  $VV \rightarrow VV$  ( $V = W, Z$ ), are the most sensitive to the symmetry breaking mechanism. By analogy with low energy QCD, or adopting one of the many schemes for turning perturbative scattering amplitudes into amplitudes which satisfy by construction the unitarity constraints, one is led to expect the presence of resonances in  $W_L W_L$  scattering. Unfortunately, the mass, spin and even number of these resonances are not uniquely determined [451].

Six fermion processes are also related to the production of three vector bosons and give access to  $t\bar{t}$  and single-top production, enabling measurements of top mass,  $Wtb$  coupling, decay branching ratios, rare decays and all other features related to the top quark. Finally, we should mention that multi-particle final states of this kind constitute a direct background to most searches for new physics.

Three are the key features of PHASE [452]. The first one consists in the use of a modular helicity formalism for computing matrix elements. Scattering amplitudes get contributions from thousands of diagrams and the computation efficiency has a primary role. The helicity method [453, 454] we use is suited to compute in a fast and compact way parts of diagrams of increasing size, and recombine them later in order to obtain the final set. In this manner, parts common to various diagrams are evaluated just once for all possible helicity configurations, optimizing the computation procedure. The second main feature concerns the integration. We have devised a new integration method to address the crucial point of reaching good stability and efficiency in event generation. Our integration strategy combines the commonly used multichannel approach [455] with the adaptivity of VEGAS. As the number of particles increases, the multichannel technique becomes rather cumbersome, given the thousands of resonant structures which can appear in the amplitude at the same time. Conversely, the VEGAS adaptivity is not powerful enough to deal with all possible peaks of the amplitude.

We have merged the two strategies in a single procedure. The outcome is that PHASE adapts to different kinematic cuts and peaks with good efficiency, using only a few channels per process. As third main feature, PHASE employs the *one-shot* method developed for WPHACT [456, 457]. In this running mode, all processes are simultaneously generated in the correct relative proportion for any set of experimental cuts, and directly interfaced to hadronization and detector simulation programs giving a fully comprehensive physical description. Preliminary results have been presented in [458, 459].

A number of samples of events, representative of all possible processes, have been produced with

---

<sup>59</sup>Contributed by: E. Accomando, A. Ballestrero, A. Belhouari, S. Bolognesi, E. Maina, C. Mariotti

<sup>60</sup>A detailed review and an extensive bibliography can be found in Ref. [450].

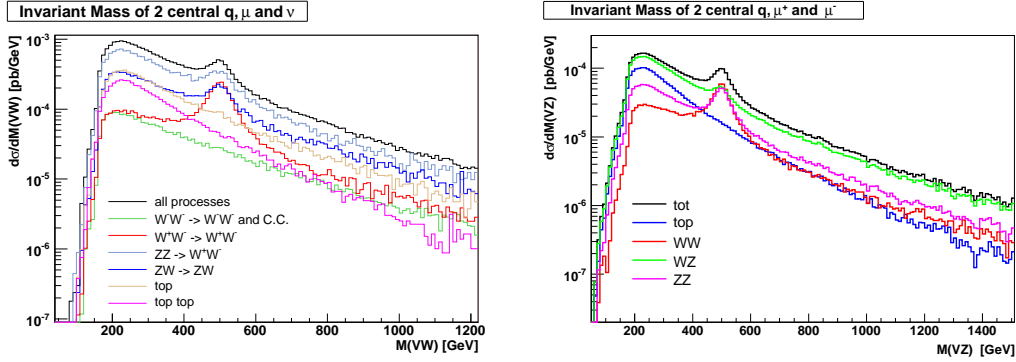


Fig. 159: Distribution of the invariant mass of the two candidate vector bosons for  $qq \rightarrow 4q + \mu\nu$  and  $qq \rightarrow 4q\mu^+\mu^-$ .

PHASE. In order to comply with the acceptance and trigger requirements of the CMS experiment, the cuts in Table 36 have been applied. We have used the CTEQ5L PDF set with the scale  $Q^2 = M_W^2 + \sum_{i=1}^6 p_{Ti}^2/6$ .

Table 36: Standard acceptance cuts applied in all results. Here lepton refers to  $l^\pm$  only.

$E(\text{lepton}) > 20 \text{ GeV}$	$p_T(\text{lepton}) > 10 \text{ GeV}$	$ \eta(\text{lepton})  < 3$
$E(\text{quarks}) > 20 \text{ GeV}$	$p_T(\text{quarks}) > 10 \text{ GeV}$	$ \eta(\text{quark})  < 6.5$
$M(qq) > 20 \text{ GeV}$	$M(l^+l^-) > 20 \text{ GeV}$	

### 29.11 Physical sub-processes

Many subprocesses (i.e.  $WW \rightarrow WW$ ,  $ZW \rightarrow ZW$ ,  $ZZ \rightarrow WW$ ,  $ZZ \rightarrow ZZ$ ,  $t\bar{t}$ ) will in general contribute to a specific six fermion reaction. It is impossible to separate and compute individually the cross section due to a single subprocess, since there are large interference effects between the different contributions. We can however select all complete  $2 \rightarrow 6$  processes which include a specific set of sub-diagrams. For instance,  $ZW \rightarrow ZW$  with on shell bosons is described by 5 Feynman diagrams. These diagrams, with all external vector bosons connected to a fermion line, constitute the  $ZW \rightarrow ZW$  set of  $2 \rightarrow 6$  diagrams. Several sets can contribute to a single process and therefore the same process can appear in different groups. Figure 159 shows the invariant mass distribution of the two most central quarks (when ordered in  $\eta$ ), the lepton and the neutrino for the reactions  $PP \rightarrow qq \rightarrow 4ql\nu$  (LHS) and  $PP \rightarrow qq \rightarrow 4ql^+l^-$  (RHS). The distributions for the different subprocesses as well as the one for the total are presented for  $M(H) = 500 \text{ GeV}$ .

It should be pointed out that the total cross section in Fig. 159 is smaller than the sum of the cross sections for the various groups. Notice that the Higgs peak is present in the  $ZW \rightarrow ZW$  curve. This is due to processes that in addition to the  $ZW \rightarrow ZW$  set of diagrams include also diagrams describing Higgs production, e.g.  $u\bar{u} \rightarrow u\bar{u}d\bar{d}\mu^-\bar{\nu}$ . The groups comprising single top and  $t\bar{t}$  diagrams have a large cross section. An invariant mass analysis reveals that they are indeed dominated by top production. Simple invariant mass vetoes reduce drastically the EW top background and produce a much sharper Higgs peak.

## 29.2 The VV-fusion signal

In the absence of firm predictions in the strong scattering regime, trying to gauge the possibilities of discovering signals of new physics at the LHC requires the definition of a model of  $V_L V_L$  scattering beyond the SM. Some of these models predict the formation of spectacular resonances which will be

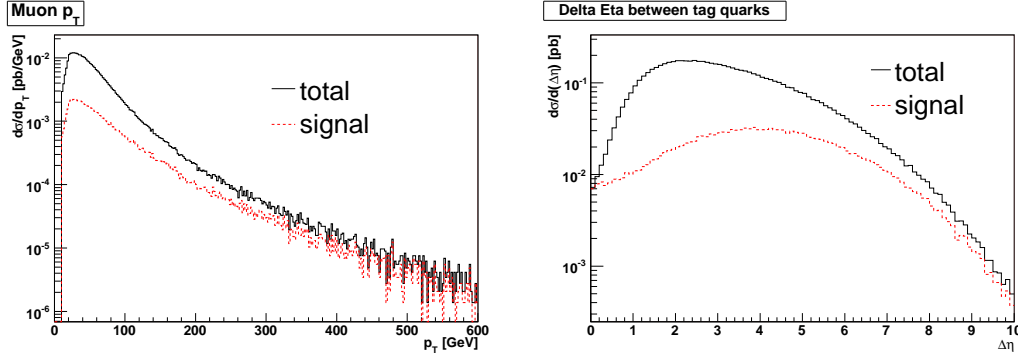


Fig. 160: Distributions of the transverse momentum of the muon, and of  $\Delta\eta$  between the two tagging quarks for all the events (black) and for the signal events (red).

easily detected, while in other cases only rather small effects are expected. The simplest approach is to consider the SM in the presence of a very heavy Higgs boson. While this entails the violation of perturbative unitarity, the linear rise of the cross section with  $\hat{s}$  - the invariant mass squared in the hard scattering - will be swamped by the decrease of the parton luminosities at large momentum fractions and, as a consequence, will be particularly challenging to detect. At the LHC for  $M_H > 10$  TeV, all Born diagrams with Higgs propagators become completely negligible in the unitary gauge and all expectations reduce to those in the  $M_H \rightarrow \infty$  limit. We have compared this minimalistic definition of physics beyond the Standard Model with the predictions of the SM for Higgs masses within the reach of the LHC.

In addition to the diagrams which are related to the process we would like to measure, VV fusion, there will be diagrams in which a pair of V's are produced without undergoing VV scattering. Furthermore, diagrams related to Higgs production via Higgsstrahlung will also be present, as well as diagrams which can be interpreted as  $t\bar{t}$  EW production or as single top production. Finally, diagrams describing three vector boson production, which include triple gauge coupling and quartic gauge coupling, will contribute as well, since they produce the same kind of six fermion final states. Depending on the flavour of the quarks the various subprocesses will contribute and interfere to a different degree. All processes will be experimentally indistinguishable, apart from heavy quark tagging, and will have to be studied simultaneously.

In the following, we will concentrate on the  $Aql\nu$  final states. In order to isolate the VV fusion process from all the other six fermion final states and investigate EWSB, different kinematic cuts have been applied to the simulated events, after vetoing top quarks. The invariant mass of the muon and the neutrino has to reconstruct the mass of a W, and is required to be in the range  $M_W \pm 10$  GeV. In VV fusion an additional W or a Z decaying hadronically is expected to be present. Therefore, events are required to contain two quarks with the correct flavours to be produced in the W or Z decay, with an invariant mass of  $\pm 10$  GeV around the central value of the appropriate EW boson. If more than one combination of two quarks satisfies these requirements, the one closest to the corresponding central mass value is selected. In the following, this combination will be assumed to originate from the decay of an EW vector boson.

In order to reject events which can be identified with the production of three vector bosons, the flavour content and the invariant mass of the two remaining quarks is compared with a W and a Z in a second step. If compatible within 10 GeV with either vector boson, the event is rejected. This happens in about 2% of the cases. The events, satisfying all these constraints, will constitute the “signal” sample.

These requirements are not fully realistic: no flavour information will be available for light quarks and b's will be tagged only in the central part of the detector. Our aim however, is to define a “signal” in the same spirit as CC03 was adopted as such at LEP 2, which could be used to compare the results from

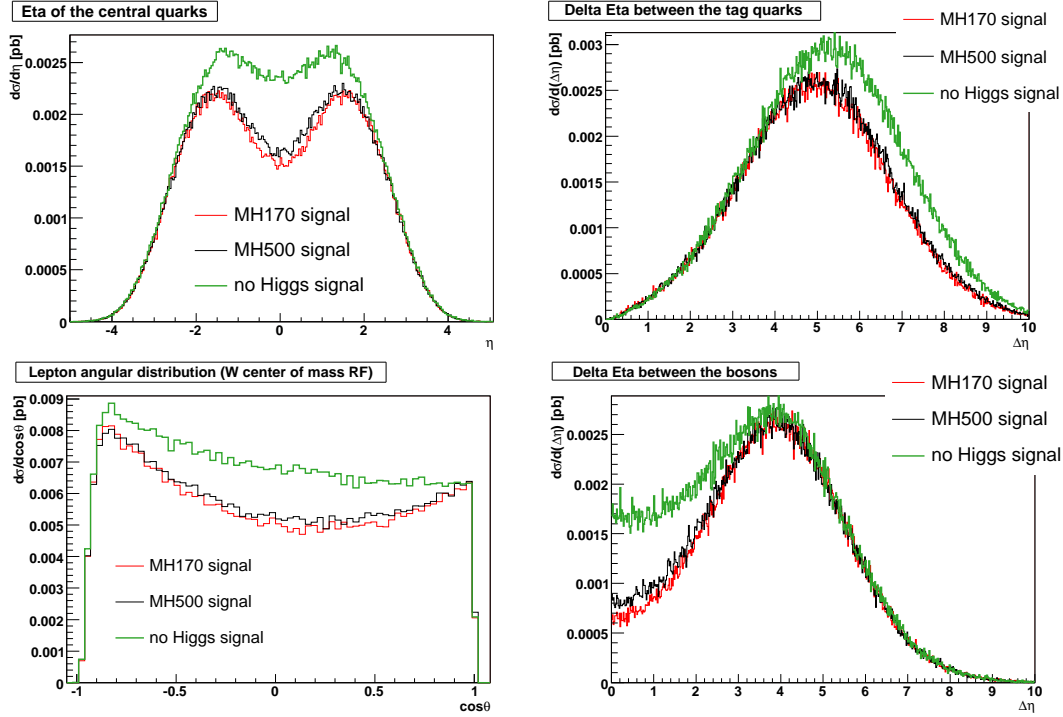


Fig. 161: The  $\eta$  of the two central jets, the  $\Delta\eta$  of the two tagging quarks, the  $\Delta\eta$  of the two vector bosons, the cosine of the angle between the muon and the W boson in the W boson rest frame. In green (full line) for the no-Higgs case, in black (dashed) for  $M(H) = 500$  GeV and in red for  $M(H) = 170$  GeV. All events satisfy  $M(VW) > 800$  GeV.

the different collaborations. The signal is not necessarily directly observable but it should be possible to relate it via Monte Carlo to measurable quantities. If such a definition is to be useful, it must correspond as closely as possible to the process which needs to be studied and the Monte Carlo corrections must be small. At this stage, we want to isolate the VV fusion signal from all other production channels, while following reasonably close the experimental practice and taking into account the full set of diagrams required by gauge invariance. It becomes then possible to analyze the differences between the VV fusion signal sample and its intrinsic background. This also provides some preliminary experience at the generator level which could guide more realistic and complete studies.

In Fig. 160, we show the distribution of the transverse momentum of the muon, and of the difference in pseudorapidity between the two tagging quarks for all the events and for the signal. The “no-Higgs” case is chosen as an example, but there are no significant differences with the case of a finite mass Higgs boson. The muons in the “signal” tend to have a larger  $p_T$  than the sum of all subprocesses, and the  $\Delta\eta$  between tagging quarks tends to be larger.

### 29.3 Higgs production in PHASE

Higgs production in VV fusion, followed by the Higgs decay to WW or ZZ, is an important channel over the full range of Higgs masses which will be explored at the LHC. It is the channel with the highest statistical significance for an intermediate mass Higgs boson [414]. PHASE is capable of simulating Higgs production in VV fusion together with all its EW irreducible backgrounds for any Higgs mass and is particularly useful in the intermediate mass range, where only one of the vector bosons can be approximately treated in a production times decay approach.

## 29.4 The high mass region

An interesting physics possibility is to investigate, whether an elementary Higgs boson exists by measuring the  $VW$  cross section at large  $M(VW)$ . For this purpose, kinematic distributions for  $M(H) = 170$  GeV,  $M(H) = 500$  GeV and the no-Higgs case have been compared for  $M(VW) > 800$  GeV since the cross section at large  $M(VW)$  for  $M(H) = 170$  GeV and  $M(H) = 500$  GeV is essentially due to transversely polarized vector bosons, while the cross section for the no-Higgs case is due to a mixture of the two polarizations. Figure 161 shows that the distributions are quite insensitive to the value of the Higgs mass, provided it is much smaller than the invariant mass of the  $VW$  system. This raises the stimulating possibility of defining Standard Model predictions for high invariant mass production of  $VV$  pairs. These predictions will obviously suffer from the usual PDF and scale uncertainties, which could in principle be controlled by comparing with the cross section of some appropriate “standard candle” process.

We have tried several sets of cuts and we believe that using a Neural Network (NN) is the most effective way of increasing the separation between the no-Higgs case and the presence of a relatively light Higgs. Two samples of events, satisfying the cuts in Table 36, for  $M(H) = 500$  GeV and the no-Higgs case, respectively, have been employed to train a NN. The following set of weakly correlated variables have been used in the training: the difference in pseudorapidity between the two bosons and between the two tagging quarks, the transverse momentum of the tagging quarks and the cosine of the angle between the muon and the  $W$  boson in the  $W$  center of mass system. Some kinematic variables are shown in Fig. 161 for the no-Higgs and the  $M(H) = 500$  GeV case.

Applying a cut on the output variable, the NN can enhance the separation between the heavy and light Higgs case. In Table 37, the integrated cross section and the number of events for  $M(VW) > 800$  GeV are shown for different values of the cut.

Table 37: Integrated cross section for the number of expected events in a year at high luminosity in the two cases and their corresponding ratios.

	$\sigma_{no-Higgs}$	$\mathcal{L} = 100 fb^{-1}$	$\sigma_{mH=500GeV}$	$\mathcal{L} = 100 fb^{-1}$	ratio
all events	13.6 fb	$1360 \pm 37$	11.6 fb	$1160 \pm 34$	1.2
NN >0.54	3.17 fb	$317 \pm 18$	1.95 fb	$195 \pm 14$	1.6
NN >0.58	2.28 fb	$228 \pm 15$	1.13 fb	$113 \pm 11$	2.0

## Acknowledgements

This work is supported by MIUR contract 26-01-2001 N.13 and under contract 2004021808\_009

## Part III

# NLO AND NNLO QCD COMPUTATIONS

## 30. NLO PREDICTIONS FOR MANY-PARTICLE PRODUCTION <sup>61</sup>

### 30.1 Introduction

At the LHC, most of the interesting processes will involve multi-particle final states, either through the decay of resonances or from direct multi-particle production. However, only a few theoretical predictions beyond leading order are available up to now for processes with more than two particles in the final

<sup>61</sup>Contributed by: T. Binoth, F. Boudjema, A. Denner, S. Dittmaier, J. Fujimoto, J.-Ph. Guillet, G. Heinrich, J. Huston, T. Ishikawa, T. Kaneko, K. Kato, Y. Kurihara, E. Pilon



state. On the other hand, it is well known that leading order predictions have serious deficiencies like limited predictive power due to large scale dependence, large sensitivity to kinematic cuts and poor jet modelling. Parton shower Monte Carlos on the other hand cannot predict the overall normalisation of a process and do not perform well in describing large angle radiation. As a consequence of the latter, shapes of certain distributions may not be well described. This is especially worrisome if backgrounds need to be extrapolated to signal regions using theoretical predictions.

A lot of activity has been going on recently to improve this situation. The following sections should serve to summarize the current situation and to assess the needs and prospects for the near future.

### 30.2 Status

There are already a few QCD NLO  $2 \rightarrow 3$  processes in hadronic collisions that have been calculated so far, see Table 38.

Table 38: List of existing predictions for  $pp \rightarrow 3$  particles.

<sup>a</sup> Although this is a  $2 \rightarrow 3$  process, because of its colour singlet nature the NLO QCD corrections are simple and do not involve more than vertex corrections. Strictly speaking, genuine corrections involving 5-point loop functions do appear if one considers the same final state initiated through  $Z$ -strahlung. These contributions are small compared to VBF and have, so far, not been considered.

<sup>b</sup> This refers to the *effective* NLO QCD correction where the Higgs is produced at “leading order” through the effective coupling to two gluons. Compared to VBF this process is characterised by extra central jet activity.

pp $\rightarrow$ 3 particles		
process ( $V = Z, W^\pm$ )	references	comments
$pp \rightarrow 3$ jets	[460–464]	public code available [464]
$pp \rightarrow V + 2$ jets	[408, 465]	public code available
$pp \rightarrow Z b \bar{b}$	[466, 467]	massless $b$ quarks
$W^\pm + g^* (\rightarrow b \bar{b})$	[468]	massless $b$ quarks
$pp \rightarrow H + 2$ jets	[469–472]	$H$ through VBF, Vector Boson Fusion <sup>a</sup>
$pp \rightarrow H + 2$ jets	[473]	“Background” to VBF <sup>b</sup> , under construction
$pp \rightarrow \gamma\gamma$ jet	[474, 475]	
$pp \rightarrow t\bar{t}H, b\bar{b}H$	[348–351, 391–393, 476]	
$pp \rightarrow t\bar{t}h^0$	[477]	SUSY QCD corrections
$pp \rightarrow t\bar{b}H^-$	[478]	SUSY QCD corrections
$pp \rightarrow t\bar{t}$ jet	[479]	under construction

Very recently there has also been major progress in electroweak NLO corrections to  $2 \rightarrow 3$  processes, see Table 39. These involve a considerable number of diagrams with many different mass scales. The past year has even witnessed the first complete calculation of NLO electroweak corrections to  $2 \rightarrow 4$  processes, Table 40.

Besides, a few calculation of NLO corrections to  $2 \rightarrow 4, 5$  in toy models or for specific helicity configurations have been performed successfully, see Table 41. One important development has been the computation of the *virtual* corrections to the 6 gluon amplitude [505]. Results at the amplitude level have been given for a specific point in phase space. This is an important step towards the computation of the cross section at NLO. At the same time, based on the newly developed twistor techniques [504, 508–515], the major part of the 6-gluon amplitude at one-loop has been derived [516]. We therefore expect that the NLO correction to the 4-jet cross section at the LHC are within sight.

Table 39: List of existing calculations for  $e^+e^- \rightarrow \gamma^* \rightarrow 4$  jets and  $e^+e^-, \gamma\gamma \rightarrow 3$  particles

$e^+e^-$ and $\gamma\gamma \rightarrow 3$ particles.		
process	type of corrections	references
$e^+e^- \rightarrow 4$ jets	QCD	[480–486]
$e^+e^- \rightarrow \nu\bar{\nu}H$	EW	[433, 487–489]
$e^+e^- \rightarrow e^+e^-H$	EW	[490]
$e^+e^- \rightarrow t\bar{t}H$	EW and QCD	[491–494]
$e^+e^- \rightarrow ZHH$	EW	[495, 496]
$e^+e^- \rightarrow \nu\bar{\nu}\gamma$	EW	[497]
$\gamma\gamma \rightarrow t\bar{t}H$	EW and QCD	[498]

Table 40:  $2 \rightarrow 4$  cross sections presently available.

$2 \rightarrow 4$		
process	references	comments
$e^+e^- \rightarrow 4$ fermions	[429, 499] [500]	cross sections status report
$e^+e^- \rightarrow HH\nu\bar{\nu}$	[501]	cross sections

The present panorama of the multi-leg one-loop corrections together with the recent emergence of new and improved loop techniques as well as novel approaches such as the twistor string inspired makes it now possible to tackle  $2 \rightarrow 3$  and  $2 \rightarrow 4$  processes that are of importance for the LHC.

### 30.3 A realistic NLO wishlist for multi-particle final states

A somewhat whimsical experimenter’s *wishlist* was first presented at the Run 2 Monte Carlo workshop at Fermilab in 2001 [517]. Since then the list has gathered a great deal of notoriety and has appeared in numerous LHC-related theory talks. This list contained a great number of multi-particle processes with many particles in the final state. Although it was well motivated from a data analysis point of view, many of the processes are far beyond present calculational methods and tools. For example, it is unlikely that  $WWW + b\bar{b} + 3$  jets will be calculated at NLO soon, no matter the level of physics motivation, but there are a number of high priority calculations, primarily of backgrounds to new physics, that are accessible with the present technology. However, the manpower available before the LHC turns on is limited. Thus, it is necessary to prioritize the calculations, both in terms of the importance of the calculation and the effort expected to bring it to completion.

A prioritized list, determined at the Les Houches workshop, is shown in Table 42, along with a brief discussion of the physics motivation. Later in this section, there will be a discussion of some of the specific theoretical difficulties to expect. Note that the list contains only  $2 \rightarrow 3$  and  $2 \rightarrow 4$  processes. It will be much more of a challenge to tackle higher multiplicities before addressing these cross sections.

First, a few general statements: usually, signatures for new physics will involve high  $p_T$  leptons and jets (especially  $b$  jets) and missing transverse momentum. Thus, backgrounds to new physics will tend to involve (multiple) vector boson production (with jets) and  $t\bar{t}$  pair production (with jets). The best manner in which to understand the normalization of a cross section is to measure it; however the rates for

Table 41: Other  $2 \rightarrow 4(5)$  calculations.

2 $\rightarrow$ 4(5): special models, specific helicity amplitudes, special kinematics.		
process	references	comments
N-photon helicity amplitudes	[502]	only specific helicity configurations
6- and 7 - gluon amplitudes	[503, 504]	for non-Susy Yang-Mills only specific helicity configurations
6- gluon amplitude	[505]	Result for one phase space point (only virtual corrections)
6-scalar amplitudes in the Yukawa model	[506]	
2-photon 4-scalar amplitudes in the Yukawa model	[507]	only specific helicity configurations

some of the complex final states listed here may be limited and (at least in the early days) must be known from NLO theory. NLO is the first order at which both the normalization and shape can be calculated with any degree of confidence.

Table 42: The LHC “priority” wishlist for which a NLO computation seems now feasible.

process ( $V \in \{Z, W, \gamma\}$ )	relevant for
1. $pp \rightarrow V V$ jet	$t\bar{t}H$ , new physics
2. $pp \rightarrow t\bar{t} b\bar{b}$	$t\bar{t}H$
3. $pp \rightarrow t\bar{t} + 2$ jets	$t\bar{t}H$
4. $pp \rightarrow V V b\bar{b}$	VBF $\rightarrow H \rightarrow VV$ , $t\bar{t}H$ , new physics
5. $pp \rightarrow V V + 2$ jets	VBF $\rightarrow H \rightarrow VV$
6. $pp \rightarrow V + 3$ jets	various new physics signatures
7. $pp \rightarrow V V V$	SUSY trilepton

- $pp \rightarrow VV + \text{jet}$ : One of the most promising channels for Higgs production in the low mass range is through the  $H \rightarrow WW^*$  channel, with the W’s decaying semi-leptonically. It is useful to look both in the  $H \rightarrow WW$  exclusive channel, along with the  $H \rightarrow WW + \text{jet}$  channel. The calculation of  $pp \rightarrow WW + \text{jet}$  will be especially important in understanding the background to the latter.
- $pp \rightarrow t\bar{t}b\bar{b}$  and  $pp \rightarrow t\bar{t} + 2$  jets: Both of these processes serve as background to  $t\bar{t}H$ , where the Higgs decays into a  $b\bar{b}$  pair. The rate for  $t\bar{t}jj$  is much greater than that for  $t\bar{t}b\bar{b}$  and thus, even if 3  $b$ -tags are required, there may be a significant chance for the heavy flavor mistag of a  $t\bar{t}jj$  event to contribute to the background.
- $pp \rightarrow VVb\bar{b}$ : Such a signature serves as non-resonant background to  $t\bar{t}$  production as well as to possible new physics.
- $pp \rightarrow VV + 2$  jets: The process serves as a background to VBF production of a Higgs boson.
- $pp \rightarrow V + 3$  jets: The process serves as background for  $t\bar{t}$  production where one of the jets may not be reconstructed, as well as for various new physics signatures involving leptons, jets and missing transverse momentum.

- $pp \rightarrow VVV$ : The process serves as a background for various new physics subprocesses such as SUSY tri-lepton production.

Work on (at least) the processes 1. to 3. of Table 42 is already in progress by several groups, and clearly all of them aim at a setup which allows for an application to other processes.

From an experimentalist’s point-of-view, the NLO calculations discussed thus far may be used to understand changes in normalization and/or shape that occur for a given process when going from LO to NLO [518]. Direct comparisons to the data require either a determination of parton-to-hadron corrections for the theory or hadron-to-parton corrections for the data [519]. (Of course, one is just the inverse of the other.) Both types of correction take into account the effects of the underlying event and of fragmentation. For multi-parton final states, it is also necessary to model the effects of jet algorithms, when two or more partons may be combined into one jet [520].

### 30.4 Review of theoretical approaches

In this section, first a brief overview of the existing methods to tackle one-loop multi-leg amplitudes will be given. More detailed descriptions of the individual methods are given in section 30.41.

The majority of the one-loop cross sections available up to now has been calculated by following the approach pioneered by Ellis Ross and Terrano [521,522] to calculate real and virtual corrections and treat the soft/collinear singularities, applying the Passarino-Veltman algorithm [438], or some variation of it, for the tensor reduction and the evaluation of the one-loop integrals. This “traditional” approach consists of the following steps for the calculation of a  $2 \rightarrow N$  particle process at partonic level:

1. diagram generation
2. calculation of the real radiation corrections (requires  $2 \rightarrow N + 1$  amplitudes at tree level and subtraction of poles due to soft/collinear massless particles)
3. calculation of the one-loop amplitude (involves  $(N + 2)$ -point integrals)
4. combination of real and virtual contributions, integration over the phase space

The issue of subtraction of long distance singularities in step 2. above has been solved once and for all by the general methods, of phase space slicing [236, 523–525], and of subtraction [227, 366, 526–528], so that, for multi-particle processes, step 3. is now the bottleneck. We will therefore concentrate on the calculation of one-loop amplitudes in the following.

A loop integral for an  $N$ -point function consists of products of denominators representing the propagators circulating in the loop and a numerator consisting of a tensor structure that generally depends on the loop momentum. When the numerator of an integral is independent of the loop momentum, it is called a scalar integral. The traditional method for the calculation of one-loop tensor integrals consists, through recursion, of an *algebraic* reduction of the tensor integrals to a set of scalar “basis integrals”. As the basis integrals are known in analytic form, the virtual amplitude is expressed by analytic functions which depend on the invariants of the given process, thus having maximal analytic control when proceeding to the phase space integration. All tensor integrals can be expressed in terms of scalar integrals and form factors carrying the Lorentz structure by solving a system of equations where the unknowns are the tensor coefficients. The determinant of this system of equations, the Gram determinant, can vanish or get extremely small for some particular configurations of phase space. This can lead to numerical instability as the Gram determinant appears with inverse powers if the “traditional” reduction method is used.  $N$ -point functions for  $N \geq 5$ , including scalar functions, can also be reduced to a system of four-and lower-point functions, and in this process inverse determinants are generated as well. To deal with this problem, a few methods have been worked out recently. One can for example use a Taylor expansion in the Gram determinant [439, 529–531] or resort to a numerical evaluation of some of the integrals [439, 530, 532], at least for these critical points. By stopping the reduction before only scalar functions are reached and integrating the endpoints of such a reduction numerically, the occurrence of inverse Gram determinants can be avoided completely [439, 532].

Another way of tackling the problem is to revert to a numerical evaluation of all the loop integrals, which is generally called "semi-numerical" or "numerical" approach, depending on the extent of algebraic reductions carried out before evaluating certain integrals numerically. The borderline between "algebraic" and "semi-numerical" cannot be drawn in a clear way. Below we first list the most recent variants of the "algebraic/partly numerical" approach.

- Denner, Dittmaier  
*massive and massless,*  
*applied to calculate the first cross section for a 6-point process* [429, 437, 439, 499, 533]
- Ellis R.K., Giele, Glover, Zanderighi  
*massless propagators only* [473, 505, 530, 534]
- Binoth, Guillet, Heinrich, Pilon, Schubert  
*massless and massive* [532, 535]
- GRACE group  
*applications so far massive, massless under development* [500, 536]
- Del Aguila, Pittau [537];  
Van Hameren, Vollinga, Weinzierl [538]  
*based on spinor helicity*
- Duplancic, Nizic  
*massless propagators only* [539]
- Fleischer, Jegerlehner, Tarasov  
*massive only* [540, 541]
- Bern, Dixon, Kosower  
*massless propagators only* [542, 543]

Besides this mostly algebraic approach, there are semi-numerical methods, which do split into real and virtual corrections, but largely rely on the numerical evaluation of loop integrals, either by doing already the integration over the loop momenta numerically, or by evaluating the Feynman parameter representation of the integrals numerically. This requires the elaboration of a scheme to remove the poles from the integrals before the numerical integration. The following groups have worked in this direction recently: (*historical order*)

- Fujimoto, Shimizu, Kato, Oyanagi [544]
- Ferroglia, Passera, Passarino, Uccirati [545]
- Binoth, Heinrich, Kauer [546]
- Nagy, Soper [547, 548]
- Kurihara, Kaneko [549]
- Anastasiou, Daleo [550]

Further, there is an approach [551–553] which avoids the splitting into real and virtual parts by first performing the sum over cuts for a given graph and then integrating over all momenta, including the loop momenta, numerically. In this way unitarity is exploited to cancel soft and collinear divergences before they show up as explicit poles. However, this method has only been applied to the process  $e^+e^- \rightarrow 3$  jets at NLO so far.

Very recently, a novel approach to the calculation of one-loop amplitudes has emerged, which is often referred to as "twistor-space-inspired" methods [504, 508–515]. Using these methods, compact expressions for very complex tree-level amplitudes could be achieved, and their extension to loop level has seen a very rapid development [504, 516, 554–561]. In particular, the unitarity-based method of [562, 563] has seen a successful revival due to the use of on-shell recursion relations [559, 564, 565]. A very recent breakthrough is the derivation of the major part of the 6-gluon amplitude at NLO (the rational

parts are still missing). However, this approach being very new, it is difficult to judge whether it can be applied to processes where several different mass scales are involved.

### 30.41 *More detailed descriptions of recent methods*

**The DD approach** In the following we describe the salient features of the methods described in Refs. [437, 439] that have been successfully applied in the calculation of a complete one-loop correction to a  $2 \rightarrow 4$  scattering reaction, viz. the electroweak corrections to the charged-current processes  $e^+e^- \rightarrow 4f$  [429, 499]. The described methods, thus, have proven their reliability in practice.

Particular attention is paid to the issue of numerical stability. For 1- and 2-point integrals of arbitrary tensor rank, general numerically stable results are used. For 3- and 4-point tensor integrals, serious numerical instabilities are known to arise in the frequently used Passarino–Veltman reduction [438] if Gram determinants built of external momenta become small. While Passarino–Veltman reduction is applied if Gram determinants are not too small, for the remaining problematic cases dedicated reduction techniques have been developed. One of the techniques replaces the standard scalar integral by a specific tensor coefficient that can be safely evaluated numerically and reduces the remaining tensor coefficients as well as the standard scalar integral to the new set of basis integrals. In this scheme no dangerous inverse Gram determinants occur, but inverse modified Cayley determinants instead. In a second class of techniques, the basis set of standard scalar integrals is kept, and the tensor coefficients are iteratively deduced up to terms that are systematically suppressed by small Gram determinants or by other small kinematical determinants in specific kinematical configurations; the numerical accuracy can be systematically improved upon including higher tensor ranks. For 5- and 6-point tensor integrals, reductions to 4- and 5-point integrals, respectively, are employed that do not involve inverse Gram determinants either.

Finally, we summarize some information that is relevant for the practical use of the methods.

1. The methods are valid for massive and massless cases. More precisely, the formulas given in Refs. [437, 439] are valid without modifications if IR divergences are regularized with mass parameters or dimensionally.<sup>62</sup> The IR, i.e. soft or collinear, singularities naturally appear in the standard scalar 2-point, 3-point and 4-point functions. Finite masses can be either real or complex.
2. The input and output structure of the methods is the same as for conventional Passarino–Veltman reduction, where momenta and masses are used as input and the numerical values of all tensor coefficients (and the scalar integrals) are delivered as output. This means that no specific algebraic manipulations are needed in applications, so that the whole method can be (and in fact is) organized as a numerical library for scalar integrals and tensor coefficients.
3. Up to now, the methods are explicitly worked out for  $N$ -point integrals with  $N \leq 6$ , which is sufficient for  $2 \rightarrow 4$  particle reactions. The extension to higher-point functions is straightforward.
4. All relevant formulas are published and ready for direct implementation without further manipulations. Only the scalar 3- and 4-point functions are needed from elsewhere.

**The BGHPS approach** The method described in [532] to compute multi-particle processes relevant for the LHC at one-loop level has the following main features:

1. validity for an arbitrary number  $N$  of external legs
2. validity for both, massive and massless particles
3. algebraic isolation of IR divergences
4. flexibility in applying reduction algorithms algebraically/numerically, depending on phase space regions
5. numerically stable representations of reduction building blocks

---

<sup>62</sup>For the method of Ref. [437], this has been shown in Ref. [533].



In our approach, point 3. above is achieved by means of an iterative algebraic reduction which decomposes any  $N$ -point one-loop scalar/tensor integral into an infrared-finite part and an infrared-divergent part. No regulator masses for soft and collinear divergences are needed in our formalism as we regulate all divergences by working in  $n = 4 - 2\epsilon$  dimensions. Our reduction endpoints (“basis integrals”) are chosen such that all IR divergences are contained in 3-point and 2-point integrals, which have simple analytical representations, allowing for a straightforward isolation of the  $1/\epsilon$  poles. The most complicated building blocks of our reduced amplitude, the 4-point functions in  $n + 2$  and  $n + 4$  dimensions, are always free from IR divergences.

We thus express all loop diagrams algebraically as linear combinations of spinors, (contracted) Lorentz tensors and form factors. The form factors are represented on a basis of 1-,2-,3- and 4-point functions. The special feature of our set of basis integrals consists in the fact that it is carefully designed not to introduce dangerous denominators which are present in many standard approaches. As proven in [532], this can only be achieved if some of the basis integrals are not purely scalar integrals, but do have Feynman parameters in the numerator. More in detail, our basis integrals are, apart from trivial 1- and 2-point functions: 3-point functions  $I_3$  in  $d = n$  and  $d = n + 2$  dimensions and 4-point functions  $I_4$  in  $d = n + 2$  and  $d = n + 4$  dimensions, where  $I_3^n$  and  $I_4^6$  can have up to three Feynman parameters in the numerator, and  $I_3^{n+2}$  and  $I_4^{n+4}$  can have up to one Feynman parameter in the numerator. The short-hand notation for this basis set is thus

$$\{I_3^n(1, j_1, j_1 j_2, j_1 j_2 j_3), I_3^{n+2}(1, j_1), I_4^6(1, j_1, j_1 j_2, j_1 j_2 j_3), I_4^{n+4}(1, j_1)\}. \quad (69)$$

We have shown that *any*  $N$ -point one-loop amplitude can be expressed in terms of this basis, such that no inverse Gram determinants are introduced at all, and a proliferation of further higher dimensional integrals is avoided. The evaluation of any  $N$ -point amplitude represented in this way is therefore reduced to the evaluation of the basis elements. This point refers to item 4. of the above list. In our approach, the evaluation of the integrals in (69) can be done optionally by further algebraic reduction, which offers the possibility to algebraically simplify the expressions further. This proved useful in the amplitude computations for  $gg \rightarrow \gamma\gamma g$  [475] and  $gg \rightarrow V^*V^* \rightarrow l\nu l'\nu'$  [314, 566], both relevant to Higgs phenomenology at the LHC. On the other hand, we provide switches to numerical representations of our building blocks. The latter are completely free of algebraic objects which might induce numerical problems. By combining these two possibilities, using always the one which is more appropriate in the corresponding phase space regions, one arrives at algebraic amplitude representations – which allow for a fast evaluation – in the bulk of the phase space and robust numerical representations in critical phase space regions. For the latter we propose a method based on contour deformation of multi-dimensional parameter integrals to numerically evaluate our basis integrals. The evaluation of processes given in the “wishlist” using these methods is presently under construction.

**The GRACE approach** The GRACE system is a highly automatised tool for the computation of total cross sections both at tree and loop level, starting from the Feynman diagram generation, complex Dirac and tensor algebra, loop integration and integration over phase space and event generation. Recently a series of  $2 \rightarrow 3$  and a couple of  $2 \rightarrow 4$  (see Tables 39,40) processes in the electroweak sector that involve a very large number of Feynman diagrams have been computed demonstrating the power of the system. To carry this success to NLO QCD multi-leg processes, some new techniques have recently been developed in particular to deal with massless particles.

For the electro-weak processes with massive particles circulating in the loop, all tensor reductions of two, three and four-point functions are performed by solving a system of equations obtained by taking derivatives with respect to the Feynman parameters [567]. All higher orders parametric integrals corresponding to the tensor integrals can then be recursively derived from the scalar integral. The two-point integrals are implemented using simple analytical formulas. The scalar 3-point function and all but the infra-red divergent 4-point scalar functions are evaluated through a call to the FF package [568]. For the

infrared four-point function, GRACE supplies its own optimized routines through some rather simple analytical results [569] that lead to an efficient complete cancellation of infrared divergences between these loop functions and the infrared factors from the real soft bremsstrahlung part. Although this tensor reduction can potentially lead to instabilities due to inverse Gram determinants, this has not been an issue for the host of multi-leg processes that we studied.

To extend the system, a fully numerical method to calculate loop integrals, a numerical contour-integration method, has recently been developed [549]. Loop integrals can be interpreted as a contour integral in a complex plane for an integrand with multi-poles in the plane. Stable and efficient numerical integrations along an appropriate contour can be performed for scalar and tensor integrals appearing in the loop calculations of the standard model.

For the massless case as would be needed for NLO-QCD processes, a set of one-loop vertex and box tensor integrals with massless internal particles has been obtained directly without any reduction method to scalar-integrals [536]. Results with one or two massive external lines for the vertex integral and up to one massive external line for the box integral have been developed. The dimensionally regularised functions allow to extract the infra-red and collinear poles. The results are expressed through very compact formulas for an easy numerical implementation. The tensor integrals for the box with two or more off-shell external legs are under development.

A method to construct event-generators based on next-to-leading order QCD matrix-elements and leading-logarithmic parton showers is developed by a GRACE group [570]. Matrix elements of loop diagrams as well as those of a tree level can be generated using an automatic system. A soft/collinear singularity is treated using a leading-log subtraction method.

The PDF and PS include leading-log(LL) terms of the initial-state parton emission. If one combines the matrix element with the PDF or PS very naively, one cannot avoid double-counting of these LL-terms. Our proposal to solve this problem is to subtract the LL-terms from the exact matrix elements as

$$\begin{aligned}\sigma_{LLsub} &= \frac{1}{(2p_1^0)(2p_2^0)v_{rel}} \int_{\Omega_{vis}} d\Phi_{N+1}^{(4)} \left[ \left| \mathcal{M}_{N+1}^{(4)} \right|^2 - \left| \mathcal{M}_N^{(4)}(sx) \right|^2 f_{LL}(x, s) \right], \\ f_{LL}(x, s) &= 16\pi^2 \left( \frac{\alpha_s}{2\pi} \right) \frac{P^{(1)}(x)}{k_{\perp}^2} \left( \frac{1-x}{x} \right).\end{aligned}$$

The second term of the integrand is the LL-approximation of the real-emission matrix-elements under the collinear condition. Higher soft/collinear correction by the parton shower method is combined with the NLO matrix-element without any double-counting in this method.

### 30.42 Combination with parton showers

To date, experimentalists have been more comfortable with predictions at the hadron level produced by interfaces to parton shower and hadronization programs. The Les Houches Accord (2001) provides an interface between matrix element and parton shower/hadronization programs but cannot be used directly for the NLO processes discussed thus far. There is the danger of double-counting of some of the higher order corrections since these can also be produced by the parton shower as well as by the matrix element. In addition, the more complex matrix element calculations contain many contributions with large negative weights, which are not conducive to a Monte Carlo framework.

In a parton shower interface, a specific subtraction scheme must be implemented to preserve the NLO cross section. As each parton shower Monte Carlo may produce a different real radiation component, the subtraction scheme must necessarily depend on the Monte Carlo program to which the matrix element program is matched. The presence of interference effects with NLO calculations requires that a relatively small fraction ( $\sim 10\%$ ) of events have negative weights (of value -1).

Several groups have worked on the subject to consistently combine partonic NLO calculations with parton showers.

- Collins, Zu [571,572]
- Frixione, Nason, Webber (MC@NLO) [308,309]
- Nason [573]
- Kurihara, Fujimoto, Ishikawa, Kato, Kawabata, Munehisa, Tanaka [570]
- Krämer, Soper [574–576]
- Nagy, Soper [577,578]

MC@NLO is the only publically available program that combines NLO calculations with parton showering and hadronization. The Herwig Monte Carlo is used for the latter. The processes included to date are:  $(W, Z, \gamma^*, H, b\bar{b}, t\bar{t}, HW, HZ, WW, WZ, ZZ)$ . Recently, single top hadroproduction has been added to MC@NLO [579]. This is the first implementation of a process that has both initial- and final-state singularities. This allows a more general category of additional processes to be added in the future. Work is proceeding on inclusion of inclusive jet production and WW fusion to Higgs. Adding spin correlations to a process increases the level of difficulty but is important for processes such as single top production.

### 31. ONE LOOP GLUON INITIATED CORRECTIONS IN DIPHOX <sup>63</sup>

#### 31.1 Introduction

Direct photon pair production is an important background for the low mass Higgs. An analysis of the diphoton background at LHC has been performed in [580]. A full next to leading order study of direct photon pair production in hadronic colliders is also incorporated in DIPHOX [581], except for  $gg \rightarrow \gamma\gamma + X$  at NLO.

Because LHC is a gluon factory, gluon fusion is a very important background for Higgs search at LHC. In this work, we focus on the implementation of the real contribution of gluon initiated processes of photoproduction, *i.e.* one loop  $gg \rightarrow \gamma\gamma + g$  diagrams, into DIPHOX<sup>64</sup>. We consider the result of the direct calculation of this amplitude [582]. After reviewing the analytical framework, we will investigate some numerical results from DIPHOX.

#### 31.2 Analytical framework

Two topologies are associated to  $gg \rightarrow \gamma\gamma + g$ :

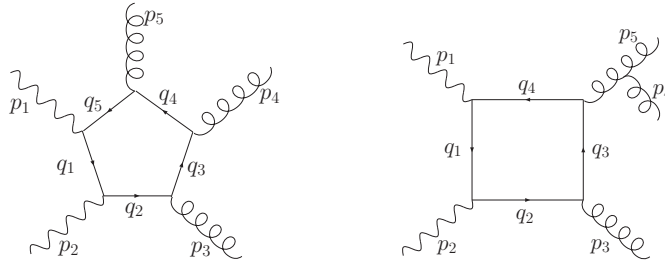


Fig. 162: The two topologies of  $gg \rightarrow \gamma\gamma + g$ .

The calculation of the matrix element squared has been performed thanks to an analytic FORM [583]/MAPLE [584] code, and a numerical Fortran code.

The analytical amplitudes can be written in function of the field strength tensor  $\mathcal{F}$ , where  $\mathcal{F}$  is defined

<sup>63</sup>Contributed by: F. Mahmoudi

<sup>64</sup>Note that in order to have the complete NLO corrections, one has to add the two loop virtual corrections as well.

as [582]:

$$\mathcal{F}_j^{\mu\nu} = p_j^\mu \epsilon_j^\nu - p_j^\nu \epsilon_j^\mu . \quad (70)$$

The representation in function of the field strength tensor is not unique, and it is possible to find a common structure for all helicity amplitudes:

$$\mathcal{A}^{+++++} = \frac{\text{Tr}(\mathcal{F}_1^+ \mathcal{F}_2^+) \text{Tr}(\mathcal{F}_3^+ \mathcal{F}_4^+ \mathcal{F}_5^+)}{2 s_{34} s_{45} s_{35}} \quad (71)$$

$$\mathcal{A}^{-++++} = \frac{\text{Tr}(\mathcal{F}_2^+ \mathcal{F}_3^+) \text{Tr}(\mathcal{F}_4^+ \mathcal{F}_5^+)}{s_{23}^2 s_{45}^2} \left( C_1^{-++++} (p_2 \cdot \mathcal{F}_1^- \cdot p_4) + C_2^{-++++} (p_2 \cdot \mathcal{F}_1^- \cdot p_5) \right) \quad (72)$$

$$\mathcal{A}^{++++-} = \frac{\text{Tr}(\mathcal{F}_1^+ \mathcal{F}_2^+) \text{Tr}(\mathcal{F}_3^+ \mathcal{F}_4^+)}{s_{12}^2 s_{34}^2} \left( C_1^{++++-} (p_1 \cdot \mathcal{F}_5^- \cdot p_3) + C_2^{++++-} (p_1 \cdot \mathcal{F}_5^- \cdot p_4) \right) \quad (73)$$

$$\mathcal{A}^{--+++} = \frac{\text{Tr}(\mathcal{F}_1^- \mathcal{F}_2^-) \text{Tr}(\mathcal{F}_3^+ \mathcal{F}_4^+)}{s_{12}^2 s_{34}^2} \left( C_1^{--+++} (p_3 \cdot \mathcal{F}_5^+ \cdot p_2) + C_2^{--+++} (p_3 \cdot \mathcal{F}_5^+ \cdot p_1) \right) \quad (74)$$

$$\mathcal{A}^{+++--} = \frac{\text{Tr}(\mathcal{F}_1^+ \mathcal{F}_2^+) \text{Tr}(\mathcal{F}_4^- \mathcal{F}_5^-)}{s_{12}^2 s_{45}^2} \left( C_1^{+++--} (p_4 \cdot \mathcal{F}_3^+ \cdot p_2) + C_2^{+++--} (p_4 \cdot \mathcal{F}_3^+ \cdot p_1) \right) \quad (75)$$

$$\mathcal{A}^{-+++-} = \frac{\text{Tr}(\mathcal{F}_2^+ \mathcal{F}_3^+) \text{Tr}(\mathcal{F}_1^- \mathcal{F}_5^-)}{s_{23}^2 s_{15}^2} \left( C_1^{-+++-} (p_2 \cdot \mathcal{F}_4^+ \cdot p_5) + C_2^{-+++-} (p_2 \cdot \mathcal{F}_4^+ \cdot p_3) \right) \quad (76)$$

One can obtain the coefficients  $C_1$  et  $C_2$  using the  $C$ 's of [582].  $C_1$  and  $C_2$  contain logarithmic terms (from two point functions), 6 dimensional integrals (four point functions) and constant terms. These amplitudes share a basic structure in  $\text{Tr}(\mathcal{F}_i^\pm \mathcal{F}_j^\pm)$ ,  $p_i \cdot \mathcal{F}_k^\pm \cdot p_j$ , with real and complex coefficients. It is possible to write the field strength tensor terms in function of spinor products [585]. One can show that:

$$\text{Tr}(\mathcal{F}_i^+ \mathcal{F}_j^+) = -(\langle p_i p_j \rangle^*)^2 , \quad (77)$$

$$\text{Tr}(\mathcal{F}_i^- \mathcal{F}_j^-) = -(\langle p_i p_j \rangle)^2 , \quad (78)$$

and

$$\text{Tr}(\mathcal{F}_i^+ \mathcal{F}_j^+ \mathcal{F}_k^+) = \frac{1}{\sqrt{2}} \langle p_i p_j \rangle^* \langle p_j p_k \rangle^* \langle p_k p_i \rangle^* . \quad (79)$$

And for the scalar products:

$$p_i \cdot \mathcal{F}_k^+ \cdot p_j = \frac{1}{2\sqrt{2}} \langle p_i p_j \rangle \langle p_i p_k \rangle^* \langle p_k p_j \rangle^* , \quad (80)$$

$$p_i \cdot \mathcal{F}_k^- \cdot p_j = \frac{1}{2\sqrt{2}} \langle p_i p_j \rangle^* \langle p_i p_k \rangle \langle p_k p_j \rangle . \quad (81)$$

The six dimensional box integrals can be calculated analytically [586], and written as:

$$\frac{1}{a+b-c} I_4^6(a, b, c) = Li_2\left(1 - \frac{c}{a}\right) + Li_2\left(1 - \frac{c}{b}\right) - Li_2\left(-\frac{b}{a}\right) - Li_2\left(-\frac{a}{b}\right) . \quad (82)$$

Thanks to these relations, it is possible to calculate the total squared amplitude. This result has been implemented into DIPHOX.

Another interesting study concerns the collinear limits of the amplitudes, which on one side, allows the study of the cancellations of singularities, and on the other side, can be used as a cross-check of the

results. For example, in the case of  $3 \parallel 5$ , one can define  $p_3 = z P_{35}$  and  $p_5 = (1 - z) P_{35}$  and show that [585]:

$$\begin{aligned} \mathcal{A}_{p_3 \parallel p_5}^{++++-} &= \frac{1}{2\sqrt{2}} \frac{1}{\langle p_3 p_5 \rangle^*} \frac{z^2}{\sqrt{z(1-z)}} \frac{\langle p_1 p_2 \rangle^* \langle P_{35} p_4 \rangle^*}{\langle p_1 p_2 \rangle \langle P_{35} p_4 \rangle} \\ &+ \frac{1}{2\sqrt{2}} \frac{1}{\langle p_3 p_5 \rangle} \frac{(1-z)^2}{\sqrt{z(1-z)}} \frac{\langle P_{35} p_4 \rangle \langle P_{35} p_2 \rangle \langle p_2 p_4 \rangle^*}{\langle p_1 p_2 \rangle \langle p_1 p_4 \rangle \langle p_2 p_4 \rangle} . \end{aligned} \quad (83)$$

Thus, the amplitude appears as the superposition of the amplitude of 2 gluons  $\rightarrow$  2 photons with a positive helicity for particle 3, plus the amplitude with a negative helicity for particle 3. The coefficients  $z^2/\sqrt{z(1-z)}$  and  $(1-z)^2/\sqrt{z(1-z)}$  are related to the well-known splitting functions [587, 588], the first one corresponding to the case where a gluon of positive helicity produces a collinear gluon of positive helicity and of momentum fraction  $z$ , whereas the second one corresponds to the case where a gluon of positive helicity produces a collinear gluon of negative helicity. Hence, one can write the amplitude under the form:

$$\mathcal{A}_{p_3 \parallel p_5}^{\lambda_1 \lambda_2 \lambda_3 \lambda_4 \lambda_5}(p_1, p_2, p_3, p_4, p_5) = \sum_{\lambda=\pm} S_\lambda(p_3^{\lambda_3}, p_5^{\lambda_5}) \mathcal{A}^{\lambda_1 \lambda_2 (-\lambda) \lambda_4}(p_1, p_2, p_3 + p_5, p_4) , \quad (84)$$

where  $\lambda$  refers to the helicity and  $S$  are the splitting functions. Reproducing this well-known result constitutes another test of the amplitudes.

### 31.3 Numerical results

We use for the spinor products definitions given in [589]. Considering a quadrivector  $k^\mu$  one can use the following notations:

$$k_\pm = k_0 \pm k_z , \quad (85)$$

and

$$k_\perp = k_x + i k_y = |k_\perp| e^{i\varphi_k} = \sqrt{k_+ k_-} e^{i\varphi_k} . \quad (86)$$

With an adequate choice of phase, we can find:

$$|k_+\rangle = \begin{bmatrix} \sqrt{k_+} \\ \sqrt{k_-} e^{i\varphi_k} \\ 0 \\ 0 \end{bmatrix} , \quad (87)$$

and

$$|k_-\rangle = \begin{bmatrix} 0 \\ 0 \\ \sqrt{k_-} e^{-i\varphi_k} \\ -\sqrt{k_+} \end{bmatrix} . \quad (88)$$

Consequently, one has:

$$\langle k_1 k_2 \rangle = \langle k_{1-} | k_{2+} \rangle = \sqrt{k_{1-} k_{2+}} e^{i\varphi_1} - \sqrt{k_{1+} k_{2-}} e^{i\varphi_2} . \quad (89)$$

Using these relations, one can evaluate the numerical value of each amplitude, and so the matrix element squared. To avoid the numerical difficulties concerning collinear singularities, we used a multiprecision package [590] which enables an arbitrary level of numeric precision.

To implement this matrix element squared into DIPHOX, we follow the same procedure as presented in [581]. Let us consider the physical case:

$$g(p_1) + g(p_2) \longrightarrow \gamma(p_3) + \gamma(p_4) + g(p_5) . \quad (90)$$

In this case, the only possible collinear singularities come from  $p_1 \parallel p_5$  or if  $p_2 \parallel p_5$ . To isolate the part containing potential collinear or infrared singularities, we consider in the matrix element squared the coefficient of the eikonal factor:

$$E_{12} = \frac{p_1 \cdot p_2}{p_1 \cdot p_5 p_2 \cdot p_5} , \quad (91)$$

which we call  $H_{12}(p_5)$ . Therefore the matrix element squared can be written as:

$$|M|^2 = H_{12}(p_5) E_{12} . \quad (92)$$

$H_{12}$  can then be implemented into DIPHOX to obtain the cross section.

We consider the LHC energy and use the kinematic cuts from the ATLAS and CMS proposals [591,592], specifically for the transverse momentum of the most energetic photon (photon 1):  $p_{T(\gamma_1)} > 40$  GeV, and the rapidity:  $|\eta| < 2.5$ . The isolation criterion of photons requires that the amount of hadronic transverse energy deposited inside a cone of a certain radius and oriented towards the photon is smaller than  $E_{Tmax}$ , fixed by the experiment. We used the CTEQ 6 set of parton distribution functions [593].

In Fig. 163 is plotted the invariant mass distribution of the photon pair for the exclusive production of two photons and one jet. We require each pair of particles to be separated by at least 0.3 in the rapidity–azimuthal angle space:

$$\Delta R_{sep} = \sqrt{\Delta\phi^2 + \Delta\eta^2} > 0.3 , \quad (93)$$

where  $\phi$  is the azimuthal angle between the photons. The factorization and renormalization scales are given by:

$$\mu^2 = M^2 = m_{\gamma\gamma}^2 + p_T^2(\text{jet}) , \quad (94)$$

where  $m_{\gamma\gamma}$  corresponds to the invariant mass of the photon pair. The results are in agreement with those of [594].

In Fig. 164 is represented the cross-section of inclusive production of two photons in function of the transverse momentum of the photon pair, and in function of the azimuthal angle between the photons. Using the kinematic cuts of ATLAS and CMS, one imposes for the transverse momentum of photon 1:

$$p_{T(\gamma_1)} > 40 \text{ GeV} , \quad (95)$$

and for the transverse momentum of photon 2:

$$p_{T(\gamma_2)} > 25 \text{ GeV} . \quad (96)$$

Here we choose the renormalization and factorization scales as:

$$\mu^2 = M^2 = \frac{1}{4} m_{\gamma\gamma}^2 . \quad (97)$$

The results depend on the scale choice. For the isolation criterion of the photons, we now impose:

$$E_{Tmax} > 15 \text{ GeV} , \quad (98)$$



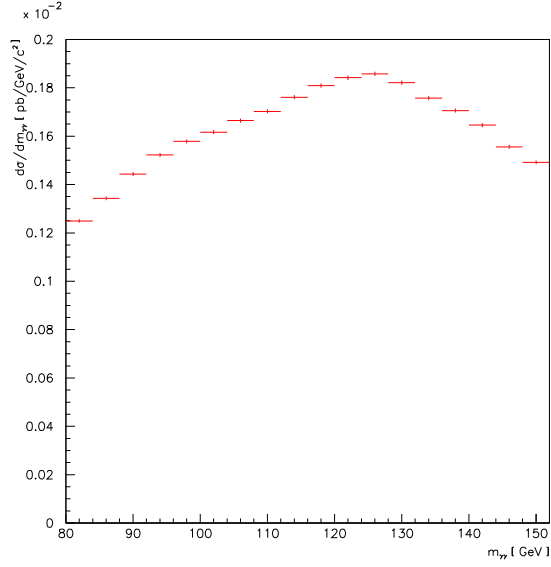


Fig. 163: Invariant mass distribution of exclusive production of two photons and one jet.

and, for the radius of the isolation cone:

$$R = \sqrt{\Delta\phi^2 + \Delta\eta^2} > 0.4 \quad , \quad (99)$$

with an acollinearity cut between photons of:

$$m_{\gamma\gamma} > 80 \text{ GeV} \quad . \quad (100)$$

For the transverse momentum distribution, we require a transverse momentum cut  $q_T > 20 \text{ GeV}$  for the photon pair.

As a comparison, the contributions of *direct*, *one fragmentation* and *two fragmentations* photoproduction processes are also presented on the figure. One can notice that, for this choice of scales, the contribution of  $gg \rightarrow \gamma\gamma + jet$  is smaller than the direct and one fragmentation contributions, but bigger than the two fragmentation contribution.

### 31.4 Conclusions

The one loop  $3g2\gamma$  corrections ( $\alpha_S^3$  order) have been incorporated into DIPHOX using the results of the direct calculation of the matrix element squared. The results are in agreement with those extracted from the  $5g$  amplitude. A comparison between transverse momentum and azimuthal distributions of the photon pair of direct, one fragmentation, two fragmentation and gluon initiated processes has been performed. The next step would consist in the implementation of the virtual correction of two loop gluon initiated process into DIPHOX to obtain the complete NLO accuracy.

### Acknowledgements

I would like to thank Jean-Philippe Guillet for his help regarding DIPHOX, and for his remarks and suggestions. I would like to thank also Thomas Binoth for useful discussions. I acknowledge the support of the McCain Fellowship at Mount Allison University. Feynman diagrams in this paper are drawn with Jaxodraw [595].

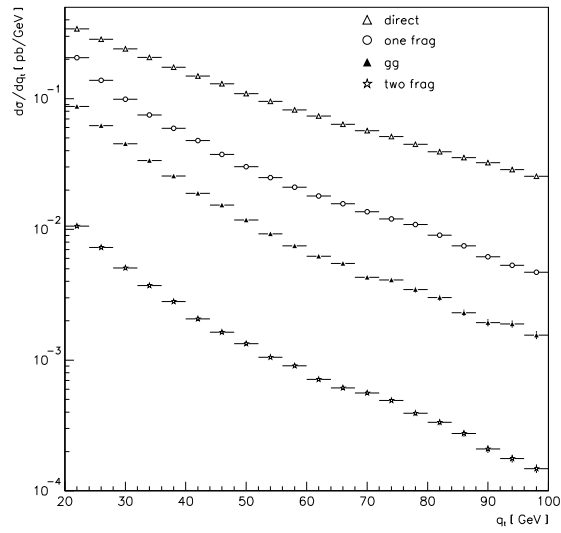
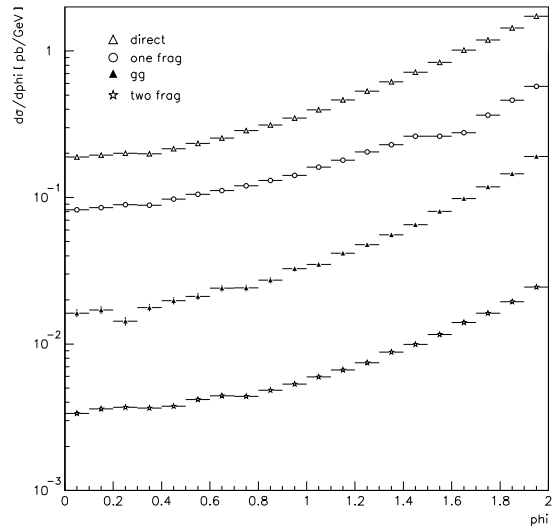


Fig. 164: Gluon initiated cross section versus transverse momentum of the photon pair (on the left) and versus the azimuthal angle between the two photons (on the right), compared to the cross sections of direct, one and two fragmentation photoproduction processes, for  $\mu^2 = M^2 = \frac{1}{4}m_{\gamma\gamma}^2$ .

## 32. THE ARCHITECTURE OF NNLO CROSS SECTIONS <sup>65</sup>

### 32.1 Introduction

QCD is an important component of the Standard Model, and will play a fundamental role at the LHC. Within the known Standard Model, it will be important to have an evaluation as precise as possible of the strong coupling constant  $\alpha_S$ , of the parton distributions, of the electroweak parameters, and of the LHC parton luminosity. Beyond that, a precise determination of Higgs and New-Physics production, and particularly of their backgrounds, will be essential, in order to interpret New-Physics signals.

At high  $Q^2$  any production rate can be expressed as a series expansion in  $\alpha_S$ . Because QCD is asymptotically free, the simplest approximation is to evaluate any series expansion at leading order in  $\alpha_S$ . However, for most processes a leading-order evaluation yields unreliable predictions. The next simplest approximation is a NLO evaluation, which usually allows for a satisfying assessment of the production rates. In the past 25 years, many efforts have been made to compute production rates at NLO and to devise process-independent methods [485, 523, 524, 526, 527, 596–600] to compute rates at NLO accuracy (see the NLO section of these proceedings). In some cases, though, the NLO corrections may not be accurate enough. Specimen cases are: the extraction of  $\alpha_S$  from the data, where in order to avoid that the main source of uncertainty be due to the NLO evaluation of some production rates, like the event shapes of jet production in  $e^+e^-$  collisions, only observables evaluated at next-to-next-to-leading order (NNLO) accuracy are considered [601]; open  $b$ -quark production at the Tevatron, where the NLO uncertainty bands are too large to test the theory [602] vs. the data [603]; Higgs production from gluon fusion in hadron collisions, where it is known that the NLO corrections are large [604, 605], while the NNLO corrections [606–608], which have been evaluated in the large- $m_t$  limit, display a modest increase, of the order of less than 20%, with respect to the NLO evaluation; Drell-Yan productions of  $W$  and  $Z$  vector bosons at LHC, which can be used as “standard candles” to measure the parton luminosity at the LHC [609–612].

In the last few years the NNLO corrections have been computed to the total cross section [606, 613] and to the rapidity distribution [207, 614] of Drell-Yan production, to the total cross section for the production of a scalar [606–608] and a pseudoscalar [615, 616] Higgs from gluon fusion as well as to a fully differential cross section [617, 618], and to jet production in  $e^+e^-$  collisions [619–621]. The methods which have been used are disparate: analytic integration, which is the first method to have been used [613], cancels the divergences analytically, and is flexible enough to include a limited class of acceptance cuts by modelling cuts as propagators [207, 607, 614, 616]; sector decomposition [617, 619, 622–627], which is flexible enough to include any acceptance cuts and for which the cancellation of the divergences is performed numerically; subtraction [621, 626, 628–635], for which the cancellation of the divergences is organised in a process-independent way by exploiting the universal structure of the infrared divergences of a gauge theory, in particular the universal structure of the three-parton tree-level splitting functions [636–641] and the two-parton one-loop splitting functions [563, 642–645].

The standard approach of subtraction to NNLO relies on defining approximate cross sections which match the singular behaviour of the QCD cross sections in all the relevant unresolved limits. In general, the definition of the approximate cross sections must rely on the single and double unresolved limits of the QCD squared matrix elements. Although, as outlined above, the infrared limits of the QCD matrix elements have been extensively studied, the formulae presented in the literature do not lend themselves directly for devising the approximate cross sections for two reasons. The first problem is that the various single and double soft and/or collinear limits overlap in a very complicated way and the infrared-factorisation formulae have to be written in such forms that these overlaps can be disentangled, so that the double subtraction is avoided. The second problem is that even if the factorisation formulae are written such that the double subtraction does not occur, the expressions cannot straightforwardly be

---

<sup>65</sup>Contributed by: V. Del Duca, A. Gehrmann-De Ridder, T. Gehrmann, E.W.N. Glover, G. Heinrich, G. Somogyi, Z. Trócsányi

used as subtraction formulae, because the momenta of the partons in the factorised matrix elements are unambiguously defined only in the strict soft and collinear limits. In order to define the approximate cross sections, one also has to factorise the phase space of the unresolved partons such that the singular factors can be integrated and the remaining expressions can be combined with the virtual correction, leading to cross sections which are finite and integrable in four dimensions.

In the sector decomposition approach, the singularities are isolated by an algebraic procedure acting on the integration variables, which is iterated in an automated way. The pole coefficients are integrated numerically. This method avoids the manual setup of a subtraction scheme, but leads to rather large expressions as the number of original functions is increased in each iteration of the sector decomposition.

In the following, variants of both the ‘‘standard subtraction’’ and the sector decomposition approach will be described briefly.

## 32.2 The approach of Del Duca, Somogyi, Trócsányi <sup>66</sup>

In the context of the standard subtraction, a subtraction scheme was presented in [635] for processes without coloured partons in the initial state. Namely, subtraction terms were explicitly constructed, which regularise the kinematical singularities of the squared matrix element in all singly- and doubly-unresolved parts of the phase space, in such a way that the subtraction terms avoid all possible double and triple subtractions. Thus, the regularised squared matrix element is integrable over all the phase space regions where at most two partons become unresolved. In particular, new factorisation formulae were presented in the iterated singly-unresolved limits for the colour-correlated and the spin-correlated squared matrix elements. It was pointed out that soft factorisation formulae do not exist for the simultaneously spin- and colour-correlated squared matrix elements, which indicates that within the scheme envisaged in [635] the azimuthally correlated singly-collinear subtraction terms must not contain colour correlations. This can be achieved naturally for those processes where the colour charges in the colour-correlated squared matrix elements can be factorized completely, which occurs only for processes with no more than three coloured hard partons [521], that is for  $e^+e^- \rightarrow 2, 3$  jets in this context. For processes with more coloured hard partons a subtraction scheme that avoids such correlations was outlined in Ref. [635]. However, that paper did not consider the second problem mentioned above, namely the phase space of the subtraction terms. In the following, we outline a possible solution to that. In order to avoid a lengthy introduction to the notation, we use the same notation as Ref. [635].

### 32.21 Subtraction scheme at NNLO

The NNLO correction to any  $m$ -jet production rate is a sum of three contributions, the doubly-real, the one-loop singly-unresolved real-virtual and the two-loop doubly-virtual terms,

$$\sigma^{\text{NNLO}} = \int_{m+2} d\sigma_{m+2}^{\text{RR}} J_{m+2} + \int_{m+1} d\sigma_{m+1}^{\text{RV}} J_{m+1} + \int_m d\sigma_m^{\text{VV}} J_m . \quad (101)$$

The three contributions in Eq.(101) are separately divergent, but their sum is finite for infrared-safe observables. As explained in Ref. [635], we rewrite Eq. (101) as

$$\sigma^{\text{NNLO}} = \int_{m+2} d\sigma_{m+2}^{\text{NNLO}} + \int_{m+1} d\sigma_{m+1}^{\text{NNLO}} + \int_m d\sigma_m^{\text{NNLO}} , \quad (102)$$

where the integrands

$$d\sigma_{m+2}^{\text{NNLO}} = \left[ d\sigma_{m+2}^{\text{RR}} J_{m+2} - d\sigma_{m+2}^{\text{RR,A}_2} J_m - d\sigma_{m+2}^{\text{RR,A}_1} J_{m+1} + d\sigma_{m+2}^{\text{RR,A}_{12}} J_m \right]_{\varepsilon=0} , \quad (103)$$

<sup>66</sup>Authors: V. Del Duca, G. Somogyi, Z. Trócsányi

$$d\sigma_{m+1}^{\text{NNLO}} = \left[ d\sigma_{m+1}^{\text{RV}} J_{m+1} - d\sigma_{m+1}^{\text{RV},A_1} J_m + \int_1 \left( d\sigma_{m+2}^{\text{RR},A_1} J_{m+1} - d\sigma_{m+2}^{\text{RR},A_{12}} J_m \right) \right]_{\varepsilon=0}, \quad (104)$$

and

$$d\sigma_m^{\text{NNLO}} = \left[ d\sigma_m^{\text{VV}} + \int_2 d\sigma_{m+2}^{\text{RR},A_2} + \int_1 d\sigma_{m+1}^{\text{RV},A_1} \right]_{\varepsilon=0} J_m, \quad (105)$$

are separately finite, thus integrable in four dimensions by construction. Above  $d\sigma_{m+2}^{\text{RR},A_2}$  and  $d\sigma_{m+2}^{\text{RR},A_1}$  are the counterterms regularising the doubly- and singly-unresolved limits of  $d\sigma_{m+2}^{\text{RR}}$  respectively while the overlap of these is accounted for by  $d\sigma_{m+2}^{\text{RR},A_{12}}$ . The singly-unresolved limits of  $d\sigma_{m+1}^{\text{RV}}$  are regularised by the counterterm  $d\sigma_{m+1}^{\text{RV},A_1}$ . In this contribution we will deal exclusively with the subtractions needed to regularise the doubly-real emission.

### 32.22 Subtraction terms for doubly-real emission

**The general setup** The cross section  $d\sigma_{m+2}^{\text{RR}}$ , is the integral of the tree-level squared matrix element for  $m+2$  parton production over the  $m+2$  parton phase space

$$d\sigma_{m+2}^{\text{RR}} = d\phi^{(m+2)} |\mathcal{M}_{m+2}^{(0)}|^2. \quad (106)$$

We disentangled the overlap structure of the singularities of  $|\mathcal{M}_{m+2}^{(0)}|^2$  into the pieces  $\mathbf{A}_2 |\mathcal{M}_{m+2}^{(0)}|^2$ ,  $\mathbf{A}_1 |\mathcal{M}_{m+2}^{(0)}|^2$  and  $\mathbf{A}_{12} |\mathcal{M}_{m+2}^{(0)}|^2$  in Ref. [635]. These expressions are, as they stand, only defined in the strict soft and/or collinear limits. To define true counterterms, they need to be extended over the full phase-space. This extension requires a phase-space factorisation that maintains momentum conservation exactly, but such that in addition it respects the structure of delicate cancellations among the various subtraction terms. Then the counterterms may symbolically be written as

$$d\sigma_{m+2}^{\text{RR},A_2} = d\phi^{(m)} [dp^{(2)}] \mathcal{A}_2 |\mathcal{M}_{m+2}^{(0)}|^2, \quad (107)$$

$$d\sigma_{m+2}^{\text{RR},A_1} = d\phi^{(m+1)} [dp^{(1)}] \mathcal{A}_1 |\mathcal{M}_{m+2}^{(0)}|^2, \quad (108)$$

and

$$d\sigma_{m+2}^{\text{RR},A_{12}} = d\phi^{(m)} [dp^{(1)}] [dp^{(1)}] \mathcal{A}_{12} |\mathcal{M}_{m+2}^{(0)}|^2, \quad (109)$$

where in Eqs.(107)–(109) we used a calligraphic notation to indicate the extension of the terms  $\mathbf{A}_2 |\mathcal{M}_{m+2}^{(0)}|^2$ ,  $\mathbf{A}_1 |\mathcal{M}_{m+2}^{(0)}|^2$  and  $\mathbf{A}_{12} |\mathcal{M}_{m+2}^{(0)}|^2$  over the whole phase space.

**Singly-singular counterterms** The singly-singular counterterm  $\mathcal{A}_1 |\mathcal{M}_{m+2}^{(0)}|^2$  reads

$$\mathcal{A}_1 |\mathcal{M}_{m+2}^{(0)}|^2 = \sum_r \left[ \sum_{i \neq r} \frac{1}{2} \mathcal{C}_{ir} + \left( \mathcal{S}_r - \sum_{i \neq r} \mathcal{C}_{ir} \mathcal{S}_r \right) \right]. \quad (110)$$

Here the singly-collinear term is

$$\mathcal{C}_{ir} = 8\pi\alpha_s \mu^{2\varepsilon} \frac{1}{s_{ir}} \langle \mathcal{M}_{m+1}^{(0)} | \hat{P}_{f_i f_r}^{(0)}(\tilde{z}_{i,r}, \tilde{z}_{r,i}, \tilde{k}_{\perp,ir}; \varepsilon) | \mathcal{M}_{m+1}^{(0)} \rangle, \quad (111)$$

where  $\hat{P}_{f_i f_r}^{(0)}(z_i, z_r, k_{\perp}, \varepsilon)$  is the Altarelli-Parisi splitting function. We define the momentum fractions  $\tilde{z}_{i,r}$  and  $\tilde{z}_{r,i}$  as

$$\tilde{z}_{i,r} = \frac{s_{iQ}}{s_{iQ} + s_{rQ}} \quad \text{and} \quad \tilde{z}_{r,i} = \frac{s_{rQ}}{s_{iQ} + s_{rQ}}, \quad (112)$$

i.e., the energy fractions of the daughter momenta of the splitting with respect to the energy of the parent parton. The transverse momentum  $\tilde{k}_{\perp,ir}$  is given by

$$\tilde{k}_{\perp,ir}^{\mu} = \left( \tilde{z}_{i,r} - \frac{s_{ir}}{\alpha_{ir}(s_{iQ} + s_{rQ})} \right) p_r^{\mu} - \left( \tilde{z}_{r,i} - \frac{s_{ir}}{\alpha_{ir}(s_{iQ} + s_{rQ})} \right) p_i^{\mu} + (\tilde{z}_{r,i} - \tilde{z}_{i,r}) \tilde{p}_{ir}^{\mu}, \quad (113)$$

where we used the abbreviations  $s_{iQ} = 2p_i \cdot Q$ ,  $s_{rQ} = 2p_r \cdot Q$ .

The  $m + 1$  momenta entering the matrix elements on the right hand side of Eq.(111) are defined as follows

$$\tilde{p}_{ir}^{\mu} = \frac{1}{1 - \alpha_{ir}} (p_i^{\mu} + p_r^{\mu} - \alpha_{ir} Q^{\mu}), \quad \tilde{p}_n^{\mu} = \frac{1}{1 - \alpha_{ir}} p_n^{\mu}, \quad n \neq i, r, \quad (114)$$

where

$$\alpha_{ir} = \frac{(p_i + p_r) \cdot Q - \sqrt{[(p_i + p_r) \cdot Q]^2 - s_{ir} s}}{s} \quad (115)$$

and  $Q^{\mu}$  is the total four-momentum of the incoming electron and positron and  $s = Q^2$ . Clearly, the total four-momentum is conserved,

$$\tilde{p}_{ir}^{\mu} + \sum_n \tilde{p}_n^{\mu} = p_i^{\mu} + p_r^{\mu} + \sum_n p_n^{\mu}. \quad (116)$$

The singly-soft term is

$$\mathcal{S}_r = -8\pi\alpha_s\mu^{2\varepsilon} \sum_i \sum_{k \neq i} \frac{1}{2} \mathcal{S}_{ik}(r) \langle \mathcal{M}_{m+1}^{(0)} | \mathbf{T}_i \mathbf{T}_k | \mathcal{M}_{m+1}^{(0)} \rangle, \quad (117)$$

if  $r$  is a gluon, and  $\mathcal{S}_r = 0$  if  $r$  is a quark or antiquark. The  $m + 1$  momenta entering the matrix element on the right hand side of Eq. (117) are defined in by first rescaling all the hard momenta by a factor  $1/\lambda_r$  and then transforming all of the rescaled momenta by a Lorentz transformation  $\Lambda_{\nu}^{\mu}$ ,

$$\tilde{p}_n^{\mu} = \Lambda_{\nu}^{\mu} [Q, (Q - p_r)/\lambda_r] (p_n^{\nu}/\lambda_r), \quad n \neq r, \quad (118)$$

where

$$\lambda_r = \sqrt{1 - \frac{s_{rQ}}{s}}, \quad \Lambda_{\nu}^{\mu} [K, \tilde{K}] = g_{\nu}^{\mu} - \frac{2(K + \tilde{K})^{\mu} (K + \tilde{K})_{\nu}}{(K + \tilde{K})^2} + \frac{2K^{\mu} \tilde{K}_{\nu}}{K^2}. \quad (119)$$

The matrix  $\Lambda_{\nu}^{\mu} [K, \tilde{K}]$  generates a (proper) Lorentz transformation, provided  $K^2 = \tilde{K}^2 \neq 0$ . Since  $p_r^{\mu}$  is massless ( $p_r^2 = 0$ ), the total four-momentum is again conserved.

The eikonal factor in Eq. (117) is

$$\mathcal{S}_{ik}(r) = \frac{2s_{ik}}{s_{ir}s_{rk}}, \quad (120)$$

and the sum in Eq. (117) runs over the external partons of the  $m + 1$  parton matrix element on the right hand side.

The soft-collinear subtraction is given by

$$\mathcal{C}_{ir} \mathcal{S}_r = 8\pi\alpha_s\mu^{2\varepsilon} \frac{1}{s_{ir}} \frac{2\tilde{z}_{i,r}}{\tilde{z}_{r,i}} \mathbf{T}_i^2 | \mathcal{M}_{m+1}^{(0)} |^2, \quad (121)$$

if  $r$  is a gluon, and  $\mathcal{C}_{ir} \mathcal{S}_r = 0$  if  $r$  is a quark or antiquark. The momentum fractions are given by Eq. (112). As pointed out in Ref. [635], the correct variables in the squared matrix element in the soft-collinear limit are those that appear in the soft limit. Thus the  $m + 1$  momenta entering the matrix elements on the right hand side are again given by Eq. (118).



The momentum mappings introduced in Eqs. (114) and (118) both lead to exact phase-space factorisation in the form

$$d\phi^{(m+2)} = d\phi^{(m+1)} [dp^{(1)}], \quad (122)$$

where the  $m + 1$  momenta in the first factor on the right hand side are exactly those defined in Eq. (114) or Eq. (118). The explicit expressions for  $[dp^{(1)}]$  read

$$[dp^{(1)}] = \frac{(1 - \alpha_{ir})^{m(d-2)-1} s_{irQ}}{\sqrt{(s_{r\tilde{ir}} + s_{irQ} - s_{rQ})^2 + 4s_{r\tilde{ir}}(s - s_{irQ})}} \Theta(1 - \alpha_{ir}) \frac{d^d p_r}{(2\pi)^{d-1}} \delta_+(p_r^2), \quad (123)$$

$$[dp^{(1)}] = \lambda_r^{m(d-2)-2} \Theta(\lambda_r) \frac{d^d p_r}{(2\pi)^{d-1}} \delta_+(p_r^2), \quad (124)$$

for the collinear and soft phase-space factorisations (Eqs. (114) and (118)) respectively. In Eq. (123)  $\alpha_{ir}$  is understood to be expressed in terms of the variable  $\tilde{p}_{ir}$ ,

$$\alpha_{ir} = \frac{\sqrt{(s_{r\tilde{ir}} + s_{irQ} - s_{rQ})^2 + 4s_{r\tilde{ir}}(s - s_{irQ})} - (s_{r\tilde{ir}} + s_{irQ} - s_{rQ})}{2(s - s_{irQ})}. \quad (125)$$

The analytical integration of the counterterms over the factorised one-parton phase-space  $[dp^{(1)}]$  is then possible. Details of these integrations will be given elsewhere.

### 32.23 Doubly-singular and iterated counterterms

The doubly-singular and iterated counterterms are respectively defined by

$$\begin{aligned} \mathcal{A}_2 |\mathcal{M}_{m+2}^{(0)}|^2 = \sum_r \sum_{s \neq r} \left\{ \sum_{i \neq r, s} \left[ \frac{1}{6} \mathcal{C}_{irs} + \sum_{j \neq i, r, s} \frac{1}{8} \mathcal{C}_{ir;js} + \frac{1}{2} \left( \mathcal{C}_{ir;s} - \mathcal{C}_{irs} \mathcal{C}_{ir;s} - \sum_{j \neq i, r, s} \mathcal{C}_{ir;js} \mathcal{C}_{ir;s} \right) \right] \right. \\ \left. + \frac{1}{2} \mathcal{S}_{rs} - \sum_{i \neq r, s} \left[ \mathcal{C}_{ir;s} \mathcal{S}_{rs} + \frac{1}{2} \mathcal{C}_{irs} (\mathcal{S}_{rs}^N - \mathcal{S}_{rs}^A) + \sum_{j \neq i, r, s} \frac{1}{2} \mathcal{C}_{ir;js} \mathcal{S}_{rs} \right] \right\} \quad (126) \end{aligned}$$

and

$$\mathcal{A}_{12} |\mathcal{M}_{m+2}^{(0)}|^2 = \sum_t \left[ \mathcal{S}_t \mathcal{A}_2 |\mathcal{M}_{m+2}^{(0)}|^2 + \sum_{k \neq t} \frac{1}{2} \mathcal{C}_{kt} \mathcal{A}_2 |\mathcal{M}_{m+2}^{(0)}|^2 - \sum_{k \neq t} \mathcal{C}_{kt} \mathcal{S}_t \mathcal{A}_2 |\mathcal{M}_{m+2}^{(0)}|^2 \right], \quad (127)$$

where the three terms in Eq. (127) each evaluate further into long expressions. Leaving all details to a further publication, here we only note that similarly to the singly-unresolved counterterms in Eq. (110), each term in Eqs. (126) and (127) represents an extension of one of the limits discussed in Ref. [635]. The momentum mappings used for the various terms are either combinations of those introduced in Eqs. (114) and (118) or simple generalisations thereof. Exact phase-space factorisation is again possible. Using those factorised phase spaces, it is straightforward to write Eq. (103) explicitly. We have coded Eq. (103) for the case when  $d\sigma_{m+2}^{\text{RR}}$  is the fully differential cross section for the process  $e^+e^- \rightarrow q\bar{q}ggg$  ( $m = 3$ ) and  $J_5$  defines the  $C$ -parameter. We found that the integral of  $d\sigma_{m+2}^{\text{NNLO}}$  is indeed finite and integrable in four dimensions using standard Monte Carlo methods.

### 32.24 Outlook

The subtraction scheme outlined here uses the known singly- and doubly-singular limits of the squared matrix elements. These limits overlap and a way of disentanglement was presented in Ref. [635]. In this contribution we discussed how to make the next step, namely we outlined the exact phase space

factorisations we propose for the collinear and soft subtraction terms. Putting the subtraction terms on the factorised phase space allows us the integration of the singular factors such that the remaining expressions can be combined with the virtual correction. This integration and combination is left for future work.

### 32.3 The antenna subtraction approach <sup>67</sup>

#### 32.31 Method

An  $m$ -jet cross section at NLO is obtained by summing contributions from  $(m+1)$ -parton tree level and  $m$ -parton one-loop processes:

$$d\sigma_{NLO} = \int_{d\Phi_{m+1}} (d\sigma_{NLO}^R - d\sigma_{NLO}^S) + \left[ \int_{d\Phi_{m+1}} d\sigma_{NLO}^S + \int_{d\Phi_m} d\sigma_{NLO}^V \right].$$

The cross section  $d\sigma_{NLO}^R$  is the  $(m+1)$ -parton tree-level cross section, while  $d\sigma_{NLO}^V$  is the one-loop virtual correction to the  $m$ -parton Born cross section  $d\sigma^B$ . Both contain infrared singularities, which are explicit poles in  $1/\epsilon$  in  $d\sigma_{NLO}^V$ , while becoming explicit in  $d\sigma_{NLO}^R$  only after integration over the phase space. In general, this integration involves the (often iterative) definition of the jet observable, such that an analytic integration is not feasible (and also not appropriate). Instead, one would like to have a flexible method that can be easily adapted to different jet observables or jet definitions. Therefore, the infrared singularities of the real radiation contributions should be extracted using infrared subtraction terms. One introduces  $d\sigma_{NLO}^S$ , which is a counter-term for  $d\sigma_{NLO}^R$ , having the same unintegrated singular behaviour as  $d\sigma_{NLO}^R$  in all appropriate limits. Their difference is free of divergences and can be integrated over the  $(m+1)$ -parton phase space numerically. The subtraction term  $d\sigma_{NLO}^S$  has to be integrated analytically over all singular regions of the  $(m+1)$ -parton phase space. The resulting cross section added to the virtual contribution yields an infrared finite result. Several methods for constructing NLO subtraction terms systematically were proposed in the literature [485, 523, 526, 527, 596, 599, 600]. For some of these methods, extension to NNLO was discussed [628, 629, 631, 632, 635] and partly worked out. In this section, focus is on the antenna subtraction method [485, 599], which is extended to NNLO [621].

The basic idea of the antenna subtraction approach at NLO is to construct the subtraction term  $d\sigma_{NLO}^S$  from antenna functions. Each antenna function encapsulates all singular limits due to the emission of one unresolved parton between two colour-connected hard partons (tree-level three-parton antenna function). This construction exploits the universal factorisation of phase space and squared matrix elements in all unresolved limits, depicted in Figure 165. The individual antenna functions are obtained by normalising three-parton tree-level matrix elements to the corresponding two-parton tree-level matrix elements.

At NNLO, the  $m$ -jet production is induced by final states containing up to  $(m+2)$  partons, including the one-loop virtual corrections to  $(m+1)$ -parton final states. As at NLO, one has to introduce subtraction terms for the  $(m+1)$ - and  $(m+2)$ -parton contributions. Schematically the NNLO  $m$ -jet cross section reads,

$$\begin{aligned} d\sigma_{NNLO} = & \int_{d\Phi_{m+2}} (d\sigma_{NNLO}^R - d\sigma_{NNLO}^S) + \int_{d\Phi_{m+2}} d\sigma_{NNLO}^S \\ & + \int_{d\Phi_{m+1}} (d\sigma_{NNLO}^{V,1} - d\sigma_{NNLO}^{VS,1}) + \int_{d\Phi_{m+1}} d\sigma_{NNLO}^{VS,1} \\ & + \int_{d\Phi_m} d\sigma_{NNLO}^{V,2}, \end{aligned}$$

where  $d\sigma_{NNLO}^S$  denotes the real radiation subtraction term coinciding with the  $(m+2)$ -parton tree level cross section  $d\sigma_{NNLO}^R$  in all singular limits [636–641]. Likewise,  $d\sigma_{NNLO}^{VS,1}$  is the one-loop virtual

<sup>67</sup> Authors: A. Gehrmann-De Ridder, T. Gehrmann, E.W.N. Glover

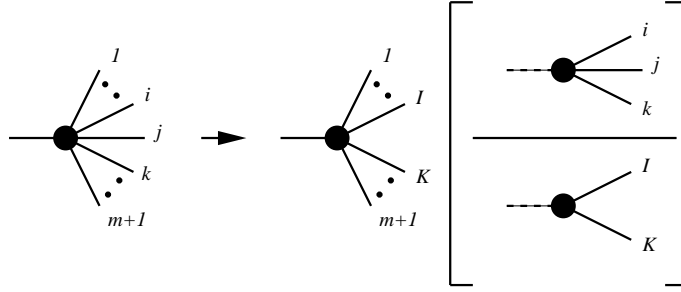


Fig. 165: Illustration of NLO antenna factorisation representing the factorisation of both the squared matrix elements and the  $(m + 1)$ -particle phase space. The term in square brackets represents both the antenna function and the antenna phase space.

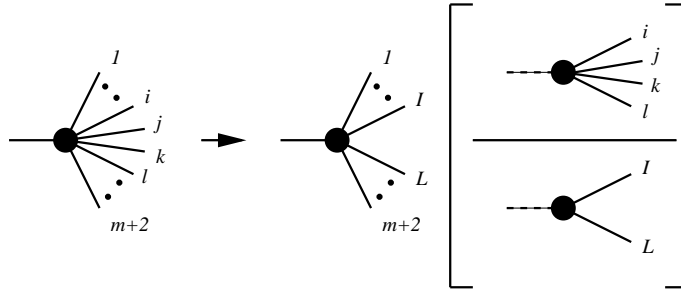


Fig. 166: Illustration of NNLO antenna factorisation representing the factorisation of both the squared matrix elements and the  $(m + 2)$ -particle phase space when the unresolved particles are colour connected. The term in square brackets represents both the antenna function and the antenna phase space.

subtraction term coinciding with the one-loop  $(m + 1)$ -parton cross section  $d\sigma_{NNLO}^{V,1}$  in all singular limits [563, 642–645]. Finally, the two-loop correction to the  $m$ -parton cross section is denoted by  $d\sigma_{NNLO}^{V,2}$ .

Both types of NNLO subtraction terms can be constructed from antenna functions. In  $d\sigma_{NNLO}^S$ , one has to distinguish four different types of unresolved configurations: (a) One unresolved parton but the experimental observable selects only  $m$  jets; (b) Two colour-connected unresolved partons (colour-connected); (c) Two unresolved partons that are not colour connected but share a common radiator (almost colour-unconnected); (d) Two unresolved partons that are well separated from each other in the colour chain (colour-unconnected). Among those, configuration (a) is properly accounted for by a single tree-level three-parton antenna function like used already at NLO. Configuration (b) requires a tree-level four-parton antenna function (two unresolved partons emitted between a pair of hard partons) as shown in Figure 166, while (c) and (d) are accounted for by products of two tree-level three-parton antenna functions.

In single unresolved limits, the one-loop cross section  $d\sigma_{NNLO}^{V,1}$  is described by the sum of two terms [563, 642–645]: a tree-level splitting function times a one-loop cross section and a one-loop splitting function times a tree-level cross section. Consequently, the one-loop single unresolved subtraction term  $d\sigma_{NNLO}^{VS,1}$  is constructed from tree-level and one-loop three-parton antenna functions, as sketched in Figure 167. Several other terms in  $d\sigma_{NNLO}^{VS,1}$  cancel with the results from the integration of terms in the double real radiation subtraction term  $d\sigma_{NNLO}^S$  over the phase space appropriate to one of the unresolved partons, thus ensuring the cancellation of all explicit infrared poles in the difference  $d\sigma_{NNLO}^{V,1} - d\sigma_{NNLO}^{VS,1}$ .

Finally, all remaining terms in  $d\sigma_{NNLO}^S$  and  $d\sigma_{NNLO}^{VS,1}$  have to be integrated over the four-parton and three-parton antenna phase spaces. After integration, the infrared poles are rendered explicit and cancel with the infrared pole terms in the two-loop squared matrix element  $d\sigma_{NNLO}^{V,2}$ .

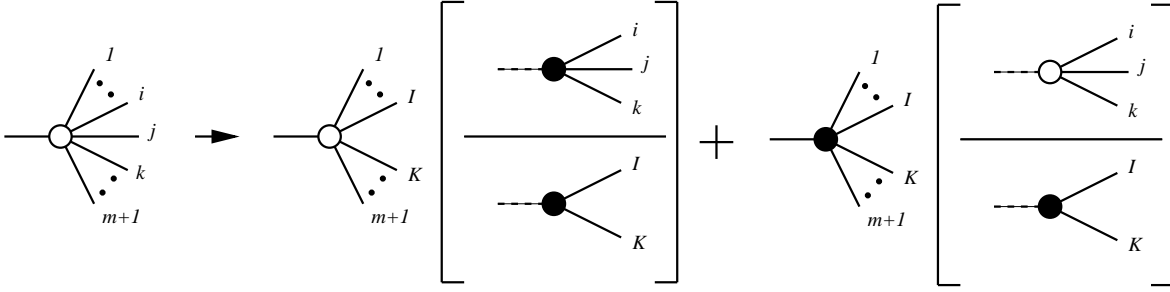


Fig. 167: Illustration of NNLO antenna factorisation representing the factorisation of both the one-loop “squared” matrix elements (represented by the white blob) and the  $(m + 1)$ -particle phase space when the unresolved particles are colour connected.

### 32.32 Derivation of antenna functions

The subtraction terms  $d\sigma_{NLO}^S$ ,  $d\sigma_{NNLO}^S$  and  $d\sigma_{NNLO}^{VS,1}$  require three different types of antenna functions corresponding to the different pairs of hard partons forming the antenna: quark-antiquark, quark-gluon and gluon-gluon antenna functions. In the past [485, 599], NLO antenna functions were constructed by imposing definite properties in all single unresolved limits (two collinear limits and one soft limit for each antenna). This procedure turns out to be impractical at NNLO, where each antenna function must have definite behaviours in a large number of single and double unresolved limits. Instead, one can derive these antenna functions in a systematic manner from physical matrix elements known to possess the correct limits. The quark-antiquark antenna functions can be obtained directly from the  $e^+e^- \rightarrow 2j$  real radiation corrections at NLO and NNLO [620]. For quark-gluon and gluon-gluon antenna functions, effective Lagrangians are used to obtain tree-level processes yielding a quark-gluon or gluon-gluon final state. The antenna functions are then obtained from the real radiation corrections to these processes. Quark-gluon antenna functions were derived [633] from the purely QCD (i.e. non-supersymmetric) NLO and NNLO corrections to the decay of a heavy neutralino into a massless gluino plus partons [646], while gluon-gluon antenna functions [634] result from the QCD corrections to Higgs boson decay into partons [647, 648].

All tree-level three-parton and four-parton antenna functions and three-parton one-loop antenna functions are listed in [621], where they are also integrated, using the phase space integration techniques described in [626].

### 32.33 Application to $e^+e^- \rightarrow 3 \text{ jets}$

To illustrate the application of antenna subtraction on a non-trivial example, in [621, 649] the  $1/N^2$ -contribution to the NNLO corrections to  $e^+e^- \rightarrow 3 \text{ jets}$  was derived. This colour factor receives contributions from  $\gamma^* \rightarrow q\bar{q}ggg$  and  $\gamma^* \rightarrow q\bar{q}q\bar{q}g$  at tree-level [650–652],  $\gamma^* \rightarrow q\bar{q}gg$  and  $\gamma^* \rightarrow q\bar{q}q\bar{q}$  at one-loop [480–482, 653, 654] and  $\gamma^* \rightarrow q\bar{q}g$  at two-loops [655, 656]. The four-parton and five-parton final states contain infrared singularities, which need to be extracted using the antenna subtraction formalism.

In this contribution, all gluons are effectively photon-like, and couple only to the quarks, but not to each other. Consequently, only quark-antiquark antenna functions appear in the construction of the subtraction terms.

Starting from the program EERAD2 [485], which computes the four-jet production at NLO, the NNLO antenna subtraction method for the  $1/N^2$  colour factor contribution to  $e^+e^- \rightarrow 3j$  was implemented. EERAD2 already contains the five-parton and four-parton matrix elements relevant here, as well as the NLO-type subtraction terms.

The implementation contains three channels, classified by their partonic multiplicity: (a) in the five-parton channel, one integrates  $d\sigma_{NNLO}^R - d\sigma_{NNLO}^S$ ; (b) in the four-parton channel, one integrates

$d\sigma_{NNLO}^{V,1} - d\sigma_{NNLO}^{VS,1}$ ; (c) in the three-parton channel, one integrates  $d\sigma_{NNLO}^{V,2} + d\sigma_{NNLO}^S + d\sigma_{NNLO}^{VS,1}$ . The numerical integration over these channels is carried out by Monte Carlo methods.

By construction, the integrands in the four-parton and three-parton channel are free of explicit infrared poles. In the five-parton and four-parton channel, the proper implementation of the subtraction was tested by generating trajectories of phase space points approaching a given single or double unresolved limit. Along these trajectories, one observes that the antenna subtraction terms converge locally towards the physical matrix elements, and that the cancellations among individual contributions to the subtraction terms take place as expected. Moreover, the correctness of the subtraction was checked by introducing a lower cut (slicing parameter) on the phase space variables, and observing that our results are independent of this cut (provided it is chosen small enough). This behaviour indicates that the subtraction terms ensure that the contribution of potentially singular regions of the final state phase space does not contribute to the numerical integrals, but is accounted for analytically.

Finally, it was noted in [621] that the infrared poles of the two-loop (including one-loop times one-loop) correction to  $\gamma^* \rightarrow q\bar{q}g$  are cancelled in all colour factors by a combination of integrated three-parton and four-parton antenna functions. This highly non-trivial cancellation clearly illustrates that the antenna functions derived here correctly approximate QCD matrix elements in all infrared singular limits at NNLO. They also outline the structure of infrared cancellations in  $e^+e^- \rightarrow 3j$  at NNLO, and indicate the structure of the subtraction terms in all colour factors.

### 32.34 Outlook

The antenna subtraction method presented here allows the subtraction of infrared singularities in the calculation of jet observables at NNLO. It introduces subtraction terms for double real radiation at tree level and single real radiation at one loop based on antenna functions. These antenna functions describe the colour-ordered radiation of unresolved partons between a pair of hard (radiator) partons. All antenna functions at NLO and NNLO can be derived systematically from physical matrix elements. To demonstrate the application of the new method on a non-trivial example, the NNLO corrections to the subleading colour contribution to  $e^+e^- \rightarrow 3$  jets were implemented.

An immediate application of the method presented here is the calculation of the full NNLO corrections to  $e^+e^- \rightarrow 3$  jets. The antenna subtraction method can be further generalised to NNLO corrections to jet production in lepton-hadron or hadron-hadron collisions. In these kinematical situations, the subtraction terms are constructed using the same antenna functions, but in different phase space configurations: instead of the  $1 \rightarrow n$  decay kinematics considered here,  $2 \rightarrow n$  scattering kinematics are required, which can also contain singular configurations due to single or double initial state radiation. These require new sets of integrated antenna functions, accounting for the different phase space configurations in these cases.

## 32.4 The sector decomposition approach to NNLO cross sections <sup>68</sup>

### 32.41 General aspects

Sector decomposition is a general method to disentangle and isolate overlapping singularities, of both ultraviolet and infrared nature. As the infrared singularities occurring in NNLO calculations involving massless particles can be entangled in a very complicated way – in the virtual two-loop integrals as well as in the real radiation parts – sector decomposition is particularly helpful in the context of NNLO calculations. Originally, it has been conceived by K. Hepp [657] for overlapping ultraviolet singularities. Its first phenomenological application can be found in [622], and in [623] it has been developed to an automated tool to calculate multi-loop integrals numerically in the Euclidean region. It has been successfully applied to various types of multi-loop integrals [658–662]. Its application to NNLO phase space integrals, first proposed in [624], saw a very rapid development recently [625–627] and already

<sup>68</sup> Author: G. Heinrich

lead to NNLO results for  $e^+e^- \rightarrow 2$  jets [619], Higgs production [618] and muon decay [662]. In [663], first results on its application to  $e^+e^- \rightarrow 3$  jets were presented.

The advantages of the sector decomposition approach reside in the fact that the extraction of the infrared poles is algorithmic, being done by an algebraic subroutine, and that the subtraction terms can be arbitrarily complicated as they are integrated only numerically. However, the size of the expressions produced by the iterated sector decomposition is rather large. On the other hand, the methods based on the manual construction of an analytic subtraction scheme [620, 621, 628–635, 649] allow maximal (i.e. analytical) control over the pole terms, and insure a minimal number of subtraction terms.

### 32.42 The method

The universal applicability of sector decomposition goes back to the fact that it acts in parameter space by a simple mechanism. The parameters can be Feynman parameters in the case of multi-loop integrals, or phase space integration parameters, or a combination of both. In the following, the working mechanism of sector decomposition will be outlined only briefly, details can be found in [623, 627].

An overlapping singularity in parameter space is of the type

$$I = \int_0^1 dx \int_0^1 dy x^{-1-\epsilon} (x+y)^{-1},$$

where a naive subtraction of the singularity for  $x \rightarrow 0$  of the form

$$\int_0^1 dx \int_0^1 dy x^{-1-\epsilon} f(x, y) = -\frac{1}{\epsilon} \int_0^1 dy f(0, y) + \int_0^1 dx \int_0^1 dy x^{-\epsilon} \frac{f(x, y) - f(0, y)}{x} \quad (128)$$

fails. To solve this problem, one can split the integration region into sectors where the variables  $x$  and  $y$  are ordered:

$$I = \int_0^1 dx \int_0^1 dy x^{-1-\epsilon} (x+y)^{-1} \left[ \underbrace{\Theta(x-y)}_{(a)} + \underbrace{\Theta(y-x)}_{(b)} \right].$$

Then the integration domain is remapped to the unit cube: After the substitutions  $y = xt$  in sector (a) and  $x = yt$  in sector (b), one has

$$I = \int_0^1 dx x^{-1-\epsilon} \int_0^1 dt (1+t)^{-1} + \int_0^1 dy y^{-1-\epsilon} \int_0^1 dt t^{-1-\epsilon} (1+t)^{-1},$$

where all singularities are factorised. For more complicated functions, several iterations of this procedure may be necessary, which can be easily implemented into an automated subroutine. Once all singularities are factored out, subtractions of the type (128) are possible and the result can subsequently be expanded in  $\epsilon$ . Note that the subtractions of the pole terms naturally lead to plus distributions [625] by the identity

$$x^{-1+\kappa\epsilon} = \frac{1}{\kappa\epsilon} \delta(x) + \sum_{n=0}^{\infty} \frac{(\kappa\epsilon)^n}{n!} \left[ \frac{\ln^n(x)}{x} \right]_+ \quad \text{where} \quad \int_0^1 dx f(x) [g(x)/x]_+ = \int_0^1 dx \frac{f(x) - f(0)}{x} g(x).$$

In this way, a Laurent series in  $\epsilon$  is obtained, where the pole coefficients are sums of finite parameter integrals which can be evaluated numerically.

For the numerical evaluation of loop integrals it has to be assured that no integrable singularities (e.g. thresholds) are crossed which spoil the numerical convergence. For integrals depending only on a single scale, which can be factored out, this does not pose a problem at all. For integrals with more than one scale, like for example two-loop box diagrams, the situation is more difficult, but in the case of  $e^+e^-$  annihilation to massless final state particles, evaluation over the whole physical region is possible, as the kinematics of these processes is such that all Mandelstam variables are always non-negative.



### 32.43 Application to $e^+e^- \rightarrow 3 \text{ jets}$ at NNLO

In order to focus on a concrete example of phenomenological relevance, we will discuss the application of sector decomposition to the calculation of  $e^+e^- \rightarrow 3 \text{ jets}$  at NNLO in the following.

**Virtual contributions** The contributions to the amplitude which involve virtual integrals are composed of the two-loop corrections combined with a  $1 \rightarrow 3$  particle phase space, and the one-loop corrections combined with a  $1 \rightarrow 4$  particle phase space where one particle can become soft and/or collinear. In both cases, sector decomposition for loop integrals [623] can serve to extract the poles in  $1/\epsilon$  from the integrals. In what concerns the two-loop integrals, this part could also be taken from the literature, as the full two-loop matrix element is known analytically [655, 656]. This would save a considerable amount of CPU time. The two-loop matrix element will only depend on the invariants  $y_1 = s_{12}/q^2$ ,  $y_2 = s_{13}/q^2$  and  $y_3 = s_{23}/q^2$ , where  $q^2$  is the invariant mass of the  $e^+e^-$  system and  $\sum_{i=1}^3 y_i = 1$ . The subsequent phase space integration over the  $y_i$  is trivial, and the 3-jet measurement function will make sure that all events where a singular limit  $y_i \rightarrow 0$  is approached will be rejected.

In the case of the one-loop contributions, the most complicated objects will be 5-point integrals with one off-shell external leg. Sector decomposition will lead to a result in terms of five independent scaled Mandelstam invariants  $y_i$ . This result has to be calculated up to order  $\epsilon^2$ , as it will be combined with the  $1 \rightarrow 4$  parton phase space where one parton can become unresolved, leading to  $1/\epsilon^2$  poles. This does not constitute a problem, as the expansions to higher order in  $\epsilon$ , as well as  $1 \rightarrow 4$  parton phase space integrals, are well under control within sector decomposition. It is also possible to do parts of the loop integrations analytically to achieve a form which is suitable for subsequent sector decomposition [662, 664]. However, these contributions have not yet been implemented completely into a Monte Carlo program, because priority has been given to the most challenging part, which is the integration over the  $1 \rightarrow 5$  parton phase space where up to two partons can become unresolved.

**Real radiation at NNLO** As mentioned above, the main difficulty in calculating the real radiation part of  $e^+e^- \rightarrow 3 \text{ jets}$  at NNLO is the isolation and subtraction of the infrared poles which occur when integrating the squared amplitude over the phase space for  $\gamma^* \rightarrow 5$  partons. In [663], a method has been developed to tackle this problem. The correctness of the results for the integrals over the  $1 \rightarrow 5$  particle phase space can be checked by exploiting the fact that the sum over all cuts of a given (UV renormalised) diagram must be infrared finite. This is shown in Figure 168 for a sample diagram: Summing over all cuts of this diagram and performing UV renormalisation, we obtain the condition

$$T_{1 \rightarrow 5} + z_1 T_{1 \rightarrow 4} + z_2 T_{1 \rightarrow 3} + z_3 T_{1 \rightarrow 2} = \text{finite}, \quad (129)$$

where  $T_{1 \rightarrow i}$  denotes the diagram with  $i$  cut lines. The renormalisation constants  $z_i$  (in Feynman gauge)

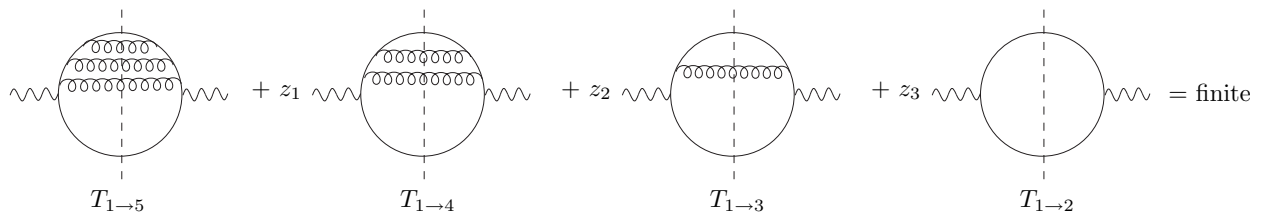


Fig. 168: Cancellation of IR divergences in the sum over all cuts of the renormalised graph

are given by [627, 663]

$$z_1 = C_F \frac{\alpha_s}{4\pi} \frac{1}{\epsilon}, \quad z_2 = C_F^2 \left( \frac{\alpha_s}{4\pi} \right)^2 \left( \frac{1}{2\epsilon^2} - \frac{1}{4\epsilon} \right), \quad z_3 = C_F^3 \left( \frac{\alpha_s}{4\pi} \right)^3 \left( \frac{1}{6\epsilon^3} - \frac{1}{4\epsilon^2} + \frac{1}{6\epsilon} \right). \quad (130)$$

The important new ingredient in eq. (129) is the calculation of  $T_{1\rightarrow 5}$ . The sector decomposition method leads to [663]

$$T_{1\rightarrow 5} = -C_F^3 \left(\frac{\alpha_s}{4\pi}\right)^3 T_{1\rightarrow 2} \left\{ \frac{0.16662}{\varepsilon^3} + \frac{1}{\varepsilon^2} [1.4993 - 0.4999 \log\left(\frac{q^2}{\mu^2}\right)] + \frac{1}{\varepsilon} [5.5959 - 4.4978 \log\left(\frac{q^2}{\mu^2}\right) + 0.7498 \log^2\left(\frac{q^2}{\mu^2}\right)] + \text{finite} \right\}, \quad (131)$$

where the numerical accuracy is 1%. The expressions entering eq. (129) for  $i < 5$  combine to [663]

$$z_1 T_{1\rightarrow 4} + z_2 T_{1\rightarrow 3} + z_3 T_{1\rightarrow 2} = C_F^3 \left(\frac{\alpha_s}{4\pi}\right)^3 T_{1\rightarrow 2} \left\{ \frac{1}{6\varepsilon^3} + \frac{1}{2\varepsilon^2} [3 - \log\left(\frac{q^2}{\mu^2}\right)] + \frac{1}{\varepsilon} [5.61 - \frac{9}{2} \log\left(\frac{q^2}{\mu^2}\right) + \frac{3}{4} \log^2\left(\frac{q^2}{\mu^2}\right)] + \text{finite} \right\}. \quad (132)$$

We can see that the poles in (132) are exactly cancelled by the 5-parton contribution (131) within the numerical precision.

**Differential cross sections for various observables** Although the sector decomposition approach is considered to be a “numerical method”, as the pole coefficients are only calculated numerically, the isolation of the poles is an algebraic procedure, leading to a set of finite functions for each pole coefficient as well as for the finite part. This feature allows the inclusion of any (infrared safe) measurement function, at the level of the final Monte Carlo program, which means that the subtractions and expansions in  $\varepsilon$  do *not* have to be redone each time a different observable is considered. However, some optional information about the physical singular limits, which does not spoil the above property, can be included at the stage of the  $\varepsilon$ -expansion, thus avoiding the subtraction of certain “spurious” singularities.

In [663], it is shown how the four-momenta of the final state particles in terms of energies and angles can be reconstructed from the variables in which the sector decomposition is performed. In this way, fully differential information about the final state is available, such that observables can be calculated which cannot be cast into analytic functions, being complicated subroutines in the numerical program. As an example, the JADE algorithm [665] to define 3-, 4- and 5-jet events has been implemented into a Monte Carlo program built upon the output of sector decomposition [663], using the multi-dimensional integration package BASES [666]. The architecture of the program, being the one of a partonic event generator, is such that the JADE algorithm can be easily replaced by a different jet algorithm, and shape observables can also be defined.

### 32.44 Outlook

The method outlined here is a very powerful tool, especially for what concerns the double real radiation part of NNLO calculations, as it requires neither the manual construction of subtraction terms, nor the factorisation of the phase space and the analytic integration of the subtraction terms in the singular limits. A disadvantage of the sector decomposition approach is given by the fact that it produces very large expressions, as in each decomposition step, the number of original functions increases. Therefore, CPU time is an issue for the treatment of processes with a large number of massless particles in the final state. However, the method sketched here relies on a division of the amplitude squared into different “topologies” corresponding to different classes of denominator structures, such that the problem is naturally split into smaller subparts. If such a “trivial parallelisation” is not sufficient, there is still the possibility to parallelise the evaluation of the functions produced by sector decomposition. Furthermore, the size of the expressions can be reduced by including information about physical limits already at the level of the  $\varepsilon$ -expansion, without losing any flexibility for what concerns the definition of observables at the Monte Carlo level.

For the parts of the full matrix element for  $e^+e^- \rightarrow 3\text{jets}$  at NNLO considered so far, the numerical stability is very good. A reason might be that the subtractions within the sector decomposition method are local in the sense of plus distributions, i.e. the singular limits in each integration variable are directly subtracted.

As the method is based on a universal algorithm acting on integration variables, it will surely see a number of interesting applications in the future, in particular for what concerns the production of massive particles.

## Part IV

# MONTE CARLO ISSUES

### 33. ON REWEIGHTING TECHNIQUES <sup>69</sup>

Fixed-order computations in perturbation theory are characterized by low-multiplicity, parton-level final states. These are by far and large unrealistic, and cannot be used in complex simulations such as those performed by experiments to compute acceptances and to study detector responses. For such purposes, parton shower Monte Carlos (MCs) are used instead. It is well known, however, that MCs lack the capability of giving reliable predictions for total rates and for observables sensitive to large- $p_T$  emissions. To compensate for this, MC results are typically multiplied by N<sup>i</sup>LO  $K$  factors, i.e. the ratios of N<sup>i</sup>LO cross sections over LO ones; this procedure is called reweighting. Obviously, there are as many  $K$  factors as observables; the standard approach is that of using the  $K$  factor relevant to total rates. It is easy to realize, however, that such a  $K$  factor does not lead to any improvement of the MC results as far as shapes are concerned. An alternative approach [312] is that of selecting a given observable  $O$ , and reweight with the “differential”  $K$  factor  $K(O)$ . This will certainly correct the shape of  $O$  to the N<sup>i</sup>LO accuracy, as well as the total rate. The question is what happens to the shapes of other observables (and even to  $O$ , in the case in which cuts are applied, which cannot be implemented in the fixed-order computation used to obtain  $K(O)$ ).

The purpose of this note is to show that unweighting may actually lead to worsening, rather than to improving, leading-order Monte Carlo results. In order to do this, it is sufficient to find an example in which this happens. Such example can be easily worked out in the context of a simple two-dimensional model. Thus, I consider the case of two kinematic variables with the following ranges

$$p, \quad 0 \leq p \leq 1; \quad x, \quad 0 \leq x \leq 1. \quad (133)$$

I assume that the doubly-differential cross section is

$$\begin{aligned} \frac{d\sigma^T}{dxdp} &= \frac{2}{\Gamma(a-1,1)} \\ &\times \frac{e^{-1/p}}{p^a} \left[ \Theta\left(\frac{1}{2} - x\right) \left(\frac{1}{2} + \alpha \frac{1-p}{2}\right) + \Theta\left(x - \frac{1}{2}\right) \left(\frac{1}{2} - \alpha \frac{1-p}{2}\right) \right], \end{aligned} \quad (134)$$

where

$$\Gamma(a, x) = \int_x^\infty dt t^{a-1} e^{-t} \quad (135)$$

is the incomplete  $\Gamma$  function, and the superscript T means “true”. In Eq. (134),  $a$  and  $\alpha$  are free parameters; I assume that

$$a \geq 1; \quad -1 \leq \alpha \leq 1, \quad (136)$$

---

<sup>69</sup>Contributed by: S. Frixione

where the latter condition implies that the cross section is positive definite. It is a matter of simple algebra to compute the single-inclusive and total cross sections

$$\frac{d\sigma^T}{dp} = \frac{1}{\Gamma(a-1, 1)} \frac{e^{-1/p}}{p^a}, \quad (137)$$

$$\begin{aligned} \frac{d\sigma^T}{dx} &= \Theta\left(\frac{1}{2} - x\right) \left(1 + \alpha - \alpha \frac{\Gamma(a-2, 1)}{\Gamma(a-1, 1)}\right) \\ &+ \Theta\left(x - \frac{1}{2}\right) \left(1 - \alpha + \alpha \frac{\Gamma(a-2, 1)}{\Gamma(a-1, 1)}\right), \end{aligned} \quad (138)$$

$$\sigma^T = 1. \quad (139)$$

The total rate is equal to one thanks to the prefactor that contains the  $\Gamma$  function in Eq. (134), which has actually been chosen for this purpose. Eqs. (134)–(138) suggest that  $p$  may be seen as a rescaled (transverse) momentum; the larger the parameter  $a$ , the more steeply falling the distribution. The nature of  $x$  doesn't need to be specified here, since what follows actually applies to *any* observable; in order to simplify the discussion, I assume that the cross section is a constant in the ranges  $x < 1/2$  and  $x > 1/2$  (see Eq. (138)); the difference between its values in those ranges (i.e. the steepness of  $d\sigma^T/dx$ ) is proportional to  $\alpha$ . Notice that  $x$  and  $p$  are correlated, and that the slope in  $x$  is flatter the larger  $p$ .

I now want to apply the reweighting procedure of ref. [312] to compute  $d\sigma/dx$ . The correct answer is that of Eq. (138), which in an MC simulation is obtained by filling  $x$  bins with the weights computed with Eq. (134) for all of the phase-space points  $(x, p)$  sampled during the run. However, in order to follow the procedure of ref. [312], I must assume that the true doubly-differential cross section (i.e., the correct MC simulation) is not available. What is available is an MC simulation which is known to necessitate corrections. In the present simplified approach, this corresponds to a doubly-differential cross section that I write as follows:

$$\begin{aligned} \frac{d\sigma^U}{dx dp} &= \frac{2}{\Gamma(b-1, 1)} \\ &\times \frac{e^{-1/p}}{p^b} \left[ \Theta\left(\frac{1}{2} - x\right) \left(\frac{1}{2} + \beta \frac{1-p}{2}\right) + \Theta\left(x - \frac{1}{2}\right) \left(\frac{1}{2} - \beta \frac{1-p}{2}\right) \right], \end{aligned} \quad (140)$$

where the superscript U stands for “uncorrected”. The functional form of Eq. (140) is identical to that of Eq. (134); this obviously doesn't need to be so, but it simplifies the computations. The two cross sections are different, however, since in general  $a \neq b$  and  $\alpha \neq \beta$ . The single-inclusive “uncorrected” cross section can be obtained from Eqs. (137) and (138) with the formal replacements  $a \rightarrow b$  and  $\alpha \rightarrow \beta$ . In particular, we have

$$\begin{aligned} \frac{d\sigma^U}{dx} &= \Theta\left(\frac{1}{2} - x\right) \left(1 + \beta - \beta \frac{\Gamma(b-2, 1)}{\Gamma(b-1, 1)}\right) \\ &+ \Theta\left(x - \frac{1}{2}\right) \left(1 - \beta + \beta \frac{\Gamma(b-2, 1)}{\Gamma(b-1, 1)}\right). \end{aligned} \quad (141)$$

Ref. [312] proceeds by computing the  $p$ -dependent correction factor

$$K(p) \equiv \frac{d\sigma^T}{dp} \bigg/ \frac{d\sigma^U}{dp} = \frac{\Gamma(b-1, 1)}{\Gamma(a-1, 1)} p^{b-a}, \quad (142)$$

which is then applied event-by-event in the MC simulation. In the formalism of this note, this is equiva-

lent to defining a “corrected” doubly-differential cross section

$$\begin{aligned} \frac{d\sigma^C}{dx dp} &\equiv K(p) \frac{d\sigma^U}{dx dp} \\ &= \frac{2}{\Gamma(a-1, 1)} \\ &\times \frac{e^{-1/p}}{p^a} \left[ \Theta\left(\frac{1}{2} - x\right) \left(\frac{1}{2} + \beta \frac{1-p}{2}\right) + \Theta\left(x - \frac{1}{2}\right) \left(\frac{1}{2} - \beta \frac{1-p}{2}\right) \right], \end{aligned} \quad (143)$$

from which we obtain the “corrected” differential distribution

$$\begin{aligned} \frac{d\sigma^C}{dx} &= \Theta\left(\frac{1}{2} - x\right) \left(1 + \beta - \beta \frac{\Gamma(a-2, 1)}{\Gamma(a-1, 1)}\right) \\ &+ \Theta\left(x - \frac{1}{2}\right) \left(1 - \beta + \beta \frac{\Gamma(a-2, 1)}{\Gamma(a-1, 1)}\right). \end{aligned} \quad (144)$$

We must now understand whether Eq. (144) is a good approximation of Eq. (138). In order to study this, I introduce the shorthand notation

$$\frac{d\sigma_{<}^A}{dx} = \frac{d\sigma^A}{dx} \Theta\left(\frac{1}{2} - x\right), \quad (145)$$

$$\frac{d\sigma_{>}^A}{dx} = \frac{d\sigma^A}{dx} \Theta\left(x - \frac{1}{2}\right), \quad (146)$$

where A = T, U, C and define

$$R_{<}^{U,C} = \frac{d\sigma_{<}^{U,C}}{dx} \bigg/ \frac{d\sigma_{<}^T}{dx}, \quad (147)$$

$$R_{>}^{U,C} = \frac{d\sigma_{>}^{U,C}}{dx} \bigg/ \frac{d\sigma_{>}^T}{dx}, \quad (148)$$

$$S^{U,C} = \left( \frac{d\sigma_{>}^{U,C}}{dx} - \frac{d\sigma_{<}^{U,C}}{dx} \right) \bigg/ \left( \frac{d\sigma_{>}^T}{dx} - \frac{d\sigma_{<}^T}{dx} \right). \quad (149)$$

If the “uncorrected” cross sections were coincident with the “true” ones, the  $R$ ’s and  $S$ ’s defined in Eqs. (147)–(149) would be all equal to one. On the other hand, the larger the values of  $|R - 1|$  and  $|S - 1|$ , the worse the agreement between the “true” cross section and the “uncorrected” or “corrected” ones. By construction,  $R_{<}$  and  $R_{>}$  are relevant to the rate for  $x < 1/2$  and  $x > 1/2$  respectively, while  $S$  is relevant to the slope.

Using Eqs. (138), (141), and (144) we readily get

$$R_{<}^U = \frac{\Gamma(a-1, 1)}{\Gamma(b-1, 1)} \frac{(1+\beta)\Gamma(b-1, 1) - \beta\Gamma(b-2, 1)}{(1+\alpha)\Gamma(a-1, 1) - \alpha\Gamma(a-2, 1)}, \quad (150)$$

$$R_{<}^C = \frac{(1+\beta)\Gamma(a-1, 1) - \beta\Gamma(a-2, 1)}{(1+\alpha)\Gamma(a-1, 1) - \alpha\Gamma(a-2, 1)}, \quad (151)$$

$$S^U = \frac{\beta\Gamma(a-1, 1)}{\alpha\Gamma(b-1, 1)} \frac{\Gamma(b-1, 1) - \Gamma(b-2, 1)}{\Gamma(a-1, 1) - \Gamma(a-2, 1)}, \quad (152)$$

$$S^C = \frac{\beta}{\alpha}, \quad (153)$$

and the results for  $R_{>}^{U,C}$  can be obtained from Eqs. (150) and (151) with the formal replacements  $\alpha \rightarrow -\alpha$ ,  $\beta \rightarrow -\beta$ . With the equations above we can explicitly verify that when  $b = a$  and  $\beta = \alpha$  (i.e., the “uncorrected” cross section is identical to the “true” one), then  $R = S = 1$ .

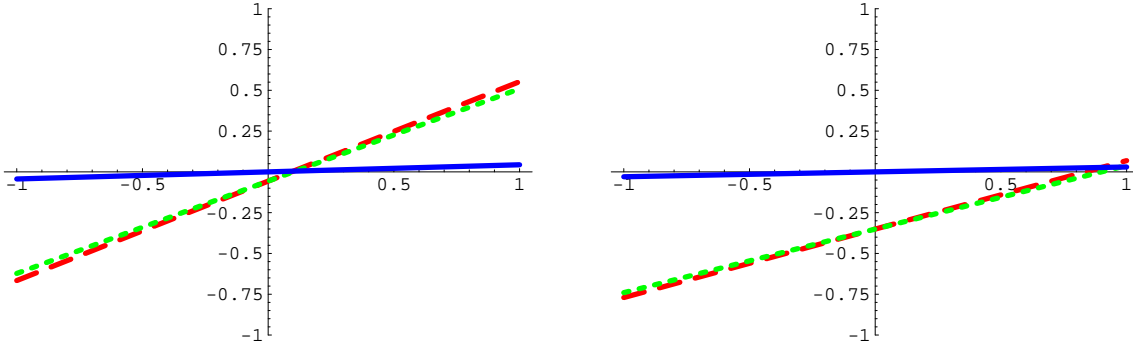


Fig. 169: I plot here  $1 - R_{<sup>U</sup>}^<sub><sup>C</sup></sub>$  (red long-dashed line),  $1 - R_{<sup>C</sup>}^<sub><sup>U</sup></sub>$  (green short-dashed line), and  $R_{<sup>C</sup>}^<sub><sup>C</sup></sub> - R_{<sup>U</sup>}^<sub><sup>C</sup></sub>$  (blue solid line) as a function of  $\beta$ , for  $a = 4, b = 4.5$ , and  $\alpha = 0.1$  (left panel) or  $\alpha = 0.9$  (right panel).

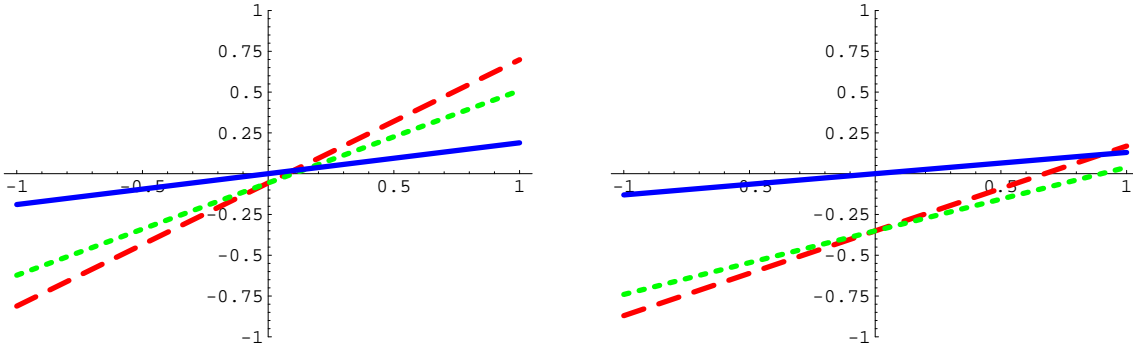


Fig. 170: As in Fig. 169, except for the value of  $b$ ; here  $b = 7$ .

I proceed by observing that, if the derivative of the “true”  $x$  distribution has the opposite sign of that of the “uncorrected”  $x$  distribution (say, the former is decreasing while the latter is increasing, i.e.  $\alpha > 0$  and  $\beta < 0$ ), then clearly the reweighting cannot correct this behaviour, as is most evident from Eq. (153). In order to have an idea of what happens in general, I plot in Figs. 169 and 170 the quantities  $1 - R_{<sup>U</sup>}^<sub><sup>C</sup></sub>$ ,  $1 - R_{<sup>C</sup>}^<sub><sup>U</sup></sub>$ , and  $R_{<sup>C</sup>}^<sub><sup>C</sup></sub> - R_{<sup>U</sup>}^<sub><sup>C</sup></sub>$ , as functions of  $\beta$  for given values of  $\alpha, a$ , and  $b$ . In Figs. 171 and 172 I plot  $1 - S^U, 1 - S^C$ , and  $S^U - S^C$ . By inspection of the figures, we can see that when the  $p$  “true” and “uncorrected” distributions are similar ( $a = 4, b = 4.5$ ), the difference between the “uncorrected” and “corrected”  $x$  distributions is fairly marginal; the “corrected”  $x$  distribution may display a disagreement with respect to the “true”  $x$  distributions that can be as large as 50%. The agreement with the “true” result obviously improves when  $\beta \simeq \alpha$ , but in such a case one wouldn’t advocate the necessity of a reweighting procedure at all. In the case in which the  $p$  “uncorrected” distribution is much steeper than the “true” one ( $a = 4, b = 7$ ), the effect of the reweighting is more pronounced, but this doesn’t imply that the “corrected”  $x$  distribution improves the “uncorrected” one, since this appears to depend on the value of  $\alpha$ . In any case, the “corrected”  $x$  distribution agrees better with the “uncorrected” than with the “true” one.

In conclusions: it is obvious that the functional form chosen here for the cross section is too simplistic to give a proper description of the complex final state which emerges from a hadronic collision. It does show, however, that the results of reweighting may be contrary to expectations, since the corrected cross section may have a larger disagreement with the physical cross section than the uncorrected one. As expected, this is more likely to happen when the reweighting function (Eq. (142) in the context of the model discussed in this note) is not flat, which is precisely when the use of an observable-dependent  $K$  factor would be advocated. For the majority of the parameter choices considered here, reweighting



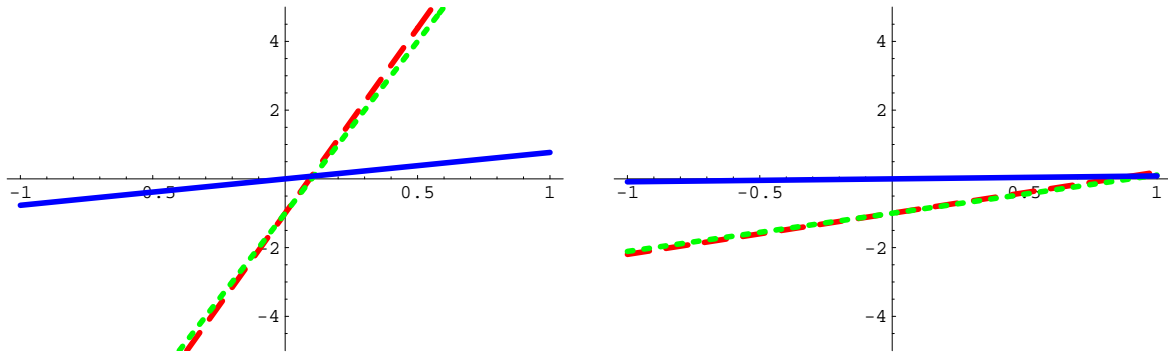


Fig. 171: As in Fig. 169, for  $S^U$  and  $S^C$ .

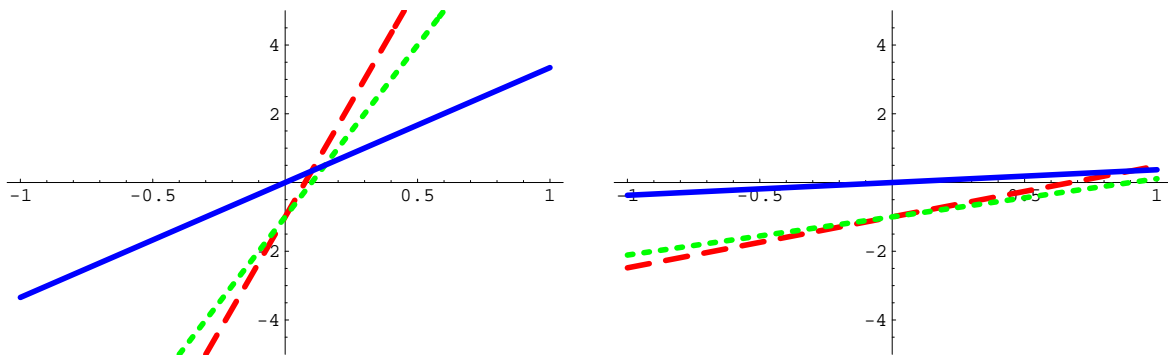


Fig. 172: As in Fig. 170, for  $S^U$  and  $S^C$ .

does improve the “uncorrected” result, but the improvement is pretty marginal. It is impossible to say whether this will also be the case for a physical observable. It appears in fact that only the comparison with the “true” result allows one to assess the accuracy with which the reweighting does its job. If the “true” result is not available, it is impossible to give a sound estimate of the uncertainties involved in the procedure. Clearly, the availability of the “true” result would render the whole procedure useless; a practical strategy may then be that of checking that the corrected cross sections obtained starting from two or more different “uncorrected” predictions (say, resulting from different Monte Carlos) are in better mutual agreement than the “uncorrected” ones; it is clear, however, that such a strategy may easily fail.

## 34. LCG MCDB — DATABASE OF MONTE-CARLO SIMULATED EVENTS <sup>70</sup>

### 34.1 LCG MCDB Overview

The LCG MCDB proposal was presented at the Les Houches workshop in 2003 [667, 668] This paper gives a status report of the LCG MCDB project.

The LCG MCDB project has been created to facilitate communication between experts of Monte-Carlo (MC) generators and users of the LHC collaborations. It provides flexible infrastructure to share generated MC event samples (MC samples) and the corresponding book-keeping in a convenient way, with dedicated interfaces to the users and to the authors.

The LCG MCDB tool is particularly useful for samples that require a frequent interaction between users and MC experts, or significant CPU resources. Nowadays, the LCG MCDB project is ready for LHC community and provides many useful interfaces for authors of MC samples and for the users. A

<sup>70</sup>Contributed by: P. Bartalini, S. Belov, L. Dudko, A. Gusev, A. Sherstnev

dedicated web server has been deployed: <http://mcdb.cern.ch>.

The adoption of a central database of MC events is motivated by simulation needs which are specific to the high energy physics domain. In general, the correct MC simulation of complex processes requires a rather sophisticated expertise. Often, different physics groups in various experimental collaborations approach the same experts and authors of MC generators, respectively, in order to generate MC samples for a particular physics process. Having these events stored in a public place along with the corresponding documentation, allows for direct cross checks of the performances on reference samples, and prevents possible waste of precious human and computing resources.

The main motivation behind the MCDB project is to make sophisticated MC event samples available for various physics groups. For example, the same MC samples of Standard Model (SM) processes can be used for the investigations in some SM effects as well as a background for some studies of new phenomena. Public availability of the event samples helps to speed up the validation procedure of the events and provides the public stage for rapid communication between authors of the samples and their users. The previous version [669] of MCDB was launched by the CMS collaboration in 2002. The main limitations of the CMS MCDB are the AFS based storage supporting only small size MC samples (basically only parton level events from matrix element tools) and the lack of search functionalities, mostly based on phonetic keys.

The significant interest shown by the potential users motivated the MCDB migration to the LCG framework, benefiting from a much more powerful, standardized and exportable software tools that are available to all the LHC collaborations. The LCG MCDB [670] is now almost ready. In the next sections we will briefly describe the subsystems and modules of the LCG MCDB, providing instructions for the users.

## 34.2 LCG MCDB Description

The subsystems and software technologies adopted in the LCG MCDB are described in this section. The LCG MCDB is based on the following software technologies: WEB, CGI, PERL, SQL, XML, CASTOR and GRID. All of the developed software is available in LCG CVS [671]. The software is organized as a set of modules with the possibility to export the LCG MCDB software to other sites on the grid. We provide a daily backup of the SQL DB and double mirroring of the samples in CASTOR.

The main concept of the LCG MCDB is the ARTICLE, which is a document describing a set of event samples. MCDB articles are divided into CATEGORIES, i.e. a set of articles concerning a particular type of physics process (e.g. top physics, Higgs physics) or theoretical model (e.g. supersymmetry, extra dimensions). There are four different types of permissions to access the LCG MCDB. The USER access is reserved for users who are interested in requesting a new event sample or in downloading or documenting comments to the already published event samples. The AUTHOR access is reserved to authorized users (MC experts). Only an AUTHOR can upload a new event sample. The MODERATOR access is reserved to moderators who manage author profiles and monitor other information. The ADMINISTRATOR access is reserved to software developers and maintainers who take care of the LCG MCDB itself. The scheme of the LCG MCDB is shown in Fig. 173.

### 34.21 WEB interface

The main interface of the LCG MCDB is based on WEB technologies. It is split in two parts:

- ▷ The user interface, where any user can apply for new event samples, search and browse for the already available samples, read the description of the events, download the samples, ask a question about the samples and read the previous discussion concerning it.
- ▷ Author area, where authorized authors can upload new samples to the database and describe them using a template system. The system has a lot of pre-entered information. Authors can interact

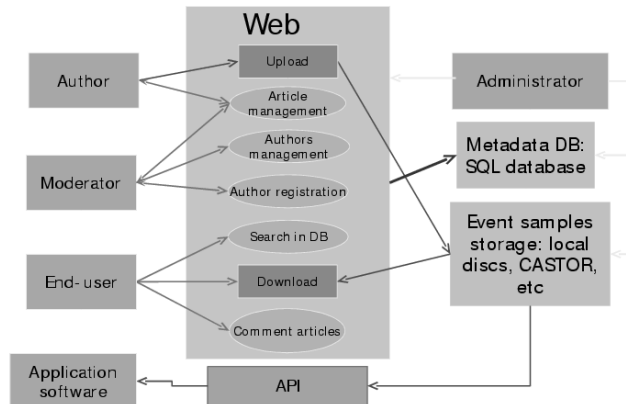


Fig. 173: Scheme of the LCG MCDB

with users on the public forums attached to each article. With the same interface authors can edit previous articles or make the articles temporarily inaccessible to users.

### 34.22 SQL DB

The LCG MCDB adopts MySQL. The SQL technology provides a possibility to keep information in a very structured way. Authors provide documentation of their event samples through forms with pre-filled forms from the cache or from the selection menu. In this way the description of new events (e.g. MC generator, theoretical model, parameters of generation, kinematic cuts, etc.) turns out to be much simplified.

### 34.23 Storage

For the native storage of event samples we have selected CASTOR [672], because of the absence of serious space limitations and considering its popularity in the LHC collaborations. We provide direct CASTOR paths for all LCG MCDB samples along with the possibility to get the samples through different interfaces (http, GridFtp etc.). A local disk cache system is used to speed up the storage operations.

### 34.24 Search engine

Since we use a SQL DB, it is possible to provide the possibility for a variety of complex search queries, including those specifying relations between DB objects. The deployed WEB search interface is realized as a dynamic query construction wizard which is based on the JavaScript XML-query constructor. The development of application programming interfaces to specific external software (for example a simulation framework of a LHC collaboration) may benefit of similar tools in order to simplify the query construction.

### 34.25 Authorization

We pay a special attention to the security of the transactions in all LCG MCDB operations. There are two possibilities of authorization. The first one is the authorization with CERN AFS/Kerberos login/password, all of the transactions are encrypted by SSL technology. The second possibility is to

authorize with LCG GRID certificates. Authors can choose any of these two types of authorizations or both of them. Both of these authorization methods are standard at CERN and any CERN user can use at least one of these two methods.

#### *34.26 Documentation*

Most of the LCG MCDB documentation is available from the dedicated web server. The information is separated in two parts, corresponding to the technical and the user part. The first part describes the implementation of the LCG MCDB itself. The second part is organized as a set of HOW-TOs for users and authors. A separate documentation (available from the CVS repository) is devoted to the developers of the LCG MCDB software.

In most of the cases it is appropriate to refer to the set in the HOW-TO for the users and authors, which provides short answers on the most common questions with corresponding links to solutions of the problems. A brief start-up manual for not experienced LCG MCDB users is also available in the next section of this document. In addition, there are two freely accessible mailing lists dedicated to users and developers. Their addresses are available in the documentation section at the main web page.

#### *34.27 API to collaboration software*

In the near future, some emphasis will be put on the development of application programming interfaces (API) specific to the simulation environments of the LHC collaborations. This work will require constant interaction with contact persons in the LHC collaborations. The main idea of this subsystem is to write a set of routines for the collaboration software which would allow a direct access to the LCG MCDB files during the MC production on computer farms. Access to LCG MCDB samples should not represent a big issues as, at present, collaboration software can already use the direct CASTOR paths to get the event samples or download the samples from web interfaces.

#### *34.28 HEPML, unified XML format of simulated events*

Another useful feature, which we plan to implement in the LCG MCDB, is a unified XML format of event samples. At present, each MC generator supports its own output format.

Some authors of matrix element tools provide interface programs to pass the events of a particular MC generator to the subsequent level of simulation (e.g. showering, hadronization decays) which are based on the Les Houches Accord number one .

However, there is still no agreement on a possible unified format to save intermediate MC information to a file. The most appropriate technology for the unified event format seems to be XML, which provides the possibility to describe the stored information in a very flexible and standardized way. Different MC generators may use the same tag for the description of a physics parameter, or may need to keep specific information (through the introduction of a dedicated tag). In other words, the HEPML format should consist of many possible XML tags, separated in two different sets describing general and MC specific information respectively. Possible internal adaption of this representation to the most popular Monte Carlo generators would result in a significant improvement of the Monte Carlo documentation and book-keeping. The LCG MCDB project will in any case support a set of HEPML tags to document event samples internally, and will promote its usage in other environments. The first practical attempts to introduce a standardized set of MC tags has been performed already, for example by the CEDAR collaboration [673]. A dedicated document discussing the details of the requirements and describing the HEPML proposal will appear in the near future.

### 34.3 How to use the LCG MCDB.

A user who needs simulated events for a particular process can browse the MCDB categories and sub-categories (menu at the left side of the main LCG MCDB web page [670]) and verify, whether an appropriate sample has been already generated. If this is the case, the users may want to read the article describing how the event sample has been prepared (parameters of the theoretical model, generator name and generation parameters, kinematic cuts, etc.). At the bottom of the page a link to the uploaded file(s) is provided, as well as the CASTOR path. On top of that, the web page also contains a link to the "Users Comments" interface, where users can ask questions about the sample and browse the previous discussion on the article. Users do not need any authorization for the steps described above.

The following procedure has to be followed if one needs to publish a sample in the LCG MCDB (becoming author):

1. Register as a new author with the link at the right side menu of the web page [670], wait for the confirmation e-mail
2. Login to the LCG MCDB authors area
3. Choose "Create New Article" in the authors menu which will appear at the right side after the authorization.
4. Fill all necessary fields in the documentation template, which will appear (title, generator, theoretical model, cuts, etc.)
5. Upload your event files in the "Event Files" sub-window.
6. Click "Preview/Save" slice and check the box "Publish"

To be authorized in the LCG MCDB, the author needs a valid CERN AFS login or a LCG digital certificate. Authors can save unfinished articles in MCDB and resume to correct them at any moment. Authors can edit their previous articles that are already published on the web or make the articles publicly inaccessible for a while.

The LCG MCDB team will appreciate any possible bug report, feedback, comments or suggestions for possible new implementations concerning the LCG MCDB.

## 35. SUPPORTING MONTE CARLO GENERATORS AT THE LHC <sup>71</sup>

### 35.1 Introduction

The LCG Simulation project covers a range of activities in the simulation as part of the LCG Applications Area, encompassing common development and validation work among the LHC experiments on the GEANT4, FLUKA and GARFIELD simulation engines as well as on Monte Carlo generators.

The mandate of the LCG Generator project is to collaborate with Monte Carlo (MC) generators authors and with LHC experiments in order to prepare, validate and maintain LCG code for both the theoretical and experimental communities at the LHC, sharing the user support duties, providing assistance for the development of the new object oriented generators and guaranteeing the maintenance of the older packages on the LCG supported platforms. Contact persons for most of MC generator packages relevant for the LHC and representatives for all the LHC experiments have been agreed. Four different work packages (WP) have been defined:

WP1 Generator services library;

WP2 Event interfaces and particle services;

WP3 Production, storage and book-keeping of public generator level events;

WP4 Monte Carlo Validation.

This paper describes the status and the development guidelines in the four different work packages, concentrating on the main activity, i.e. the MC generator services library (GENSER).

---

<sup>71</sup>Contributed by: P. Bartalini, L. Dudko, M. Kirsanov, A. Sherstnev

## 35.2 WP1: the generator services library

Two different options are available to support Monte Carlo packages in LCG: they can be simply stored in the LCG external area [674] or they can be rather migrated in the dedicated LCG Generator Services module (GENSER) [675], adapting the directory structure according to the LCG policy. This second solution has been adopted for most of the installed packages. However, for each MC package, an ad-hoc solution is found taking into account the authors directives and the user requirements. Top priority and second priority packages pursued for inclusion in the generator library have been indicated in the report of the RTAG 9 working group.

### 35.21 GENSER

GENSER is the LCG module for MC generators and generator tools. It was the first module in the LCG Simulation CVS repository. The sources and the binaries are installed in AFS and the tarballs are made available by the Software Process and Infrastructure group (LCG-SPI). This new library has gradually replaced the obsolete CERN library for what concerns the MC generators support. In fact GENSER is currently widely adopted as the standard Monte Carlo generators library by most of the LHC experiments.

The management of the GENSER releases has been recently improved and is currently coordinated by the central LCG librarian from CERN PH/SFT. GENSER is fully independent from other large libraries and currently follows a quarterly release scheme. Quick bug fixes and special versions can be produced under request. Most of the MC sub-package versions produced by the authors are installed. Old versions are maintained as long as they are used.

Configuration and build systems for the librarian and end users are based on the SCRAM technology [676]; future versions of GENSER will support Makefiles as well. At the moment GENSER is considered to be at the “production quality” stage. The current version of GENSER (1.2.1) comprises both shared and static libraries for the platform slc3\_ia32\_gcc323.

### 35.22 External Monte Carlo packages

The following MC generator packages are stored in the LCG external area, however they are completely supported in GENSER with corresponding examples and test suites:

- EVTGEN [677] version alpha-00-11-07;
- SHERPA [678] version 1.0.5, 1.0.6;
- COMPHEP [286] versions 4.2.p1, 4.4.0.

### 35.23 Internal Monte Carlo packages

The following MC generator packages have been migrated in GENSER, along with the corresponding test and validation code:

- PYTHIA [183, 284] versions 6.205, 6.217, 6.220, 6.221, 6.222, 6.223, 6.224, 6.227, 6.304, 6.319, 6.320, 6.321, 6.324;
- HERWIG [33] versions 6.500, 6.503, 6.504, 6.505, 6.506, 6.507, 6.508, 6.510;
- JIMMY [34] version 4.1, 4.2;
- ISAJET [679] versions 7.67, 7.69, 7.71;
- HIJING [680] versions 1.36, 1.37, 1.383;
- MC@NLO [308, 309] version 2.3.1, 3.1.0;
- ALPGEN [397] version 1.3.2, 2.0, 2.01, 2.03, 2.05;
- TOPREX [321] version 4.09;
- MADGRAPH [325] version 3.2;



- FEYNHIGGS [681] version 2.2.9, 2.2.10;
- LHAPDF [46] versions 1.1, 2.0, 3.0, 4.0, 4.1.1, 5.0;
- PHOTOS [682] versions 207, 209, 2.14, 2.15;
- PHOJET [683] version 1.10;
- GLAUBER Xs [684] version 1.0;
- CHARYBDIS [685] version 1.001;
- STAGEN [686] version 1.07 (including TRUENOIR and two GRAVITON codes);
- EVTGENLHC [687] versions 1.2, 1.3.

In this list, EVTGENLHC represents a special case. EVTGENLHC is the LHC version of EVTGEN, a Monte Carlo following the spin density matrix formalism that is particularly dedicated to the simulation of B decays and specifically designed for B production at the  $\Upsilon(4S)$  resonance. EVTGEN currently comprises one of the largest tuneable and upgradeable collection of decay models.

EVTGENLHC has been set-up and provided in GENSER by the LHCb collaboration. It includes an interface to the HEPMC event record that allows for modularization with plug-in to the most popular general purpose Monte Carlo generators (typically parton shower QCD models). Mixing description and CP violation implementation have been adapted to the case of incoherent B meson production.

Common work between the LHC collaborations is currently developing as a LCG Generator activity, with the participation of the original EVTGEN authors. This project is concentrating on the implementation of particle polarizations and on the extension of the decay models to  $B_s$ ,  $B_c$  and to B baryons. LCG Generator also pursues a common initiative between experiments at LHC, Tevatron and at the B factories for the tuning of the EVTGEN decay tables (to be developed in WP4).

### 35.3 WP2: event interfaces and particle services

The goal of WP2 is to contribute to the definition of the standards for generator interfaces and formats, collaborating in the development of the corresponding application programming interfaces (API).

#### 35.31 *ThePEG*

In order to favor the adoption of the new object oriented MC generators in the experiment simulation frameworks, the LCG Generator project will share some responsibilities on the development and maintenance of the Toolkit for High Energy Physics Event Generation (THEPEG) [688]. LCG Generator has set a common milestone with the PHENOGRID initiative [689] for mid 2005: the first test of ThePEG and EvtGenLHC integration in Herwig++.

#### 35.32 *HEPML*

HEPML [668] is a meta-data format where the information is sub-divided in two parts:

- The header, that contains the general information concerning the event sample, i.e. author, creation date, collider description, generator specific data, generation cuts, other physical parameters, parser directives etc.
- The event records, i.e. the variable data of events written in some compact format to one string (particle momenta, colour chains etc.).

The header is stored in a text file with XML Syntax. The event records are zip-compressed and attached to the header file. The HEPML meta-data format provides the basis to the SQL search for public generator level events (WP3).

### 35.4 WP3: production, storage and book-keeping of public generator level events

The goal of WP3 is to produce "certified" public generator event files to be used for benchmarks, comparisons and combinations. The format and the structure of the files will be accessible to the simulation

frameworks of the LHC experiments. Three different activities have been started in this work package: simulation framework, production and book-keeping and storage.

#### 35.41 *Simulation framework*

The development of a simple production and validation framework at generator level is a common software project between LCG and CMS. A new package has been designed which is relying on HepMC (event interface), ROOT and POOL (event storage). The beta version of the framework will be available in the end of 2005.

#### 35.42 *Production*

A dedicated production centre integrated in the grid middleware will provide the LHC experiments and the other end-users with a transparent access to the public event files. This will be essential for those samples requiring an huge amount of CPU time and parallelization techniques.

#### 35.43 *Book-keeping and storage*

The LCG Monte Carlo Data Base (MCDB) [668] is a public service for the configuration, book-keeping and storage of the generator level event files. A prototype is currently in production on a dedicated web server [690]. Details on MCDB are given in another section of these proceedings.

### 35.5 **WP4: Monte Carlo validation**

The Monte Carlo validation work package is divided in two different parts: basic sanity checks and the physics validation.

The activity is currently concentrating on the functional validation of the generator packages inserted in GENSER. The basic sanity checks are currently performed in a standalone way. The code is provided by the authors, beta testers and librarians and it is stored under the TEST module in the simulation repository. It will be subsequently integrated with the simple generator level production framework (developed in WP3).

In the long term the physics validation will be performed with JETWEB [691], assuming that it will be interfaced to GENSER in a reasonable time scale (i.e. by mid 2006).

### **Acknowledgements**

We are indebted with all the other members of the LCG Generator team: F. Ambroglini, (INFN-Perugia); M. Bargiotti, A. Pfeiffer and A. Ribon (CERN); S. Belov, S. Korobov and V. Uzhinsky (JINR); J. Cuevas Maestro and H. Naves (Cantabria); I. Katchaev and S. Slabospitsky (IFVE); S. Makarychev and I. Seluzhenkov (ITEP).

We are particularly grateful to all the contributors to the EVTGENLHC project. In particular we wish to thank D. Lange (Livermore); A. Ryd (Cornell); P. Robbe (LHCb, LAL Paris XI); M. Smizanska and J. Catmore (ATLAS, Lancaster); Michela Biglietti (ATLAS, Michigan).

We wish to thank also the LCG-SPI team, as well as our contact persons in the LHC experiments and in the MC generator projects.

### **References**

- [1] A. Donnachie and P. V. Landshoff, *Phys. Lett.* **B296** (1992) 227–232, [[hep-ph/9209205](#)].
- [2] A. Donnachie and P. V. Landshoff, *Phys. Lett.* **B595** (2004) 393–399, [[hep-ph/0402081](#)].
- [3] N. Amos *et. al.*, **E710** Collaboration *Phys. Rev. Lett.* **68** (1992) 2433–2436.

- [4] C. Avila *et. al.*, **E811** Collaboration *Phys. Lett.* **B445** (1999) 419–422.
- [5] F. Abe *et. al.*, **CDF** Collaboration *Phys. Rev.* **D50** (1994) 5550–5561.
- [6] M. M. Block and F. Halzen, hep-ph/0510238.
- [7] M. M. Block and F. Halzen, *Phys. Rev.* **D72** (2005) 036006, [hep-ph/0506031].
- [8] K. Igi and M. Ishida, *Phys. Lett.* **B622** (2005) 286–294, [hep-ph/0505058].
- [9] R. F. Avila, E. G. S. Luna, and M. J. Menon, *Phys. Rev.* **D67** (2003) 054020, [hep-ph/0212234].
- [10] J. R. Cudell *et. al.*, **COMPETE** Collaboration *Phys. Rev. Lett.* **89** (2002) 201801, [hep-ph/0206172].
- [11] J. R. Cudell *et. al.*, hep-ph/0212101.
- [12] D. Cline, F. Halzen, and J. Luthe, *Phys. Rev. Lett.* **31** (1973) 491–494.
- [13] G. Pancheri and C. Rubbia, *Nucl. Phys.* **A418** (1984) 117c–138c.
- [14] T. K. Gaisser and F. Halzen, *Phys. Rev. Lett.* **54** (1985) 1754.
- [15] L. Durand and P. Hong, *Phys. Rev. Lett.* **58** (1987) 303.
- [16] G. Pancheri and Y. N. Srivastava, *Phys. Lett.* **B182** (1986) 199–207.
- [17] A. Grau, G. Pancheri, and Y. N. Srivastava, *Phys. Rev.* **D60** (1999) 114020, [hep-ph/9905228].
- [18] R. M. Godbole, A. Grau, G. Pancheri, and Y. N. Srivastava, *Phys. Rev.* **D72** (2005) 076001, [hep-ph/0408355].
- [19] K. Igi and S. Matsuda, *Phys. Rev. Lett.* **18** (1967) 625–629.
- [20] Y. N. Srivastava and A. Widom, *Phys. Rev.* **D63** (2001) 077502, [hep-ph/0010064].
- [21] P. V. Landshoff, hep-ph/0108156.
- [22] H. Meyer and T. M.J., *Phys. Lett.* **B 605** (2005) 344–354.
- [23] M. Gluck, E. Reya, and A. Vogt, *Z. Phys.* **C53** (1992) 127–134.
- [24] M. Gluck, E. Reya, and A. Vogt, *Z. Phys.* **C67** (1995) 433–448.
- [25] M. Gluck, E. Reya, and A. Vogt, *Eur. Phys. J.* **C 5** (1998) 461–470, [hep-ph/9806404].
- [26] A. D. Martin, R. G. Roberts, W. J. Stirling, and R. S. Thorne, *Phys. Lett.* **B531** (2002) 216–224, [hep-ph/0201127].
- [27] T. Sjostrand, L. Lonnblad, S. Mrenna, and P. Skands, hep-ph/0308153.
- [28] T. Sjostrand, *PYTHIA (and JETSET) webpage*, 2005.  
<http://www.thep.lu.se/~torbjorn/Pythia.html>.
- [29] T. Sjostrand and M. van Zijl, *Phys. Rev.* **D36** (1987) 2019.
- [30] A. Moraes, C. Buttar, and I. Dawson, ATL-PHYS-PUB-2005-007.

- [31] R. Field, *Min-Bias and the Underlying Event at the Tevatron and the LHC*, October, 2002. (talk presented at the Fermilab ME/MC Tuning Workshop, Fermilab).
- [32] J. M. Butterworth and M. H. Seymour, *JIMMY4: Multiparton Interactions in Herwig for the LHC*, October, 2004. (<http://jetweb.hep.ucl.ac.uk/JIMMY/index.html>).
- [33] G. Corcella *et al.*, *JHEP* **01** (2001) 010, [[hep-ph/0011363](http://arxiv.org/abs/hep-ph/0011363)].
- [34] J. M. Butterworth, J. R. Forshaw, and M. H. Seymour, *Z. Phys.* **C72** (1996) 637–646, [[hep-ph/9601371](http://arxiv.org/abs/hep-ph/9601371)].
- [35] A. Breakstone *et al.*, **Ames-Bologna-CERN-Dortmund-Heidelberg-Warsaw** Collaboration *Phys. Rev.* **D30** (1984) 528.
- [36] G. J. Alner *et al.*, **UA5** Collaboration *Phys. Rept.* **154** (1987) 247–383.
- [37] F. Abe *et al.*, **CDF** Collaboration *Phys. Rev.* **D41** (1990) 2330.
- [38] T. Alexopoulos *et al.*, *Phys. Lett.* **B435** (1998) 453–457.
- [39] S. G. Matinyan and W. D. Walker, *Phys. Rev.* **D59** (1999) 034022, [[hep-ph/9801219](http://arxiv.org/abs/hep-ph/9801219)].
- [40] T. Affolder *et al.*, **CDF** Collaboration *Phys. Rev.* **D65** (2002) 052006, [[hep-ex/0106012](http://arxiv.org/abs/hep-ex/0106012)].
- [41] D. Acosta *et al.*, **CDF** Collaboration *Phys. Rev.* **D70** (2004) 072002, [[hep-ex/0404004](http://arxiv.org/abs/hep-ex/0404004)].
- [42] *List of Rome samples*, June, 2005. ATLAS list of samples Wiki: <https://uimon.cern.ch/twiki/bin/view/Atlas/RomeListOfSamples>.
- [43] *Generator Job Options for Rome*, 2005. ATLAS CVS: <http://atlassw1.phy.bnl.gov/lxr/source/atlas/Generators/GeneratorOptionsRome/share/>.
- [44] R. C. E. Devenish and A. M. Cooper-Sarkar, *Deep Inelastic Scattering Chap.9*. Oxford University Press, 2004.
- [45] S. ZEUS Coll., Chekanov, *Phys. Rev.* **D 67** (2003) 012007.
- [46] M. Whalley, *Eur. Phys. J.*
- [47] J. Pumplin, *JHEP* **0207** (2002) 012.
- [48] A. D. Martin, *Eur. Phys. J C* **23** (2002) 73.
- [49] A. M. Tricoli, A. Cooper-Sarkar and G. Gwenlan, *hep-ex* **0509002** (2005).
- [50] R. D. Ball and S. Forte, *Phys. Lett.* **B335** (1994) 77–86, [[hep-ph/9405320](http://arxiv.org/abs/hep-ph/9405320)].
- [51] R. D. Ball and S. Forte, *Phys. Lett.* **B336** (1994) 77–79, [[hep-ph/9406385](http://arxiv.org/abs/hep-ph/9406385)].
- [52] R. D. Ball and S. Forte, *Phys. Lett.* **B358** (1995) 365–378, [[hep-ph/9506233](http://arxiv.org/abs/hep-ph/9506233)].
- [53] A. Vogt, S. Moch, and J. A. M. Vermaseren, *Nucl. Phys.* **B691** (2004) 129–181, [[hep-ph/0404111](http://arxiv.org/abs/hep-ph/0404111)].
- [54] E. A. Kuraev, L. N. Lipatov, and V. S. Fadin, *Sov. Phys. JETP* **44** (1976) 443–450.
- [55] E. A. Kuraev, L. N. Lipatov, and V. S. Fadin, *Sov. Phys. JETP* **45** (1977) 199–204.
- [56] I. I. Balitsky and L. N. Lipatov, *Sov. J. Nucl. Phys.* **28** (1978) 822–829.

- [57] V. S. Fadin and L. N. Lipatov, *Phys. Lett.* **B429** (1998) 127–134, [hep-ph/9802290].
- [58] R. D. Ball and S. Forte, hep-ph/9805315.
- [59] D. A. Ross, *Phys. Lett.* **B431** (1998) 161–165, [hep-ph/9804332].
- [60] R. D. Ball and S. Forte, *Phys. Lett.* **B465** (1999) 271–281, [hep-ph/9906222].
- [61] G. P. Salam, *JHEP* **07** (1998) 019, [hep-ph/9806482].
- [62] G. Altarelli, R. D. Ball, and S. Forte, *Nucl. Phys.* **B575** (2000) 313–329, [hep-ph/9911273].
- [63] G. Altarelli, R. D. Ball, and S. Forte, *Nucl. Phys.* **B599** (2001) 383–423, [hep-ph/0011270].
- [64] G. Altarelli, R. D. Ball, and S. Forte, *Nucl. Phys.* **B621** (2002) 359–387, [hep-ph/0109178].
- [65] G. Altarelli, R. D. Ball, and S. Forte, *Nucl. Phys.* **B674** (2003) 459–483, [hep-ph/0306156].
- [66] G. Altarelli, R. D. Ball, and S. Forte, hep-ph/0310016.
- [67] G. Altarelli, R. D. Ball, and S. Forte, *Nucl. Phys. Proc. Suppl.* **135** (2004) 163–167, [hep-ph/0407153].
- [68] G. Altarelli, R. D. Ball, and S. Forte, hep-ph/0512237.
- [69] M. Ciafaloni, D. Colferai, and G. P. Salam, *Phys. Rev.* **D60** (1999) 114036, [hep-ph/9905566].
- [70] M. Ciafaloni, D. Colferai, D. Colferai, G. P. Salam, and A. M. Stasto, *Phys. Lett.* **B576** (2003) 143–151, [hep-ph/0305254].
- [71] M. Ciafaloni, D. Colferai, G. P. Salam, and A. M. Stasto, *Phys. Rev.* **D68** (2003) 114003, [hep-ph/0307188].
- [72] M. Ciafaloni and D. Colferai, *JHEP* **09** (2005) 069, [hep-ph/0507106].
- [73] R. D. Ball and S. Forte, *Phys. Lett.* **B405** (1997) 317–326, [hep-ph/9703417].
- [74] V. S. Fadin and L. N. Lipatov, *JETP Lett.* **49** (1989) 352.
- [75] V. Del Duca, *Phys. Rev.* **D54** (1996) 989–1009, [hep-ph/9601211].
- [76] V. S. Fadin and L. N. Lipatov, *Nucl. Phys.* **B477** (1996) 767–808, [hep-ph/9602287].
- [77] V. Del Duca, *Phys. Rev.* **D54** (1996) 4474–4482, [hep-ph/9604250].
- [78] V. S. Fadin, R. Fiore, A. Flachi, and M. I. Kotsky, *Phys. Lett.* **B422** (1998) 287–293, [hep-ph/9711427].
- [79] S. Catani, M. Ciafaloni, and F. Hautmann, *Phys. Lett.* **B242** (1990) 97.
- [80] S. Catani, M. Ciafaloni, and F. Hautmann, *Nucl. Phys.* **B366** (1991) 135–188.
- [81] V. S. Fadin and L. N. Lipatov, *Nucl. Phys.* **B406** (1993) 259–292.
- [82] V. S. Fadin, R. Fiore, and A. Quartarolo, *Phys. Rev.* **D50** (1994) 5893–5901, [hep-th/9405127].
- [83] V. S. Fadin, R. Fiore, and M. I. Kotsky, *Phys. Lett.* **B389** (1996) 737–741, [hep-ph/9608229].

- [84] V. Del Duca and C. R. Schmidt, *Phys. Rev.* **D59** (1999) 074004, [hep-ph/9810215].
- [85] V. S. Fadin, M. I. Kotsky, and R. Fiore, *Phys. Lett.* **B359** (1995) 181–188.
- [86] V. S. Fadin, R. Fiore, and M. I. Kotsky, *Phys. Lett.* **B387** (1996) 593–602, [hep-ph/9605357].
- [87] V. S. Fadin, R. Fiore, and A. Quartarolo, *Phys. Rev.* **D53** (1996) 2729–2741, [hep-ph/9506432].
- [88] J. Blumlein, V. Ravindran, and W. L. van Neerven, *Phys. Rev.* **D58** (1998) 091502, [hep-ph/9806357].
- [89] V. Del Duca and E. W. N. Glover, *JHEP* **10** (2001) 035, [hep-ph/0109028].
- [90] M. Ciafaloni and G. Camici, *Phys. Lett.* **B430** (1998) 349–354, [hep-ph/9803389].
- [91] G. Camici and M. Ciafaloni, *Phys. Lett.* **B412** (1997) 396–406, [hep-ph/9707390].
- [92] S. Abachi *et. al.*, **D0** Collaboration *Phys. Rev. Lett.* **77** (1996) 595–600, [hep-ex/9603010].
- [93] B. Abbott *et. al.*, **D0** Collaboration *Phys. Rev. Lett.* **84** (2000) 5722–5727, [hep-ex/9912032].
- [94] A. H. Mueller and H. Navelet, *Nucl. Phys.* **B282** (1987) 727.
- [95] V. Del Duca and C. R. Schmidt, *Phys. Rev.* **D49** (1994) 4510–4516, [hep-ph/9311290].
- [96] W. J. Stirling, *Nucl. Phys.* **B423** (1994) 56–79, [hep-ph/9401266].
- [97] J. R. Andersen, V. Del Duca, S. Frixione, C. R. Schmidt, and W. J. Stirling, *JHEP* **02** (2001) 007, [hep-ph/0101180].
- [98] J. R. Andersen, V. Del Duca, F. Maltoni, and W. J. Stirling, *JHEP* **05** (2001) 048, [hep-ph/0105146].
- [99] R. K. Ellis and D. A. Ross, *Nucl. Phys.* **B345** (1990) 79–103.
- [100] J. R. Andersen, V. Del Duca, S. Frixione, F. Maltoni, and W. J. Stirling, *JHEP* **11** (2004) 061, [hep-ph/0408239].
- [101] S. Aid *et. al.*, **H1** Collaboration *Phys. Lett.* **B356** (1995) 118–128, [hep-ex/9506012].
- [102] J. Breitweg *et. al.*, **ZEUS** Collaboration *Eur. Phys. J.* **C6** (1999) 239–252, [hep-ex/9805016].
- [103] C. Adloff *et. al.*, **H1** Collaboration *Nucl. Phys.* **B538** (1999) 3–22, [hep-ex/9809028].
- [104] A. Aktas *et. al.*, **H1** Collaboration hep-ex/0508055.
- [105] A. H. Mueller, *Nucl. Phys. Proc. Suppl.* **18C** (1991) 125–132.
- [106] W.-K. Tang, *Phys. Lett.* **B278** (1992) 363–366.
- [107] J. Bartels, A. de Roeck, and M. Loewe, *Z. Phys.* **C54** (1992) 635–642.
- [108] A. J. Askew, J. Kwiecinski, A. D. Martin, and P. J. Sutton, *Phys. Rev.* **D47** (1993) 3775–3782.
- [109] J. Bartels, V. Del Duca, A. De Roeck, D. Graudenz, and M. Wusthoff, *Phys. Lett.* **B384** (1996) 300–306, [hep-ph/9604272].



- [110] E. Mirkes and D. Zeppenfeld, *Phys. Rev. Lett.* **78** (1997) 428–431, [hep-ph/9609231].
- [111] J. Bartels, V. Del Duca, and M. Wusthoff, *Z. Phys.* **C76** (1997) 75–79, [hep-ph/9610450].
- [112] C. Adloff *et. al.*, **H1** Collaboration *Phys. Lett.* **B462** (1999) 440–452, [hep-ex/9907030].
- [113] A. Aktas *et. al.*, **H1** Collaboration *Eur. Phys. J.* **C36** (2004) 441–452, [hep-ex/0404009].
- [114] C. Adloff *et. al.*, **H1** Collaboration *Eur. Phys. J.* **C12** (2000) 595–607, [hep-ex/9907027].
- [115] M. Acciarri *et. al.*, **L3** Collaboration *Phys. Lett.* **B453** (1999) 333–342.
- [116] G. Abbiendi *et. al.*, **OPAL** Collaboration *Eur. Phys. J.* **C24** (2002) 17–31, [hep-ex/0110006].
- [117] P. Achard *et. al.*, **L3** Collaboration *Phys. Lett.* **B531** (2002) 39–51, [hep-ex/0111012].
- [118] A. Heister *et. al.*, **ALEPH** Collaboration hep-ex/0305107.
- [119] J. Bartels, A. De Roeck, and H. Lotter, *Phys. Lett.* **B389** (1996) 742–748, [hep-ph/9608401].
- [120] S. J. Brodsky, F. Hautmann, and D. E. Soper, *Phys. Rev.* **D56** (1997) 6957–6979, [hep-ph/9706427].
- [121] J. Bartels, C. Ewerz, and R. Staritzbichler, *Phys. Lett.* **B492** (2000) 56–62, [hep-ph/0004029].
- [122] M. Cacciari, V. Del Duca, S. Frixione, and Z. Trocsanyi, *JHEP* **02** (2001) 029, [hep-ph/0011368].
- [123] V. Del Duca, F. Maltoni, and Z. Trocsanyi, *JHEP* **05** (2002) 005, [hep-ph/0202237].
- [124] S. D. Ellis, Z. Kunszt, and D. E. Soper, *Phys. Rev. Lett.* **69** (1992) 3615–3618, [hep-ph/9208249].
- [125] F. Abe *et. al.*, **CDF** Collaboration *Phys. Rev. Lett.* **69** (1992) 2896–2900.
- [126] F. Abe *et. al.*, **CDF** Collaboration *Phys. Rev. Lett.* **77** (1996) 5336–5341, [hep-ex/9609011].
- [127] B. Abbott *et. al.*, **D0** Collaboration *Phys. Rev. Lett.* **80** (1998) 666–671, [hep-ex/9707016].
- [128] Z. Nagy and Z. Trocsanyi, *Phys. Rev. Lett.* **87** (2001) 082001, [hep-ph/0104315].
- [129] C. R. Schmidt, *Phys. Rev. Lett.* **78** (1997) 4531–4535, [hep-ph/9612454].
- [130] L. H. Orr and W. J. Stirling, *Phys. Rev.* **D56** (1997) 5875–5884, [hep-ph/9706529].
- [131] L. H. Orr and W. J. Stirling, *Phys. Lett.* **B429** (1998) 135–144, [hep-ph/9801304].
- [132] J. R. Andersen and A. Sabio Vera, *Phys. Lett.* **B567** (2003) 116–124, [hep-ph/0305236].
- [133] J. R. Andersen and A. Sabio Vera, *Nucl. Phys.* **B679** (2004) 345–362, [hep-ph/0309331].
- [134] M. A. Dobbs *et. al.*, hep-ph/0403045.
- [135] D. Stump *et. al.*, *JHEP* **10** (2003) 046, [hep-ph/0303013].
- [136] R. K. Ellis, W. J. Stirling, and B. R. Webber, *Camb. Monogr. Part. Phys. Nucl. Phys. Cosmol.* **8** (1996) 1–435.

- [137] A. Pukhov, hep-ph/0412191.
- [138] <http://durpdg.dur.ac.uk/hepdata/pdf3.html>.
- [139] G. Sterman, *Nucl. Phys.* **B281** (1987) 310.
- [140] S. Catani and L. Trentadue, *Nucl. Phys.* **B327** (1989) 323.
- [141] E. Laenen and S.-O. Moch, *Phys. Rev.* **D59** (1999) 034027, [hep-ph/9809550].
- [142] G. Corcella and A. D. Mitov, *Nucl. Phys.* **B676** (2004) 346–364, [hep-ph/0308105].
- [143] M. Tzanov *et. al.*, **NuTeV** Collaboration hep-ex/0509010.
- [144] M. Arneodo *et. al.*, **New Muon** Collaboration *Nucl. Phys.* **B483** (1997) 3–43, [hep-ph/9610231].
- [145] A. C. Benvenuti *et. al.*, **BCDMS** Collaboration *Phys. Lett.* **B223** (1989) 485.
- [146] A. C. Benvenuti *et. al.*, **BCDMS** Collaboration *Phys. Lett.* **B237** (1990) 592.
- [147] G. Corcella and L. Magnea, *Phys. Rev.* **D72** (2005) 074017, [hep-ph/0506278].
- [148] L. Del Debbio, S. Forte, J. I. Latorre, A. Piccione, and J. Rojo, **NNPDF** Collaboration *JHEP* **03** (2005) 080, [hep-ph/0501067].
- [149] S. Forte, L. Garrido, J. I. Latorre, and A. Piccione, *JHEP* **05** (2002) 062, [hep-ph/0204232].
- [150] G. Corcella and L. Magnea, hep-ph/0507042.
- [151] U.-K. Yang *et. al.*, **CCFR/NuTeV** Collaboration *Phys. Rev. Lett.* **86** (2001) 2742–2745, [hep-ex/0009041].
- [152] V. Drollinger, T. Muller, and D. Denegri, hep-ph/0201249.
- [153] E. Richter-Was and M. Sapinski, *Acta Phys. Polon.* **B30** (1999) 1001–1040.
- [154] V. Drollinger, T. Muller, and D. Denegri, hep-ph/0111312.
- [155] B. Mele and P. Nason, *Nucl. Phys.* **B361** (1991) 626–644.
- [156] T. Sjostrand, L. Lonnblad, and S. Mrenna, hep-ph/0108264.
- [157] K. Abe *et. al.*, **SLD** Collaboration *Phys. Rev. Lett.* **84** (2000) 4300–4304, [hep-ex/9912058].
- [158] A. Heister *et. al.*, **ALEPH** Collaboration *Phys. Lett.* **B512** (2001) 30–48, [hep-ex/0106051].
- [159] G. Abbiendi *et. al.*, **OPAL** Collaboration *Eur. Phys. J.* **C29** (2003) 463–478, [hep-ex/0210031].
- [160] V. G. Kartvelishvili, A. K. Likhoded, and V. A. Petrov, *Phys. Lett.* **B78** (1978) 615.
- [161] G. Barker *et. al.*, **DELPHI** Collaboration *DELPHI 2002-069, CONF 603*.
- [162] G. Corcella and A. D. Mitov, *Nucl. Phys.* **B623** (2002) 247–270, [hep-ph/0110319].
- [163] G. Corcella, *Nucl. Phys.* **B705** (2005) 363–383, [hep-ph/0409161].
- [164] M. Cacciari and S. Catani, *Nucl. Phys.* **B617** (2001) 253–290, [hep-ph/0107138].

- [165] M. Cacciari, G. Corcella, and A. D. Mitov, *JHEP* **12** (2002) 015, [hep-ph/0209204].
- [166] S. Catani, B. R. Webber, and G. Marchesini, *Nucl. Phys.* **B349** (1991) 635–654.
- [167] G. Miu and T. Sjostrand, *Phys. Lett.* **B449** (1999) 313–320, [hep-ph/9812455].
- [168] E. Norrbin and T. Sjostrand, *Nucl. Phys.* **B603** (2001) 297–342, [hep-ph/0010012].
- [169] M. H. Seymour, *Comp. Phys. Commun.* **90** (1995) 95–101, [hep-ph/9410414].
- [170] M. H. Seymour, *Z. Phys.* **C56** (1992) 161–170.
- [171] G. Corcella and M. H. Seymour, *Phys. Lett.* **B442** (1998) 417–426, [hep-ph/9809451].
- [172] G. Corcella and V. Drollinger, *Nucl. Phys.* **B730** (2005) 82–102, [hep-ph/0508013].
- [173] S. Gieseke, A. Ribon, M. H. Seymour, P. Stephens, and B. Webber, *JHEP* **02** (2004) 005, [hep-ph/0311208].
- [174] G. C. B. *et al.*, hep-ex/0005012.
- [175] t. L. E. W. Group,, **OPAL** Collaboration hep-ex/0511027.
- [176] V. M. Abazov *et al.*, **CDF** Collaboration *Phys. Rev.* **D70** (2004) 092008, [hep-ex/0311039].
- [177] R. D. Field, hep-ph/0201192 CDF Note 6403; further recent talks available from webpage <http://www.phys.ufl.edu/~rfield/cdf/>.
- [178] T. Affolder *et al.*, **CDF** Collaboration *Phys. Rev.* **D65** (2002) 092002.
- [179] C. M. Buttar, D. Clements, I. Dawson, and A. Moraes, *Acta Phys. Polon.* **B35** (2004) 433–441.
- [180] R. Field and R. C. Group,, **CDF** Collaboration hep-ph/0510198.
- [181] T. Sjöstrand and P. Z. Skands, *Nucl. Phys.* **B659** (2003) 243, [hep-ph/0212264].
- [182] T. Sjöstrand and P. Z. Skands, *JHEP* **03** (2004) 053, [hep-ph/0402078].
- [183] T. Sjostrand and P. Z. Skands, *Eur. Phys. J.* **C39** (2005) 129–154, [hep-ph/0408302].
- [184] G. Gustafson, U. Pettersson, and P. M. Zerwas, *Phys. Lett.* **B209** (1988) 90.
- [185] T. Sjöstrand and V. A. Khoze, *Phys. Rev. Lett.* **72** (1994) 28–31, [hep-ph/9310276].
- [186] T. Sjöstrand and V. A. Khoze, *Z. Phys.* **C62** (1994) 281–310, [hep-ph/9310242].
- [187] B. Andersson, G. Gustafson, G. Ingelman, and T. Sjöstrand, *Phys. Rept.* **97** (1983) 31.
- [188] M. G. Jackson, N. T. Jones, and J. Polchinski, *JHEP* **10** (2005) 013, [hep-th/0405229].
- [189] A. L. Cotrone, L. Martucci, and W. Troost, hep-th/0511045.
- [190] V. A. Khoze and T. Sjostrand, *Phys. Lett.* **B328** (1994) 466–476, [hep-ph/9403394].
- [191] G. Gustafson and J. Hakkinen, *Z. Phys.* **C64** (1994) 659–664.
- [192] L. Lonnblad, *Z. Phys.* **C70** (1996) 107–114.
- [193] C. Friberg, G. Gustafson, and J. Hakkinen, *Nucl. Phys.* **B490** (1997) 289–305, [hep-ph/9604347].

- [194] B. R. Webber, *J. Phys.* **G24** (1998) 287–296, [hep-ph/9708463].
- [195] W. Buchmuller and A. Hebecker, *Phys. Lett.* **B355** (1995) 573–578, [hep-ph/9504374].
- [196] A. Edin, G. Ingelman, and J. Rathsman, *Phys. Lett.* **B366** (1996) 371–378, [hep-ph/9508386].
- [197] R. Enberg, G. Ingelman, and N. Timneanu, *Phys. Rev.* **D64** (2001) 114015, [hep-ph/0106246].
- [198] A. Edin, G. Ingelman, and J. Rathsman, *Phys. Rev.* **D56** (1997) 7317–7320, [hep-ph/9705311].
- [199] G. Abbiendi *et. al.*, **OPAL** Collaboration *Phys. Lett.* **B453** (1999) 153–168, [hep-ex/9901019].
- [200] G. Abbiendi *et. al.*, **OPAL** Collaboration hep-ex/0508062.
- [201] B. Andersson, G. Gustafson, and B. Söderberg, *Z. Phys.* **C20** (1983) 317.
- [202] T. Sjöstrand *et. al.*, PYTHIA update notes, see <http://www.thep.lu.se/~torbjorn/pythia/pythia6326.update>.
- [203] T. Sjöstrand, S. Mrenna, and P. Skands, hep-ph/0603175.
- [204] M. Sandhoff., Diploma Thesis, Bergische Universität Wuppertal, WU D 05-08.
- [205] J. M. Butterworth, J. P. Couchman, B. E. Cox, and B. M. Waugh., *KtJet: A C++ implementation of the  $K_{\perp}$  clustering algorithm*. October, 2002. MAN/HEP/2002/02, UCL/HEP 2002-02.
- [206] W. L. van Neerven and E. B. Zijlstra, *Nucl. Phys.* **B382** (1992) 11–62.
- [207] C. Anastasiou, L. J. Dixon, K. Melnikov, and F. Petriello, *Phys. Rev. Lett.* **91** (2003) 182002, [hep-ph/0306192].
- [208] C. M. Carloni Calame, G. Montagna, O. Nicrosini, and M. Treccani, *Phys. Rev.* **D69** (2004) 037301, [hep-ph/0303102].
- [209] C. M. Carloni Calame, G. Montagna, O. Nicrosini, and M. Treccani, *JHEP* **05** (2005) 019, [hep-ph/0502218].
- [210] C. Balazs and C. P. Yuan, *Phys. Rev.* **D56** (1997) 5558–5583, [hep-ph/9704258].
- [211] F. Landry, R. Brock, P. M. Nadolsky, and C. P. Yuan, *Phys. Rev.* **D67** (2003) 073016, [hep-ph/0212159].
- [212] W. Placzek and S. Jadach, *Eur. Phys. J.* **C29** (2003) 325–339, [hep-ph/0302065].
- [213] U. Baur, S. Keller, and D. Wackerroth, *Phys. Rev.* **D59** (1999) 013002, [hep-ph/9807417].
- [214] U. Baur, O. Brein, W. Hollik, C. Schappacher, and D. Wackerroth, *Phys. Rev.* **D65** (2002) 033007, [hep-ph/0108274].
- [215] Q.-H. Cao and C. P. Yuan, *Phys. Rev. Lett.* **93** (2004) 042001, [hep-ph/0401026].
- [216] S. Haywood *et. al.*, hep-ph/0003275.
- [217] S. Catani *et. al.*, hep-ph/0005025.

- [218] P. M. Nadolsky, *AIP Conf. Proc.* **753** (2005) 158–170, [hep-ph/0412146].
- [219] U. Baur, hep-ph/0511064.
- [220] F. A. Berends and R. Kleiss, *Z. Phys.* **C27** (1985) 365.
- [221] S. Dittmaier and M. Krämer, *Phys. Rev.* **D65** (2002) 073007, [hep-ph/0109062].
- [222] U. Baur and D. Wackerth, *Phys. Rev.* **D70** (2004) 073015, [hep-ph/0405191].
- [223] U. Baur, S. Keller, and W. K. Sakumoto, *Phys. Rev.* **D57** (1998) 199–215, [hep-ph/9707301].
- [224] C. M. Carloni Calame, S. Jadach, G. Montagna, O. Nicrosini, and W. Placzek, *Acta Phys. Polon.* **B35** (2004) 1643–1674, [hep-ph/0402235].
- [225] A. D. Martin, R. G. Roberts, W. J. Stirling, and R. S. Thorne, *Eur. Phys. J.* **C39** (2005) 155–161, [hep-ph/0411040].
- [226] K. P. O. Diener, S. Dittmaier, and W. Hollik, *Phys. Rev.* **D72** (2005) 093002, [hep-ph/0509084].
- [227] S. Dittmaier, *Nucl. Phys.* **B565** (2000) 69–122, [hep-ph/9904440].
- [228] A. Bredenstein, S. Dittmaier, and M. Roth, *Eur. Phys. J.* **C44** (2005) 27–49, [hep-ph/0506005].
- [229] C. M. Carloni Calame, C. Lunardini, G. Montagna, O. Nicrosini, and F. Piccinini, *Nucl. Phys.* **B584** (2000) 459–479, [hep-ph/0003268].
- [230] C. M. Carloni Calame, *Phys. Lett.* **B520** (2001) 16–24, [hep-ph/0103117].
- [231] C. M. Carloni Calame, G. Montagna, O. Nicrosini, and A. Vicini, *in preparation*.
- [232] A. Andonov *et. al.*, hep-ph/0411186.
- [233] A. Arbuzov *et. al.*, hep-ph/0506110.
- [234] H. Baer, J. Ohnemus, and J. F. Owens, *Phys. Rev.* **D40** (1989) 2844.
- [235] H. Baer, J. Ohnemus, and J. F. Owens, *Phys. Rev.* **D42** (1990) 61–71.
- [236] B. W. Harris and J. F. Owens, *Phys. Rev.* **D65** (2002) 094032, [hep-ph/0102128].
- [237] S. Eidelman *et. al.*, **Particle Data Group** Collaboration *Phys. Lett.* **B592** (2004) 1.
- [238] P. Azzi *et. al.*, **CDF Collaborattion** Collaboration hep-ex/0404010.
- [239] F. Jegerlehner, hep-ph/0105283.
- [240] V. Lendermann, H. Spiesberger, J. Stirling, and A. Tapper, *private communications*.
- [241] W. Hollik *et. al.*, *Acta Phys. Polon.* **B35** (2004) 2533–2555, [hep-ph/0501246].
- [242] J. H. Kühn, A. Kulesza, S. Pozzorini, and M. Schulze, *Nucl. Phys.* **B727** (2005) 368–394, [hep-ph/0507178].
- [243] J. H. Kühn, A. Kulesza, S. Pozzorini, and M. Schulze, hep-ph/0508253.
- [244] E. Maina, S. Moretti, and D. A. Ross, *Phys. Lett.* **B593** (2004) 143–150, [hep-ph/0403050].

- [245] J. H. Kühn, A. Kulesza, S. Pozzorini, and M. Schulze, *Phys. Lett.* **B609** (2005) 277–285, [hep-ph/0408308].
- [246] A. Denner and S. Pozzorini, *Eur. Phys. J.* **C18** (2001) 461–480, [hep-ph/0010201].
- [247] A. Denner, M. Melles, and S. Pozzorini, *Nucl. Phys.* **B662** (2003) 299–333, [hep-ph/0301241].
- [248] M. Melles, *Phys. Rev.* **D63** (2001) 034003, [hep-ph/0004056].
- [249] S. Pozzorini, *Ph.D. Thesis, Universität Zürich* (2001) [hep-ph/0201077].
- [250] M. Ciafaloni, P. Ciafaloni, and D. Comelli, *Phys. Rev. Lett.* **84** (2000) 4810–4813, [hep-ph/0001142].
- [251] E. Maina, S. Moretti, M. R. Nolten, and D. A. Ross, *Phys. Lett.* **B570** (2003) 205–214, [hep-ph/0307021].
- [252] E. Maina, S. Moretti, M. R. Nolten, and D. A. Ross, hep-ph/0401093.
- [253] E. Maina, S. Moretti, M. R. Nolten, and D. A. Ross, hep-ph/0407150.
- [254] W. Beenakker *et. al.*, *Nucl. Phys.* **B411** (1994) 343–380.
- [255] W. Hollik, W. M. Mosle, and D. Wackerroth, *Nucl. Phys.* **B516** (1998) 29–54, [hep-ph/9706218].
- [256] C. Kao, G. A. Ladinsky, and C. Yuan, *Int. J. Mod. Phys.* **A12** (1997) 1341–1372.
- [257] C. Kao and D. Wackerroth, *Phys. Rev.* **D61** (2000) 055009, [hep-ph/9902202].
- [258] W. Bernreuther, M. Fückler, and Z. G. Si, hep-ph/0508091.
- [259] W. Bernreuther, M. Fückler, and Z. G. Si, hep-ph/0509210.
- [260] J. H. Kühn, A. Scharf, and P. Uwer, hep-ph/0508092.
- [261] M. Beccaria, F. M. Renard, and C. Verzegnassi, hep-ph/0405036.
- [262] M. Beccaria, F. M. Renard, and C. Verzegnassi, *Phys. Rev.* **D72** (2005) 093001, [hep-ph/0506230].
- [263] S. Moretti, M. R. Nolten, and D. A. Ross, hep-ph/0509254.
- [264] S. Moretti, M. R. Nolten, and D. A. Ross, hep-ph/0503152.
- [265] U. Baur, E. W. N. Glover, and A. D. Martin, *Phys. Lett.* **B232** (1989) 519.
- [266] J. R. Ellis, S. Moretti, and D. A. Ross, *JHEP* **06** (2001) 043, [hep-ph/0102340].
- [267] F. Abe *et. al.*, **CDF** Collaboration *Phys. Rev. Lett.* **74** (1995) 2626–2631, [hep-ex/9503002].
- [268] S. Abachi *et. al.*, **D0** Collaboration *Phys. Rev. Lett.* **74** (1995) 2632–2637, [hep-ex/9503003].
- [269] A. Abulencia *et. al.*, **CDF-Run II** Collaboration hep-ex/0511023.
- [270] V. M. Abazov *et. al.*, **D0** Collaboration *Phys. Rev.* **D72** (2005) 011104, [hep-ex/0505031].



- [271] E. Boos, L. Dudko, and T. Ohl, *Eur. Phys. J.* **C11** (1999) 473–484, [hep-ph/9903215].
- [272] D. Acosta *et. al.*, **CDF** Collaboration *Phys. Rev.* **D71** (2005) 012005, [hep-ex/0410058].
- [273] V. M. Abazov *et. al.*, **D0** Collaboration *Phys. Lett.* **B622** (2005) 265–276, [hep-ex/0505063].
- [274] Y. Sumino and S. Tsuno, *Phys. Lett.* **B633** (2006) 715–720, [hep-ph/0512205].
- [275] S. Tsuno, I. Nakano, Y. Sumino, and R. Tanaka, *Phys. Rev.* **D73** (2006) 054011, [hep-ex/0512037].
- [276] W. Bernreuther, A. Brandenburg, Z. G. Si, and P. Uwer, *Phys. Lett.* **B509** (2001) 53–58, [hep-ph/0104096].
- [277] W. Bernreuther, A. Brandenburg, and Z. G. Si, *Phys. Lett.* **B483** (2000) 99–104, [hep-ph/0004184].
- [278] G. Mahlon and S. J. Parke, *Phys. Rev.* **D53** (1996) 4886–4896, [hep-ph/9512264].
- [279] T. Stelzer and S. Willenbrock, *Phys. Lett.* **B374** (1996) 169–172, [hep-ph/9512292].
- [280] S. J. Parke and Y. Shadmi, *Phys. Lett.* **B387** (1996) 199–206, [hep-ph/9606419].
- [281] M. Jezabek and J. H. Kuhn, *Phys. Rev.* **D48** (1993) 1910–1913, [hep-ph/9302295].
- [282] B. Grzadkowski and Z. Hioki, *Phys. Lett.* **B476** (2000) 87–94, [hep-ph/9911505].
- [283] S. Tsuno *et. al.*, *Comput. Phys. Commun.* **151** (2003) 216–240, [hep-ph/0204222].
- [284] T. Sjostrand *et. al.*, *Comput. Phys. Commun.* **135** (2001) 238–259, [hep-ph/0010017].
- [285] K. Ikematsu, K. Fujii, Z. Hioki, Y. Sumino, and T. Takahashi, *Eur. Phys. J.* **C29** (2003) 1–10, [hep-ph/0302214].
- [286] E. Boos *et. al.*, **CompHEP** Collaboration *Nucl. Instrum. Meth.* **A534** (2004) 250–259, [hep-ph/0403113].
- [287] M. Beneke *et. al.*, hep-ph/0003033.
- [288] Z. Sullivan, *Phys. Rev.* **D70** (2004) 114012, [hep-ph/0408049].
- [289] T. Stelzer, Z. Sullivan, and S. Willenbrock, *Phys. Rev.* **D56** (1997) 5919–5927, [hep-ph/9705398].
- [290] B. W. Harris, E. Laenen, L. Phaf, Z. Sullivan, and S. Weinzierl, *Phys. Rev.* **D66** (2002) 054024, [hep-ph/0207055].
- [291] E. Boos, L. Dudko, and V. Savrin, CMS Note 2000/065.
- [292] E. E. .Boos, V. E. Bunichev, L. V. Dudko, V. I. Savrin, and A. V. Sherstnev, *accepted for publication in Physics of Atomic Nuclei* [SINP MSU 2005-16/782].
- [293] J. Campbell, R. K. Ellis, and F. Tramontano, *Phys. Rev.* **D70** (2004) 094012, [hep-ph/0408158].
- [294] V. M. Abazov *et. al.*, **D0** Collaboration *Phys. Rev. Lett.* **94** (2005) 151801, [hep-ex/0410066].

- [295] D. Acosta *et. al.*, **CDF Collaboration** *Phys. Rev. Lett.* **94** (2005) 211801, [hep-ex/0501050].
- [296] M. Dittmar and H. K. Dreiner, *Phys. Rev.* **D55** (1997) 167–172, [hep-ph/9608317].
- [297] M. Dittmar and H. K. Dreiner, hep-ph/9703401.
- [298] J. Ohnemus, *Phys. Rev.* **D44** (1991) 1403–1414.
- [299] S. Frixione, *Nucl. Phys.* **B410** (1993) 280–324.
- [300] L. J. Dixon, Z. Kunszt, and A. Signer, *Phys. Rev.* **D60** (1999) 114037, [hep-ph/9907305].
- [301] J. M. Campbell and R. K. Ellis, *Phys. Rev.* **D60** (1999) 113006, [hep-ph/9905386].
- [302] M. Grazzini, hep-ph/0510337.
- [303] L. J. Dixon, Z. Kunszt, and A. Signer, *Nucl. Phys.* **B531** (1998) 3–23, [hep-ph/9803250].
- [304] D. de Florian and M. Grazzini, *Phys. Rev. Lett.* **85** (2000) 4678–4681, [hep-ph/0008152].
- [305] D. de Florian and M. Grazzini, *Nucl. Phys.* **B616** (2001) 247–285, [hep-ph/0108273].
- [306] G. Bozzi, S. Catani, D. de Florian, and M. Grazzini, *Phys. Lett.* **B564** (2003) 65–72, [hep-ph/0302104].
- [307] G. Bozzi, S. Catani, D. de Florian, and M. Grazzini, hep-ph/0508068.
- [308] S. Frixione and B. R. Webber, *JHEP* **06** (2002) 029, [hep-ph/0204244].
- [309] S. Frixione, P. Nason, and B. R. Webber, *JHEP* **08** (2003) 007, [hep-ph/0305252].
- [310] S. Frixione and B. R. Webber, hep-ph/0506182.
- [311] A. D. Martin, R. G. Roberts, W. J. Stirling, and R. S. Thorne, *Eur. Phys. J.* **C28** (2003) 455–473, [hep-ph/0211080].
- [312] G. Davatz, G. Dissertori, M. Dittmar, M. Grazzini, and F. Pauss, *JHEP* **05** (2004) 009, [hep-ph/0402218].
- [313] D. L. Rainwater and D. Zeppenfeld, *Phys. Rev.* **D60** (1999) 113004, [hep-ph/9906218].
- [314] T. Binoth, M. Ciccolini, N. Kauer, and M. Kramer, *JHEP* **03** (2005) 065, [hep-ph/0503094].
- [315] M. Dührssen, K. Jakobs, J. J. van der Bij, and P. Marquard, *JHEP* **05** (2005) 064, [hep-ph/0504006].
- [316] G. Davatz, M. Dittmar, and A.-S. Giolo-Nicollerat, CERN-CMS-NOTE 2006/047.
- [317] T. Binoth, M. Ciccolini, N. Kauer, and M. Kramer, in these proceedings.
- [318] Z. Bern, L. J. Dixon, and C. Schmidt, *Phys. Rev.* **D66** (2002) 074018, [hep-ph/0206194].
- [319] G. Corcella *et. al.*, hep-ph/0210213.
- [320] V. Drollinger, T. Binoth, M. Ciccolini, M. Dührssen, and N. Kauer, CERN-CMS-NOTE-2005-024.
- [321] S. R. Slabospitsky and L. Sonnenschein, *Comput. Phys. Commun.* **148** (2002) 87–102, [hep-ph/0201292].

- [322] G. Davatz, A.-S. Giolo-Nicollerat, and M. Zanetti,, **CMS** Collaboration. CERN-CMS-NOTE 2006/048.
- [323] N. Kauer, *Phys. Rev.* **D70** (2004) 014020, [hep-ph/0404045].
- [324] F. Palla, A. Rizzi, and G. Segneri,. CMS Note, in preparation.
- [325] F. Maltoni and T. Stelzer, *JHEP* **02** (2003) 027, [hep-ph/0208156].
- [326] G. Davatz, A. S. Giolo-Nicollerat, and M. Zanetti,. In this proceedings.
- [327] J. D’Hondt, J. Heyninck, S. Lowette, and V. P.,. CMS Note, in preparation.
- [328] T. M. P. Tait, *Phys. Rev.* **D61** (2000) 034001, [hep-ph/9909352].
- [329] A. Belyaev and E. Boos, *Phys. Rev.* **D63** (2001) 034012, [hep-ph/0003260].
- [330] J. Campbell and F. Tramontano, *Nucl. Phys.* **B726** (2005) 109–130, [hep-ph/0506289].
- [331] J. M. Campbell and R. K. Ellis, <http://mcfm.fnal.gov>.
- [332] P. Bartalini, R. Chierici, and A. De Roeck,. CERN-CMS-NOTE-2005-013.
- [333] W. Giele and M. R. Whalley, <http://durpdg.dur.ac.uk/lhapdf/>.
- [334] J. Pumplin *et. al.*, *Phys. Rev.* **D65** (2002) 014013, [hep-ph/0101032].
- [335] R. W. L. Jones, M. Ford, G. P. Salam, H. Stenzel, and D. Wicke, *JHEP* **12** (2003) 007, [hep-ph/0312016].
- [336] E. Accomando, A. Denner, and A. Kaiser, *Nucl. Phys.* **B706** (2005) 325–371, [hep-ph/0409247].
- [337] E. Accomando, A. Denner, and C. Meier, hep-ph/0509234.
- [338] D. R. Stump,. Prepared for 31st International Conference on High Energy Physics (ICHEP 2002), Amsterdam, The Netherlands, 24-31 Jul 2002.
- [339] P. Bartalini, R. Chierici, and A. De Roeck,. CMS Note 2005/013.
- [340] P. Nason *et. al.*, hep-ph/0003142.
- [341] C. 2002-26,. CMS TDR 6.2, 15, p.317.
- [342] A. De Roeck, *AIP Conf. Proc.* **792** (2005) 107–120.
- [343] H. Jung and G. P. Salam, *Eur. Phys. J.* **C19** (2001) 351–360, [hep-ph/0012143].
- [344] G. Corcella and S. Moretti, *Phys. Lett.* **B590** (2004) 249–257, [hep-ph/0402146].
- [345] I. Dawson, C. Buttar, and A. Moraes, *Czech. J. Phys.* **54** (2004) A221–A228.
- [346] R. Kinnunen, S. Lehti, F. Moortgat, A. Nikitenko, and M. Spira, *Eur. Phys. J.* **C40N5** (2005) 23–32, [hep-ph/0503075].
- [347] J. Campbell, R. K. Ellis, F. Maltoni, and S. Willenbrock, *Phys. Rev.* **D67** (2003) 095002, [hep-ph/0204093].
- [348] S. Dittmaier, M. Kramer, and M. Spira, *Phys. Rev.* **D70** (2004) 074010, [hep-ph/0309204].

- [349] S. Dawson, C. B. Jackson, L. Reina, and D. Wackerroth, *Phys. Rev.* **D69** (2004) 074027, [hep-ph/0311067].
- [350] S. Dawson, C. B. Jackson, L. Reina, and D. Wackerroth, *Phys. Rev. Lett.* **94** (2005) 031802, [hep-ph/0408077].
- [351] S. Dawson, C. B. Jackson, L. Reina, and D. Wackerroth, hep-ph/0508293.
- [352] D. Dicus, T. Stelzer, Z. Sullivan, and S. Willenbrock, *Phys. Rev.* **D59** (1999) 094016, [hep-ph/9811492].
- [353] C. Balazs, H.-J. He, and C. P. Yuan, *Phys. Rev.* **D60** (1999) 114001, [hep-ph/9812263].
- [354] F. Maltoni, Z. Sullivan, and S. Willenbrock, *Phys. Rev.* **D67** (2003) 093005, [hep-ph/0301033].
- [355] R. V. Harlander and W. B. Kilgore, *Phys. Rev.* **D68** (2003) 013001, [hep-ph/0304035].
- [356] J. Campbell *et. al.*, hep-ph/0405302.
- [357] M. A. G. Aivazis, J. C. Collins, F. I. Olness, and W.-K. Tung, *Phys. Rev.* **D50** (1994) 3102–3118, [hep-ph/9312319].
- [358] M. A. G. Aivazis, F. I. Olness, and W.-K. Tung, *Phys. Rev.* **D50** (1994) 3085–3101, [hep-ph/9312318].
- [359] F. I. Olness and R. J. Scalise, *Phys. Rev.* **D57** (1998) 241–244, [hep-ph/9707459].
- [360] M. Kramer, F. I. Olness, and D. E. Soper, *Phys. Rev.* **D62** (2000) 096007, [hep-ph/0003035].
- [361] J. C. Collins, *Phys. Rev.* **D58** (1998) 094002, [hep-ph/9806259].
- [362] R. Doria, J. Frenkel, and J. C. Taylor, *Nucl. Phys.* **B168** (1980) 93.
- [363] C. Di’Lieto, S. Gendron, I. G. Halliday, and C. T. Sachrajda, *Nucl. Phys.* **B183** (1981) 223.
- [364] S. Catani, M. Ciafaloni, and G. Marchesini, *Nucl. Phys.* **B264** (1986) 588–620.
- [365] S. Catani, *Z. Phys.* **C37** (1988) 357.
- [366] S. Catani, S. Dittmaier, M. H. Seymour, and Z. Trocsanyi, *Nucl. Phys.* **B627** (2002) 189–265, [hep-ph/0201036].
- [367] E. Laenen, S. Riemersma, J. Smith, and W. L. van Neerven, *Nucl. Phys.* **B392** (1993) 162–228.
- [368] W.-K. Tung, S. Kretzer, and C. Schmidt, *J. Phys.* **G28** (2002) 983–996, [hep-ph/0110247].
- [369] M. Buza, Y. Matiounine, J. Smith, R. Migneron, and W. L. van Neerven, *Nucl. Phys.* **B472** (1996) 611–658, [hep-ph/9601302].
- [370] M. Buza, Y. Matiounine, J. Smith, and W. L. van Neerven, *Phys. Lett.* **B411** (1997) 211–217, [hep-ph/9707263].
- [371] M. Buza, Y. Matiounine, J. Smith, and W. L. van Neerven, *Eur. Phys. J.* **C1** (1998) 301–320, [hep-ph/9612398].
- [372] Y. Matiounine, J. Smith, and W. L. van Neerven, *Phys. Rev.* **D57** (1998) 6701–6722, [hep-ph/9801224].

- [373] A. Chuvakin, J. Smith, and W. L. van Neerven, *Phys. Rev.* **D61** (2000) 096004, [hep-ph/9910250].
- [374] A. Chuvakin, J. Smith, and W. L. van Neerven, *Phys. Rev.* **D62** (2000) 036004, [hep-ph/0002011].
- [375] A. Chuvakin and J. Smith, *Comput. Phys. Commun.* **143** (2002) 257–286, [hep-ph/0103177].
- [376] A. Vogt, *Comput. Phys. Commun.* **170** (2005) 65–92, [hep-ph/0408244].
- [377] W. Bernreuther and W. Wetzel, *Nucl. Phys.* **B197** (1982) 228.
- [378] W. Bernreuther, *Ann. Phys.* **151** (1983) 127.
- [379] S. A. Larin, T. van Ritbergen, and J. A. M. Vermaseren, *Nucl. Phys.* **B438** (1995) 278–306, [hep-ph/9411260].
- [380] K. G. Chetyrkin, B. A. Kniehl, and M. Steinhauser, *Phys. Rev. Lett.* **79** (1997) 2184–2187, [hep-ph/9706430].
- [381] F. Maltoni, T. McElmurry, and S. Willenbrock, *Phys. Rev.* **D72** (2005) 074024, [hep-ph/0505014].
- [382] A. Chuvakin, J. Smith, and B. W. Harris, *Eur. Phys. J.* **C18** (2001) 547–553, [hep-ph/0010350].
- [383] F. I. Olness, R. J. Scalise, and W.-K. Tung, *Phys. Rev.* **D59** (1999) 014506, [hep-ph/9712494].
- [384] K. Assamagan *et. al.*, **Higgs Working Group** Collaboration hep-ph/0406152.
- [385] G. Belanger, F. Boudjema, and K. Sridhar, *Nucl. Phys.* **B568** (2000) 3–39, [hep-ph/9904348].
- [386] M. Dubinin, V. Ilyin, and V. Savrin, CMS Note 1997/101.
- [387] R. Kinnunen and D. Denegri, CMS Note 1997/057.
- [388] CERN-LHCC-94-38.
- [389] CERN-LHCC-99-15.
- [390] P. Beauchemin, G. Azuelos, and C. Burgess, *J. Phys.* **G30** (2004) N17, [hep-ph/0407196].
- [391] W. Beenakker, S. Dittmaier, M. Kraemer, B. Pluemper, M. Spira, and P. Zerwas, *Phys. Rev. Lett.* **87** (2001) 201805, [hep-ph/0107081].
- [392] W. Beenakker, S. Dittmaier, M. Kraemer, B. Pluemper, M. Spira, and P. Zerwas, *Nucl. Phys.* **B653** (2003) 151–203, [hep-ph/0211352].
- [393] S. Dawson, L. Orr, L. Reina, and D. Wackerroth, *Phys. Rev.* **D67** (2003) 071503, [hep-ph/0211438].
- [394] A. Djouadi, J. Kalinowski, and M. Spira, *Comput. Phys. Commun.* **108** (1998) 56–74, [hep-ph/9704448].
- [395] T. Stelzer and W. Long, *Comput. Phys. Commun.* **81** (1994) 357–371, [hep-ph/9401258].

- [396] H. Murayama, I. Watanabe, and K. Hagiwara, KEK-91-11.
- [397] M. L. Mangano, M. Moretti, F. Piccinini, R. Pittau, and A. D. Polosa, *JHEP* **07** (2003) 001, [hep-ph/0206293].
- [398] M. Mangano, M. Moretti, and R. Pittau, *Nucl. Phys.* **B632** (2002) 343–362, [hep-ph/0108069].
- [399] F. Caravaglios, M. Mangano, M. Moretti, and R. Pittau, *Nucl. Phys.* **B539** (1999) 215–232, [hep-ph/9807570].
- [400] M. Spira, *Fortsch. Phys.* **46** (1998) 203–284, [hep-ph/9705337].
- [401] J. Gunion and X.-G. He, *Phys. Rev. Lett.* **76** (1996) 4468–4471, [hep-ph/9602226].
- [402] S. Lehti, *CMS Note 2002/035*.
- [403] J. Campbell, *Private communication*.
- [404] *CERN Program Library Long Writeup W5013* (1994).
- [405] <http://cmsdoc.cern.ch/cms/cpt/Software/html/General>.
- [406] e. . Sphicas, P., **CMS** Collaboration. CERN-LHCC-2002-026.
- [407] *CERN/LHCC 05-xx (to be published) CMS TDR 8 Vol 1* (2006).
- [408] J. Campbell, R. K. Ellis, and D. L. Rainwater, *Phys. Rev.* **D68** (2003) 094021, [hep-ph/0308195].
- [409] B. Mellado, G. Unal, and S. L. Wu, *ATLAS internal note ATL-COM-PHYS-2004-062*.
- [410] T. Sjostrand, *Comput. Phys. Commun.* **82** (1994) 74–90.
- [411] E. Richter-Was, D. Froidevaux, and L. Poggioli, *ATLAS Internal Note ATL-PHYS-98-131*.
- [412] N. Kauer and D. Zeppenfeld, *Phys. Rev.* **D65** (2002) 014021, [hep-ph/0107181].
- [413] B. Mellado, W. Quayle, and S. L. Wu, *ATLAS internal note ATL-COM-PHYS-2005-074*.
- [414] S. Asai *et. al.*, *Eur. Phys. J.* **C32S2** (2004) 19–54, [hep-ph/0402254].
- [415] S. Abdullin *et. al.*, *Eur. Phys. J.* **C39S2** (2005) 41–61.
- [416] L. Zivkovic, *Czech. J. Phys.* **54** (2004) A73–A82.
- [417] V. D. Barger, K.-m. Cheung, A. Djouadi, B. A. Kniehl, and P. M. Zerwas, *Phys. Rev.* **D49** (1994) 79–90, [hep-ph/9306270].
- [418] S. Y. Choi, D. J. Miller, M. M. Mühlleitner, and P. M. Zerwas, *Phys. Lett.* **B553** (2003) 61–71, [hep-ph/0210077].
- [419] J. Fleischer and F. Jegerlehner, *Phys. Rev.* **D23** (1981) 2001–2026.
- [420] B. A. Kniehl, *Nucl. Phys.* **B352** (1991) 1–26.
- [421] B. A. Kniehl, *Nucl. Phys.* **B357** (1991) 439–466.
- [422] D. Y. Bardin, P. K. Khristova, and B. M. Vilensky, *Sov. J. Nucl. Phys.* **54** (1991) 833–844.



- [423] C. M. Carloni Calame,, “QED corrections to Higgs boson decay into 4 fermions at the LHC.” , talk given at the RADCOR05 conference, Shonan Village, October 2-7, 2005.
- [424] A. Bredenstein,, “Electroweak corrections to  $H \rightarrow WW/ZZ \rightarrow 4$  fermions.” , talk given at the RADCOR05 conference, Shonan Village, October 2-7, 2005, 2005.
- [425] A. Bredenstein, A. Denner, S. Dittmaier, and M. M. Weber, in preparation.
- [426] A. Denner, *Fortschr. Phys.* **41** (1993) 307–420.
- [427] A. Denner, G. Weiglein, and S. Dittmaier, *Nucl. Phys.* **B440** (1995) 95–128, [hep-ph/9410338].
- [428] A. Denner, S. Dittmaier, M. Roth, and D. Wackerroth, *Nucl. Phys.* **B560** (1999) 33–65, [hep-ph/9904472].
- [429] A. Denner, S. Dittmaier, M. Roth, and L. H. Wieders, *Nucl. Phys.* **B724** (2005) [hep-ph/0505042].
- [430] J. Küblbeck, M. Böhm, and A. Denner, *Comput. Phys. Commun.* **60** (1990) 165–180.
- [431] T. Hahn, *Comput. Phys. Commun.* **140** (2001) 418–431, [hep-ph/0012260].
- [432] T. Hahn and M. Perez-Victoria, *Comput. Phys. Commun.* **118** (1999) 153–165, [hep-ph/9807565].
- [433] A. Denner, S. Dittmaier, M. Roth, and M. M. Weber, *Nucl. Phys.* **B660** (2003) 289–321, [hep-ph/0302198].
- [434] G. ’t Hooft and M. J. G. Veltman, *Nucl. Phys.* **B153** (1979) 365–401.
- [435] W. Beenakker and A. Denner, *Nucl. Phys.* **B338** (1990) 349–370.
- [436] A. Denner, U. Nierste, and R. Scharf, *Nucl. Phys.* **B367** (1991) 637–656.
- [437] A. Denner and S. Dittmaier, *Nucl. Phys.* **B658** (2003) 175–202, [hep-ph/0212259].
- [438] G. Passarino and M. J. G. Veltman, *Nucl. Phys.* **B160** (1979) 151.
- [439] A. Denner and S. Dittmaier, hep-ph/0509141.
- [440] A. Ghinculov, *Nucl. Phys.* **B455** (1995) 21–38, [hep-ph/9507240].
- [441] A. Frink, B. A. Kniehl, D. Kreimer, and K. Riesselmann, *Phys. Rev.* **D54** (1996) 4548–4560, [hep-ph/9606310].
- [442] S. Dittmaier, *Phys. Rev.* **D59** (1999) 016007, [hep-ph/9805445].
- [443] M. Roth,, *Precise predictions for four-fermion production in electron positron annihilation.* PhD thesis, ETH Zürich No.13363, 1999. hep-ph/0008033.
- [444] M. Böhm and S. Dittmaier, *Nucl. Phys.* **B409** (1993) 3–21.
- [445] S. Dittmaier and M. Böhm, *Nucl. Phys.* **B412** (1994) 39–56.
- [446] W. Beenakker *et. al.*, hep-ph/9602351.
- [447] S. Dittmaier and M. Roth, *Nucl. Phys.* **B642** (2002) 307–343, [hep-ph/0206070].

- [448] G. P. Lepage, *J. Comput. Phys.* **27** (1978) 192.
- [449] W. Beenakker, F. A. Berends, and A. P. Chapovsky, *Nucl. Phys.* **B548** (1999) 3–59, [hep-ph/9811481].
- [450] A. Djouadi, hep-ph/0503172.
- [451] J. M. Butterworth, B. E. Cox, and J. R. Forshaw, *Phys. Rev.* **D65** (2002) 096014, [hep-ph/0201098].
- [452] E. Accomando, A. Ballestrero, and E. Maina, *JHEP* **07** (2005) 016, [hep-ph/0504009].
- [453] A. Ballestrero and E. Maina, *Phys. Lett.* **B350** (1995) 225–233, [hep-ph/9403244].
- [454] A. Ballestrero, hep-ph/9911318.
- [455] F. A. Berends, R. Pittau, and R. Kleiss, *Comput. Phys. Commun.* **85** (1995) 437–452, [hep-ph/9409326].
- [456] E. Accomando, A. Ballestrero, and E. Maina, *Comput. Phys. Commun.* **150** (2003) 166–196, [hep-ph/0204052].
- [457] E. Accomando and A. Ballestrero, *Comput. Phys. Commun.* **99** (1997) 270–296, [hep-ph/9607317].
- [458] E. Accomando, A. Ballestrero, and E. Maina, *Nucl. Instrum. Meth.* **A534** (2004) 265–268, [hep-ph/0404236].
- [459] E. Accomando, A. Ballestrero, A. Belhouari, and E. Maina, hep-ph/0505225.
- [460] Z. Bern, L. J. Dixon, and D. A. Kosower, *Phys. Rev. Lett.* **70** (1993) 2677–2680, [hep-ph/9302280].
- [461] Z. Kunszt, A. Signer, and Z. Trocsanyi, *Phys. Lett.* **B336** (1994) 529–536, [hep-ph/9405386].
- [462] Z. Bern, L. J. Dixon, and D. A. Kosower, *Nucl. Phys.* **B437** (1995) 259–304, [hep-ph/9409393].
- [463] W. B. Kilgore and W. T. Giele, *Phys. Rev.* **D55** (1997) 7183–7190, [hep-ph/9610433].
- [464] Z. Nagy, *Phys. Rev. Lett.* **88** (2002) 122003, [hep-ph/0110315].
- [465] J. Campbell, R. K. Ellis, F. Maltoni, and S. Willenbrock, hep-ph/0510362.
- [466] R. K. Ellis and S. Veseli, *Phys. Rev.* **D60** (1999) 011501, [hep-ph/9810489].
- [467] J. M. Campbell and R. K. Ellis, *Phys. Rev.* **D62** (2000) 114012, [hep-ph/0006304].
- [468] J. M. Campbell, hep-ph/0105226.
- [469] T. Han, G. Valencia, and S. Willenbrock, *Phys. Rev. Lett.* **69** (1992) 3274–3277, [hep-ph/9206246].
- [470] T. Figy, C. Oleari, and D. Zeppenfeld, *Phys. Rev.* **D68** (2003) 073005, [hep-ph/0306109].
- [471] E. L. Berger and J. Campbell, *Phys. Rev.* **D70** (2004) 073011, [hep-ph/0403194].
- [472] T. Figy and D. Zeppenfeld, *Phys. Lett.* **B591** (2004) 297–303, [hep-ph/0403297].

- [473] R. K. Ellis, W. T. Giele, and G. Zanderighi, *Phys. Rev.* **D72** (2005) 054018, [hep-ph/0506196].
- [474] V. Del Duca, F. Maltoni, Z. Nagy, and Z. Trocsanyi, *JHEP* **04** (2003) 059, [hep-ph/0303012].
- [475] T. Binoth, J. P. Guillet, and F. Mahmoudi, *JHEP* **02** (2004) 057, [hep-ph/0312334].
- [476] L. Reina, S. Dawson, and D. Wackerroth, *Phys. Rev.* **D65** (2002) 053017, [hep-ph/0109066].
- [477] W. Peng *et. al.*, hep-ph/0505086.
- [478] W. Peng *et. al.*, hep-ph/0601069.
- [479] A. Brandenburg, S. Dittmaier, P. Uwer, and S. Weinzierl, *Nucl. Phys. Proc. Suppl.* **135** (2004) 71–75, [hep-ph/0408137].
- [480] E. W. N. Glover and D. J. Miller, *Phys. Lett.* **B396** (1997) 257–263, [hep-ph/9609474].
- [481] J. M. Campbell, E. W. N. Glover, and D. J. Miller, *Phys. Lett.* **B409** (1997) 503–508, [hep-ph/9706297].
- [482] Z. Bern, L. J. Dixon, and D. A. Kosower, *Nucl. Phys.* **B513** (1998) 3–86, [hep-ph/9708239].
- [483] L. J. Dixon and A. Signer, *Phys. Rev.* **D56** (1997) 4031–4038, [hep-ph/9706285].
- [484] Z. Nagy and Z. Trocsanyi, *Phys. Rev.* **D59** (1999) 014020, [hep-ph/9806317].
- [485] J. M. Campbell, M. A. Cullen, and E. W. N. Glover, *Eur. Phys. J.* **C9** (1999) 245–265, [hep-ph/9809429].
- [486] S. Weinzierl and D. A. Kosower, *Phys. Rev.* **D60** (1999) 054028, [hep-ph/9901277].
- [487] G. Belanger *et. al.*, *Nucl. Phys. Proc. Suppl.* **116** (2003) 353–357, [hep-ph/0211268].
- [488] G. Belanger *et. al.*, *Phys. Lett.* **B559** (2003) 252–262, [hep-ph/0212261].
- [489] A. Denner, S. Dittmaier, M. Roth, and M. M. Weber, *Phys. Lett.* **B560** (2003) 196–203, [hep-ph/0301189].
- [490] F. Boudjema *et. al.*, *Phys. Lett.* **B600** (2004) 65–76, [hep-ph/0407065].
- [491] Y. You *et. al.*, *Phys. Lett.* **B571** (2003) 85–91, [hep-ph/0306036].
- [492] G. Belanger *et. al.*, *Phys. Lett.* **B571** (2003) 163–172, [hep-ph/0307029].
- [493] A. Denner, S. Dittmaier, M. Roth, and M. M. Weber, *Phys. Lett.* **B575** (2003) 290–299, [hep-ph/0307193].
- [494] A. Denner, S. Dittmaier, M. Roth, and M. M. Weber, *Nucl. Phys.* **B680** (2004) 85–116, [hep-ph/0309274].
- [495] R.-Y. Zhang, W.-G. Ma, H. Chen, Y.-B. Sun, and H.-S. Hou, *Phys. Lett.* **B578** (2004) 349–358, [hep-ph/0308203].
- [496] G. Belanger *et. al.*, *Phys. Lett.* **B576** (2003) 152–164, [hep-ph/0309010].
- [497] F. Boudjema *et. al.*, *Nucl. Instrum. Meth.* **A534** (2004) 334–338, [hep-ph/0404098].
- [498] H. Chen *et. al.*, *Nucl. Phys.* **B683** (2004) 196–218, [hep-ph/0309106].

- [499] A. Denner, S. Dittmaier, M. Roth, and L. H. Wieders, *Phys. Lett.* **B612** (2005) 223–232, [hep-ph/0502063].
- [500] F. Boudjema *et. al.*, *Nucl. Phys. Proc. Suppl.* **135** (2004) 323–327, [hep-ph/0407079].
- [501] F. Boudjema *et. al.*, hep-ph/0510184.
- [502] G. Mahlon, *Phys. Rev.* **D49** (1994) 2197–2210, [hep-ph/9311213].
- [503] Z. Bern, L. J. Dixon, D. C. Dunbar, and D. A. Kosower, hep-ph/9405248.
- [504] Z. Bern, V. Del Duca, L. J. Dixon, and D. A. Kosower, *Phys. Rev.* **D71** (2005) 045006, [hep-th/0410224].
- [505] R. K. Ellis, W. T. Giele, and G. Zanderighi, hep-ph/0602185.
- [506] T. Binoth, J. P. Guillet, G. Heinrich, and C. Schubert, *Nucl. Phys.* **B615** (2001) 385–401, [hep-ph/0106243].
- [507] T. Binoth, *Nucl. Phys. Proc. Suppl.* **116** (2003) 387–391, [hep-ph/0211125].
- [508] E. Witten, *Commun. Math. Phys.* **252** (2004) 189–258, [hep-th/0312171].
- [509] F. Cachazo, P. Svrcek, and E. Witten, *JHEP* **09** (2004) 006, [hep-th/0403047].
- [510] F. Cachazo, P. Svrcek, and E. Witten, *JHEP* **10** (2004) 074, [hep-th/0406177].
- [511] A. Brandhuber, B. J. Spence, and G. Travaglini, *Nucl. Phys.* **B706** (2005) 150–180, [hep-th/0407214].
- [512] F. Cachazo, P. Svrcek, and E. Witten, *JHEP* **10** (2004) 077, [hep-th/0409245].
- [513] R. Britto, F. Cachazo, and B. Feng, *Nucl. Phys.* **B725** (2005) 275–305, [hep-th/0412103].
- [514] F. Cachazo and P. Svrcek, *PoS RTN2005* (2005) 004, [hep-th/0504194].
- [515] L. J. Dixon, hep-ph/0512111.
- [516] R. Britto, B. Feng, and P. Mastrolia, hep-ph/0602178.
- [517] *Workshop On Monte Carlo Generator Physics For Run II At The Tevatron, 18-20 Apr 2001, Batavia, Illinois.*
- [518] J. Campbell and J. Huston, *Phys. Rev.* **D70** (2004) 094021.
- [519] G. U. Flanagan, FERMILAB-THESIS-2005-58.
- [520] S. D. Ellis, J. Huston, and M. Tonnesmann, *eConf C010630* (2001) P513, [hep-ph/0111434].
- [521] R. K. Ellis, D. A. Ross, and A. E. Terrano, *Nucl. Phys.* **B178** (1981) 421.
- [522] R. K. Ellis and J. C. Sexton, *Nucl. Phys.* **B269** (1986) 445.
- [523] W. T. Giele and E. W. N. Glover, *Phys. Rev.* **D46** (1992) 1980–2010.
- [524] W. T. Giele, E. W. N. Glover, and D. A. Kosower, *Nucl. Phys.* **B403** (1993) 633–670, [hep-ph/9302225].
- [525] S. Keller and E. Laenen, *Phys. Rev.* **D59** (1999) 114004, [hep-ph/9812415].

- [526] S. Frixione, Z. Kunszt, and A. Signer, *Nucl. Phys.* **B467** (1996) 399–442, [hep-ph/9512328].
- [527] S. Catani and M. H. Seymour, *Nucl. Phys.* **B485** (1997) 291–419, [hep-ph/9605323].
- [528] L. Phaf and S. Weinzierl, *JHEP* **04** (2001) 006, [hep-ph/0102207].
- [529] W. Giele, E. W. N. Glover, and G. Zanderighi, *Nucl. Phys. Proc. Suppl.* **135** (2004) 275–279, [hep-ph/0407016].
- [530] R. K. Ellis, W. T. Giele, and G. Zanderighi, hep-ph/0508308.
- [531] F. Boudjema, A. Semenov, and D. Temes, *Phys. Rev.* **D72** (2005) 055024, [hep-ph/0507127].
- [532] T. Binoth, J. P. Guillet, G. Heinrich, E. Pilon, and C. Schubert, *JHEP* **10** (2005) 015, [hep-ph/0504267].
- [533] S. Dittmaier, *Nucl. Phys.* **B675** (2003) 447–466, [hep-ph/0308246].
- [534] W. T. Giele and E. W. N. Glover, *JHEP* **04** (2004) 029, [hep-ph/0402152].
- [535] T. Binoth, J. P. Guillet, and G. Heinrich, *Nucl. Phys.* **B572** (2000) 361–386, [hep-ph/9911342].
- [536] Y. Kurihara, hep-ph/0504251.
- [537] F. del Aguila and R. Pittau, *JHEP* **07** (2004) 017, [hep-ph/0404120].
- [538] A. van Hameren, J. Vollinga, and S. Weinzierl, *Eur. Phys. J.* **C41** (2005) 361–375, [hep-ph/0502165].
- [539] G. Duplancic and B. Nizic, *Eur. Phys. J.* **C35** (2004) 105–118, [hep-ph/0303184].
- [540] O. V. Tarasov, *Acta Phys. Pol.* **B29** (1998) 2655, [hep-ph/9812250].
- [541] J. Fleischer, F. Jegerlehner, and O. V. Tarasov, *Nucl. Phys.* **B566** (2000) 423–440, [hep-ph/9907327].
- [542] Z. Bern, L. J. Dixon, and D. A. Kosower, *Phys. Lett.* **B302** (1993) 299–308, [hep-ph/9212308].
- [543] Z. Bern, L. J. Dixon, and D. A. Kosower, *Nucl. Phys.* **B412** (1994) 751–816, [hep-ph/9306240].
- [544] J. Fujimoto, Y. Shimizu, K. Kato, and Y. Oyanagi, *Prog. Theor. Phys.* **87** (1992) 1233–1248.
- [545] A. Ferroglia, M. Passera, G. Passarino, and S. Uccirati, *Nucl. Phys.* **B650** (2003) 162–228, [hep-ph/0209219].
- [546] T. Binoth, G. Heinrich, and N. Kauer, *Nucl. Phys.* **B654** (2003) 277–300, [hep-ph/0210023].
- [547] Z. Nagy and D. E. Soper, *JHEP* **09** (2003) 055, [hep-ph/0308127].
- [548] Z. Nagy and D. E. Soper, *Acta Phys. Polon.* **B35** (2004) 2557–2572.
- [549] Y. Kurihara and T. Kaneko, hep-ph/0503003.
- [550] C. Anastasiou and A. Daleo, hep-ph/0511176.
- [551] D. E. Soper, *Phys. Rev. Lett.* **81** (1998) 2638–2641, [hep-ph/9804454].

- [552] D. E. Soper, *Phys. Rev.* **D62** (2000) 014009, [hep-ph/9910292].
- [553] D. E. Soper, *Phys. Rev.* **D64** (2001) 034018, [hep-ph/0103262].
- [554] S. J. Bidder, N. E. J. Bjerrum-Bohr, L. J. Dixon, and D. C. Dunbar, *Phys. Lett.* **B606** (2005) 189–201, [hep-th/0410296].
- [555] A. Brandhuber, S. McNamara, B. J. Spence, and G. Travaglini, *JHEP* **10** (2005) 011, [hep-th/0506068].
- [556] Z. Bern, L. J. Dixon, and D. A. Kosower, hep-ph/0507005.
- [557] Z. Bern, L. J. Dixon, and D. A. Kosower, hep-ph/0505055.
- [558] R. Britto, E. Buchbinder, F. Cachazo, and B. Feng, *Phys. Rev.* **D72** (2005) 065012, [hep-ph/0503132].
- [559] Z. Bern, L. J. Dixon, and D. A. Kosower, *Phys. Rev.* **D71** (2005) 105013, [hep-th/0501240].
- [560] Z. Bern, L. J. Dixon, and D. A. Kosower, *Phys. Rev.* **D72** (2005) 045014, [hep-th/0412210].
- [561] J. Bedford, A. Brandhuber, B. J. Spence, and G. Travaglini, *Nucl. Phys.* **B712** (2005) 59–85, [hep-th/0412108].
- [562] Z. Bern, L. J. Dixon, D. C. Dunbar, and D. A. Kosower, *Nucl. Phys.* **B435** (1995) 59–101, [hep-ph/9409265].
- [563] Z. Bern, L. J. Dixon, D. C. Dunbar, and D. A. Kosower, *Nucl. Phys.* **B425** (1994) 217–260, [hep-ph/9403226].
- [564] D. Forde and D. A. Kosower, hep-th/0507292.
- [565] D. Forde and D. A. Kosower, hep-ph/0509358.
- [566] V. Drollinger, *in these proceedings*.
- [567] G. Belanger *et. al.*, hep-ph/0308080.
- [568] G. J. van Oldenborgh, *Comput. Phys. Commun.* **66** (1991) 1–15.
- [569] J. Fujimoto, M. Igarashi, N. Nakazawa, Y. Shimizu, and K. Tobimatsu, *Prog. Theor. Phys. Suppl.* **100** (1990) 1–379.
- [570] Y. Kurihara *et. al.*, *Nucl. Phys.* **B654** (2003) 301–319, [hep-ph/0212216].
- [571] Y.-j. Chen, J. Collins, and X.-m. Zu, *JHEP* **04** (2002) 041, [hep-ph/0110257].
- [572] J. C. Collins and X. Zu, *JHEP* **03** (2005) 059, [hep-ph/0411332].
- [573] P. Nason, *JHEP* **11** (2004) 040, [hep-ph/0409146].
- [574] M. Kramer and D. E. Soper, *Phys. Rev.* **D69** (2004) 054019, [hep-ph/0306222].
- [575] D. E. Soper, *Phys. Rev.* **D69** (2004) 054020, [hep-ph/0306268].
- [576] M. Kramer, S. Mrenna, and D. E. Soper, hep-ph/0509127.
- [577] Z. Nagy and D. E. Soper, *JHEP* **10** (2005) 024, [hep-ph/0503053].



- [578] Z. Nagy and D. E. Soper, hep-ph/0601021.
- [579] S. Frixione, E. Laenen, P. Motylinski, and B. R. Webber, hep-ph/0512250.
- [580] Z. Bern, L. Dixon, and C. Schmidt, *Phys.Rev.* **D66** (2002) 074018, [hep-ph/0206194].
- [581] T. Binoth, J. P. Guillet, E. Pilon, and M. Werlen, *Eur. Phys. J.* **C16** (2000) 311–330, [hep-ph/9911340].
- [582] T. Binoth, J. P. Guillet, and F. Mahmoudi, *JHEP* **02** (2004) 57, [hep-ph/0312334].
- [583] J. Vermaseren, math-ph/0010025.
- [584] Maplesoft, <http://www.maplesoft.com>.
- [585] F. Mahmoudi, *PhD. Thesis, Université de Savoie* (2004) [LAPTH-thèse-1058].
- [586] T. Binoth, J. P. Guillet, G. Heinrich, and C. Schubert, *Nucl. Phys.* **B615** (2001) 385, [hep-ph/0106243].
- [587] F. Berends and W. Giele, *Nucl. Phys.* **B306** (1988) 759.
- [588] Z. Bern, L. Dixon, D. Dunbar, and D. Kosower, *Nucl. Phys.* **B425** (1994) 217, [hep-ph/9403226].
- [589] Z. Xu, D. Zhang, and L. Chang, *Nucl. Phys.* **B291** (1987) 392.
- [590] D. Bailey, *RNR Technical Report RNR-90-022* (1993) [<http://crd.lbl.gov/~dhbailey/mpdist/>].
- [591] CMS-Collaboration, *CERN-LHCC-94-38* (1994).
- [592] ATLAS-Collaboration, *CERN-LHCC-94-43* (1994).
- [593] J. J. Pumplin, D. Stump, J. Huston, H. Lai, P. Nadolsky, and W. Tung, *JHEP* **07** (2002) 012, [hep-ph/0201195].
- [594] D. De Florian and Z. Kunszt, *Phys. Lett.* **B460** (1999) 184, [hep-ph/9905283].
- [595] D. Binosi and L. Theussl, *Comp. Phys. Comm.* (2004) [hep-ph/0309015].
- [596] Z. Kunszt and D. E. Soper, *Phys. Rev.* **D46** (1992) 192–221.
- [597] Z. Nagy and Z. Trocsanyi, *Nucl. Phys.* **B486** (1997) 189–226, [hep-ph/9610498].
- [598] S. Frixione, *Nucl. Phys.* **B507** (1997) 295–314, [hep-ph/9706545].
- [599] D. A. Kosower, *Phys. Rev.* **D57** (1998) 5410–5416, [hep-ph/9710213].
- [600] D. A. Kosower, *Phys. Rev.* **D71** (2005) 045016, [hep-ph/0311272].
- [601] S. Bethke, *Nucl. Phys. Proc. Suppl.* **135** (2004) 345–352, [hep-ex/0407021].
- [602] M. Cacciari, S. Frixione, M. L. Mangano, P. Nason, and G. Ridolfi, *JHEP* **07** (2004) 033, [hep-ph/0312132].
- [603] D. Acosta *et. al.*, **CDF** Collaboration *Phys. Rev.* **D71** (2005) 032001, [hep-ex/0412071].
- [604] D. Graudenz, M. Spira, and P. M. Zerwas, *Phys. Rev. Lett.* **70** (1993) 1372–1375.

- [605] M. Spira, A. Djouadi, D. Graudenz, and P. M. Zerwas, *Nucl. Phys.* **B453** (1995) 17–82, [hep-ph/9504378].
- [606] R. V. Harlander and W. B. Kilgore, *Phys. Rev. Lett.* **88** (2002) 201801, [hep-ph/0201206].
- [607] C. Anastasiou and K. Melnikov, *Nucl. Phys.* **B646** (2002) 220–256, [hep-ph/0207004].
- [608] V. Ravindran, J. Smith, and W. L. van Neerven, *Nucl. Phys.* **B665** (2003) 325–366, [hep-ph/0302135].
- [609] M. Dittmar, F. Pauss, and D. Zurcher, *Phys. Rev.* **D56** (1997) 7284–7290, [hep-ex/9705004].
- [610] V. A. Khoze, A. D. Martin, R. Orava, and M. G. Ryskin, *Eur. Phys. J.* **C19** (2001) 313–322, [hep-ph/0010163].
- [611] W. T. Giele and S. A. Keller, hep-ph/0104053.
- [612] S. Frixione and M. L. Mangano, *JHEP* **05** (2004) 056, [hep-ph/0405130].
- [613] R. Hamberg, W. L. van Neerven, and T. Matsuura, *Nucl. Phys.* **B359** (1991) 343–405.
- [614] C. Anastasiou, L. J. Dixon, K. Melnikov, and F. Petriello, *Phys. Rev.* **D69** (2004) 094008, [hep-ph/0312266].
- [615] R. V. Harlander and W. B. Kilgore, *JHEP* **10** (2002) 017, [hep-ph/0208096].
- [616] C. Anastasiou and K. Melnikov, *Phys. Rev.* **D67** (2003) 037501, [hep-ph/0208115].
- [617] C. Anastasiou, K. Melnikov, and F. Petriello, *Phys. Rev. Lett.* **93** (2004) 262002, [hep-ph/0409088].
- [618] C. Anastasiou, K. Melnikov, and F. Petriello, *Nucl. Phys.* **B724** (2005) 197–246, [hep-ph/0501130].
- [619] C. Anastasiou, K. Melnikov, and F. Petriello, *Phys. Rev. Lett.* **93** (2004) 032002, [hep-ph/0402280].
- [620] A. Gehrmann-De Ridder, T. Gehrmann, and E. W. N. Glover, *Nucl. Phys.* **B691** (2004) 195–222, [hep-ph/0403057].
- [621] A. Gehrmann-De Ridder, T. Gehrmann, and E. W. N. Glover, *JHEP* **09** (2005) 056, [hep-ph/0505111].
- [622] M. Roth and A. Denner, *Nucl. Phys.* **B479** (1996) 495–514, [hep-ph/9605420].
- [623] T. Binoth and G. Heinrich, *Nucl. Phys.* **B585** (2000) 741–759, [hep-ph/0004013].
- [624] G. Heinrich, *Nucl. Phys. Proc. Suppl.* **116** (2003) 368–372, [hep-ph/0211144].
- [625] C. Anastasiou, K. Melnikov, and F. Petriello, *Phys. Rev.* **D69** (2004) 076010, [hep-ph/0311311].
- [626] A. Gehrmann-De Ridder, T. Gehrmann, and G. Heinrich, *Nucl. Phys.* **B682** (2004) 265–288, [hep-ph/0311276].
- [627] T. Binoth and G. Heinrich, *Nucl. Phys.* **B693** (2004) 134–148, [hep-ph/0402265].
- [628] D. A. Kosower, *Phys. Rev.* **D67** (2003) 116003, [hep-ph/0212097].

- [629] S. Weinzierl, *JHEP* **03** (2003) 062, [hep-ph/0302180].
- [630] S. Weinzierl, *JHEP* **07** (2003) 052, [hep-ph/0306248].
- [631] W. B. Kilgore, *Phys. Rev.* **D70** (2004) 031501, [hep-ph/0403128].
- [632] S. Frixione and M. Grazzini, *JHEP* **06** (2005) 010, [hep-ph/0411399].
- [633] A. Gehrmann-De Ridder, T. Gehrmann, and E. W. N. Glover, *Phys. Lett.* **B612** (2005) 36–48, [hep-ph/0501291].
- [634] A. Gehrmann-De Ridder, T. Gehrmann, and E. W. N. Glover, *Phys. Lett.* **B612** (2005) 49–60, [hep-ph/0502110].
- [635] G. Somogyi, Z. Trocsanyi, and V. Del Duca, *JHEP* **06** (2005) 024, [hep-ph/0502226].
- [636] F. A. Berends and W. T. Giele, *Nucl. Phys.* **B313** (1989) 595.
- [637] A. Gehrmann-De Ridder and E. W. N. Glover, *Nucl. Phys.* **B517** (1998) 269–323, [hep-ph/9707224].
- [638] J. M. Campbell and E. W. N. Glover, *Nucl. Phys.* **B527** (1998) 264–288, [hep-ph/9710255].
- [639] S. Catani and M. Grazzini, *Phys. Lett.* **B446** (1999) 143–152, [hep-ph/9810389].
- [640] S. Catani and M. Grazzini, *Nucl. Phys.* **B570** (2000) 287–325, [hep-ph/9908523].
- [641] V. Del Duca, A. Frizzo, and F. Maltoni, *Nucl. Phys.* **B568** (2000) 211–262, [hep-ph/9909464].
- [642] Z. Bern, V. Del Duca, and C. R. Schmidt, *Phys. Lett.* **B445** (1998) 168–177, [hep-ph/9810409].
- [643] D. A. Kosower, *Nucl. Phys.* **B552** (1999) 319–336, [hep-ph/9901201].
- [644] D. A. Kosower and P. Uwer, *Nucl. Phys.* **B563** (1999) 477–505, [hep-ph/9903515].
- [645] Z. Bern, V. Del Duca, W. B. Kilgore, and C. R. Schmidt, *Phys. Rev.* **D60** (1999) 116001, [hep-ph/9903516].
- [646] H. E. Haber and D. Wyler, *Nucl. Phys.* **B323** (1989) 267.
- [647] F. Wilczek, *Phys. Rev. Lett.* **39** (1977) 1304.
- [648] M. A. Shifman, A. I. Vainshtein, and V. I. Zakharov, *Phys. Lett.* **B78** (1978) 443.
- [649] A. Gehrmann-De Ridder, T. Gehrmann, and E. W. N. Glover, *Nucl. Phys. Proc. Suppl.* **135** (2004) 97–101, [hep-ph/0407023].
- [650] K. Hagiwara and D. Zeppenfeld, *Nucl. Phys.* **B313** (1989) 560.
- [651] F. A. Berends, W. T. Giele, and H. Kuijff, *Nucl. Phys.* **B321** (1989) 39.
- [652] N. K. Falck, D. Graudenz, and G. Kramer, *Nucl. Phys.* **B328** (1989) 317.
- [653] Z. Bern, L. J. Dixon, D. A. Kosower, and S. Weinzierl, *Nucl. Phys.* **B489** (1997) 3–23, [hep-ph/9610370].
- [654] Z. Nagy and Z. Trocsanyi, *Phys. Lett.* **B414** (1997) 187–194, [hep-ph/9708342].

- [655] L. W. Garland, T. Gehrmann, E. W. N. Glover, A. Koukoutsakis, and E. Remiddi, *Nucl. Phys.* **B627** (2002) 107–188, [hep-ph/0112081].
- [656] L. W. Garland, T. Gehrmann, E. W. N. Glover, A. Koukoutsakis, and E. Remiddi, *Nucl. Phys.* **B642** (2002) 227–262, [hep-ph/0206067].
- [657] K. Hepp, *Commun. Math. Phys.* **2** (1966) 301–326.
- [658] T. Binoth and G. Heinrich, *Nucl. Phys.* **B680** (2004) 375–388, [hep-ph/0305234].
- [659] A. Denner and S. Pozzorini, *Nucl. Phys.* **B717** (2005) 48–85, [hep-ph/0408068].
- [660] G. Heinrich and V. A. Smirnov, *Phys. Lett.* **B598** (2004) 55–66, [hep-ph/0406053].
- [661] M. Czakon, J. Gluza, and T. Riemann, *Phys. Rev.* **D71** (2005) 073009, [hep-ph/0412164].
- [662] C. Anastasiou, K. Melnikov, and F. Petriello, hep-ph/0505069.
- [663] G. Heinrich, hep-ph/0601062.
- [664] G. Heinrich, *Nucl. Phys. Proc. Suppl.* **135** (2004) 290–294, [hep-ph/0406332].
- [665] S. Bethke et al., **JADE** Collaboration *Phys. Lett.* **B213** (1988) 235.
- [666] S. Kawabata, *Comp. Phys. Commun.* **88** (1995) 309–326.
- [667] M. Dobbs *et. al.*, hep-ph/0403100.
- [668] P. Bartalini *et. al.*, hep-ph/0404241.
- [669] L. Dudko and A. Sherstnev, <http://cmsdoc.cern.ch/cms/generators/mcdb>.
- [670] L. M. team, <http://mcdb.cern.ch>.
- [671] CVS, <http://savannah.cern.ch/projects/mcdb>.
- [672] J.-P. Baud *et. al.*, *ECONF C0303241* (2003) TUDT007, [cs.oh/0305047].
- [673] CEDAR, <http://www.cedar.ac.uk/xml/>.
- [674] The LCG Software Process and Infrastructure, “External Software Web Page.” <http://spi.cern.ch/extsoft/>.
- [675] The LCG Generator collaboration, “Web Page.” <http://lcgapp.cern.ch/project/simu/generator/>.
- [676] J. P. Wellisch, C. Williams, and S. Ashby, *ECONF C0303241* (2003) TUJP001, [cs.oh/0306014].
- [677] D. J. Lange, *Nucl. Instrum. Meth.* **A462** (2001) 152–155.
- [678] T. Gleisberg *et. al.*, *JHEP* **02** (2004) 056, [hep-ph/0311263].
- [679] F. E. Paige, S. D. Protopopescu, H. Baer, and X. Tata, hep-ph/0312045.
- [680] X.-N. Wang and M. Gyulassy, *Phys. Rev.* **D44** (1991) 3501–3516.
- [681] S. Heinemeyer, W. Hollik, and G. Weiglein, *Comput. Phys. Commun.* **124** (2000) 76–89, [hep-ph/9812320].
- [682] P. Golonka and Z. Was, *Eur. Phys. J.* **C45** (2006) 97–107, [hep-ph/0506026].

- [683] F. W. Bopp, R. Engel, and J. Ranft, [hep-ph/9803437](#).
- [684] K. Abdel-Waged, A. Abdel-Hafiez, and V. V. Uzhinsky, *J. Phys.* **G26** (2000) 1105–1115.
- [685] C. M. Harris, P. Richardson, and B. R. Webber, *JHEP* **08** (2003) 033, [[hep-ph/0307305](#)].
- [686] S. Dimopoulos and G. Landsberg, *Phys. Rev. Lett.* **87** (2001) 161602, [[hep-ph/0106295](#)].
- [687] The LHCb collaboration, “EvtGenLHC Web Page.”  
<http://lhcb-comp.web.cern.ch/lhcb-comp/Simulation/evtgen.htm>.
- [688] L. Lonnblad, Prepared for 12th International Workshop on Deep Inelastic Scattering (DIS 2004), Strbske Pleso, Slovakia, 14-18 Apr 2004.
- [689] The PHENOGRID collaboration, “Web Page.” <http://www.phenogrid.dur.ac.uk/>.
- [690] The MCDB collaboration, “Web Page.” <http://mcdb.cern.ch/>.
- [691] J. M. Butterworth and S. Butterworth, *Comput. Phys. Commun.* **153** (2003) 164–178, [[hep-ph/0210404](#)].